12-1995

A Differential GPS Aided INS for Aircraft Landings

Ryan L. Britton

AFIT/GE/ENG/95D-03

A DIFFERENTIAL GPS AIDED INS FOR AIRCRAFT LANDINGS

THESIS

RYAN L. BRITTON
CAPTAIN, USAF

AFIT/GE/ENG/95D-03

DISCLAIMER NOTICE

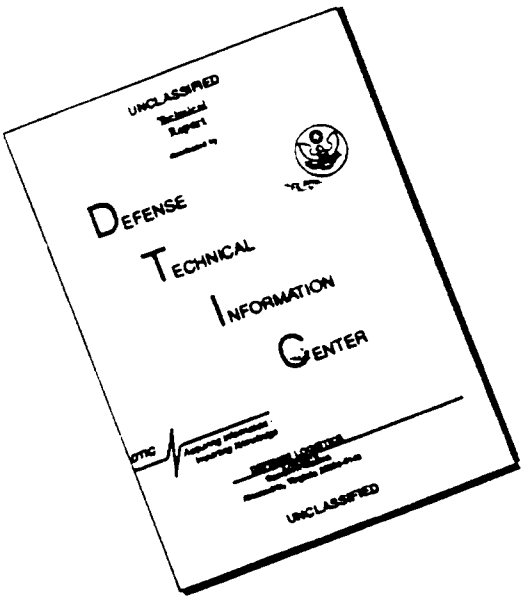

THIS DOCUMENT IS BEST QUALITY AVAILABLE. THE COPY FURNISHED TO DTIC CONTAINED A SIGNIFICANT NUMBER OF PAGES WHICH DO NOT REPRODUCE LEGIBLY.

The views expressed in this thesis are those of the author and do not reflect the official policy or position of the Department of Defense or the U.S. Government.

AFIT/GE/ENG/95D-03

A DIFFERENTIAL GPS AIDED INS FOR AIRCRAFT LANDINGS

THESIS

Presented to the Faculty of the Graduate School of Engineering

of the Air Force Institute of Technology

Air University

In Partial Fulfillment of the

Requirements for the Degree of

Master of Science in Electrical Engineering

Ryan L. Britton, B.S.E.E.

Captain, USAF

December 1995

Preface

This thesis applies the knowledge obtained over the years by several students at AFIT. It is a direct follow-on to the research done by Robert Gray in the area of aircraft precision approach landings. This thesis will focus on optimally combining an INS, DGPS, Baro altimeter and Radar altimeter using an extended Kalman filter for aircraft precision landing approaches.

I have met some great classmates at AFIT. Thanks to everyone in class GE-95D for all your patience, support, and guidance in the completion of this work. I wish you all the best in you military careers, and hope we will see each other again in the future. Also, special thanks to Stan Musick for taking the time to explain MSOFE, PROFGEN, and MPLOT, and to Bob Gray for all the help in explaining his work and getting me started prior to his leaving.

I also would like to thank my committee members, Lt Col Bob Riggins and Capt Ron Delap for aiding me in my AFIT education and reviewing this thesis research effort. I especially would like to thank my thesis advisor, Dr. Peter Maybeck, for his support, patience, prayers, and continued guidance throughout the thesis development. Dr. Maybeck is definitely one of the brightest men with whom I have ever had the pleasure of meeting and working.

To my Christian family at the Central Avenue Church of Christ, thanks for your spiritual guidance and during my time in Dayton. Your continued interest and support has

been instrumental in the completion of this thesis. Without God's help, this work would never have been completed.

I want to thank my parents, Richard and Dale Britton, for their support throughout the past 19 months. I would not be where I am today if not for their continued guidance in my life. Thanks to my brothers, Rickie, Randy and Ronnie, for all the calls and visits to take my mind off things. Finally, I want my son Drew to know how much I love him. The time I have spent away has been hard on him, but he was always there to cheer me up no matter how much time I had available to spend with him. Thanks for all your hugs, kisses, cards, and letters. They meant everything to me.

Table of Contents

Page

Page

Page

Page

List of Figures

Page

Page

Page

Page

Page

Page

Page

List of Tables

Page

Page

Abstract

The Department of Defense (DOD) and the commercial airline industry are in the process of replacing the instrument landing system (ILS) for aircraft precision approach landings. The use of the *differential* Global Positioning System (DGPS) is thought to be a viable replacement for ILS precision approaches. This thesis explores the integration of an INS, DGPS, Barometric Altimeter, Pseudolite, and Radar Altimeter for a tanker type and a single engine aircraft precision approach. These devices are integrated using an extended Kalman filter (EKF). For the tanker type aircraft, Federal Aviation Administration (FAA) requirements for a Category I and a Category II precision approach were met when an INS, DGPS, Barometric Altimeter, and Radar Altimeter were integrated. Category III precision approach requirements were met for the single engine type aircraft when the same sensors were integrated.

A Differential GPS Aided INS for Aircraft Landing

I. Introduction

For precision approaches during aircraft landings, the Department of Defense (DOD) and the commercial airline industry currently use the Instrument Landing System (ILS) [20,23]. Originally, the replacement for the ILS was thought to be the Microwave Landing System (MLS). However, with a full constellation of satellites now available for use and recent advances made in determination accuracy, the Global Positioning System (GPS) is now thought to be a viable replacement for aircraft ILS precision approaches [27].

The DOD and Department of Transportation (DOT) are under extreme pressure from users to certify GPS for precision landing approaches. The use of GPS for precision makes sense financially for the DOD and DOT. GPS will eventually be installed on all DOD and commercial transports [2,21,22,62,71,74], and if an MLS receiver does not have to be purchased, billions of dollars will be saved [41]. To meet the accuracy and integrity requirements of the Federal Aviation Administration (FAA) for precision approaches, the author believes it is necessary to integrate the GPS with an INS. The accuracy requirements for aircraft precision approaches are presented in Table 1 - 2. To meet the integrity requirements for an aircraft precision approach, fault detection must notify the pilot of a possible degraded navigation solution in less than two seconds while minimizing false alarms [27]. The INS systems on-board most of the commercial and DOD aircraft are medium accuracy, stand-alone systems which cost about $100K per unit.

A medium accuracy INS has an accuracy error of one nautical mile per hour (nm/hr) circular error precision (CEP) [27,68.69]. By replacing the present day stand-alone INS with a tightly integrated INS/*differential* GPS unit capable of utilizing available barometric and radar altimeter measurements, the author believes one can meet and exceed FAA requirements for aircraft precision landings.

Cost savings are also realized because a less accurate (2-4 nm/hr CEP) INS can be used when it is tightly coupled with a GPS receiver. The less accurate INS is much less expensive than the medium accuracy INS but will be just as effective when integrated with the GPS. A tightly coupled GPS/INS unit is one in which the GPS receiver is embedded in the INS and the unprocessed GPS information is directly integrated into the navigation processor. Advantages of an embedded GPS/INS configuration include the reduction in size, weight, and power. The blending of pseudorange and pseudorange rate data from satellite vehicles instead of position, velocity and time data (as generated by an internal filter, often using a generic model for INS errors rather than one tuned to a specific INS) results in a more accurate navigation solution. The INS provides the GPS with acceleration and velocity information to aid the GPS carrier and code track loops. From a security point of view, the embedded mechanization will not require an expensive secure communication link between the INS and the GPS. The loose configuration is the other design approach. In a loosely coupled system, the INS and GPS act as stand alone units. The navigation information output from the INS and GPS is processed by an external filter to provide a more accurate navigation solution than each unit can provide separately [58,61]. The loose configuration is often used when a GPS receiver is added to an aircraft

with an INS present. This is the case with aircraft which were developed before GPS receivers were widely available. In this situation it may be cheaper to make use of the existing INS and integrate its output with GPS filter-processed output rather than raw measurements. Also, the computation time involved with the use of a loose configuration is lower because a smaller state vector is used than with the tight configuration. However, by utilizing a loose configuration, users run into problems with correlated data. Both the GPS data and the INS data have already been processed before being received by the filter to combine the information. Specifically, the GPS local filter produces its state estimates and associated error covariance matrix, to be used as "measurements" and "measurement noise covariance", respectively, in the second (integration) filter. However, this "measurement noise" is time-correlated rather than white, as assumed by the simplest form of integration filter. Therefore, this external Kalman filter must process the data at a different, reduced rate to remove any time correlation from the "measurement noise" [58,61]. There is also an issue of cross-correlation between the errors in the INS and GPS in a feedback configuration, which is also ignored in the simplest form of integration filter, causing further performance degradation. The benefits of using the GPS information are diminished because the data cannot be used at the rate at which it is available. The integrated INS/GPS already contains a host Kalman filter which is specifically tuned for the hardware and is capable of utilizing unprocessed GPS and INS information at the highest possible rates [58].

In order for GPS to replace ILS for precision approaches, areas associated with accuracy, coverage, integrity availability, and aircraft integration must be studied and

understood. In this research, the author used a model for a differential GPS (DGPS), both with and without a radar altimeter. The weakness of GPS is providing correct information for the vertical channel due to satellite vehicle (SV) geometry. Radar altimeters and GPS-aided inertial navigation systems may be incorporated into civil aviation aircraft if cost is made low enough and performance of integrated systems based on inexpensive components can be made good enough. Most military and commercial airlines have a radar altimeter available, but it is only used in the stand-alone mode. The radar altimeter provides height measurements referenced above the ground. This height above ground information is of utmost importance during aircraft landings, yet most aircraft do not integrate radar altimeter information with the differentially corrected GPS data. By integrating the height information of the radar altimeter with the GPS , one can correct the errors in the GPS vertical channel. For those civil aviation aircraft which do not have a radar altimeter, a GPS pseudolite, discussed in detail in Chapter 2, will be used to correct the problems with errors in the vertical channel [27].

The research will look at comparing several integrated systems to meet a precision approach landing. Tables 1 - 1a and 1 - 1b present the various system integrations labeled as Case I through Case XV. Cases I - VI are the basic system configurations which make use of an INS, DGPS, and barometric altimeter. Cases II, IV, and VI add a radar altimeter to improve the altitude errors. Also, three different INSs are used in these cases to demonstrate the usefulness of DGPS for precision approaches over a wide variety of aircraft. Cases I and II use an 0.4 nautical mile per hour (nm/hr) drift INS, Cases III and IV use a 2.0 nm/hr INS, and Cases V and VI use a 4.0 nm/hr INS. These are

representative of a high-precision (and expensive) INS, a moderate-precision INS, and a low-precision INS (inexpensive enough to consider for small civil aviation aircraft), respectively. With Cases VII - XII, a pseudolite is used to provide an additional measurement to Case I - VI configurations. The pseudolite will provide the most information in those areas where no radar altimeter is available. Cases XIII - XV are situations where a GPS outage occurs in the middle of the flight. These demonstrate the increase in drift seen for the different INSs and the capability of the system to correct itself when the GPS data is restored. These cases relate directly to the work done by Robert Gray [27], with DGPS replacing GPS. The improvements realized with DGPS are discussed in Chapter 4.

1.1 Key Terms

Global Positioning System (GPS): A satellite-based navigation and time system designed, developed, and maintained by the U. S. Department of Defense (DOD) [17]. The 1σ accuracy of the unaided GPS is typically 16 meters for the military and 100 meters for commercial users [27].

Case I	Case II	Case III	Case IV	Case V	Case VI
Barometric Altimeter	Barometric Altimeter	Barometric Altimeter	Barometric Altimeter	Barometric Altimeter	Barometric Altimeter
0.4 nm/hr CEP INS	0.4 nm/hr CEP INS	2.0 nm/hr CEP INS	2.0 nm/hr CEP INS	4.0 nm/hr CEP INS	4.0 nm/hr CEP INS
DGPS	DGPS	DGPS	DGPS	DGPS	DGPS
----	Radar Altimeter	----	Radar Altimeter	----	Radar Altimeter

Table 1 - 1a. Case I - VI Integration Comparisons

Case VII	Case VIII	Case IX	Case X	Case XI	Case XII	Case XIII	Case XIV	Case XV
Barometric Altimeter	Barometric Altimeter	Barometric Altimeter	Barometric Altimeter	Barometric Altimeter	Barometric Altimeter	Barometric Altimeter	Barometric Altimeter	Barometric Altimeter
0.4 nm/hr CEP INS	0.4 nm/hr CEP INS	2.0 nm/hr CEP INS	2.0 nm/hr CEP INS	4.0 nm/hr CEP INS	4.0 nm/hr CEP INS	0.4 nm/hr CEP INS	2.0 nm/hr CEP INS	4.0 nm/hr CEP INS
DGPS	DGPS	DGPS	DGPS	DGPS	DGPS	DGPS	DGPS	DGPS
Pseudolite	Radar Altimeter and Pseudolite	Pseudolite	Radar Altimeter and Pseudolite	Pseudolite	Radar Altimeter and Pseudolite	None	None	None
No GPS Outage	No GPS Outage	No GPS Outage	No GPS Outage	No GPS Outage	No GPS Outage	Single GPS Outage	Single GPS Outage	Single GPS Outage

Table 1 - 1b. Cases VII-XV Integration Comparisons

Differential GPS (DGPS): A reference receiver [an accurately surveyed, ground-based GPS receiver] is used to uplink error corrections to aircraft within 150 nautical miles (nm). The ground-based receiver information reduces common errors in GPS information to provide a better navigation solution. The 1σ accuracy of DGPS is 3 meters [27,58]. A complete description of DGPS is found in Chapter 3.

Carrier Phase GPS (CPGPS): A new receiver technique which can measure the incoming satellite-transmitted GPS signal to a fraction of a wavelength. The accuracy is less than 30 centimeters [27].

Inertial Navigation System (INS): A self-contained dead-reckoning system that uses internal gyroscopes and accelerometers to navigate. Accuracy is typically 0.4 to 4 nm/hr [27].

Kalman Filter: A recursive computer algorithm developed by R. E. Kalman in the early 1960s [27]. His work may be found in *A New Approach to Linear Filtering and Prediction Problems* [39].

Aircraft Precision Landing: Formally defined by the Federal Aviation Administration (FAA) in [23] as a Category I, II, or III precision approach. See Table 1 - 2 [40] for a brief listing of location accuracies to meet these specifications.

Pseudolite: A land-based transmitter which broadcasts GPS-like signals to approaching aircraft for improved navigation accuracy [58].

Instrument Landing System (ILS): Current land-based navigation aide used to guide aircraft safely for final approach airport landings [23,40].

Microwave Landing System (MLS): Proposed land-based replacement navigation aide for the ILS [40,48].

Precision Approach Parameters (in feet, all 1-sigma values)

Category	Azimuth	Elevation
I	+/- 28.1	+/- 6.8
II	+/- 8.6	+/- 2.8
III	+/- 6.8	+/- 1.0

Table 1 - 2. Precision Approach Parameters

1.2 Background

A review of recent technical publications [13,20,27,30,57,59] suggests very few studies have been performed which use an integrated INS/GPS for precision approaches. The majority of research has used stand-alone GPS receiver techniques and only one

technical paper [27] used a radar altimeter, pseudolite, INS, and GPS measurements integrated by a Kalman filter for aircraft precision landings.

Robert Gray, in his prior work [27] at the Air Force Institute of Technology (AFIT), has demonstrated, through computer simulation, meeting requirements for a FAA Category I and Category II precision approach landing. His work integrated a basic GPS receiver, INS, radar altimeter, barometric altimeter, and pseudolite measurements using a Kalman Filter. Jochen Hilberg and Thomas Jacob have demonstrated the ability to meet Category III precision approach landings using an INS/GPS integrated unit. The validation was performed by actual flight testing in Germany [30].

The work done by Stephen V. Rowson [59] at the NASA Wallops Flight Facility demonstrated the effectiveness of using DGPS as a stand-alone device for aircraft precision approaches. In 1993, forty DGPS guided approaches and landings were performed. Thirty-one of the approaches and landings were hands-off. Russell Paielli at the NASA Ames Research Center has demonstrated the ability of CPGPS stand-alone for aircraft precision approaches [57]. In 11 of 12 flight test approaches, the integer ambiguities (resolution errors removed by DGPS) were resolved at a minimum distance of 2.7 kilometers from landing, and the solution was maintained through touchdown. At Stanford University, Clark Cohen has developed a new system based on low power pseudolite transmitters situated underneath the approach path [13]. Real time position solutions with independent static survey measurements were shown to agree to the centimeter level.

1.3 Problem Statement

This thesis will investigate the use of an extended Kalman filter (EKF) to integrate an INS, *differential* GPS, barometric altimeter, and radar altimeter for aircraft precision approaches. The extended Kalman filter integration analysis will be performed using the Multimode Simulation for Optimal Filter Evaluation (MSOFE), a filter evaluation program [53]. In addition, the use of a single ground-based pseudolite to stabilize the vertical channel of the GPS will be analyzed. A new precision flight profile for a small instrumented rated aircraft will be developed using PROFGEN [52]. This profile will be designed around a Piper Cherokee Warrior aircraft and will be referred to as a single engine aircraft. This profile and a generic flight profile for a tanker size aircraft will be used to provide flight information for the simulation runs. True, post-processed ephemeris data [15] will replace the prior FORTRAN orbit functions used at AFIT [3,29,50,55,65]. The latitude, longitude, and altitude errors found by using the DGPS measurements will be compared to those found by Gray [27] by using standard GPS measurements. This will demonstrate the substantial improvements found by using DGPS.

1.4 Past Research at AFIT

Research at AFIT in this area began with the generation of computer models for INS, GPS, and Range/Range-Rate System (RRS), along with the development of EKF software to blend the information from these independent sources. This information was used to generate a more accurate navigation solution than each source could generate independently. Robert Gray modified this model, named it the Landing System Model (LSM), and used it in his efforts to achieve a Category III precision approach landing. He

was able to meet the requirements for a Category I and Category II landing under certain conditions, but Category III accuracy could not be achieved using the basic GPS model in the LSM. Gray also developed models for three different qualities of INSs, 0.4 nm/hr, 2.0 nm/hr, and 4.0 nm/hr, to extend the information to a wide variety of aircraft. Research at AFIT has also included the development of an accurate DGPS error model, since DGPS may provide the accuracies required for a Category III landing (and other applications). This research will modify the LSM to include the DGPS. From this point, the LSM will be called the Differential Landing System Model (DLSM).

1.5 Scope

This research will focus on a simulation-based effectiveness study of GPS integrated with an INS, barometric altimeter, radar altimeter, and pseudolites for aircraft precision approach landings. The work will be limited to:

1. The development and integration of a DGPS model with existing INS, barometric altimeter, radar altimeter, and pseudolite models [6,27,55].

2. The development of a flight profile for a single engine aircraft to demonstrate the effectiveness of using DGPS for smaller aircraft.

3. Tuning the filter model for various jamming conditions. These will be utilized eventually for multiple model adaptive estimators to detect the onset of jamming, and to adapt appropriately to the jamming.

4. The effectiveness of the integrated systems will be verified using a filter evaluation tool (MSOFE).

The tasks involved are as follows:

a. Review prior AFIT thesis of Vasquez [72], Nielsen [56], Negast [55], Gray [27], Mosle [50], and Hansen [29].

b. Study the ILS Category I, II and III precision approach techniques and performance specifications used by Robert Gray in his research [27]. Investigate the INS/GPS integration used in his research. Receive instruction from Captain David Kyger [42], a pilot, on what is required during a precision landing. His experience will allow much needed background into what is required with aircraft landing.

c. Study and utilize the developed flight profiles for an autoland at Wright-Patterson AFB, OH. Wright-Patterson AFB was chosen based on its proximity to AFIT and the readily available information about the airfield at the base. This will require the study and use of Profile Generator (PROFGEN [52]), a software tool which simulates the flight of an arbitrary vehicle responding to user defined maneuver commands. The two flight profiles of interest from PROFGEN [52] include the use of the Boeing 707 (KC-135) aircraft flight data used by Gray and the development of a single engine aircraft profile based on a smaller commercial aircraft.

d. Study the current "truth model," a complete, complex mathematical model that portrays true system behavior very accurately. Justify its continued use, update the GPS information model and make any other adjustments which are required to yield an accurate, validated model.

e. Investigate current DGPS information and modify the current GPS measurement model to be representative of DGPS instead. This effort will constitute the

major effort of this thesis. The current DGPS model will have to be checked for validity before incorporation into the current simulation software packages.

f. Learn MSOFE, a generalized Monte Carlo simulation and covariance analysis program integrated as one package. Generate the EKF based upon the truth model as a "benchmark" of performance and analyze its capabilities. This learning process will include the updating of the software developed by Gray to the latest version of MSOFE. Once this upgrade has occurred, his work must be re-accomplished to verify software integrity with the new version of the simulation package and to set a benchmark for future comparisons as the DGPS filter is incorporated.

g. Simplify the system models by removing and combining states associated with non-dominant effects. The work done by Gray [27], Negast [55], and Hansen [29] will be used as a guide for model simplification.

h. Conduct a Monte Carlo analysis of each proposed Kalman filter and tune each filter to provide the best possible performance. The Monte Carlo analysis will be the primary software evaluation tool. It is based on the use of the EKF and that filter's necessity to relinearize about each successive estimate of the state. This relinearization enhances the adequacy of the linearization process and the resulting filter performance.

i. For each separate filter (standard GPS, DGPS), select a design and implement it against the generated profile.

j. Analyze the results and compare the performance found to the current ILS, and GPS (standalone).

1.6 Assumptions

All theses are limited by the assumptions made, and no research can be adequately evaluated unless these assumptions are clearly defined [50]. This section outlines the assumptions that have been made in this thesis [27].

1. All work has been conducted through computer simulation. The "real" world in the simulation is modeled as a full-order truth error-state model. The full-order truth and filter design models are presented Chapter 3.

2. The INS platform is assumed to be stabilized with a barometric (baro) altimeter. An INS platform is unstable without an outside measurement source in the vertical channel [10], and the baro altimeter is a commonly used method to stabilize the vertical channel. The use of the baro altimeter is included in the modeling of the system.

3. This thesis will use the radar altimeter as an independent measurement device to feed additional information to an extended Kalman filter. Most commercial and military aircraft do not combine this information with other navigation data, but use it in a stand-alone mode. The radar altimeter measurements will be utilized at altitudes below 3000 feet above ground level (AGL).

4. A sample period of one second has been chosen (unless otherwise noted) for the EKF. The sample period refers to how often the GPS and radar altimeter measurements will be brought into the EKF. The decision to use one second sample period is the author's choice based primarily on the typical availability of the GPS measurement in the real world. Though faster GPS outputs are available, a one second sample period is chosen as a good, representative design choice.

5. The computer simulations have been developed using a program called Multi-mode Simulation for Optimal Filter Evaluation (MSOFE) [53]. MSOFE is well-established Air Force software to develop and test linear and extended Kalman filter algorithms.

6. The computer-simulated flight profile has been generated by the program PROFGEN [52]. PROFGEN is designed to work with MSOFE to provide the necessary data files to simulate dynamic flight profiles.

7. The plotted outputs are generated by the commercial software package MATLAB [67].

8. The SV ephemeris data using System Effectiveness Model (SEM) [19] software was obtained from the Coast Guard BBS. The ephemeris data is post-processed by the U.S. Department of Commerce, National Geodetic Information Branch [15].

9. Ephemeris data was incorporated into PROFGEN's binary output "FLIGHT" profile by making adaptations to existing FORTRAN source code [64].

10. The four SVs chosen to range during operation of MSOFE and the FLIGHT profile are chosen based on the indicated results of the System Effectiveness Model (SEM3.6) software from [19] based on position dilution of position (PDOP) criterion less than 2.5. PDOP is based on the geometry of the satellites in reference to the aircraft. The smaller the PDOP, the better the geometry and the resolution of the position errors at the aircraft.

11. The simulation software, MSOFE and MATLAB, has been coded to run in double precision to increase the numerical stability and precision of the simulation. MSOFE software utilizes a U-D factorization algorithm to increase the numerical stability in the Kalman filter measurement update equations [46,53].

12. The MSOFE runs are conducted using 15-run Monte Carlo analyses. While a larger batch size for the Monte Carlo analysis would be preferable, this value has been chosen to keep the computational burden of the thesis within reasonable bounds, while maintaining adequate confidence the resulting sample statistics properly reflect the true statistics [27].

13. Taylor series approximations truncated at first order are used for linearizing nonlinear equations in the NRS and DLSM filter.

14. It will be assumed for this thesis that, when radar altimeter measurements are available, the earth's surface will be modeled as flat and referenced approximately to the INS indicated altitude (referenced to WGS-84 ellipsoid). This assumption needs to be "upgraded" to a more realistic radar altimeter scenario at a later time by possibly using a database that contains "height of terrain" for specific locations on the earth.

15. The INS will have had a "normal" 8-minute alignment and nominal flight of 60 minutes duration prior to the terminal approach phase under investigation. "Normal" also means the INS has not been degraded nor enhanced by any means.

16. Four SV are always available, with an average PDOP of 2.1. The SEM 3.6 software selects the four best satellites available at a given time and these satellites are used without interruptions. Although some current GPS receivers allow access to more than four SVs simultaneously, all performance evalutions in this research are based on using only the four best satellites.

17. The transport aircraft flight profile will:

    a. Always be at less than 0.9g during entire flight.

    b. Have a takeoff speed of 150 knots.

c. Have a landing speed of 133 knots at a 3 degree glideslope.

d. Airspeed above 10,000 will always be greater than 250 knots.

e. Change altitude at a rate 4000 ft/min (maximum).

f. Follow the approach plate for Wright-Patterson AFB, OH.

18. The small aircraft flight profile will:

a. Always be at less than 3.0g during entire flight.

b. Have a takeoff speed of 50 knots.

c. Have a landing speed of 50 knots at a 3 degree glideslope..

d. Change altitude at a rate 500 ft/min (maximum).

e. Follow the approach plate for Wright-Patterson AFB, OH

The approach plate of WPAFB calls for the aircraft to be transitioned to the Wright-Patterson (FFO) procedure track, approximately 11 nm from the runway. The aircraft then follows the arc-turn to heading 233°. During inbound transition, the aircraft must maintain a minimum altitude of 3000 ft mean sea level (MSL). At approximately 5.6 nm from the VORTAC DME station, the aircraft maintains a minimum of 2200 ft MSL which is the *glide slope intercept altitude*. At approximately 0.5 nm from the runway end, the pilot's VORTAC DME would indicate 2.1 nm. The aircraft continues its 3° ILS glideslope to touchdown. FFO is only certified for a Category I precision approach. The approach plate shows, "S-ILS 23R 1025/24 200." This information states it is a "Precision, straight-in to Runway 23 (right-hand side); the decision height (DH) MSL is 1025 ft with prevailing visibility (runway visible range in 100's of feet) of 24." "Height of DH above touchdown zone (HAT) is 200 feet." For a precision ILS approach, the pilot:

- Transitions to the ILS Localizer Course from the published approach procedure
    - Tunes the ILS and monitors the proper identifier during the entire approach
    - Sets the published localizer course prior to localizer course interception
- Accomplishes the Approach
    - Once the localizer course is intercepted, he or she maintains glide slope interception altitude until reaching the glide slope intercept point.
    - Maintains a complete instrument cross-check throughout the approach, with increased emphasis on the baro altimeter and radar altimeter (decision height (DH) is based on the altimeters).
    - Establishes a systematic scan for the runway environment prior to reaching DH.
    - Continues descent to DH.

Note: The precision ILS approach must be discontinued if the localizer course becomes unreliable, or any time full-scale deflection of the pilot's control display indicator (CDI) occurs on final approach [17]. The pilot must not descend below localizer minimums if the aircraft is more than one dot (half scale) below or two dots (full scale) above the glide slope. One dot is 2.5° and two dots is 5°. If the glide slope is recaptured to within the above tolerance, descent may be continued to DH.

A block diagram of the NRS [50,55] is shown in Figure 1 - 1. A block diagram of the DLSM is shown in Figure 1 - 2. A "walk-through" of Figures 1 - 1 and 1 - 2 can be found in Chapter 3, Section 3.1 and Section 3.3 respectively.

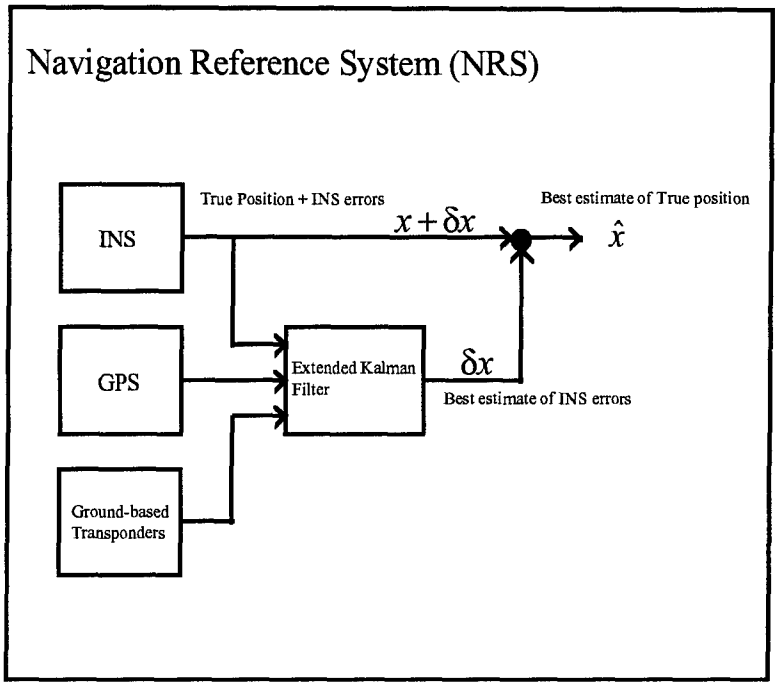

Figure 1 - 1. Navigation Reference System (NRS)

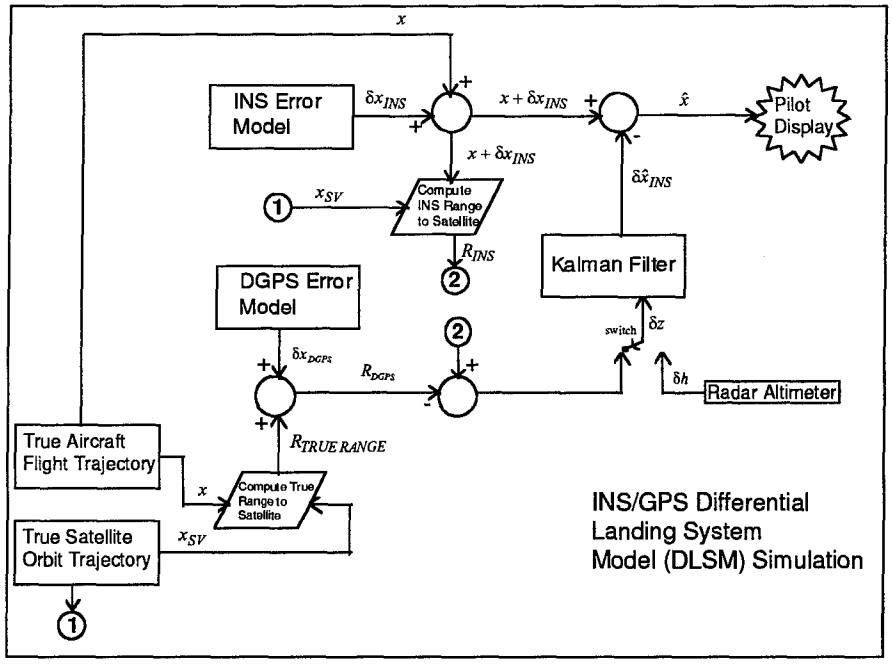

Figure 1 - 2. Differential Landing System Model (DLSM) Simulation

1.7 Summary

This chapter has given an overview of the thesis plan to develop an integrated DGPS/INS/Barometric and Radar Altimeter System for aircraft precision approaches. The background for the necessity of such a system, the various system integrations, past research, the project scope, and all assumptions were presented. The reference frames used in this project, as well as the INS, GPS, DGPS, baro altimeter, and radar altimeter subsystems, are presented in Chapter 2, along with a discussion of Kalman filter algorithms. Chapter 3 presents the DLSM and Chapter 4 presents the results and analysis of the DLSM performance. Conclusions and recommendations for future research are presented in Chapter 5.

II. Background

2.1 Introduction

The background presented in this section includes the basic theory on a ring laser gyro (RLG), an Inertial Navigation System (INS), a Global Positioning System, a Differential Global Positioning System (DGPS), a barometric altimeter and a radar altimeter. Information on ILS precision approaches, Kalman filter, and extended Kalman filter (EKF) theory will also be discussed. More information on Kalman filter development and uses may be found in [45,46,47]. Deterministic and stochastic processes used in this section will presented in roman typeface. Vectors will be displayed in bold-faced type, **x**, and scalars will be shown in normal type, x. Matrices will be displayed in bold-faced upper case, **X.** A particular realization of a variable will be displayed in italics, *x*. The credit for the development of large portions of this chapter belongs to Gray [27].

2.2 RLG Strapdown INS

An RLG strapdown INS provides aircraft information on the present position, bearing, velocity, and distance from destination. An inertial navigatior is a self-contained, dead-reckoning navigation aid using inertial sensors, a reference direction, an initial and/or subsequent fixes to determine direction, distance, and speed; single integration of acceleration provides speed information and a double integration provides distance information [36].

A strapdown system is a type of inertial navigator characterized by the lack of a gimbal support structure [10]. The non-gimbaled INS is advantageous because no moving parts are required to keep a stable element level. Without the moving parts, the system is less prone to failures and cheaper to build. Also, when gyro failures occur in a strapdown

system, the gyros may be replaced; the entire inertial measurement unit (IMU) would have to be replaced in a gimbaled system. The disadvantage with a strapdown system is the platform is physically strapped to the aircraft body. This forces the gyroscopes, accelerometers, and strapdown computer algorithms to be rugged enough to maintain integrity in whatever harsh dynamic environment the aircraft may encounter. The sensors must also provide *precise* measurements over a substantially larger range of values than would a similar sensor on a gimbaled platform.

The strapdown system is mechanized by mounting three gyros and three accelerometers directly to the vehicle for which the navigation function is to be provided. More than three of each can be used to provide enhanced reliability through redundancy. A digital computer is used to keep track of the vehicle's attitude with respect to some reference frame, based on information from the gyros. This enables the computer to provide the coordinate transformation necessary to coordinatize the accelerometer outputs in a desired computational reference frame, such as East-North-Up or wander azimuth [27].

To provide navigation information, the RLG detects and measures angular rates by measuring the frequency difference between two counter-rotating (laser) beams [32]. The two laser beams circulate in a ring-shaped optical cavity simultaneously. The beams are reflected around the optical cavity using mirrors. The resonant frequency of a contained laser beam is a function of its optical path length. Since the path traveled by each of the beams is identical, the two laser beams have the same frequencies when the gyro is at rest. If the cavity is rotating in an inertial sense, the propagation times of the two light beams are different. The delay in the propagation time manifests itself in the form of a phase shift

between the two beams, and the phase shift is detected by a pair of photo detectors. The magnitude of the phase shift provides a direct indication of the angular rate of rotation of the instrument with respect to inertial space [60,65].

2.3 Barometric Altimeter

Errors in navigation information from an INS are due in part to the inherent instability present in the vertical channel. This instability results in unbounded error growth in vertical position and velocity [3,10,26,58]. The instability may be controlled by aiding the vertical channel with a barometric (or other type of) altimeter. The barometric altimeter provides external altitude information and stabilizes the vertical channel [10].

The barometric altimeter is probably the simplest way to measure the altitude of an aircraft. The pressure of the Earth's atmosphere decreases as height above the earth increases. Barometric altimeters provide altitude information based on the pressure differences. Barometric altimeters are most inaccurate when ascending or descending at rapid rates but are realtively low in cost [17].

2.4 Global Positioning System (GPS)

GPS navigation presents opportunity for standardized worldwide civil aviation operations using a common navigation receiver [24]. GPS is a space-based positioning, velocity and time system that has three major segments: Space, Control and User.

2.4.1 GPS Space Segment

The GPS *Space* Segment is composed of 24 satellites in six orbital planes. The satellites operate in near-circular 20,200 km (10,900 NM) orbits at an inclination angle of 55 degrees and with ≈12-hour period. The spacing of satellites in orbit is arranged so that

a minimum of five satellites will be in view to users worldwide, with a position dilution of precision (PDOP) of six or less. PDOP is a measure of the error contributed by the geometric relationships of the GPS satellites as seen by the GPS receiver [18]. PDOP is mathematically defined as:

$$PDOP = (\sigma_x^2 + \sigma_y^2 + \sigma_z^2)^{1/2} \tag{2.1}$$

where σ_x^2, σ_y^2 and σ_z^2 are the variances of the estimated user position to each exis [58]. A definition for pseudorange measurement is defined in Section 2.4.3. Each satellite transmits on two L band frequencies, L1 (1575.42 MHz) and L2 (1227.6 MHz). L1 carries a precise (P) code and a coarse/acquisition (C/A) code. L2 carries the P code. A navigation data message containing the important information about about each satellite is superimposed on these codes. The same navigation data message is carried on both frequencies.

2.4.2 GPS Control Segment

The *Control* Segment has five monitor stations, three of which have uplink capabilities. The monitor stations use a GPS receiver to track all satellites in view passively and thus accumulate ranging data from the satellite signals. The information from the monitor stations is processed at the Master Control Station (MCS) to determine satellite orbits and to update the navigation message of each satellite. This updated information is transmitted to the satellites via the ground antennas, which are also used for transmitting and receiving satellite control information.

2.4.3 GPS User Segment

The *User* segment consists of an antenna and receiver processors that provide positions, velocity and precise timing to the respective user. Computing the user's positional information typically requires simultaneous solution of the following four nonlinear position equations [18]:

$$(x_1 - u_x)^2 + (y_1 - u_y)^2 + (z_1 - u_z)^2 = (R_1 - C_B)^2$$
$$(x_2 - u_x)^2 + (y_2 - u_y)^2 + (z_2 - u_z)^2 = (R_2 - C_B)^2$$
$$(x_3 - u_x)^2 + (y_3 - u_y)^2 + (z_3 - u_z)^2 = (R_3 - C_B)^2$$
$$(x_4 - u_x)^2 + (y_4 - u_y)^2 + (z_4 - u_z)^2 = (R_4 - C_B)^2$$

where the pseudorange, $R_{i=1,2,3,4}$ to each satellite is defined as

$$R_1 = c\Delta t_1$$
$$R_2 = c\Delta t_2$$
$$R_3 = c\Delta t_3$$
$$R_4 = c\Delta t_4$$

and

c = speed of light

$\Delta t_{i=1,2,3,4}$ = signal transmit time as measured by the receiver

$x_{i=1,2,3,4}$, $y_{i=1,2,3,4}$, $z_{i=1,2,3,4}$ are respective i-th satellite positions

u_x, u_y, u_z is the user position the GPS user equipment is solving numerically and recursively

C_B = the user clock bias (user equipment solves)

Normally the user equipment needs to acquire and maintain lock on at least four satellites in order to compute a 3-D position fix [49] and the clock bias C_B. The GPS pseudorange between the user and each satellite is computed based on knowledge of time (the master GPS clock) and the unique signal format which is broadcast by each satellite. Part of the problem is that the user clock is not identical to the master clock. Once the four pseudo-ranges are known, a recursive algorithm is solved to compute the user's position [49]. See [18] for further references.

2.4.4 Satellite Vehicle Data Using SEM 3.6

In his research [27], Gray made use of true SV ephemeris data as an input to MSOFE rather than utilizing the MSOFE subroutine to generate generic SV data. The ephemeris data used was obtained from the National Geodetic Office. The SV ephemeris used in the DLSM simulation was selected based upon the best four SV available for a random day by the System Effectiveness Software (SEM) 3.6 [19] software package. The four SVs chosen were based on:

- Random day (21 May 94) selected.

  (GPS week 749, Day of year 141).
- GPS Almanac data file "051994A.AL3" (See Appendix H) was obtained (downloaded) via the Coast Guard Bulletin Board Services (CGBBS).
- LAT/LONG/ALT along the Tanker flight profile was noted and entered in SEM 3.6.
    - Best 4 SV based on PDOP algorithm
    - 5° mask angle

- Scenario duration: 2 hours [Begin time 04:00 UTC (Coordinated Universal Time or 08:00 Eastern time)]

The best four SVs are then numerically displayed to the user. The mask angle was chosen as 5° based on the author's experience. Thus, all satellites in view above a 5° angle made from the GPS antenna surface (mask angle) on 21 May 94 between the hours of 04:00 - 06:00 Greenwich mean time are available for use. For further information of SEM 3.6 software and SEM 3.6 output plot format, see [19].

2.5 Differential GPS (DGPS)

Differential GPS is a method of achieving higher GPS accuracies in position measurement in a local area. The basic principle behind DGPS is based on the fact that a large portion of pseudorange measurement errors are correlated between two nearby receivers tracking a given satellite. A single DGPS reference station at a known location can compute a range error correction for each GPS satellite in view. The error corrections may then be broadcast to users in the vicinity of the reference receiver. A user can typically improve 3-D positioning accuracy from 100 meters for a standard GPS down to the 2 - 5 meter level by applying the corrections to the signals received. The accuracies do decrease as the distance between the user and the reference station increases. Beyond a separation distance of 100 kilometers, a range error correction is not sufficiently accurate to realize the full potential of DGPS [55,58].

Work accomplished by William Negast at AFIT has demonstrated the effectiveness of using differential corrections to increase GPS precision. He was able to eliminate the satellite vehicle (SV) clock error from each pseudorange measurement, and the SV position errors was nearly eliminated. The atmospheric propagation errors can be almost

totally eliminated when the two GPS receivers are within 200 miles of each other [55]. The work by Negast provided the new DGPS error model used in this effort. Detailed equations for DGPS and explanations for the errors removed from standard GPS after the application of DGPS corrections are presented in Section 3.4.3.

2.6 Radar Altimeter

A radar altimeter provides measurement of absolute clearance over all types of terrain [31]. The system operates by measuring the time it takes for an electromagnetic energy pulse to travel from the aircraft to the terrain below and return to the aircraft. Radar altimeters are normally all-weather devices. Performance specifications (3-σ) are typically $\pm$ [3ft + 3% of altitude range], with $\pm$ 30° pitch and $\pm$ 45° roll maneuverability at or above ground level (AGL) heights, which typically vary from 0 feet to 10,000 feet. Figure 2 - 1 provides an elementary block diagram of this operation.

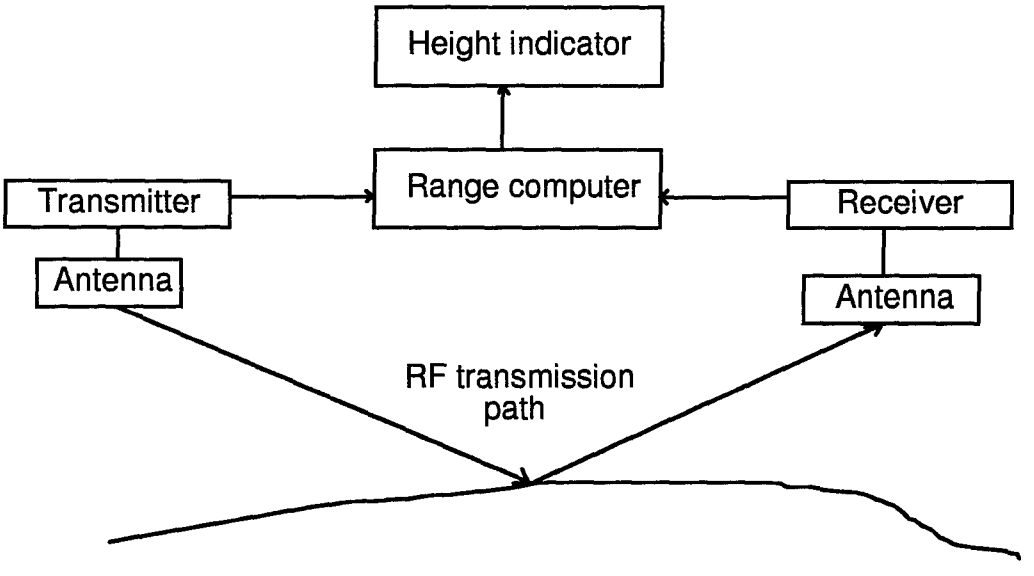

Figure 2 - 1. Elementary Radar Altimeter Block Diagram

2.7 Instrument Landing System (ILS) Precision Approach

An *instrument approach*, by definition [36], is the process of making an approach to a landing by the use of navigation instruments without dependence upon direct visual reference to the terrain. The *Instrument Landing System* (ILS) is designed to provide an approach path for exact alignment and descent of an aircraft on final approach to a runway [17]. The ground equipment consists of two highly directional transmitting systems, and along the approach, three (or fewer) marker beacons. The directional transmitters are known as the localizer and glide slope transmitters. See Figure 2 - 2.

The *localizer* transmitter, operating on one of the 40 ILS channels within the frequency range of 108.10 MHz to 111.95 MHz, emits signals which provide the pilot with course guidance to the runway centerline in the horizontal plane. The localizer signal is usable and accurate to a range of 18 nautical miles (NM) from the localizer antenna unless otherwise depicted on the Instrument approach procedure (IAP) [17]. See Figure 2 - 2.

The ultra high frequency *glide slope* transmitter, operating on one of the 40 ILS channels within the frequency range 329.15 MHz to 335.00 MHz, radiates its signals primarily in the direction of the localizer front course, i.e., so as to measure angular vertical displacement from the desired glide path, as seen from the side. The glide slope signal is usable to a distance of 10 NM unless otherwise depicted on the Instrument approach procedure (IAP) [17].

A *marker beacon* light and (or) aural tone may be included in the cockpit display to indicate aircraft position along the localizer. The marker beacons are identified by continuous dashes for the outer marker, alternating dashes and dots for the middle marker, and continuous dots for the inner marker (see Figure 2 - 2). Precision ILS Approaches

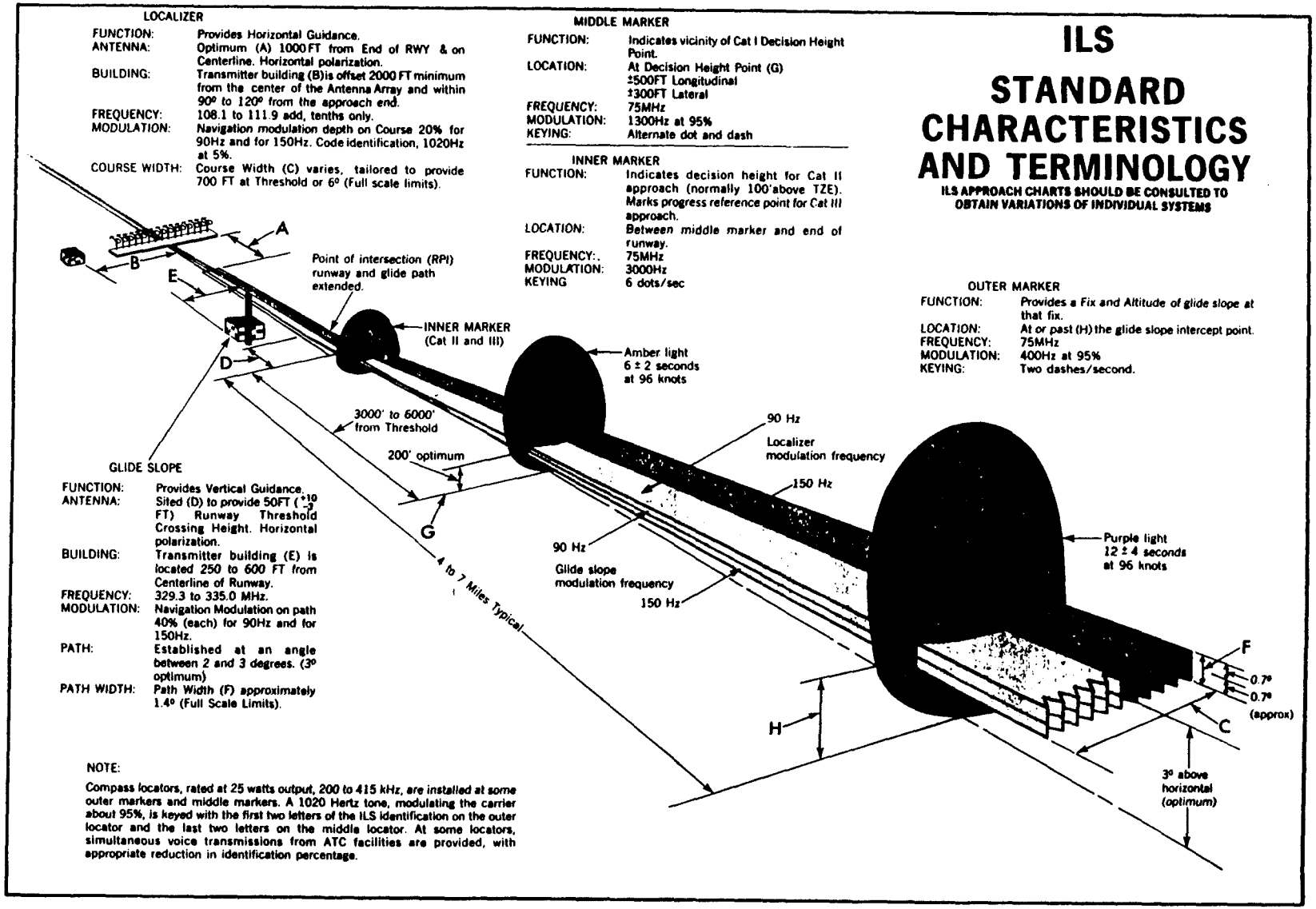

Figure 2 - 2. Standard ILS Characteristics and Terminology

ILS Precision Category	Horizontal Accuracy	Vertical Accuracy
1	± 56.1 ft	± 13.5 ft
2	± 17.1 ft	± 5.6 ft
3	± 13.5 ft	± 2.0 ft

Table 2 - 1. 2-σ Precision ILS Approach Criteria at Decision Height

follow the 2-σ decision height accuracy shown in Table 2 - 1.

2.8 Reference Frames

A navigation "solution" has significance only if the corresponding frame in which the solution is expressed is clearly understood [65]. While the preceding statement may seem obvious, it cannot be overemphasized. Consider that a typical INS "owner's manual" defines *earth* frame, *true* frame, *computer* frame, *platform* frame, *sensor* frame, *accelerometer* frame and the *body* frame [41,65]. From a student's perspective this may at first be overwhelming, but to make matters worse, another INS vendor may well define every frame mentioned above, such as "*earth* frame" in an entirely *different* manner! Therefore, the frames used in this project and the coordinate transformations, will briefly be discussed (all reference frame figures with permission from [8]). All the figures are presented at the end of Section 2.8

2.8.1 Inertial Frame (x^i, y^i, z^i)

An inertial frame is an orthogonal, right-handed coordinate system; its origin is coincident with the earth's center-of-mass and the frame is oriented as follows. The x^i, z^i plane lies in the earth's equatorial plane and does not rotate with respect to the fixed stars.

The y^i axis projects from the earth's center-of-mass directly through the North pole. The inertial frame is depicted by the $[x^i, y^i, z^i]$ frame shown in Figure 2 - 3.

2.8.2 Earth Frame (x^e, y^e, z^e)

The earth frame or "earth-centered-earth-fixed" (ECEF) frame is an orthogonal, right-hand coordinate system; its origin is coincident with the earth's center-of-mass, with the x^e, z^e plane located in the earth's equatorial plane. The z^e axis is aligned with the Greenwich meridian and rotates at exactly the earth rate, Ω, about the y^e axis, which projects from the earth's center-of-mass directly through the North pole. The Earth frame is depicted as $[x^e, y^e, z^e]$ in Figure 2 - 4.

2.8.3 Geographic Frame (x^g, y^g, z^g) = (E, N, U)

The geographic frame or "local-level" frame is an orthogonal, right-handed coordinate system; its origin is at the location of the INS (or the user), and its axes are aligned with the East, North and Up directions [E, N, U]. The geographic frame remains perpendicular to the earth's surface with respect to the earth's gravity field as the user moves over the Earth. The geographic frame is depicted as either $[x^g, y^g, z^g]$ or [E, N, U] in Figure 2 - 5.

2.8.4 Navigation Frame (x^n, y^n, z^n)

The navigation frame or "local-level-wander-azimuth" frame is an orthogonal, right-hand coordinate system; its origin is at the location of the INS (or the user). This frame coincides with the geographic frame when the wander angle, α equals 0°. The wander angle is a computed angle between a "scribe mark" on a wander azimuth angle platform

and North. For gimbaled systems, the platform is purposely not commanded to seek North, due to the high platform angular rates that this would require in polar regions, with resulting performance degradation [3,65]. The navigation frame is denoted as [x^n, y^n, z^n] shown in Figure 2 - 6.

2.8.5 Body Frame (x^b, y^b, z^b)

The body frame is an orthogonal, right-hand frame; its origin is at the vehicle (i.e., aircraft) center-of-mass. Its axes are the vehicle's roll, pitch, and yaw axes [ϕ, θ, ψ]. The x^b axis points in the forward direction, along the roll axis; the y^b axis points to the right (starboard side) of the aircraft, perpendicular to the roll axis, but along the pitch axis; and the z^b axis is positive out the underside of the aircraft. The body frame is denoted as [x^b, y^b, z^b] and is shown in Figure 2 - 7.

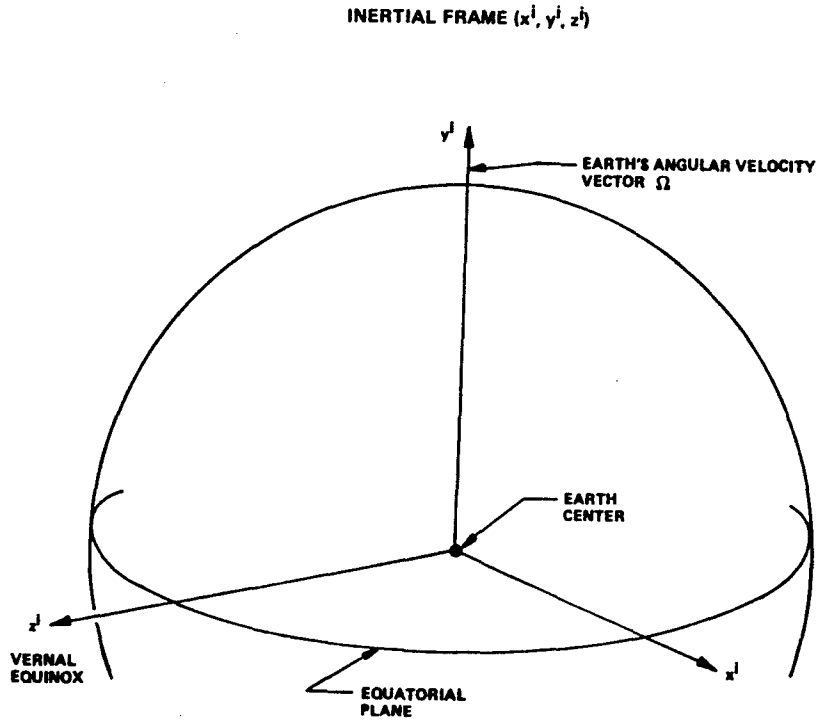

Figure 2 - 3. Inertial Frame

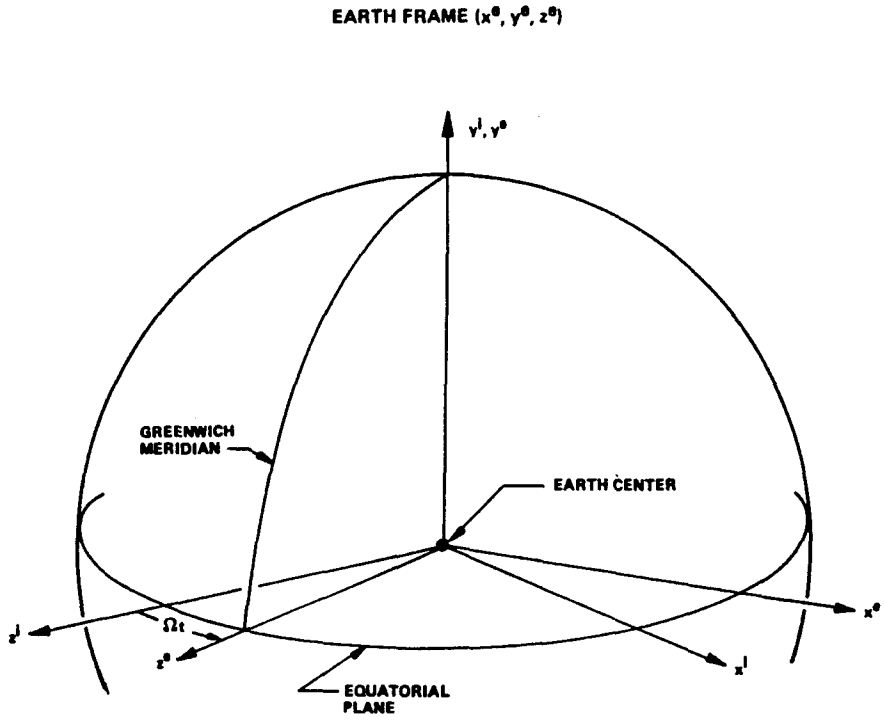

Figure 2 - 4. Earth Frame

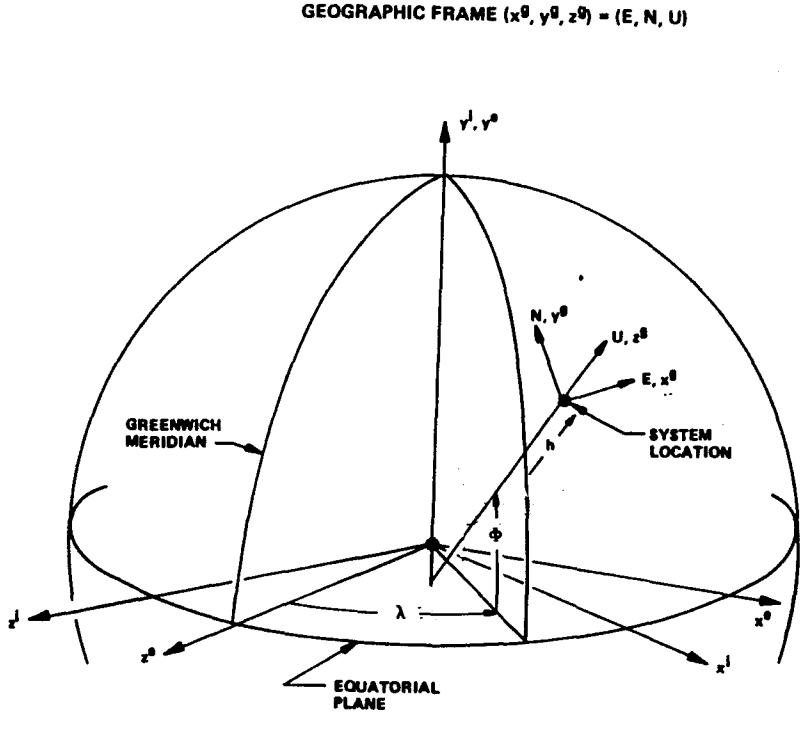

Figure 2 - 5. Geographic Frame

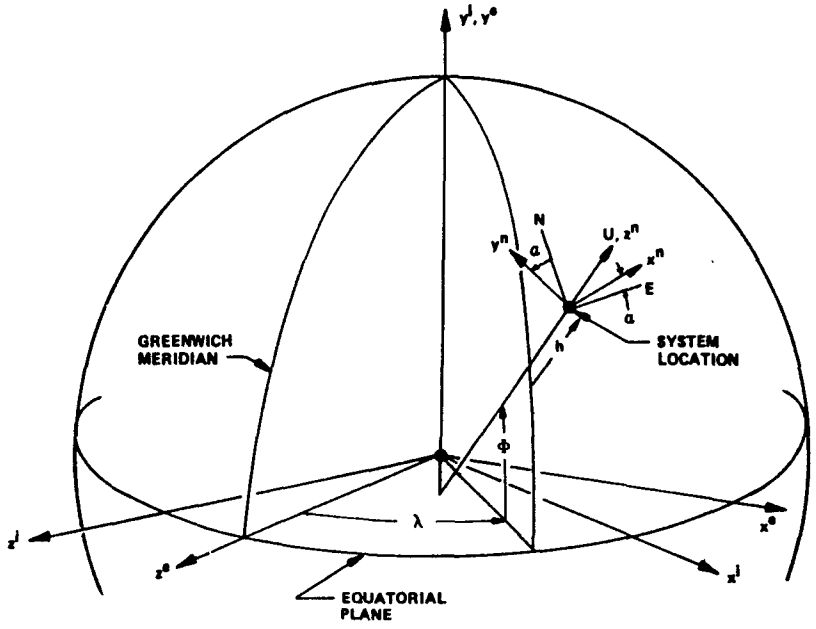

Figure 2 - 6. Navigation Frame

BODY FRAME (x^b, y^b, z^b)

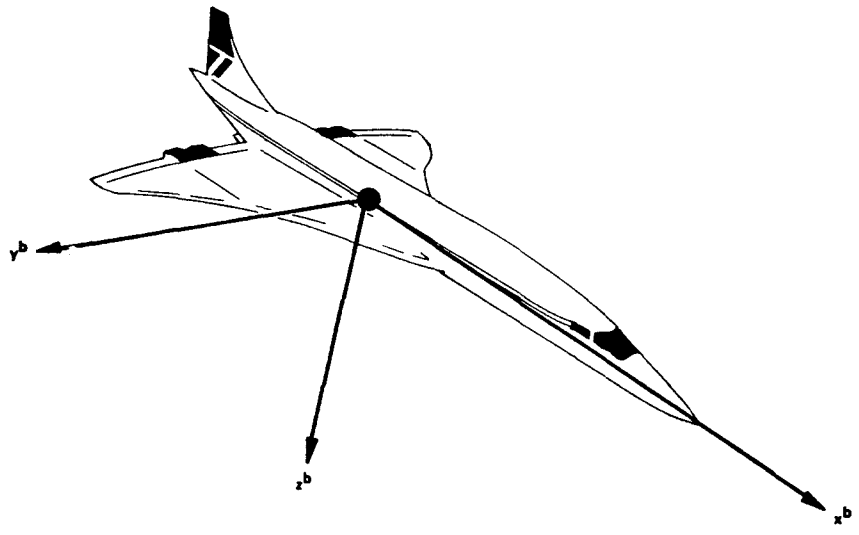

Figure 2 - 7. Body Frame

2.9 *Reference Frame Transformations*

The RLG INS modeled in this thesis uses the navigation frame or "local-level-wander-azimuth" frame. It is often necessary to express vectors such as position, attitude, velocity or acceleration in terms of several different reference frames. As an example, the INS modeled in this thesis also outputs position error in terms of an *error-angle* vector, $[\delta\theta_x, \delta\theta_y, \delta\theta_z, \delta h]^T$, where $\delta\theta_x$ is the error angle about the local level x^g (or E) axis, $\delta\theta_y$ is the error angle about the local level y^g (or N) axis, $\delta\theta_z$ is the error about the local level z^g (or U) axis, and δh is the altitude error [3,41]. Even though this definition is clear, if the error-angle vector is to have *physical* meaning, it must be transformed into a vector in *navigation* error terminology, $[\delta\phi, \delta\lambda, \delta\alpha, \delta h]^T$, where $\delta\phi$ is the error in latitude, $\delta\lambda$ is longitude error, $\delta\alpha$ is alpha (wander) angle error and δh is again the altitude error.

A *transformation matrix*, $C_{Error\ Angle}^{Navigation\ Error}$, permits compact transformation of the error-angle vector into an equivalent expression in navigation error space. The transformation matrix, $C_{Error\ Angle}^{Navigation\ Error}$ is shown below in Equation (2-2) [3,65]:

$$C_{Error\ Angle}^{Navigation\ Error} = \begin{bmatrix} -\cos\alpha & \sin\alpha & 0 & 0 \\ \sin\alpha\sec\phi & \cos\alpha\sec\phi & 0 & 0 \\ -\sin\alpha\tan\phi & -\cos\alpha\tan\phi & 1 & 0 \\ 0 & 0 & 0 & 1 \end{bmatrix} \tag{2.2}$$

ϕ = latitude
α = alpha angle

Other transformations are as follows (from [8]):

2.9.1 *Inertial Frame to Earth Frame, C_i^e*

$$C_i^e = \begin{bmatrix} \cos\Omega t & 0 & -\sin\Omega t \\ 0 & 1 & 0 \\ \sin\Omega t & 0 & \cos\Omega t \end{bmatrix} \tag{2.3}$$

$t \rightarrow$ when $t = 0$, x-axis of ECEF frame equals x-axis of inertial frame

2.9.2 *Earth Frame to Geographic Frame, C_e^g*

$$\begin{aligned} C_e^g &= \begin{bmatrix} 1 & 0 & 0 \\ 0 & \cos\phi & -\sin\phi \\ 0 & \sin\phi & \cos\phi \end{bmatrix} \begin{bmatrix} \cos\lambda & 0 & -\sin\lambda \\ 0 & 1 & 0 \\ \sin\lambda & 0 & \cos\lambda \end{bmatrix} \\ &= \begin{bmatrix} \cos\lambda & 0 & -\sin\lambda \\ -\sin\phi\sin\lambda & \cos\phi & -\sin\phi\cos\lambda \\ \cos\phi\sin\lambda & \sin\phi & \cos\phi\cos\lambda \end{bmatrix} \end{aligned} \tag{2.4}$$

where

λ = longitude
ϕ = latitude
α = alpha angle

2.9.3 *Earth Frame to Navigation Frame, C_e^n*

$$\begin{aligned} C_e^n &= \begin{bmatrix} \cos\alpha & \sin\alpha & 0 \\ -\sin\alpha & \cos\alpha & 0 \\ 0 & 0 & 1 \end{bmatrix} \begin{bmatrix} 1 & 0 & 0 \\ 0 & \cos\phi & -\sin\phi \\ 0 & \sin\phi & \cos\phi \end{bmatrix} \begin{bmatrix} \cos\lambda & 0 & -\sin\lambda \\ 0 & 1 & 0 \\ \sin\lambda & 0 & \cos\lambda \end{bmatrix} \\ &= \begin{bmatrix} \cos\alpha\cos\lambda - \sin\alpha\sin\phi\sin\lambda & \sin\alpha\cos\phi & -\cos\alpha\sin\lambda - \sin\alpha\sin\phi\cos\lambda \\ -\sin\alpha\cos\lambda - \cos\alpha\sin\phi\sin\lambda & \cos\alpha\cos\phi & \sin\alpha\sin\lambda - \cos\alpha\sin\phi\cos\lambda \\ \cos\phi\sin\lambda & \sin\phi & \cos\phi\cos\lambda \end{bmatrix} \end{aligned} \tag{2.5}$$

where

λ = longitude
ϕ = latitude
α = alpha angle

2.9.4 *Geographic Frame to Navigation Frame, C_g^n*

$$C_g^n = \begin{bmatrix} \cos\alpha & \sin\alpha & 0 \\ -\sin\alpha & \cos\alpha & 0 \\ 0 & 0 & 1 \end{bmatrix} \tag{2.6}$$

where

α = alpha angle

2.9.5 *Geographic Frame to Body Frame, C_g^b*

$$\begin{aligned} C_g^b &= \begin{bmatrix} 1 & 0 & 0 \\ 0 & \cos\rho & \sin\rho \\ 0 & -\sin\rho & \cos\rho \end{bmatrix} \begin{bmatrix} \cos\theta & 0 & -\sin\theta \\ 0 & 1 & 0 \\ \sin\theta & 0 & \cos\theta \end{bmatrix} \begin{bmatrix} \cos\psi & \sin\psi & 0 \\ -\sin\psi & \cos\psi & 0 \\ 0 & 0 & 1 \end{bmatrix} \begin{bmatrix} 0 & 1 & 0 \\ 1 & 0 & 0 \\ 0 & 0 & -1 \end{bmatrix} \\ &= \begin{bmatrix} \cos\theta\sin\psi & \cos\theta\cos\psi & \sin\theta \\ \sin\rho\sin\theta\sin\psi + \cos\rho\cos\psi & \sin\rho\sin\theta\cos\psi - \cos\rho\sin\psi & -\sin\rho\cos\theta \\ \cos\rho\sin\theta\sin\psi - \sin\rho\cos\psi & \cos\rho\sin\theta\cos\psi + \sin\rho\sin\psi & -\cos\rho\cos\theta \end{bmatrix} \end{aligned} \tag{2.7}$$

where

ρ = roll
θ = pitch
ψ = geographic heading

2.9.6 *Navigation Frame to Body Frame, C_n^b*

$$\begin{aligned} C_n^b &= \begin{bmatrix} 1 & 0 & 0 \\ 0 & \cos\rho & \sin\rho \\ 0 & -\sin\rho & \cos\rho \end{bmatrix} \begin{bmatrix} \cos\theta & 0 & -\sin\theta \\ 0 & 1 & 0 \\ \sin\theta & 0 & \cos\theta \end{bmatrix} \begin{bmatrix} \cos\psi_P & \sin\psi_P & 0 \\ -\sin\psi_P & \cos\psi_P & 0 \\ 0 & 0 & 1 \end{bmatrix} \begin{bmatrix} 0 & 1 & 0 \\ 1 & 0 & 0 \\ 0 & 0 & -1 \end{bmatrix} \\ &= \begin{bmatrix} \cos\theta\sin\psi_P & \cos\theta\cos\psi_P & \sin\theta \\ \sin\rho\sin\theta\sin\psi_P + \cos\rho\cos\psi_P & \sin\rho\sin\theta\cos\psi_P - \cos\rho\sin\psi_P & -\sin\rho\cos\theta \\ \cos\rho\sin\theta\sin\psi_P - \sin\rho\cos\psi_P & \cos\rho\sin\theta\cos\psi_P + \sin\rho\sin\psi_P & -\cos\rho\cos\theta \end{bmatrix} \end{aligned} \tag{2.8}$$

where

ρ = roll
θ = pitch
ψ_P = platform heading

2.10 Kalman Filter Theory

2.10.1 What is a Kalman Filter?

A Kalman filter is simply an optimal recursive data processing algorithm [45] that can be shown to be optimal by essentially any standard, given the appropriateness of several underlying assumptions. These assumptions are that the system in question can be adequately modeled as linear with white, Gaussian system and measurement noises.

One aspect of the word "optimal" is that the Kalman filter can incorporate all information (measurements) provided to it [45]. It processes all available measurements, regardless of their precision, to "estimate" the current value of the variables of interest with use of (from [45]):

- Knowledge of the system and measurement device dynamics
- The statistical description of the system noises, measurement errors and uncertainty in the dynamics models.
- Any available information about inertial conditions of the variables of interest.

For example, to determine the velocity of an aircraft, one could use a Doppler radar, or the velocity indications from an inertial navigation system, or the pitot and static pressure and relative wind information in the air data system. Rather than ignore any of these outputs, a Kalman filter could be built to combine all this data and knowledge of the various systems dynamics to generate an overall best estimate of velocity. Another way a Kalman filter is optimal is that it obtains the best estimate of desired quantities from data provided by a noisy environment. Here the word "optimal" means that the Kalman filter minimizes errors in essentially all respects, and it does so recursively. The word *recursive*

means that, unlike certain data processing concepts, the Kalman filter doesn't require all previous data to be kept in storage and reprocessed every time new measurements are taken.

To "see" how a Kalman filter works, a simple example taken directly from [45] will be presented. It is included here because it helped the author understand the concept of a Kalman Filter in his AFIT studies.

2.10.2 Kalman Filter Example

Suppose that you are lost at sea during the night and have no idea at all of your location. So you take a star sighting to establish your position (for the sake of simplicity, consider a one-dimensional location). At some time t_1 you determine your location to be z_1. However, because of inherent measuring device inaccuracies, human error, and the like, the result of your measurement is somewhat uncertain. Say you decide that the precision is such that the standard deviation (one-sigma value) involved is σ_{z_1} (or

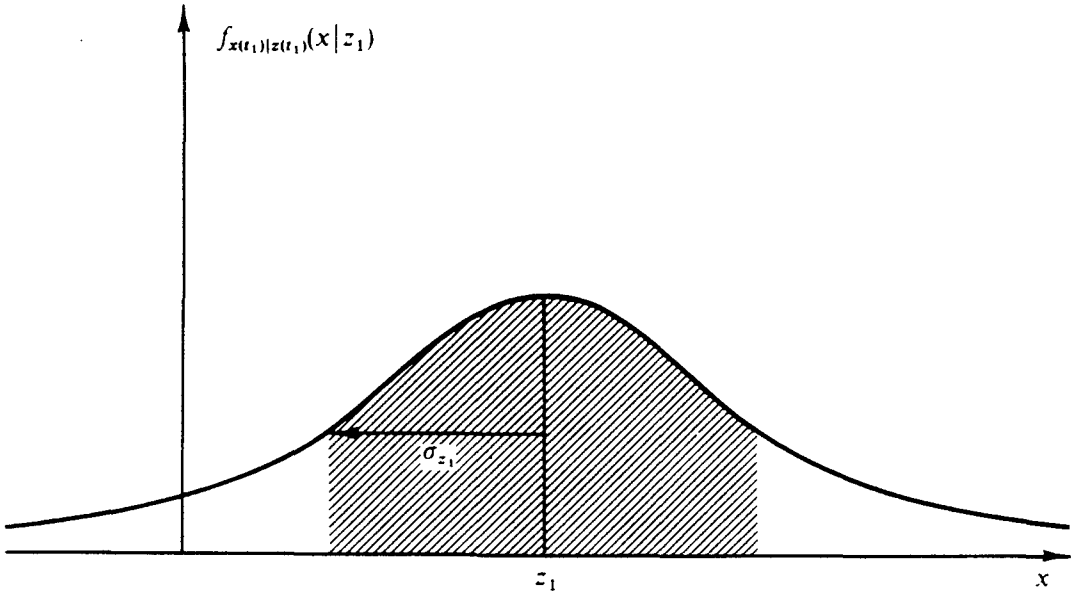

Figure 2 - 8. Conditional Density of Position Based on Measured Value z_1

equivalently, the variance, or second order central statistic, is $\sigma_{z_1}^2$). Thus, you can establish the conditional probability of $x(t_1)$, your position at time t_1, conditioned on the observed value of the measurement being z_1, as depicted in Figure 2 - 8. This is a plot of $f_{x(t_1)|z(t_1)}(x|z_1)$ as a function of the location x: it tells you the probability of being in any one location, based upon the measurement you took. Note that σ_{z_1} is a direct measure of the uncertainty: the larger σ_{z_1} is, the broader the probability peak is, spreading the probability "weight" over a larger range of x values. For a Gaussian density, 68.3% of the probability "weight" is contained within the band σ units to each side of the mean, the shaded portion in Figure 2 - 8.

Based on this conditional probability density, the best estimate of your position is

$$\hat{x}(t_1) = z_1 \tag{2.9}$$

and the variance of the error in the estimate is

$$\sigma_x^2(t_1) = \sigma_{z_1}^2 \tag{2.10}$$

Note that $\hat{x}$ is both the mode (value that locates the peak) and the median (value with 1/2 of the probability weight to each side), as well as the mean (center-of-mass).

Now say a trained navigator friend takes an independent fix right after you do, at time $t_2 \cong t_1$ (so that the true position has not changed at all), and obtains a measurement z_2 with a variance $\sigma_{z_2}^2$. Because he has a higher skill, assume the variance in his measurement to be somewhat smaller than in yours. Figure 2 - 9 presents the conditional density of your position at time t_2, based only on the measured value z_2. Note the

narrower peak due to smaller variance, indicating that you are rather certain of your position based on his measurement.

At this point, you have two measurements available for estimating your position. The question is, how do you combine these data? It can be shown that, based on the assumptions made, the conditional density of your position at $t_2 \cong t_1$, $x(t_2)$, given *both* z_1 *and* z_2, is a Gaussian density with mean μ and variance σ^2 as indicated in Figure 2 - 10 with

$$\mu = \left[\frac{\sigma_{z_2}^2}{\sigma_{z_1}^2 + \sigma_{z_2}^2}\right] z_1 + \left[\frac{\sigma_{z_1}^2}{\sigma_{z_1}^2 + \sigma_{z_2}^2}\right] z_2 \tag{2.11}$$

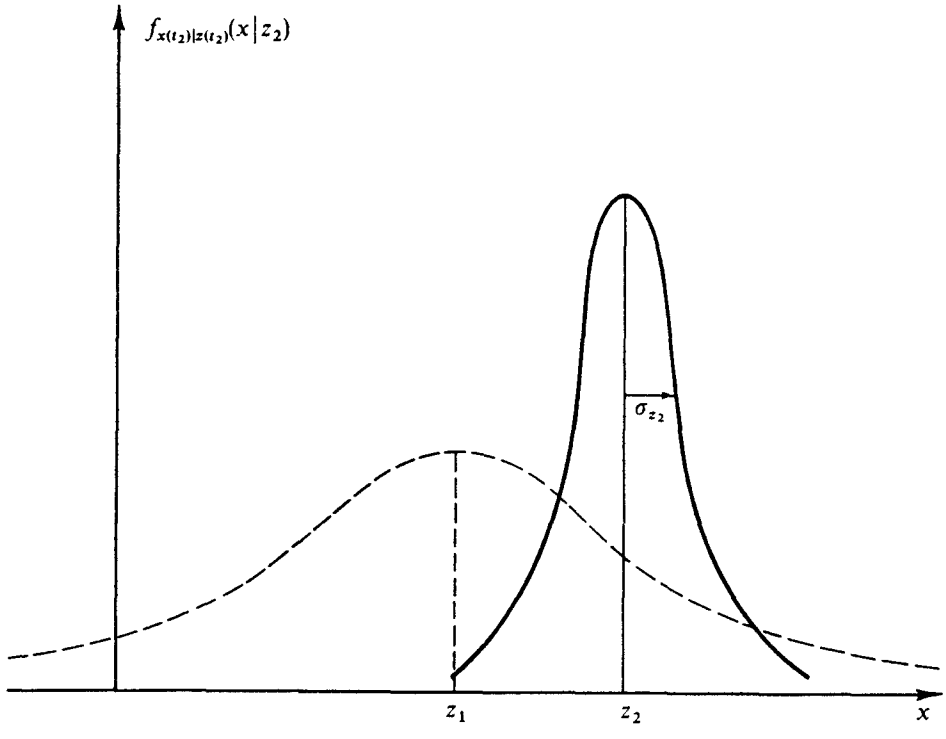

Figure 2 - 9. Conditional Density of Position Based on Measurement z_2 Alone

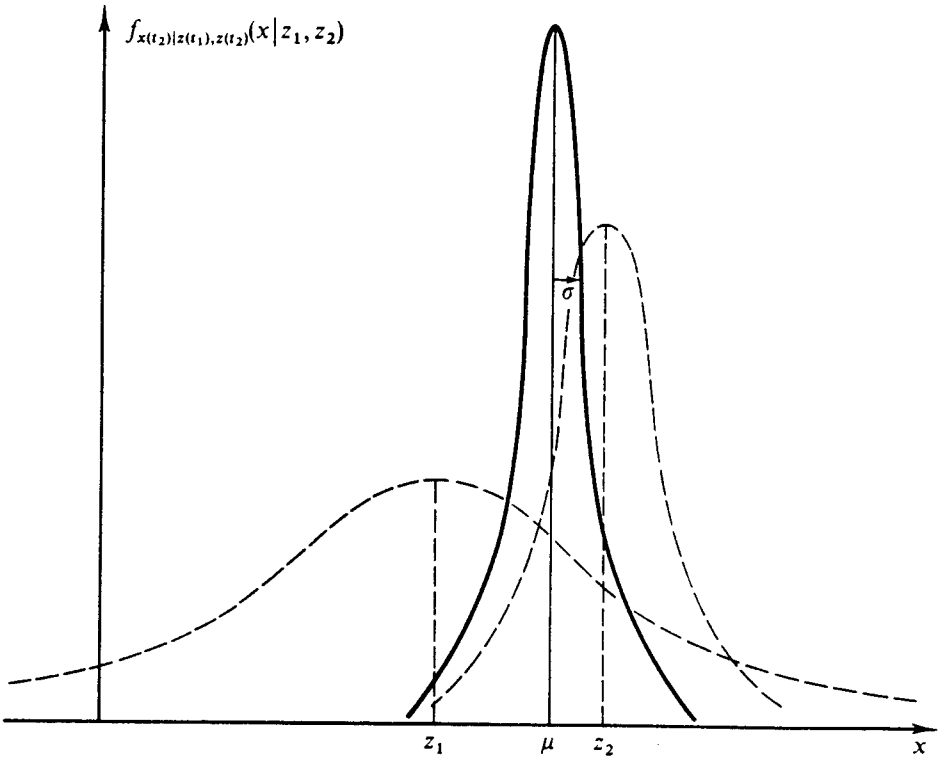

Figure 2 - 10. Conditional density of position based on data z_1 and z_2

$$\frac{1}{\sigma^2} = \frac{1}{\sigma_{z_1}^2} + \frac{1}{\sigma_{z_2}^2} \tag{2.12}$$

Note that, from (2.12), σ is less than either σ_{z_1} or σ_{z_2}, which is to say that the uncertainty in your estimate of position has been decreased by combining the two pieces of information.

Given this density, the best estimate is

$$\hat{x}(t_2) = \mu \tag{2.13}$$

with an associated error variance σ^2. It is the mode, the median and the mean (or, since it is the mean of a conditional density, it is also termed the conditional mean). Furthermore, it is also the maximum likelihood estimate, the weighted least squares estimate, and the linear unbiased estimate whose variance is less than that of any other linear unbiased

estimate. In other words, it is the "**best**" you can do according to just about any reasonable criterion.

After some study, the form of μ given in (2.11) makes good sense. If σ_{z_1} were equal to σ_{z_2}, which is to say you think the measurements are of equal precision, the equation says the optimal estimate of position is simply the average of the two measurements, as would be expected. On the other hand, if σ_{z_1} were larger than σ_{z_2}, which is to say that the uncertainty involved in the measurement z_1 is greater than that of z_2, then the equation dictates "weighting" z_2 more heavily than z_1. Finally, the variances of the estimate is less than σ_{z_1} even if σ_{z_2} is very large: even poor quality data provides some information, and should thus increase the precision of the filter output.

The equation for $\hat{x}(t_2)$ can be rewritten as

$$\hat{x}(t_2) = \left[\frac{\sigma_{z_2}^2}{\sigma_{z_1}^2 + \sigma_{z_2}^2}\right] z_1 + \left[\frac{\sigma_{z_1}^2}{\sigma_{z_1}^2 + \sigma_{z_2}^2}\right] z_2 \tag{2.14}$$

or

$$\hat{x}(t_2) = z_1 + \left[\frac{\sigma_{z_1}^2}{\sigma_{z_1}^2 + \sigma_{z_2}^2}\right] [z_2 - z_1] \tag{2.15}$$

or, in final form that is actually used in Kalman filter implementations (noting that $\hat{x}(t_1) = z_1$),

$$\hat{x}(t_2) = \hat{x}(t_1) + K(t_2)[z_2 - \hat{x}(t_1)] \tag{2.16}$$

where

$$K(t_2) = \frac{\sigma_{z_1}^2}{\sigma_{z_1}^2 + \sigma_{z_2}^2} \tag{2.17}$$

These equations say the optimal estimate at t_2, $\hat{x}(t_2)$, is equal to the best prediction of its value before z_2 is taken, $\hat{x}(t_1)$, plus a correction term of an optimal weighting value times the residual difference between z_2 and the best prediction of its value before it is actually taken, $\hat{x}(t_1)$. It is worthwhile to understand this "predictor-corrector" structure of the filter. Based on all previous information, a prediction of the value that the desired variables and measurement will have at the next measurement time is made. Then, when the next measurement is taken, the difference between it and its predicted value is used to "correct" the prediction of the desired variables.

Using the $K(t_2)$ in Equation (2.17), the variance equation given by (2.12) can be rewritten as

$$\sigma_x^2(t_2) = \sigma_x^2(t_1) - K(t_2)\sigma_x^2(t_1) \tag{2.18}$$

Note that the values of $\hat{x}(t_2)$ and $\sigma_{x_2}^2(t_2)$ embody all the information in $f_{x(t_2)|z(t_1),z(t_2)}(x|z_1, z_2)$. Stated differently, by propagating these two variables, the conditional density of your position at time t_2, given z_1 and z_2, is completely specified.

Thus we have solved the (static) estimation problem example from [45]. This will be of vital importance to the practicality of filter implementation. The filter is plain and simple, "just a computer program in a central processor" [45]. If the reader needs a further example detailing dynamics and propagations, see [45].

2.10.3 Linear Kalman Filter:

Whenever possible, a system will be modeled as a set of linear differential equations of the form [45]:

$$\dot{\mathbf{x}}(t) = \mathbf{F}(t)\mathbf{x}(t) + \mathbf{B}(t)\mathbf{u}(t) + \mathbf{G}(t)\mathbf{w}(t) \tag{2.19}$$

where:

$\mathbf{x}$ = "state" vector (n-dimensional)

$\mathbf{F}$ = homogenous state dynamics matrix (n x n)

$\mathbf{B}$ = control input matrix (n x r)

$\mathbf{u}$ = deterministic control input vector (r-dimensional)

$\mathbf{G}$ = driving noise input matrix (n x s)

$\mathbf{w}$ = white Gaussian driving noise vector (s-dimensional)

Because the deterministic control term $\mathbf{B}(t)\mathbf{u}(t)$ is zero in this research, it will be ignored hereafter. The expected value (i.e. *mean*), of the white Gaussian driving noise vector, $\mathbf{w}(t)$ is:

$$E\{\mathbf{w}(t)\} = \mathbf{0} \tag{2.20}$$

and the noise strength is $\mathbf{Q}(t)$:

$$E\{\mathbf{w}(t)\mathbf{w}^T(t+\tau)\} = \mathbf{Q}(t)\delta(\tau) \tag{2.21}$$

where $\delta(\cdot)$ is the Dirac delta function.

While Equation (2.19) is written in terms of "whole" value state variables, the models used in the thesis are those of *error* states. This choice of state variable results in simpler dynamics equations [10], and (2.19) may be rewritten as [45]:

$$\delta\dot{\mathbf{x}}(t) = \mathbf{F}(t)\delta\mathbf{x}(t) + \mathbf{B}(t)\mathbf{u}(t) + \mathbf{G}(t)\mathbf{w}(t) \tag{2.22}$$

where $\mathbf{x}(t)$ has been replaced by the error state vector $\delta\mathbf{x}(t)$, and all other quantities retain their previous definitions. The topic of error states is explored more fully in the section on extended Kalman filters.

As previously stated, the Kalman filter incorporates sampled-data measurement information from external measuring devices. Irrespective of the type of measuring device, the equation which is used to describe linear measurements is of the form [3]:

$$\mathbf{z}(t_i) = \mathbf{H}(t_i)\mathbf{x}(t_i) + \mathbf{v}(t_i) \tag{2.23}$$

or, in the case of error-state models:

$$\delta\mathbf{z}(t_i) = \mathbf{H}(t_i)\delta\mathbf{x}(t_i) + \mathbf{v}(t_i) \tag{2.24}$$

where, in both cases above, **H** is the *observation* matrix, and **v** is a discrete-time zero-mean white Gaussian measurement noise vector with covariance given by [45]:

$$E\left\{\mathbf{v}(t_i)\mathbf{v}^T(t_j)\right\} = \begin{cases} \mathbf{R}(t_i) \; for \; t_i = t_j \\ \mathbf{0} \; for \; t_i \neq t_j \end{cases} \tag{2.25}$$

The Kalman filter "propagates" the error state and its covariance from the instant in time immediately following the most recent measurement update, t_i^+, to the instant in time immediately preceding the next measurement update, t_{i+1}^-, by numerical integration of the following equations [45]:

$$\dot{\hat{\mathbf{x}}}(t \,/\, t_i) = \mathbf{F}(t)\hat{\mathbf{x}}(t \,/\, t_i) \tag{2.26}$$

$$\dot{\mathbf{P}}(t \,/\, t_i) = \mathbf{F}(t)\mathbf{P}(t \,/\, t_i) + \mathbf{P}(t \,/\, t_i)\mathbf{F}^T(t) + \mathbf{G}(t)\mathbf{Q}(t)\mathbf{G}^T(t) \tag{2.27}$$

The notation for $\hat{\mathbf{x}}(t \,/\, t_i)$ and associated error covariance $\mathbf{P}(t \,/\, t_i)$ indicate the best estimate of **x** and **P** at time t, based on measurements through time t_i. Initial conditions are given as

$$\hat{\mathbf{x}}(t_i \,/\, t_i) = \hat{\mathbf{x}}(t_i^+) \tag{2.28}$$

$$\mathbf{P}(t_i \,/\, t_i) = \mathbf{P}(t_i^+) \tag{2.29}$$

as provided by the measurement update cycle at time t_i. The variables t_i and t_{i+1} indicate the initial and final times for each integration period, respectively.

After propagation, $\hat{\mathbf{x}}(t_{i+1} \,/\, t_i) = \hat{\mathbf{x}}(t_{i+1}^-)$ and $\mathbf{P}(t_{i+1} \,/\, t_i) = \mathbf{P}(t_{i+1}^-)$ are "updated" (meaning that state estimates are revised, based on new measurement information). The pivotal element in the update equations for sample time t_i shown below is the time-varying Kalman filter gain $\mathbf{K}(t_i)$. The $\mathbf{K}(t_i)$ matrix assigns "weights" to the "measurement residual" (the residual consists of the *difference* between the actual measurement and the filter's prediction of the measurement) based on known measurement noise statistics and filter-computed state error covariance from the previous time step. This process is designed to improve the estimate of each element of the state vector. The update equations are [45]:

$$\mathbf{K}(t_i) = \mathbf{P}(t_i^-)\mathbf{H}^T(t_i)\left\{\mathbf{H}(t_i)\mathbf{P}(t_i^-)\mathbf{H}^T(t_i) + \mathbf{R}(t_i)\right\}^{-1} \tag{2.30}$$

$$\hat{\mathbf{x}}(t_i^+) = \hat{\mathbf{x}}(t_i^-) + \mathbf{K}(t_i)\left\{\mathbf{z}_i - \mathbf{H}(t_i)\hat{\mathbf{x}}(t_i)]\right\} \tag{2.31}$$

$$\mathbf{P}(t_i^+) = \mathbf{P}(t_i^-) - \mathbf{K}(t_i)\mathbf{H}(t_i)\mathbf{P}(t_i^-) \tag{2.32}$$

Although the algorithm shown above is generally applicable to any problem which lends itself to a Kalman filtering solution, it is not necessarily the algorithm which is used in practice. It is often advantageous to use a form of the algorithm known as the *U-D* factorization form [45]. In the *U-D* algorithm, the filter covariance matrix is not propagated as a single square array. The **U** and **D** matrices below representing the pre- and post-measurement filter covariances, respectively, are explicitly computed instead [45]:

$$\mathbf{P}(t_i^-) = \mathbf{U}(t_i^-)\mathbf{D}(t_i^-)\mathbf{U}(t_i^-) \tag{2.33}$$

$$\mathbf{P}(t_i^+) = \mathbf{U}(t_i^+)\mathbf{D}(t_i^+)\mathbf{U}(t_i^+) \tag{2.34}$$

where the **U** matrices are upper triangular and unitary (and thus contain ones along the main diagonal), and the **D** matrices are simply diagonal [45]. This form offers several advantages, including numerical stability, improved precision, and guaranteed non-negativity of the computed covariance's eigenvalues [45]. It is the *U-D* form of the Kalman filter algorithm which is implemented in the MSOFE software [53] that is used in this research.

2.10.4 Linearized and Extended Kalman Filtering

Unfortunately, not all problems are adequately described with linear systems driven by white Gaussian noise. In many cases, the most appropriate model is nonlinear. The navigation problem at hand falls squarely into the nonlinear category. Fortunately, a method exists whereby a nonlinear system may be treated in much the same manner as a linear one for a particular class of problems. Suppose that the nonlinear system may be described by [46]:

$$\dot{\mathbf{x}}(t) = \mathbf{f}[\mathbf{x}(t), \mathbf{u}(t), t] + \mathbf{G}(t)\mathbf{w}(t) \tag{2.35}$$

In this case, the state dynamics vector, $\mathbf{f}[\cdot, \cdot, \cdot]$, is a nonlinear function of the state vector $\mathbf{x}(\cdot)$, time t, and the control input (assumed to be zero in this research). The white Gaussian noise is defined exactly as in (2.20) and (2.21), and it still enters the dynamics model linearly. In addition, the measurement equation may also be a nonlinear function of the state vector and time [46]:

$$\mathbf{z}(t_i) = \mathbf{h}[\mathbf{x}(t_i), t_i] + \mathbf{v}(t_i) \tag{2.36}$$

The noise vector **v** is again *zero-mean*, white and Gaussian, entering the measurement equation linearly, and its covariance is described by (2.25).

Recalling that a system must be linear in order to satisfy the assumptions upon which a conventional Kalman filter is based, the nonlinear equations (2.35) and (2.36) must be linearized. The following approach is summarized from [46]:

1. Assume that a nominal state trajectory, $\mathbf{x}_n(t)$, may be generated which satisfies

$$\mathbf{x}_n(t_0) = \mathbf{x}_{n_0} \tag{2.37}$$

and

$$\dot{\mathbf{x}}_n(t) = \mathbf{f}[\mathbf{x}_n(t), \mathbf{u}(t), t] \tag{2.38}$$

where $\mathbf{f}[\cdot, \cdot, \cdot]$ is specified in (2.35), and $\mathbf{u}(t)=\mathbf{0}$.

2. The "nominal" measurements which accompany the nominal trajectory are:

$$\mathbf{z}_n(t_i) = \mathbf{h}[\mathbf{x}_n(t_i), t_i] \tag{2.39}$$

3. The "perturbation" of the state derivative is obtained by subtracting the nominal trajectory from the original nonlinear equation:

$$[\dot{\mathbf{x}}(t) - \dot{\mathbf{x}}_n(t)] = \mathbf{f}[\mathbf{x}(t), \mathbf{u}(t), t] - \mathbf{f}[\mathbf{x}_n(t), \mathbf{u}(t), t] + \mathbf{G}(t)\mathbf{w}(t) \tag{2.40}$$

4. The equation above may be approximated to first order by a Taylor series expansion:

$$\delta\dot{\mathbf{x}}(t) = \mathbf{F}[t; \mathbf{x}_n(t)]\delta\mathbf{x}(t) + \mathbf{G}(t)\mathbf{w}(t) \tag{2.41}$$

where $\delta\mathbf{x}(\cdot)$ represents a first-order approximation of the process $[\mathbf{x}(\cdot) - \mathbf{x}_n(\cdot)]$, and $\mathbf{F}[t; \mathbf{x}_n(t)]$ is a matrix of partial derivatives of **f** with respect to its first argument, evaluated along the nominal trajectory [46]:

$$\mathbf{F}[t;\mathbf{x}_n(t)] = \left.\frac{\partial \mathbf{f}[\mathbf{x},t]}{\partial \mathbf{x}}\right|_{\mathbf{x}\,=\,\mathbf{x}_n(t)} \tag{2.42}$$

5. The perturbation measurement equation is derived in like fashion and is expressed as [46]:

$$\delta\mathbf{z}(t_i) = \mathbf{H}[t_i;\mathbf{x}_n(t_i)]\delta\mathbf{x}(t) + \mathbf{v}(t_i) \tag{2.43}$$

where

$$\mathbf{H}[t_i;\mathbf{x}_n(t_i)] = \left.\frac{\partial \mathbf{h}[\mathbf{x},t_i]}{\partial \mathbf{x}}\right|_{\mathbf{x}\,=\,\mathbf{x}_n(t_i)} \tag{2.44}$$

With the "error-state" model in hand, it is possible to return to the linear filtering theory. An estimate of the whole-valued quantities of interest is obtained from [46]:

$$\hat{\mathbf{x}} \,=\, \mathbf{x}_n(t) + \delta\hat{\mathbf{x}}(t) \tag{2.45}$$

The expression above for the linearized Kalman filter is useful, provided that the linearization assumption is not violated. However, if the nominal and "true" trajectories differ by too large an amount, unacceptable errors may result [46]. It is for this reason that extended Kalman filtering is useful in many cases for which perturbation techniques alone do not suffice. Extended Kalman filtering allows for *relinearizing* about newly declared nominals at each sample time, to enhance the adequacy of the linearization process, and thus of the resulting filter performance as well [46].

The extended Kalman filter equations are summarized below. The reader is referred to [46] for details regarding their derivation. The assumed measurement model equation for an extended Kalman filter development is given by Equation (2.36), where $\mathbf{v}(\cdot)$ is once again *zero-mean*, white and Gaussian, with covariance given by (2.25).

Measurements are incorporated into the extended Kalman filter via the following set of equations [46]:

$$\mathbf{K}(t_i) = \mathbf{P}(t_i^-)\mathbf{H}^T[t_i;\hat{\mathbf{x}}(t_i^-)]\left\{\mathbf{H}[t_i;\hat{\mathbf{x}}(t_i^-)]\mathbf{P}(t_i^-)\mathbf{H}^T[t_i;\hat{\mathbf{x}}(t_i^-)]+\mathbf{R}(t_i)\right\}^{-1} \tag{2.46}$$

$$\hat{\mathbf{x}}(t_i^+) = \hat{\mathbf{x}}(t_i^-)+\mathbf{K}(t_i)\left\{\mathbf{z}_i - \mathbf{h}[\hat{\mathbf{x}}(t_i^-);t_i]\right\} \tag{2.47}$$

$$\mathbf{P}(t_i^+) = \mathbf{P}(t_i^-) - \mathbf{K}(t_i)\mathbf{H}[t_i;\hat{\mathbf{x}}(t_i^-)]\mathbf{P}(t_i^-) \tag{2.48}$$

where

$$\mathbf{H}[t_i;\hat{\mathbf{x}}(t_i^-)] = \left.\frac{\partial \mathbf{h}[\mathbf{x},t_i]}{\partial \mathbf{x}}\right|_{\mathbf{x}=\hat{\mathbf{x}}(t_i^-)} \tag{2.49}$$

The state estimate and covariance are propagated from t_i to t_{i+1} by integrating the following equations [46]:

$$\dot{\hat{\mathbf{x}}}(t \,/\, t_i) = \mathbf{f}[\hat{\mathbf{x}}(t \,/\, t_i), \mathbf{u}(t), t] \tag{2.50}$$

$$\dot{\mathbf{P}}(t \,/\, t_i) = \mathbf{F}[t;\hat{\mathbf{x}}(t \,/\, t_i)]\mathbf{P}(t \,/\, t_i) + \mathbf{P}(t \,/\, t_i)\mathbf{F}^T[t;\hat{\mathbf{x}}(t \,/\, t_i)] + \mathbf{G}(t)\mathbf{Q}(t)\mathbf{G}^T(t) \tag{2.51}$$

where

$$\mathbf{F}[t;\hat{\mathbf{x}}(t/t_i)] = \left.\frac{\partial \mathbf{f}[\mathbf{x}(t),t_i]}{\partial \mathbf{x}}\right|_{\mathbf{x}=\hat{\mathbf{x}}(t/t_i)} \tag{2.52}$$

and the initial conditions are:

$$\hat{\mathbf{x}}(t_i \,/\, t_i) = \hat{\mathbf{x}}(t_i^+) \tag{2.53}$$

$$\mathbf{P}(t_i \,/\, t_i) = \mathbf{P}(t_i^+) \tag{2.54}$$

The equations shown above for the extended Kalman filter are programmed into the MSOFE shell [53] for the problem defined by this thesis. It is the fact that the extended

Kalman filter is relinearized about each successive estimate of the state $\hat{\mathbf{x}}(t)$ which "enhances the validity of the assumption that deviations from the reference (nominal) trajectory are small enough to allow linear perturbation techniques to be employed" [46].

2.11 Single Pseudolite During the Landing Approach

A pseudolite is a ground-based "satellite" which provides very accurate pseudorange information on a precision approach because of its fixed location and its proximity to the aircraft. The placement of the pseudolite was chosen based on the near/far issue. The near/far issue determines the distance a pseudolite has to be located from the runway in order for it not to interfere with the normal satellite transmissions. Basically it is a 12 to 1 ratio, which says that if a pseudolite is place 1 nm from the runway, it can be received up to 12 nms from the runway without interference [43]. Various pseudolite locations about the runway, each being 1 nm from the runway, were tried without significant improvement. By no means is the location of the single pseudolite optimal. Several factors, including the location of the satellites overhead, would have to be taken into account to find the optimal location for the pseudolite.

The aircraft is assumed to be following a precision approach pattern, landing at Wright-Patterson AFB, OH as found in [16]. The pseudolite measurement is available and being processed once every second beginning at T = 3641 sec. It should be noted that the pseudolite is considered to be a fifth measurement. That is to say, it is like having a fifth satellite providing measurements. The designer must maintain the importance of geometry if it is necessary to replace one of the existing SVs overhead with a ground-based pseudolite. The GPS receiver must simultaneously maintain an adequate (minimal)

horizontal dilution of precision (HDOP) and PDOP at all times during the precision approach. Readers may wish to consult [13] for further reference on pseudolites.

2.12 Summary

This chapter has presented the basic theory of an RLG INS, GPS, DGPS, barometric altimeter, radar altimeter, and pseudolites. The definition of an ILS precision approach was discussed. Reference frames and coordinate transformations used in this thesis have also been defined. A Kalman filter example from [45] was given and linear, linearized and extended Kalman filter fundamentals were discussed. Chapter 3 will describe the design methodology and error models of the RLG INS, GPS, DGPS, barometric altimeter, and radar altimeter avionics used in this thesis for MSOFE simulations.

III. Design Methodology and Error Models

This chapter describes the set-up of the MSOFE computer simulation for the Differential Landing System Model (DLSM) error model. This chapter also describes the technique used to determine which "real-world" *(true)* satellite vehicle (SV) ephemeris data was used during MSOFE simulation. A brief description of the use of PROFGEN [52] to generate a transport and single engine aircraft flight profile will also be discussed. As with Chapter 2, the background work done by Gray [27] laid the foundations for large portions of this chapter.

3.1 Introduction to MSOFE

The name "MSOFE" is an acronym meaning "Multimode Simulation for Optimal Filter Evaluation." MSOFE is a general-purpose, multimode simulation program for designing integrated systems that employ optimal (Kalman) filtering techniques and for evaluating their performance [53]. Its general-purpose construction allows specific user problems to be simulated more quickly and at less cost than without its use. MSOFE has been designed to support a wide variety of system simulation and filter evaluation efforts. It provides two major operating modes:

1) Monte Carlo simulation: to generate multiple sample time histories of system truth states, filter states, and filter estimation errors, including nonlinear effects; usable for linear and extended Kalman filters;

2) Covariance simulation: to generate time histories of the second-order statistics (covariances) of system truth states, filter states, and filter estimation errors, under the assumption of linear (or linearized) models.

The Monte Carlo and covariance simulation modes of MSOFE are complementary to one another. The covariance mode can generate filter performance statistics via a single run, whereas the Monte Carlo mode requires several sample runs (say, 15 or more) to generate meaningful statistics for a given scenario. However, the covariance mode is limited to linear (or linearized) systems, whereas the Monte Carlo mode can represent nonlinear as well as linear dynamic and measurement processes. In addition, the Monte Carlo mode provides better visibility into the detailed workings of the filter models and computation processes, and can easily be reduced to a deterministic mode (by suppressing noise sampling) when required. Monte Carlo runs (15 runs) were solely performed in this thesis for each case unless otherwise noted.

MSOFE provides a general-purpose simulation environment in which the user embeds a specific problem by supplying up to 14 problem-specific subroutines. The collective set of 14 user routines is named USOFE. The name MSOFE generally references the whole program, that is the union of 63 nonvarying routines in the CSOFE "core part" with the 14 routines in the USOFE "user part". From one problem to the next, the 14 routines of USOFE vary greatly, whereas the 63 routines of CSOFE vary only in the sizes assigned to the vectors and arrays. With MSOFE, users can quickly apply their engineering skills to important filter design issues, rather than to the time-consuming development of support tools [53].

The multimode simulation program MSOFE is part of an existing set of tools developed by [53] to support the design, analysis, and evaluation of a wide variety of integrated systems. Other tools that were used in this thesis were:

- PROFGEN -- a trajectory generator for simulating the translational and rotational dynamics of an aircraft in flight [52].
- MPLOT -- a postprocessor program for satisfying the plotting needs of both MSOFE and PROFGEN, e.g. for computing ensemble statistics from Monte Carlo runs [70].

3.1.1 MSOFE Computer Requirements

MSOFE is written in ANSI standard FORTRAN 77 to provide full portability across a wide variety of computers and compilers. MSOFE was run on a 486 PC and also on a SPARC 10 UNIX machine for this thesis. MSOFE is fully compliant with the ANSI standard except for the way it manages global common blocks. These blocks, which are constructed in the form of individual files, one file per block, are inserted in the code at designated locations. This is called an "INCLUDE" approach, borrowing this name from FORTRAN 90, where this ability is an integral part of that standard. The INCLUDE ability automates common block array sizing and aids program maintenance. It can be easily eliminated or modified for non-supporting computers. This exception to ANSI compliance was permitted because of its usefulness and its wide availability as an extension to most FORTRAN implementations.

The principal system requirements necessary to run MSOFE on a given computer are:

- FORTRAN-77 compiler and linker;
- Ten input/output files open concurrently;
- Program and data memory to load the entire program at one time (it is not overlaid): approximately 200,000 words;
- Output data storage of approximately 40 (Mb) *per hour* in Monte Carlo mode was not uncommon during simulations of this thesis (15 Monte Carlo runs).

MSOFE allows models of any size, limited only by the amount of computer memory available and perhaps by array-size restrictions present in the FORTRAN compiler. There are no size restrictions whatsoever within the core code.

In order for the reader to see the "Big-MSOFE-Picture", Figure 3 - 1 (Section 3 .2) and Figure 3 - 2 (Section 3.3) illustrate the overall goal: DGPS and radar altimeter measurement information must be fed into an extended Kalman filter to determine the errors, δx, in the INS. As stated earlier, our extended Kalman filter *estimates* the true error, δx, of the INS with an output we note as "$\delta \hat{x}$". Once the best estimates, $\delta \hat{x}$, are determined by our extended Kalman filter, we then subtract them (in a feed-forward approach) from the output of the simulated INS blackbox. The feedforward approach is utilized in this thesis due to current Federal Aviation Administration (FAA) restrictions on providing "feedback" to the INS. Without going into a lengthy technical discussion about the differences between feedforward or feedback, feedforward was chosen because it is the most conservative choice, especially if one does not have faith that the extended Kalman filter feedback corrections will always be reliable. The author's belief is that, at the present time, the FAA does not want to "lose" the "pure" INS output during precision approaches. Because of this FAA requirement, a feedforward approach will be utilized in this thesis.

3.2 Introduction to PROFGEN

PROFGEN computes position, velocity, acceleration, attitude and attitude rate for an aircraft moving over the earth [52]. Position is given as (geographic) latitude, longitude and altitude. Velocity with respect to earth is coordinatized and presented in a local-

vertical frame. Acceleration consists of velocity rates-of-change summed with Coriolis effects and gravity. Attitude consists of roll, pitch and yaw: the Euler angles [52].

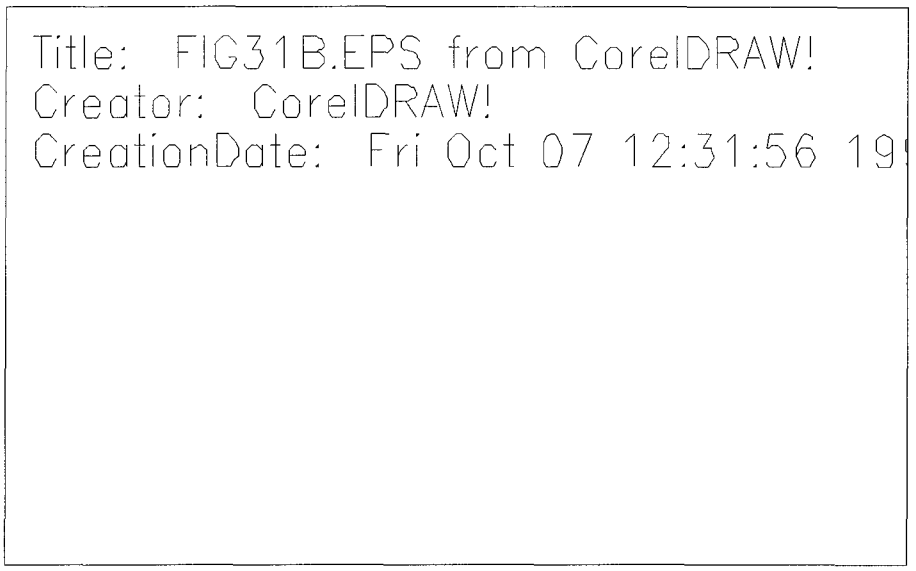

Figure 3 - 1. Overall Differential Landing System Model (DLSM) Description

PROFGEN models a point mass responding to maneuver commands specified by the user. These maneuvers are available:

- Vertical turns (pitch up or down)
- Horizontal turns (yaw left or right)
- Sinusoidal "jink" heading changes (oscillates left and right)
- Straight flights (great circle or rhumb line path)

PROFGEN is used to create an extended flight profile by concatenating a sequence of maneuvers chosen from the basic four. The user specifies how long each maneuver shall last and thereby divides the flight profile into flight segments [52]. Up to fifty flight segments, may be strung together to produce a varied total profile. The final values of the variables in each segment are passed along as the initial values for the start of the next

segment thereby creating uninterrupted time histories for all output variables. The segments for the "Tanker" flight profile used in this thesis are shown in Table 3 - 1. To augment the research performed by Gray [27] and extend the research to a wider variety of aircraft, a flight profile was also generated for a single engine aircraft that is instrument rated. The use of a smaller aircraft will establish the feasibility of utilizing a low-cost INS with DGPS measurement corrections to achieve a precision approach for civil aviation aircraft. Flight segments for the single engine aircraft profile are shown in Table 3 - 2. The earth is modeled as a perfect ellipsoid having values for eccentricity, semimajor axis length, spin velocity and gravitational constant equal to those of the DOD World Geodetic System 1972 [52].

A PROF_IN file (PROF_IN is the input file for PROFGEN [52]) was created for a Boeing 707 (KC-135) aircraft based on inputs from [4,51,66], and a similar input file was created for a Piper Cherokee Warrior aircraft based on inputs from Captain David Kyger [42]. Both the tanker and the single engine aircraft profiles consisted of a take-off from Wright-Patterson AFB, a gradual climb to cruising altitude, and several 45° turns to return each aircraft for a precision approach landing to the airfield.

PROFGEN reads in PROF_IN, and outputs a binary flight file called "FLIGHT" which contains the flight profile variables shown in Table 3 - 3. Looking at this table may seem cryptic, but note in the far right column labeled "WRITTEN TO FLIGHT" are the parameters written to the Tanker profile or the single engine aircraft profile (which are labeled "FLIGHT" in PROFGEN). Those variables followed by the word "YES" are output to the Flight file.

Segment Number	Start Time (sec)	Segment Length (sec)	Nominal Path	Centrifugal Accel (max in g's)	Accel along Velocity vector	ΔRoll (deg)	ΔPitch (deg)	ΔHeading (deg)
1	0	3	STRT	0	0	0	0	0
2	3	30	STRT	0	0.262	0	0	0
3	33	160	VERT	0.21	3.80E-02	0	5	0
4	193	329	STRT	0	1.00E-02	0	0	0
5	522	5	VERT	0.9	-8.75E-02	0	-5	0
6	527	25	HORZ	0.9	1.00E-02	0	0	45
7	552	371	STRT	0	1.00E-02	0	0	0
8	923	35	HORZ	0.9	0	1	0	45
9	958	400	STRT	0	8.00E-03	0	0	0
10	1358	35	HORZ	0.9	0	1	0	45
11	1393	340	STRT	0	0	0	0	0
12	1733	35	HORZ	0.9	0	0	0	45
13	1768	600	JINK	3.41E-02	0	0	200 (sec) for JINK	2
14	2368	35	HORZ	0.9	0	0	0	45
15	2403	120	VERT	0.311	0	0	-5	0
16	2523	35	VERT	0.9	0	0	5	0
17	2558	372	STRT	0	3.00E-03	0	0	0
18	2930	70	HORZ	0.9	-0.125	0	0	90
19	3000	40	VERT	0.63	-8.50E-02	0	-5	0
20	3040	35	VERT	0.9	0	0	5	0
21	3075	360	VERT	0.9	1.50E-02	0	-1.75	0
22	3435	45	HORZ	0.9	-5.00E-02	1	0	-45
23	3480	104	VERT	0.9	0	0	1.75	0
24	3584	35	HORZ	0.9	-5.00E-02	1	0	45
25	3619	39	VERT	0.24	-0.1882	0	-3	0
26	3658	25	HORZ	0.9	0	0	0	45
27	3683	242	STRT	0	0	0	0	0

Table 3 - 1. PROFGEN Segments for "Tanker" Flight Profile

Segment Number	Start Time (sec)	Segment Length (sec)	Nominal Path	Centrifugal Accel (max in g's)	Accel along Velocity vector	ΔRoll (deg)	ΔPitch (deg)	ΔHeading (deg)
1	0	42	STRT	0	0.1	0	0	0
2	42	130	VERT	3	0	0	3.7	0
3	172	5	VERT	3	0	0	-3.7	0
4	177	120	VERT	3	0	0	3.59	0
5	297	5	VERT	3	0	0	-3.59	0
6	302	133	VERT	3	0	0	3.24	0
7	435	5	VERT	3	0	0	-3.24	0
8	440	150	VERT	3	0	0	2.87	0
9	590	5	VERT	3	0	0	-2.87	0
10	595	170	VERT	3	0	0	2.58	0
11	765	5	VERT	3	0	0	-2.58	0
12	770	60	STRT	0	3.85E-02	0	0	0
13	830	300	STRT	0	0	0	0	0
14	1130	15	HORZ	3	0	0	0	45
15	1145	110	STRT	0	0	0	0	0
16	1255	15	HORZ	3	0	0	0	45
17	1270	260	STRT	0	0	0	0	0
18	1530	15	HORZ	3	0	0	0	45
19	1545	530	STRT	0	0	0	0	0
20	2075	15	HORZ	3	0	0	0	45
21	2090	500	STRT	0	0	0	0	0
22	2590	15	HORZ	3	0	0	0	45
23	2605	520	STRT	0	0	0	0	0
24	3125	15	HORZ	3	0	0	0	45
25	3140	300	STRT	0	0	0	0	0
26	3440	15	HORZ	3	0	0	0	45
27	3455	50	STRT	0	0	0	0	0
28	3505	15	HORZ	3	0	0	0	45
29	3520	320	VERT	3	-0.7E-02	0	-5.095	0
30	3840	5	VERT	3	0	0	5.095	0
31	3845	75	VERT	3	-2.3E-02	0	-2.0	0

Table 3 - 2. PROFGEN Segments for Single Engine Aircraft Flight Profile

	VARIABLE	DIM	PRINTED NAME(s)	PRINTED TO PROF_OUT	WRITTEN TO FLIGHT
0	time	1	TIME	YES	YES
1	terrestrial longitude	1	TLON	YES	YES
2	geographic latitude	1	GLAT	YES	YES
3	altitude	1	ALT	YES	YES
4	celestial longitude	1	CLON		
5	wander angle	1	ALPHA	YES	YES
6	heading	1	HEAD		
7	roll	1	ROLL	YES	YES
8	pitch	1	PITCH	YES	YES
9	yaw	1	YAW	YES	YES
10	terrestrial longitude rate	1	DTLON		
11	geographic latitude rate	1	DGLAT		
12	altitude rate	1	DALT		
13	celestial longitude rate	1	DCLON		
14	wander angle rate	1	DALPHA	YES	YES
15	heading rate	1	DHEAD		
16	roll rate	1	DROLL	YES	YES
17	pitch rate	1	DPITCH	YES	YES
18	yaw rate	1	DYAW	YES	YES
19	signed earth velocity magnitude	1	VET		
20	signed earth velocity magnitude rate	1	DVET		
21	position in frame i (2) (3)	3	RI		
22	earth velocity in frame i	3	VEI		
23	inertial velocity in frame i (4)	3	VII		
24	gravitation in frame i	3	GNI		
25	specific force in frame i (5)	3	FII		
26	angular rate, b/i in frame i	3	WBII		
27	DCM to inertial from body	3X3	CIB		
28	DCM to inertial from earth (6)	3X3	CIE		
29	angular rate, e/i in frame e	3	WEIE		
30	position in frame e	3	RE		
31	earth velocity in frame e	3	VEE		
32	inertial velocity in frame e	3	VIE		
33	gravity in frame e	3	GYE		
34	specific force in frame e	3	FIE		
35	angular rate, b/i in frame e	3	WBIE		
36	DCM to earth from body	3X3	CEB		
37	DCM to earth from nav	3X3	CEN		
38	angular rate, n/e in frame n	3	WNEN		
39	position in frame n	3	RN		
40	earth velocity in frame n	3	VEN	YES	YES
41	inertial velocity in frame n	3	VIN		
42	gravity in frame n	3	GYN		
43	specific force in frame n	3	FIN	YES	YES
44	angular rate, b/i in frame n	3	WBIN		
45	DCM to nav from body	3X3	CNB		
46	angular rate, b/n in frame b	3	WBNB		
47	position in frame b	3	RB		
48	earth velocity in frame b	3	VEB		
49	inertial velocity in frame b	3	VIB		
50	gravity in frame b	3	GYB		
51	specific force in frame b	3	FIB		
52	angular rate, b/i in frame b	3	WBIB		

Table 3 - 3. PROFGEN Flight Profile Outputs

3.3 The DLSM Computer Model

The NRS model [50,55] was used to model the DLSM computer model. The DLSM is divided into two parts for computer modeling, the truth model and the filter model. The truth model represents computer-generated simulation of the real-world error characteristics found in avionics black-boxes and the environment in which the units operate. The research was accomplished through computer simulation; therefore, the truth model will simulate the errors in true avionics hardware (INS, DGPS, Baro, Radar Altimeter) black-boxes. The truth model generates the measurement updates for the DLSM flter, the true flight profile of the aircraft, and a state variable baseline for evaluating filter performance [50,55]. The truth model consists of 61 error states about their nominal values. The filter model represents the DLSM as it could be hosted on-board an aircraft computer. The DLSM filter model is a 13-state extended Kalman filter developed through order reduction of the 95-state truth model of [50,55]. An advantage of using only 13 states is that the current state-of-the-art aircraft host computers can handle the computational requirements.

The block diagram, Figure 3 - 2 explains the interaction of the filter and truth models in MSOFE. A simulated flight profile is provided by PROFGEN [52], and the U.S. Coast Guard GPS Bulletin Board Service (BBS) [25] provides true SV ephemeris data for any SV. Use of the "real-world" ephemeris replaced the prior FORTRAN ORBIT functions used by past researchers at AFIT [3,50,55,65]. The best four SV were chosen by using System Effectiveness Model (SEM) software [19] and selecting the best (lowest) position dilution of precision (PDOP). With this information, the truth model is able to simulate a

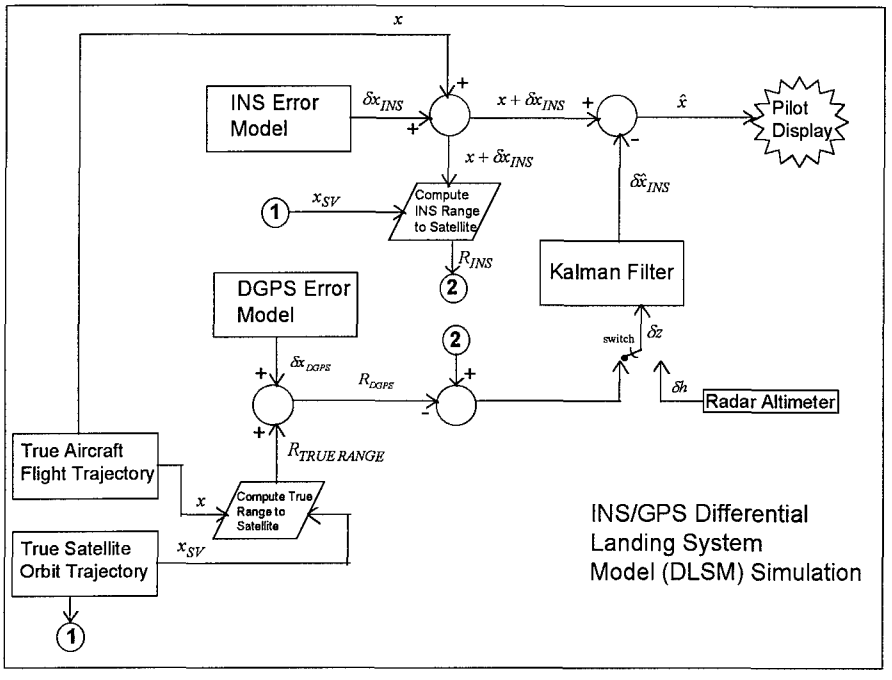

Figure 3 - 2. Truth and Filter Model Block Diagram

real world INS navigation solution, $x + \delta x_{INS}$, and generate the real world DGPS and radar altimeter measurements, R_{DGPS} and R_{ralt} respectively. The DLSM filter in Figure 3 - 2 is represented by the Kalman filter block. Corrections from the DLSM filter are subtracted from the INS navigation solution to generate the best possible navigation solution available, $\hat{x} = x + \delta x_{INS} - \delta \hat{x}_{INS}$ [50,55]. The switch in Figure 3 - 2 does not imply "either/or", instead it implies the use of radar altimeter measurements as well as DGPS receiver outputs. Now that the MSOFE implementation of the DLSM filter has been explained, the truth and filter models for the DGPS, radar altimeter and the INS subsystems will be described.

3.4 DLSM Model Description

This section presents the truth and filter model propagation and measurement equations, (2.35) and (2.36), respectively. The following presentation will be divided up by navigation subsystems with most parts taken directly from [55]. First the INS portion of the equations will be presented, then the DGPS, followed by the radar altimeter. Before the different navigation subsystems are individually described, the high-level state and measurement equations for the DLSM filter are provided, followed by those for the truth model. Equations (3.1) and (3.2) show how the different navigation subsystems models combine to form a single DLSM filter model:

$$\delta\dot{x}_f = \begin{bmatrix} F_{INS_f} & 0 \\ 0 & F_{DGPS_f} \end{bmatrix} \delta x_f + \begin{bmatrix} w_{INS_f} \\ w_{DGPS_f} \end{bmatrix} \tag{3.1}$$

$$\delta z_f = \begin{bmatrix} H_{INS_f} \\ H_{DGPS_f} \end{bmatrix} \delta x_f + \begin{bmatrix} v_{INS_f} \\ v_{INS_f} \end{bmatrix} \tag{3.2}$$

As stated earlier, the overall filter model consists of 13 states; 11 for the INS and 2 for the DGPS. A description of the 13-state vector, δx_f, implemented in the filter model can be found in Table A.4 in Appendix A. References to further descriptions of the sub-matrices in the filter equations can be found in Table 3 - 4. The barometric altimeter aiding measurements are considered to be INS measurements, while the DGPS and radar altimeter measurements are the respective updates for the baro/inertial system from the DGPS and radar altimeter.

Filter Model	Location of Description	Truth Model	Location of Description
F_{INS_f}	Section 3.4.1.3	$F_{INS\,Filter}$	Section 3.4.1.3, 3.4.2.1
-	-	$F_{INS_{t1}}$	Section 3.4.1.2
-	-	$F_{INS_{t2}}$	Section 3.4.1.2
F_{DGPS_f}	Section 3.4.2.2	F_{DGPS_t}	Section 3.4.2.1
w_{INS_f}	Section 3.4.1.3	w_{INS_t}	Section 3.4.1.2
w_{DGPS_f}	Section 3.4.2.2	w_{DGPS_t}	Section 3.4.2.1
H_{INS_f}	Section 3.4.1.4	H_{INS_t}	Section 3.4.1.4
H_{DGPS_f}	Section 3.4.2.3	H_{DGPS_t}	Section 3.4.2.3

Table 3 - 4. References for the Sub-Matrices of the DLSM Truth and Filter

The propagation and measurement equations for the DLSM *truth* model is presented in similar fashion below:

$$\delta\dot{x}_t = \begin{bmatrix} F_{Filter} & F_{INS_{t1}} & 0 \\ 0 & F_{INS_{t2}} & 0 \\ 0 & 0 & F_{DGPS_t} \end{bmatrix} \delta x_t + \begin{bmatrix} w_{Filter} \\ w_{INS_t} \\ w_{DGPS_t} \end{bmatrix} \tag{3.3}$$

$$\delta z_t = \begin{bmatrix} H_{INS_t} \\ H_{DGPS_t} \end{bmatrix} \delta x_t + \begin{bmatrix} v_{INS_t} \\ v_{DGPS_t} \end{bmatrix} \tag{3.4}$$

The DLSM truth model consists of the original thirteen states of the filter model (represented by F_{Filter} and w_{Filter}), augmented by additional INS and DGPS states (the radar altimeter measurements were modeled as corrupted only by white noise, therefore no additional states were necessary). The total number navigation subsystems states is 61; 39 INS states, and 22 DGPS states. Tables A.1 - A.3, in Appendix A, provide a full

description of each individual state of the truth model. Also Tables B.1 - B.5 and Tables B.6 - B.7 in Appendix B have a complete listing of the components of the F and the Q noise strengths associated with the w vector components in Equation (3.3).

There is one crucial difference between the first thirteen states of the filter model and the first thirteen states of the truth model [50,55]. The filter model dynamics driving noise and measurement noise do not correlate exactly with those of the first thirteen states of the truth model. To achieve good tuning against the truth model, the filter model noise statistics values have been altered [50,55]. The following sections will provide a detailed presentation into the exact make-up of the truth and filter model propagation and measurement equations for all navigation subsystems used in this thesis.

3.4.1 The Inertial Navigation System (INS) Model.

This section presents the truth and filter models used for the INS. The INS model is a strapped-down wander azimuth system that senses aircraft motion via gyros and accelerometers and is used as the primary source for navigation [50]. The INS model has been derived from a medium accuracy RLG INS 93-state model [1,41]. First, the original 93-state model will be presented, followed by the reduced-ordered 39-state truth and 11-state filter models. After the INS truth and filter state equations have been defined, barometric altimeter measurement equations will be presented.

3.4.1.1 The 93-State LN-93 Error Model.

The 93-state Litton INS MSOFE computer model has been generated by the Wright Laboratories, Avionics Directorate, Avionics System Integration and Research Team (ASIRT). Their development uses both past AFIT research and INS vendor [41]

documentation to "fine-tune" past modeling efforts [55,65,72]. The 93-state model generates a high number of documented error sources that are found in the Litton wander-azimuth LN-93 INS [41]. These errors are described using six categories of states [50,55]:

$$\delta x = \left[\delta x_1^T \; \delta x_2^T \; \delta x_3^T \; \delta x_4^T \; \delta x_5^T \; \delta x_6^T\right]^T \tag{3.5}$$

where δx is a 93 × 1 column vector and:

δx_1: represents the "general" error vector containing 13 position, velocity, attitude, and vertical channel errors (representative of a Pinson model of INS error characteristics).

δx_2: consists of 16 gyro, accelerometer, and baro-altimeter exponentially time-correlated errors, and "trend" states. These states are modeled as first order Markov processes in the truth (system) model.

δx_3: represents gyro bias errors. These 18 states are modeled as random constants in the truth model.

δx_4: is composed of the accelerometer bias error states. These 22 states are modeled in exactly the same manner as the gyro bias states.

δx_5: depicts accelerometer and gyro initial thermal transients. The 6 thermal transient states are first order Markov processes in the system model.

δx_6: models the gyro compliance errors. These 18 error states are modeled as biases in the system model.

The 93-State Litton model state space differential equation is given by:

$$\begin{Bmatrix} \delta\dot{x}_1 \\ \delta\dot{x}_2 \\ \delta\dot{x}_3 \\ \delta\dot{x}_4 \\ \delta\dot{x}_5 \\ \delta\dot{x}_6 \end{Bmatrix} = \begin{bmatrix} F_{11} & F_{12} & F_{13} & F_{14} & F_{15} & F_{16} \\ 0 & F_{22} & 0 & 0 & 0 & 0 \\ 0 & 0 & 0 & 0 & 0 & 0 \\ 0 & 0 & 0 & 0 & 0 & 0 \\ 0 & 0 & 0 & 0 & F_{55} & 0 \\ 0 & 0 & 0 & 0 & 0 & 0 \end{bmatrix} \begin{Bmatrix} \delta x_1 \\ \delta x_2 \\ \delta x_3 \\ \delta x_4 \\ \delta x_5 \\ \delta x_6 \end{Bmatrix} + \begin{Bmatrix} w_1 \\ w_2 \\ 0 \\ 0 \\ 0 \\ 0 \end{Bmatrix} \tag{3.6}$$

A full description of the sub-matrices for this equation is given in the Litton LN-93 manual [41]. This large state model represents the most accurate model available for the LN-93 navigation errors [50,55].

3.4.1.2 The 39-State INS Truth Model.

The 93-state model is a very accurate representation of the INS error characteristics, but the high dimensionality of the state equations makes the model very CPU-intensive for "first-look" projects. The intent of this thesis is to evaluate performance characteristics associated with a particular *class* of INS (medium precision or lower precision). Previous AFIT theses have demonstrated that reduced-ordered truth models can be used in place of the 93-state truth model without losing a significant degree of accuracy [50,55,58]. Therefore the INS truth model has been reduced to a 39-state model. The reduced-ordered model retains only the truly essential states from Equation (3.6). The truth model state space equation is defined in Equation (3.7):

$$\begin{Bmatrix} \delta\dot{x}_1 \\ \delta\dot{x}_2 \\ \delta\dot{x}_3 \\ \delta\dot{x}_4 \end{Bmatrix} = \begin{bmatrix} F_{11} & F_{12} & F_{13} & F_{15} \\ 0 & F_{22} & 0 & 0 \\ 0 & 0 & 0 & 0 \\ 0 & 0 & 0 & 0 \end{bmatrix} \begin{Bmatrix} \delta x_1 \\ \delta x_2 \\ \delta x_3 \\ \delta x_4 \end{Bmatrix} + \begin{Bmatrix} w_1 \\ w_2 \\ 0 \\ 0 \end{Bmatrix} \tag{3.7}$$

It should be noted that the INS truth state vector δx, is a 39-state vector. The four components of δx do not directly correlate to the first four components of the 93-state Litton model [50,55]. For a complete listing of the 39 states and how they relate to those in [41], see Tables A.1 and A.2 in Appendix A.

3.4.1.3 The 11-State INS Filter Model.

The INS filter model retains the essential states from the 39-state truth model. Through past AFIT research, the 11-state INS filter has been shown to perform adequately when given frequent DGPS measurement updates [50,55,58]. Table A.4 in Appendix A shows the 11 states used for the INS filter model. The final INS filter dynamics submatrix, **F**, as well as process noise strength **Q** and measurement noise covariance **R,** can be found in Appendix I.

3.4.1.4 INS Measurement Model.

The two measurements that are used to update the filter are the barometric altimeter and the radar altimeter. The barometric altimeter signal is used to correct for inherent instabilities of the vertical channel in the filter, and the radar altimeter is used during landing approaches when altitudes are below 3000 feet above ground level (AGL). The barometric altimeter measurement will be presented first, followed by the radar altimeter measurement. Since the DLSM filter is an error state filter, it is necessary to develop difference measurement update equations for all the measurements. The barometric altimeter measurement equation is based on the difference between the INS-predicted altitude, Alt_{INS} and the barometric altimeter-predicted altitude Alt_{Bar}:

$$\delta z_{Alt} = Alt_{INS} - Alt_{Bar} \tag{3.8}$$

Therefore it is necessary to develop the two separate measurement signals that will be differenced to attain the proper measurement update for the error state filter [50,55]. The INS-predicted altitude is the sum of the true altitude, h_t, and the INS error in vehicle altitude above the reference ellipsoid, δh. The barometric altimeter reading is modeled as the sum of the true altitude, h_t, the total time-correlated error in the barometric altimeter, δh_B, and a random measurement noise, v. The difference measurement update signal is formed in Equation (3.9) by subtracting the INS-predicted altitude from the barometric altimeter altitude:

$$\begin{aligned} \delta z_{Alt} &= Alt_{INS} - Alt_{Bar} \\ &= [h_t + \delta h] - [h_t + \delta h_B - v] \\ &= \delta h - \delta h_B + v \end{aligned} \tag{3.9}$$

Note that, since v is assumed *zero* mean, white gaussian noise, statistically speaking, one can choose v with either a plus "+" or minus "-" coefficent . The author chooses the coefficent carefully so that the end result shows a plus "+v" sign.

This completes the presentation of the INS truth and filter state equations as well as the INS measurement equations. The next section will develop similar equations for the radar altimeter used in this thesis.

3.4.2 Radar Altimeter Model.

As a "first-cut" model of the radar altimeter, the measurement equation is based on the

difference between the INS predicted altitude, Alt_{INS} and the radar altimeter predicted altitude, Alt_{Ralt}:

$$\begin{aligned} \delta z_{ALT} &= ALT_{INS} - ALT_{Ralt} \\ &= [h_t + \delta h] - [h_t - v] \\ &= \delta h + v \end{aligned} \tag{3.10}$$

Note that the errors in the radar altimeter are represented totally as white noise, with no time-correlated component at all. Though admittedly only a first-cut model, it should be sufficient to demonstrate important performance trends.

The radar altimeter measurement noise variance, R_{Filter} or R_{True}, is a function of aircraft altitude above ground level (AGL). The filter model noise variance from [31]:

$$R_{Truth} = \left\{[0.01]^2 * [Radar\ Altitude_{True(AGL)}]^2\right\} + 0.25_{Bias} \tag{3.11}$$

and the truth model noise variance is the same:

$$R_{Truth} = \left\{[0.01]^2 * [Radar\ Altitude_{True(AGL)}]^2\right\} + 0.25_{Bias} \tag{3.12}$$

Note that R_{Filter} and R_{Truth} are both time-varying rather than constant, due to the altitude dependency.

This completes the presentation of the radar altimeter measurement and noise variance equations. The next section will develop truth, filter and measurement equations for the Differential Global Positioning System (DGPS) used in this thesis.

3.4.3 The Differential Global Positioning System (DGPS) Model.

The DGPS navigation system used is based on electromagnetic signals transmitted from orbiting GPS satellites. This model has been developed throughout research at AFIT, and many of its fundamental concepts are addressed in a variety of sources [44,50.55,63,65]. GPS generates navigation information by acquiring the range to

multiple satellites of known position, called "*pseudoranges*". Inherent in the pseudorange are errors caused by ionospheric and tropospheric delays, selective availability errors incorporated by the United States, satellite clock biases, receiver noise, and ephemeris errors [4,38]. These errors work together to dilute the accuracy of standard GPS to a level which is unacceptable for aircraft precision approaches. By incorporating the *differential* corrections to the standard GPS pseudoranges, one can achieve much higher navigation precision. Several error sources can be eliminated or significantly reduced because these errors are common to both the reference station receiver and the aircraft receiver. These errors are composed of the satellite's clock error, errors in the satellites's broadcasted ephemeris data, and signal propagation delays that are not accounted for by the receiver's measurements or modeling. The dominant error source is selective availability (SA). SA is a program for controlling the accuracy of pseudorange measurements. The user is in essence given a false pseudorange for each satellite so the resulting measurement is in error by a controlled amount. The level is chosen to give navigation solutions that meet a specified accuracy. When two receivers in the same vicinity (within about 100 nautical miles) are using the same set of four satellites, the above errors will be common to both and can be removed or essentially eliminated by differential techniques [4,38]. The navigation information passed to the DLSM filter is the respective range and ephemeris data position to each of four satellites, with differential corrections applied to provide more accurate information [55]. The next three sections present all the necessary equations to define the DGPS truth and filter error models fully.

3.4.3.1 *The 22-State DGPS Truth Model*

There are five types of error sources that are modeled in the DGPS truth model state equations. The first two states represent the errors in the user clock and are modeled as follows:

$$\begin{Bmatrix} \delta\dot{R}_{clk_U} \\ \delta\dot{D}_{clk_U} \end{Bmatrix} = \begin{bmatrix} 0 & 1 \\ 0 & 0 \end{bmatrix} \begin{Bmatrix} \delta R_{clk_U} \\ \delta D_{clk_U} \end{Bmatrix} \tag{3.13}$$

where

δR_{clk_U} = range equivalent of user clock bias

δD_{clk_U} = velocity equivalent of user clock drift

The initial state estimates and covariances for these states were chosen to be consistent with previous AFIT research, [50,55,63,65] and are:

$$\begin{Bmatrix} \delta\hat{R}_{clk_U}(t_0) \\ \delta\hat{D}_{clk_U}(t_0) \end{Bmatrix} = \begin{bmatrix} 0 \\ 0 \end{bmatrix} \tag{3.14}$$

and

$$P_{\delta R_{clk_U}, \delta D_{clk_U}}(t_0) = \begin{bmatrix} 9.0 \times 10^{14}\ ft^2 & 0 \\ 0 & 9.0 \times 10^{10}\ ft^2/\sec^2 \end{bmatrix} \tag{3.15}$$

Because these error sources are a function of the user equipment, they are common to all the satellite vehicles. The remaining five sources of errors are unique to each satellite vehicle (SV), based on their individual equipment and their position with respect to the user. The first SV-specific error source for GPS is the code loop error, δR_{cloop}. Although the code loop is part of the user equipment shared by all the SV's, its error magnitude is relative to each SV. The work done by Negast [55] has shown that, with

differential corrections applied, this error can be removed from the DGPS model. The second and third SV-specific errors are the atmospheric interference with the EM signals, δR_{ion} and δR_{trop}, as related to the ionospheric and tropospheric delay in the signal's propagation. The tropospheric delay and ionospheric delay are both modeled as first order Markov processes with time constants shown in Equation (3.16), consistent with previous AFIT research [50,55,63,65]. Both are driven by zero-mean white Gaussian noise with strengths shown in Equation (3.19). The fourth SV-specific error source is due to inaccuracies in the clocks on board the SV's, δR_{Sclk}. By using differential corrections, this error source was also removed from the DGPS model. The final error source was based on line-of-sight errors between the SV's and the receiver, δx_{s_i}, δy_{s_i}, δz_{s_i}, respectively. The model for these states is shown in Equation (3.16):

$$\begin{Bmatrix} \delta\dot{R}_{trop} \\ \delta\dot{R}_{ion} \\ \delta\dot{x}_{s_i} \\ \delta\dot{y}_{s_i} \\ \delta\dot{z}_{s_i} \end{Bmatrix} = \begin{bmatrix} -\frac{1}{500} & 0 & 0 & 0 & 0 \\ 0 & -\frac{1}{1500} & 0 & 0 & 0 \\ 0 & 0 & 0 & 0 & 0 \\ 0 & 0 & 0 & 0 & 0 \\ 0 & 0 & 0 & 0 & 0 \end{bmatrix} \begin{Bmatrix} \delta R_{trop} \\ \delta R_{ion} \\ \delta x_{s_i} \\ \delta y_{s_i} \\ \delta z_{s_i} \end{Bmatrix} + \begin{Bmatrix} w_{trop} \\ w_{ion} \\ 0 \\ 0 \\ 0 \end{Bmatrix} \tag{3.16}$$

where the initial covariance for the states is given by:

$$P_{DGPS} = \begin{bmatrix} 1.0\ ft^2 & 0 & 0 & 0 & 0 \\ 0 & 1.0\ ft^2 & 0 & 0 & 0 \\ 0 & 0 & 0.35\ ft^2 & 0 & 0 \\ 0 & 0 & 0 & 0.35\ ft^2 & 0 \\ 0 & 0 & 0 & 0 & 0.35\ ft^2 \end{bmatrix} \tag{3.17}$$

and mean values and strengths of the dynamics driving noise are given by:

$$E\{w_{DGPS}(t)\} = 0 \tag{3.18}$$

$$E\left\{w_{DGPS}(t)w_{DGPS}^{T}(t+\tau)\right\}=\begin{bmatrix}0.001 & 0 & 0 & 0 & 0\\ 0 & 0.0004 & 0 & 0 & 0\\ 0 & 0 & 0 & 0 & 0\\ 0 & 0 & 0 & 0 & 0\\ 0 & 0 & 0 & 0 & 0\end{bmatrix}\frac{ft^2}{\text{sec}}\cdot\delta(\tau) \tag{3.19}$$

The reduced dynamic driving noise strengths from standard GPS are indicative of the error reduction for these remaining states when *differential* corrections are applied. A quick reference of the truth model non-zero DGPS dynamics matrix components is provided in Tables I.5 of Appendix I. This ends the description of the 22-state truth model. Now the filter model will be presented.

3.4.3.2 The 2-State DGPS Filter Model

Various research efforts have shown that two states provide a sufficient model for GPS and DGPS [50,55,58]. The primary argument is that the errors modeled by the other 20 states are small when compared to the two states common to all SV's. By adding dynamics driving noise, of strength Q, and re-tuning the filter, the overall performance of the DLSM can be maintained with the significantly reduced-order model of Equation (3.20):

$$\begin{Bmatrix}\delta\dot{R}_{clk_U}\\ \delta\dot{D}_{clk_U}\end{Bmatrix}=\begin{bmatrix}0 & 1\\ 0 & 0\end{bmatrix}\begin{Bmatrix}\delta R_{clk_U}\\ \delta D_{clk_U}\end{Bmatrix}+\begin{Bmatrix}w_{R_{clk}}\\ w_{R_{clk}}\end{Bmatrix} \tag{3.20}$$

The values implemented for the dynamics driving noise strengths can be found in Tables I.8 - I.10 of Appendix I. It should be noted that, in the tuning process, the measurement noise covariance values R (as shown in Appendix I) have also been adjusted to achieve adequate tuning of the filter [45]. This completes the description of the DGPS filter

model. The next section presents the DGPS measurement equations for both the truth and the filter models.

3.4.3.3 DGPS Measurement Model

There are four *differentially* corrected GPS measurement updates, one for each of the satellite range signals received by the DLSM filter. These measurement updates are once again *difference* measurements. First the DGPS truth model difference measurement will be fully presented, followed by a brief description of the filter measurement. The DGPS difference measurement is formed by taking the difference of the INS-calculated pseudorange, R_{INS} and actual pseudorange, R_{DGPS}.

$$\delta z_{DGPS} = R_{INS} - R_{DGPS} \tag{3.21}$$

The real pseudorange, R_{DGPS} is the sum of the true range form the user to the satellite plus all the errors in the pseudorange signal propagation. After differential corrections are applied, the measurement equation is modeled as:

$$R_{DGPS} = R_t + \delta R_{trop} + \delta R_{ion} + \delta R_{Uclk} - v \tag{3.22}$$

where

R_{DGPS} = Differentially corrected GPS pseudorange measurement, from SV to user

R_t = true range, from SV to user

R_{trop} = range error due to tropospheric delay

δR_{ion} = range error due to ionospheric delay

δR_{Uclk} = range error due to use clock error

v = zero-mean white Gaussian measurement noise

Note that, since v is assumed *zero* mean, white gaussian noise, statistically speaking, one can choose v with either a plus "+" or minus "-" coefficent . As in Equation (3.9), the author chooses the coefficent carefully so that the end result shows a plus "+ v" sign in Equation (3.25) and Equation (3.26).

The second source of a range measurement is the INS itself, R_{INS} [50,55]. R_{INS} is the difference between the DLSM-calculated position, X_U and the satellite position from the ephemeris data X_S. This difference vector is represented below in the ECEF frame

$$R_{INS} = |X_U - X_S| = \left| \begin{Bmatrix} x_U \\ y_U \\ z_U \end{Bmatrix}^e - \begin{Bmatrix} x_S \\ y_S \\ z_S \end{Bmatrix}^e \right| \tag{3.23}$$

An equivalent form for Equation (3.23) is

$$R_{INS} = \sqrt{(x_U - x_S)^2 + (y_U - y_S)^2 + (z_U - z_S)^2} \tag{3.24}$$

Based on Assumption 13 from Chapter 1, Equation (3.24) can be approximated and rewritten in terms of the true range and a truncated first-order Taylor series, with perturbations representing the errors in X_U and X_S:

$$R_{INS} = R_t + \frac{\partial R_{INS}(X_S, X_U)}{\partial X_U}\bigg|_{(X_S, X_U)_{nom}} \cdot \delta X_U + \frac{\partial R_{INS}(X_S, X_U)}{\partial X_S}\bigg|_{(X_S, X_U)_{nom}} \cdot \delta X_S \tag{3.25}$$

The solution for R_{INS} is found by substituting Equations (3.24) into Equation (3.25) and evaluating the partial derivatives to get [50,55]:

$$\begin{aligned} R_{INS} = R_t &- \left[\frac{x_S - x_U}{|R_{INS}|}\right] \cdot \delta x_U - \left[\frac{y_S - y_U}{|R_{INS}|}\right] \cdot \delta y_U - \left[\frac{z_S - z_U}{|R_{INS}|}\right] \cdot \delta z_U \\ &+ \left[\frac{x_S - x_U}{|R_{INS}|}\right] \cdot \delta x_S + \left[\frac{y_S - y_U}{|R_{INS}|}\right] \cdot \delta y_S + \left[\frac{z_S - z_U}{|R_{INS}|}\right] \cdot \delta z_S \end{aligned} \tag{3.26}$$

Finally, the DGPS pseudorange truth model *difference* measurement is given as:

$$\begin{aligned}\delta z_{DGPS_t} &= R_{INS} - R_{DGPS} \\ &= -\left[\frac{x_S - x_U}{|R_{INS}|}\right]\cdot\delta x_U - \left[\frac{y_S - y_U}{|R_{INS}|}\right]\cdot\delta y_U - \left[\frac{z_S - z_U}{|R_{INS}|}\right]\cdot\delta z_U \\ &\quad + \left[\frac{x_S - x_U}{|R_{INS}|}\right]\cdot\delta x_S + \left[\frac{y_S - y_U}{|R_{INS}|}\right]\cdot\delta y_S + \left[\frac{z_S - z_U}{|R_{INS}|}\right]\cdot\delta z_S \\ &\quad - [1]\delta R_{trop} - [1]\delta R_{ion} - [1]\delta R_{Uclk} + v\end{aligned} \tag{3.27}$$

The user position errors in Equation (3.27) can be derived from the first three states of the filter or truth model using an orthogonal transformation [10,50,55].

The filter model for the DGPS measurement will now be derived. Since the filter model does not contain the states for the errors in the satellite position, these terms are removed from the equation. The filter model measurement equation can therefore be written as:

$$\begin{aligned}\delta z_{DGPS_f} &= R_{INS} - R_{DGPS} \\ &= -\left[\frac{x_S - x_U}{|R_{INS}|}\right]\cdot\delta x_U - \left[\frac{y_S - y_U}{|R_{INS}|}\right]\cdot\delta y_U - \left[\frac{z_S - z_U}{|R_{INS}|}\right]\cdot\delta z_U \\ &\quad - [1]\delta R_{Uclk} + v\end{aligned} \tag{3.28}$$

The filter measurement noise variance, R, will be tuned to attain adequate performance despite the reduction in order from the truth model and the Taylor series approximation. The measurement noise variances for both the filter and the truth model equations are provided in Table I.11 of Appendix I. This completes the description of the DGPS measurement equations and the entire DLSM filter and truth model equations.

3.5 Chapter Summary

This chapter presents the set-up of the DLSM MSOFE computer simulation. An introduction to MSOFE and PROFGEN is provided. The truth model and filter model propagation and measurement equations are described for the INS/Baro, Radar Altimeter, and DGPS subsystems. A simple radar altimeter model has been presented. The radar altimeter measurements should play a key role in aiding the vertical channel and allowing our aircraft to meet precision approach requirements. The INS/Baro and DGPS truth model is located in tabular form in Appendix A. The dynamic submatrices F_{Filter}, F_{INSt1}, F_{INSt2}, *and* F_{DGPS}, and process noise strength and measurement noise covariance matrices for filter and truth models are presented in Appendix I. Results and analysis of the DLSM simulation are presented in Chapter 4.

IV. Results and Analysis

This chapter presents the results and analysis of the performance for the various system integrations involved in this effort. Table 4 - 1 shows the Case I - VI comparisons and Table 4 - 2 shows Cases VII - XV. Each case was evaluated using the PROFGEN-

Case I	Case II	Case III	Case IV	Case V	Case VI
Barometric Altimeter	Barometric Altimeter	Barometric Altimeter	Barometric Altimeter	Barometric Altimeter	Barometric Altimeter
0.4 nm/hr CEP INS	0.4 nm/hr CEP INS	2.0 nm/hr CEP INS	2.0 nm/hr CEP INS	4.0 nm/hr CEP INS	4.0 nm/hr CEP INS
DGPS	DGPS	DGPS	DGPS	DGPS	DGPS
----	Radar Altimeter	----	Radar Altimeter	----	Radar Altimeter

Table 4 - 1. Case I - VI Integration Comparisons

Case VII	Case VIII	Case IX	Case X	Case XI	Case XII	Case XIII	Case XIV	Case XV
Barometric Altimeter	Barometric Altimeter	Barometric Altimeter	Barometric Altimeter	Barometric Altimeter	Barometric Altimeter	Barometric Altimeter	Barometric Altimeter	Barometric Altimeter
0.4 nm/hr CEP INS	0.4 nm/hr CEP INS	2.0 nm/hr CEP INS	2.0 nm/hr CEP INS	4.0 nm/hr CEP INS	4.0 nm/hr CEP INS	0.4 nm/hr CEP INS	2.0 nm/hr CEP INS	4.0 nm/hr CEP INS
DGPS	DGPS	DGPS	DGPS	DGPS	DGPS	DGPS	DGPS	DGPS
Pseudolite	Radar Altimeter and Pseudolite	Pseudolite	Radar Altimeter and Pseudolite	Pseudolite	Radar Altimeter and Pseudolite	None	None	None
No GPS Outage	No GPS Outage	No GPS Outage	No GPS Outage	No GPS Outage	No GPS Outage	Single GPS Outage	Single GPS Outage	Single GPS Outage

Table 4 - 2. Cases VII-XV Integration Comparisons

created flight profiles for both the tanker and the light aircraft. Latitude, longitude, and altitude errors are compared for the DGPS and GPS case. The tuning values for the 13-state filter are presented for each case are presented in Appendix I.

4.1 Radar Altimeter/Barometric Altimeter/DGPS Aiding of the 0.4 nm/hr, 2.0 nm/hr INS, and 4.0 nm/hr INS with the Tanker Flight Profile

This section discusses the results for Cases I - VI for the tanker flight profile. The plots for these cases are located in Appendix B.

4.1.1 Case I and Case II - 0.4 nm/hr INS

The tanker flight profile was utilized to provide real world information for the simulations. It was assumed that there were no satellite vehicle (SV) outages for the entire flight of the aircraft. The main difference between Case I and Case II was the addition of a radar altimeter in Case II for vertical channel aiding. Several tuning runs were performed to minimize the difference between the filter-predicted errors and the truth model errors. By minimizing this difference, one is able to make more realistic decisions about the appropriateness of utilizing a reduced-order state filter for flight tests.

With the use of the radar altimeter for vertical aiding, when the aircraft went below 3000ft AGL, errors in aircraft altitude, longitude, and latitude all show a reduction. As expected, the most significant improvement occurs in the altitude errors because the altimeter is utilized to reduce the errors in the vertical channel directly. Table 4 - 3 summarizes Case I and Case II landing system performances at respective decision heights.

To meet the requirements for an aircraft precision approach, certain accuracy requirements have to be met at three decision heights (200 ft, 100 ft, and 50 ft) as an

Position Error State	Decision Height (feet)	Case I True Error (feet)	Case I Filter Error (feet)	Case II True Error (feet)	Case II Filter Error (feet)
δlatitude	200	1.04	1.37	1.14	1.32
δlatitude	100	0.99	1.37	0.92	1.32
δlatitude	50	1.0	1.37	0.86	1.31
δlongitude	200	0.76	1.62	0.81	1.59
δlongitude	100	0.91	1.62	0.97	1.59
δlongitude	50	1.06	1.62	1.15	1.59
δaltitude	200	4.55	5.96	2.49	3.36
δaltitude	100	4.68	5.96	1.47	3.06
δaltitude	50	3.19	5.96	1.19	2.95

Table 4 - 3. Case I and Case II 1σ Latitude, Longitude and Altitude Errors

Precision Approach Parameters (in feet, all 1-sigma values)

Category	Decision Height	Azimuth	Elevation
I	200 feet	+/- 28.1	+/- 6.8
II	100 feet	+/- 8.6	+/- 2.8
III	50 feet	+/- 6.8	+/- 1.0

Table 4 - 4. Precision Approach Accuracy Requirements at Decision Heights

Case Number	Horizontal (Based on True Error)	Horizontal (Based on Filter Predicted Error)	Vertical (Based on True Error)	Vertical (Based on Filter Predicted Error)
I	Cat III	Cat III	Cat I	Cat I
II	Cat III	Cat III	Cat II	Cat I

Table 4 - 5. Precision Landing Category Predicted To Achieve

aircraft approaches the runway. The accuracy requirements are presented in Table 4 - 4. Table 4 - 5 summarizes the Case I and Case II performance in terms of which precision approach category is met, based on the horizontal and vertical errors shown in Table 4 - 4. The errors predicted in the horizontal channel by the filter, as well as the true errors, meet the Category III landing requirements for Case I and Case II. This is a vast improvement over the horizontal errors using standard GPS measurements. Actual improvement values are presented later in this section. However, work needs to be done in vertical channel

aiding to meet the precision landing requirements for the vertical channel. The true error shows that a Category II landing could be met with the utilization of the radar altimeter in Case II, but the filter-predicted error and the true error for Case I in the vertical channel is limited to a Category I landing. The filter-predicted error for Case II meets the Category I landing requirements, but with some additional filter tuning it may well meet the requirements for a Category II landing.

The errors in latitude, longitude, and altitude are also reduced from those found by using standard GPS measurements. Table 4 - 6 presents a comparison of the improvement in horizontal and vertical errors using DGPS measurements versus GPS measurements for Case I. Similar improvements are found when comparisons are made for Case II when a radar altimeter is used to provide height measurements to aid the vertical channel. Table 4 - 7 presents the true and filter predicted error values for the Case II simulations using DGPS measurements and GPS measurements. Since the filter errors vary slightly with the precision of the tuning, it is useful to compare the improvements in the true errors for the

Position Error State	Decision Height (feet)	DGPS Case I True Error (feet)	DGPS Case I Filter Error (feet)	GPS Case I True Error (feet)	GPS Case I Filter Error (feet)
δlatitude	200	1.04	1.37	8.81	9.85
δlatitude	100	0.99	1.37	9.40	9.80
δlatitude	50	1.0	1.37	8.61	9.80
δlongitude	200	0.76	1.62	9.14	10.68
δlongitude	100	0.91	1.62	9.77	10.68
δlongitude	50	1.06	1.62	8.83	10.69
δaltitude	200	4.55	5.96	14.2	15.1
δaltitude	100	4.68	5.96	15.65	15.1
δaltitude	50	3.19	5.96	15.3	15.1

Table 4 - 6. DGPS vs GPS Case I 1σ Latitude, Longitude and Altitude Errors

simulations when DGPS measurements are used instead of standard GPS measurements. As can be seen in Table 4 - 8, the use of DGPS measurements improved the latitude error by almost 89%, the longitude error by 90%, and the Altitude error by 73%. Similar results are seen when the radar altimeter is used in Case II. Table 4 - 9 presents the error improvements for Case II. By comparing the altitude errors for Case I and Case II when DGPS measurements are used, one can see an additional 58% reduction in the true altitude errors when the radar altimeter is used. The averaged true errors in Tables 4 - 8 and 4 - 9 are the result of averaging the true error values from the three decision heights. Case I plots are found in Appendix B.1. Case II plots are found in Appendix B.2.

Position Error State	Decision Height (feet)	DGPS Case II True Error (feet)	DGPS Case II Filter Error (feet)	GPS Case II True Error (feet)	GPS Case II Filter Error (feet)
δlatitude	200	1.14	1.32	8.72	9.69
δlatitude	100	0.92	1.32	9.13	9.69
δlatitude	50	0.86	1.31	8.35	9.69
δlongitude	200	0.81	1.59	8.83	10.58
δlongitude	100	0.97	1.59	9.65	10.58
δlongitude	50	1.15	1.59	8.70	10.58
δaltitude	200	2.49	3.36	3.76	7.74
δaltitude	100	1.47	3.06	2.43	7.57
δaltitude	50	1.19	2.95	2.64	7.52

Table 4 - 7. DGPS vs GPS Case II 1σ Latitude, Longitude and Altitude Errors

Error State	DGPS Case I average true error (feet)	GPS Case I average true error (feet)	% Change in Error
Latitude	1.01	8.94	88.7%
Longitude	0.91	9.25	90.2%
Altitude	4.14	15.05	72.5%

Table 4 - 8. Case I Averaged True Error Reduction Using DGPS Measurements

Error State	DGPS Case II average true error (feet)	GPS Case II average true error (feet)	% Change in Error
Latitude	0.97	8.73	88.9%
Longitude	0.97	9.06	89.3%
Altitude	1.72	2.94	41.5%

Table 4 - 9. Case II Averaged True Error Reduction Using DGPS Measurements

4.1.2 Case III and Case IV - 2.0 nm/hr INS

As in Cases I and II, the tanker flight profile was flown and received DGPS measurements from 4 SV with no outages. With Case III and Case IV, a mid-range INS with a 2.0 nm/hr drift was used in place of the 0.4 nm/hr INS, to investigate the possibility of using a less accurate but more cost effective INS in the landing scenario. As with Case II, a radar altimeter is used in Case IV to provide vertical channel aiding.

Table 4 - 10 summarizes Case III and Case IV landing system performance at respective decision heights. Table 4 - 11 summarizes the Case III and Case IV performance in terms of which precision approach category is met based on the horizontal and vertical errors.

Even with the use of a less accurate INS, Category III landing requirements are still met in the horizontal errors for both Case III and Case IV. The shortcomings in the

Position Error State	Decision Height (feet)	Case III True Error (feet)	Case III Filter Error (feet)	Case IV True Error (feet)	Case IV Filter Error (feet)
δlatitude	200	1.29	1.69	1.37	1.64
δlatitude	100	0.91	1.69	0.99	1.64
δlatitude	50	1.17	1.69	0.95	1.64
δlongitude	200	0.95	2.09	0.94	2.07
δlongitude	100	1.11	2.09	1.21	2.07
δlongitude	50	1.42	2.09	1.54	2.07
δaltitude	200	3.69	6.37	2.72	3.67
δaltitude	100	4.79	6.39	1.54	3.38
δaltitude	50	3.08	6.39	1.42	3.28

Table 4 - 10. Case III and Case IV 1σ Latitude, Longitude and Altitude Errors

Case Number	Horizontal (Based on True Error)	Horizontal (Based on Filter Predicted Error)	Vertical (Based on True Error)	Vertical (Based on Filter Predicted Error)
III	Cat III	Cat III	Cat I	Cat I
IV	Cat III	Cat III	Cat II	Cat I

Table 4 - 11. Precision Landing Category Predicted To Achieve

vertical channel still limit the filter-predicted error to a Category I landing for both cases. It should be noted that the true vertical channel error for Case IV once again meets the Category II landing requirement. With some additional filter tuning, the filter-predicted errors in Case IV should also be able to meet the Category II requirements.

As expected, with the use of DGPS measurements rather than GPS measurements, the errors in latitude, longitude, and altitude are greatly reduced. This allows the Category I, II, and even III requirements for precision landings to be met, whereas standard GPS measurements limited the results to Category I and sometimes Category II approaches. Table 4 - 12 and Table 4 - 13 present the improvements for the true errors when DGPS measurements are used to replace GPS measurements for Case III and Case IV. Case III plots are in Appendix B.3. Case IV plots are in Appendix B.4.

Error State	DGPS Case III average true error (feet)	GPS Case III average true error (feet)	% Change in Error
Latitude	1.12	8.72	87.2%
Longitude	1.16	9.25	87.5%
Altitude	3.85	15.4	75.0%

Table 4 - 12. Case III Averaged True Error Reduction Using DGPS Measurements

Error State	DGPS Case IV average true error (feet)	GPS Case IV average true error (feet)	% Change in Error
Latitude	1.10	8.96	87.7%
Longitude	1.23	9.37	86.9%
Altitude	1.89	2.47	23.5%

Table 4 - 13. Case IV Averaged True Error Reduction Using DGPS Measurements

4.1.3 Case V and Case VI - 4.0 nm/hr INS

As with the previous cases, Cases V and VI use the tanker profile with DGPS information provided and no SV outages. A further reduction was made in the accuracy of the INS to help define the aircraft where this system might be useful; an INS of this level of precision ought to be affordable for civil aviation aircraft as well as for commercial airliners or military applications. Aircraft are outfitted with varying INS qualities. To make the research as usable as possible, different qualities of INSs were considered. Table 4 - 14 summarizes Case V and Case VI landing system performance at respective decision heights.

Position Error State	Decision Height (feet)	Case V True Error (feet)	Case V Filter Error (feet)	Case VI True Error (feet)	Case VI Filter Error (feet)
δlatitude	200	1.43	1.87	1.45	1.82
δlatitude	100	1.0	1.87	0.99	1.82
δlatitude	50	1.0	1.86	0.92	1.82
δlongitude	200	1.08	2.31	1.23	2.29
δlongitude	100	1.29	2.32	1.41	2.29
δlongitude	50	1.56	2.32	1.77	2.29
δaltitude	200	3.32	6.26	2.79	3.54
δaltitude	100	4.48	6.26	1.38	3.24
δaltitude	50	3.66	6.26	1.38	3.14

Table 4 - 14. Case V and Case VI 1σ Latitude, Longitude and Altitude Errors

Table 4 - 15 summarizes the Case V and Case VI performance in terms of what category of precision approach is met based on horizontal and vertical errors. Category III precision approaches are met in the horizontal direction as before, and the accuracy in the vertical is also maintained. As before, the filter-predicted errors in the vertical for Case VI meet the Category I requirements but are within the area where additional filter tuning could help achieve a Category II precision approach.

Case Number	Horizontal (Based on True Error)	Horizontal (Based on Filter Predicted Error)	Vertical (Based on True Error)	Vertical (Based on Filter Predicted Error)
V	Cat III	Cat III	Cat I	Cat I
VI	Cat III	Cat III	Cat II	Cat I

Table 4 - 15. Precision Landing Category Predicted To Achieve

With the use of the DGPS measurements, we still see major improvements in the latitude, longitude, and altitude errors for Case V and Case VI over those achievable with standard GPS measurements. Table 4 - 16 summarizes the improvements for Case V errors, and Table 4 - 17 for Case VI errors, when DGPS measurements are used instead of GPS measurements. Case V plots are in Appendix B.5. Case VI plots are in Appendix B.6.

Error State	DGPS Case V average true error (feet)	GPS Case V average true error (feet)	% Change in Error
Latitude	1.14	8.93	87.2%
Longitude	1.31	9.25	85.8%
Altitude	3.82	15.59	75.5%

Table 4 - 16. Case V Averaged True Error Reduction Using DGPS Measurements

Error State	DGPS Case VI average true error (feet)	GPS Case VI average true error (feet)	% Change in Error
Latitude	1.12	8.80	87.3%
Longitude	1.47	9.38	84.3%
Altitude	1.85	2.32	20.3%

Table 4 - 17. Case VI Averaged True Error Reduction Using DGPS Measurements

4.2 Radar Altimeter/Baro/DGPS Aiding of the 0.4 nm/hr, 2.0 nm/hr, and 4.0 nm/hr INS using a Single Pseudolite during the Landing Approach

For Cases VII - XII in this section, an additional measurement from a single pseudolite is utilized along the final approach path to improve the errors in latitude, longitude, and altitude. The final location of the pseudolite was 84° 1' 23.3" longitude and 39° 49' 15.5" latitude. This places the pseudolite at the approach end (Runway 23) of the airport. It is

positioned parallel to Runway 23, approximately one nm from the side of the landing strip. The true latitude, longitude, and altitude errors for Cases VII, IX, and XI will be averaged and compared to the average of the true errors for Cases I, III, and V to investigate the error reductions when the pseudolite is used, when no radar altimeter is employed. Similarly, the errors for Cases VIII, X, and XII will be averaged and compared to the average of the true errors for Cases II, IV, and VI, for the case when a radar altimeter is also used. Averaged values were used because no significant improvements were found in latitude, longitude, and altitude errors over Cases VII, IX, and XI (no radar altimeter used) and Cases VIII, X, and XII (radar altimeter used) when the single pseudolite was utilized. The plots for Case VII - XII are located in Appendix C.1 - C.6 respectively.

4.2.1 Cases VII, IX, and XI - Pseudolite Without Radar Altimeter

The pseudolite provides an additional range measurement to the aircraft and is available and being processed once every second. When an aircraft is following a precision approach pattern, the pseudolite data is available when the aircraft is within a 12 nm window of the runway. This distance was chosen based on a 12/1 near-far ratio. Basically this means is that, if the pseudolite is placed 1 nm from the runway, then it can broadcast data at a strength which will reach 12 times this distance without interfering with the other range measurement information received.

Other than maintaining a certain distance from the runway, the pseudolite placement was a random location at the runway. Several pseudolite positions around the runway were tried, with no significant improvement in the horizontal and vertical errors. The use of the pseudolite did decrease the VDOP, which is reflected in the decrease in altitude

Error State	Case I, III, V average true error (feet)	Case VII, IX, and XI average true error (feet)	% Change in Error
Latitude	1.09	1.14	+4.4%
Longitude	1.13	0.71	37.2%
Altitude	4.43	3.9	12.0%

Table 4 - 18. Averaged True Error Reduction Using a Single Pseudolite

error seen when Cases I, III, and V are compared to Cases VII, IX, and XI. Table 4 - 18 presents the improvements in latitude, longitude, and altitude error when a single pseudolite is used.

With the use of the pseudolite, basically no change was seen in the true errors in latitude. A 37.2% decrease in longitude error is noted, but the 12% decrease in altitude error is not enough to improve the precision landing approach above a Category I. The increase in latitude error, despite the decrease in longitude error, may be in part due to changes in HDOP and PDOP caused by the pseudolite placement. Table 4 - 19 summarizes the Case VII, IX, and XI performances in terms of which category of precision approach could be met based on horizontal and vertical errors. Category III precision approaches are maintained for the horizontal errors, but as discussed earlier, the vertical errors still limit us to a Category I approach in both true and filter predicted errors.

Case Number	Horizontal (Based on True Error)	Horizontal (Based on Filter Predicted Error)	Vertical (Based on True Error)	Vertical (Based on Filter Predicted Error)
VII, IX, and XI	Cat III	Cat III	Cat I	Cat I

Table 4 - 19. Precision Landing Category Predicted To Achieve

4.2.2 Cases VIII, X, and XII - Pseudolite and Radar Altimeter

Cases VIII, X, and XII are identical to cases in the previous section except for the addition of radar altimeter measurements when the aircraft goes below 3000 feet (AGL). Cases VIII, X, and XII will be compared to Cases II, IV, and VI, where the radar altimeter was also used in the configuration. The improvements realized when the pseudolite and radar altimeter are used together versus just the use of the pseudolite are presented in Table 4 - 20. The performance enhancements obtained by the pseudolite and radar altimeter combination, compared to just the use of a radar altimeter, are presented in Table 4 - 21.

Once again, we were able to maintain a Category III precision approach for the horizontal errors when the pseudolite was introduced along with the radar altimeter in Cases VIII, X, and XII. The pseudolite improved the longitude errors by 44% over the cases when only the radar altimeter was used, but this time only a marginal improvement of 2.2% was seen in the altitude errors from Cases II, IV, and VI to Cases VIII, X, and

Error State	Case II, IV, VI average true error (feet)	Case VIII, X, XII average true error (feet)	% Change in Error
Latitude	1.07	1.11	+ 3.6%
Longitude	1.23	0.69	44.0%
Altitude	1.82	1.78	2.2%

Table 4 - 20. Averaged True Error Reduction, Case II-IV-VI vs. Case VIII-X-XII

Error State	Case VII, IX, XI average true error (feet)	Case VIII, X, XII average true error (feet)	% Change in Error
Latitude	1.14	1.11	2.6%
Longitude	0.71	0.69	2.8%
Altitude	3.9	1.78	54.4%

Table 4 - 21. Averaged True Error Reduction, Case VII-IX-XI vs. Case VIII-X-XII

XII. This can be attributed to the fact that the radar altimeter is providing adequate vertical channel aiding to the aircraft, and the improvements provided by the pseudolite are not as significant. Table 4 - 21 presents the significance of the radar altimeter for altitude error performance. When the radar altimeter is used with the pseudolite, a 54% improvement in average altitude errors is seen over the pseudolite only case. The average true altitude errors for Cases VII, IX, and XI show only a modest improvement when the the pseudolite is used, when compared to Cases I, III, and V when no pseudolite is used. In the cases where the altimeter is used, the performance requirements for a Category II precision approach are met in the vertical channel. In Cases VII, IX, and XI where no altimeter is used, only a Category I precision approach can be maintained. Table 4 - 22 summarizes the Case VIII, X, and XII precision approach performances.

Case Number	Horizontal (Based on True Error)	Horizontal (Based on Filter Predicted Error)	Vertical (Based on True Error)	Vertical (Based on Filter Predicted Error)
VIII, IX, and XII	Cat III	Cat III	Cat II	Cat I

Table 4 - 22. Precision Landing Category Predicted To Achieve

4.3 Example of 0.4 nm/hr, 2.0 nm/hr, and 4.0 nm/hr INS Drift during a Loss of GPS Measurements for 1/8 Schuler Period

Research done in Cases I - XII was based on the assumption that range measurement information from 4 satellites was available without interruption. In this section, the loss of GPS for approximately 650 seconds (1/8 Schuler period) was examined to view the performance of the true and filter-predicted parameters under real world conditions. During an actual flight, loss of GPS measurements will inevitably occur. If a low accuracy INS is used in a DGPS/INS Kalman filter integration for a landing system implementation, one needs to know the effects of the loss of DGPS measurements. The continuous DGPS

measurements enabled the performance differences between each of the INSs to be minimized, allowing the aided navigation systems to maintain their accuracies. The increased drift caused by the less accurate INSs will increase the errors substantially if the DGPS measurements are lost. The plots for Cases XIII - XV are located in Appendixes D.1 - D.3. By comparing the plots for Cases XIII - XV, one can see the errors for the INSs increase as the quality of the INSs degrade.

The four SV measurements were assumed lost at time T = 2000 sec. into the flight. This loss represents a situation where the GPS receiver may be unusable or a terrorist jamming has occurred. In Appendix D, one can compare the outputs for the three different INSs and see the errors increasing until the GPS measurements are re-acquired. Figure D.1 through Figure D.3 represent the 0.4 nm/hr, 2.0 nm/hr, and 4.0 nm/hr INS, respectively. Once the re-acquisition has occurred, the INS errors are once again bounded. The latitude, longitude, and altitude errors once again approach the range required for precision approach landings. Table 4 - 23 presents the averaged true errors and Table 4 - 24 summarizes the precision landing performance for Cases XIII, XIV, and XV. There were no precision landing category degradations caused by the interruption in DGPS information due to the time period over which DGPS information was lost, relative to the time of landing. As before a Category III precision approach was realized with the horizontal errors, but the vertical errors limited the landing to a Category I.

Error State	Case XIII average true error (feet)	Case XIV average true error (feet)	Case XV average true error (feet)
Latitude	1.19	1.29	1.39
Longitude	0.44	0.51	0.54
Altitude	4.16	4.31	4.25

Table 4 - 23. Averaged True Error for Case XIII, XIV, and XV

Case Number	Horizontal (Based on True Error)	Horizontal (Based on Filter Predicted Error)	Vertical (Based on True Error)	Vertical (Based on Filter Predicted Error)
XIII, XIV, and XV	Cat III	Cat III	Cat I	Cat I

Table 4 - 24. Precision Landing Category Predicted To Achieve

4.4 Radar Altimeter/Barometric Altimeter/DGPS Aiding of the 0.4 nm/hr, 2.0 nm/hr INS, and 4.0 nm/hr INS with the Single Engine Aircraft Flight Profile

This section discusses the Case I - XV results for the single engine aircraft flight profile. The scenarios for the set-up of each of these scenarios is identical to the set-up for the cases in Sections 4.1, 4.2, and 4.3. Also the filter-predicted errors for these cases using the single engine aircraft flight profile are nearly identical to the errors found with the tanker flight profile. Therefore, the information discussed will be limited to the true errors and the precision approach performance for each case. The plots for Cases I - VI are located in Appendices E.1 - E.6; these are directly comparable to plots in Appendices B.1 - B.6 for the case of the tanker trajectory profile. The plots for Cases VII - XII are located in Appendices F.1 - F.6; these can be compared to plots in Appendices C.1 - C.6 for the tanker profile. The plots for Cases XIII - XV are located in Appendices G.1 - G.3; these can be compared to results in Appendices D.1 - D.3.

4.4.1 Case I, III, and V - 0.4 nm/hr, 2.0 nm/hr, and 4.0 nm/hr INS

For these three cases, no radar altimeter was used for vertical channel aiding. The only difference in the scenarios is the accuracy of the INS used. The true error information presented is an average of the errors for Cases I, III, and V. Averaged values were used because no significant improvements were found in latitude, longitude, and altitude errors at the three decision heights. Table 4 - 25 presents the averaged true errors for each individual case and Table 4 - 26 summarizes the precision approach capabilities for each case.

Error State	Case I average true error (feet)	Case III average true error (feet)	Case V average true error (feet)
Latitude	0.6	0.44	0.58
Longitude	1.81	1.74	1.73
Altitude	4.65	3.96	4.92

Table 4 - 25. Averaged True Error for Case I, III, and V

Case Number	Horizontal (Based on True Error)	Horizontal (Based on Filter Predicted Error)	Vertical (Based on True Error)	Vertical (Based on Filter Predicted Error)
I, III, and V	Cat III	Cat III	Cat I	Cat I

Table 4 - 26. Precision Landing Category Predicted To Achieve

Once again, Category III precision approach requirements are met with the horizontal errors, but we are still limited to Category I with the vertical error precision. This matches exactly the precision approach requirements seen with the tanker aircraft. When one compares the average true errors of the tanker with the average true errors of the single engine aircraft, some interesting trends are noted. Table 4 - 27 presents the true error comparisons for latitude, longitude, and altitude for Cases I, III, and V (tanker and single engine aircraft). A significant decrease in the latitude error is seen from the tanker to the

single engine aircraft. However, the gains in latitude errors are lost by an increase in longitude errors for the single engine aircraft. The difference in altitude errors shows no significant differences between the tanker and the single engine aircraft, except for Case V where a difference of one foot is found. These differences can be associated with the difference in the flight profiles flown by the two aircraft. The approach speed for the single engine aircraft and the altitude from which it began its descent is much different from that of the tanker. These variations show up in the final output.

Error State	Case I average true error (feet) tanker	Case I average true error (feet) single engine	Case III average true error (feet) tanker	Case III average true error (feet) single engine	Case V average true error (feet) tanker	Case V average true error (feet) single engine
Latitude	1.01	0.6	1.12	0.44	1.14	0.58
Longitude	0.91	1.81	1.16	1.74	1.31	1.73
Altitude	4.14	4.65	3.85	3.96	3.82	4.92

Table 4 - 27. Average True Errors of Tanker vs Single Engine Aircraft

4.4.2 Case II, IV, and VI - 0.4 nm/hr, 2.0 nm/hr, and 4.0 nm/hr INS with Radar Altimeter

With the addition of the radar altimeter for these cases, the true errors in the vertical channel have been reduced enough to warrant a close look at the altitude errors at each decision height. Once again, the latitude and longitude errors will be will be averaged over the three decision heights because no significant improvements were noted, and a Category III precision approach is met at all three heights. Table 4 - 28 shows the averaged true error for Cases II, IV, and VI.

Error State	Case II average true error (feet)	Case IV average true error (feet)	Case VI average true error (feet)
Latitude	0.85	1.0	0.98
Longitude	0.99	1.12	1.18

Table 4 - 28. Averaged True Error for Case II, IV, and VI

Enough of an improvement in the radar-altimeter-assisted latitude errors has led to the requirements for a Category III precision approach landing being met for the true vertical errors. It should be noted that the filter-predicted vertical errors still maintain only a Category I precision approach, but with some additional tuning a Category III approach should be possible. Table 4 - 29 outlines the true latitude errors for each decision height and Table 4 - 30 summarizes the precision approach category for each case.

Position Error State	Decision Height (feet)	Case II True Error (feet)	Case IV True Error (feet)	Case VI True Error (feet)	Vertical (Based on True Error)
δaltitude	200	1.98	2.38	1.92	Cat III
δaltitude	100	0.79	1.1	0.78	Cat III
δaltitude	50	0.47	0.82	0.51	Cat III

Table 4 - 29. Case II, IV, and VI 1σ Altitude Errors

Case Number	Horizontal (Based on True Error)	Horizontal (Based on Filter Predicted Error)	Vertical (Based on True Error)	Vertical (Based on Filter Predicted Error)
II, IV, and VI	Cat III	Cat III	Cat III	Cat I

Table 4 - 30. Precision Landing Category Predicted To Achieve

The Category III precision approach met in the vertical channel for the true errors is one level higher than the Category II approach met by the tanker aircraft scenario. Table 4 - 31 outlines the Case II, IV, and IV comparisons for the tanker and single engine aircraft errors. As can be seen, the altitude errors in the single engine aircraft cases has been reduced by an amount large enough to maintain a Category III precision approach. Although the true altitude errors in the tanker scenarion are less than one foot more, this difference is enough to maintain the precision approach at a Category II. This is counterintuitive since the small aircraft will "bounce around" more in an approach than a tanker. The different speed of the approaches is the determining factor here. The small

aircraft has decreased speed to 50 knots at touchdown while the tanker has a speed of 133 knots. Since the PROFGEN simulation does not simulate the greater buffetting of the single engine aircraft during landing, the lower velocity minimizes the effects of some of the errors. The addition of the radar altimeter for Cases II, IV, and VI has also eliminated the differences in latitude and longitude errors between the tanker and single engine aircraft which were seen in Cases I, III, and V. This additional measurement is very significant during the precision approach landing.

Error State	Case II average true error (feet) tanker	Case II average true error (feet) single engine	Case IV average true error (feet) tanker	Case IV average true error (feet) single engine	Case VI average true error (feet) tanker	Case VI average true error (feet) single engine
Latitude	0.97	0.85	1.10	1.0	1.12	0.98
Longitude	0.97	0.99	1.23	1.12	1.47	1.18
Altitude	1.72	1.08	1.89	1.43	1.85	1.07

Table 4 - 31. Average True Errors of Tanker vs Single Engine Aircraft

4.4.3 Case VII, IX, and XI - 0.4 nm/hr, 2.0 nm/hr, and 4.0 nm/hr INS with a Single Pseudolite

With the addition of the single pseudolite, no significant improvements were noted over Cases I, III, and V where no pseudolite was used. "Significant" implies the changing of a precision landing category based on the changes in either filter-predicted or true errors. Table 4 - 32 summarizes the precision landing category met for each case. As with the non-pseudolite case, Category III precision is met in the horizontal errors, but only Category I is met with the vertical errors.

Case Number	Horizontal (Based on True Error)	Horizontal (Based on Filter Predicted Error)	Vertical (Based on True Error)	Vertical (Based on Filter Predicted Error)
VII, IX, and XI	Cat III	Cat III	Cat I	Cat I

Table 4 - 32. Precision Landing Category Predicted To Achieve

4.4.4 Case VIII, X, and XII - 0.4 nm/hr, 2.0 nm/hr, and 4.0 nm/hr INS with a Single Pseudolite and radar altimeter

As in the previous section, no significant changes were found when the pseudolite was added to the radar altimeter case. We were able to realize a Category III precision approach in the true errors in for both the horizontal and vertical. Table 4 - 33 summarizes the precision approach capabilities for Cases VIII, X, and XII.

Case Number	Horizontal (Based on True Error)	Horizontal (Based on Filter Predicted Error)	Vertical (Based on True Error)	Vertical (Based on Filter Predicted Error)
VIII, X, and XII	Cat III	Cat III	Cat III	Cat I

Table 4 - 33. Precision Landing Category Predicted To Achieve

4.4.5 Example of 0.4 nm/hr, 2.0 nm/hr, and 4.0 nm/hr INS Drift during a Loss of GPS Measurement for 1/8 Schuler Period

Section 4.3 presents a detailed discussion for the reasoning behind the loss of range measurements from the 4 satellites. With the flight profile of the single engine aircraft used in place of the tanker profile, we see the increase in errors when the DGPS measurements are lost and the subsequent error improvements when the measurements are returned. The plots in Figure G.1 can be compared to the plots in Figure G.2 and Figure G.3 to see the increase in errors for the different INSs. Table 4 - 34 summarizes the precision approach performance for these last cases. As with the tanker profile scenarios, the horizontal errors meet a Category III precision approach while the vertical errors still

V. Conclusions and Recommendations

This chapter presents recommendations and conclusions based on the results which were presented in Chapter 4. This includes a basic introduction on the focus of the thesis, the conclusions which were drawn from the research, and recommendations for future work which may provide a solution to fully implementing a Category III precision approach.

5.1 Introduction

This thesis focused on the integration of information from several different stand-alone devices located on an aircraft to provide a more accurate answer about the location of an aircraft. The information was integrated using an extended Kalman filter to meet the FAA Category I, II, and III precision approach accuracy requirements. The stand-alone devices integrated included an INS, differentially corrected GPS, barometric altimeter, radar altimeter, and a ground-based pseudolite.

This thesis focused on the investigation of using differentially corrected GPS data to improve the accuracy of the integrated system. It also developed a generic precision approach flight profile (using PROFGEN [52]) for a small single engine aircraft. This would extend the research of Gray [27] to a new class of aircraft. The use of a single ground-based pseudolite to improve accuracy was also investigated. MSOFE [53] was utilized to perform extended Kalman Filter integration analysis.

5.2 Conclusions

The first conclusion which can be drawn is that the use of DGPS measurements is a giant step forward from standard GPS measurements towards realizing a Category III precision approach landing. Category I requirements were met under all scenarios. A

Category II precision approach was met with the true errors when a radar altimeter was also used to aid the inertial navigation system, and for the single engine aircraft, a Category III precision approach with the true errors was met when the radar altimeter was used as well as DGPS for INS aiding. This points out the necessity of performing additional filter tuning to have the performance of the filter-predicted errors match the performance of the true errors in order to meet a Category II and Category III precision approach landing.

The use of the single pseudolite provided negligible improvements in the latitude and altitude errors when a radar altimeter is used, but when a radar altimeter was not available, the altitude errors decreased by over 10%. The latitude errors increased by a small margin when the single pseudolite was used. This may be partially explained by changes in PDOP and HDOP caused by pseudolite placement. The longitude errors decreased by a substantial margin when the pseudolite was used, both with and without the use of a radar altimeter. However, a more substantial improvement is required in the vertical errors to meet a Category III approach. The radar altimeter, or some other device which accurately measures the height above ground level, is necessary to achieve the goal of a Category III precision approach landing. A 54% decrease in altitude errors was seen when a radar altimeter was used with the pseudolite, compared to when the radar altimeter was not used. Accurate height above ground information is required to meet higher precision landing requirements. The DGPS measurements removed most of the errors that the single pseudolite was helping to correct; therefore, the usefulness of that pseudolite was not as evident as when basic GPS measurements were used. The weakness of DGPS in the vertical channel still exists, and a device which provides improved vertical

measurements over the radar altimeter model used will close the gap for a Category III approach.

The use of DGPS on smaller instrument-rated aircraft is a viable option based on the results of the analysis done. Even a very inaccurate (4 nm/hr) INS, when coupled with DGPS measurements and a barometric altimeter, is capable of meeting a Category I precision approach. When a radar altimeter is used to aid the vertical channel, a Category III precision approach is capable of being met when the true errors are considered. The filter-predicted errors seen in this research would seem to limit the system to a Category I precision approach, but filter tuning should be able to remove enough of this error to reach a Category II approach at a minimum.

The loss of DGPS measurement information is a major concern, especially during final approach. The information provided for Cases XIII - XV show how quickly errors begin to grow when a DGPS outage occurs. The use of ground-based pseudolites would help in this area because each ground-based pseudolite could replace a lost satellite during final approach. However, if there are problems with receiving the data at the aircraft, this would not be a viable solution. The use of a Multiple Model Adaptive Estimator (MMAE) [56] which has the capability to adapt to changes in noise levels would be a great asset in minimizing the effects of such problems.

5.3 Recommendations

This thesis has taken the work begun by Gray [27] and increased the capabilities of the integrated system by introducing more precise equipment to improve the overall accuracy. To meet a Category III precision approach landing, several recommendations are presented to improve the accuracy of the system further.

1. Utilize carrier-phase GPS signals to increase the accuracy of the GPS measurements to the centimeter level. A viable carrier-phase model was not available for the MSOFE package during this effort. By developing and utilizing such an accurate measurement system, one will be able to reduce the vertical errors even further and hopefully be able to make the final step to meet a Category III precision approach.

2. The use of a second pseudolite should be investigated. Even though the improvements brought on by using a single pseudolite was minimal, the integrated system is close enough to a Category III approach that a second pseudolite may provide the necessary improvements.

3. Investigate varying the locations of the two pseudolites to determine the optimal geometry for pseudolite placement. It should be noted that the geometry will be different for every runway location.

4. Investigate the use of a MMAE structure to adapt to varying noise levels from the DGPS measurements, and to jamming. This will help assure the proper tuning of the filters based on the changing quality of the measurements actually received.

5. Explore new methods to compensate for the vertical errors in the integrated system. The radar altimeter is useful, but more accuracy is required.

Appendix A. Error State Definitions for the DLSM Truth and Filter Models

Tabular listings of the truth and filter models are presented. Tables A.1 and A.2 show the 39 INS states for the truth model, with the SNU 84-1 [41] and NRS [50,55] state numbers given for cross-reference. Table A.3 list the GPS states respectively, and Table A.4 lists the states in the reduced-ordered DLSM filter model.

Note: In Table A.1, the DLSM states 12 and 13 are not included; these are found in Table A.3.

DLSM State	State Symbol	Definition	SNU 84-1 State	NRS State
1	$\delta\theta_X$	X-component of vector angle from true to computer frame	1	1
2	$\delta\theta_Y$	Y-component of vector angle from true to computer frame	2	2
3	$\delta\theta_Z$	Z-component of vector angle from true to computer frame	3	3
4	ϕ_X	X- component of vector angle from true to platform frame	4	4
5	ϕ_Y	Y- component of vector angle from true to platform frame	5	5
6	ϕ_Z	Z- component of vector angle from true to platform frame	6	6
7	δV_X	X-component of error in computed velocity	7	7
8	δV_Y	Y-component of error in computed velocity	8	8
9	δV_Z	Z-component of error in computed velocity	9	9
10	δh	Error in vehicle altitude above reference ellipsoid	10	10
11	δh_B	Total baro-altimeter correclated error	23	11
14	δh_L	Error in lagged inertial	11	16
15	δS_3	Error in vertical channel aiding state	12	17
16	δS_4	Error in vertical channel aiding state	13	18
17	Δx_C	X-component of accelerometer and velocity quantizer correlated noise	17	19
18	Δy_C	Y-component of accelerometer and velocity quantizer correlated noise	18	20
19	Δz_C	Z-component of accelerometer and velocity quantizer correlated noise	19	21
20	δg_X	X-component of gravity vector errors	20	22
21	δg_Y	Y-component of gravity vector errors	21	23
22	δg_Z	Z-component of gravity vector errors	22	24

Table A.1 39-State INS System Model: First 20 States

Note: DLSM state 12 and state 13 are located in Table A - 3

State Number	State Symbol	Definition	SNU 84-1 State	NRS State
23	b_x	X-component of gyro drift rate repeatability	30	25
24	b_y	Y-component of gyro drift rate repeatability	31	26
25	b_z	Z-component of gyro drift rate repeatability	32	27
26	S_{gx}	X-component of gyro scale factor error	33	28
27	S_{gy}	Y-component of gyro scale factor error	34	29
28	S_{gz}	Z-component of gyro scale factor error	35	30
29	∇_{bx}	X-component of accelerometer bias repeatability	48	31
30	∇_{by}	Y-component of accelerometer bias repeatability	49	32
31	∇_{bz}	Z-component of accelerometer bias repeatability	50	33
32	S_{Ax}	X-component of accelerometer and velocity quantizer scale factor error	51	34
33	S_{Ay}	Y-component of accelerometer and velocity quantizer scale factor error	52	35
34	S_{Az}	Z-component of accelerometer and velocity quantizer scale factor error	53	36
35	S_{QAx}	X-component of accelerometer and velocity quantizer scale factor asymmetry	54	37
36	S_{QAy}	Y-component of accelerometer and velocity quantizer scale factor asymmetry	55	38
37	S_{QAz}	Z-component of accelerometer and velocity quantizer scale factor asymmetry	56	39
38	μ_1	X accelerometer misalignment about Z-axis	66	40
39	μ_2	Y accelerometer misalignment about Z-axis	67	41
40	μ_3	Z accelerometer misalignment about Y-axis	68	42
41	σ_1	X accelerometer misalignment about Y-axis	69	43

Table A.2 39-state INS System Model: Second 19 States

State Number	State Symbol	Definition	NRS State
12	δR_{clku}	User clock bias	14
13	δD_{clku}	User clock drift	15
43	δR_{trop1}	SV 1 tropospheric error	69
44	δR_{ion1}	SV 1 ionospheric error	70
46	δx_{sv1}	SV 1 x-component of position error	72
47	δy_{sv1}	SV 1 y-component of position error	73
48	δz_{sv1}	SV 1 z-component of position error	74
50	δR_{trop2}	SV 2 tropospheric error	76
51	δR_{ion2}	SV 2 ionospheric error	77
53	δx_{sv2}	SV 2 x-component of position error	79
54	δy_{sv2}	SV 2 y-component of position error	80
55	δz_{sv2}	SV 2 z-component of position error	81
57	δR_{trop3}	SV 3 tropospheric error	83
58	δR_{ion3}	SV 3 ionospheric error	84
60	δx_{sv3}	SV 3 x-component of position error	86
61	δy_{sv3}	SV 3 y-component of position error	87
62	δz_{sv3}	SV 3 z-component of position error	88
64	δR_{trop4}	SV 4 tropospheric error	90
65	δR_{ion4}	SV 4 ionospheric error	91
67	δx_{sv4}	SV 4 x-component of position error	93
68	δy_{sv4}	SV 4 y-component of position error	94
69	δz_{sv4}	SV 4 z-component of position error	95

Table A.3 22-State DGPS System Model

State Number	State Symbol	Definition	NRS State
1	$\delta\theta_X$	X-component of vector angle from true to computer frame	1
2	$\delta\theta_Y$	Y-component of vector angle from true to computer frame	2
3	$\delta\theta_Z$	Z-component of vector angle from true to computer frame	3
4	ϕ_X	X- component of vector angle from true to platform frame	4
5	ϕ_Y	Y- component of vector angle from true to platform frame	5
6	ϕ_Z	Z- component of vector angle from true to platform frame	6
7	δV_X	X-component of error in computed velocity	7
8	δV_Y	Y-component of error in computed velocity	8
9	δV_Z	Z-component of error in computed velocity	9
10	δh	Error in vehicle altitude above reference ellipsoid	10
11	δh_B	Total baro-altimeter correclated error	11
12	δclk_b	User clock bias	14
13	δclk_{dr}	User clock drift	15

Table A.4 13-State Reduced-Order Filter Model

Appendix B.

Plots of Case I through Case VI for Tanker Flight Profile.

Plot Legend

$\cdots$ true error (mean error $\pm$ σ_{true})

- - - filter predicted error ($0 \pm \sigma_{filter}$)

— mean error

B.1 Plots of Case I: Barometric Altimeter, 0.4 nm/hr INS, and DGPS Using the Tanker Flight Profile.

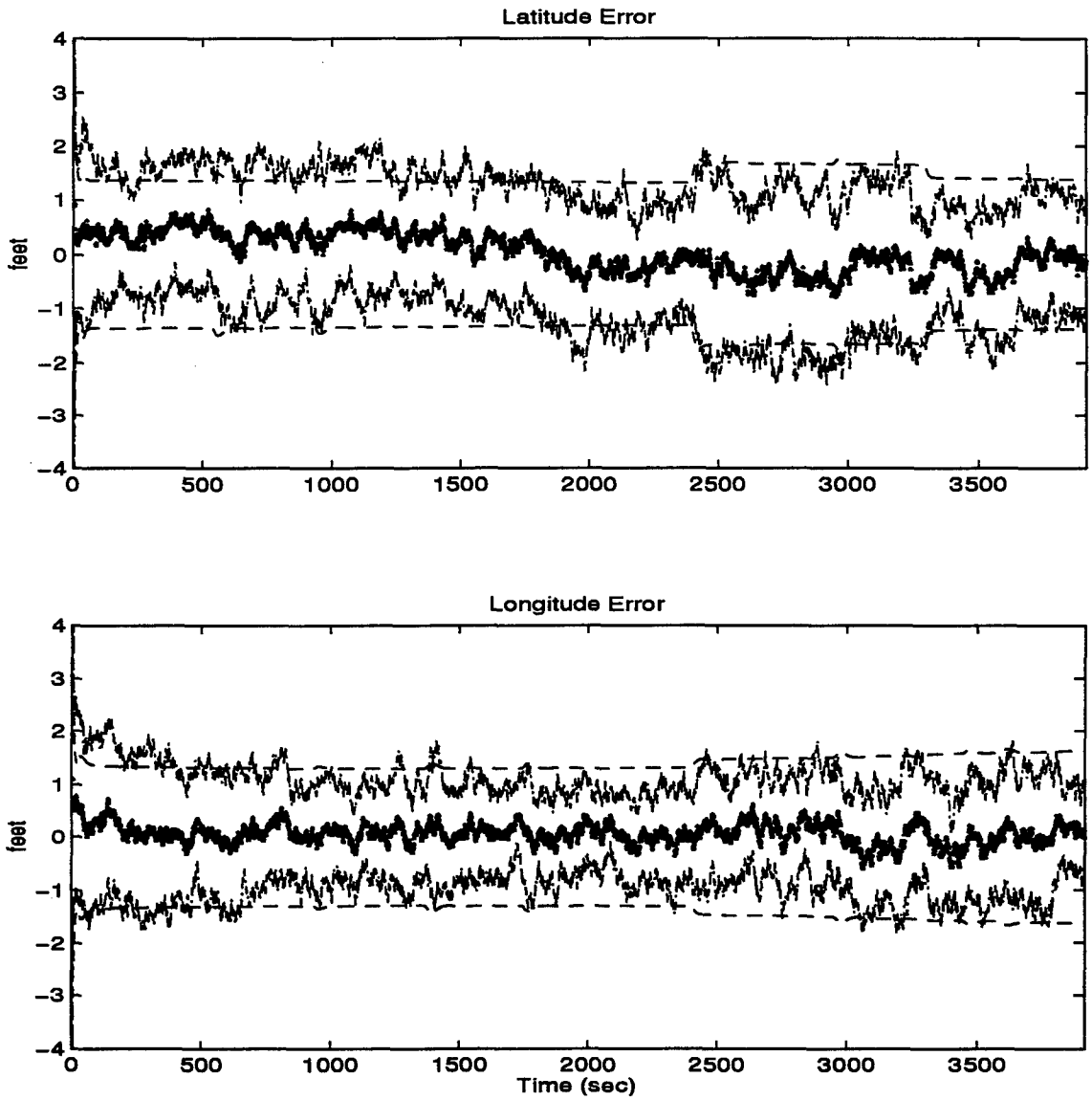

Figure B.1 Latitude and Longitude Error

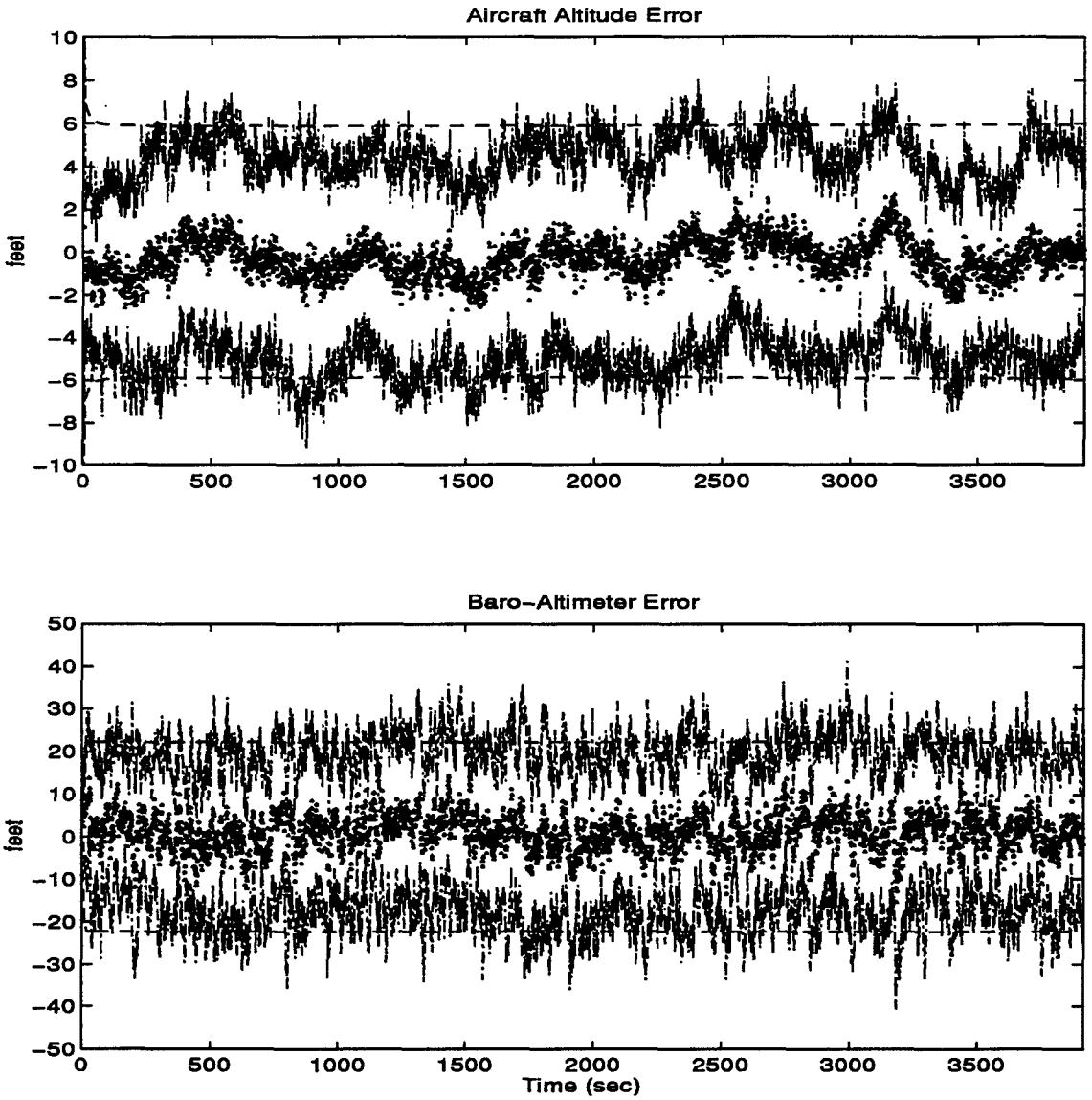

Figure B.2 Aircraft Altitude and Baro-Altimeter Error

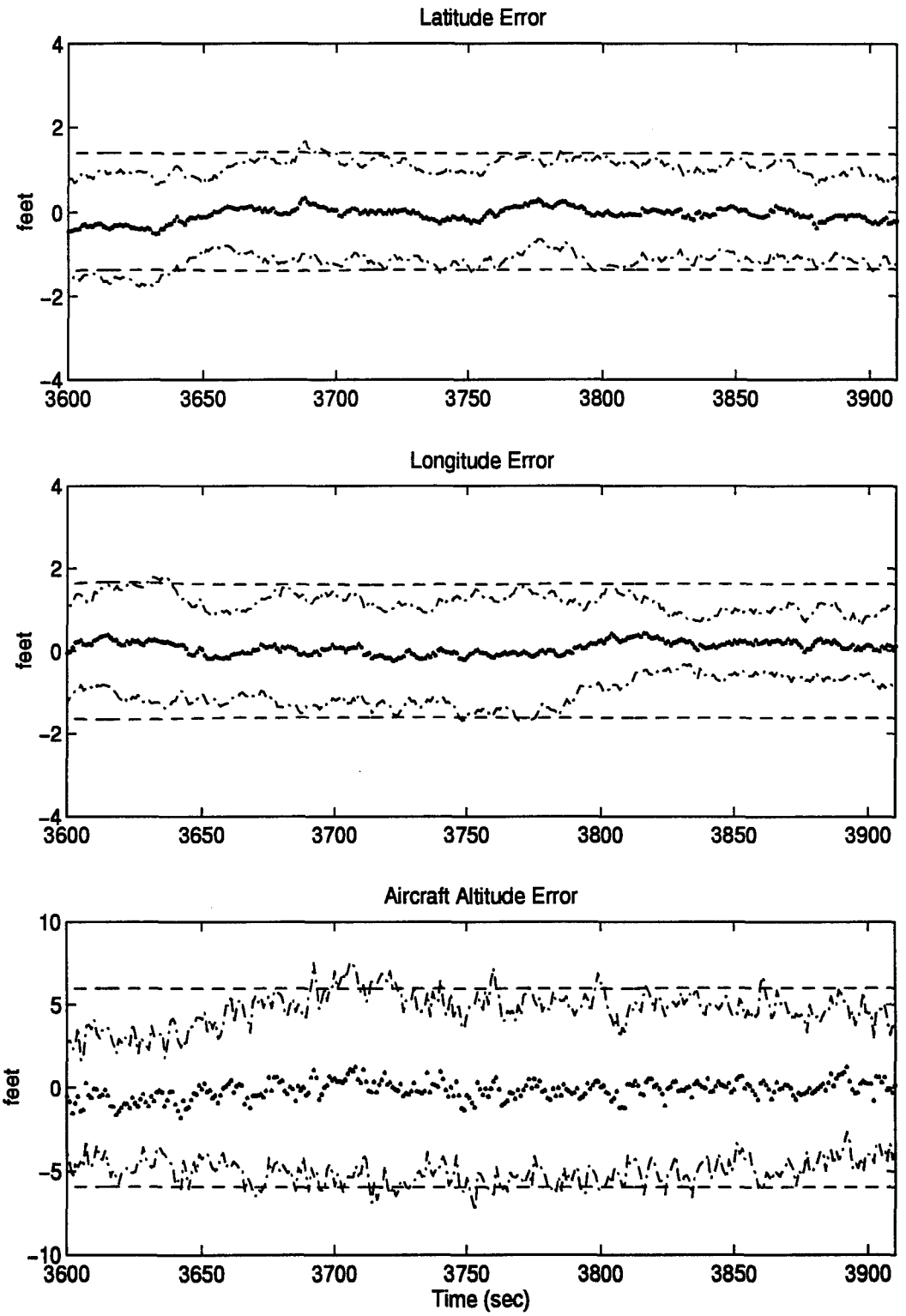

Figure B.3 Latitude, Longitude, and Aircraft Altitude Error

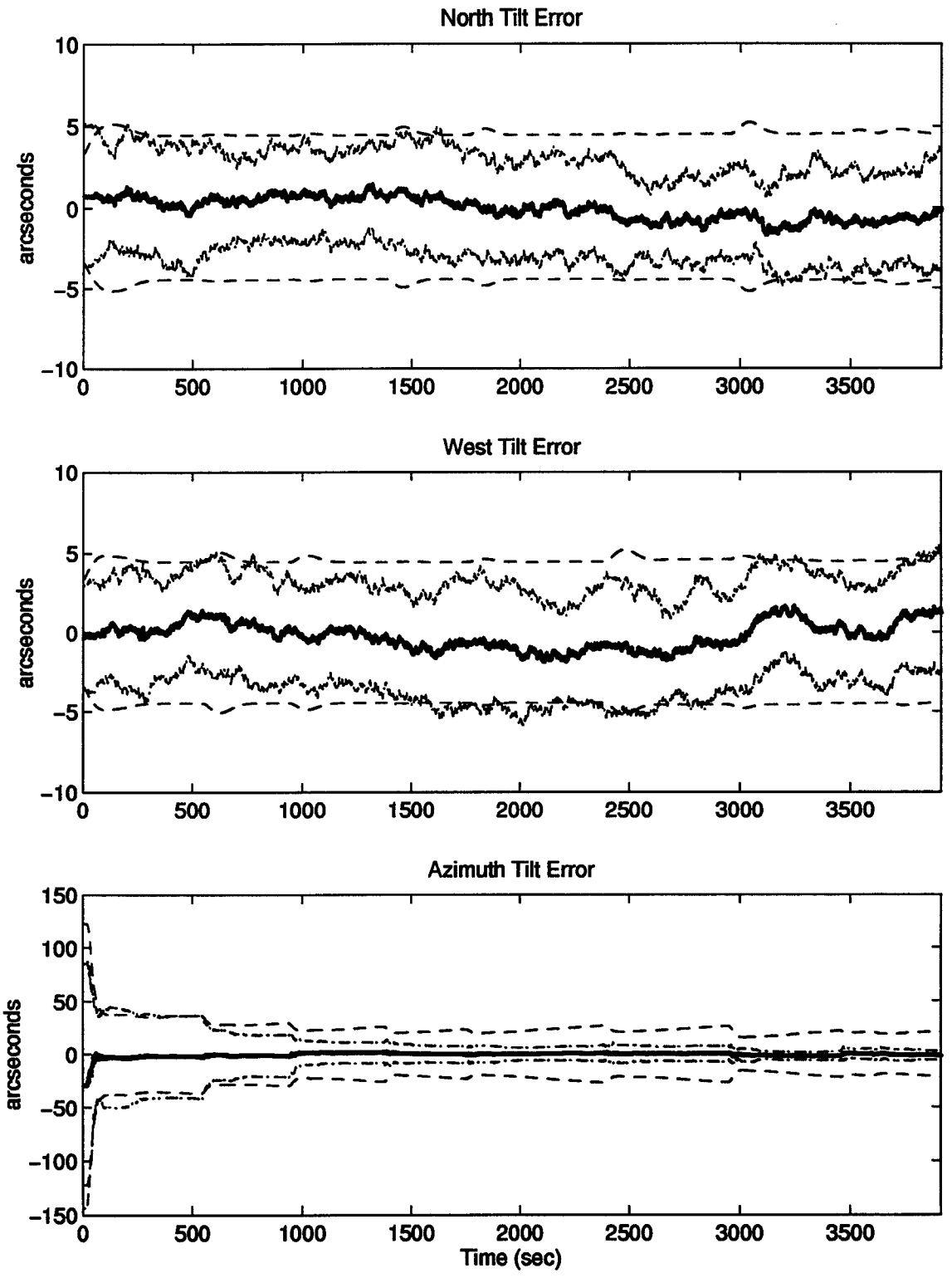

Figure B.4 North, West, and Azimuth Tilt Errors

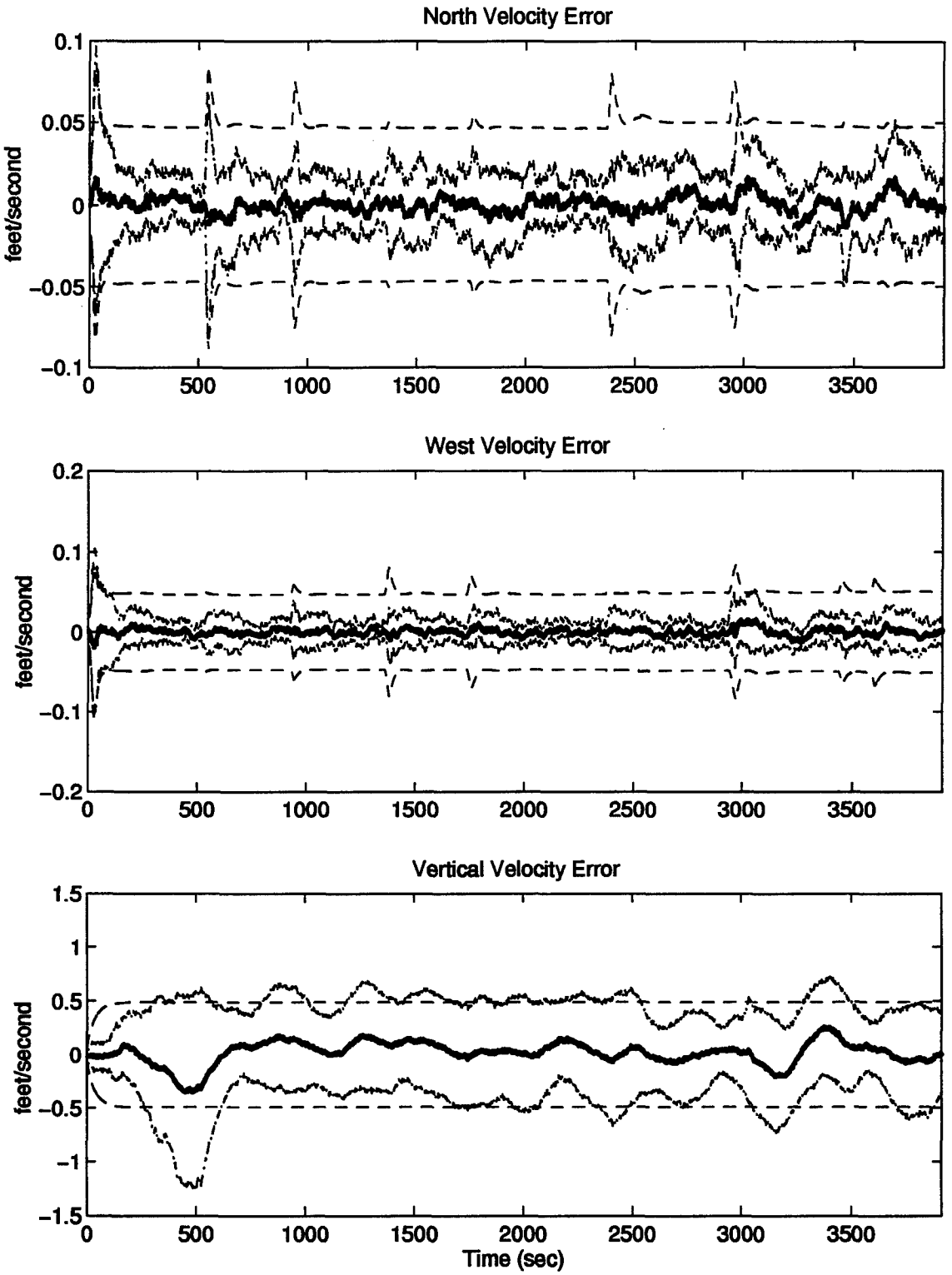

Figure B.5 North, West, and Vertical Velocity Errors

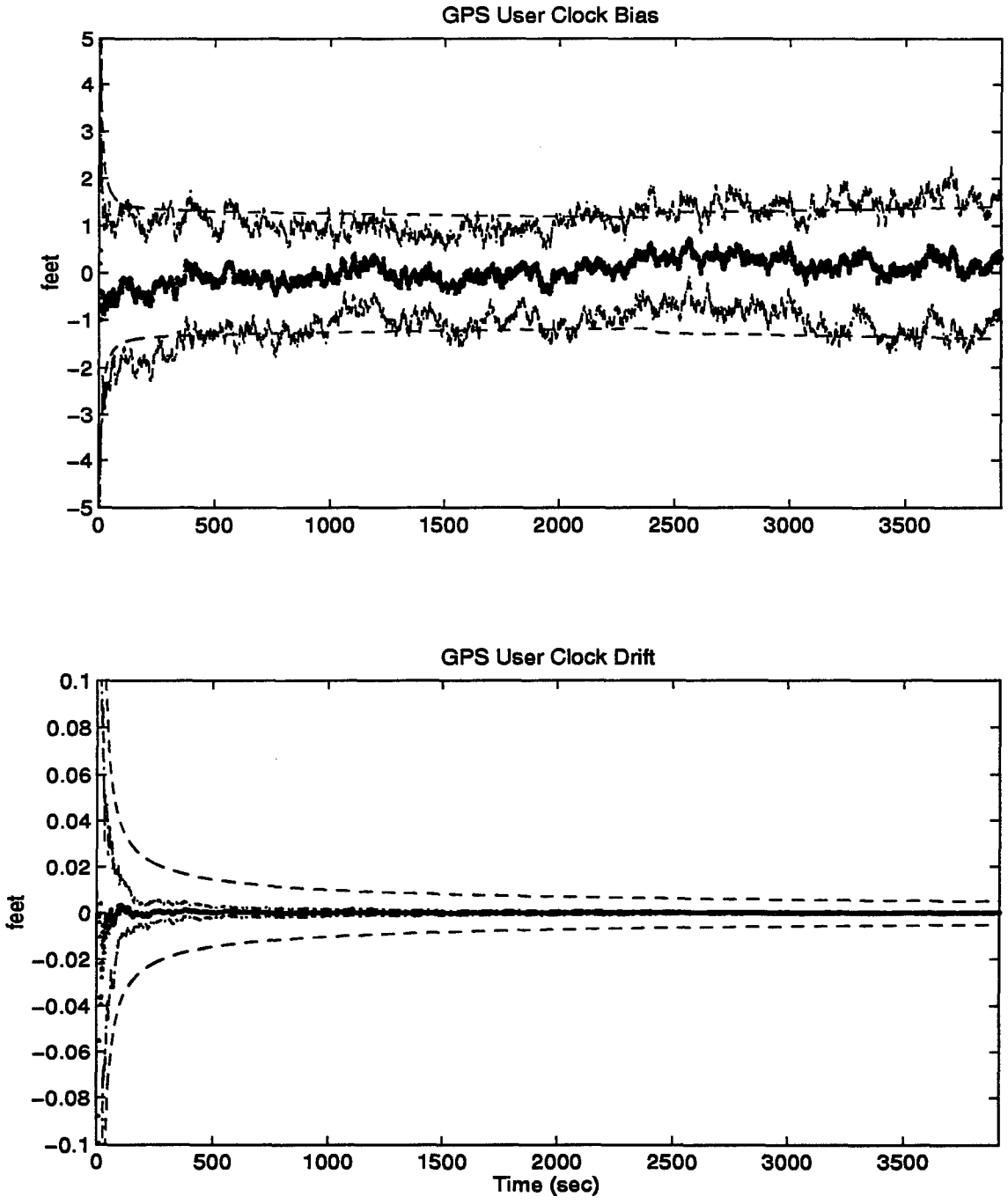

Figure B.6 GPS User Clock Bias and GPS User Clock Drift

B.2 Plots of Case II: Barometric Altimeter, 0.4 nm/hr INS, Radar Altimeter, and DGPS Using the Tanker Flight Profile.

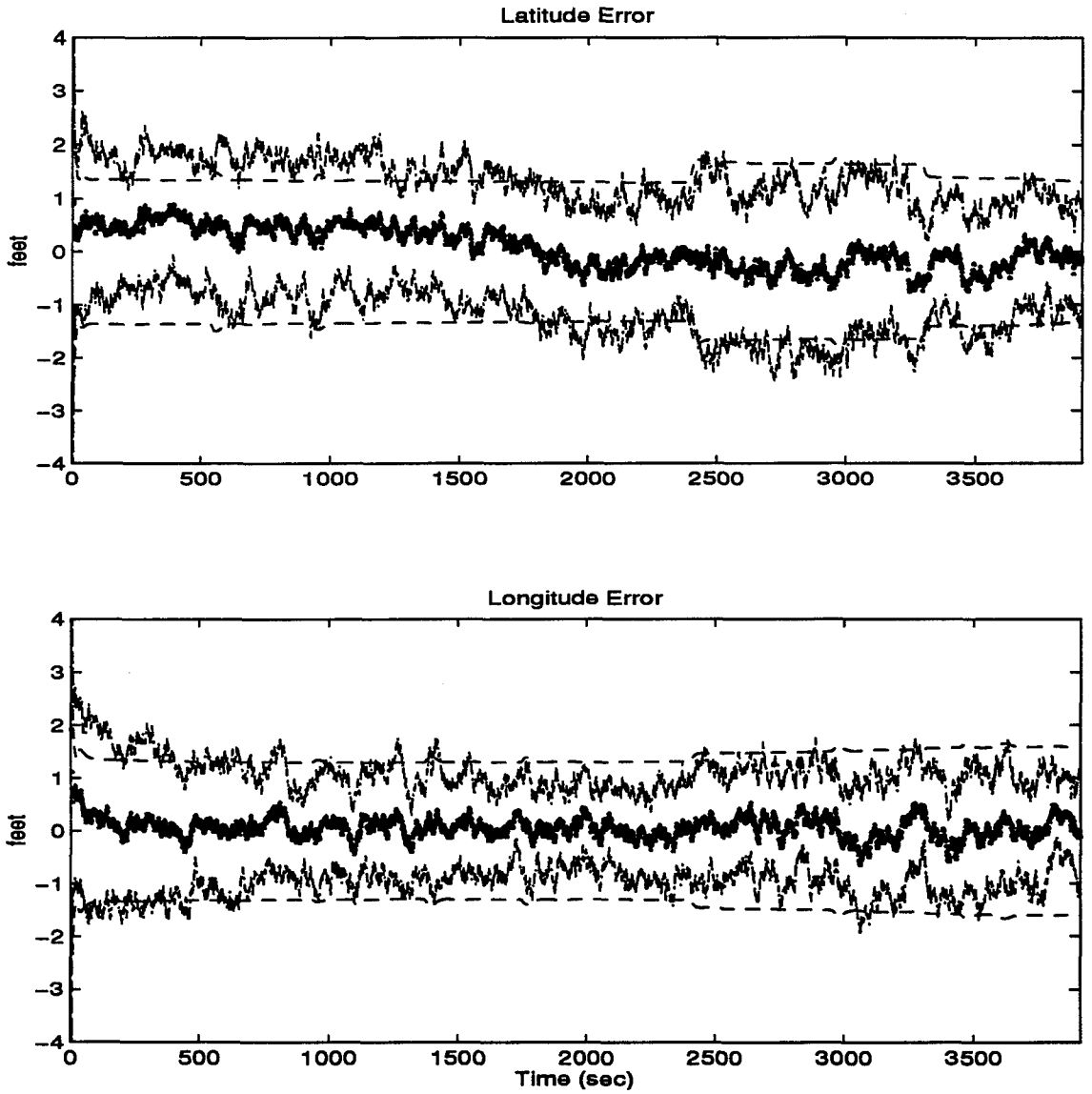

Figure B.7 Latitude and Longitude Error

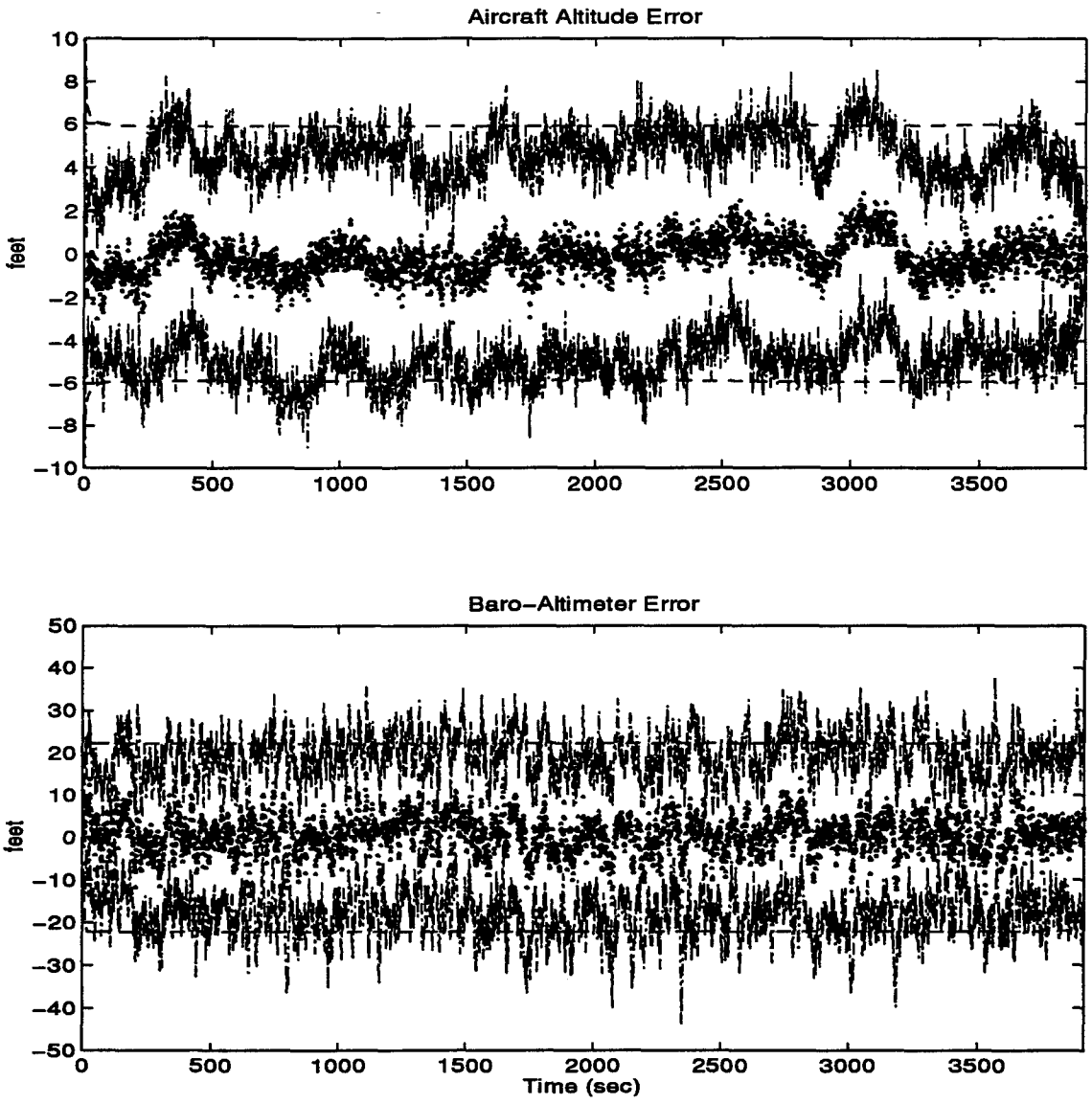

Figure B.8 Aircraft Altitude and Baro-Altimeter Error

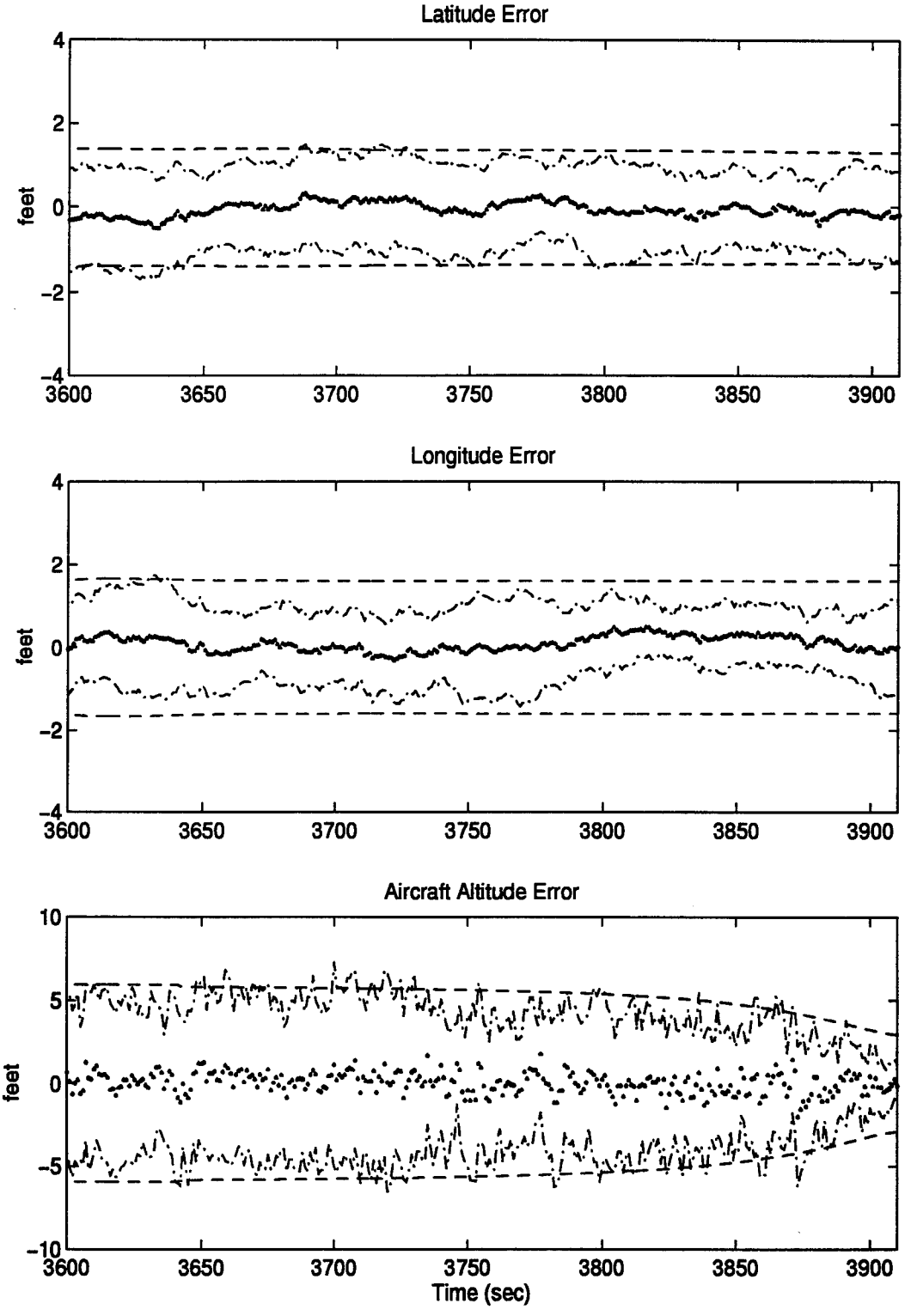

Figure B.9 Latitude, Longitude, and Aircraft Altitude Error

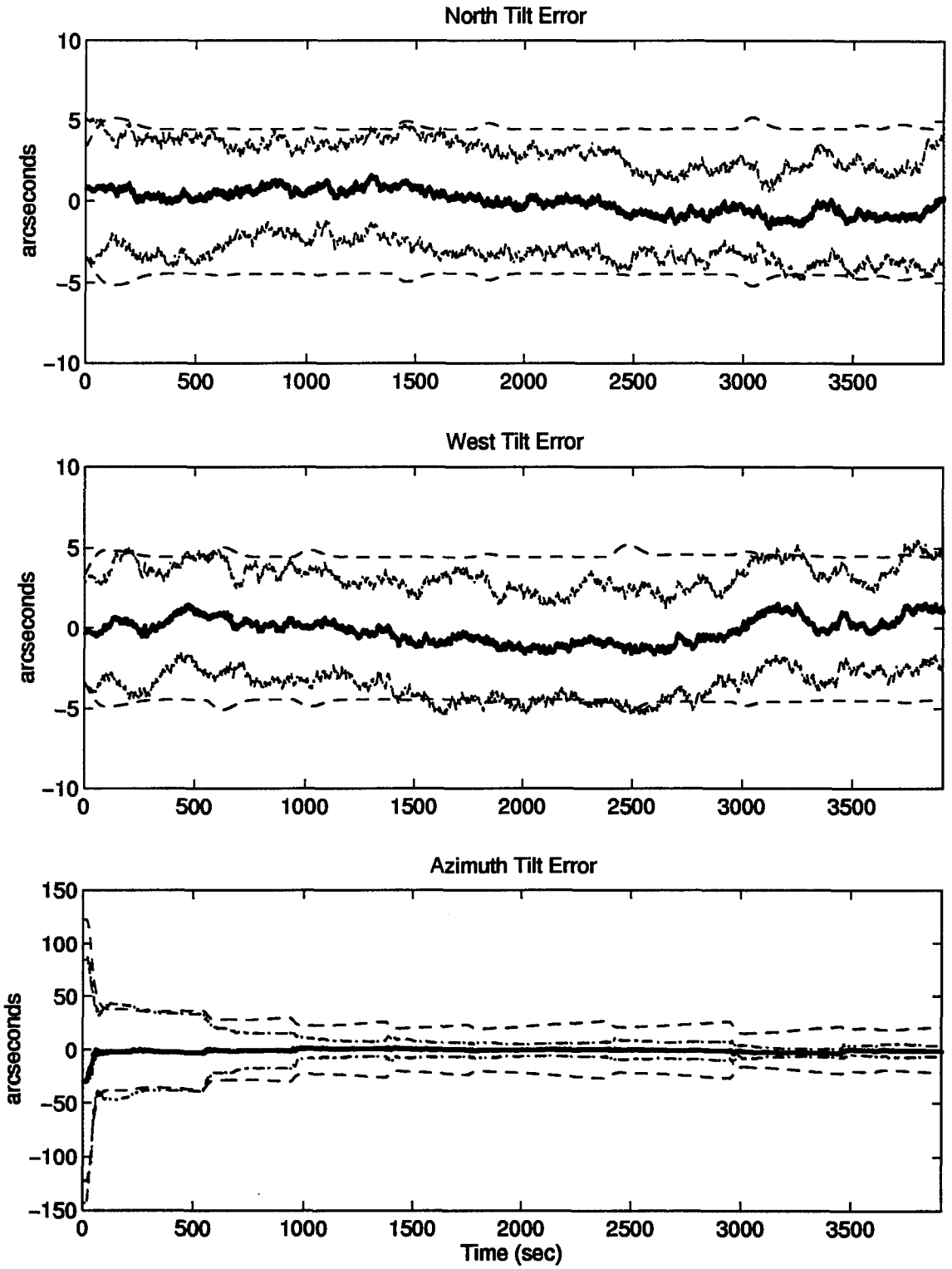

Figure B.10 North, West, and Azimuth Tilt Errors

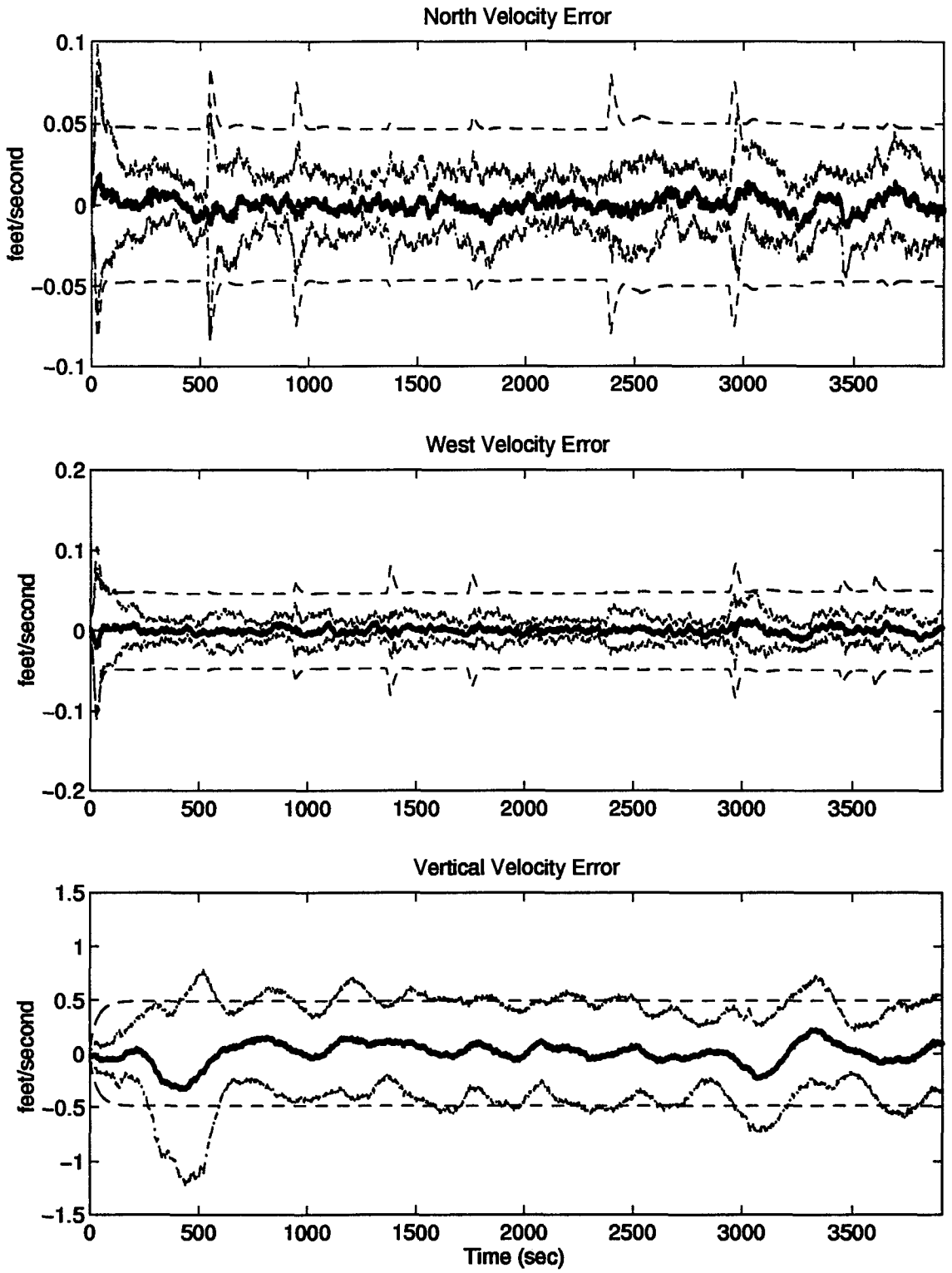

Figure B.11 North, West, and Vertical Velocity Errors

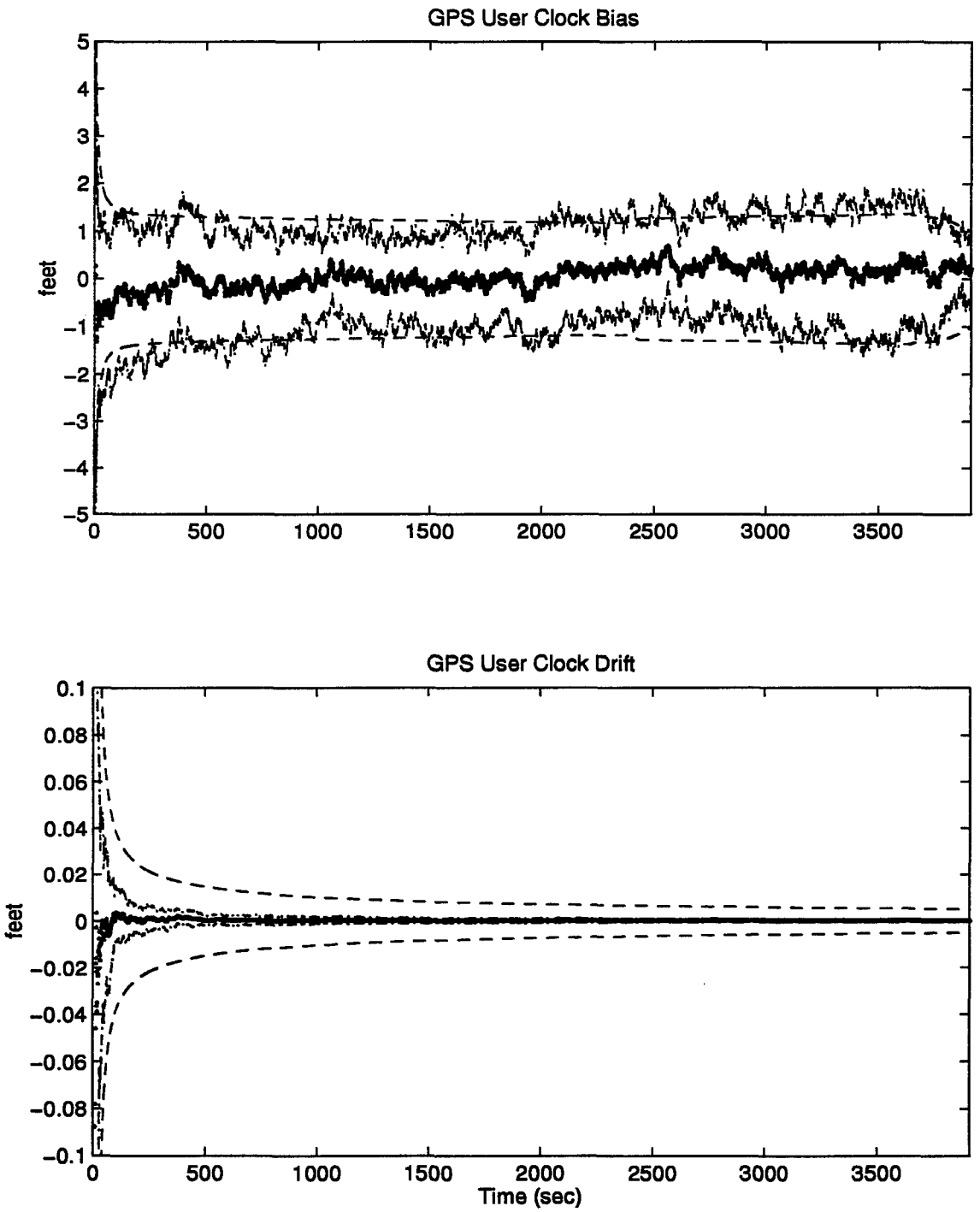

Figure B.12 GPS User Clock Bias and GPS User Clock Drift

B.3 Plots of Case III: Barometric Altimeter, 2.0 nm/hr INS, and DGPS Using the Tanker Flight Profile.

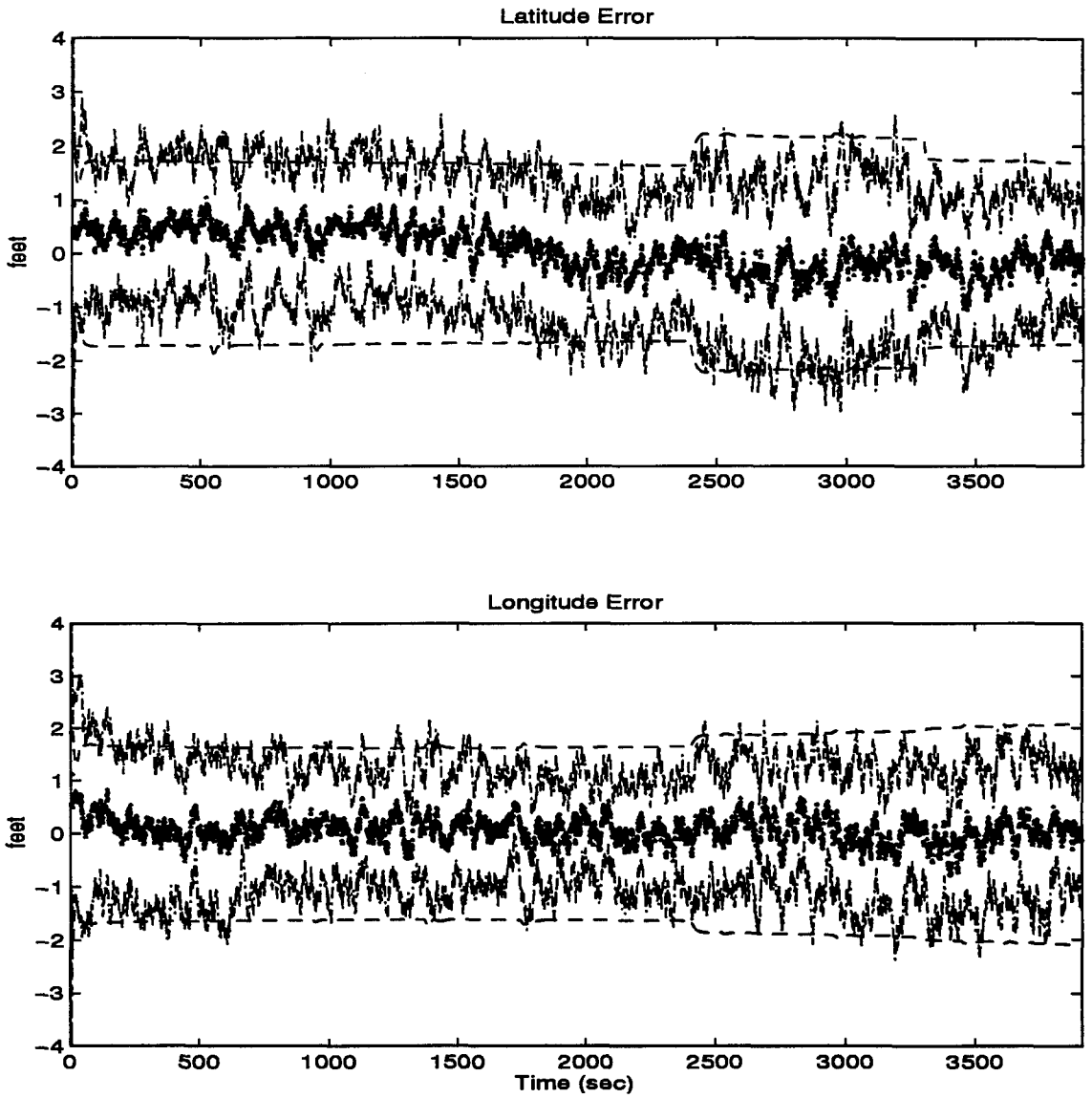

Figure B.13 Latitude and Longitude Error

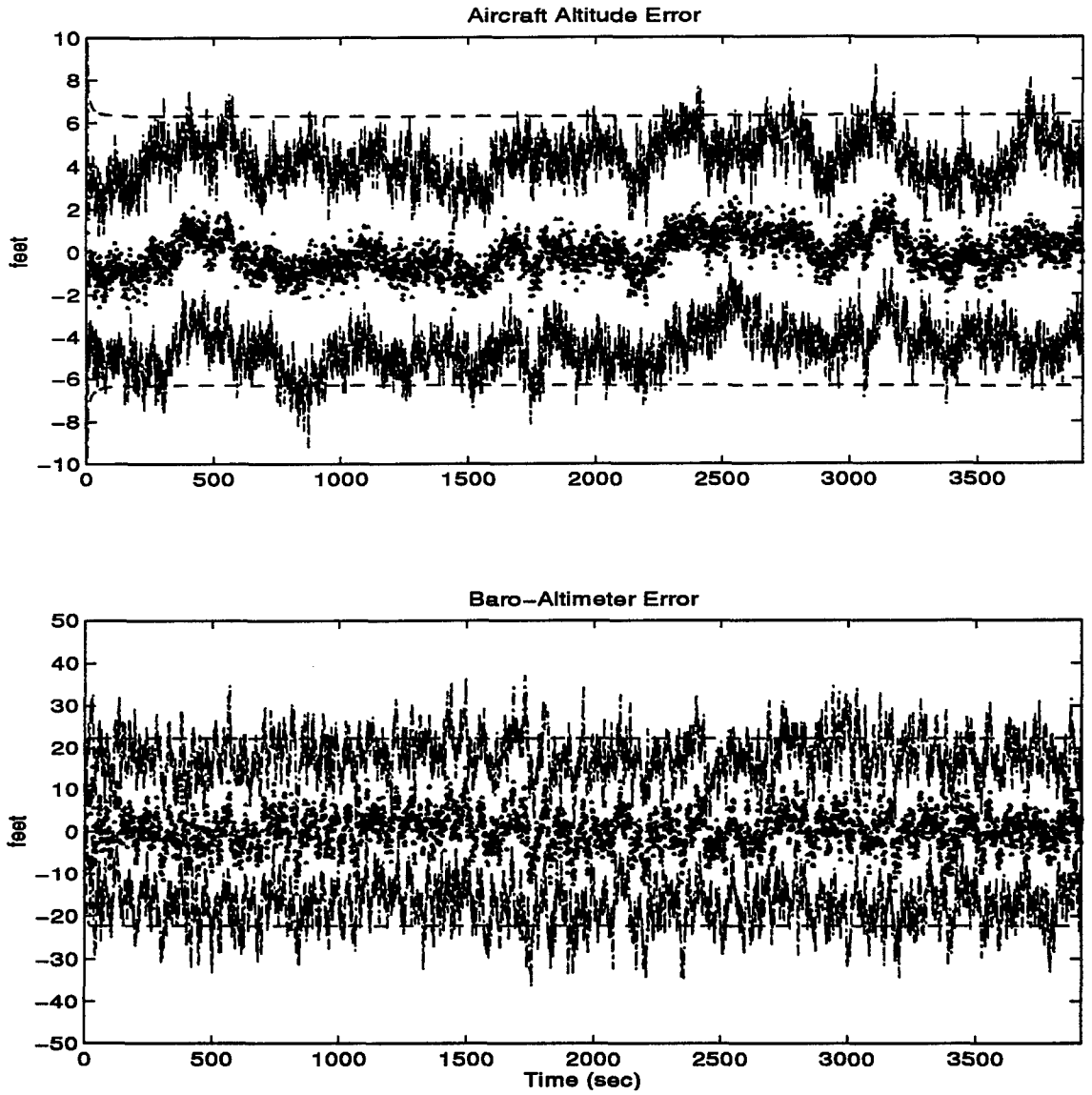

Figure B.14 Aircraft Altitude and Baro-Altimeter Error

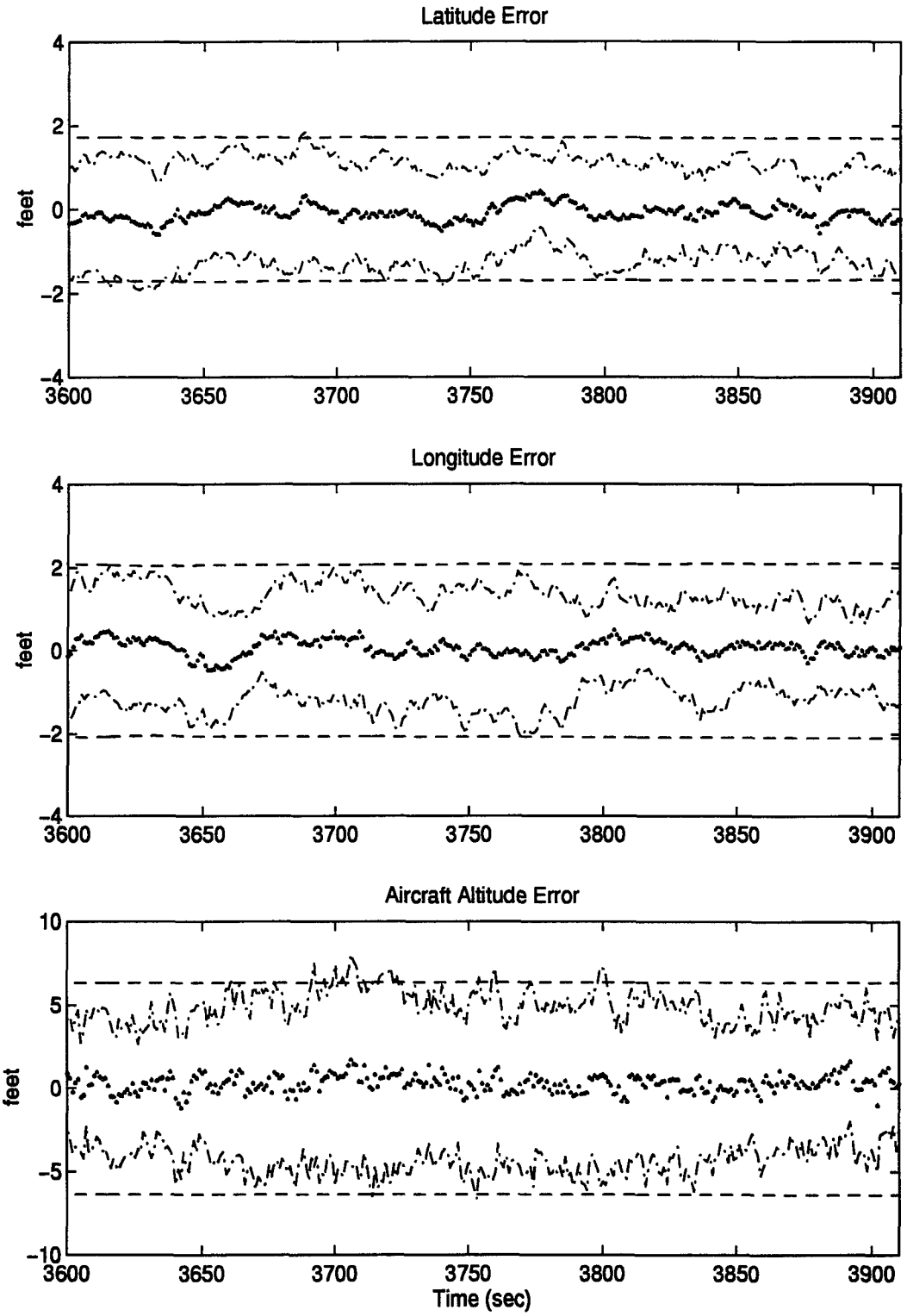

Figure B.15 Latitude, Longitude, and Aircraft Altitude Error

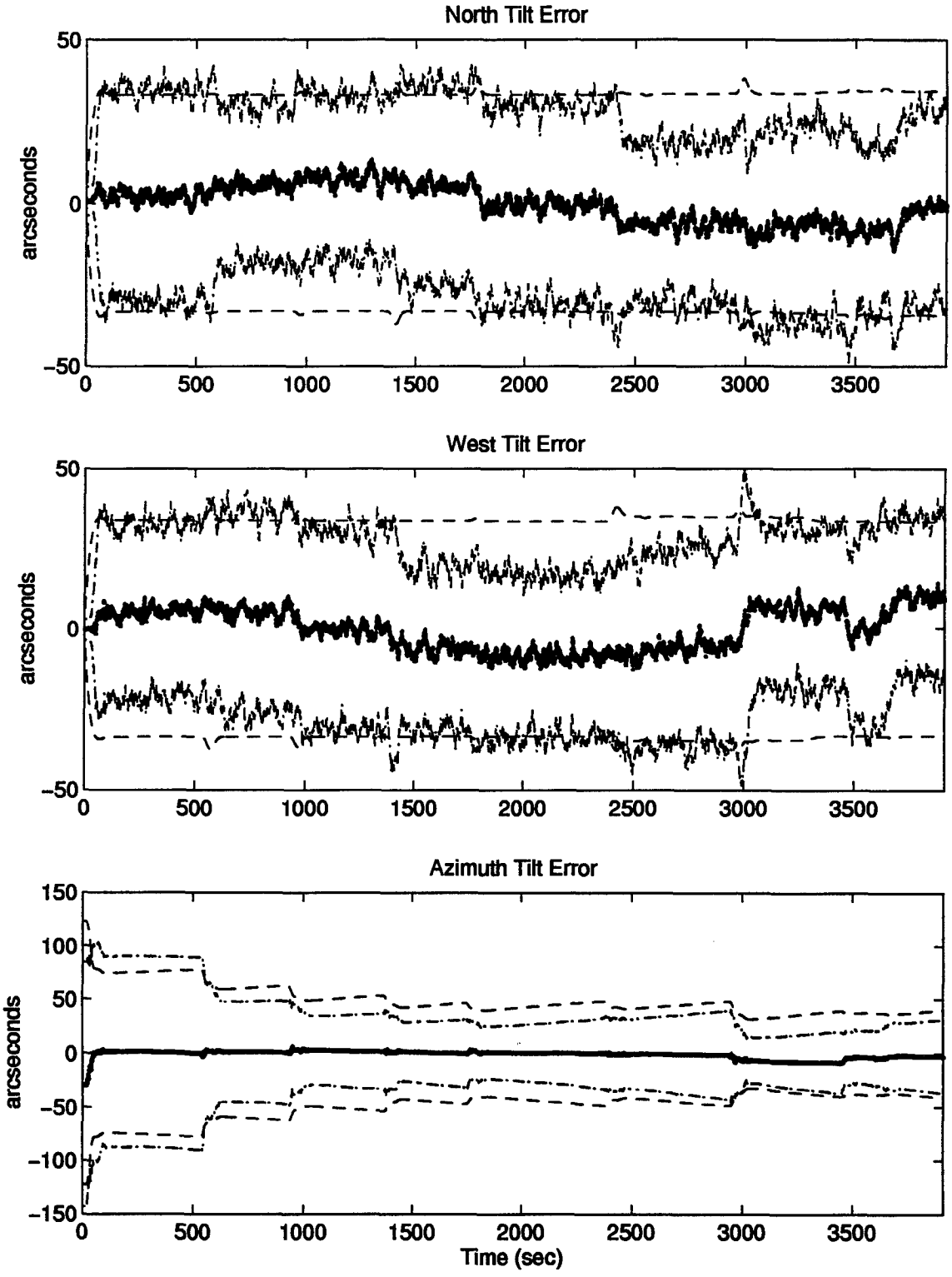

Figure B.16 North, West, and Azimuth Tilt Errors

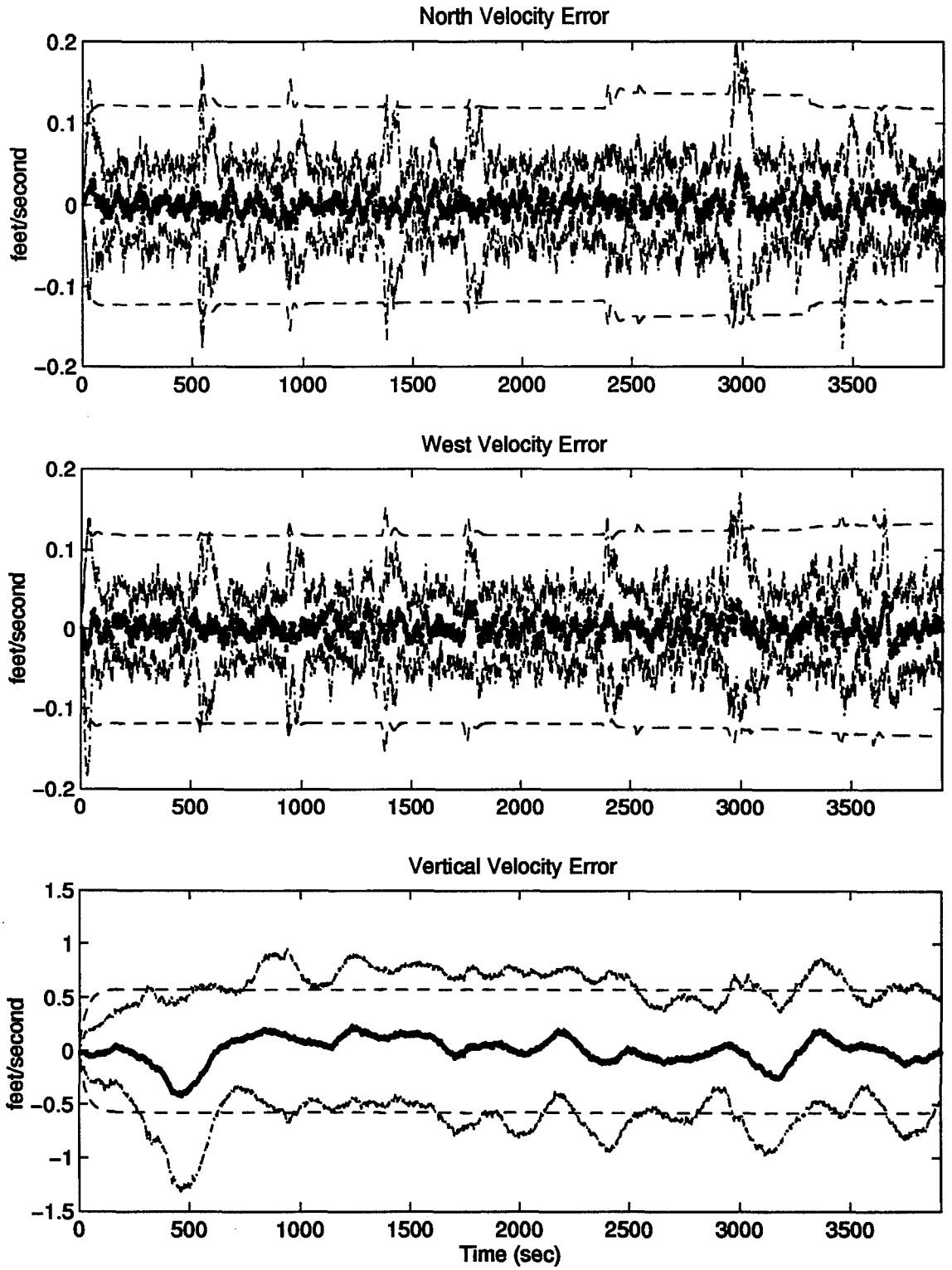

Figure B.17 North, West, and Vertical Velocity Errors

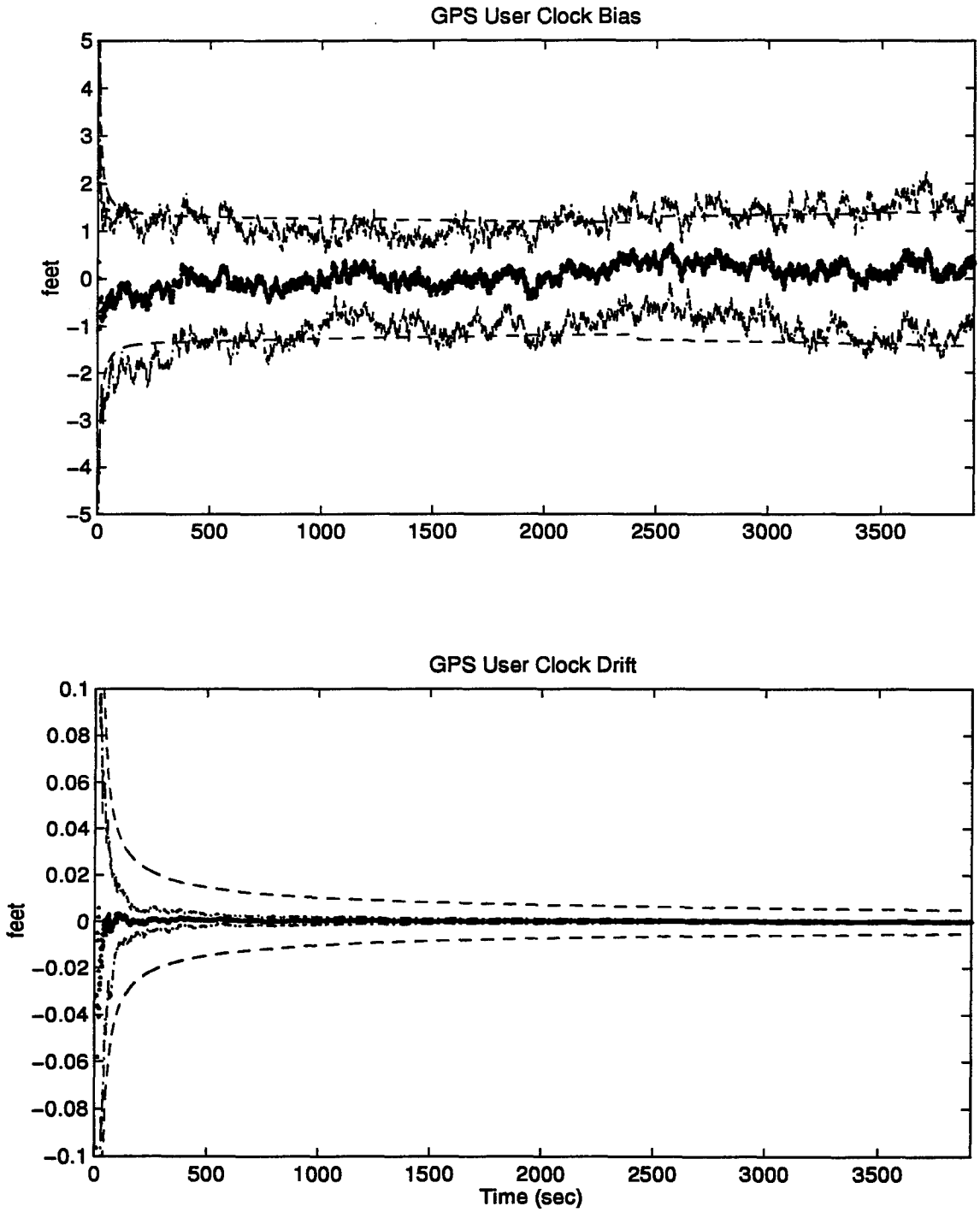

Figure B.18 GPS User Clock Bias and GPS User Clock Drift

B.4 Plots of Case IV: Barometric Altimeter, 2.0 nm/hr INS, Radar Altimeter, and DGPS Using the Tanker Flight Profile.

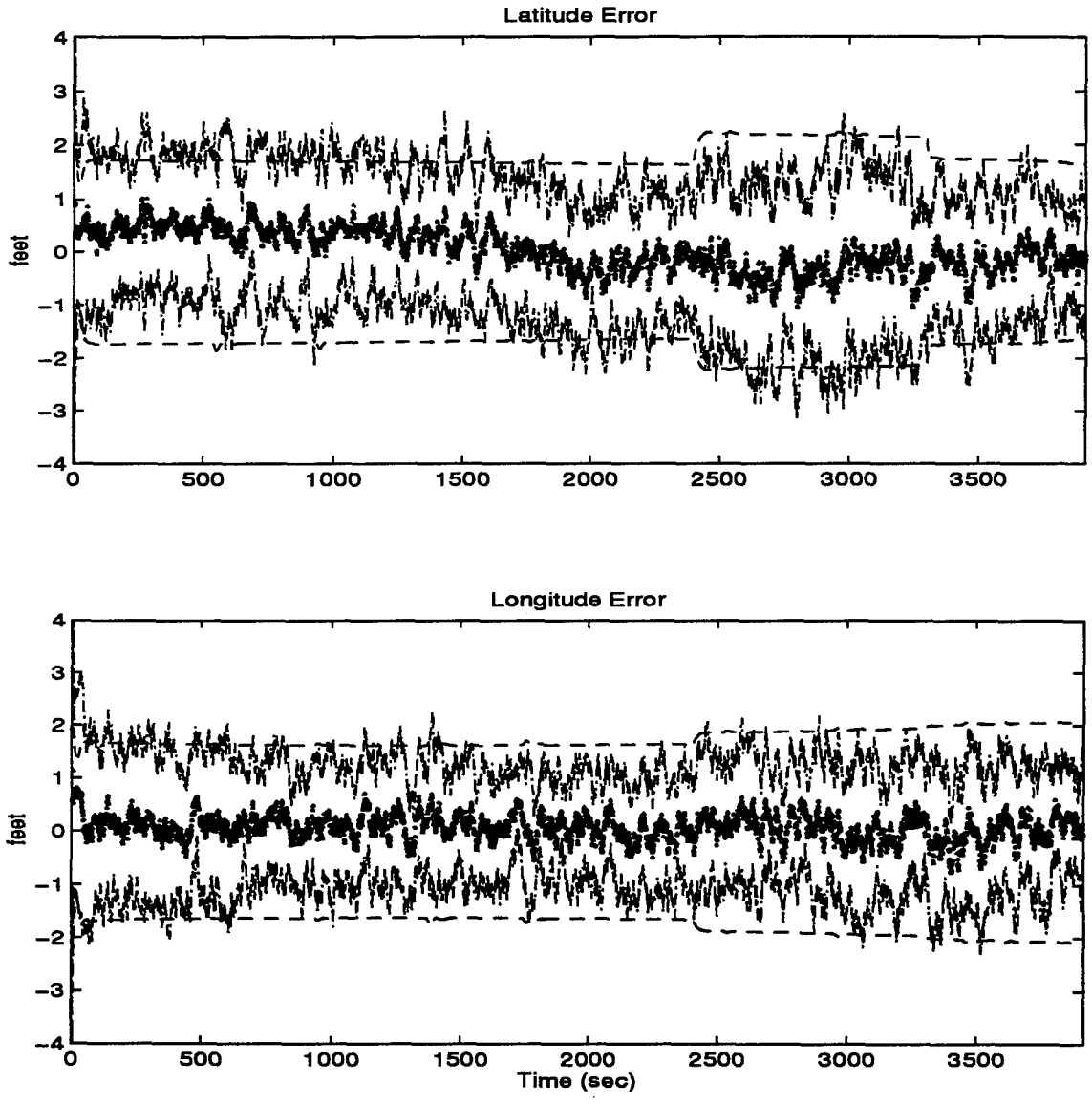

Figure B.19 Latitude and Longitude Error

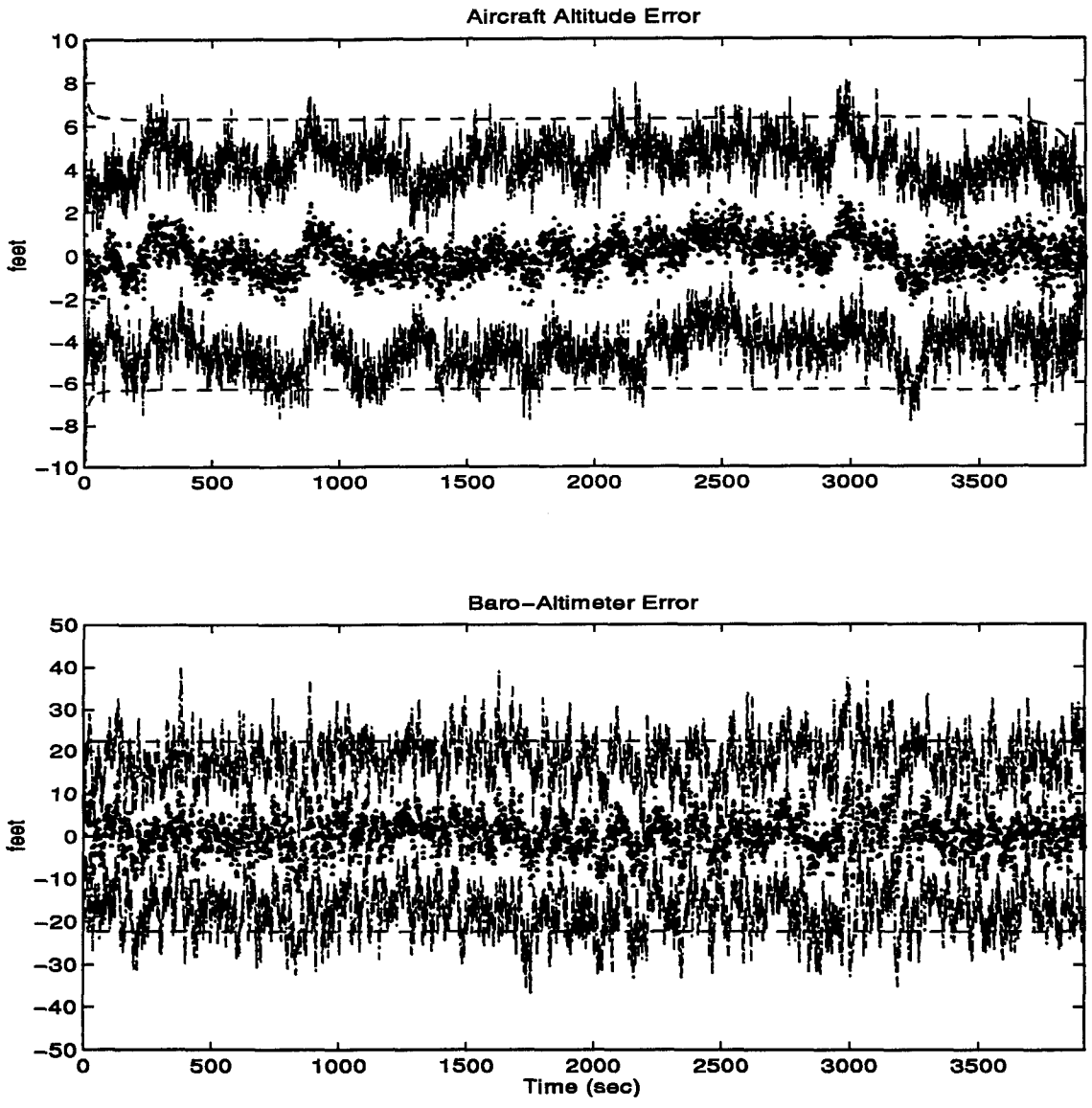

Figure B.20 Aircraft Altitude and Baro-Altimeter Error

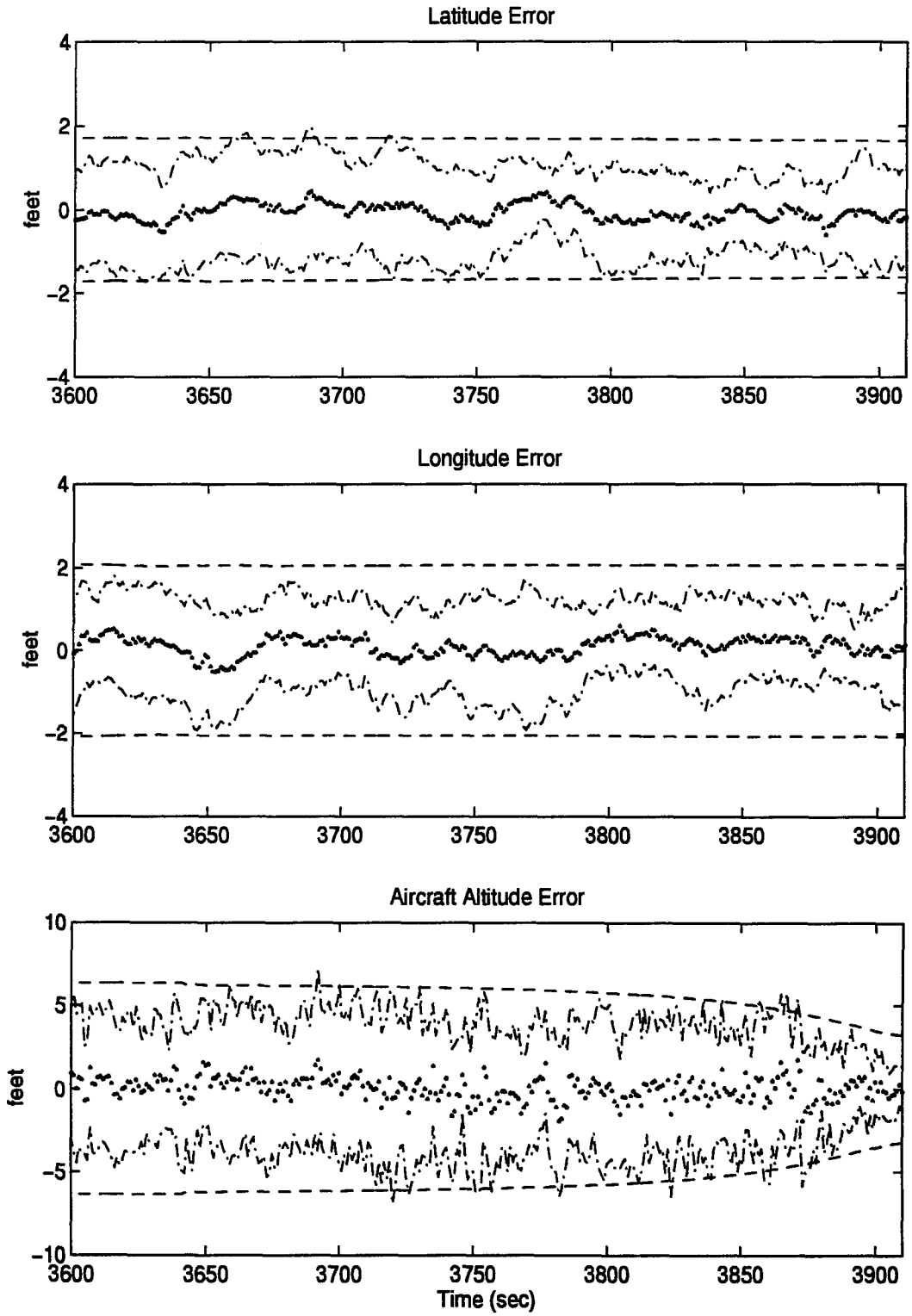

Figure B.21 Latitude, Longitude, and Aircraft Altitude Error

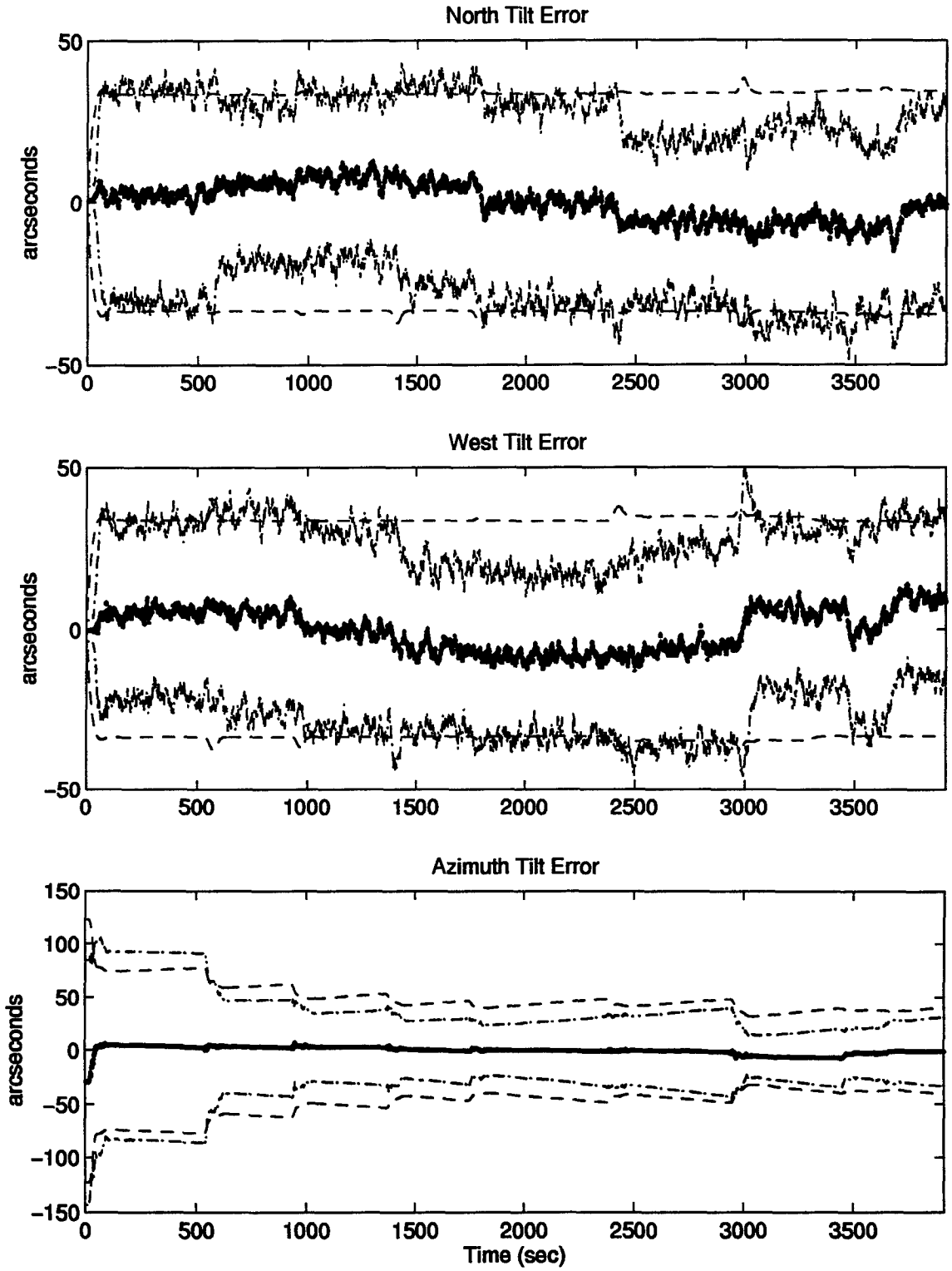

Figure B.22 North, West, and Azimuth Tilt Errors

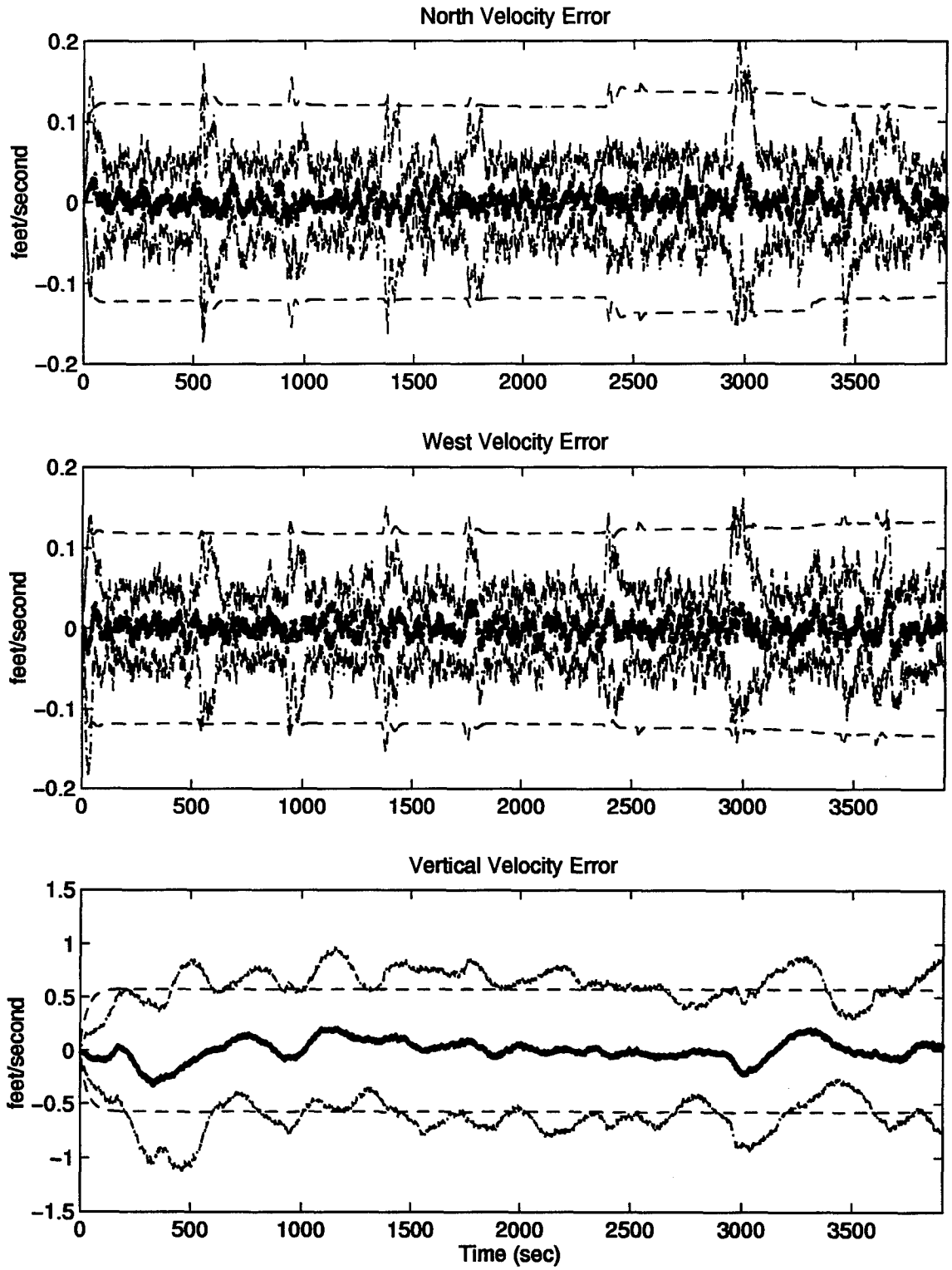

Figure B.23 North, West, and Vertical Velocity Errors

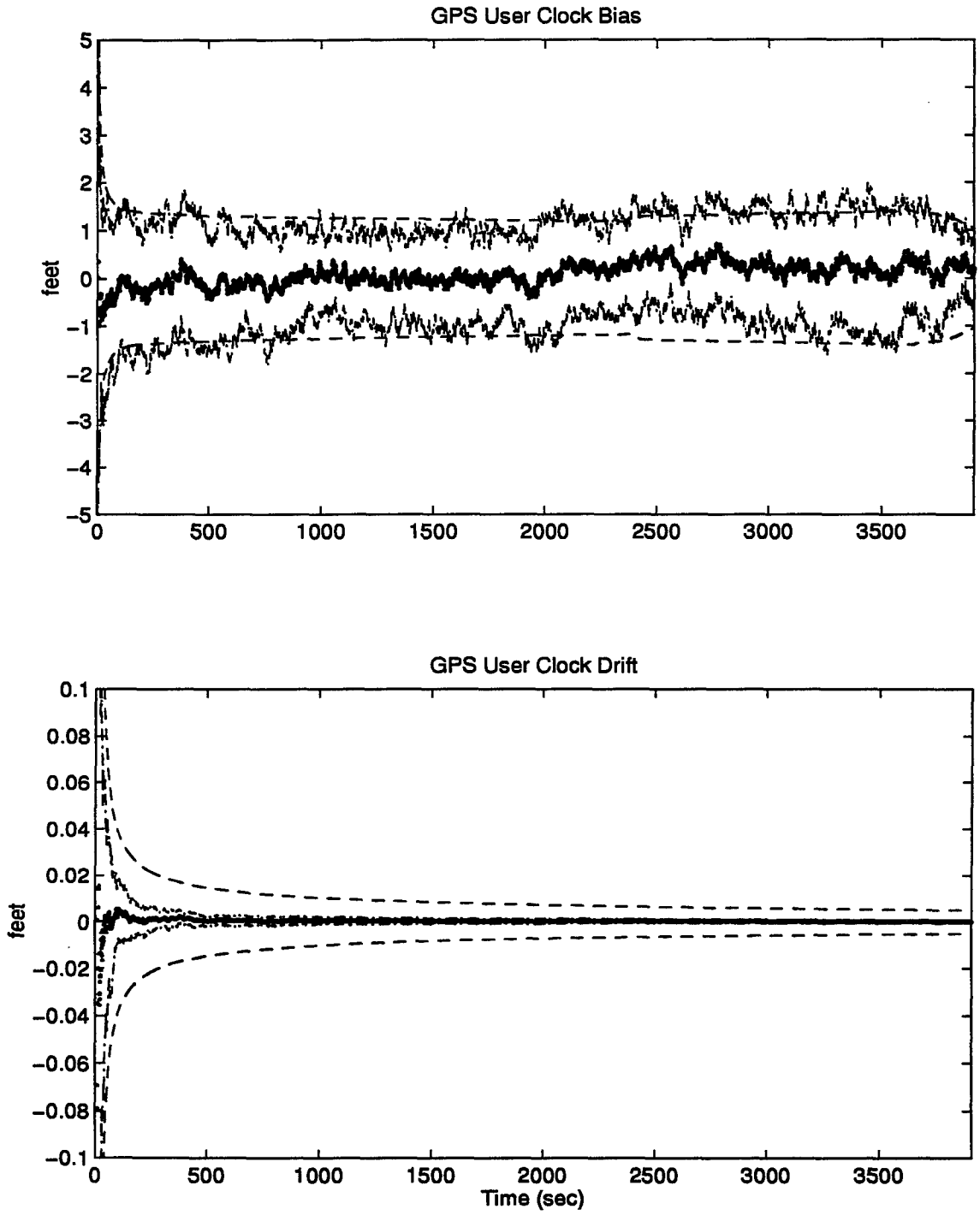

Figure B.24 GPS User Clock Bias and GPS User Clock Drift

B.5 Plots of Case V: Barometric Altimeter, 4.0 nm/hr INS, and DGPS Using the Tanker Flight Profile.

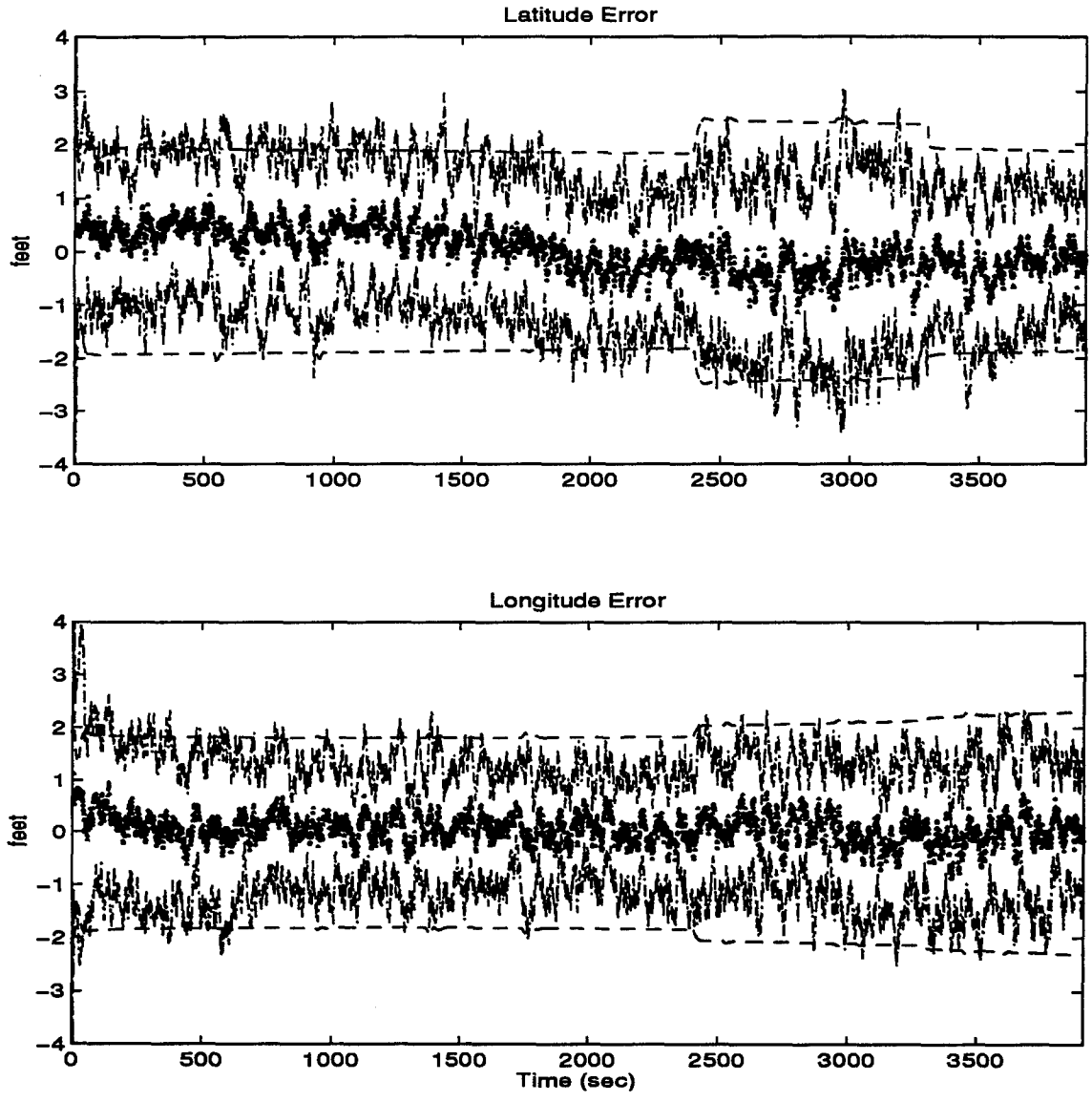

Figure B.25 Latitude and Longitude Error

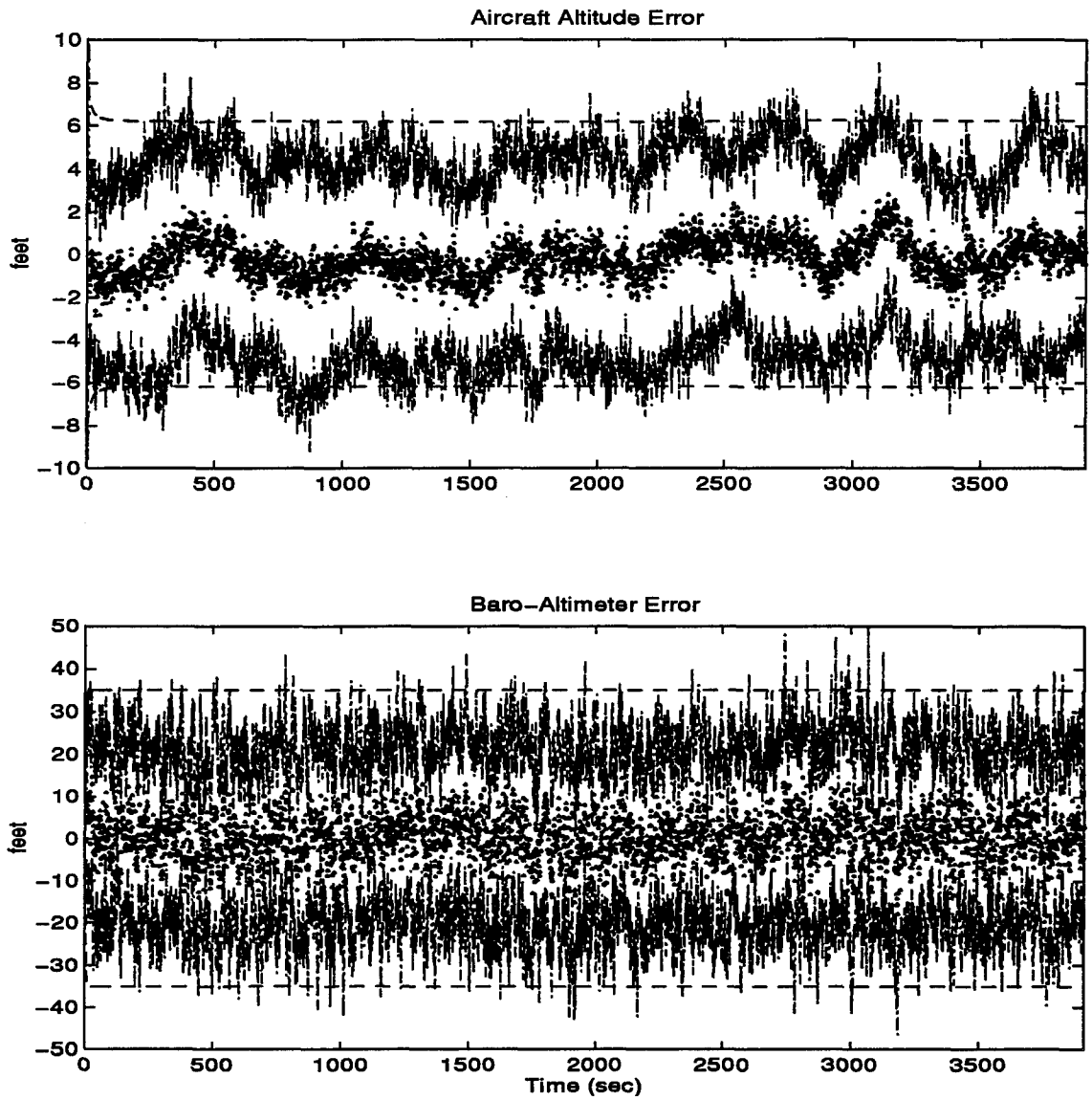

Figure B.26 Aircraft Altitude and Baro-Altimeter Error

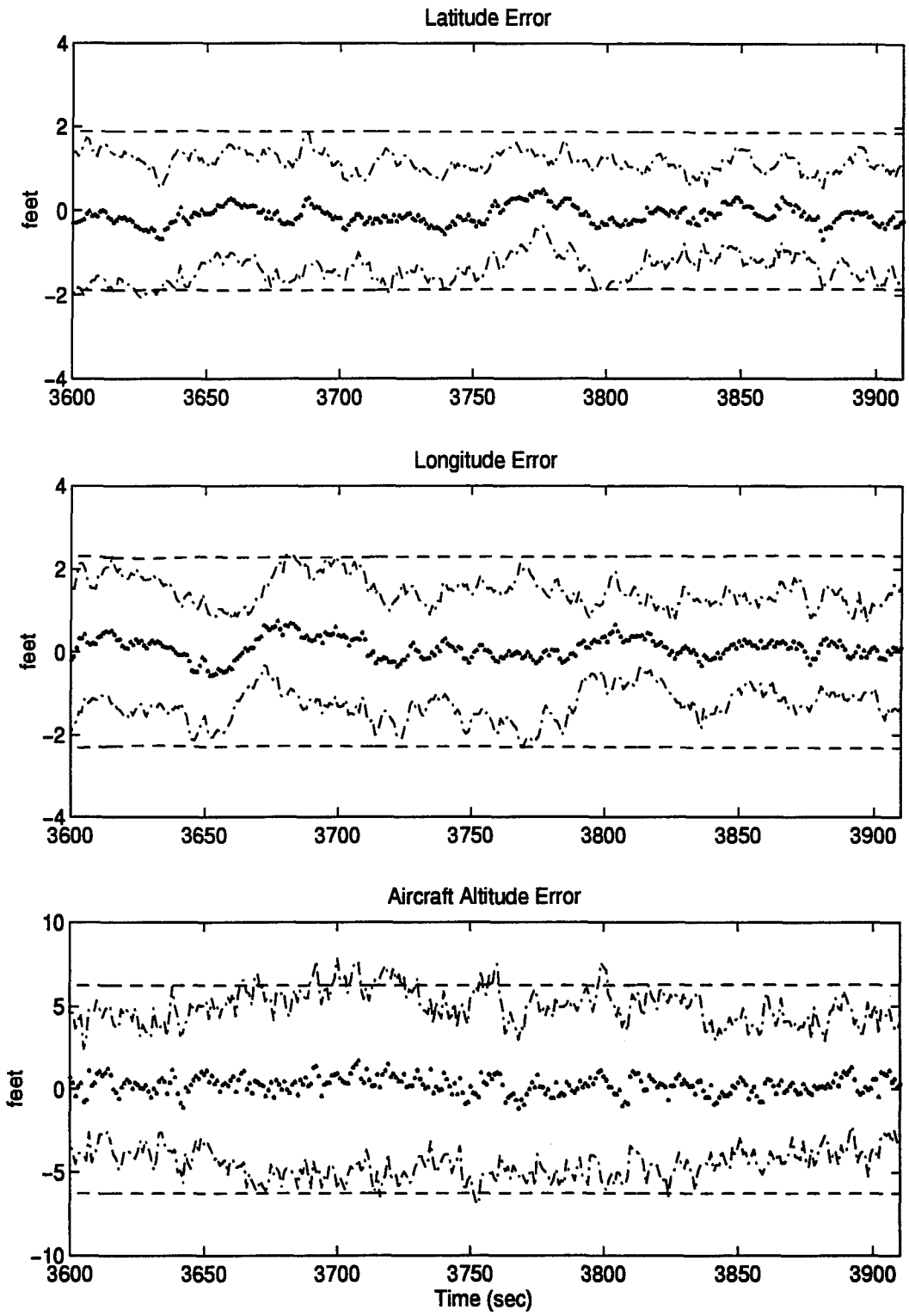

Figure B.27 Latitude, Longitude, and Aircraft Altitude Error

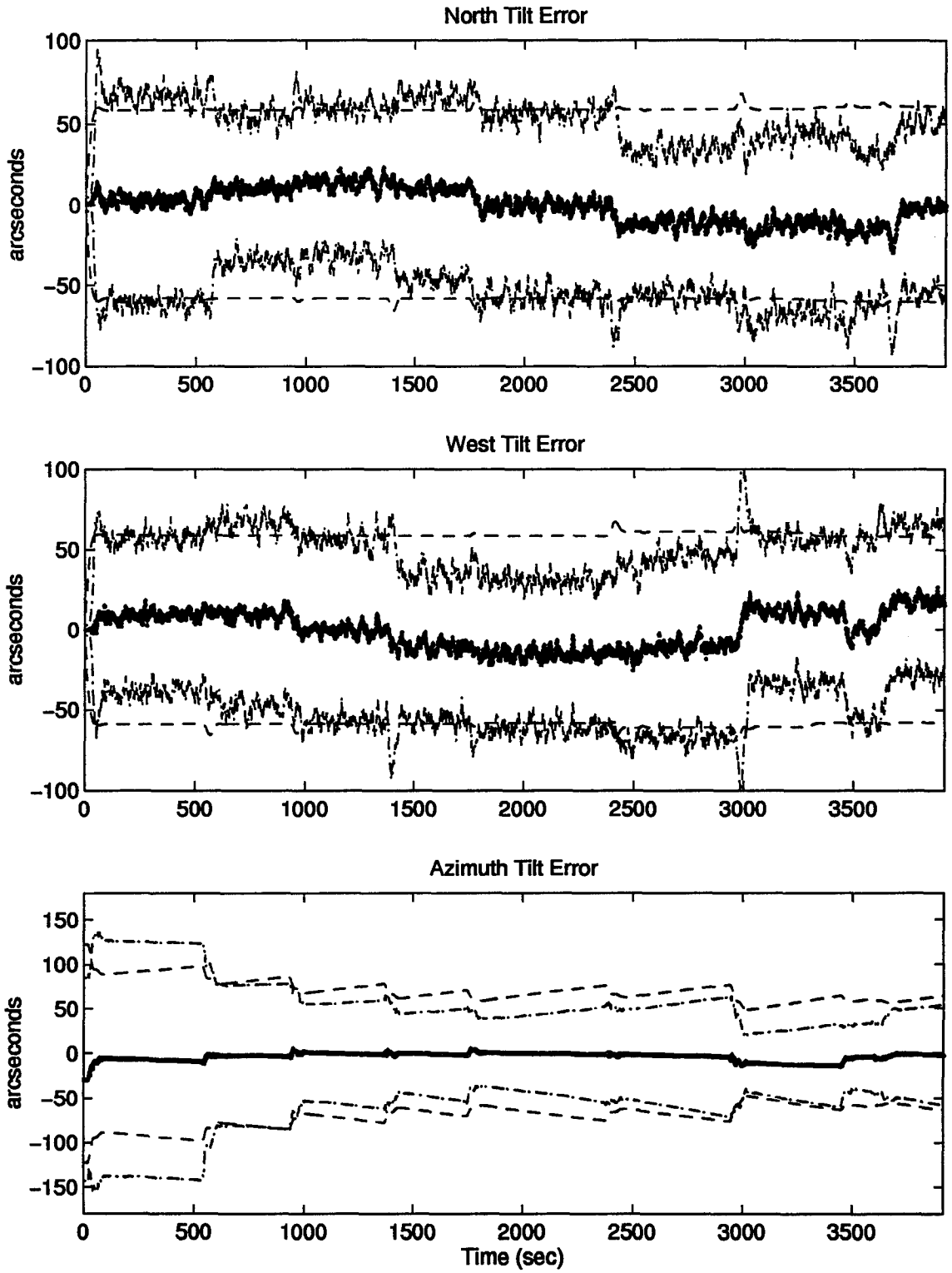

Figure B.28 North, West, and Azimuth Tilt Errors

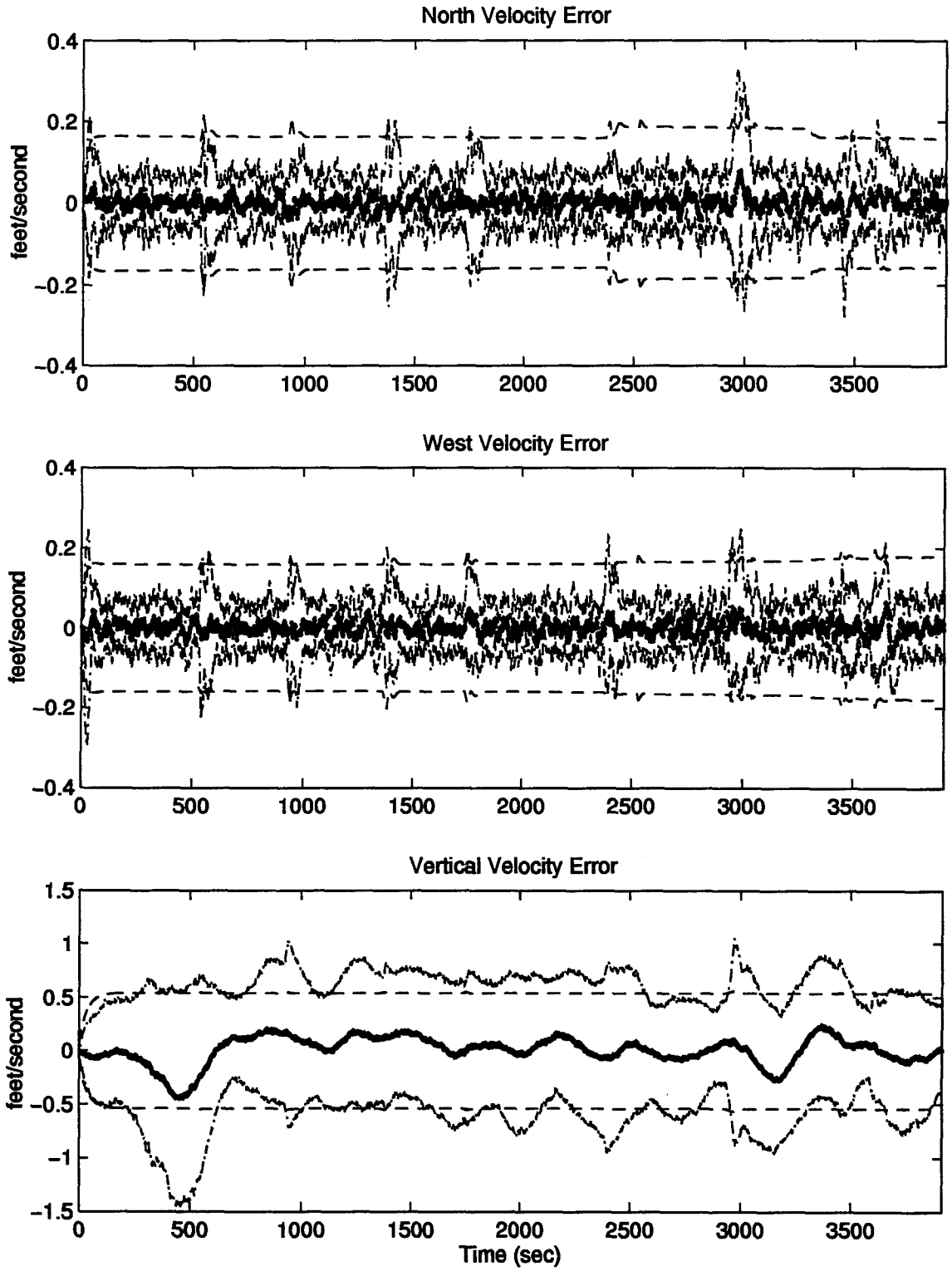

Figure B.29 North, West, and Vertical Velocity Errors

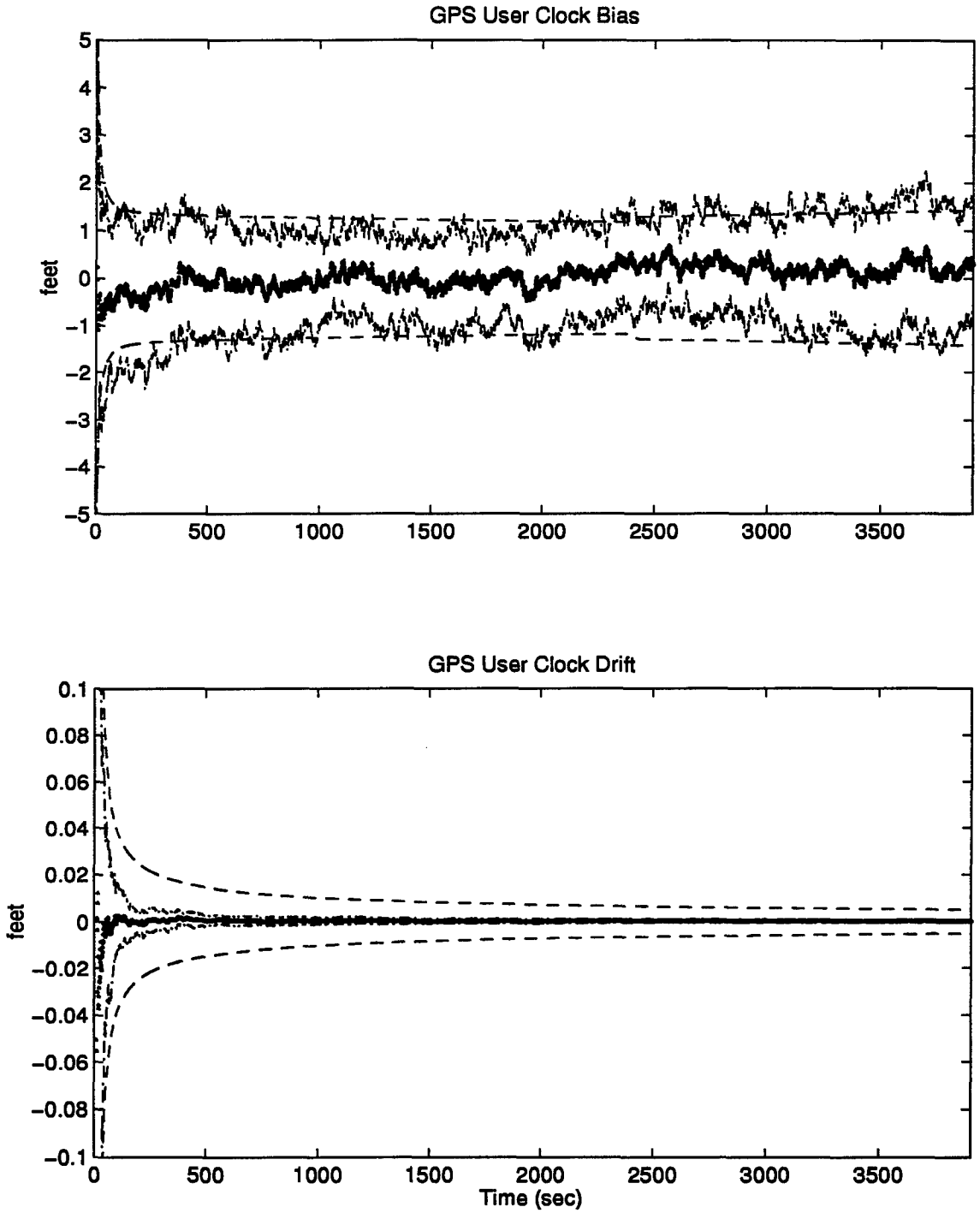

Figure B.30 GPS User Clock Bias and GPS User Clock Drift

B.6 Plots of Case VI: Barometric Altimeter, 4.0 nm/hr INS, Radar Altimeter, and DGPS Using the Tanker Flight Profile.

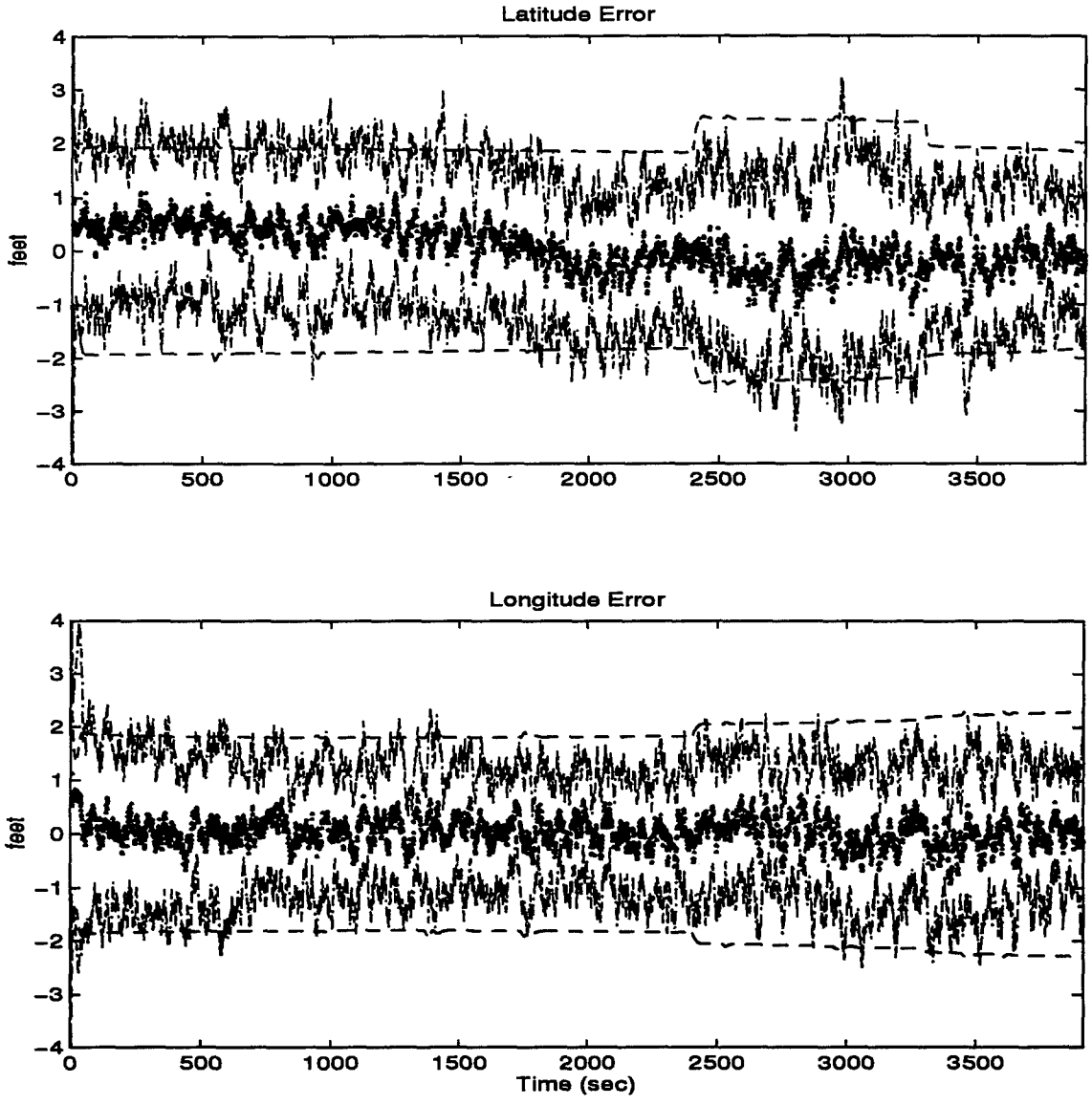

Figure B.31 Latitude and Longitude Error

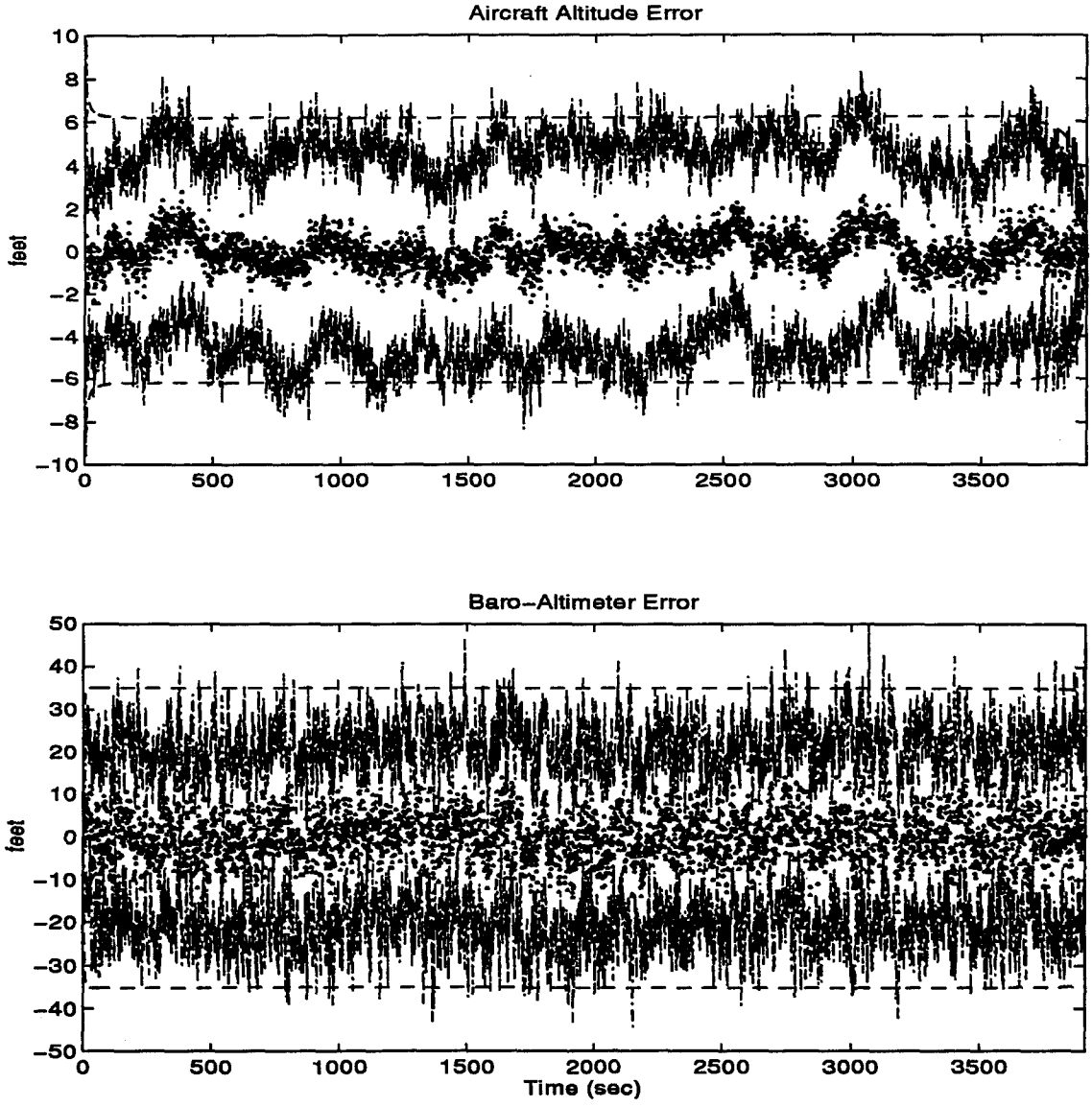

Figure B.32 Aircraft Altitude and Baro-Altimeter Error

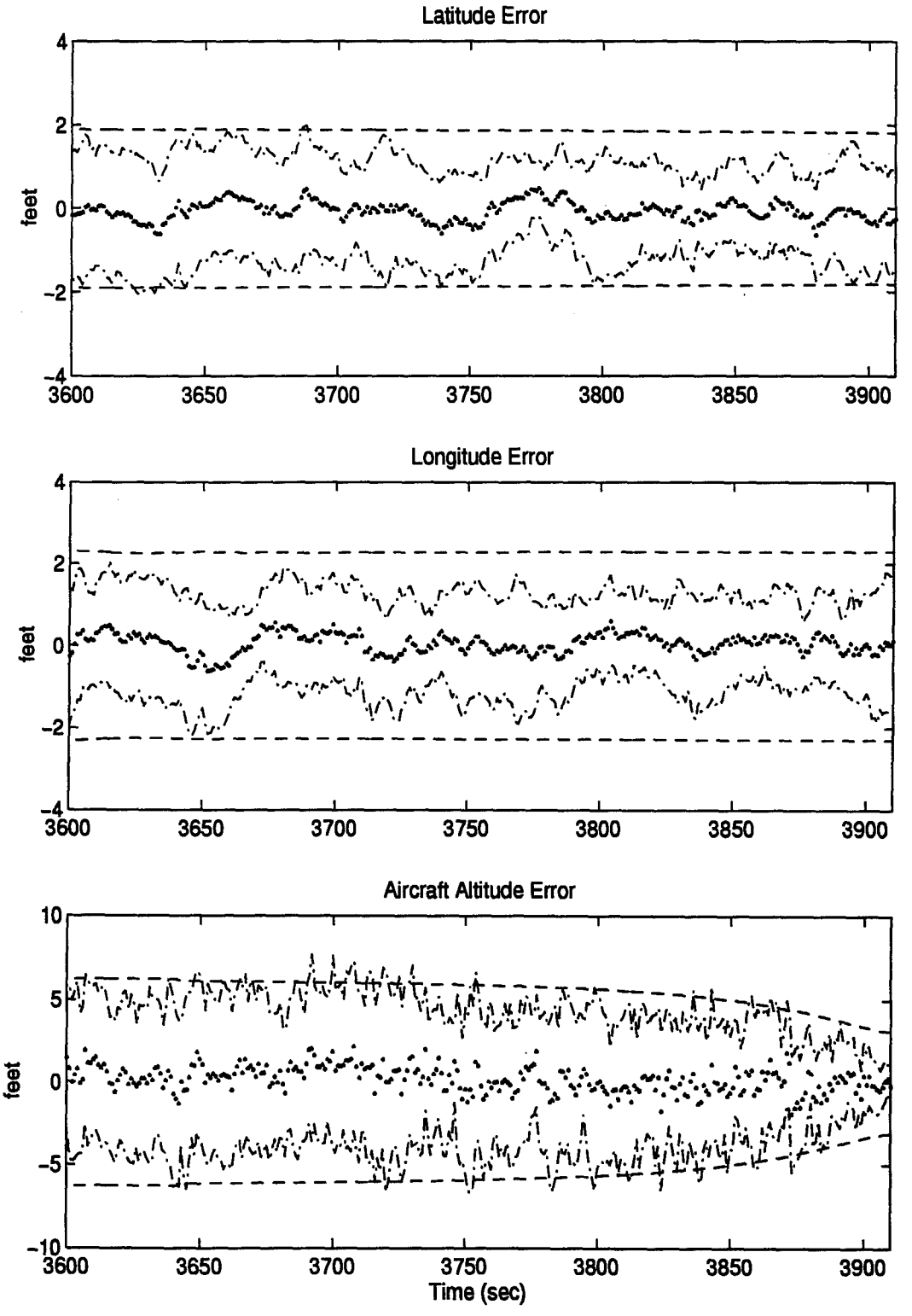

Figure B.33 Latitude, Longitude, and Aircraft Altitude Error

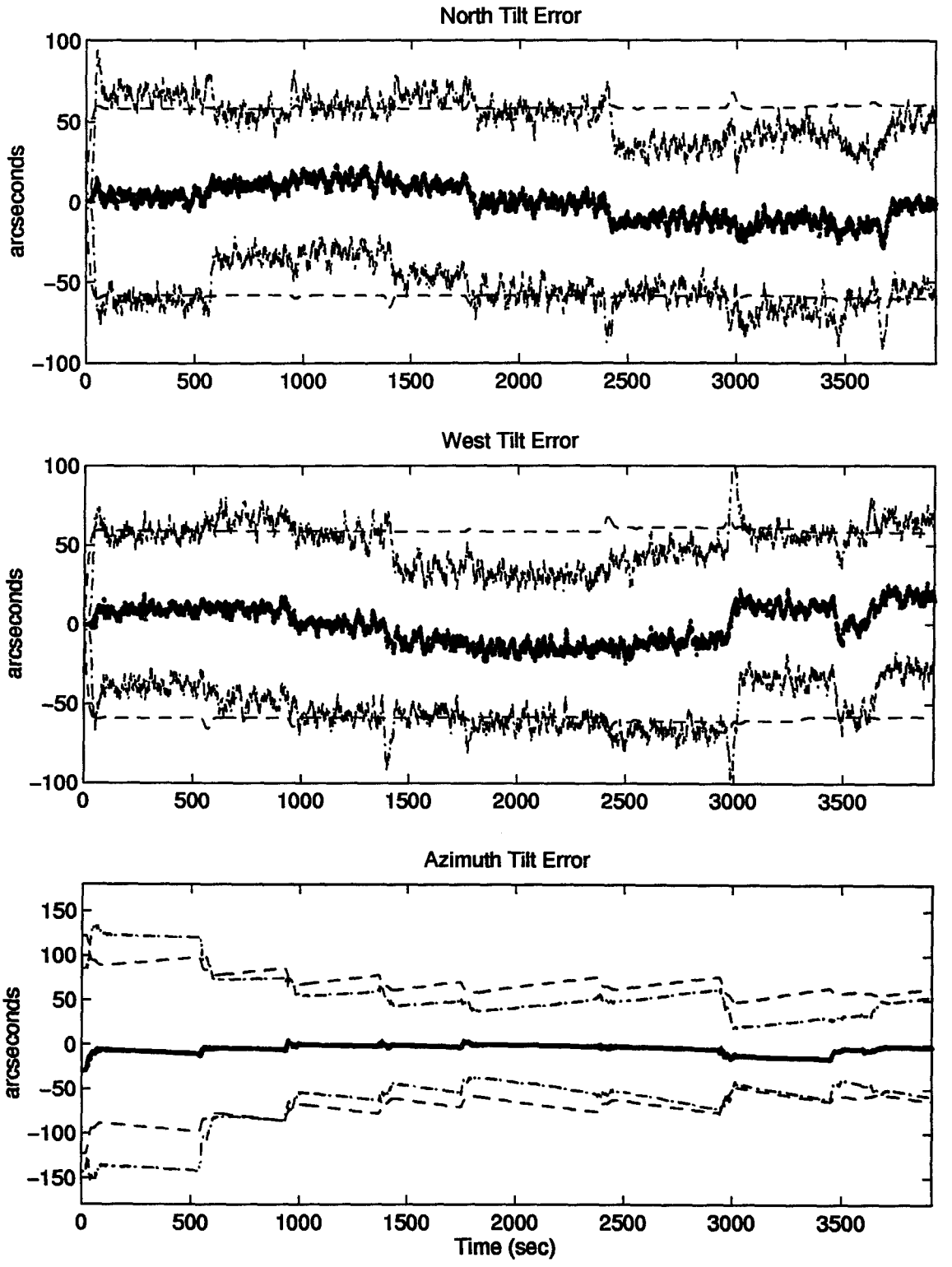

Figure B.34 North, West, and Azimuth Tilt Errors

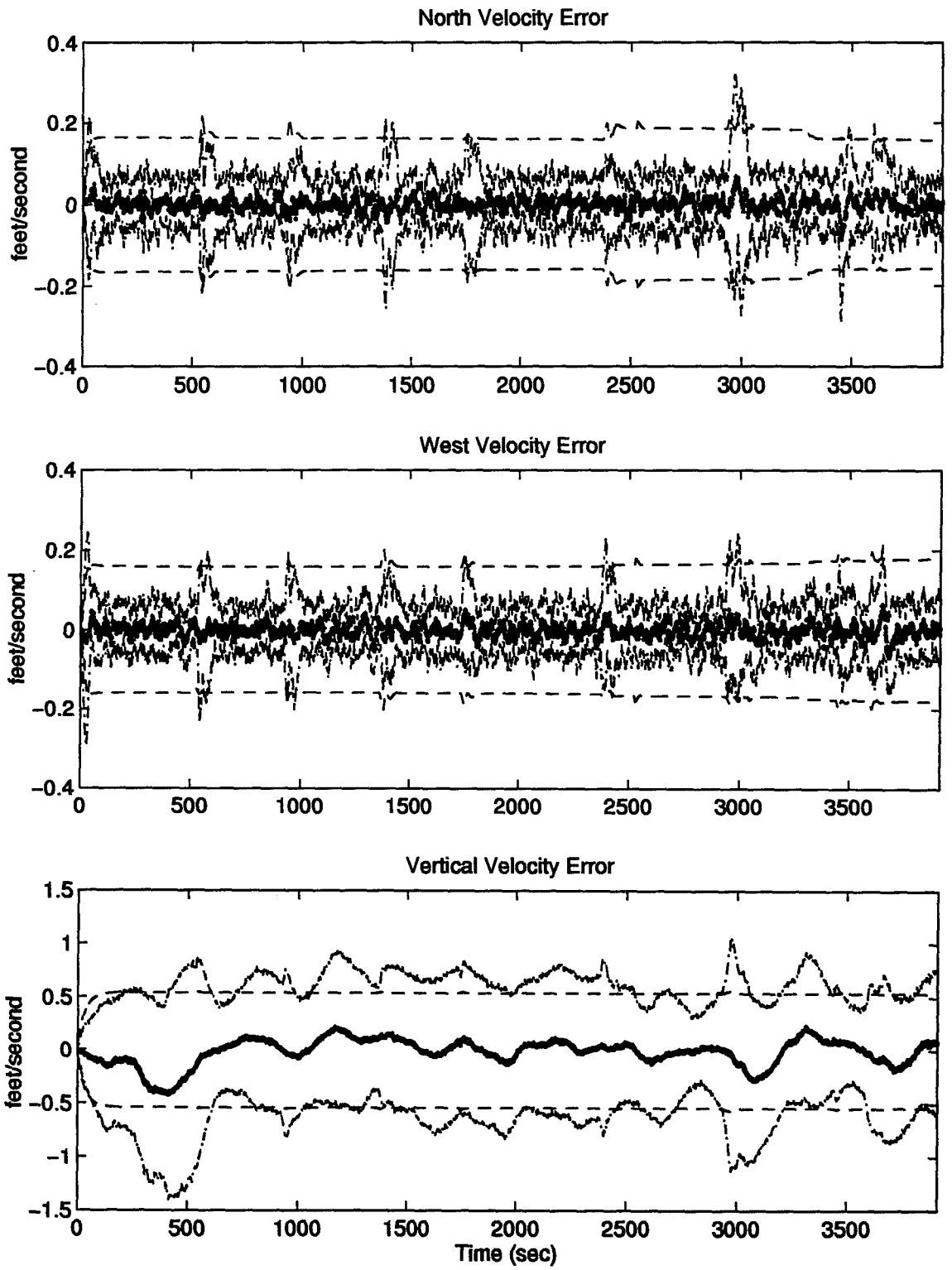

Figure B.35 North, West, and Vertical Velocity Errors

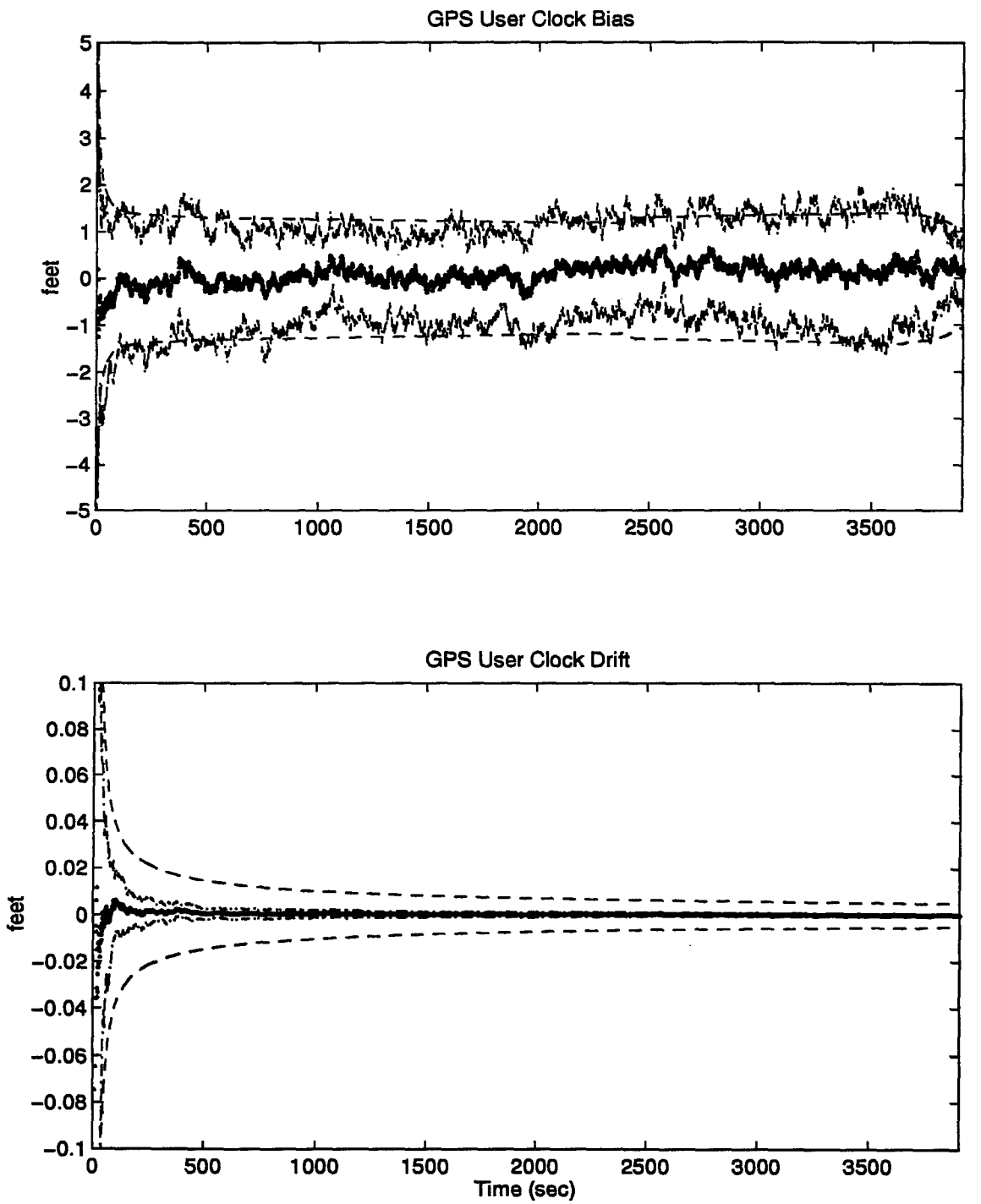

Figure B.36 GPS User Clock Bias and GPS User Clock Drift

Appendix C.

Plots of Case VII through Case XII for Tanker Flight Profile.

Plot Legend

$\cdots$ true error (mean error $\pm$ σ_{true})

- - - filter predicted error ($0 \pm \sigma_{filter}$)

— mean error

C.1 Plots of Case VII: Barometric Altimeter, 0.4 nm/hr INS, Single Pseudolite, and DGPS Using the Tanker Flight Profile.

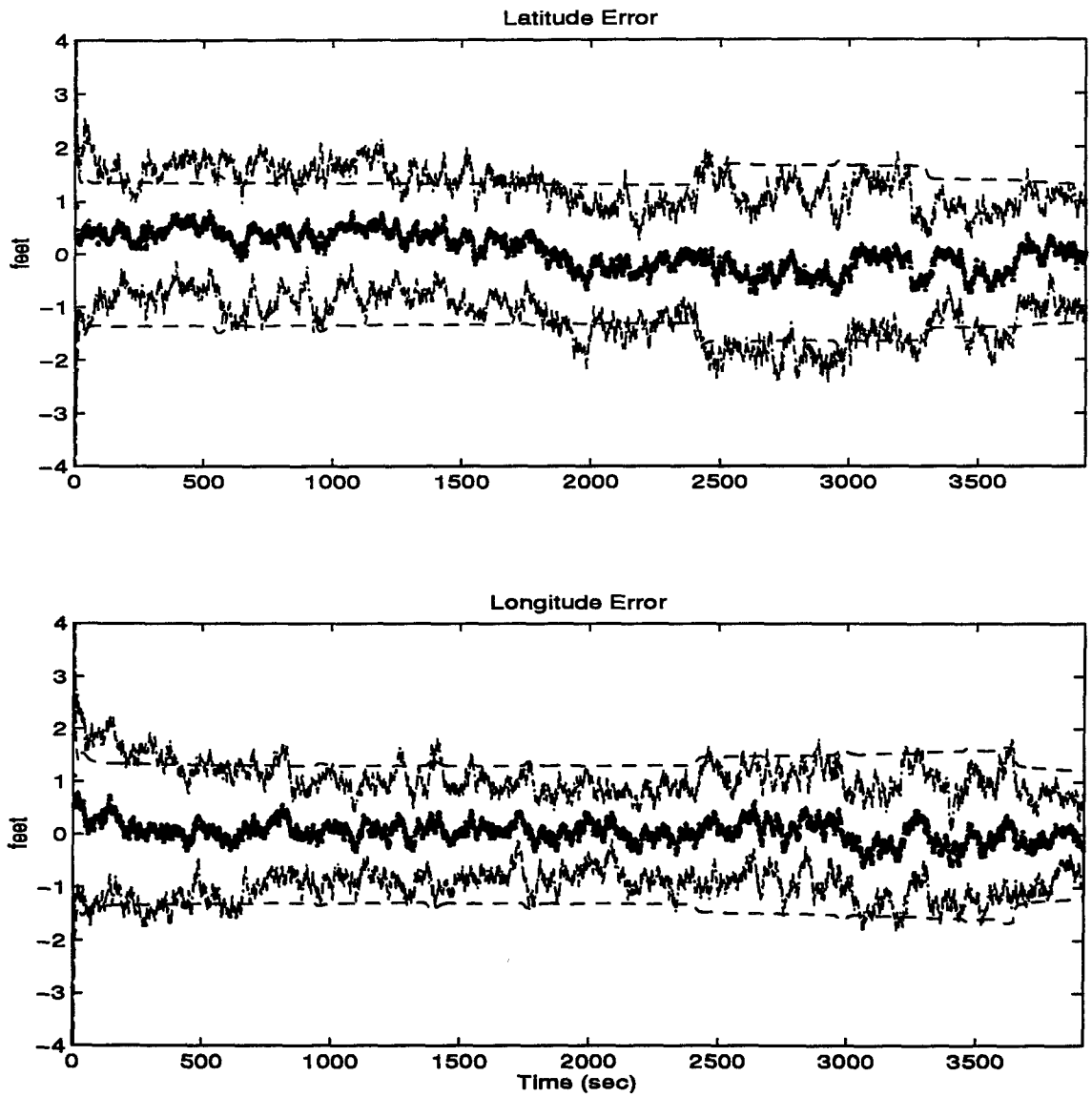

Figure C.1 Latitude and Longitude Error

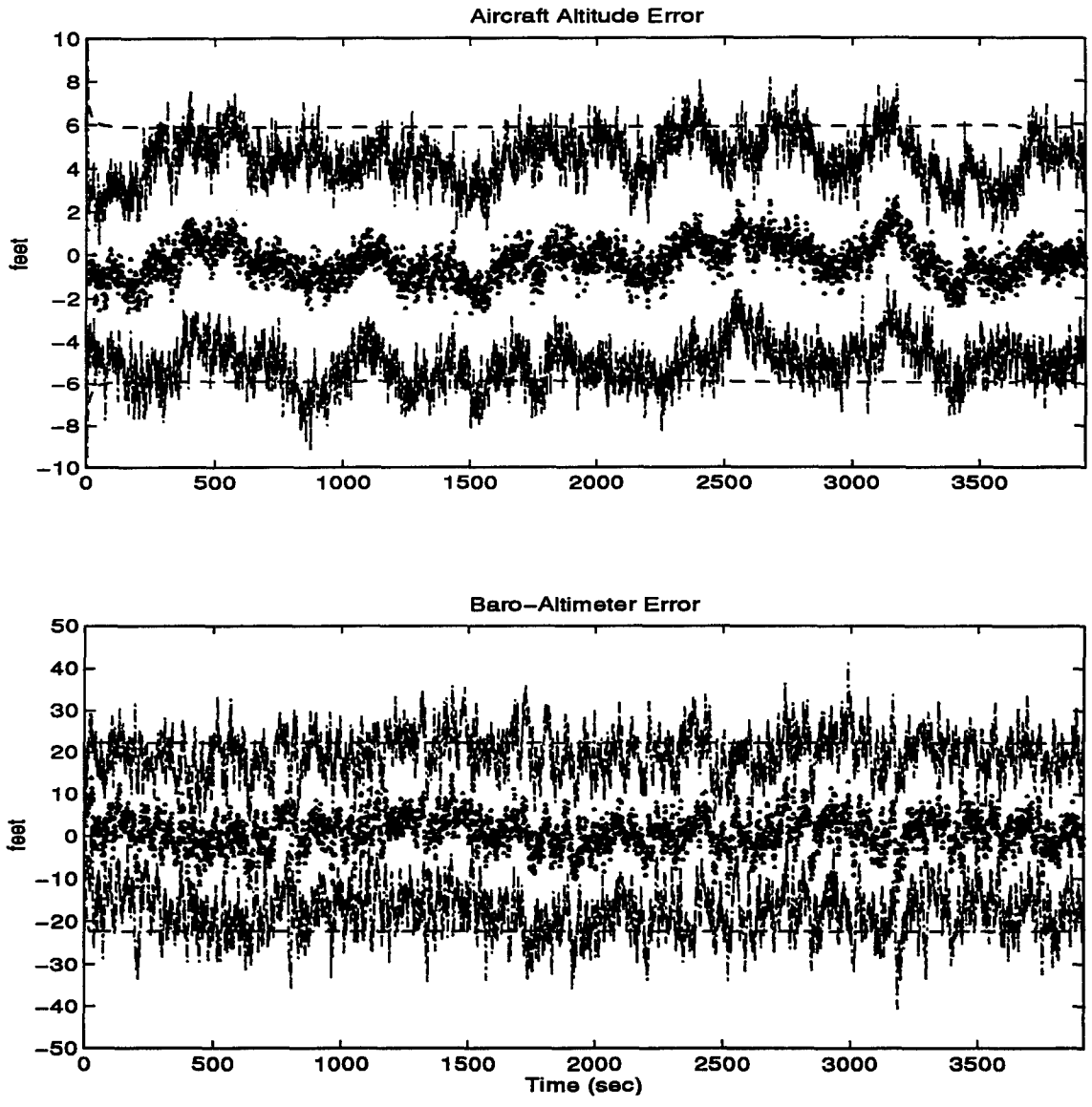

Figure C.2 Aircraft Altitude and Baro-Altimeter Error

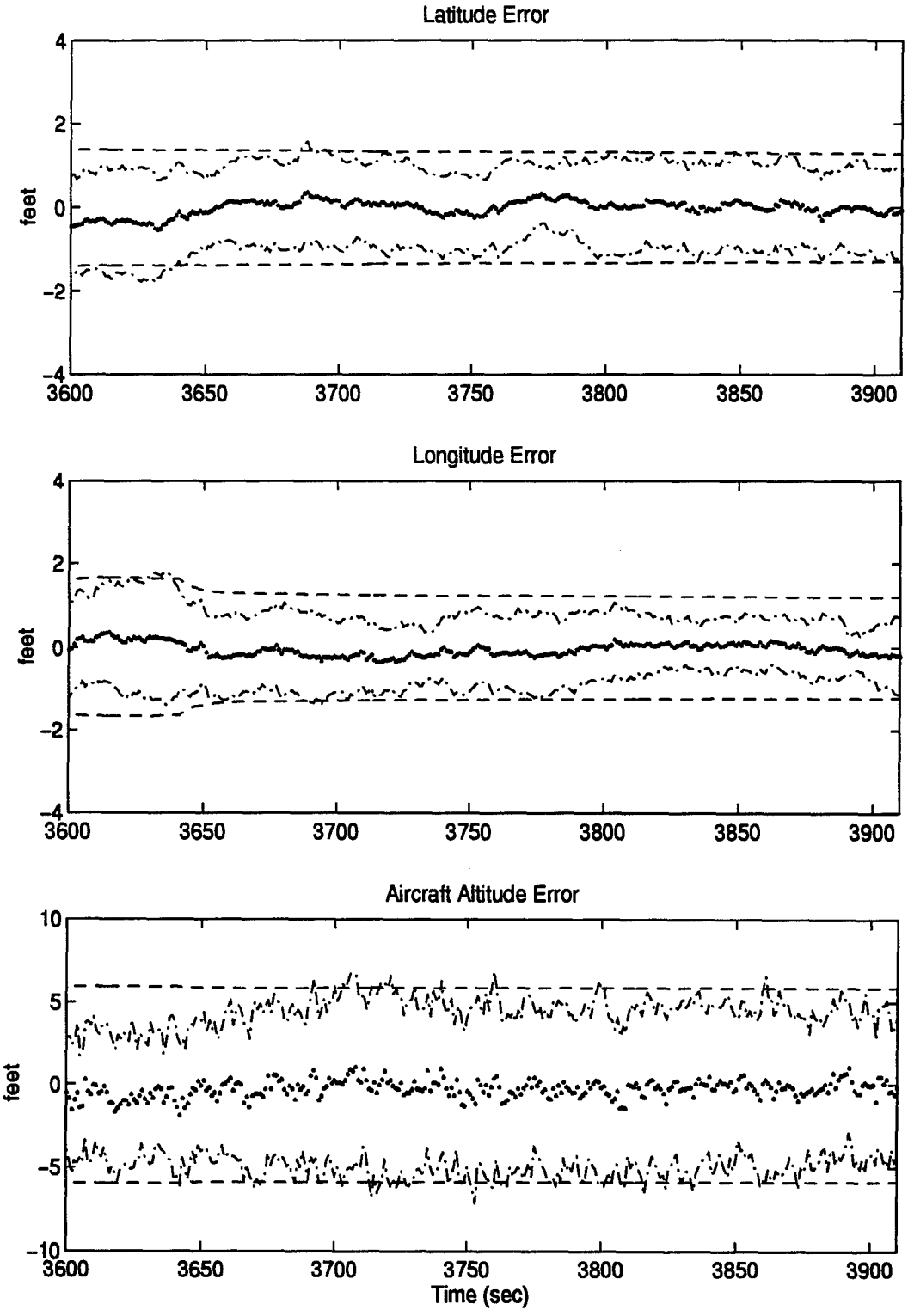

Figure C.3 Latitude, Longitude, and Aircraft Altitude Error

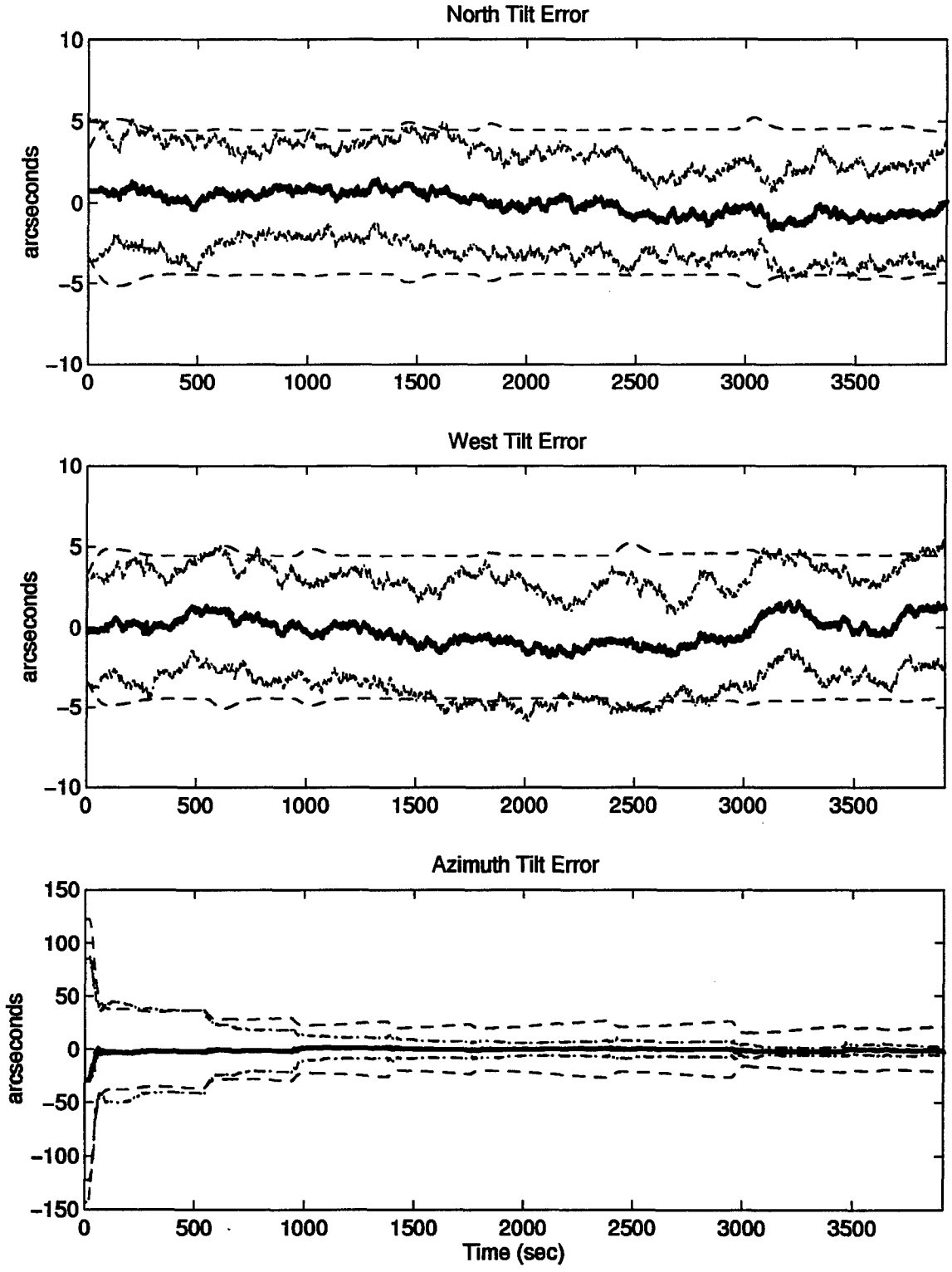

Figure C.4 North, West, and Azimuth Tilt Errors

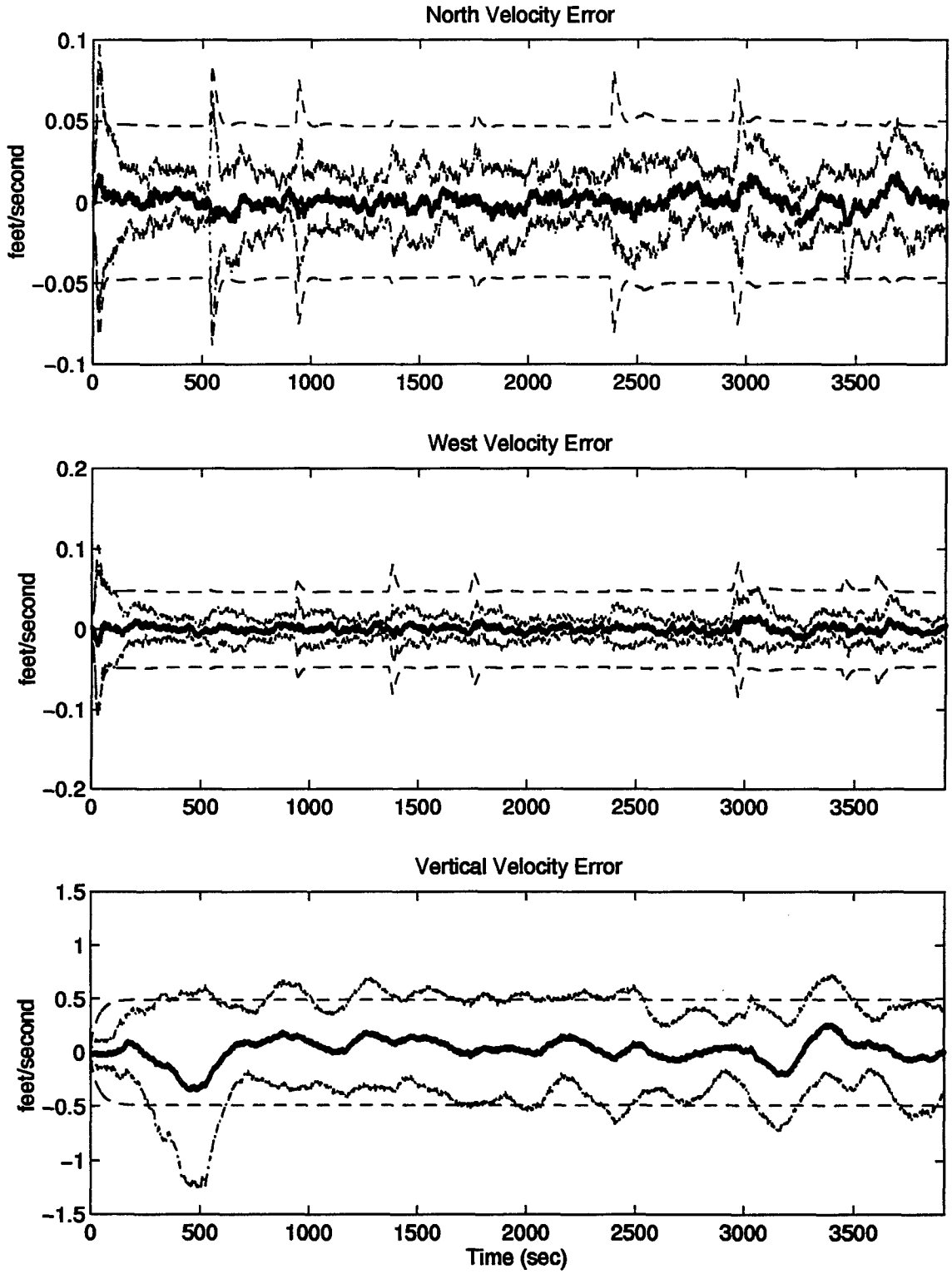

Figure C.5 North, West, and Vertical Velocity Errors

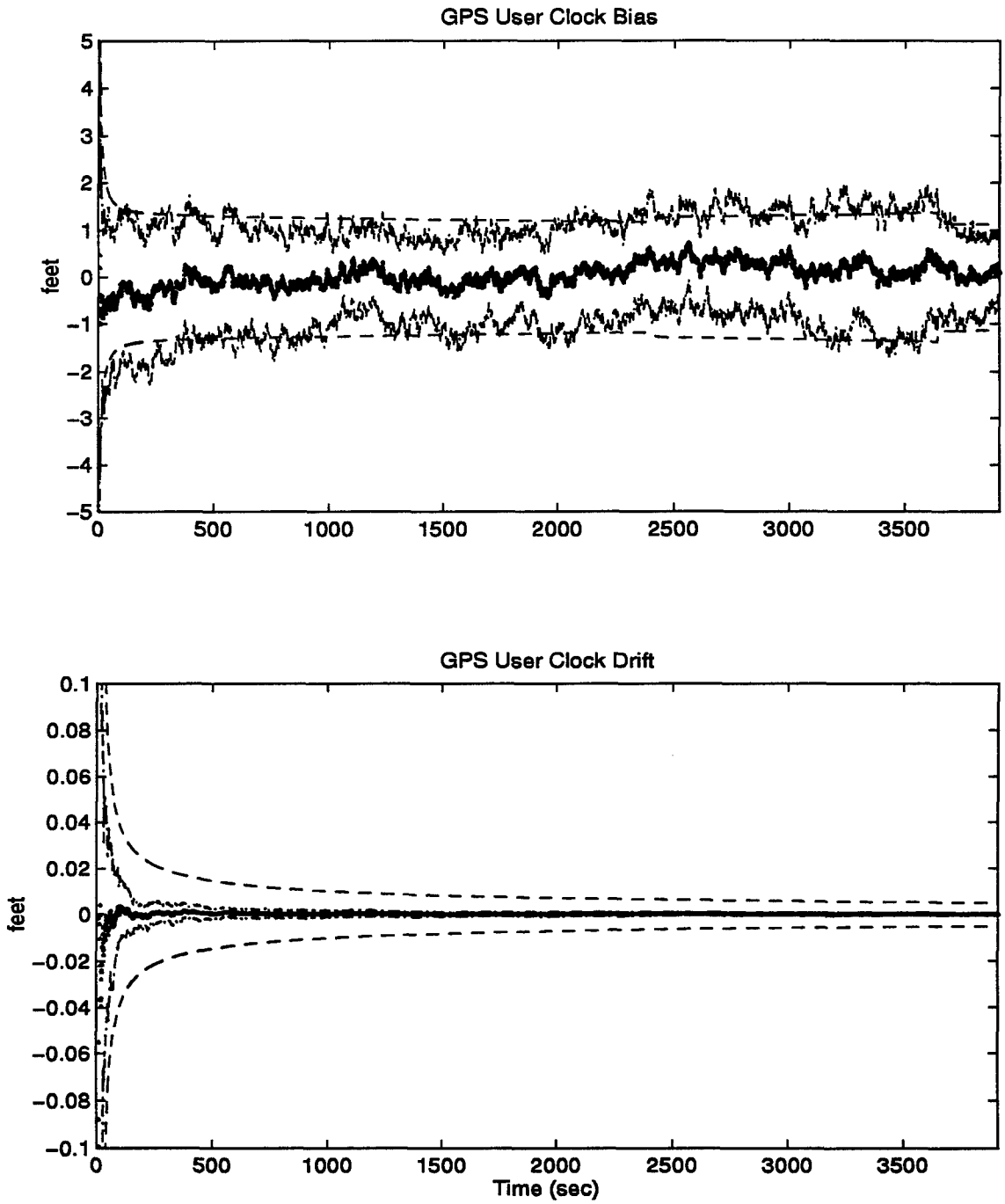

Figure C.6 GPS User Clock Bias and GPS User Clock Drift

C.2 Plots of Case VIII: Barometric Altimeter, 0.4 nm/hr INS, Radar Altimeter, Single Pseudolite, and DGPS Using the Tanker Flight Profile.

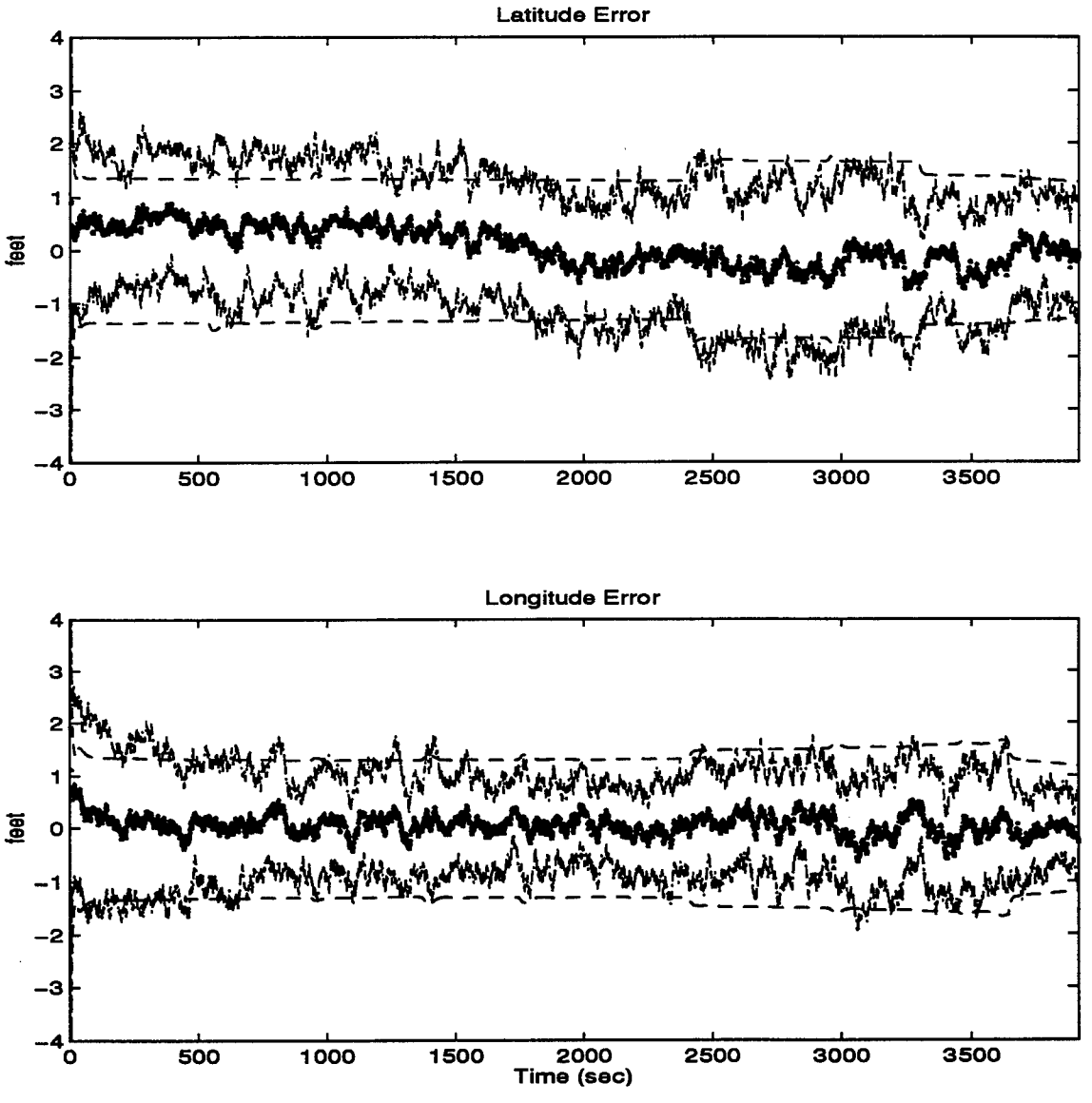

Figure C.7 Latitude and Longitude Error

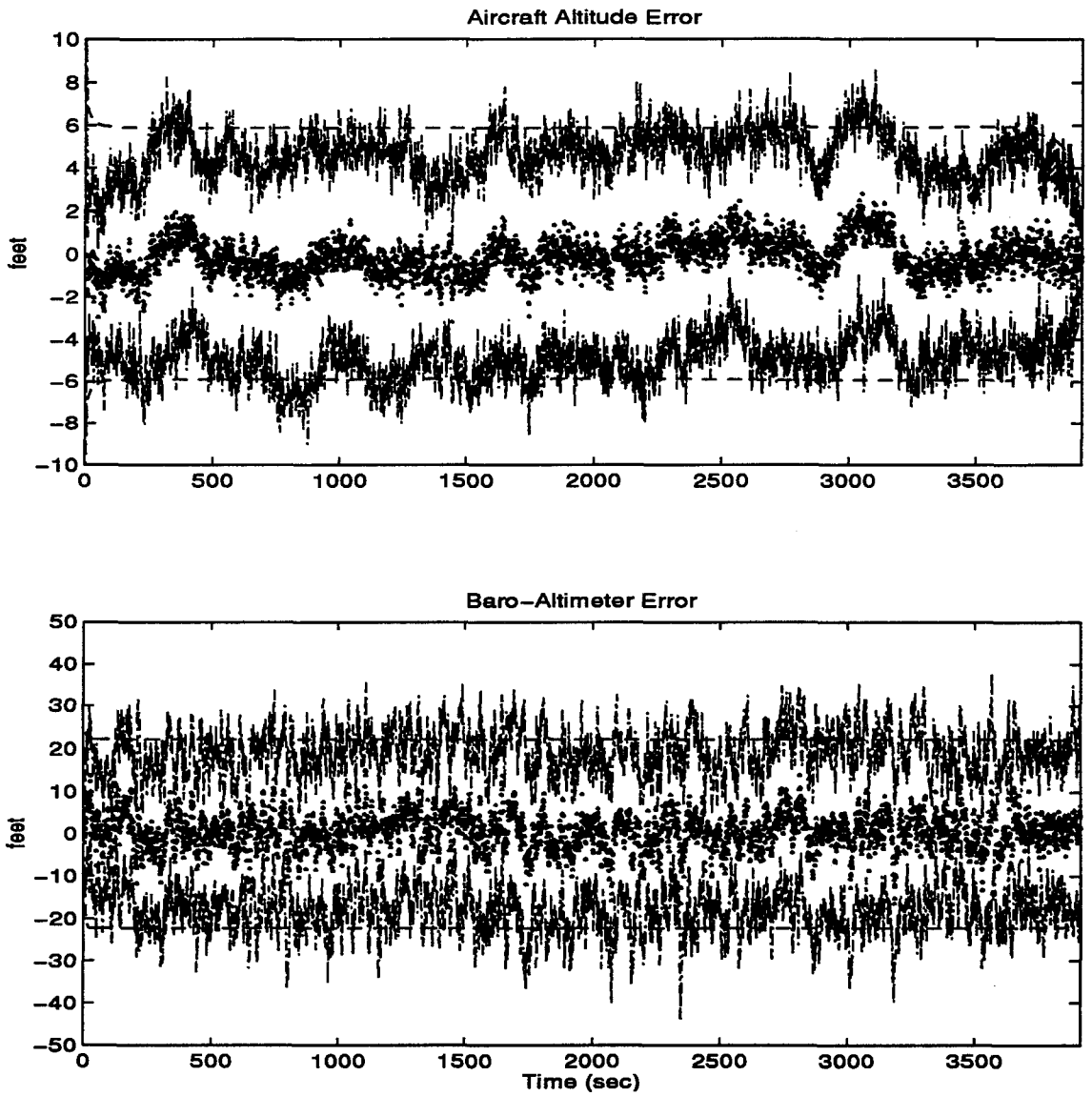

Figure C.8 Aircraft Altitude and Baro-Altimeter Error

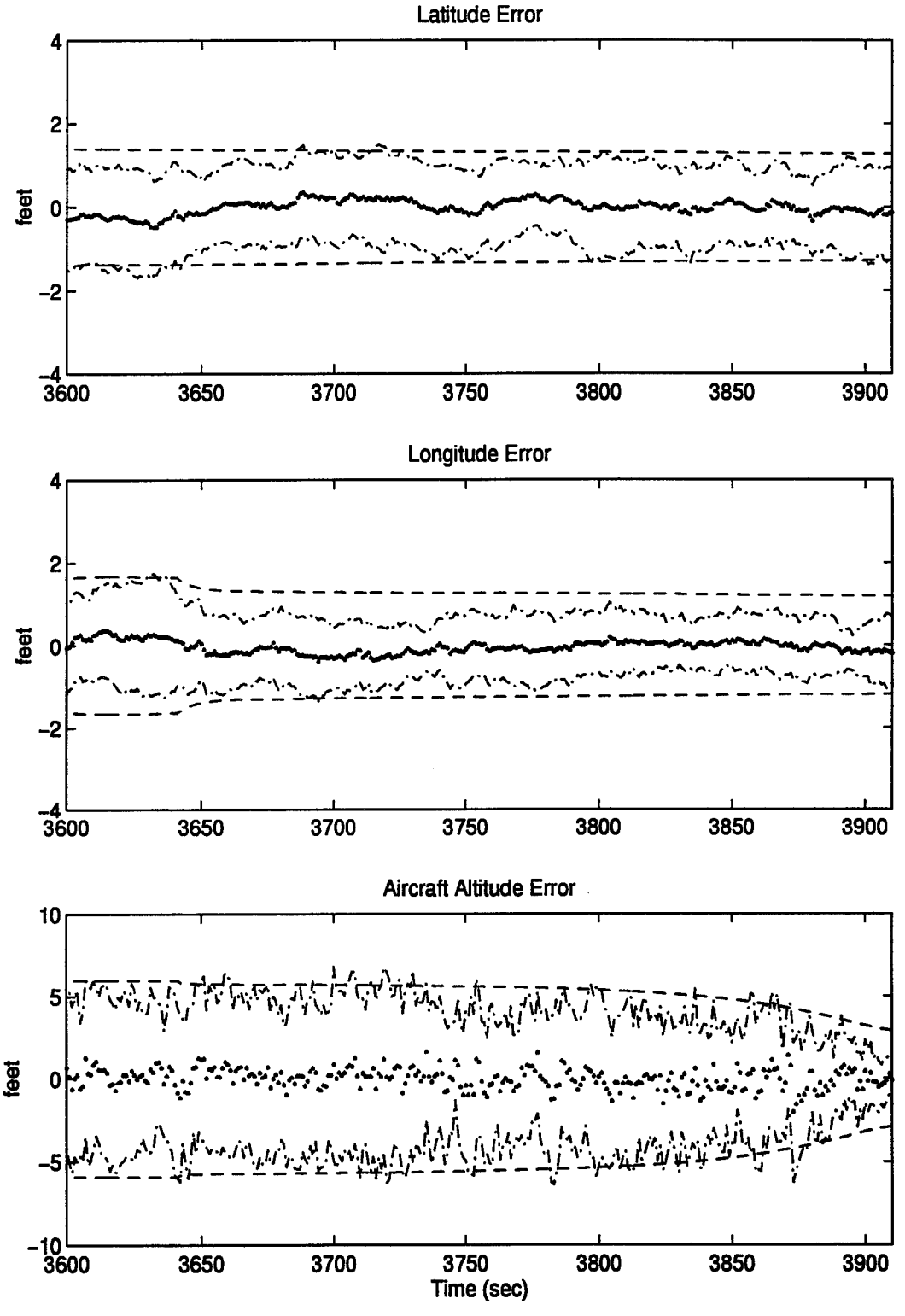

Figure C.9 Latitude, Longitude, and Aircraft Altitude Error

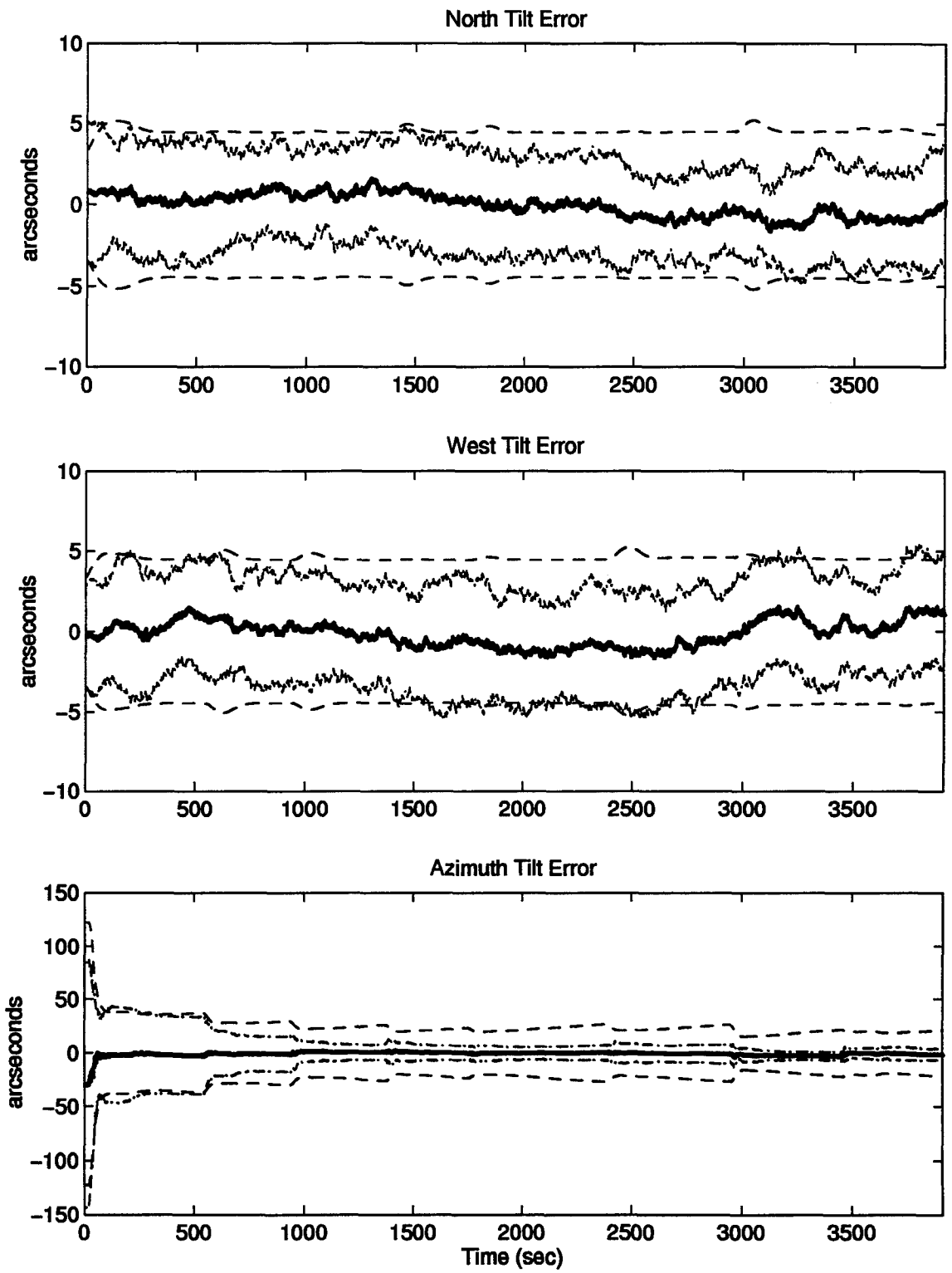

Figure C.10 North, West, and Azimuth Tilt Errors

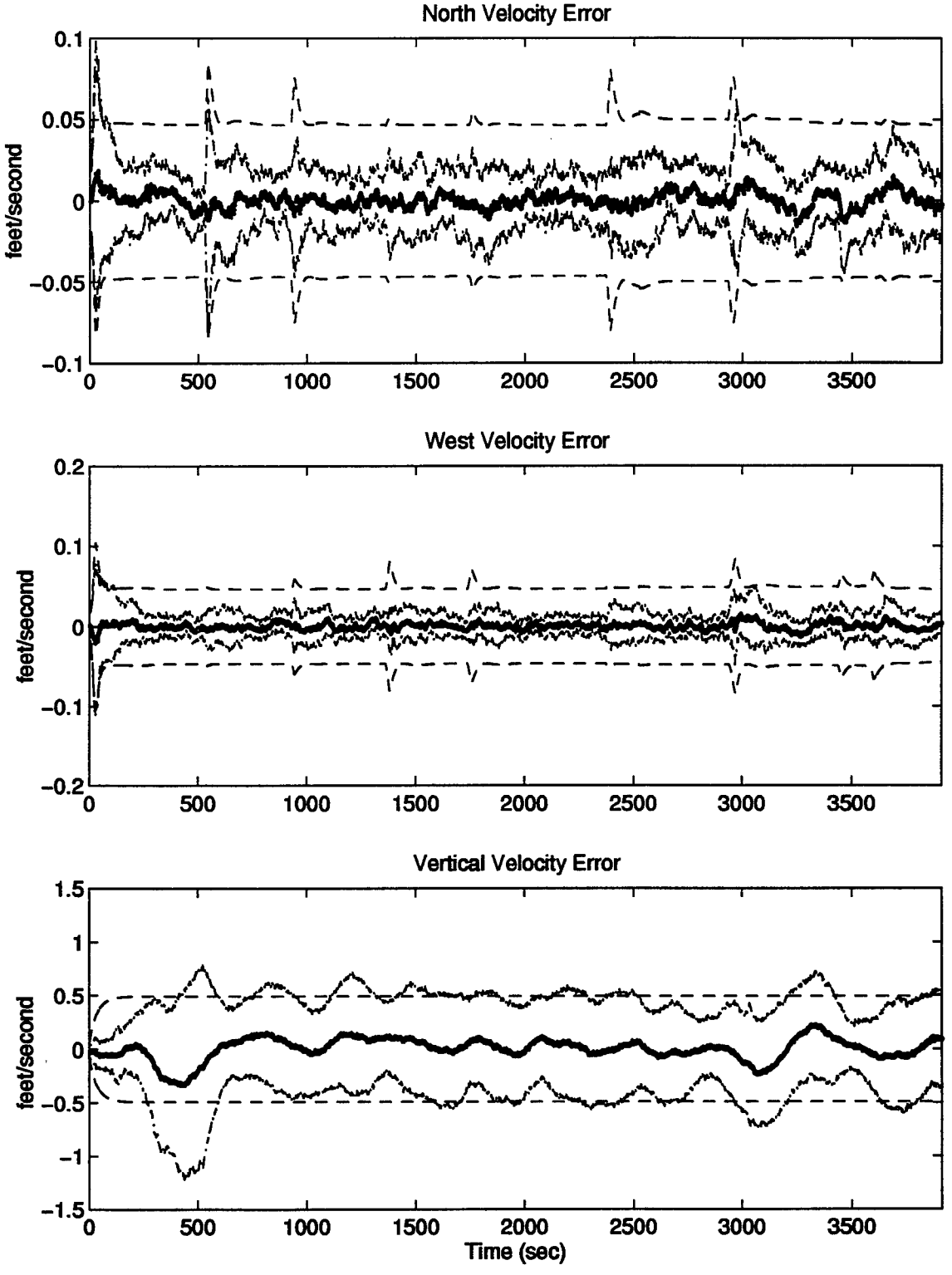

Figure C.11 North, West, and Vertical Velocity Errors

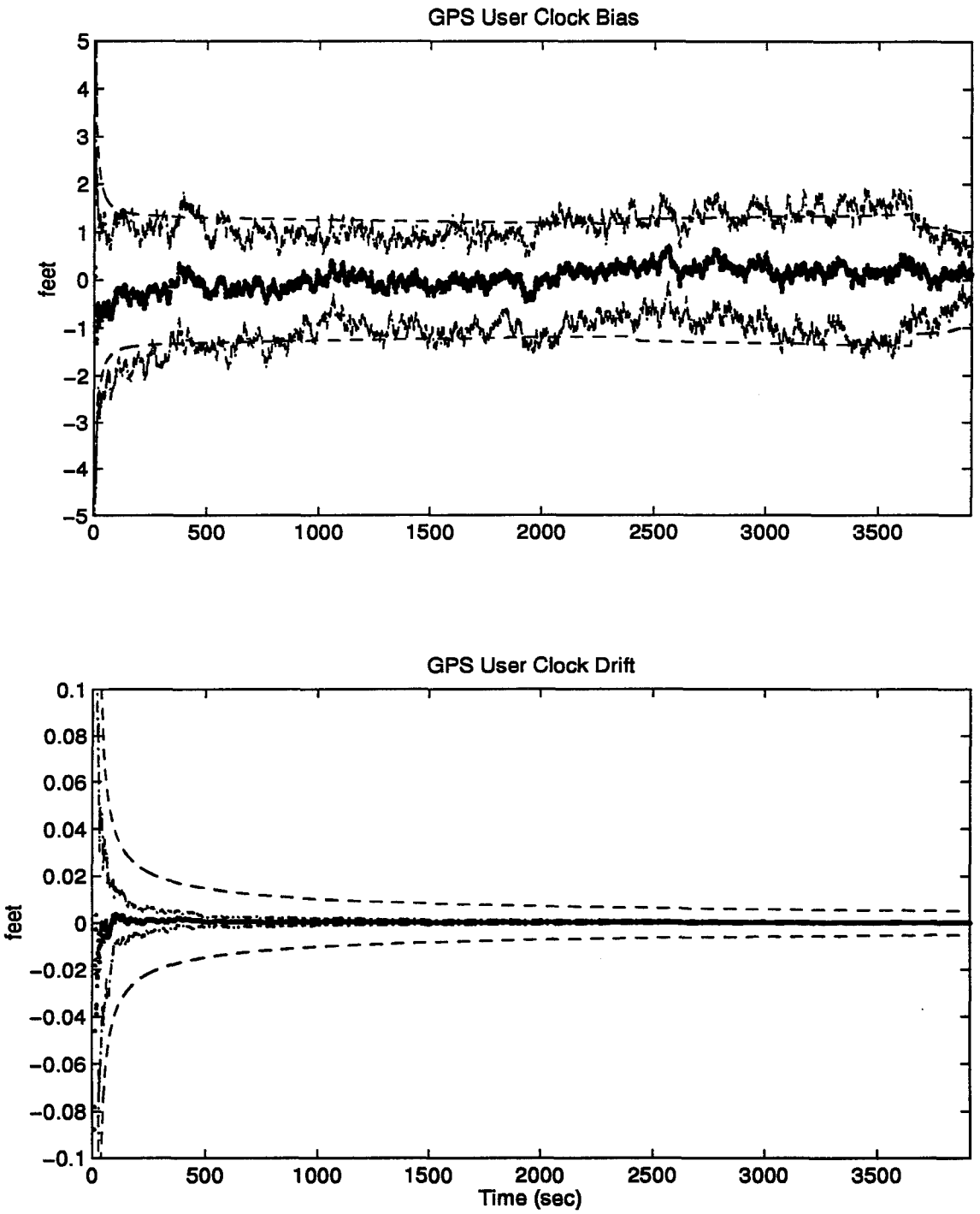

Figure C.12 GPS User Clock Bias and GPS User Clock Drift

C.3 Plots of Case IX: Barometric Altimeter, 2.0 nm/hr INS, Radar Altimeter, Single Pseudolite, and DGPS Using the Tanker Flight Profile.

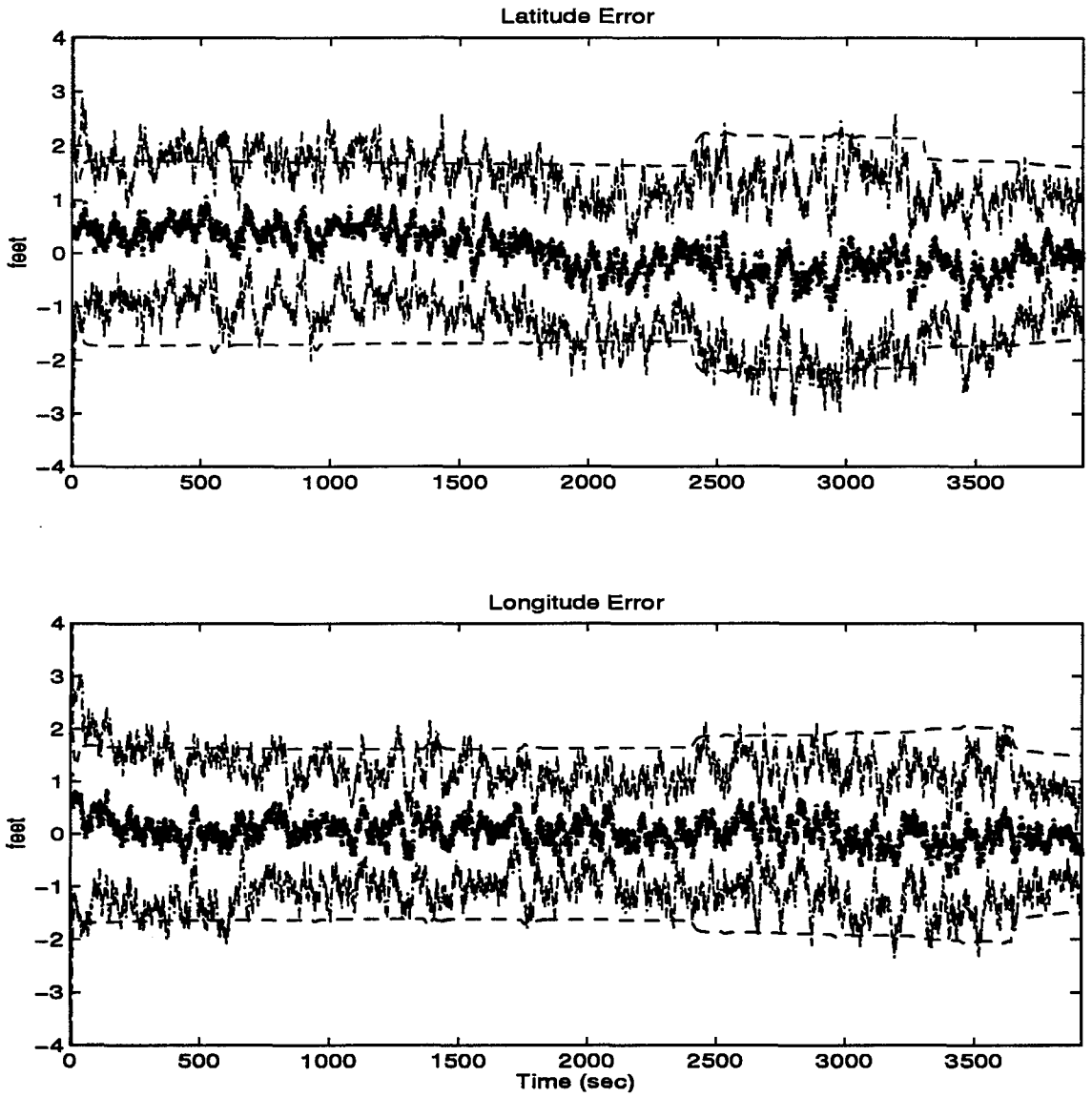

Figure C.13 Latitude and Longitude Error

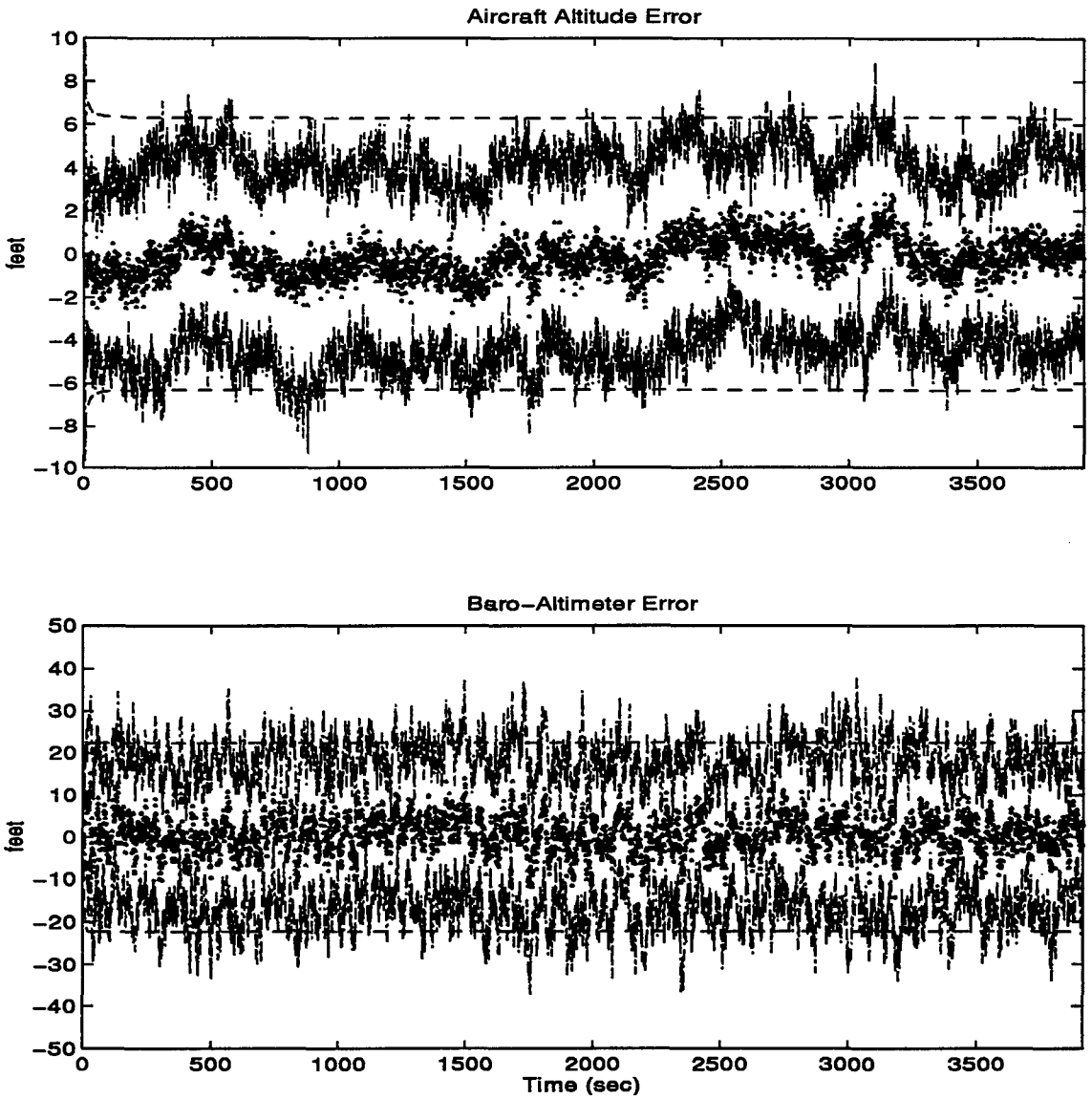

Figure C.14 Aircraft Altitude and Baro-Altimeter Error

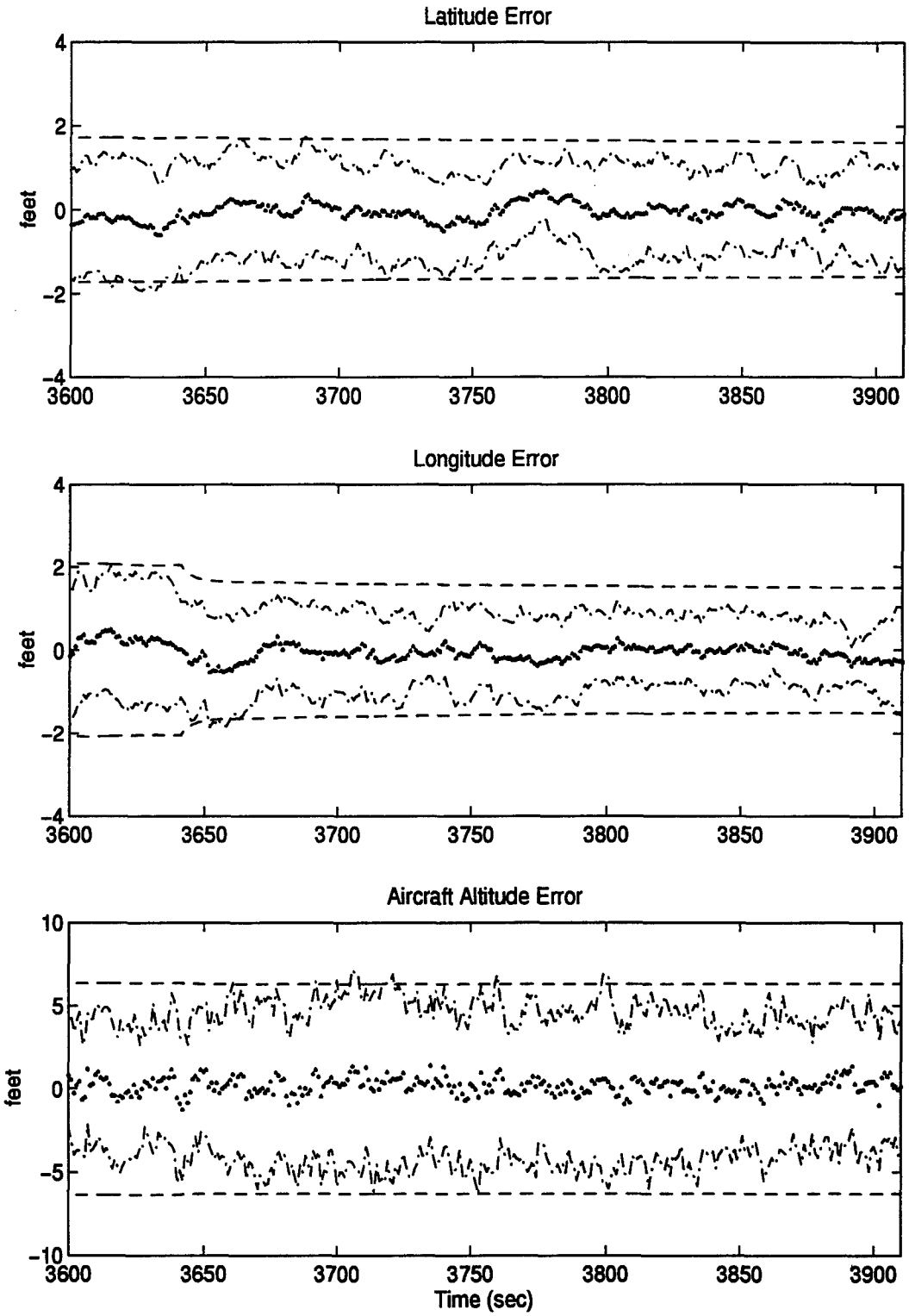

Figure C.15 Latitude, Longitude, and Aircraft Altitude Error

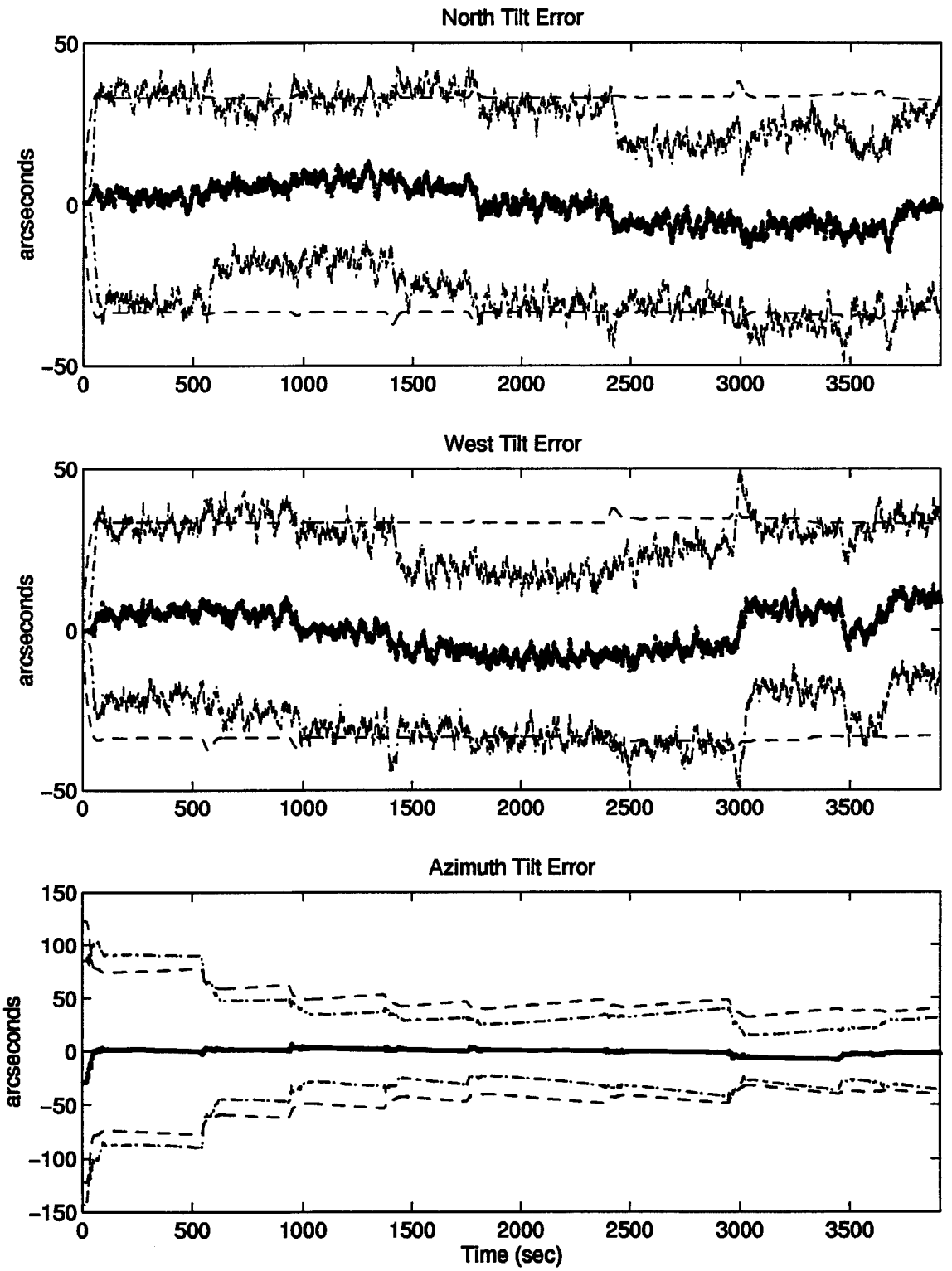

Figure C.16 North, West, and Azimuth Tilt Errors

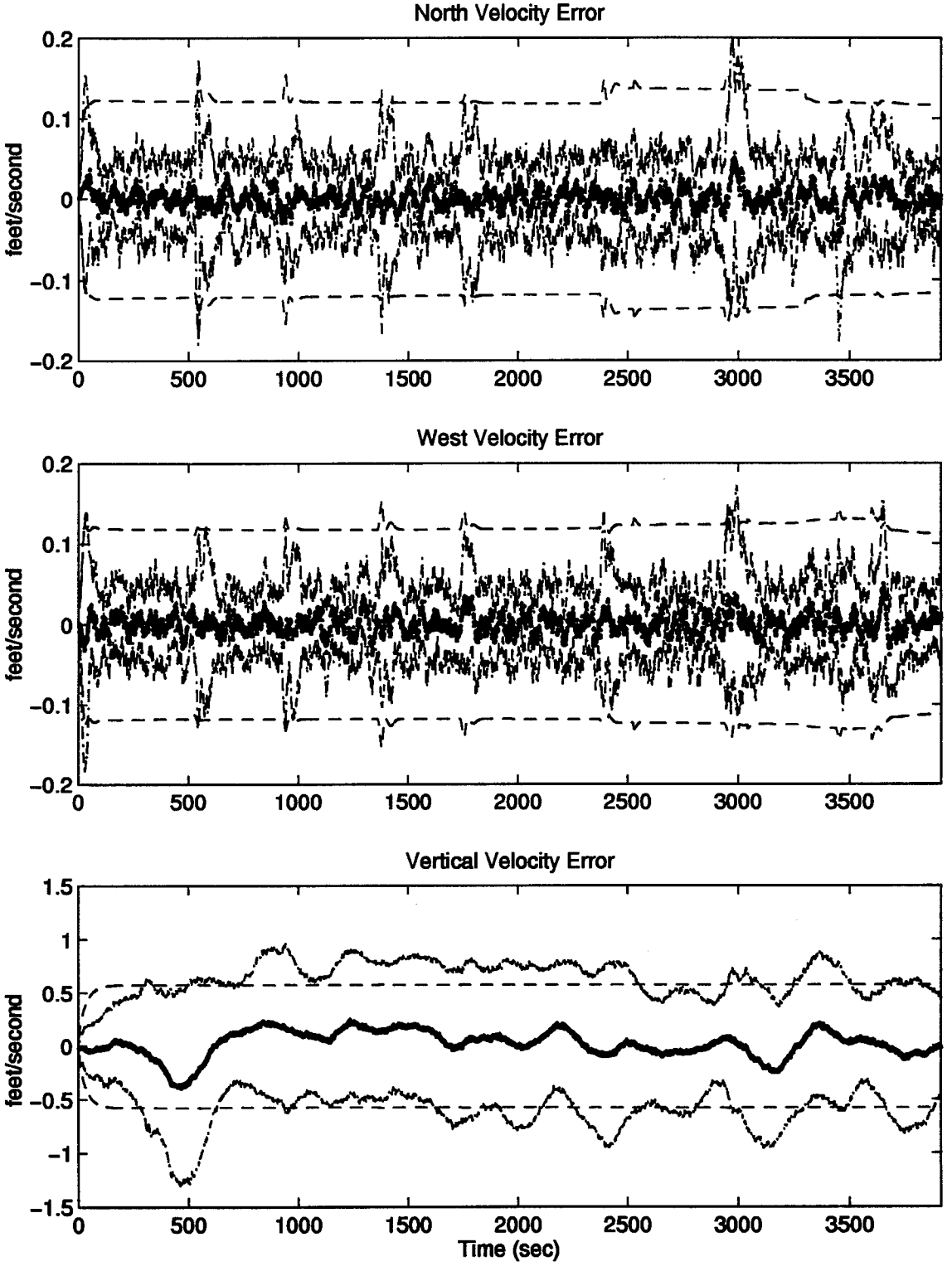

Figure C.17 North, West, and Vertical Velocity Errors

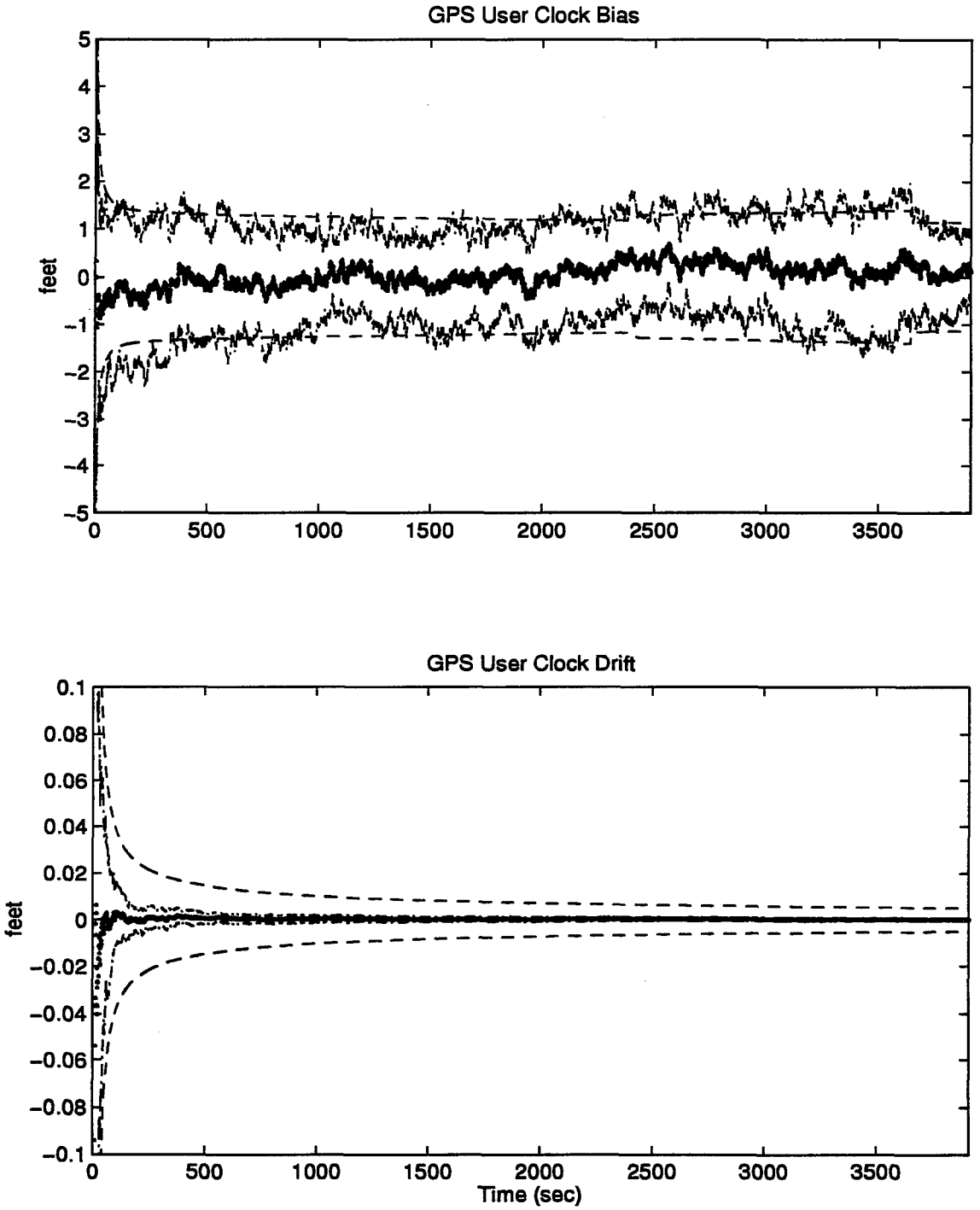

Figure C.18 GPS User Clock Bias and GPS User Clock Drift

C.4 Plots of Case X: Barometric Altimeter, 2.0 nm/hr INS, Radar Altimeter, Single Pseudolite, and DGPS Using the Tanker Flight Profile.

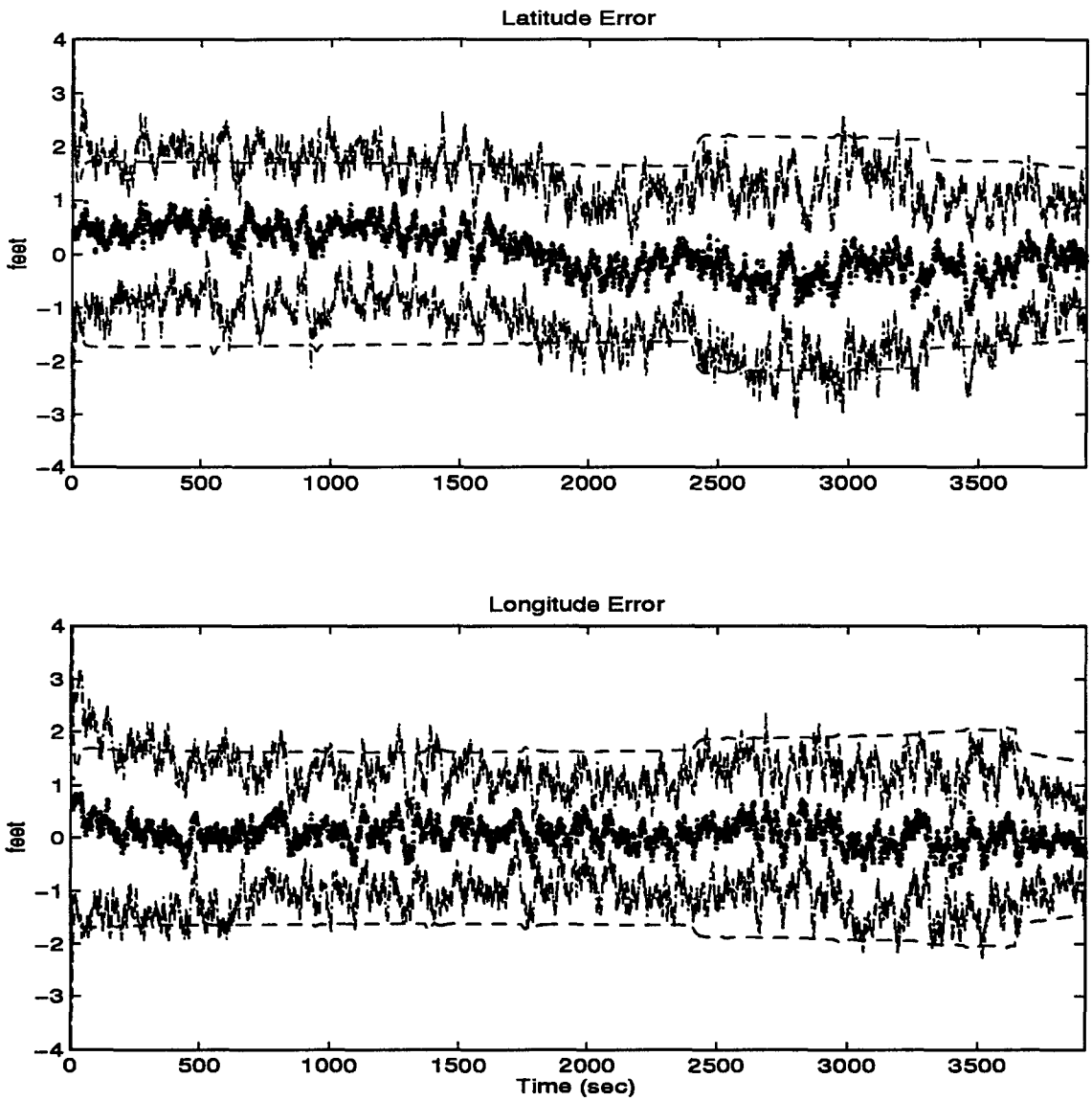

Figure C.19 Latitude and Longitude Error

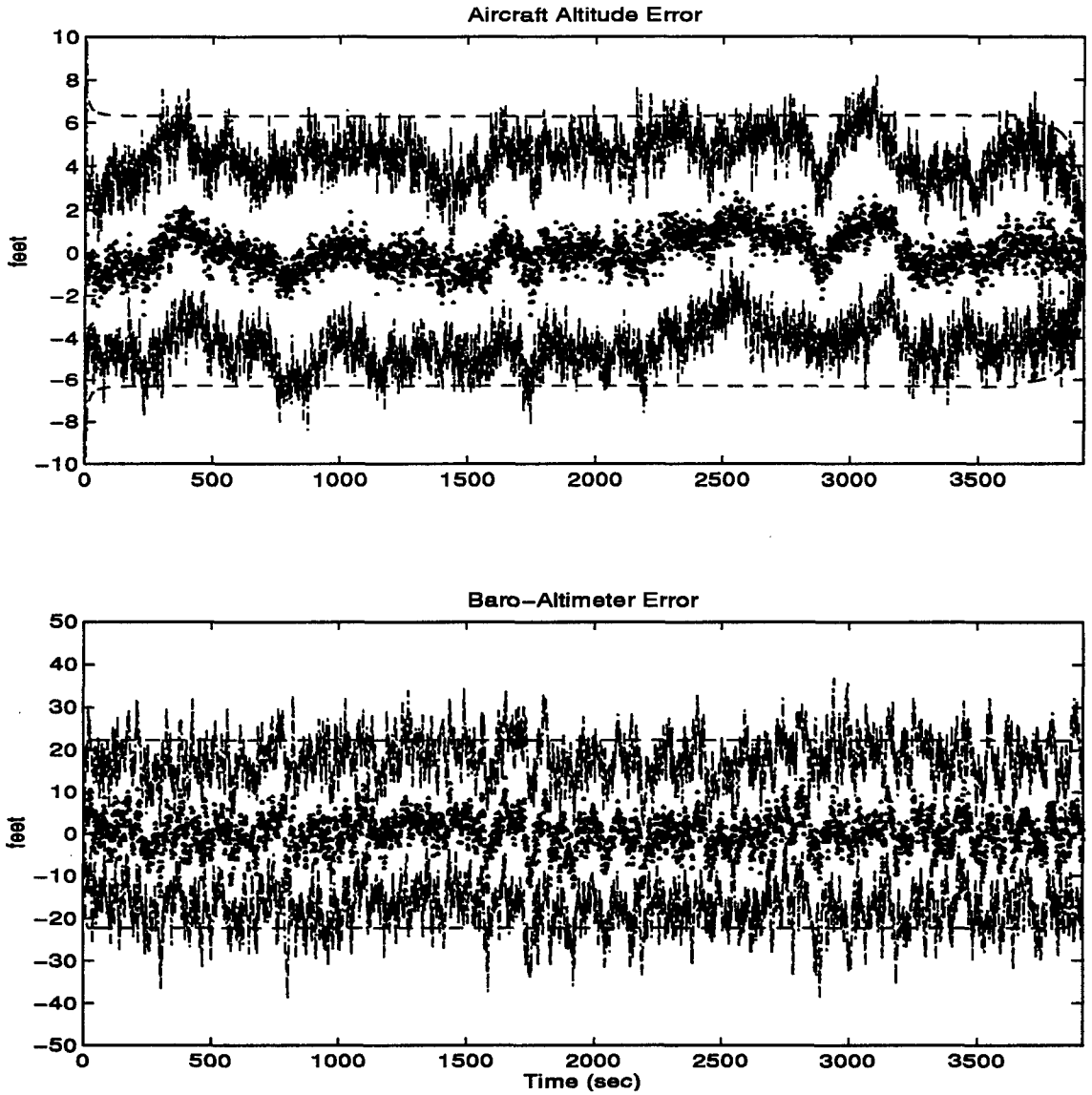

Figure C.20 Aircraft Altitude and Baro-Altimeter Error

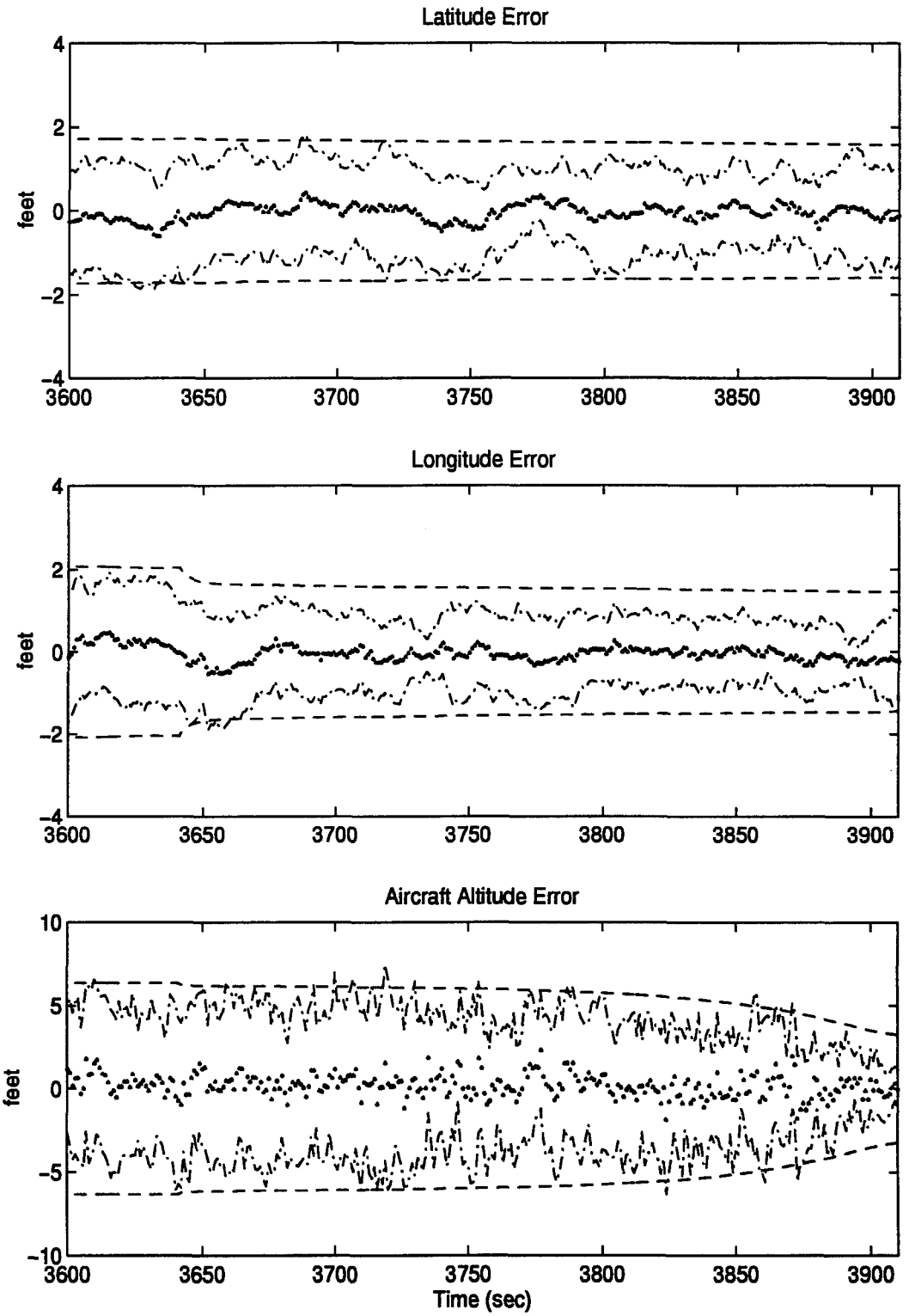

Figure C.21 Latitude, Longitude, and Aircraft Altitude Error

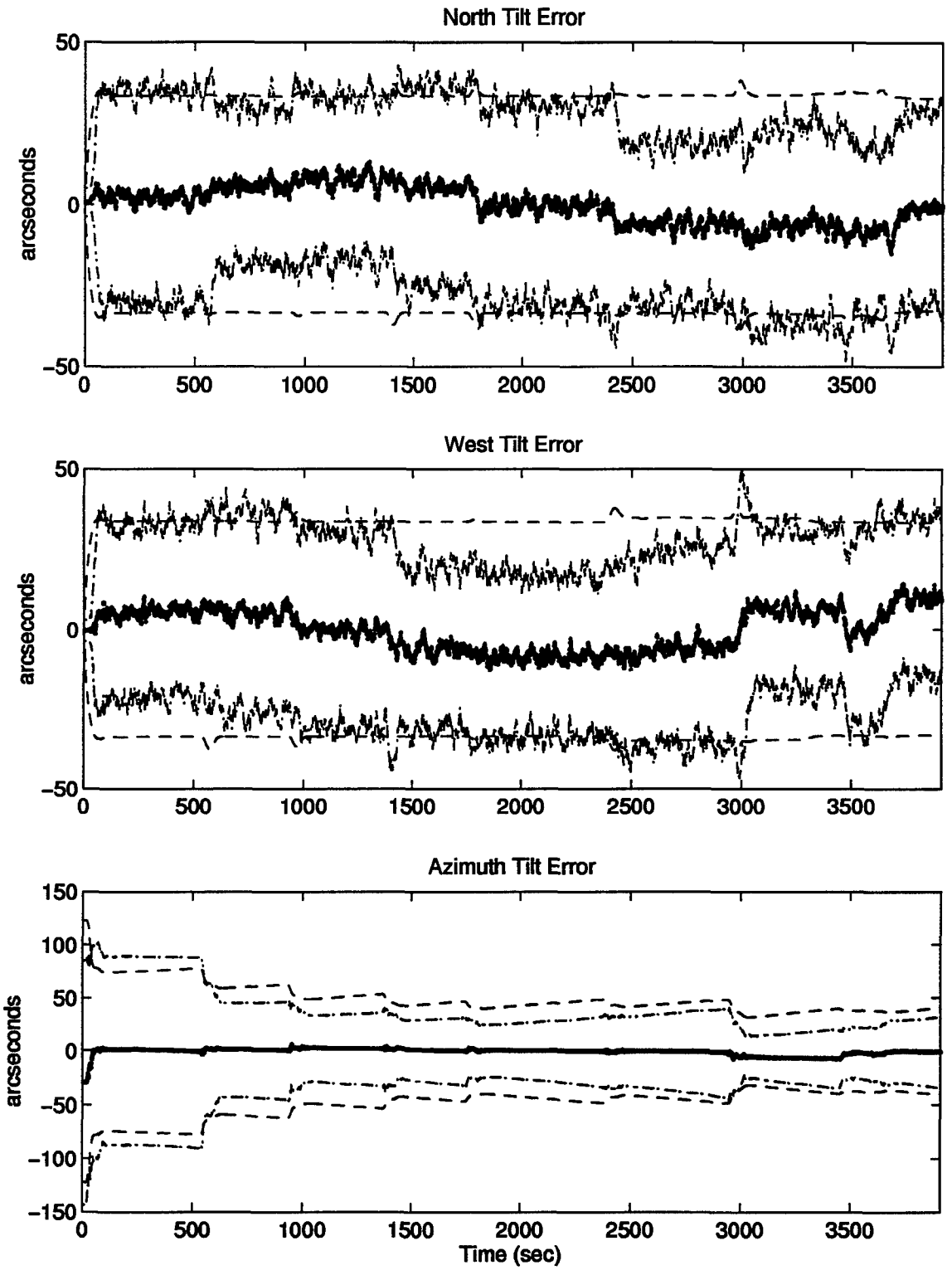

Figure C.22 North, West, and Azimuth Tilt Errors

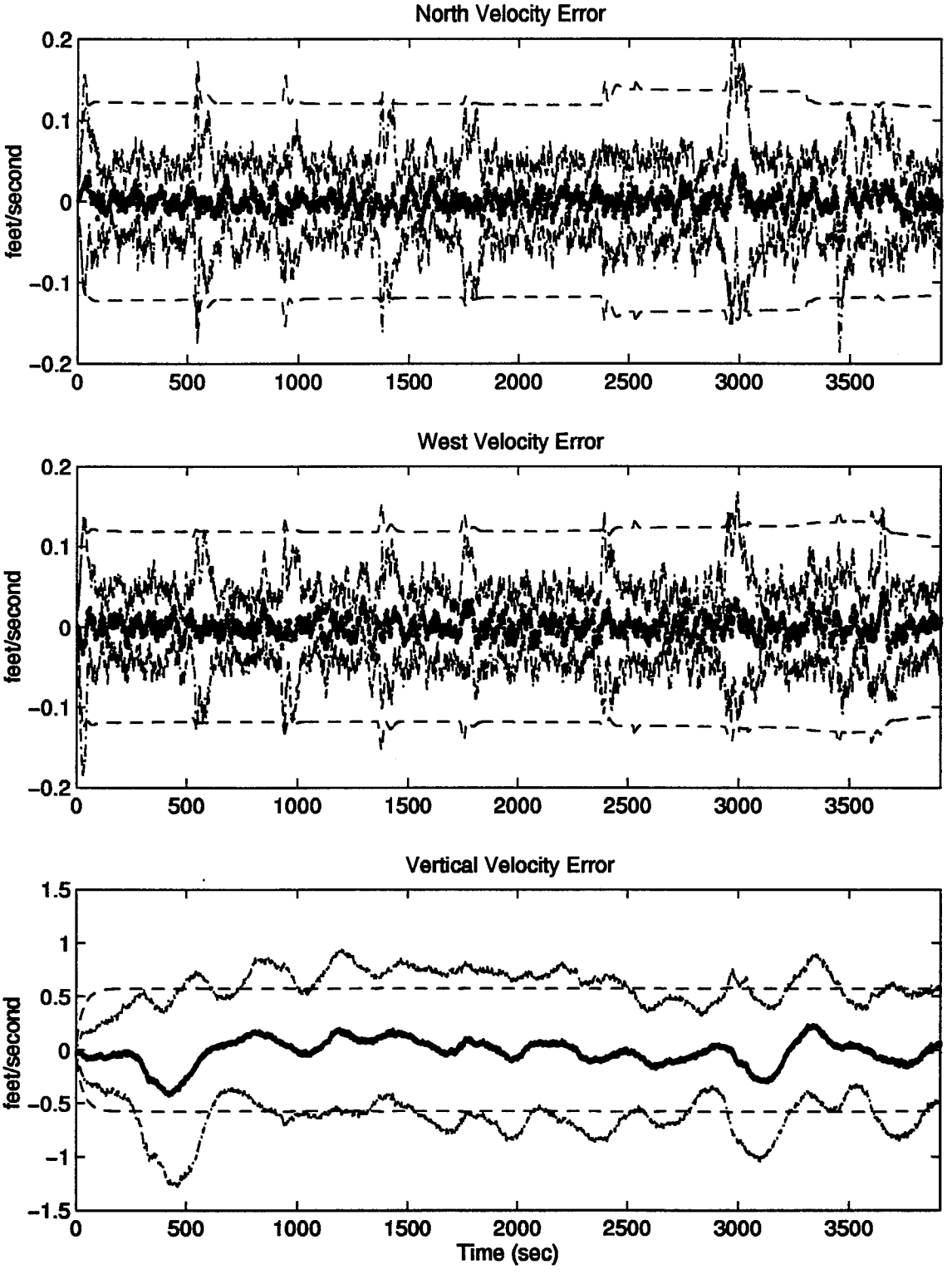

Figure C.23 North, West, and Vertical Velocity Errors

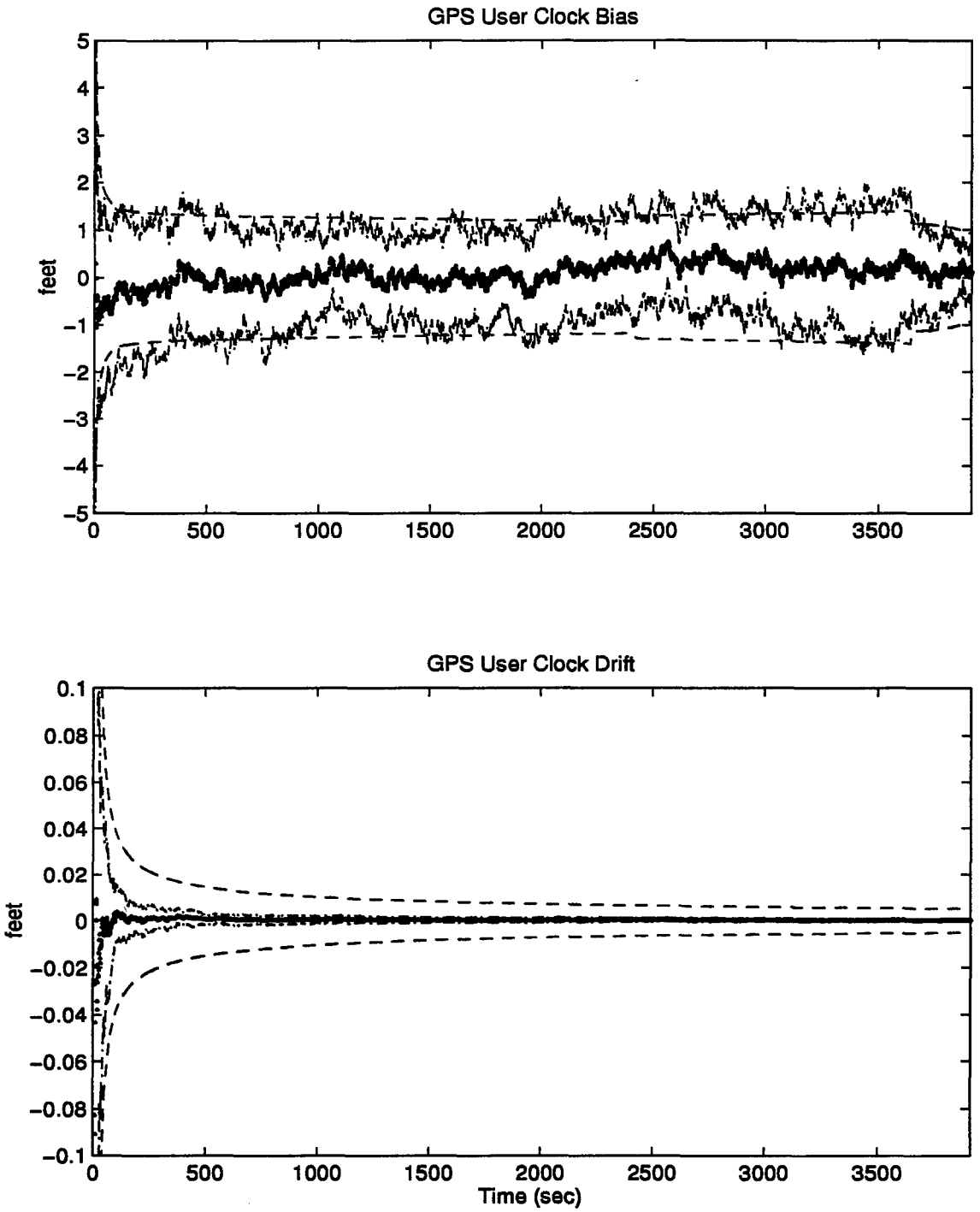

Figure C.24 GPS User Clock Bias and GPS User Clock Drift

C.5 Plots of Case XI: Barometric Altimeter, 4.0 nm/hr INS, Single Pseudolite, and DGPS Using the Tanker Flight Profile.

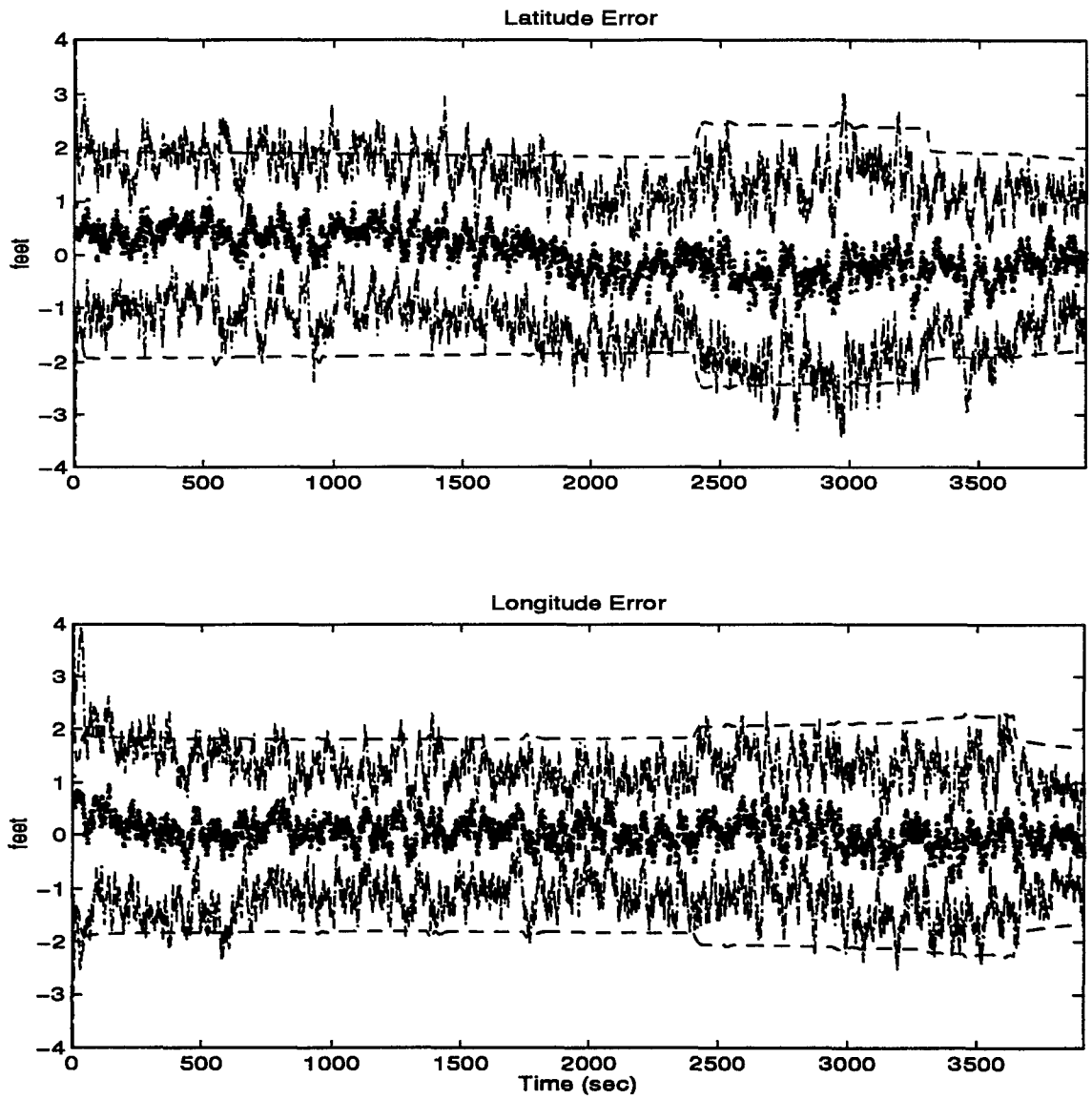

Figure C.25 Latitude and Longitude Error

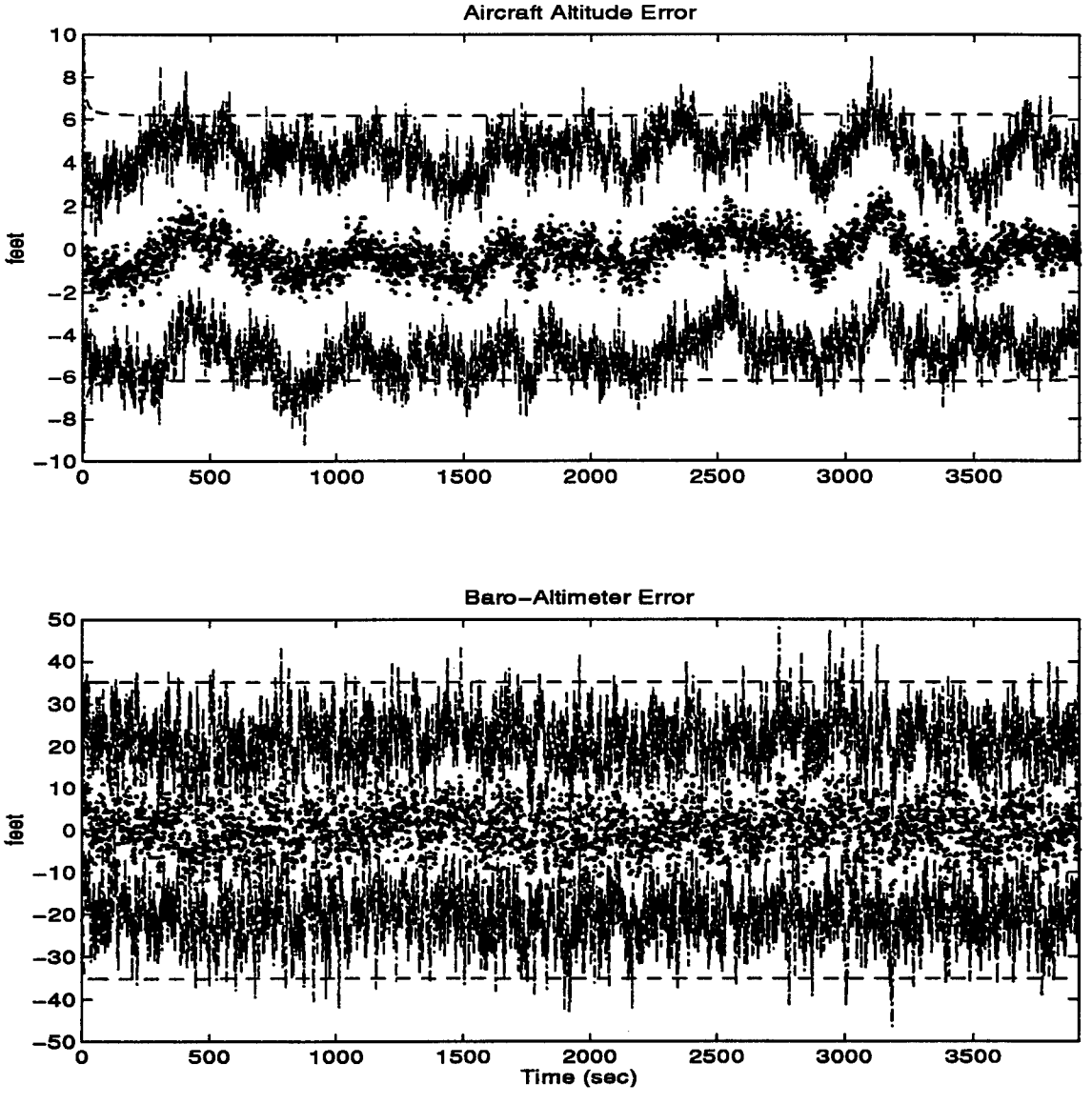

Figure C.26 Aircraft Altitude and Baro-Altimeter Error

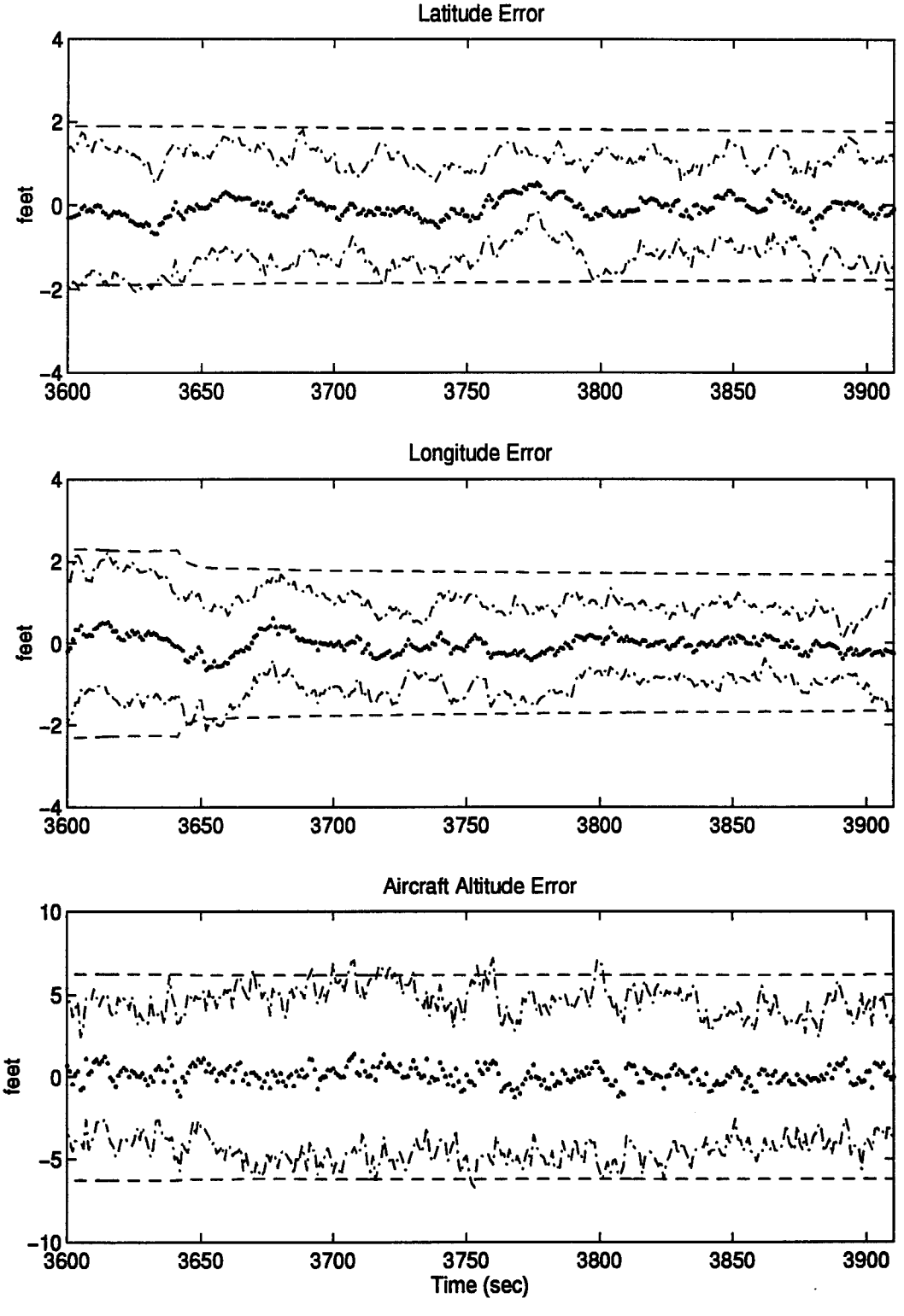

Figure C.27 Latitude, Longitude, and Aircraft Altitude Error

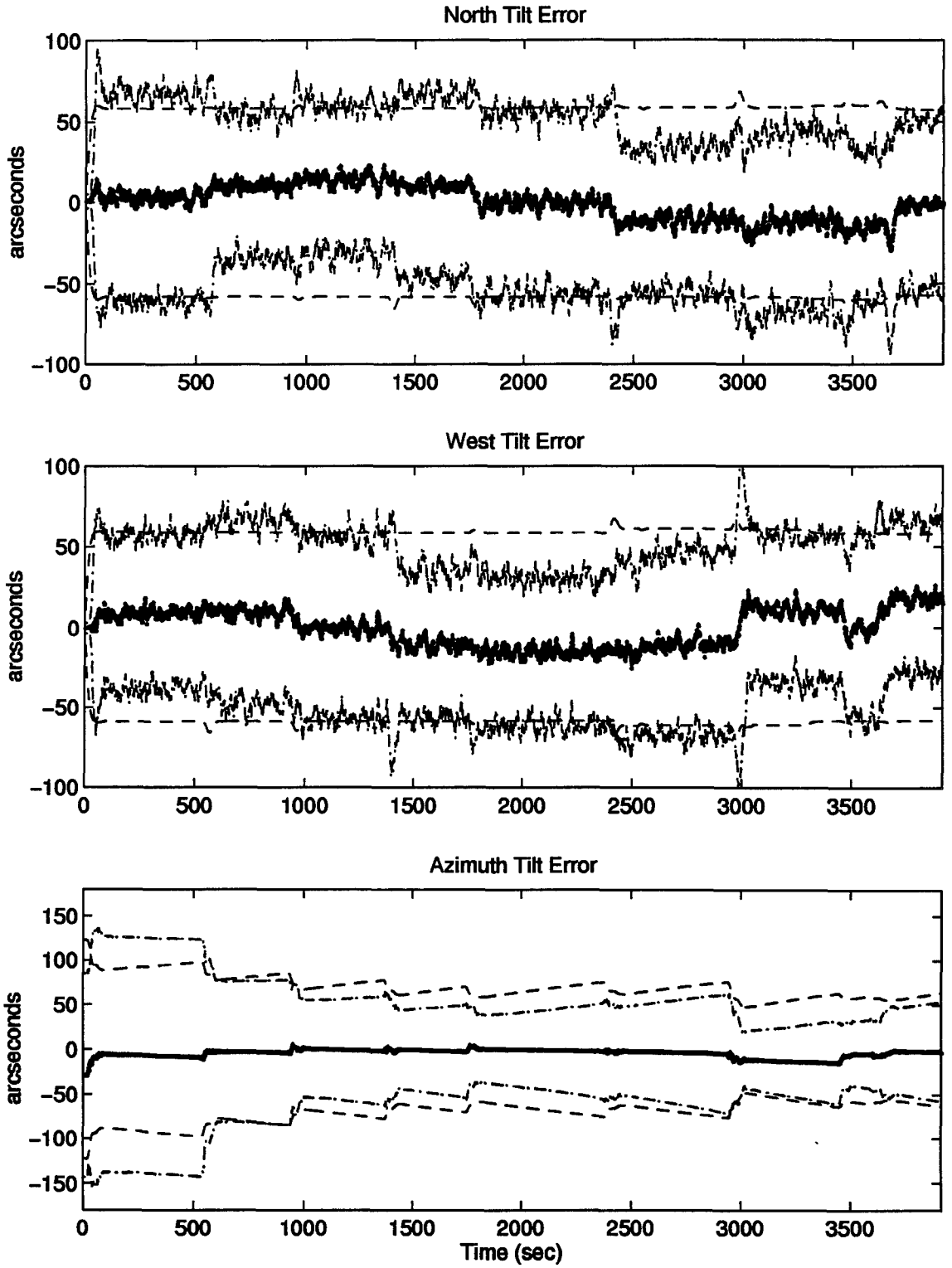

Figure C.28 North, West, and Azimuth Tilt Errors

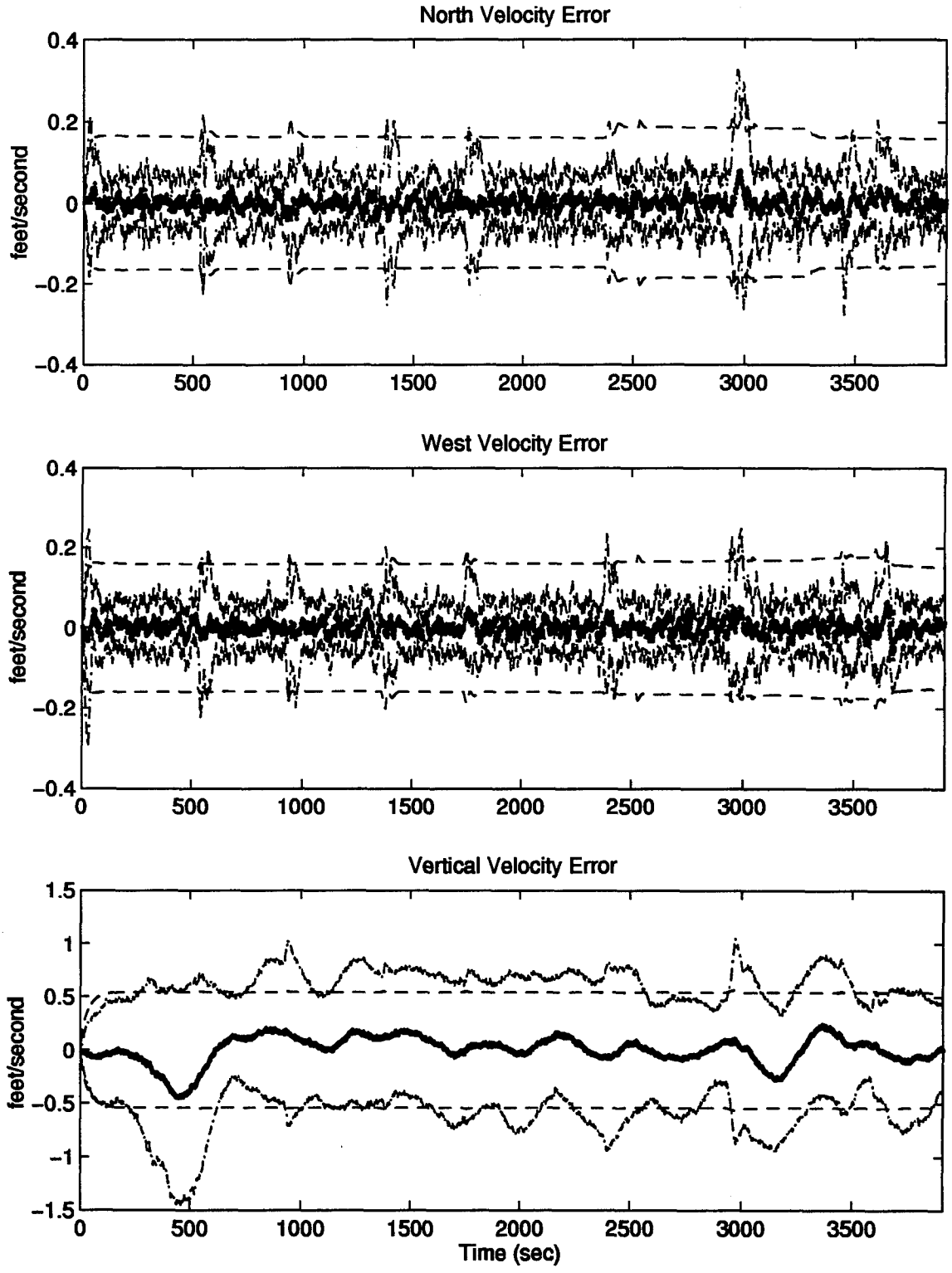

Figure C.29 North, West, and Vertical Velocity Errors

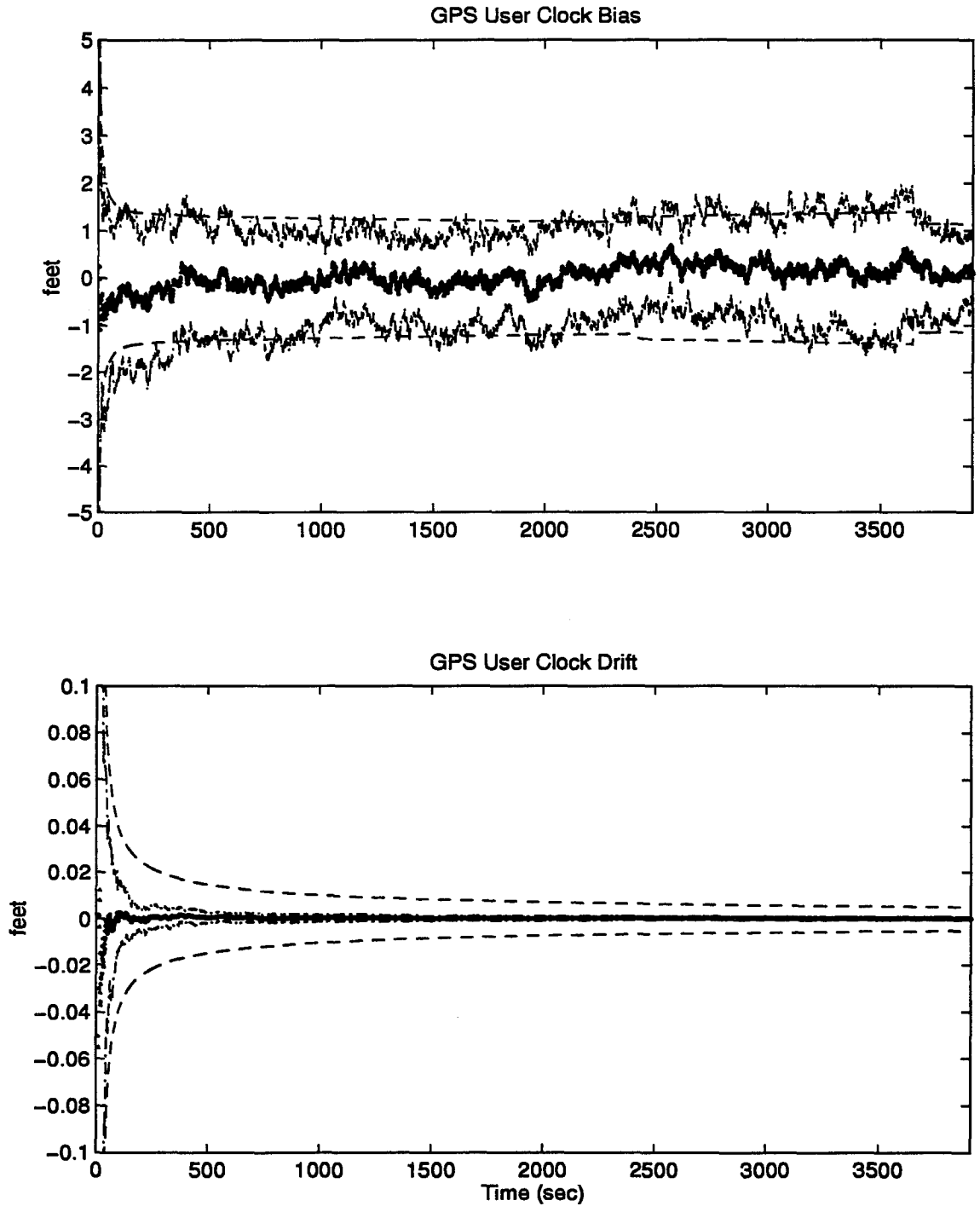

Figure C.30 GPS User Clock Bias and GPS User Clock Drift

C.6 Plots of Case XII: Barometric Altimeter, 4.0 nm/hr INS, Radar Altimeter, Single Pseudolite, and DGPS Using the Tanker Flight Profile.

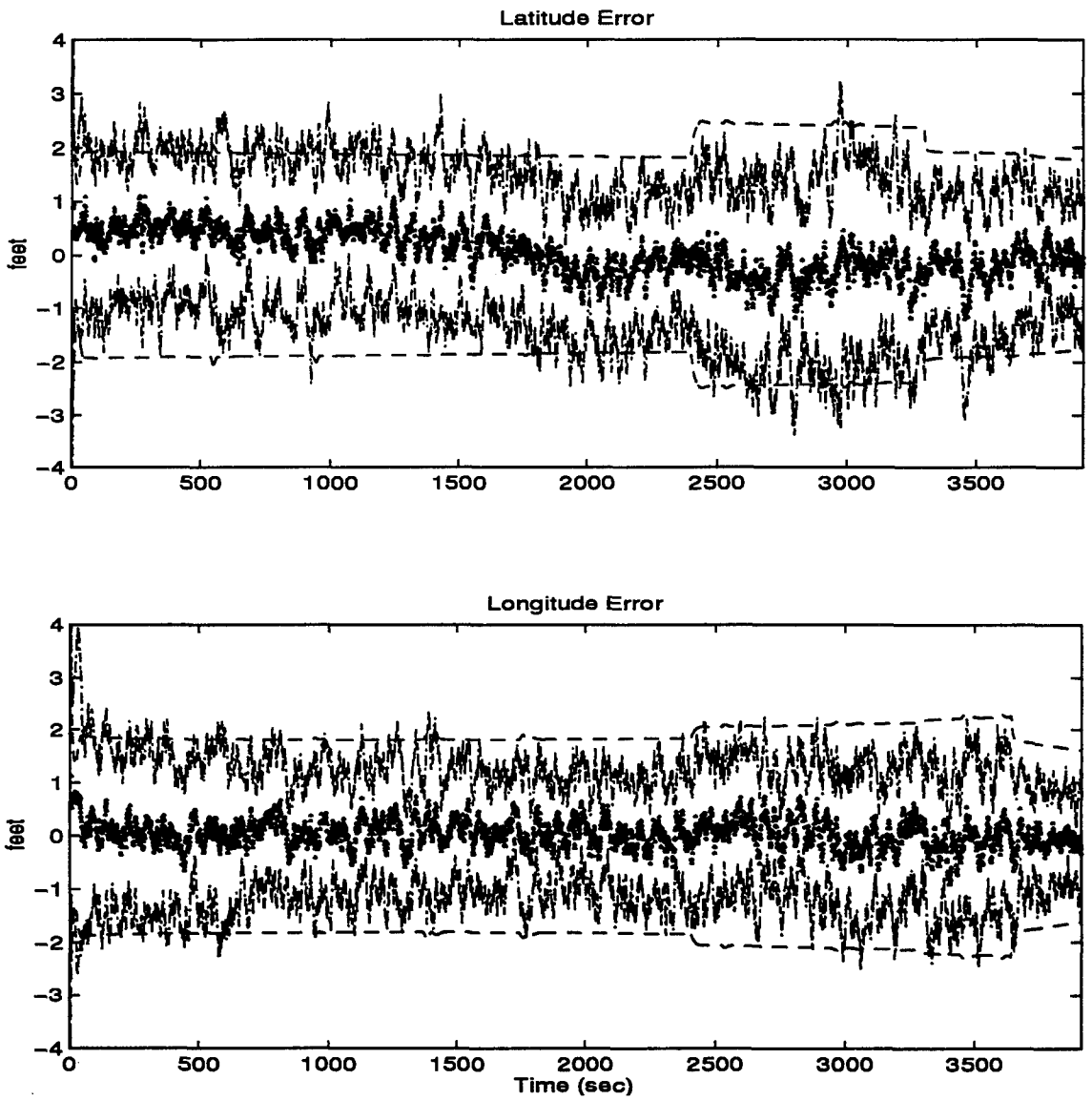

Figure C.31 Latitude and Longitude Error

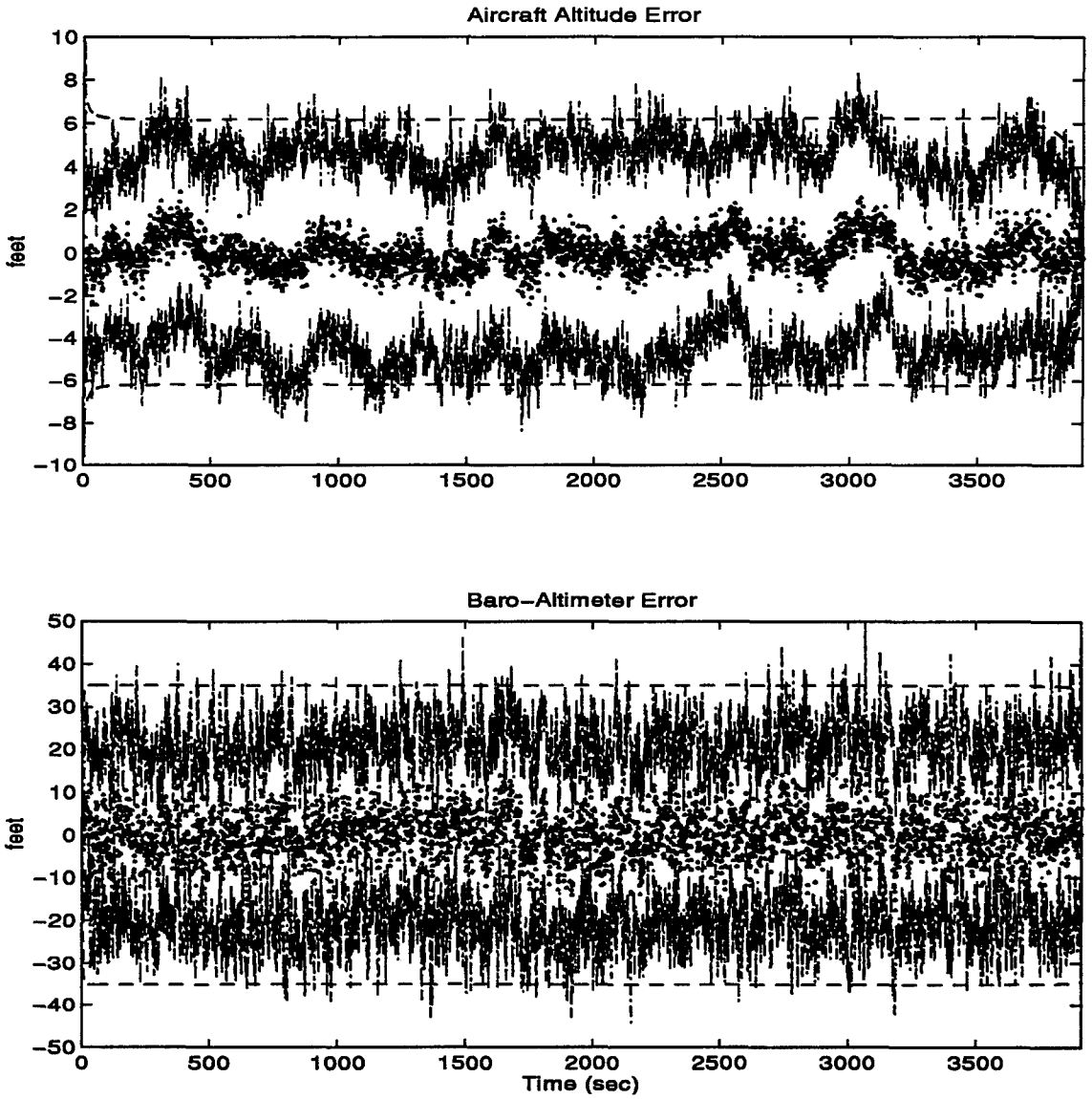

Figure C.32 Aircraft Altitude and Baro-Altimeter Error

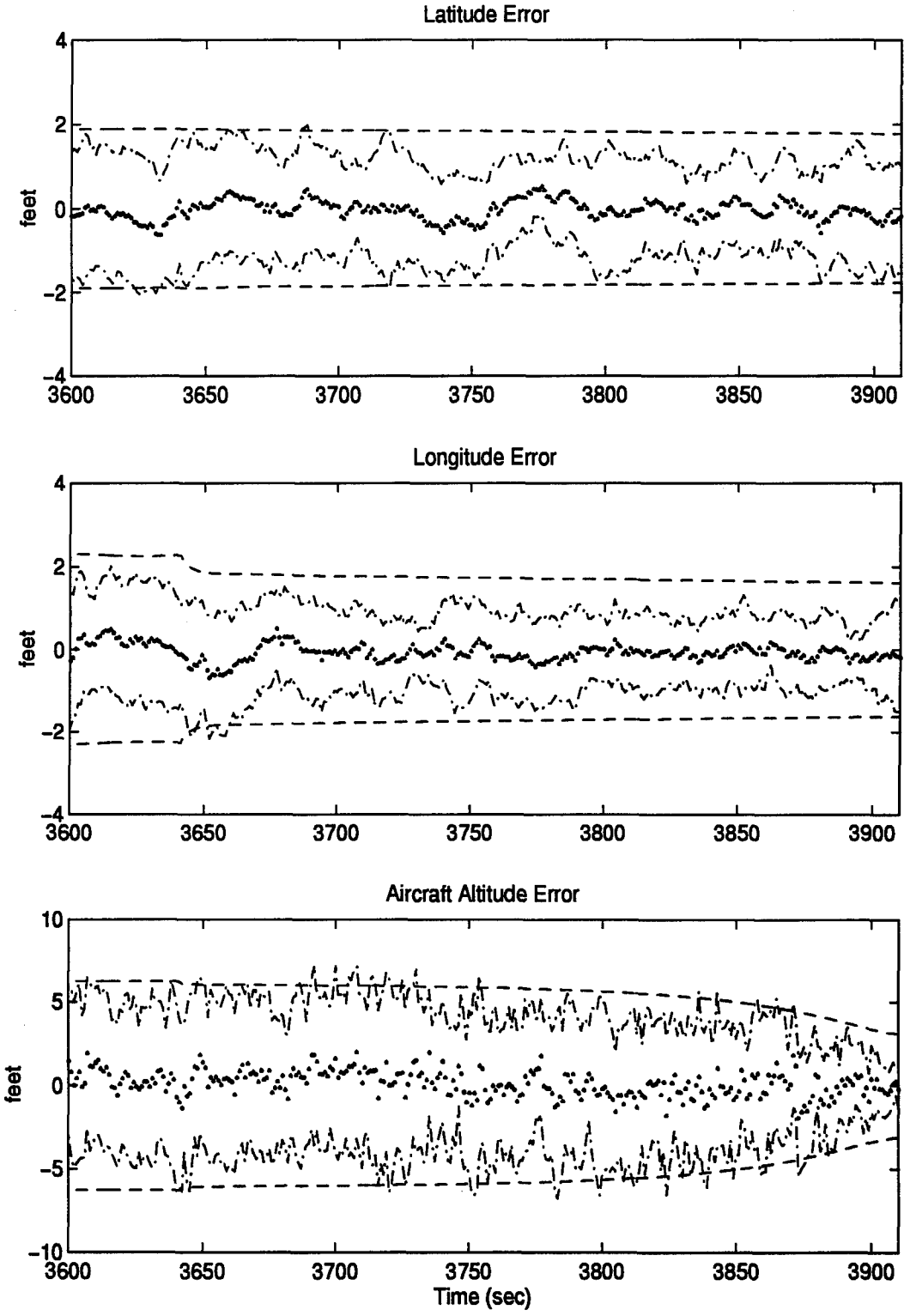

Figure C.33 Latitude, Longitude, and Aircraft Altitude Error

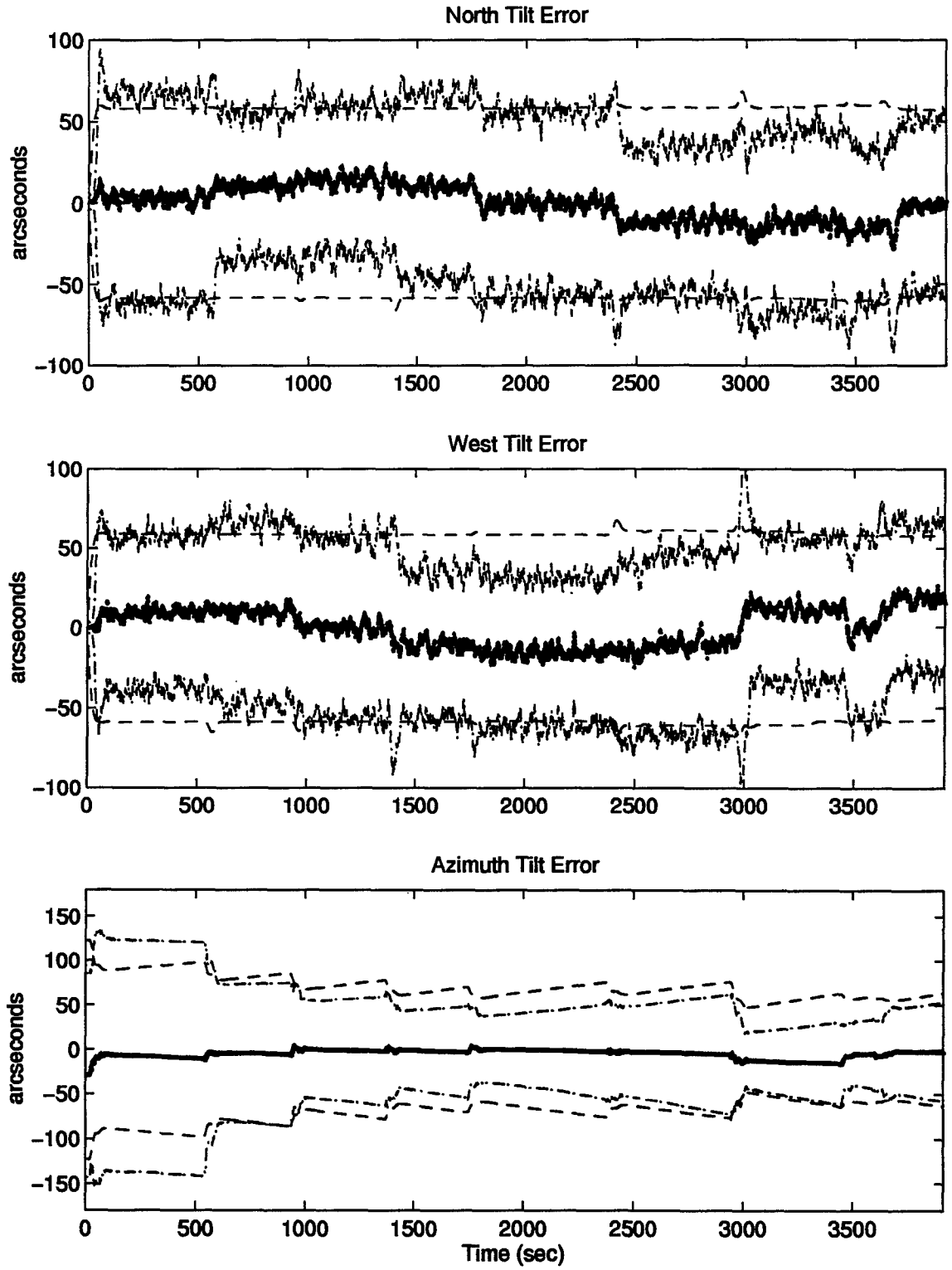

Figure C.34 North, West, and Azimuth Tilt Errors

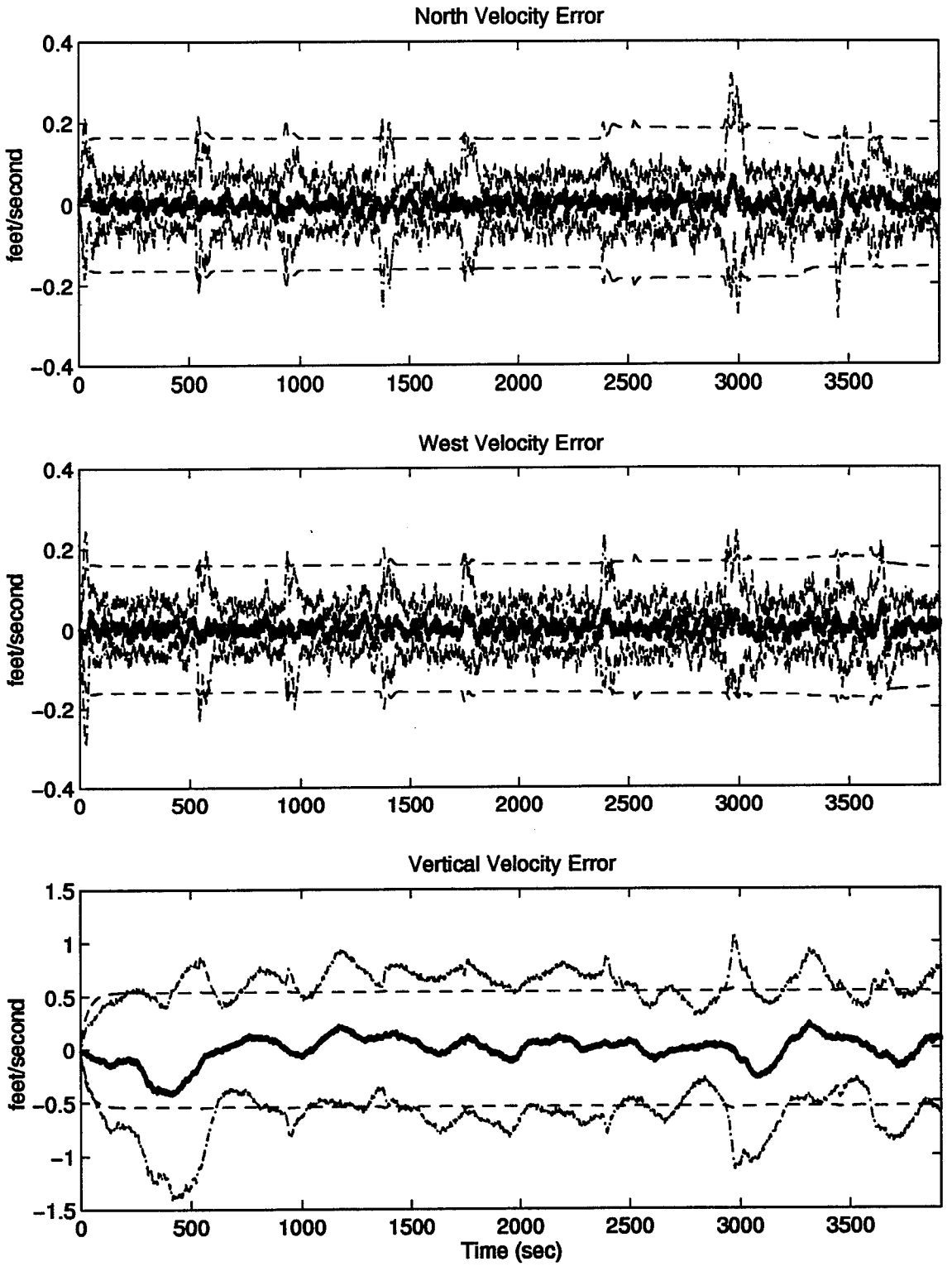

Figure C.35 North, West, and Vertical Velocity Errors

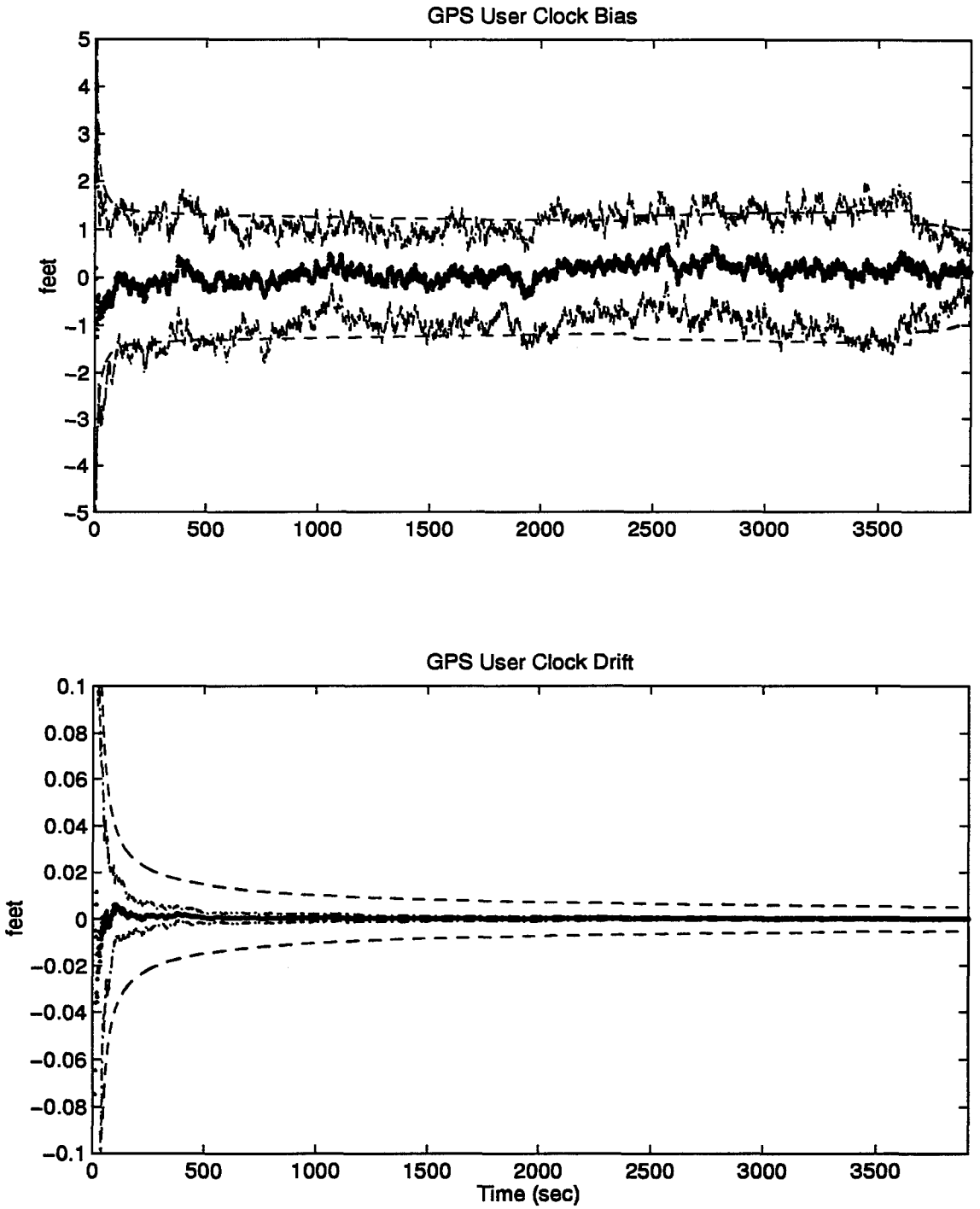

Figure C.36 GPS User Clock Bias and GPS User Clock Drift

Appendix D.

Plots of Case XIII, Case XIV, and Case XV for Tanker Flight Profile. These Cases Present DGPS Measurement Failure in Case I, Case III, and Case V.

Plot Legend

$\cdots$ true error (mean error $\pm$ σ_{true})

- - - filter predicted error ($0 \pm \sigma_{filter}$)

— mean error

D.1 Plots of Case XIII: Barometric Altimeter, 0.4 nm/hr INS, and DGPS Using the Tanker Flight Profile.

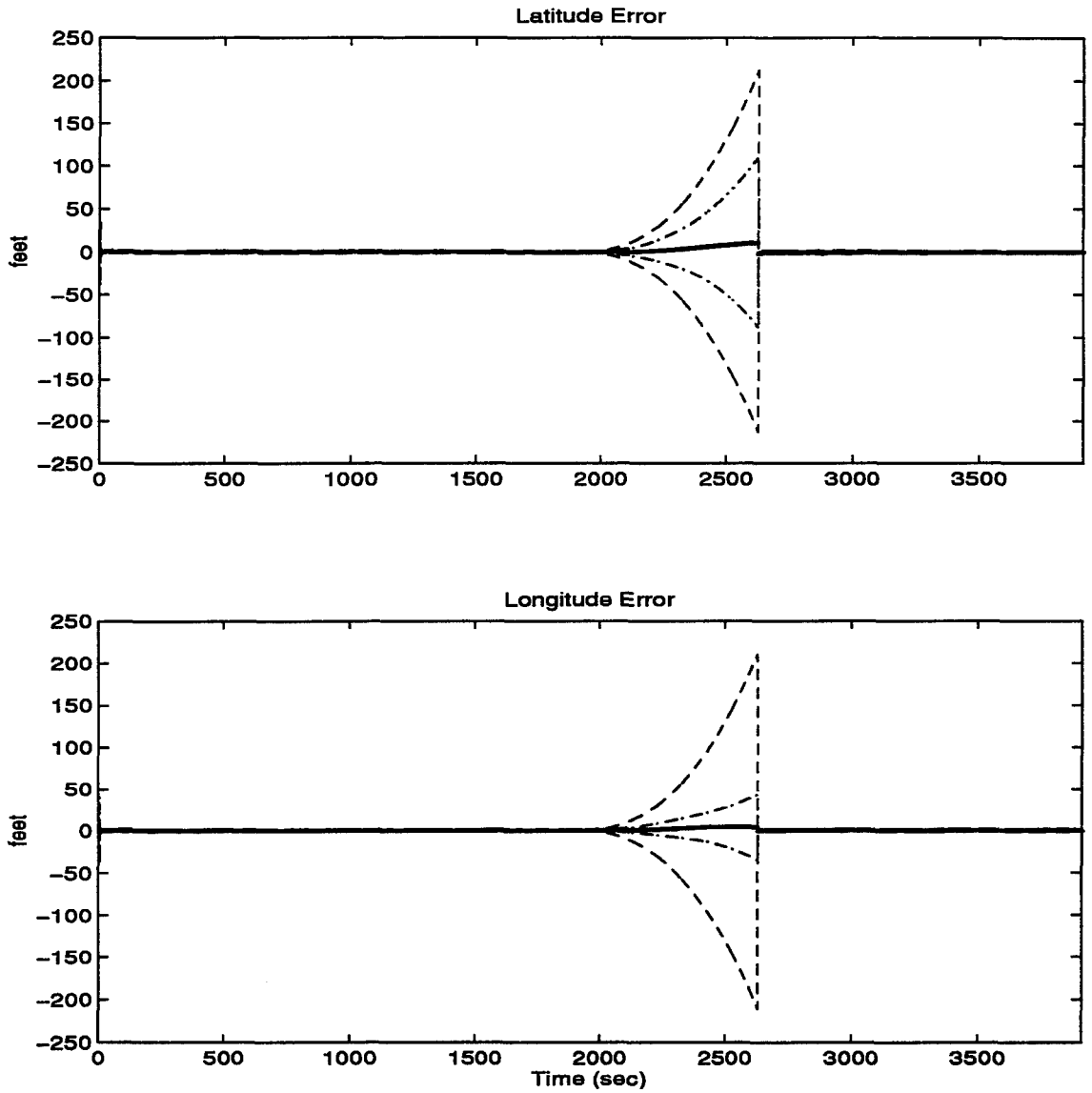

Figure D.1 Latitude and Longitude Error

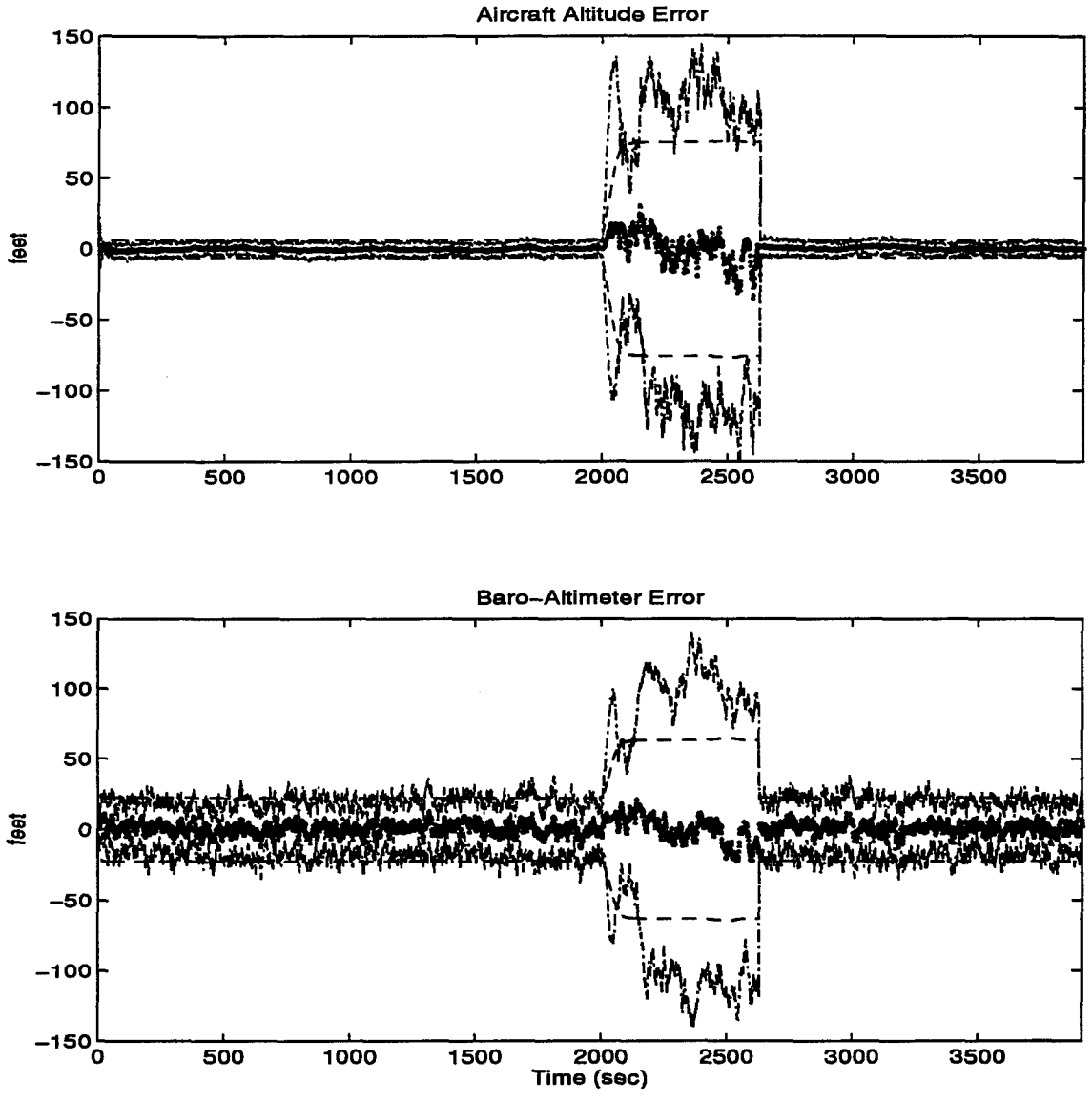

Figure D.2 Aircraft Altitude and Baro-Altimeter Error

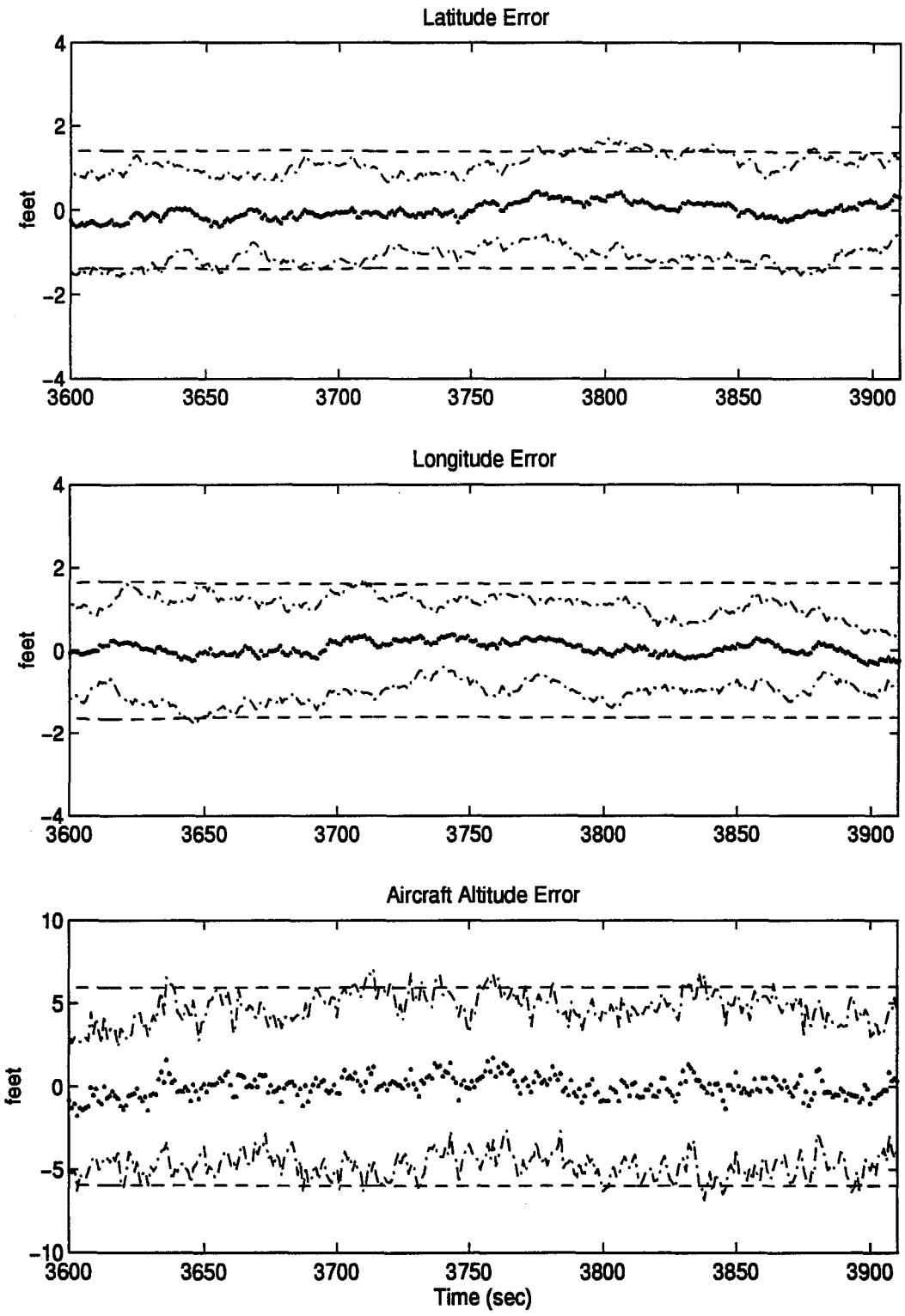

Figure D.3 Latitude, Longitude, and Aircraft Altitude Error

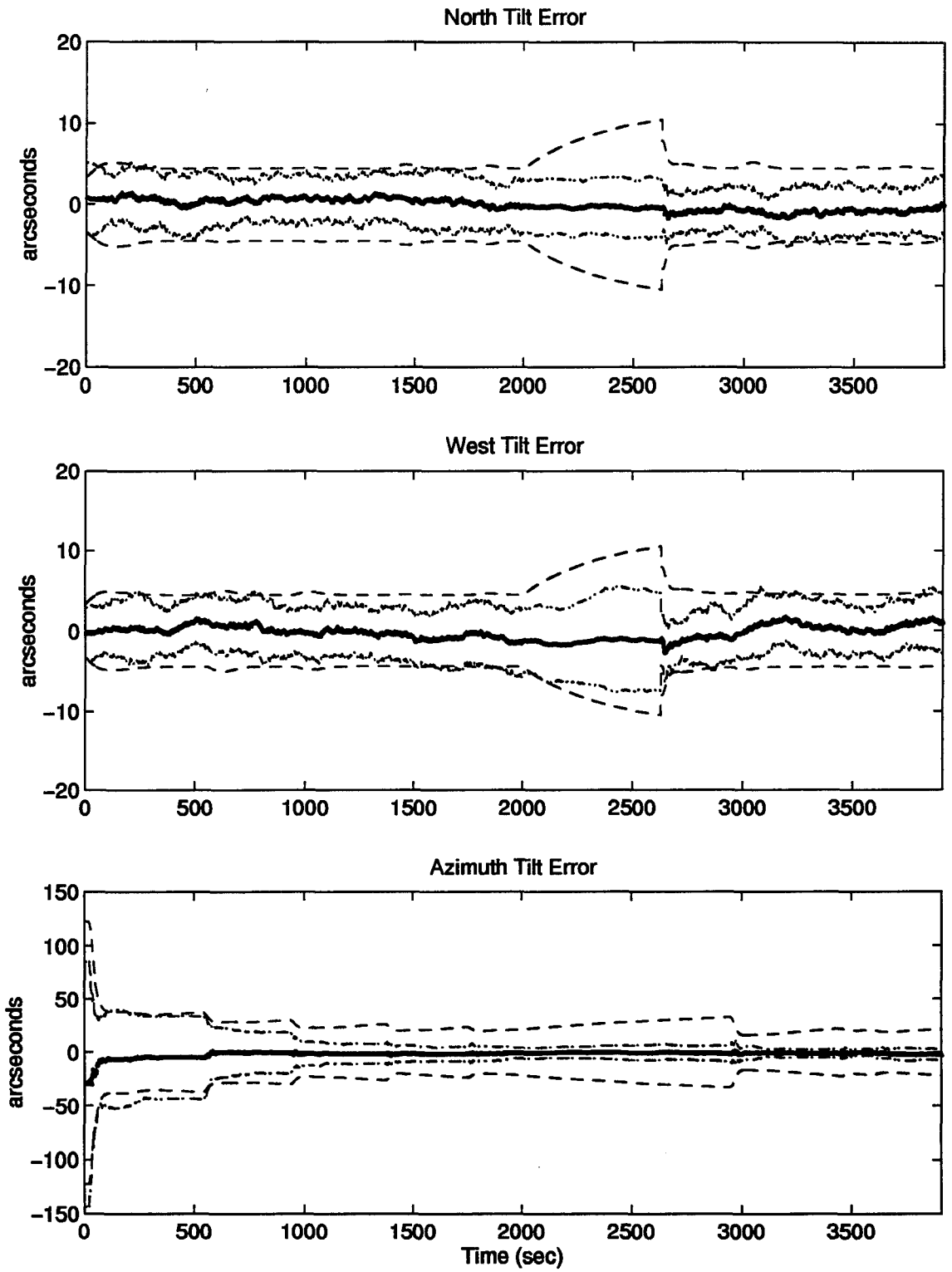

Figure D.4 North, West, and Azimuth Tilt Errors

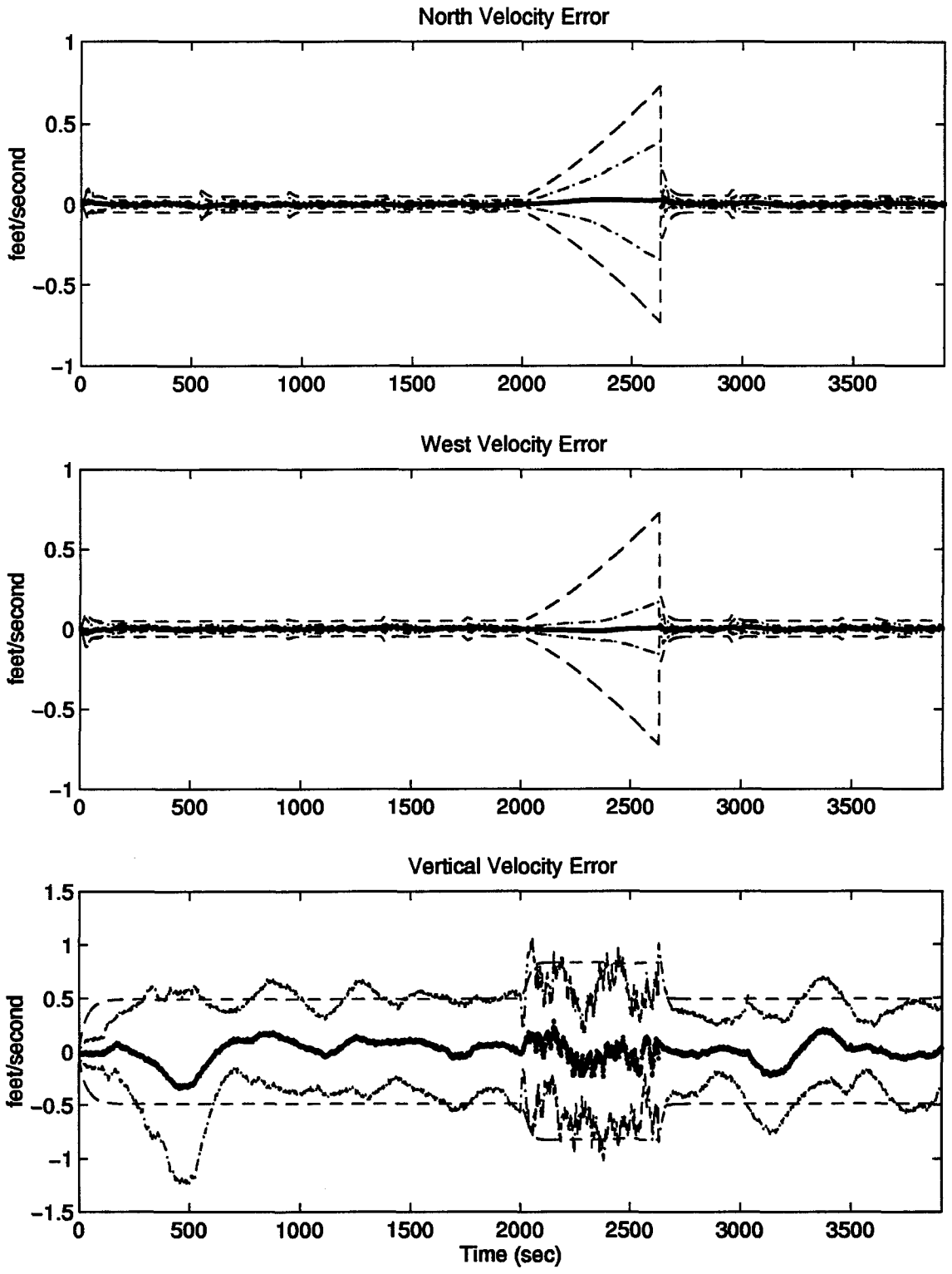

Figure D.5 North, West, and Vertical Velocity Errors

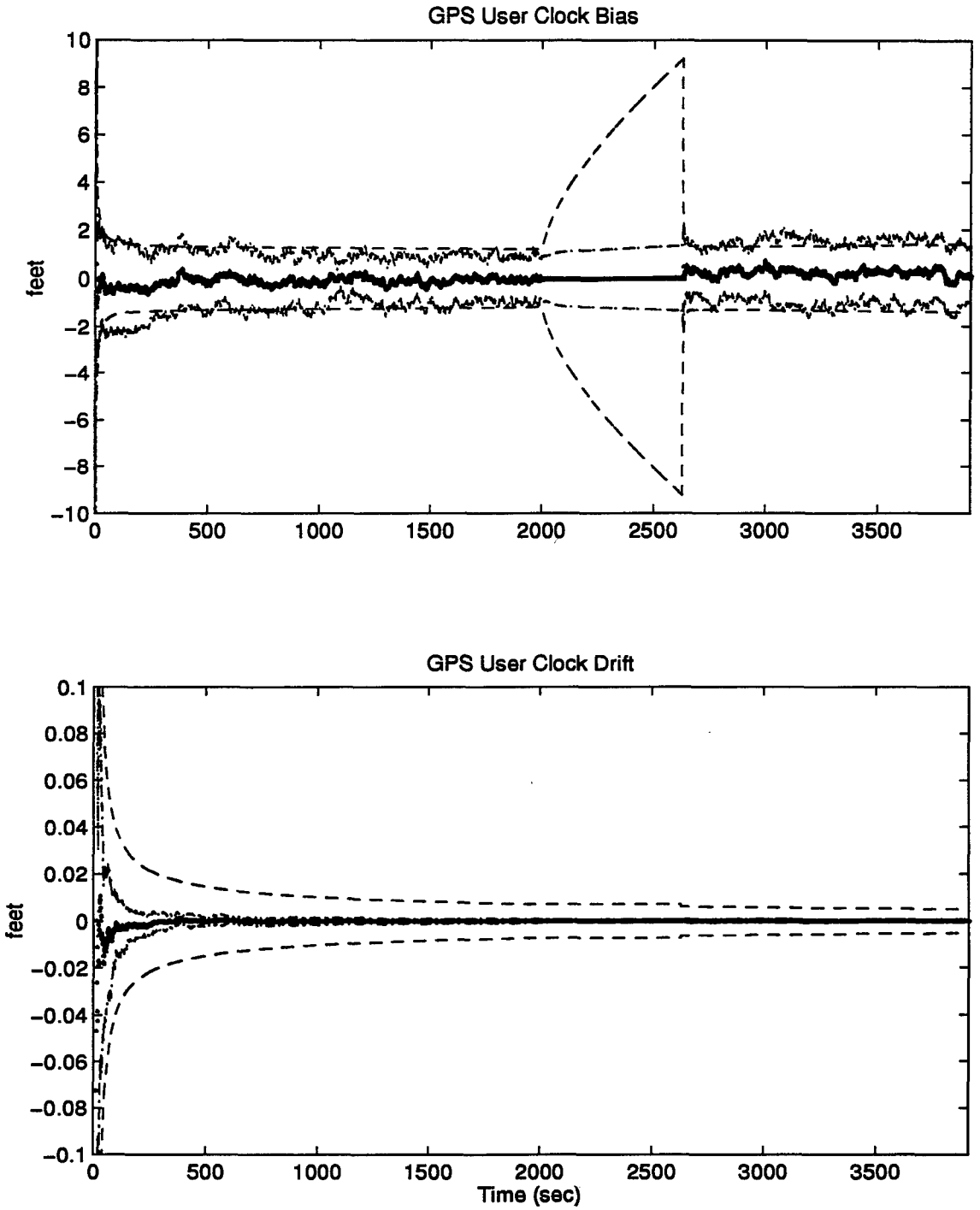

Figure D.6 GPS User Clock Bias and GPS User Clock Drift

D.2 Plots of Case XIV: Barometric Altimeter, 2.0 nm/hr INS, and DGPS Using the Tanker Flight Profile.

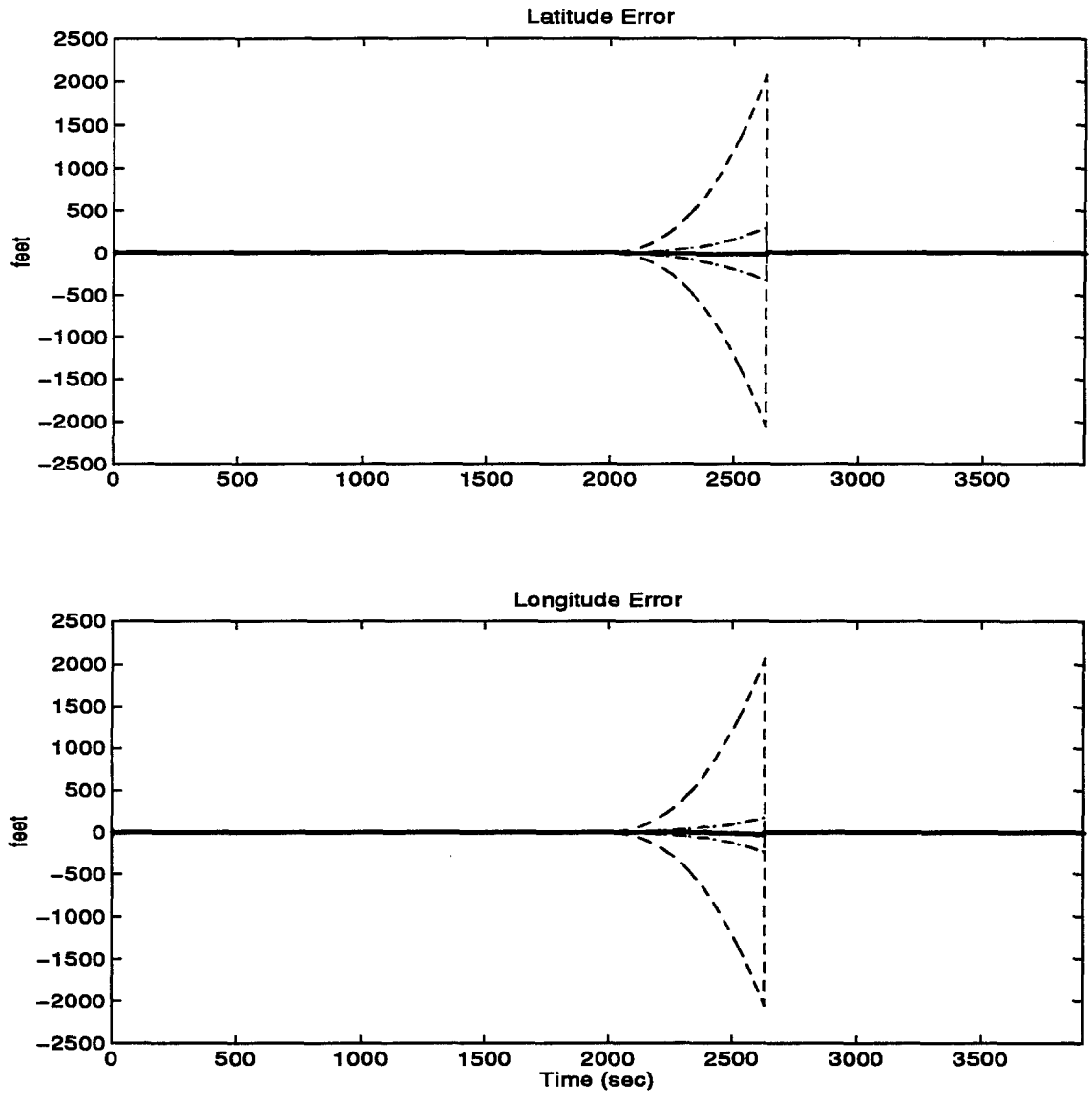

Figure D.7 Latitude and Longitude Error

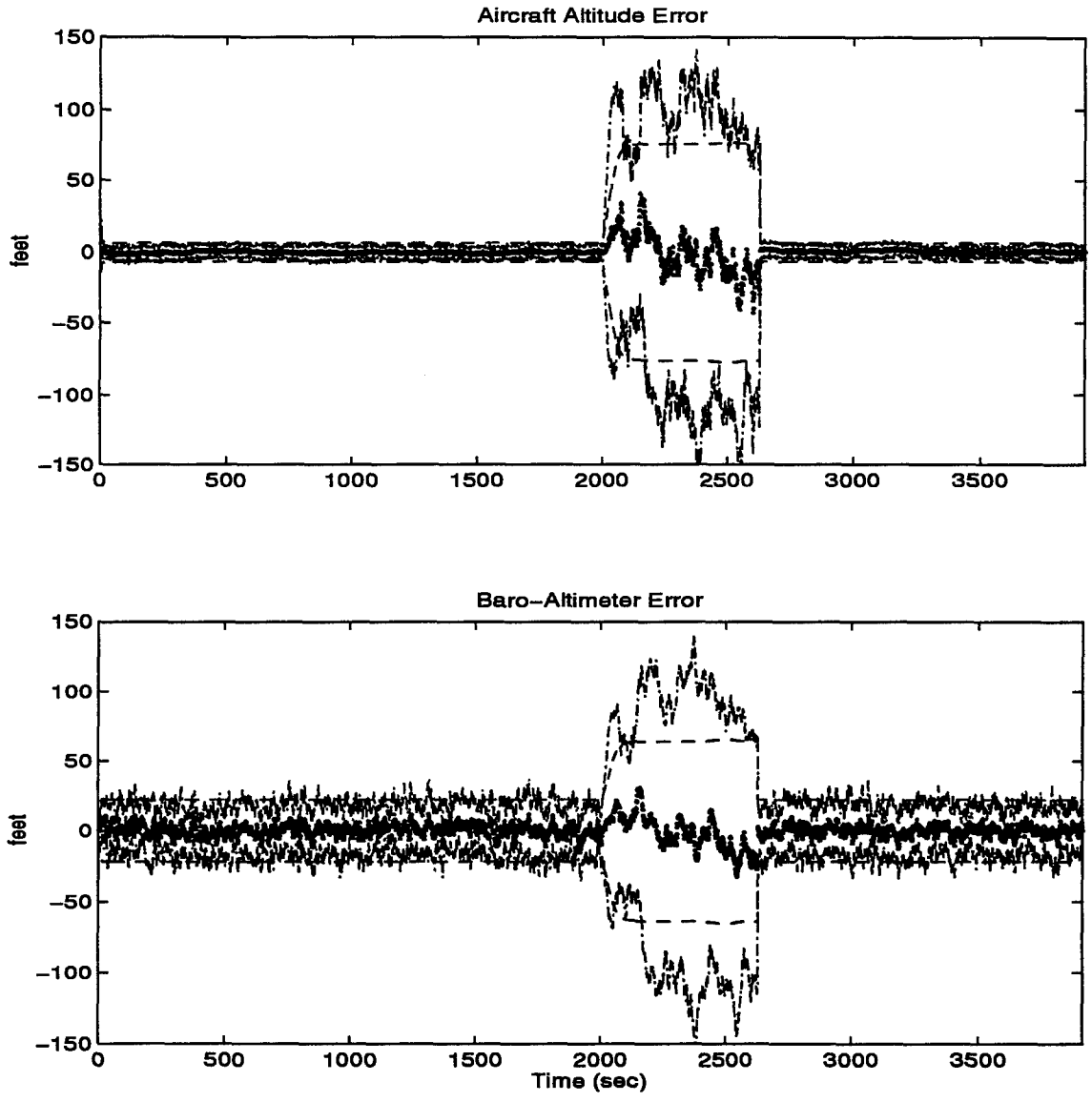

Figure D.8 Aircraft Altitude and Baro-Altimeter Error

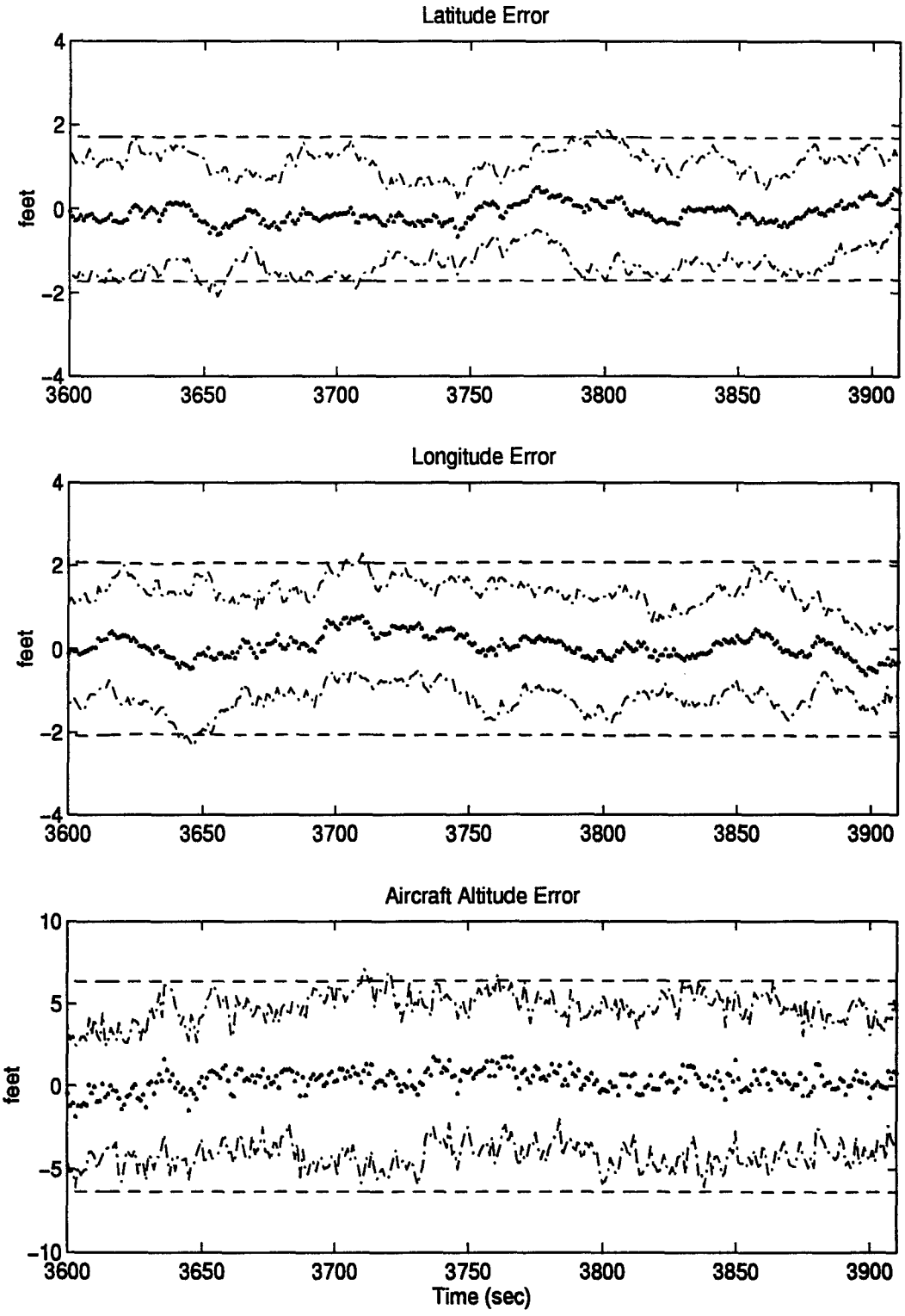

Figure D.9 Latitude, Longitude, and Aircraft Altitude Error

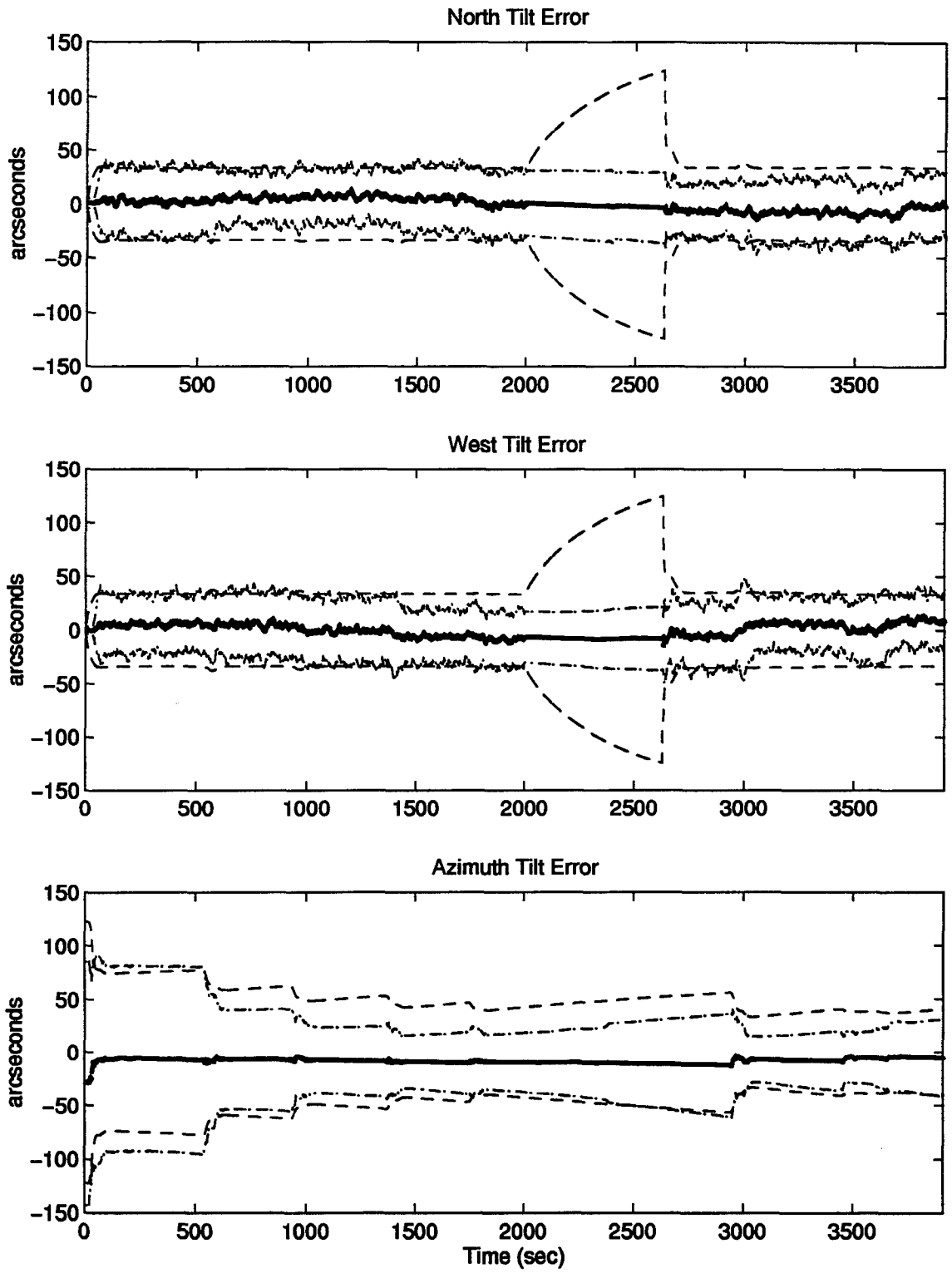

Figure D.10 North, West, and Azimuth Tilt Errors

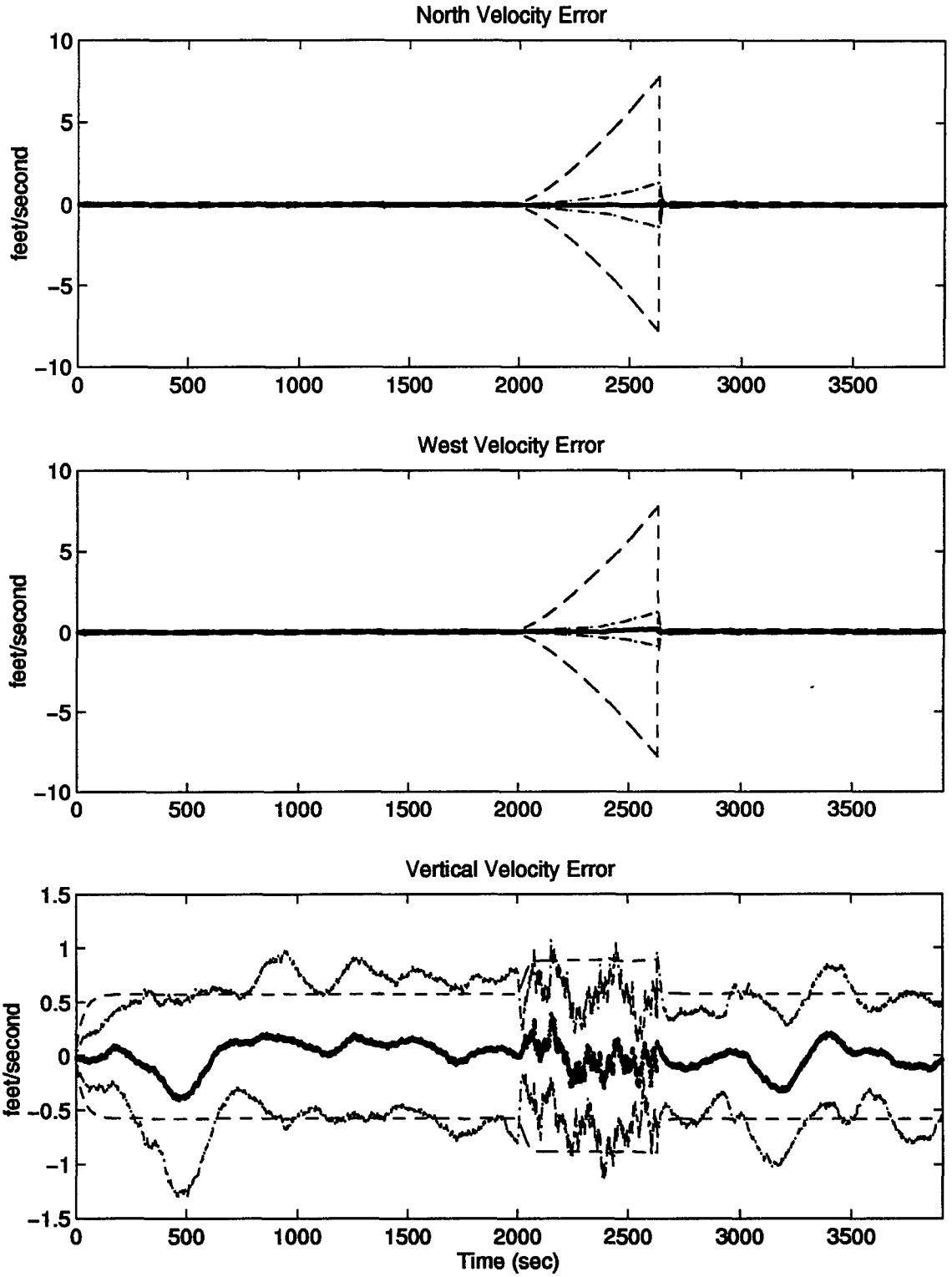

Figure D.11 North, West, and Vertical Velocity Errors

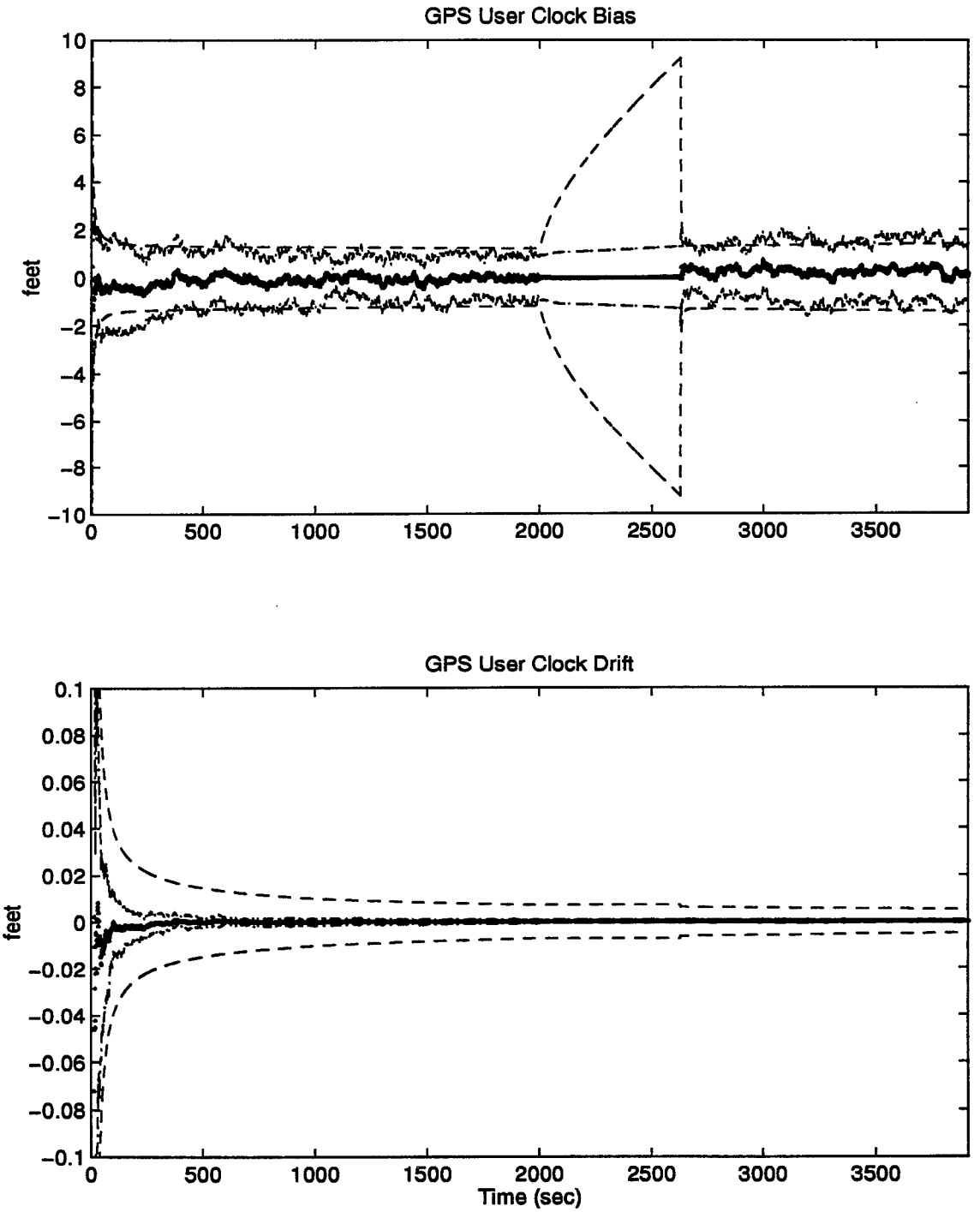

Figure D.12 GPS User Clock Bias and GPS User Clock Drift

D.3 Plots of Case XV: Barometric Altimeter, 4.0 nm/hr INS, and DGPS Using the Tanker Flight Profile.

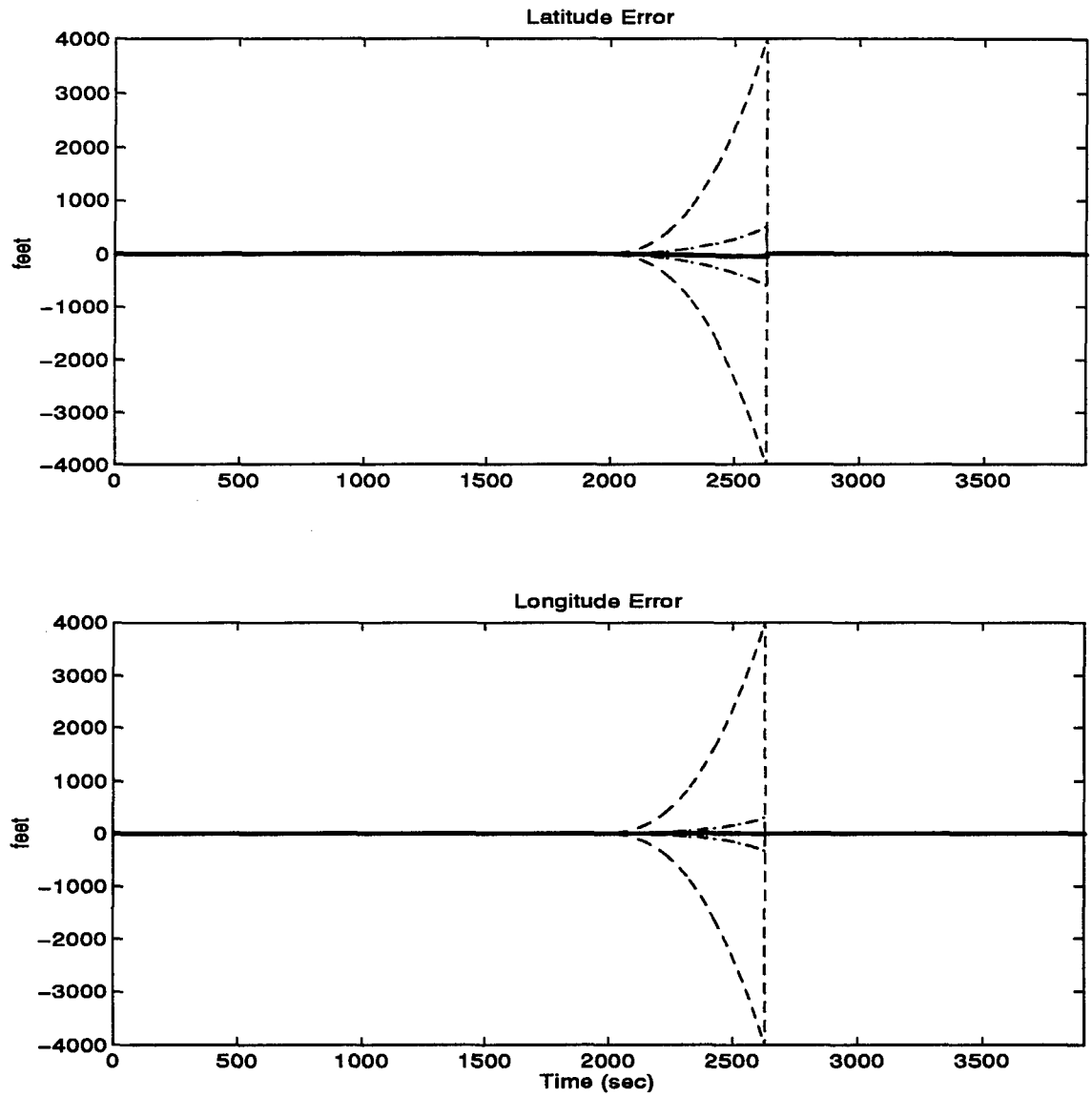

Figure D.13 Latitude and Longitude Error

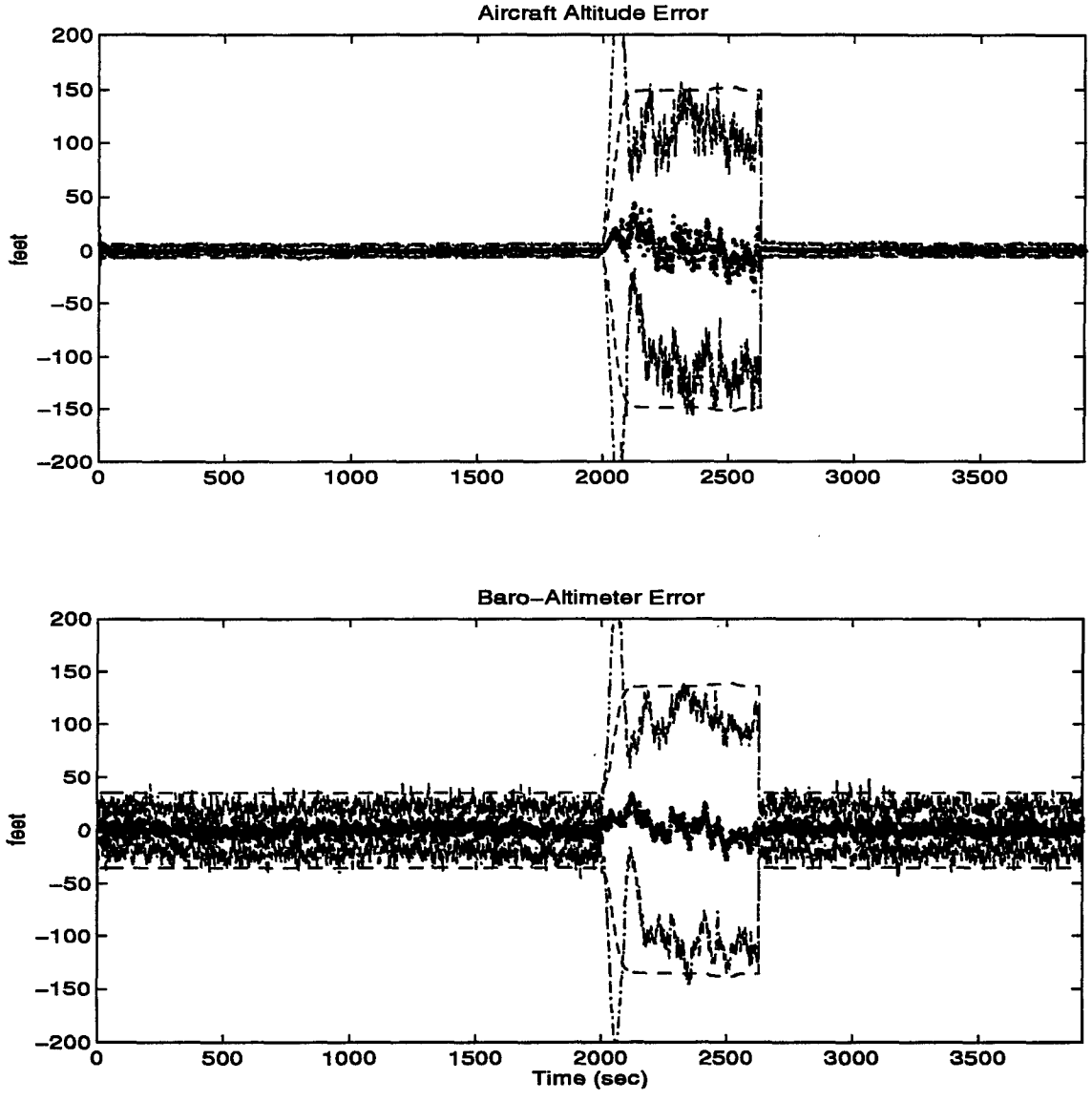

Figure D.14 Aircraft Altitude and Baro-Altimeter Error

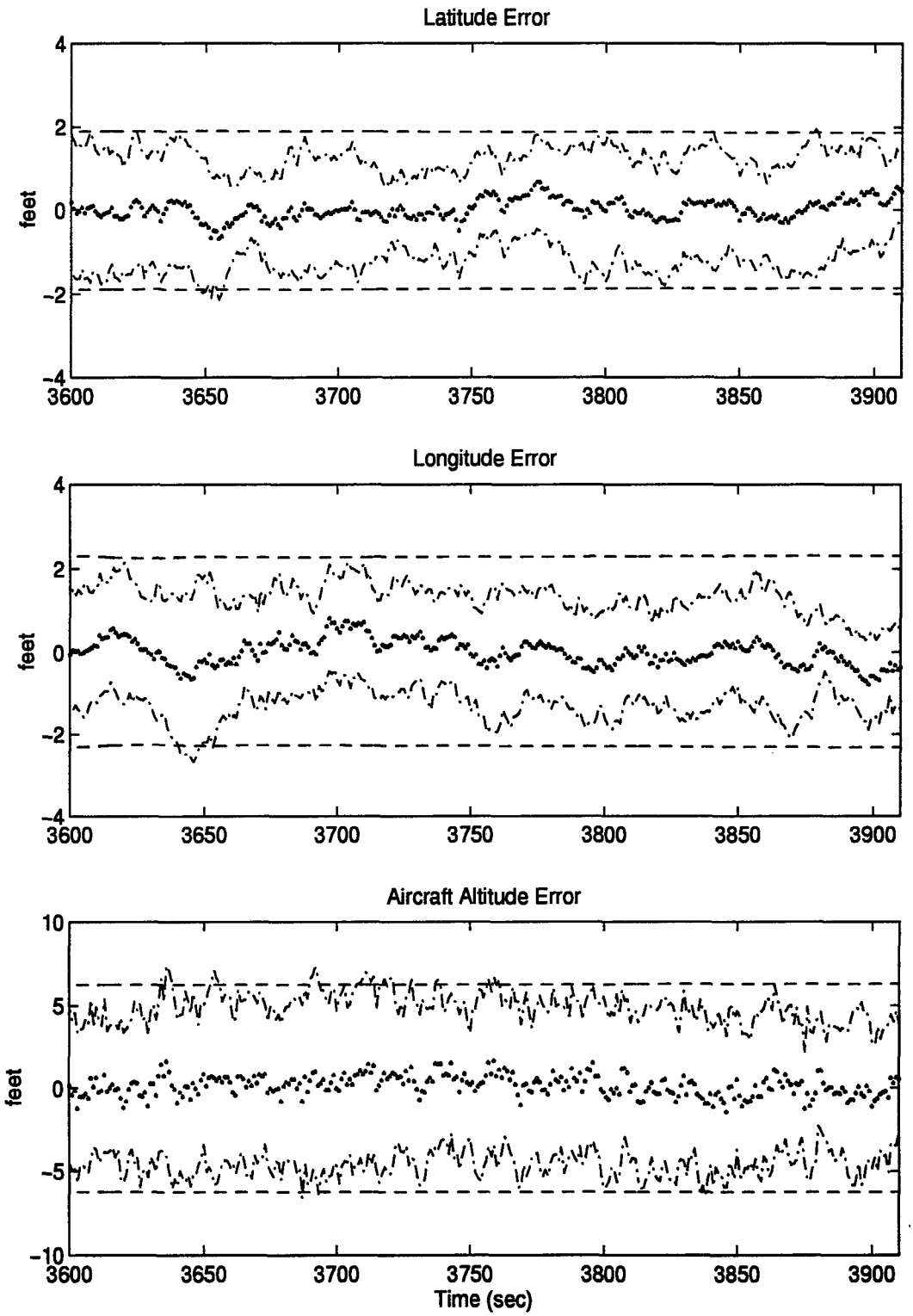

Figure D.15 Latitude, Longitude, and Aircraft Altitude Error

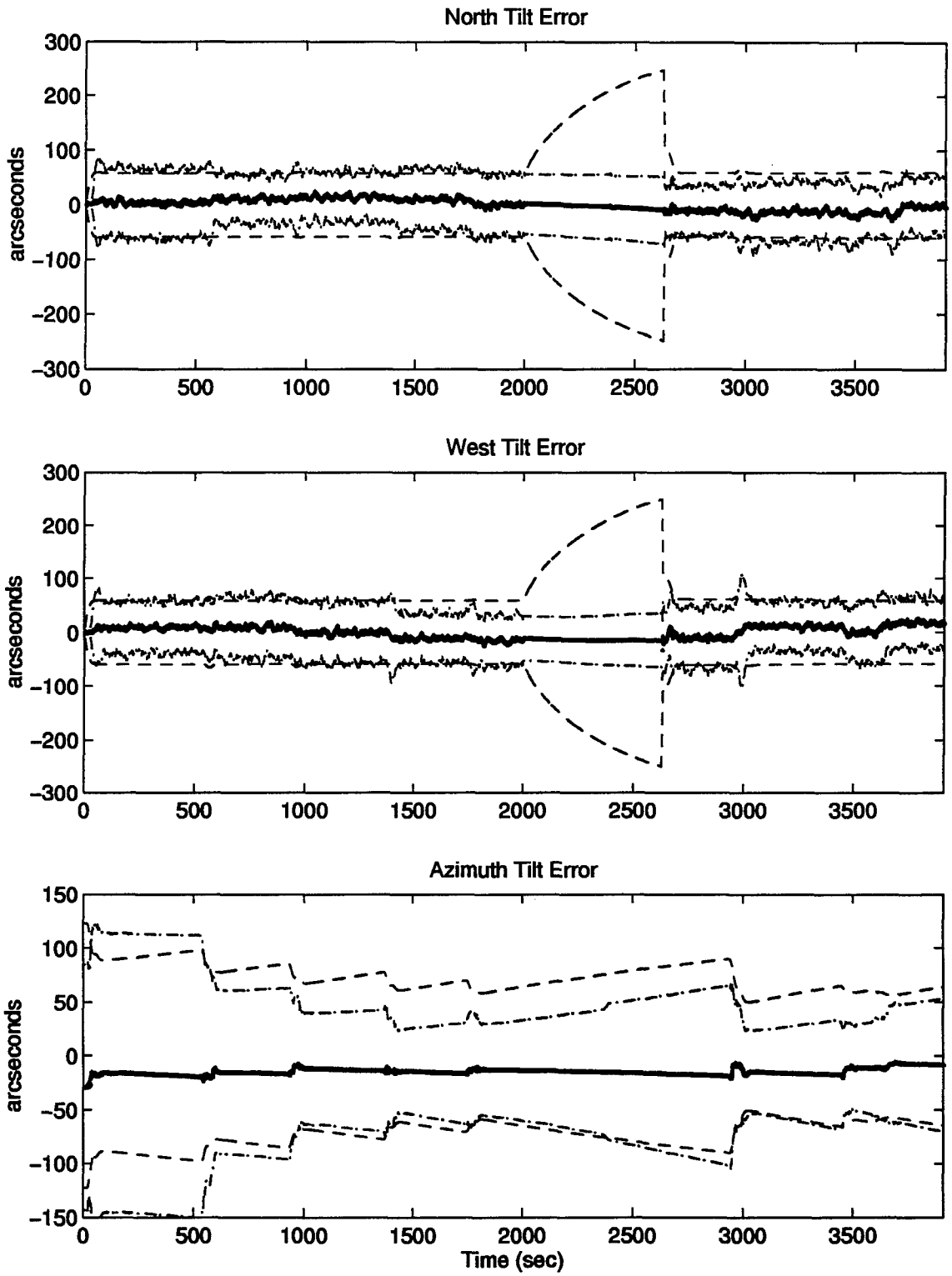

Figure D.16 North, West, and Azimuth Tilt Errors

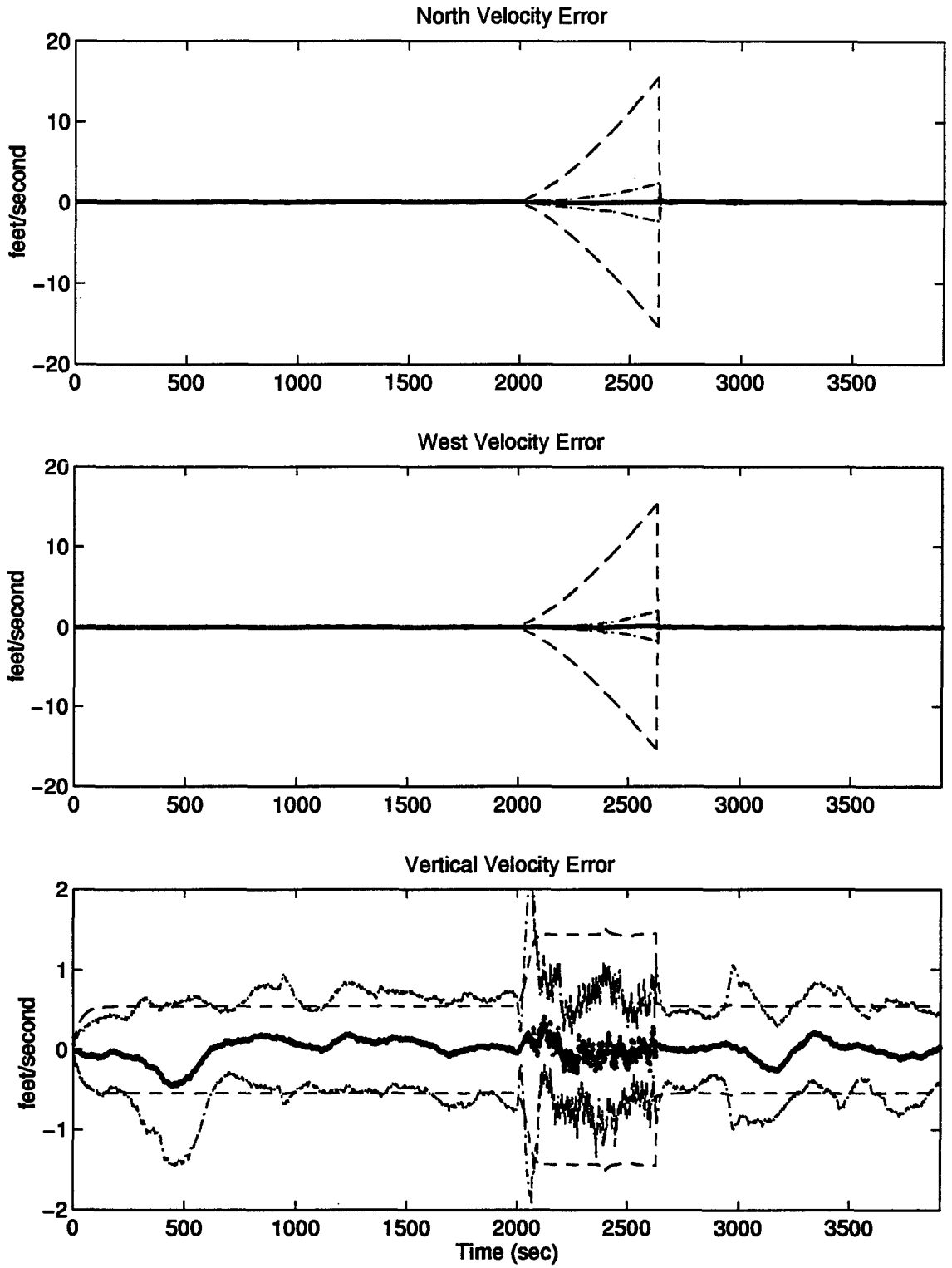

Figure D.17 North, West, and Vertical Velocity Errors

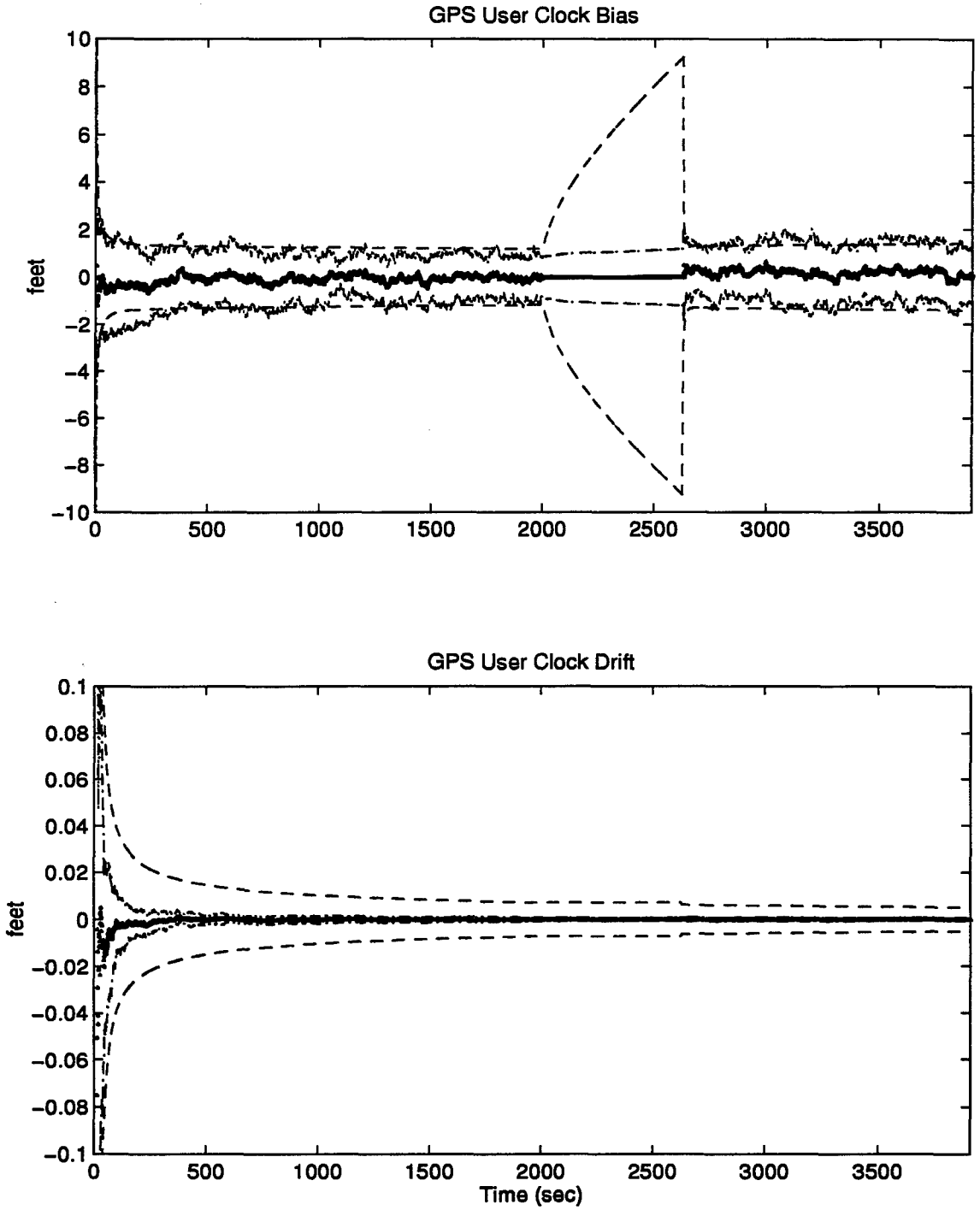

Figure D.18 GPS User Clock Bias and GPS User Clock Drift

Appendix E.

Plots of Case I through Case VI for Single Engine Aircraft Flight Profile.

Plot Legend

$\cdots$ true error (mean error $\pm$ σ_{true})

- - - filter predicted error ($0 \pm \sigma_{filter}$)

— mean error

E.1 Plots of Case I: Barometric Altimeter, 0.4 nm/hr INS, and DGPS Using the Single Engine Aircraft Flight Profile.

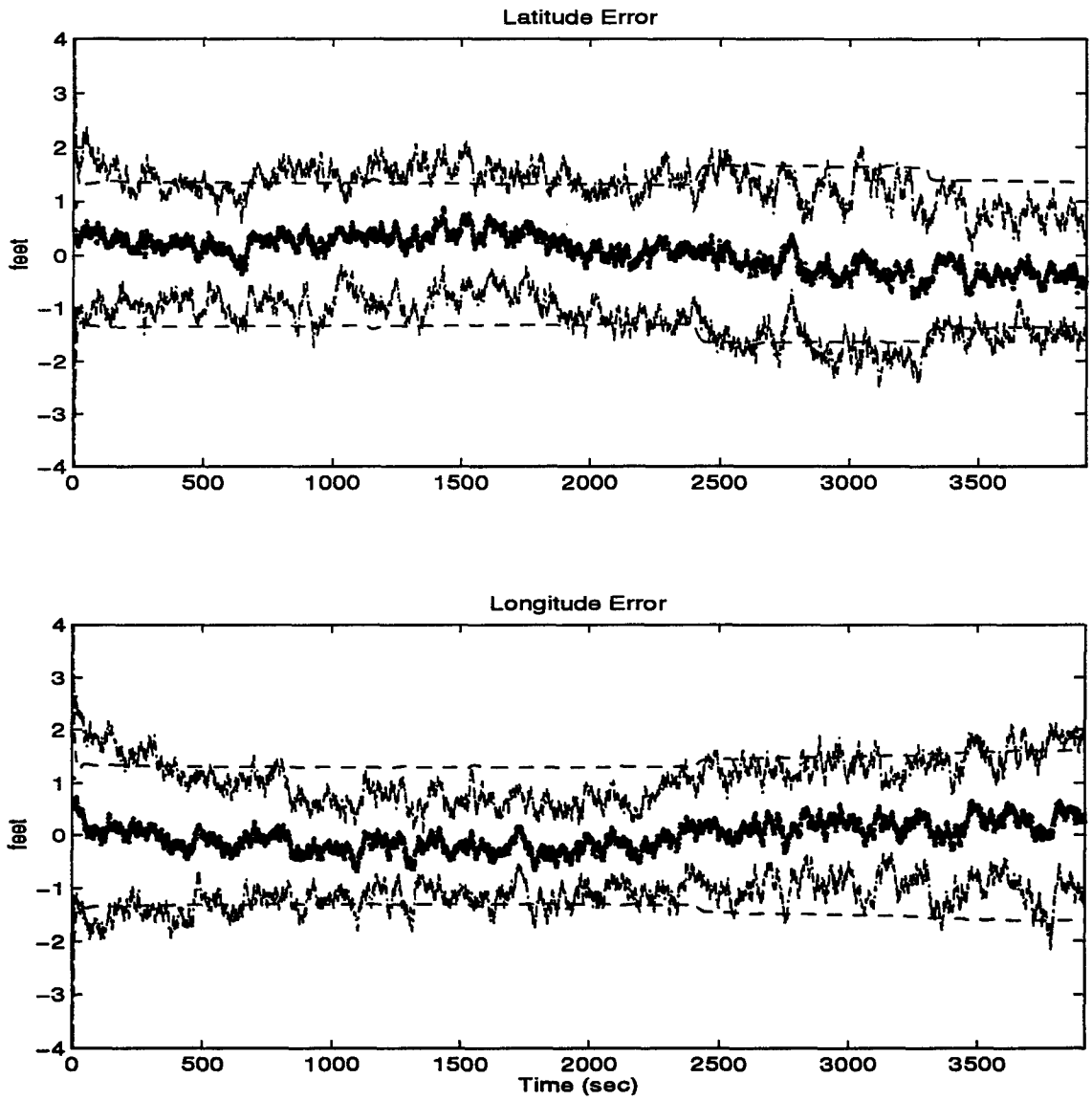

Figure E.1 Latitude and Longitude Error

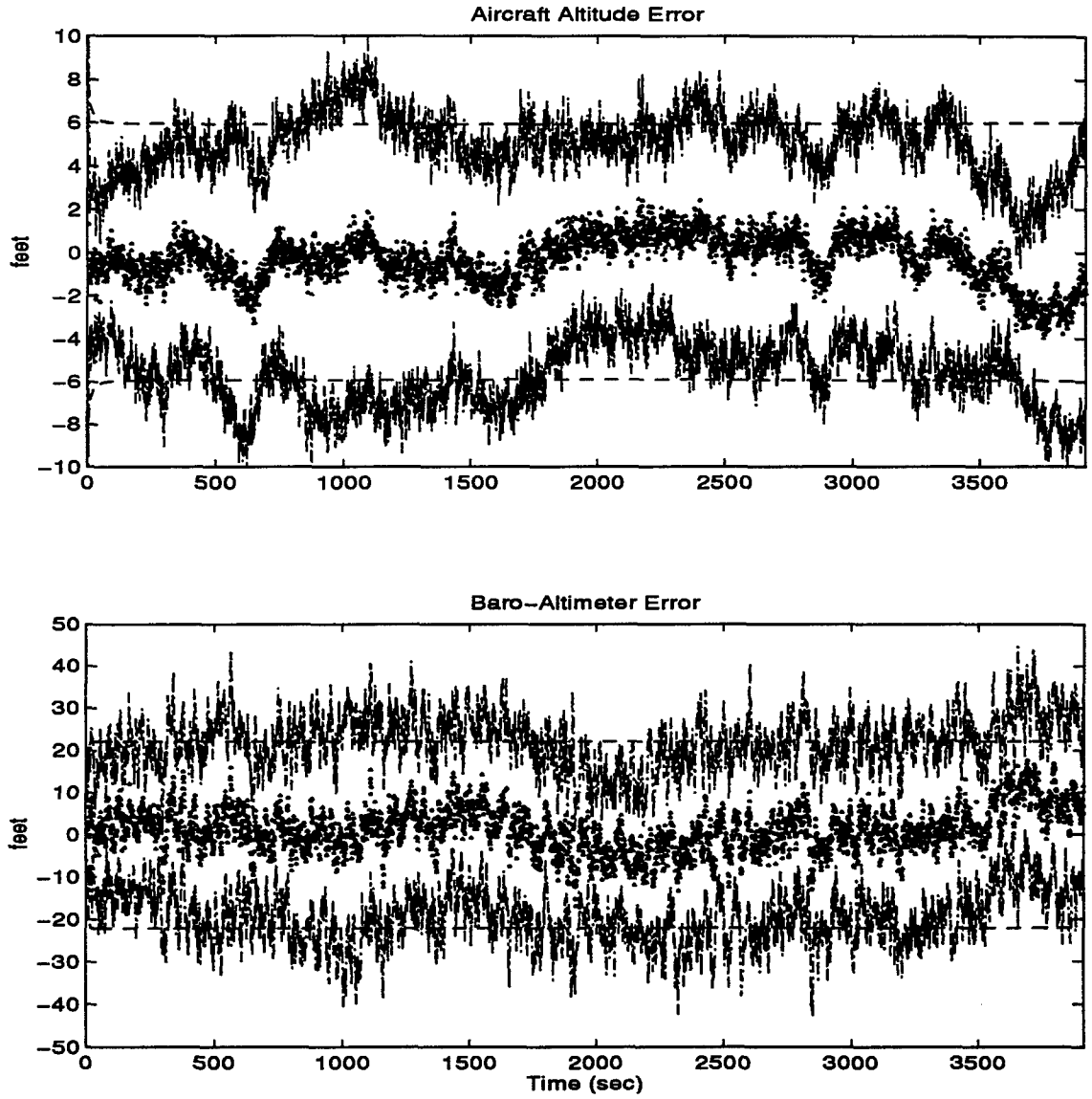

Figure E.2 Aircraft Altitude and Baro-Altimeter Error

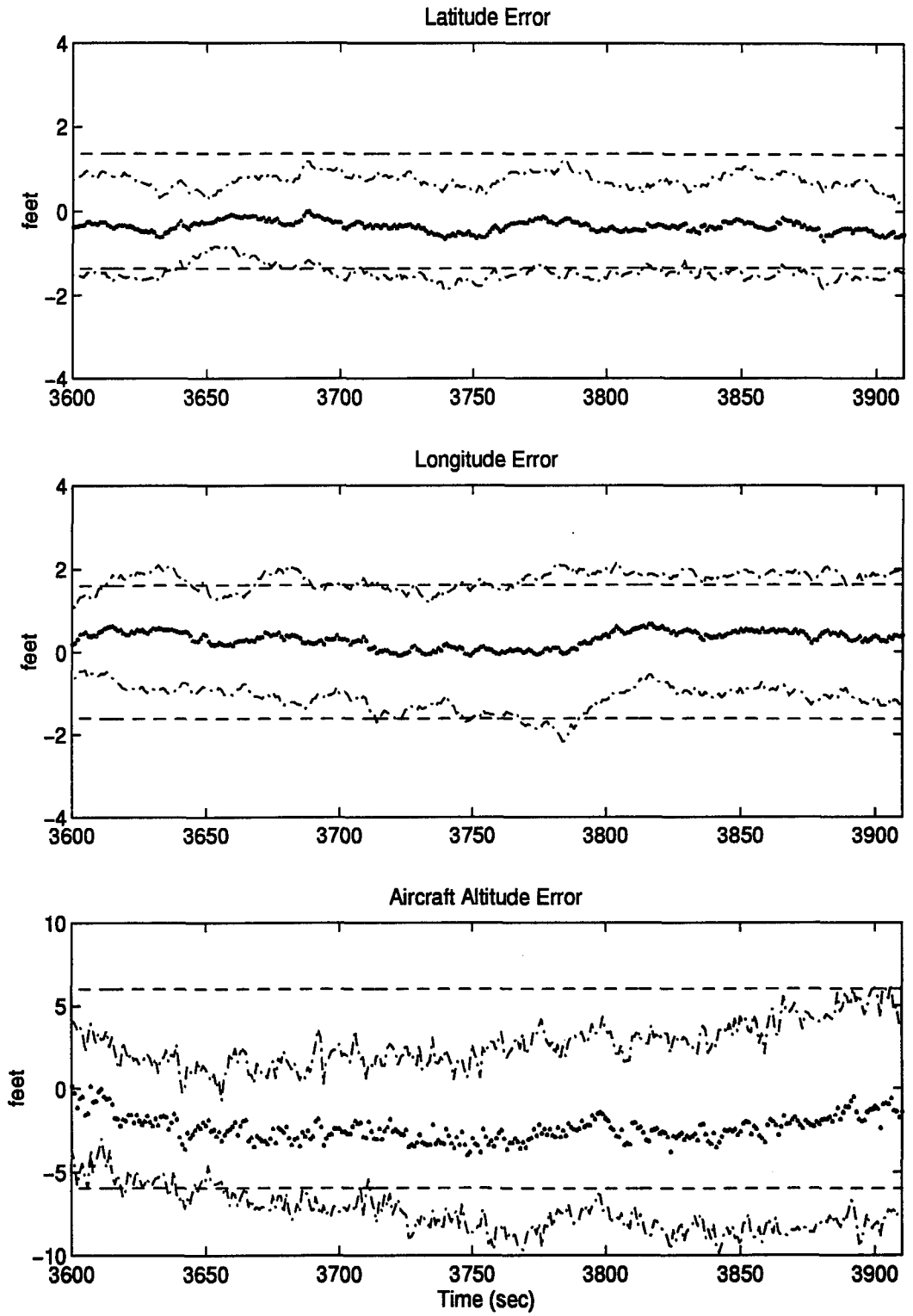

Figure E.3 Latitude, Longitude, and Aircraft Altitude Error

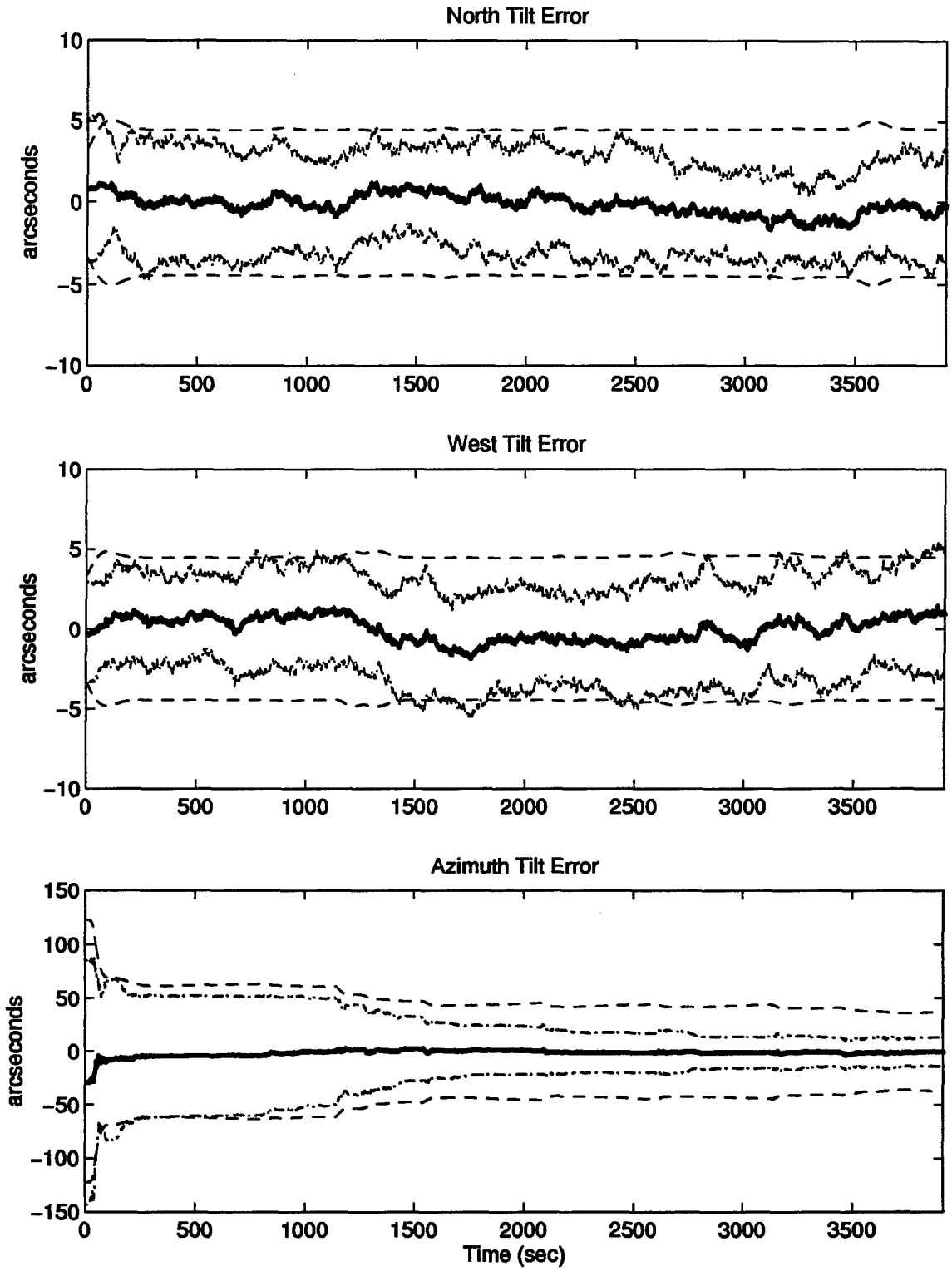

Figure E.4 North, West, and Azimuth Tilt Errors

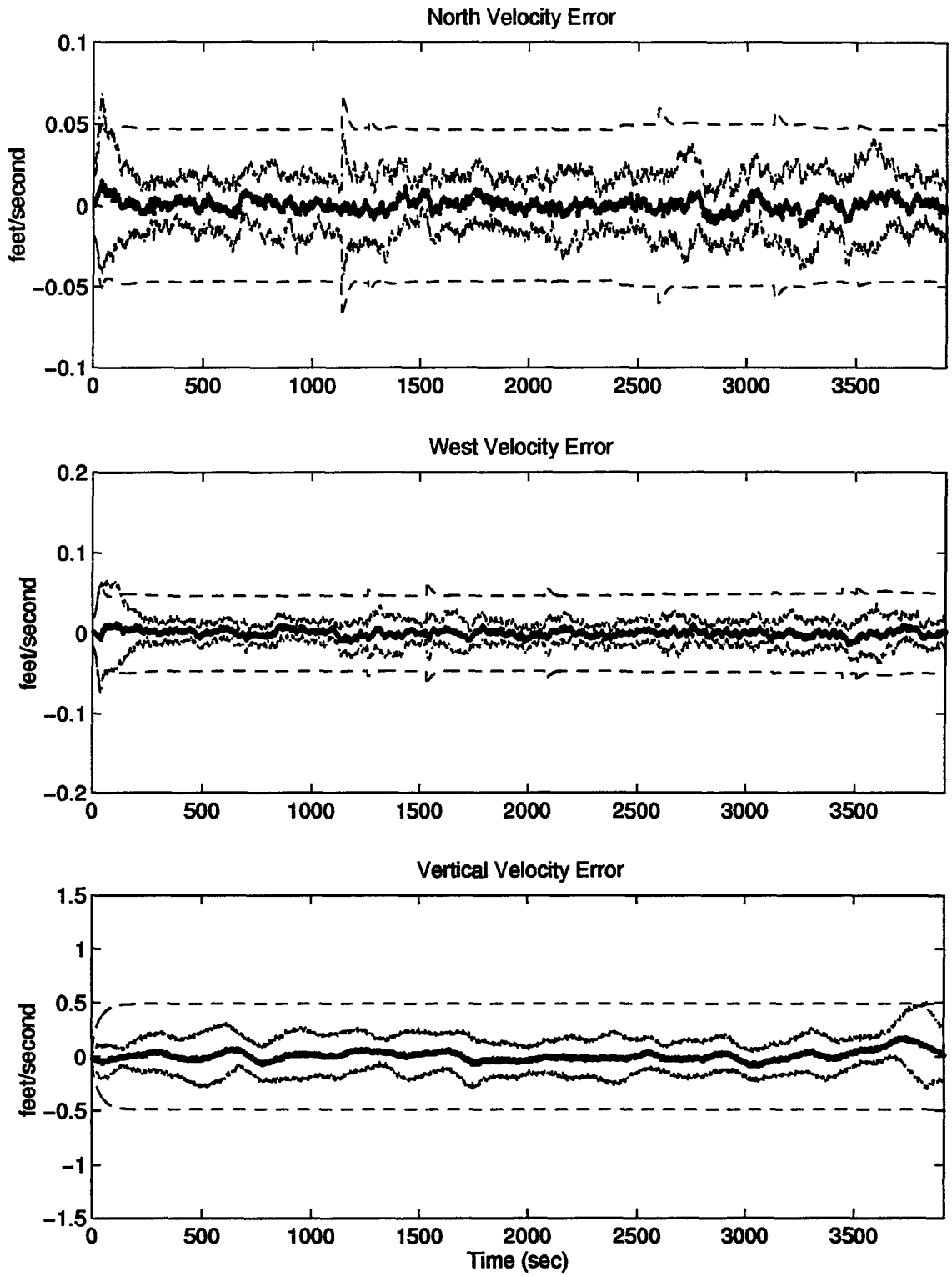

Figure E.5 North, West, and Vertical Velocity Errors

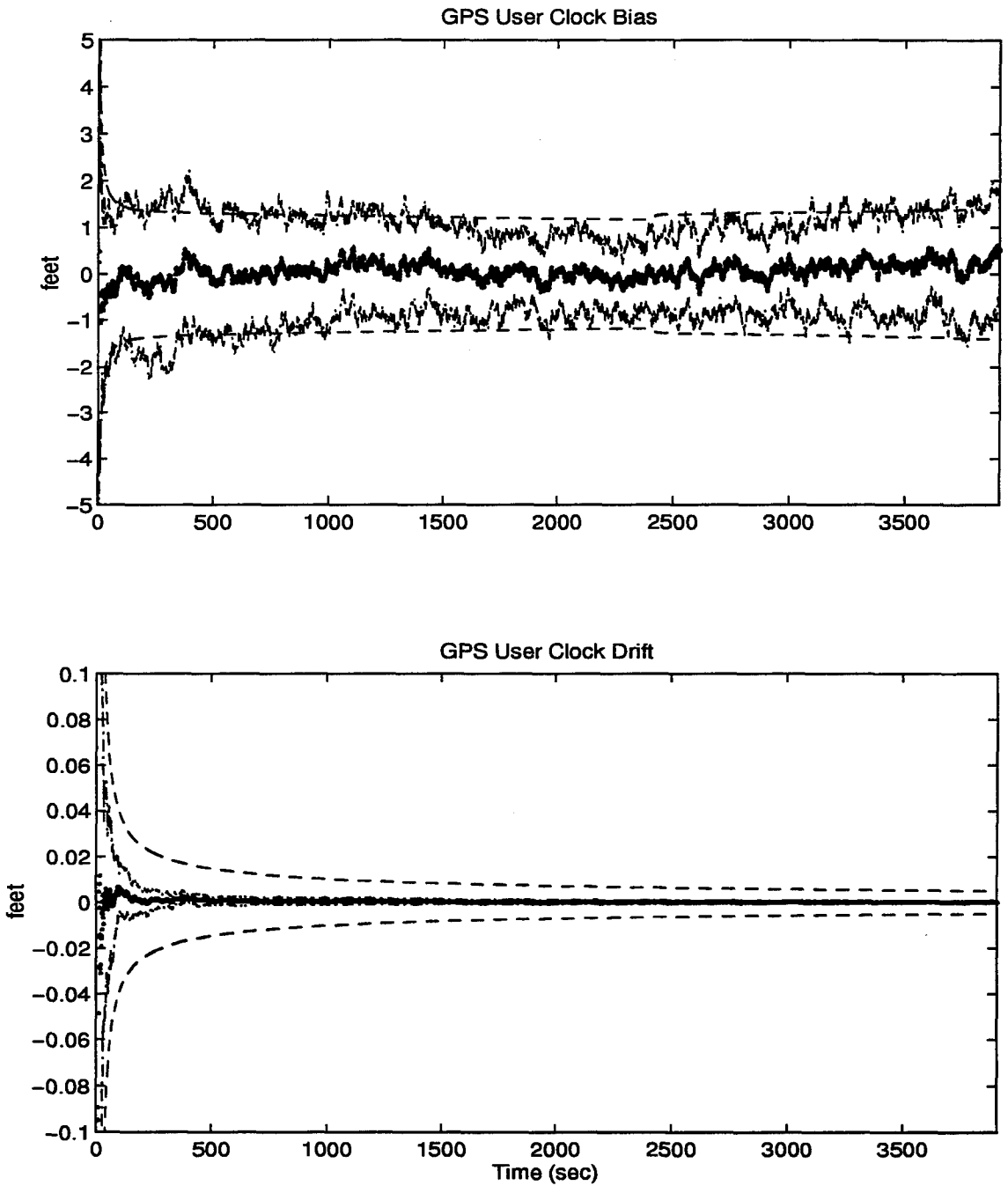

Figure E.6 GPS User Clock Bias and GPS User Clock Drift

E.2 Plots of Case II: Barometric Altimeter, 0.4 nm/hr INS, Radar Altimeter, and DGPS Using the Single Engine Aircraft Flight Profile.

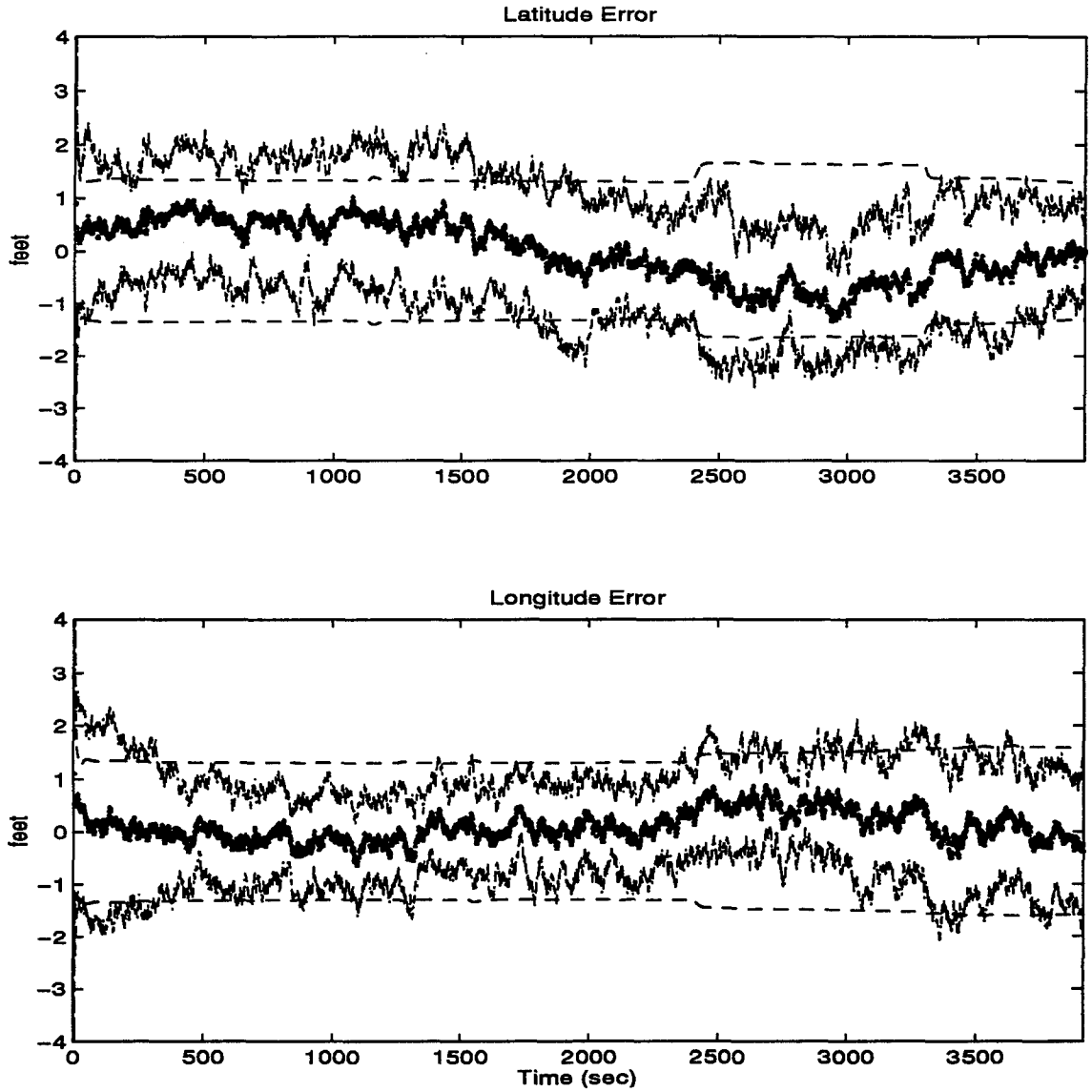

Figure E.7 Latitude and Longitude Error

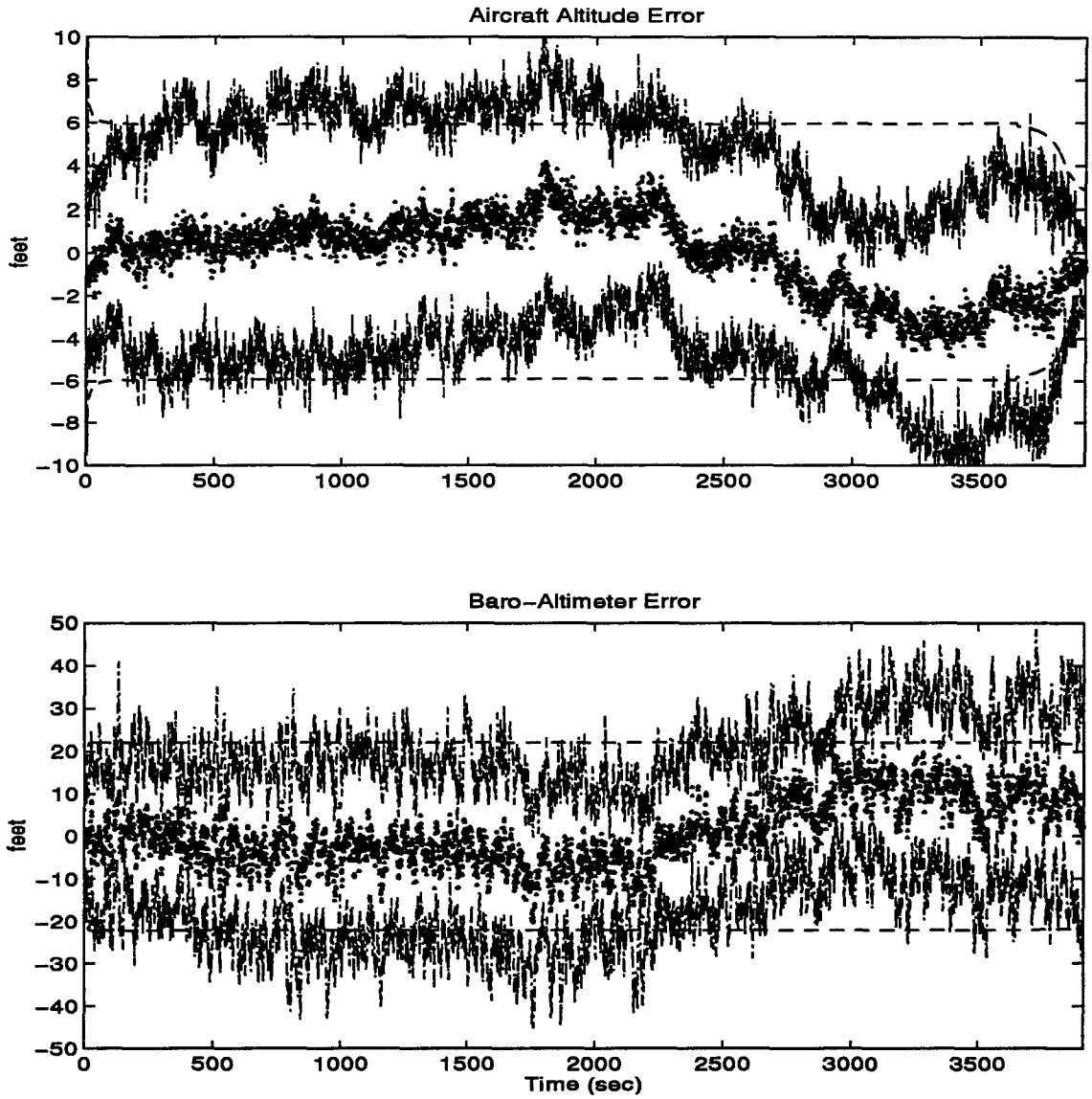

Figure E.8 Aircraft Altitude and Baro-Altimeter Error

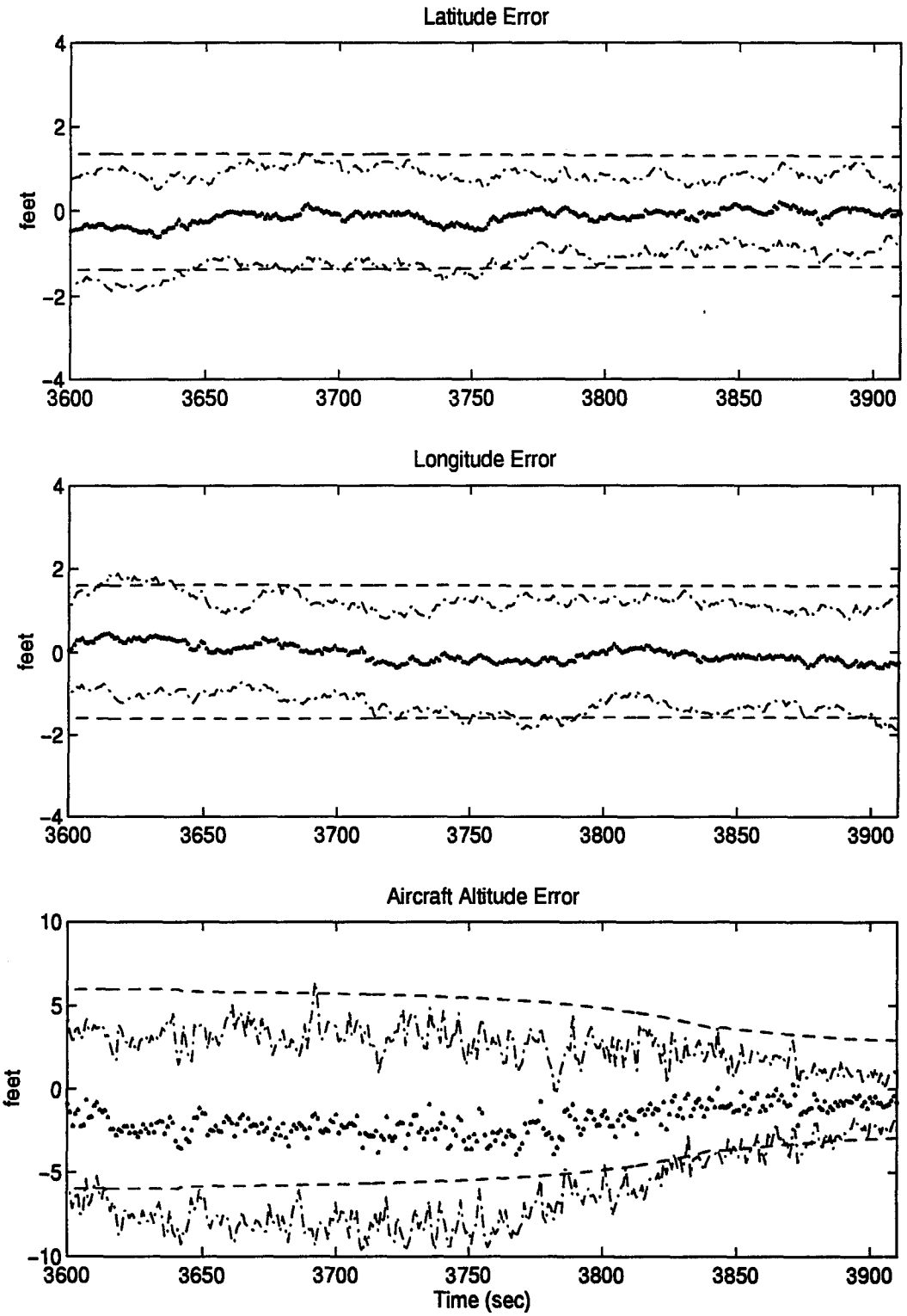

Figure E.9 Latitude, Longitude, and Aircraft Altitude Error

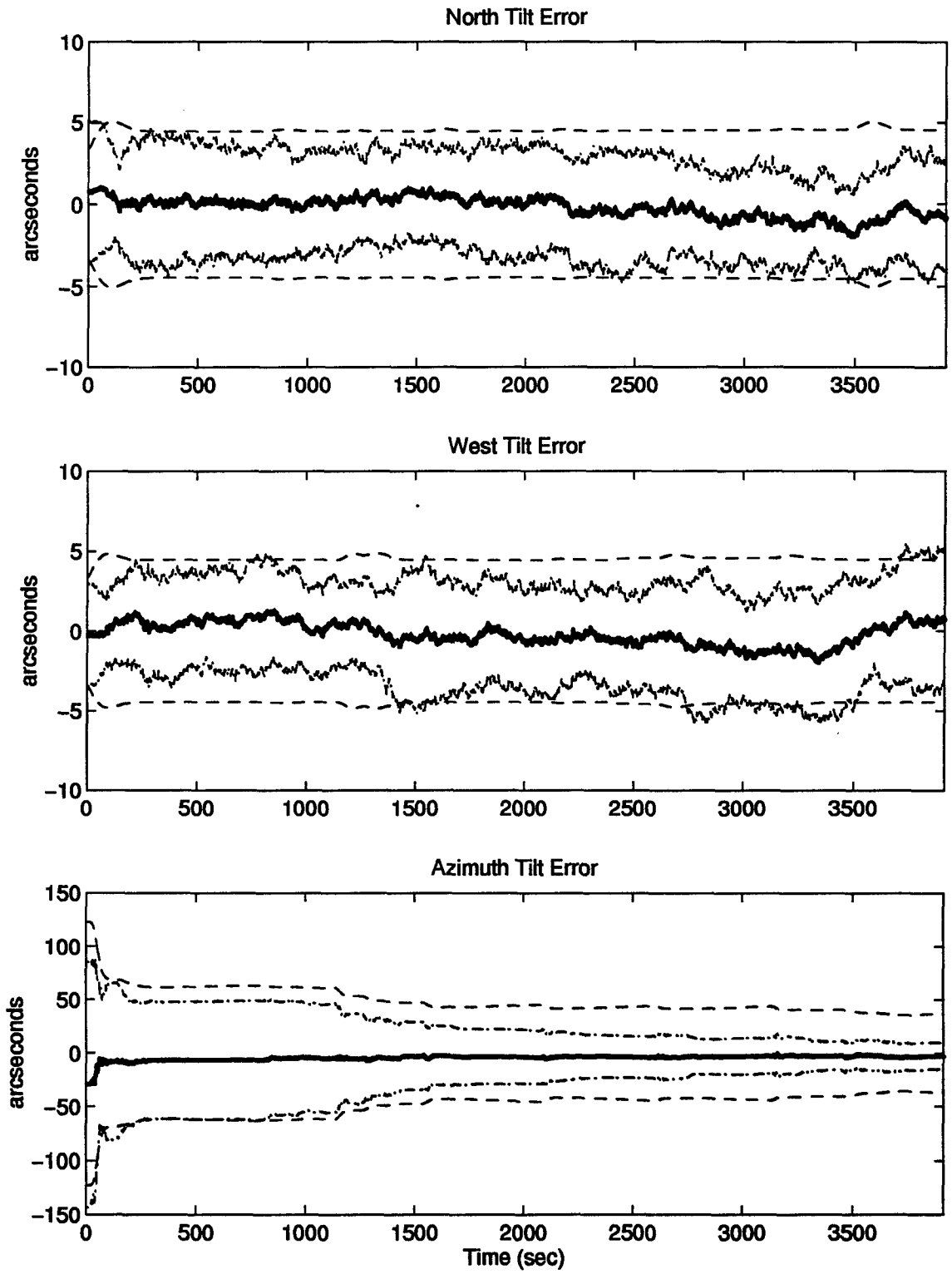

Figure E.10 North, West, and Azimuth Tilt Errors

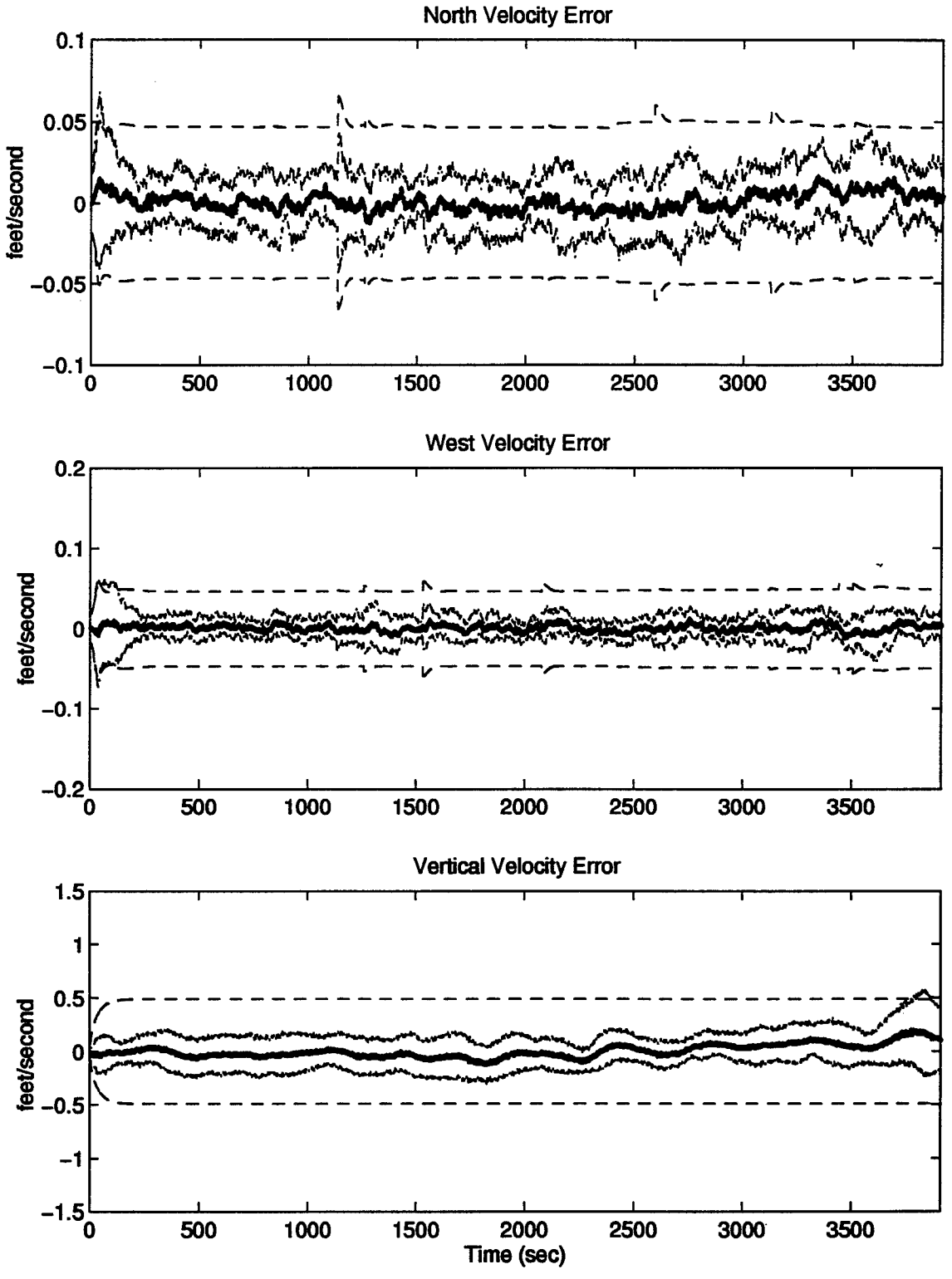

Figure E.11 North, West, and Vertical Velocity Errors

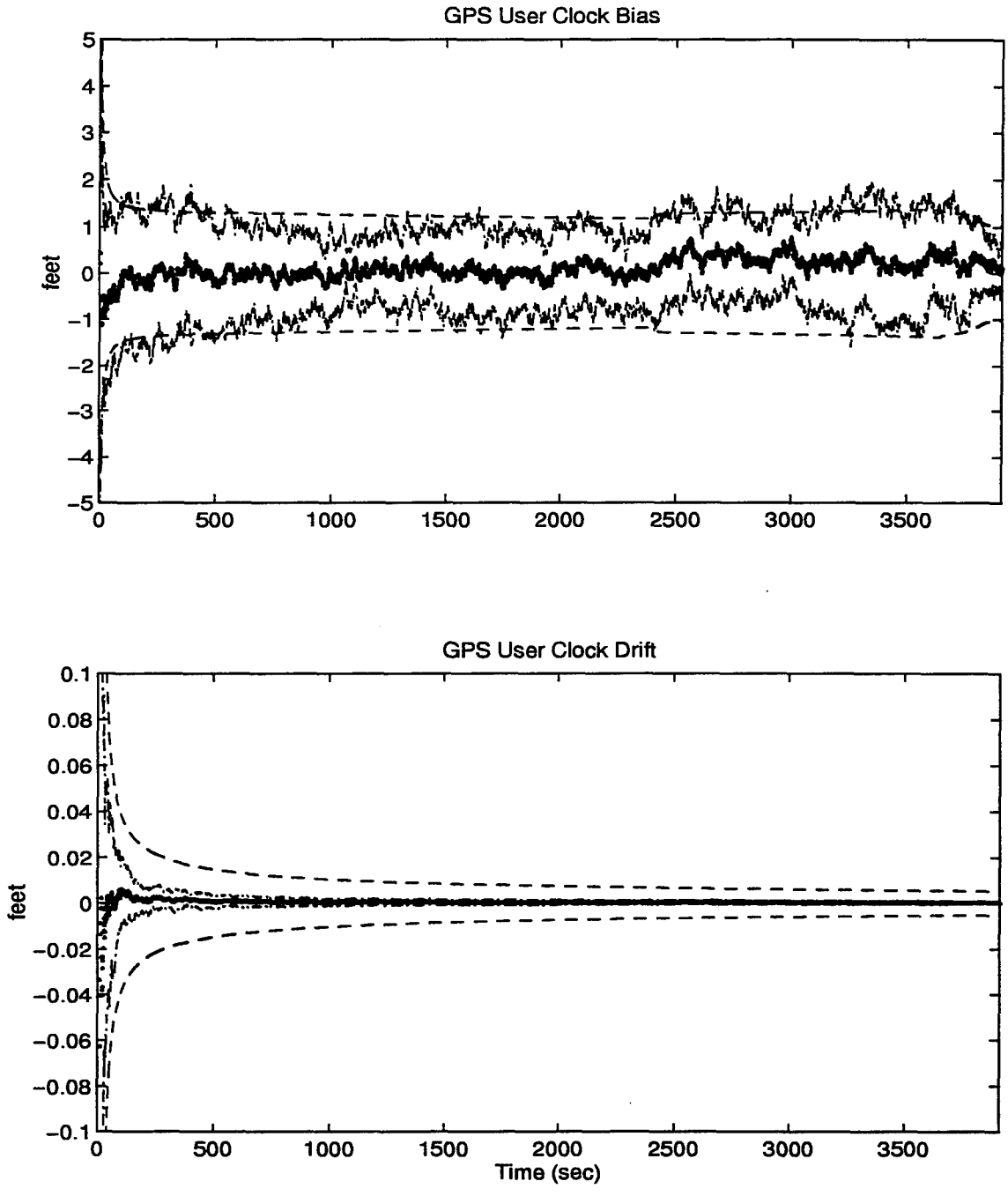

Figure E.12 GPS User Clock Bias and GPS User Clock Drift

E.3 Plots of Case III: Barometric Altimeter, 2.0 nm/hr INS, and DGPS Using the Single Engine Aircraft Flight Profile.

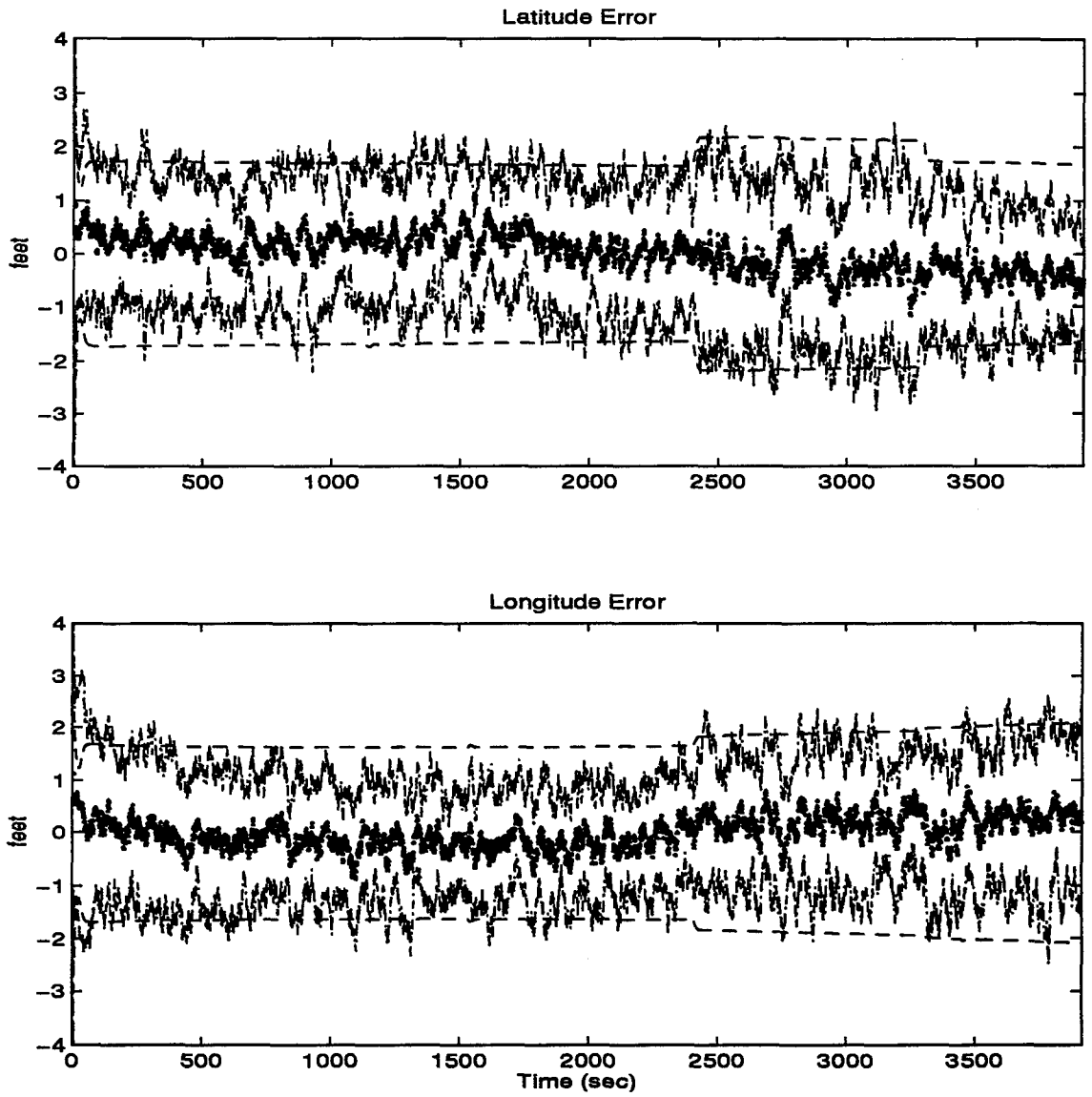

Figure E.13 Latitude and Longitude Error

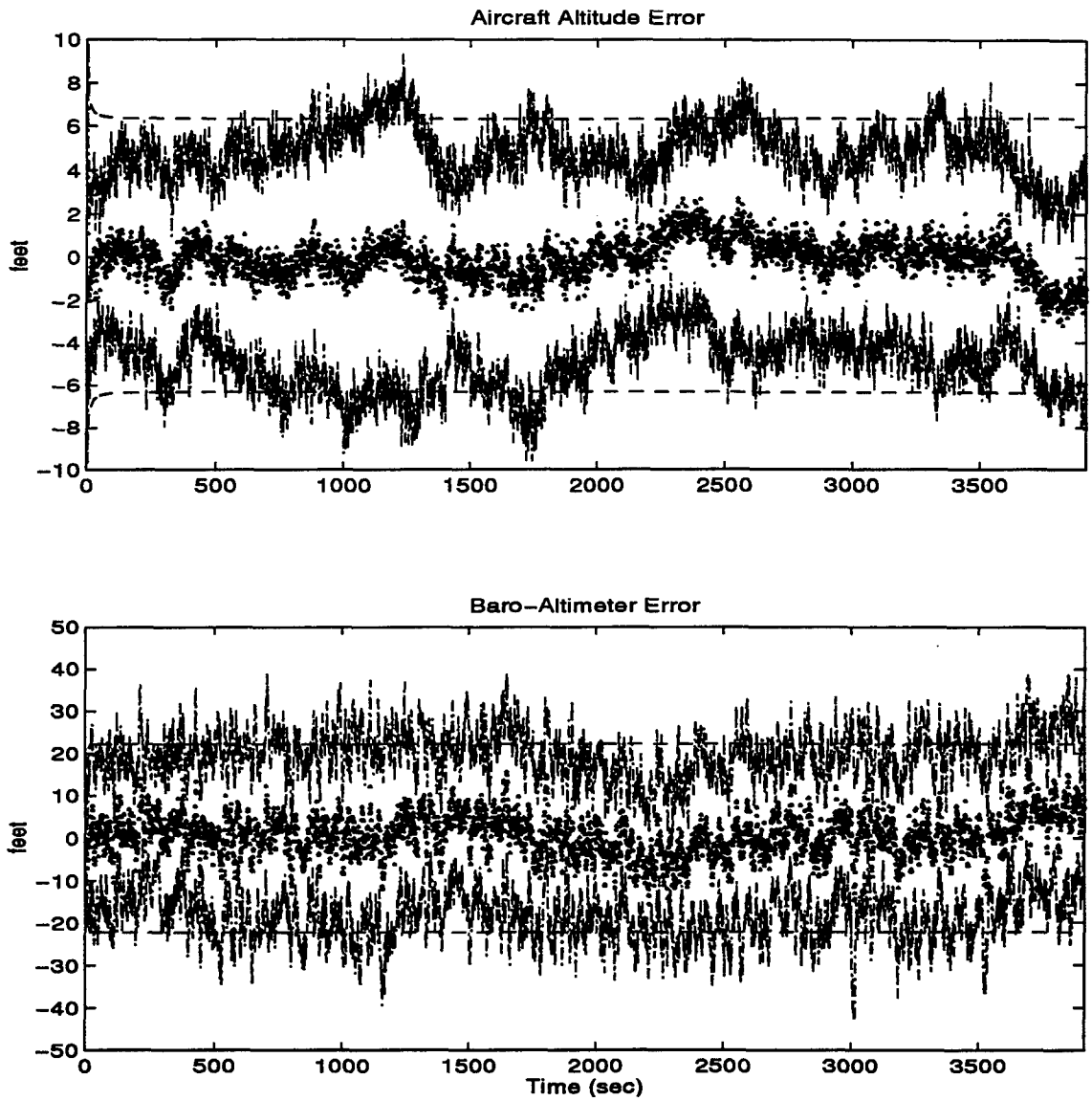

Figure E.14 Aircraft Altitude and Baro-Altimeter Error

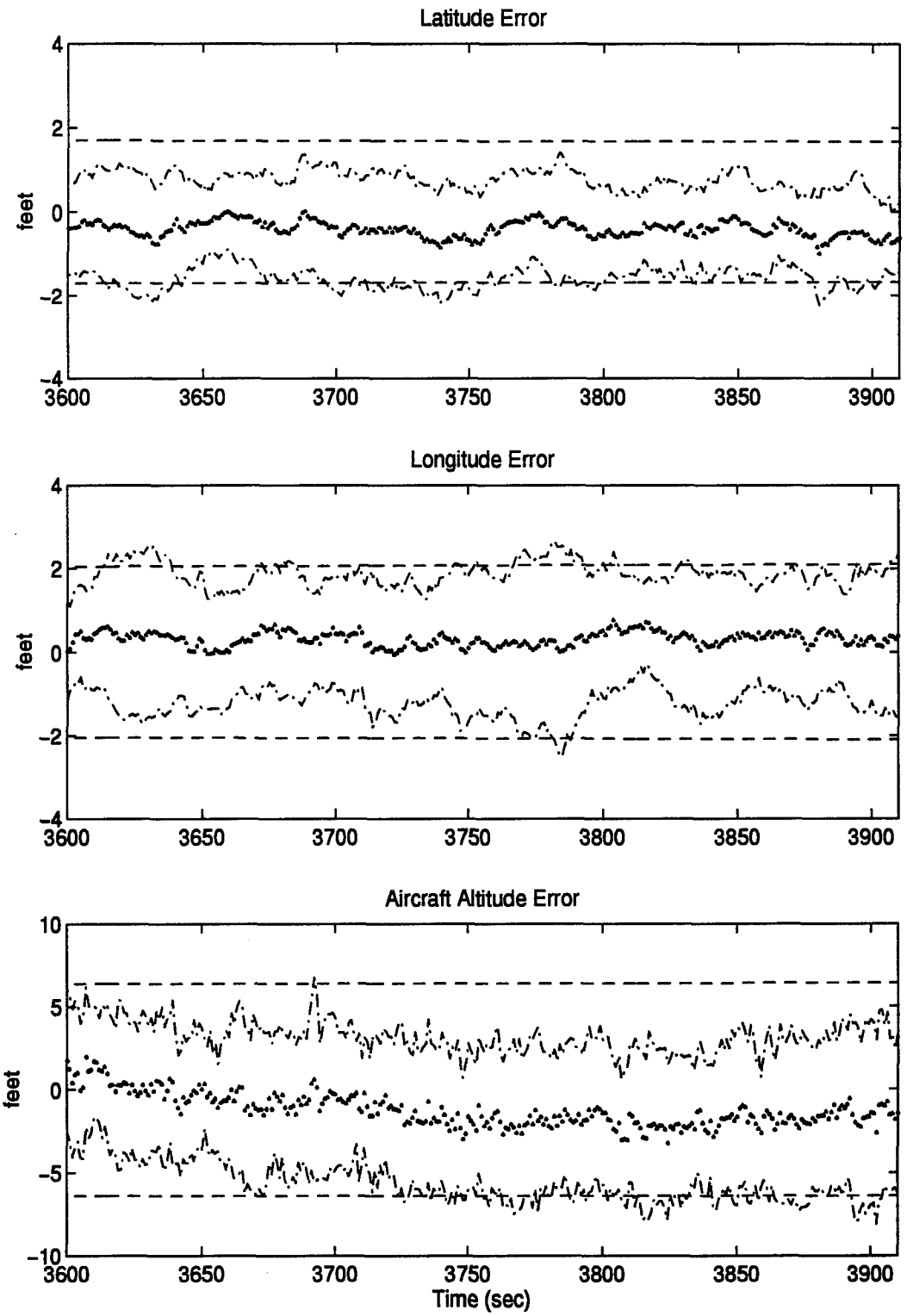

Figure E.15 Latitude, Longitude, and Aircraft Altitude Error

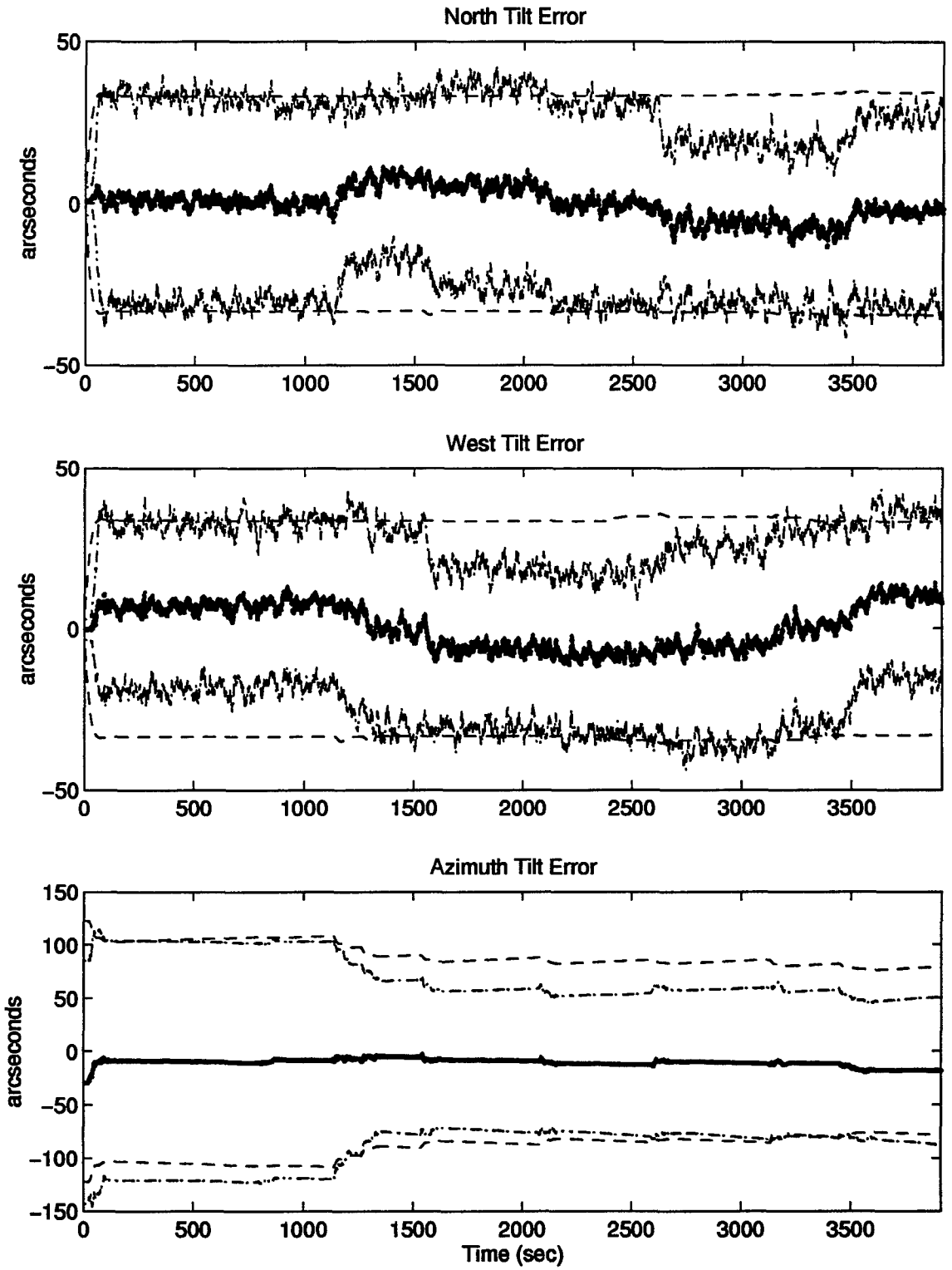

Figure E.16 North, West, and Azimuth Tilt Errors

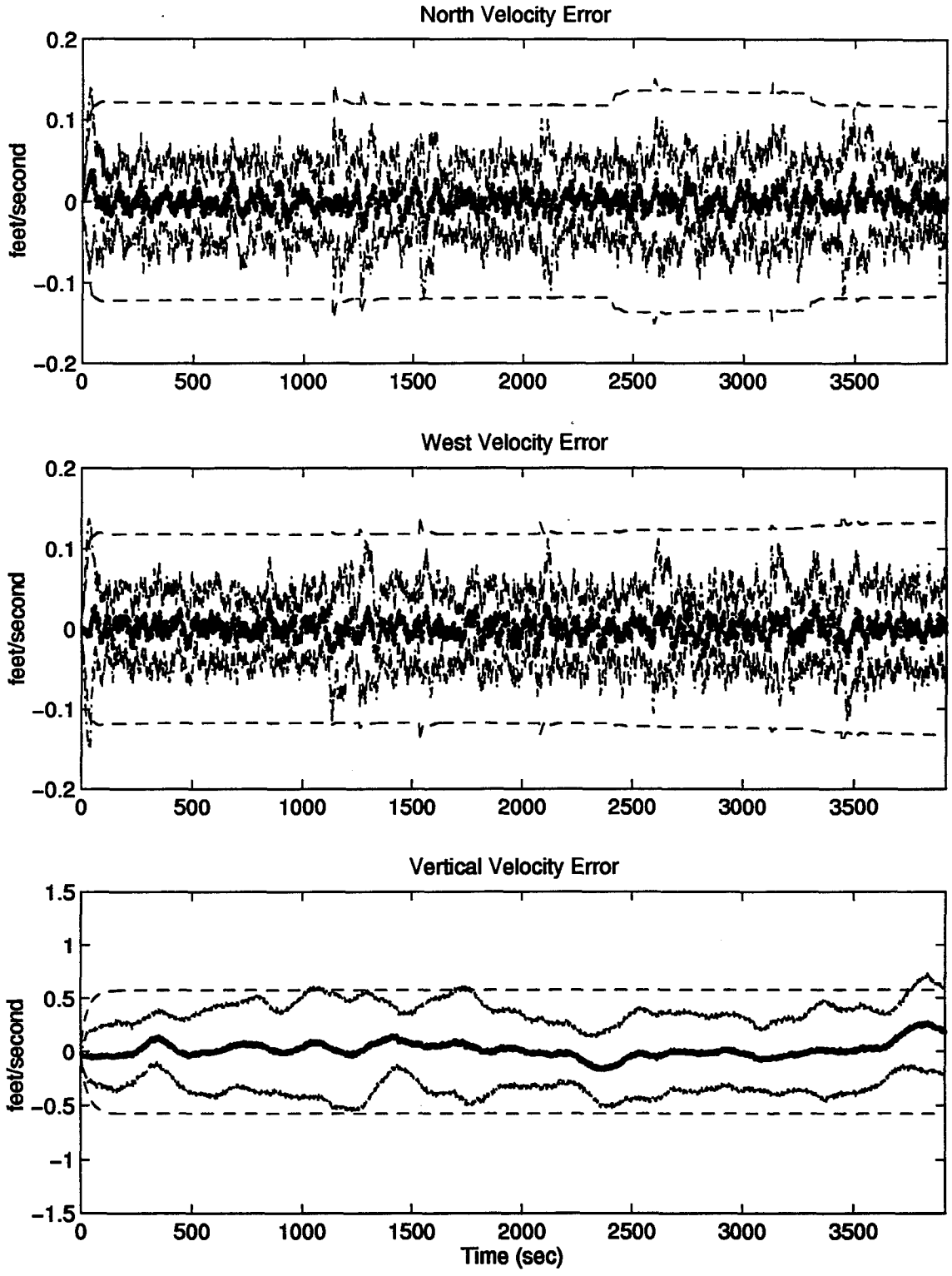

Figure E.17 North, West, and Vertical Velocity Errors

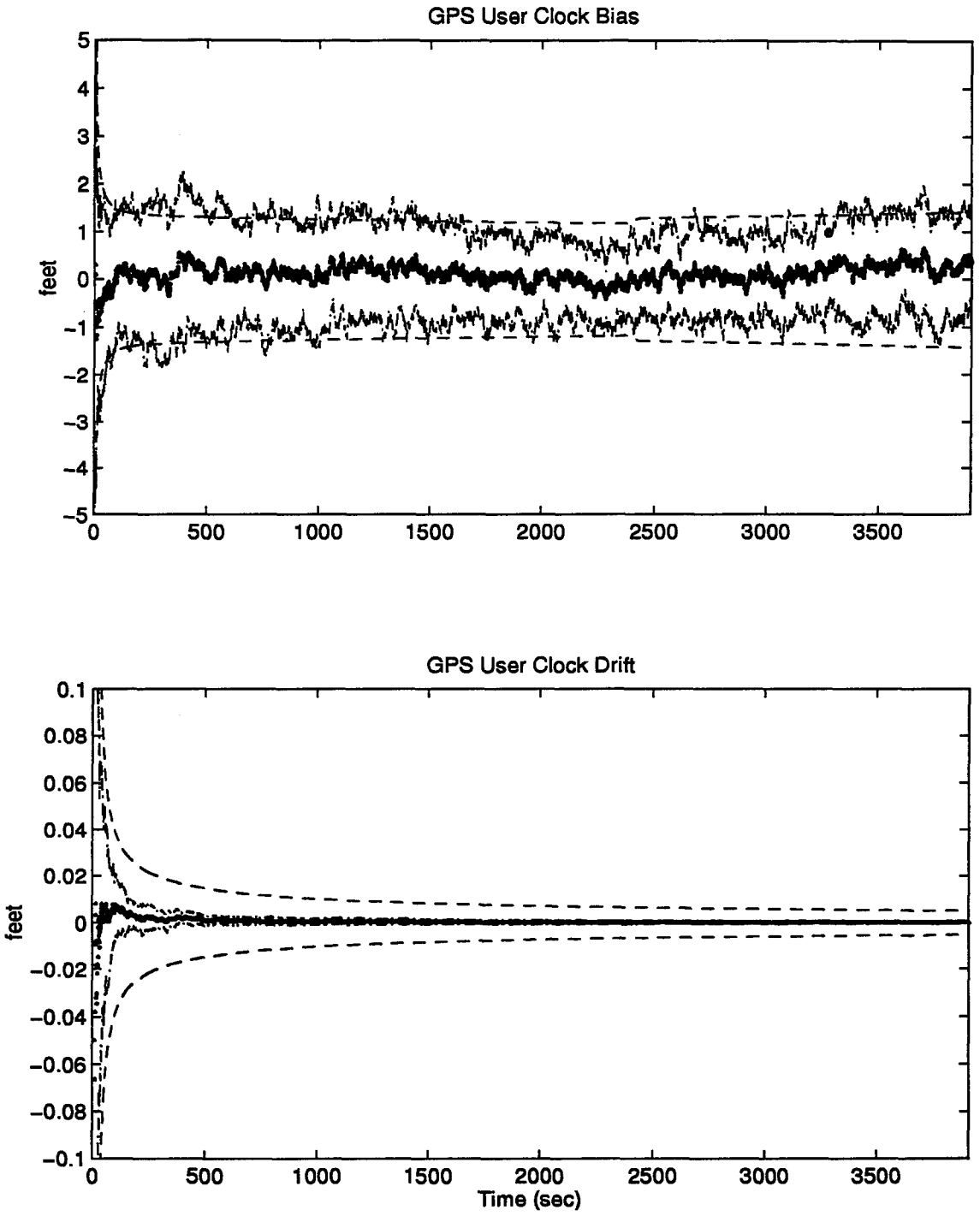

Figure E.18 GPS User Clock Bias and GPS User Clock Drift

E.4 Plots of Case IV: Barometric Altimeter, 2.0 nm/hr INS, Radar Altimeter, and DGPS Using the Single Engine Aircraft Flight Profile.

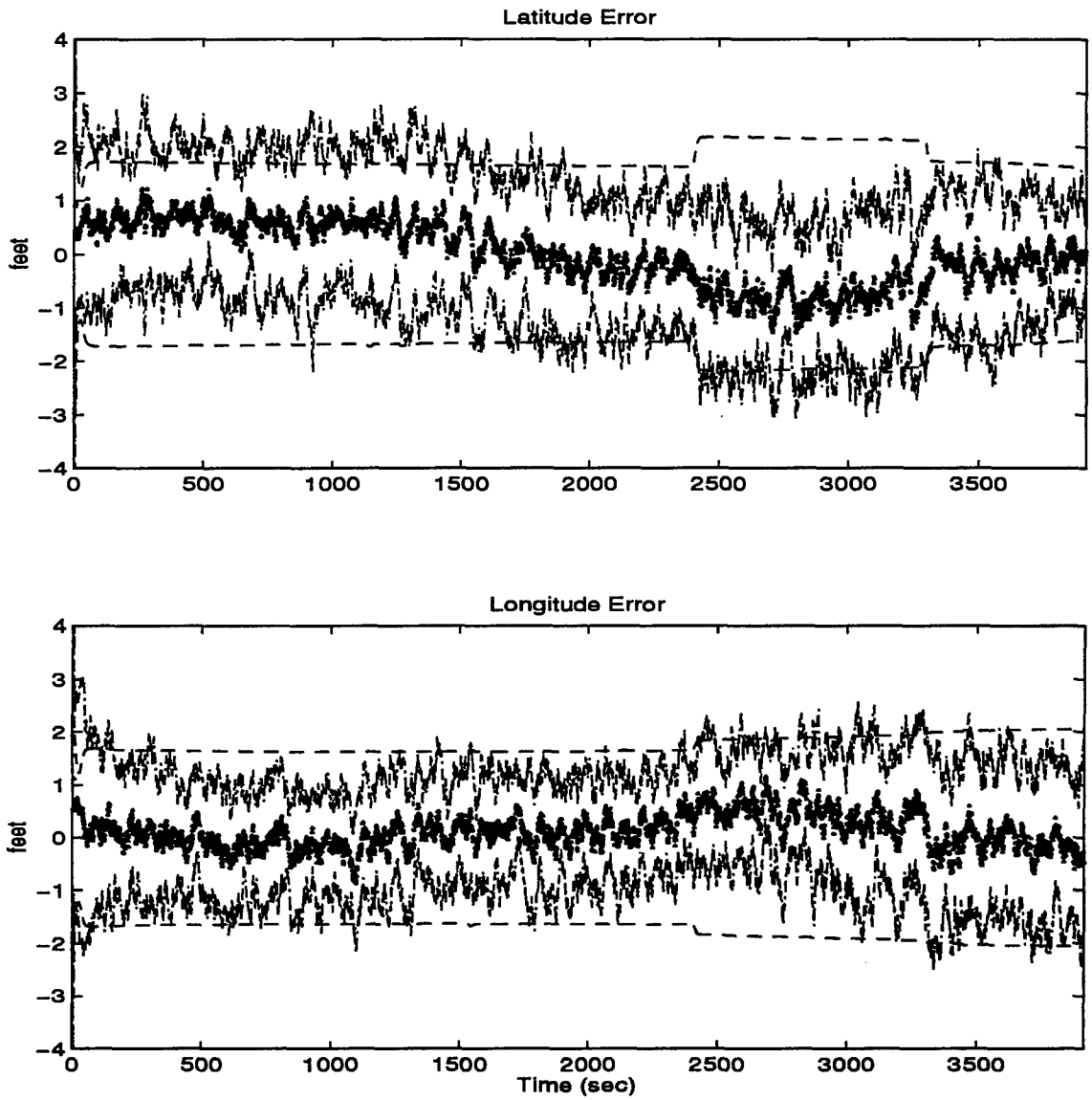

Figure E.19 Latitude and Longitude Error

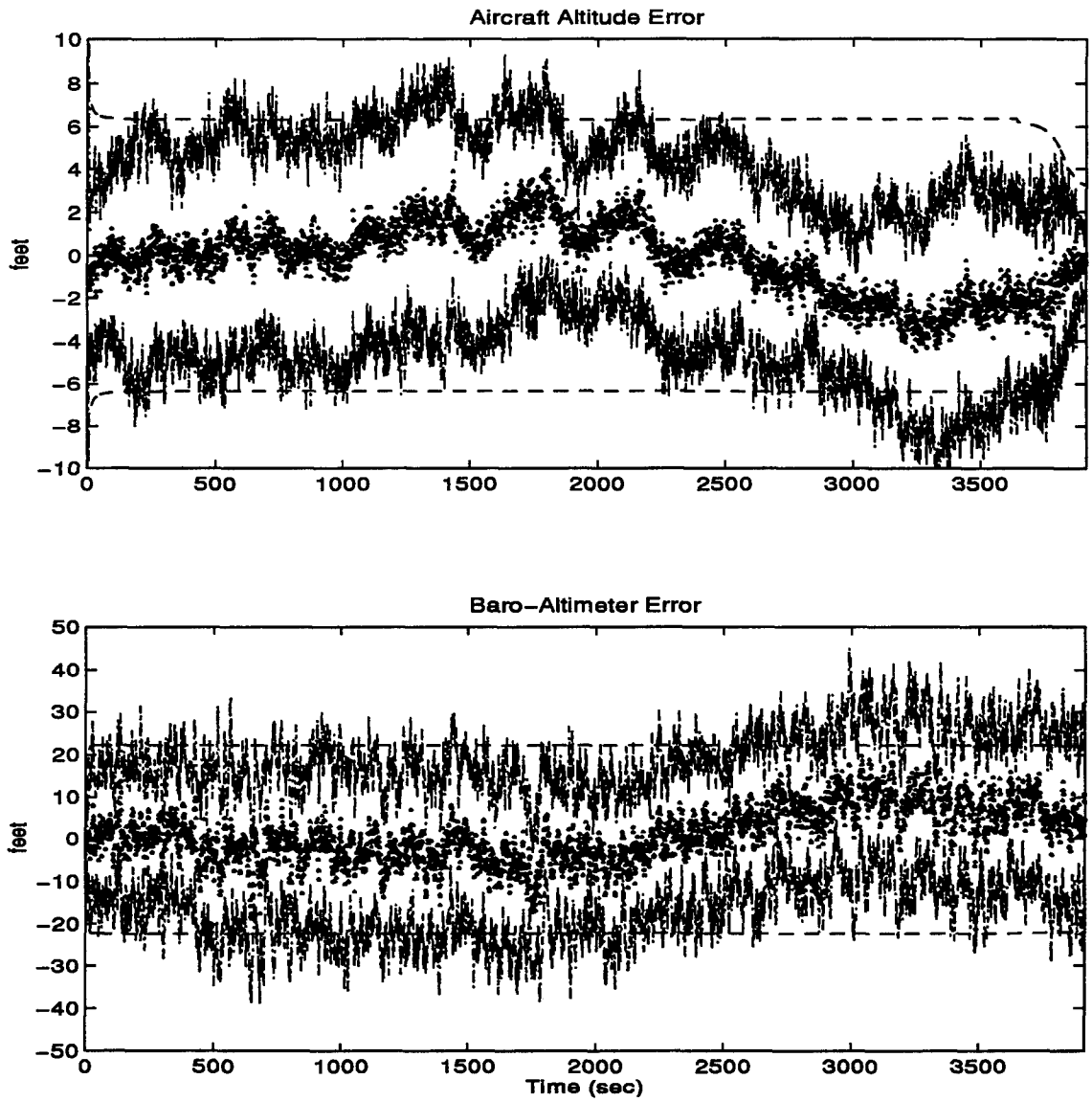

Figure E.20 Aircraft Altitude and Baro-Altimeter Error

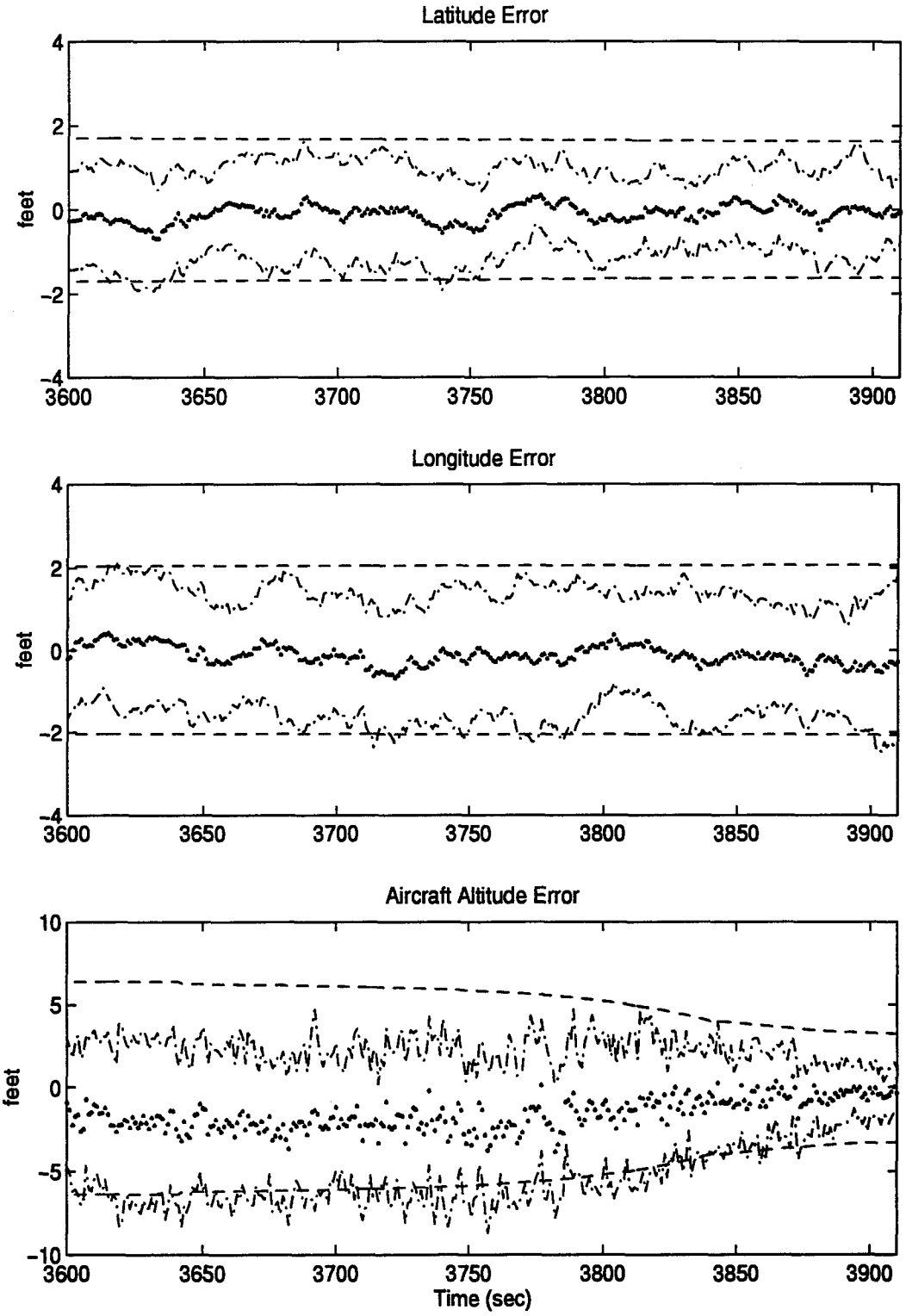

Figure E.21 Latitude, Longitude, and Aircraft Altitude Error

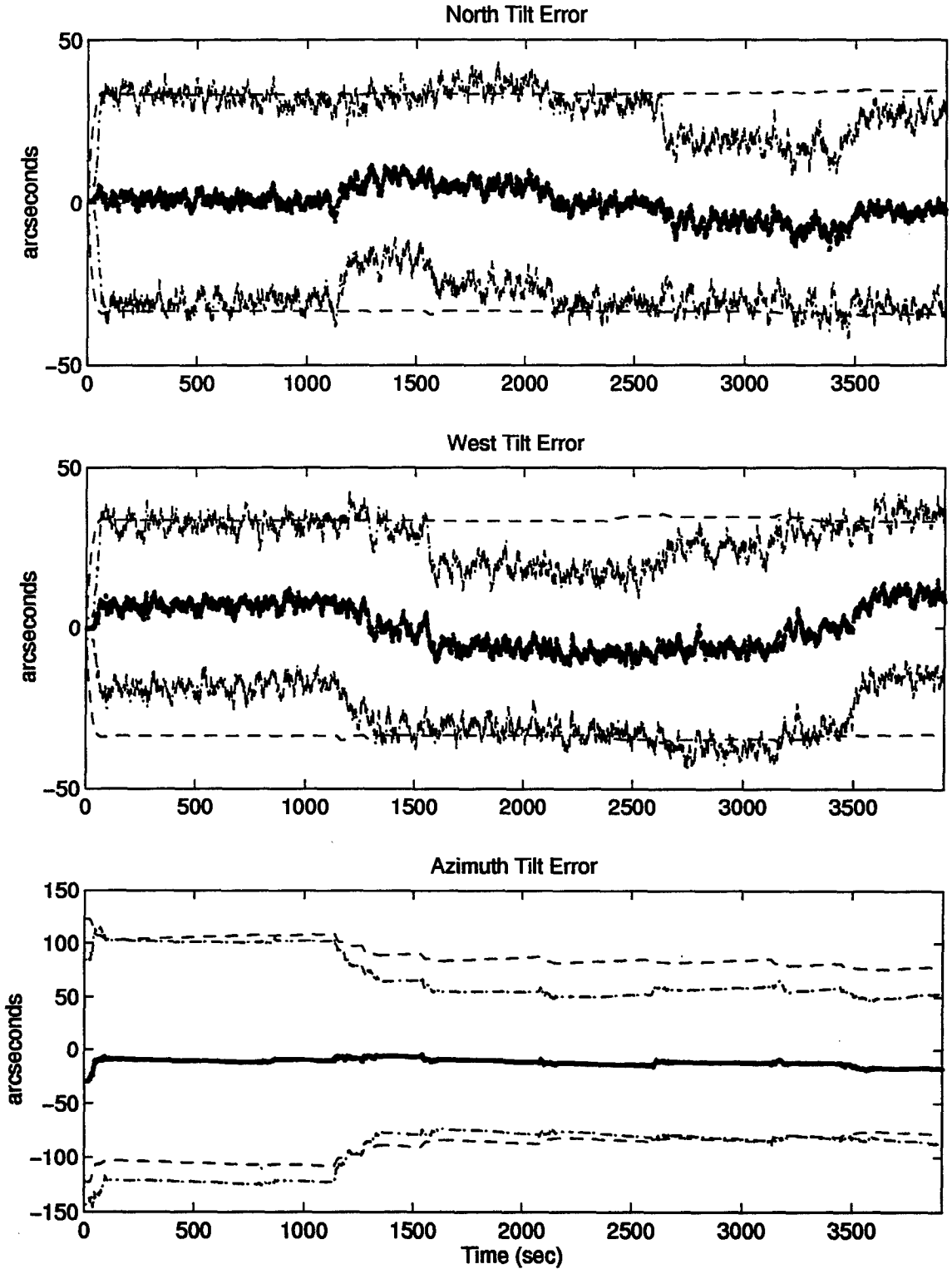

Figure E.22 North, West, and Azimuth Tilt Errors

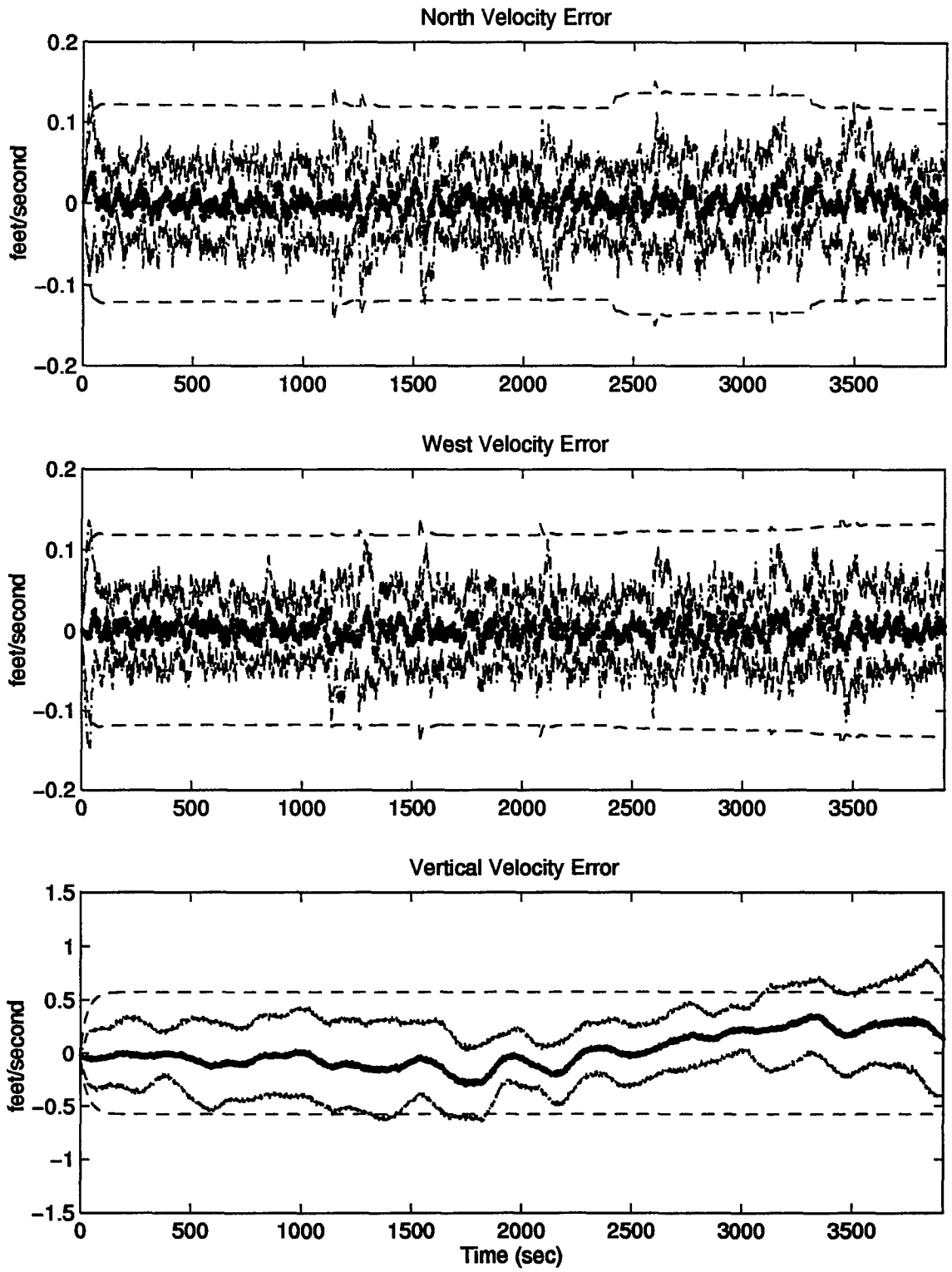

Figure E.23 North, West, and Vertical Velocity Errors

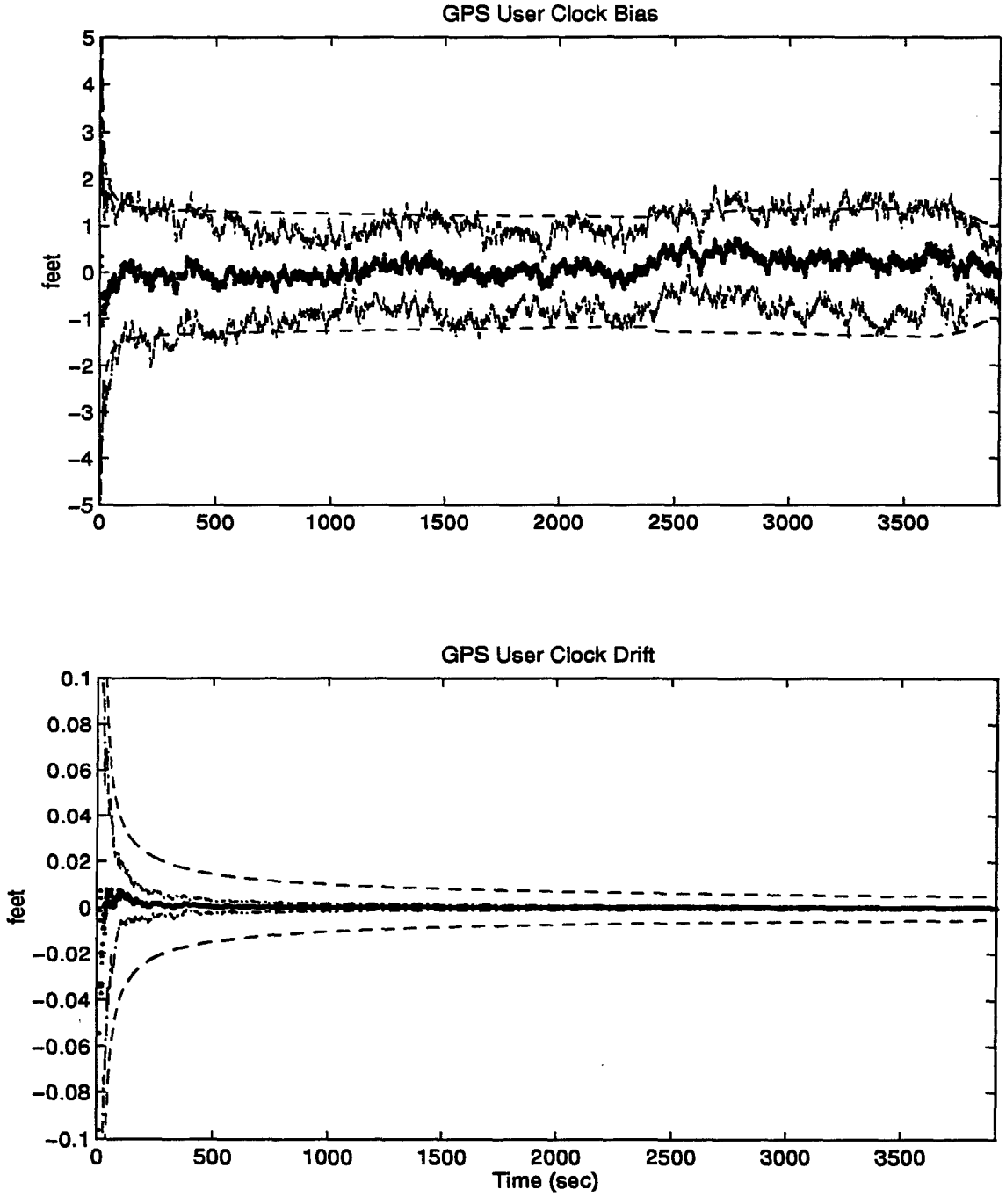

Figure E.24 GPS User Clock Bias and GPS User Clock Drift

E.5 Plots of Case V: Barometric Altimeter, 4.0 nm/hr INS, and DGPS Using the Single Engine Aircraft Flight Profile.

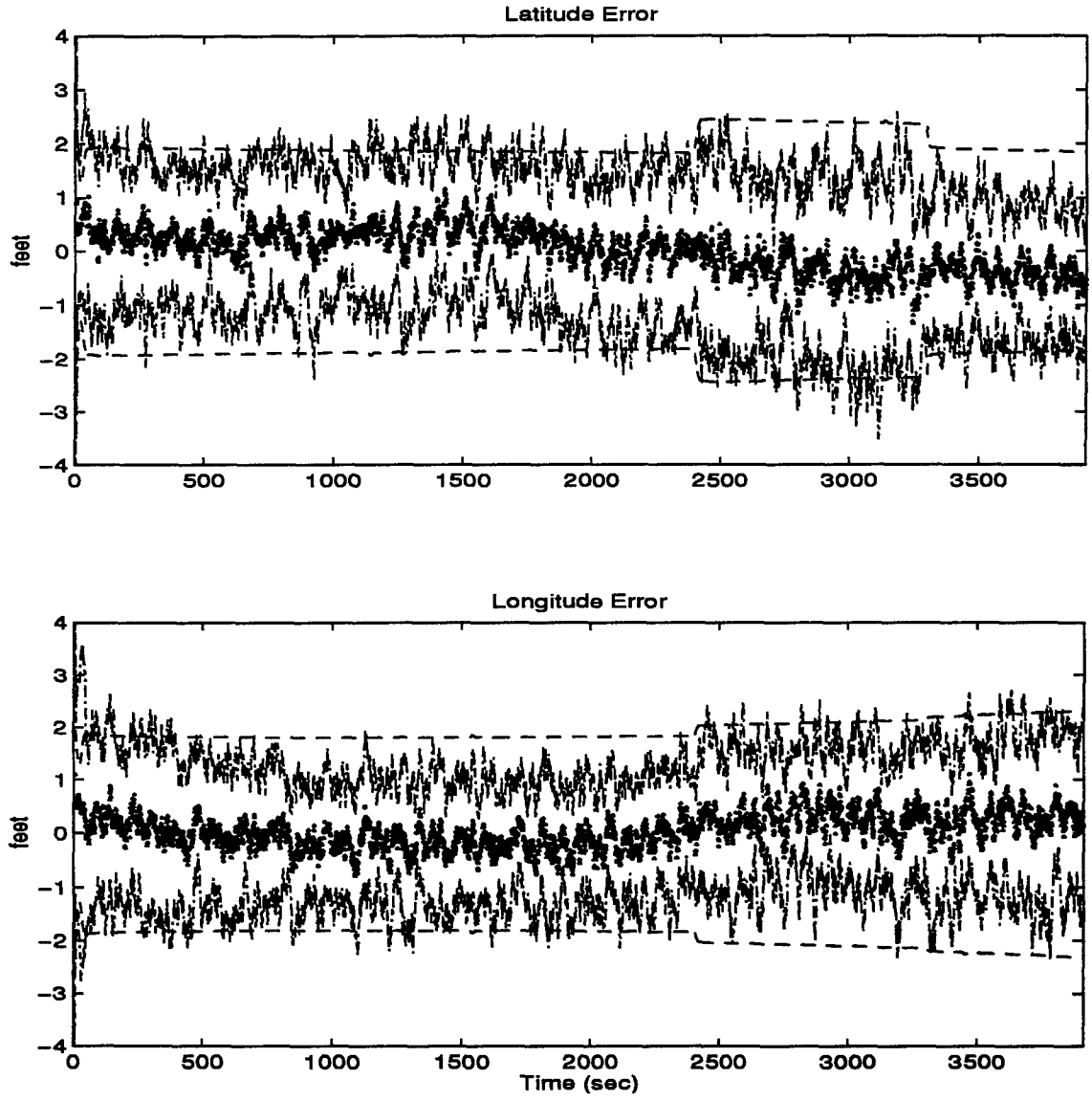

Figure E.25 Latitude and Longitude Error

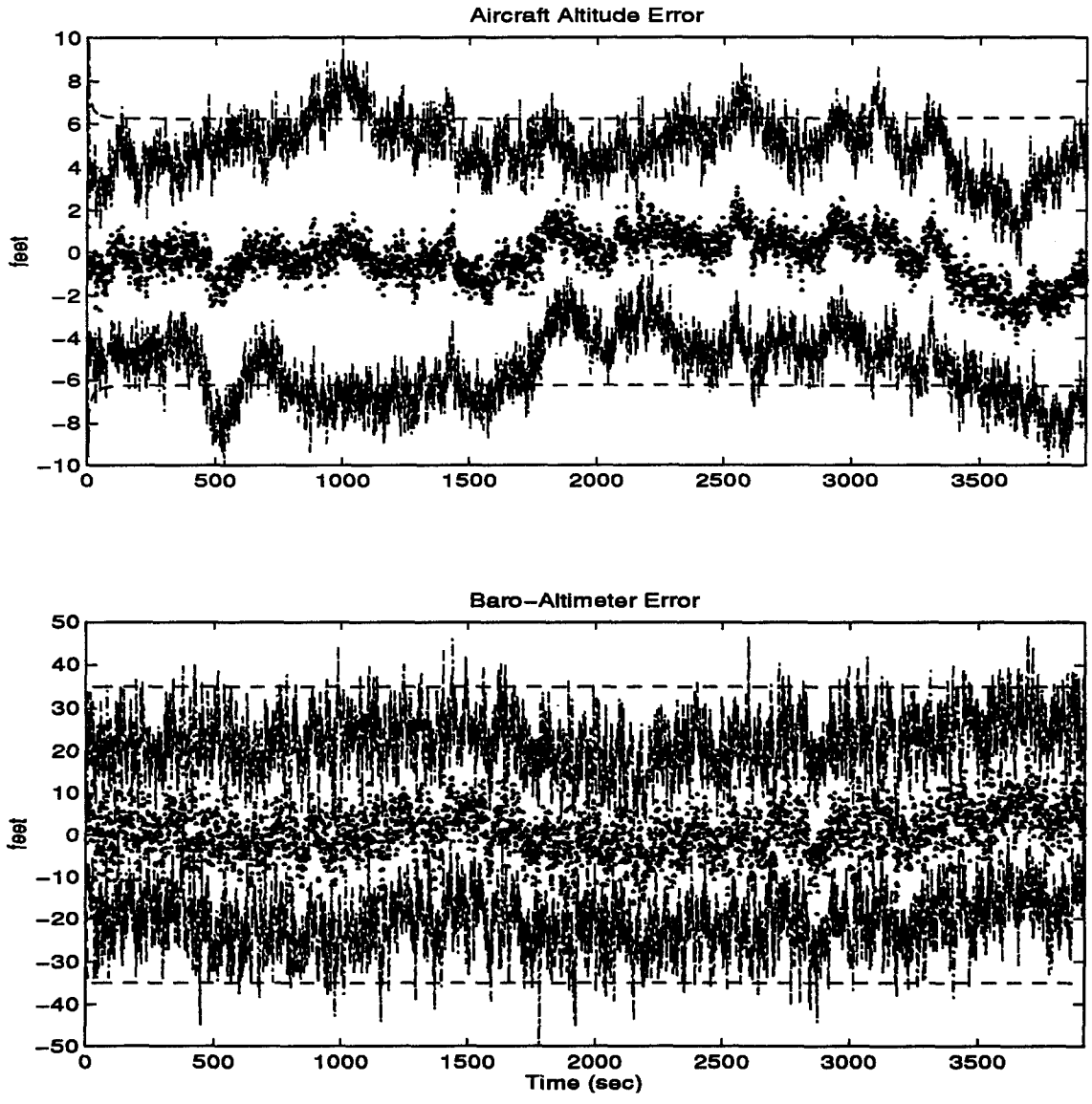

Figure E.26 Aircraft Altitude and Baro-Altimeter Error

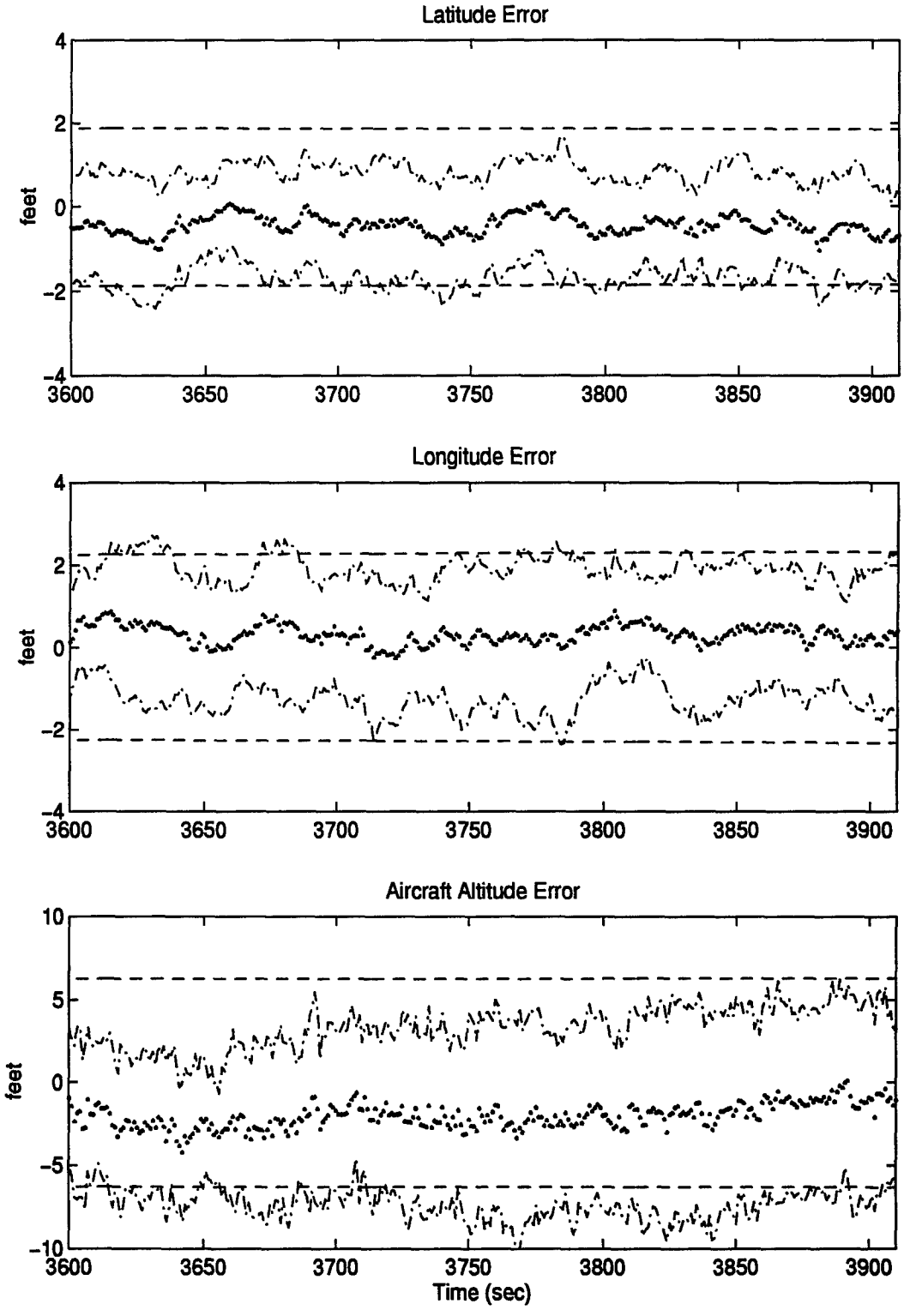

Figure E.27 Latitude, Longitude, and Aircraft Altitude Error

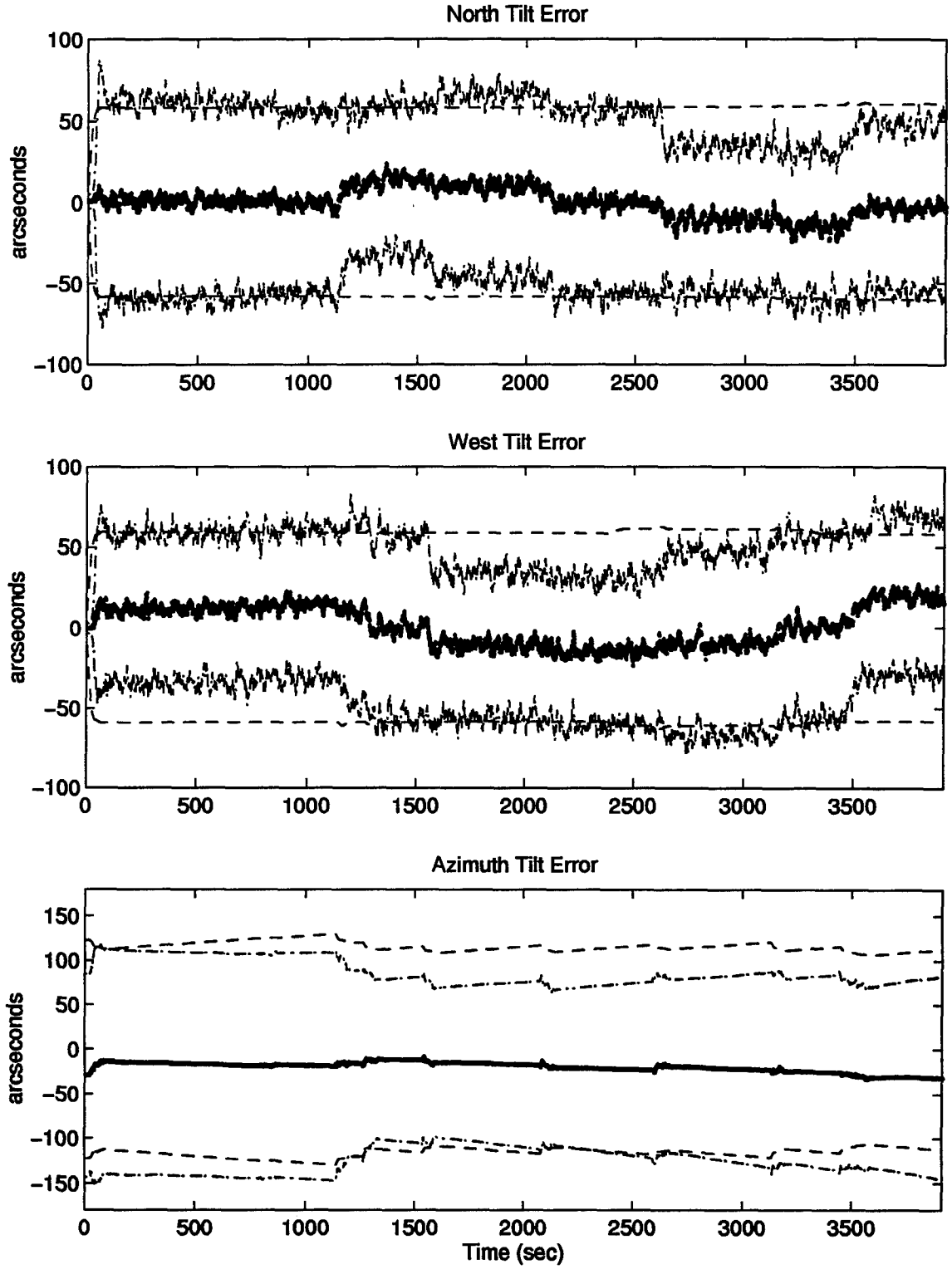

Figure E.28 North, West, and Azimuth Tilt Errors

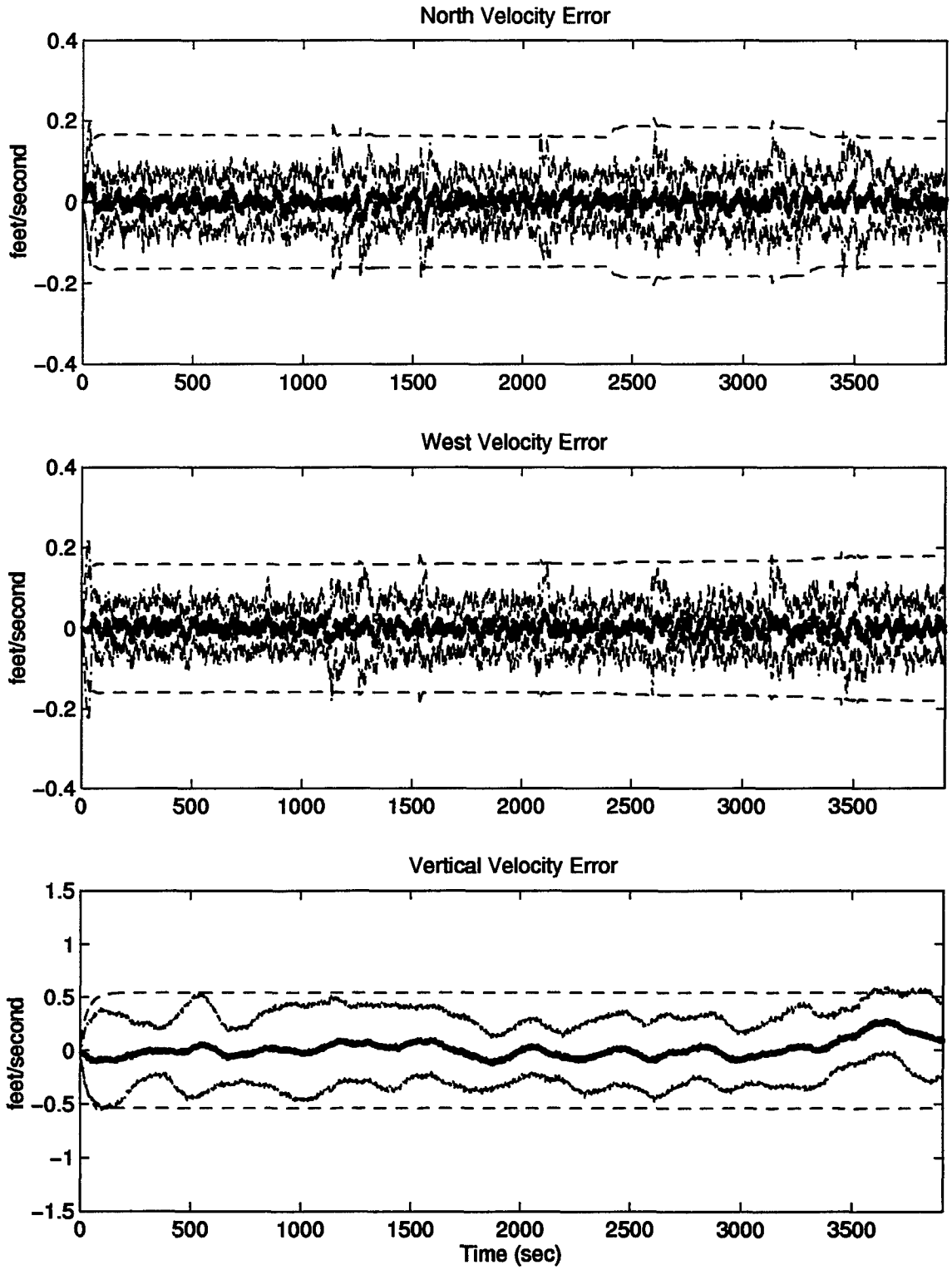

Figure E.29 North, West, and Vertical Velocity Errors

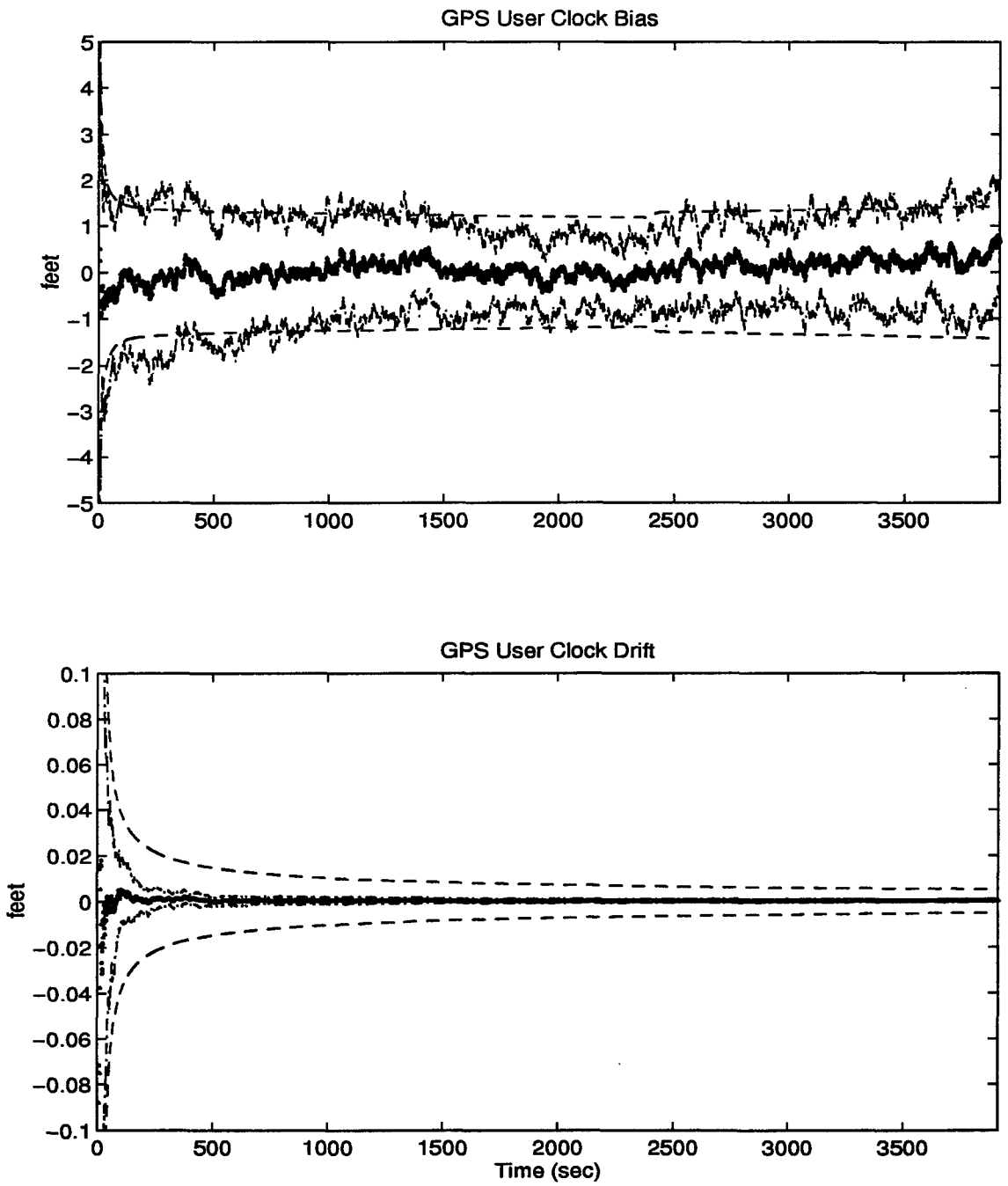

Figure E.30 GPS User Clock Bias and GPS User Clock Drift

E.6 Plots of Case VI: Barometric Altimeter, 4.0 nm/hr INS, Radar Altimeter, and DGPS Using the Single Engine Aircraft Flight Profile.

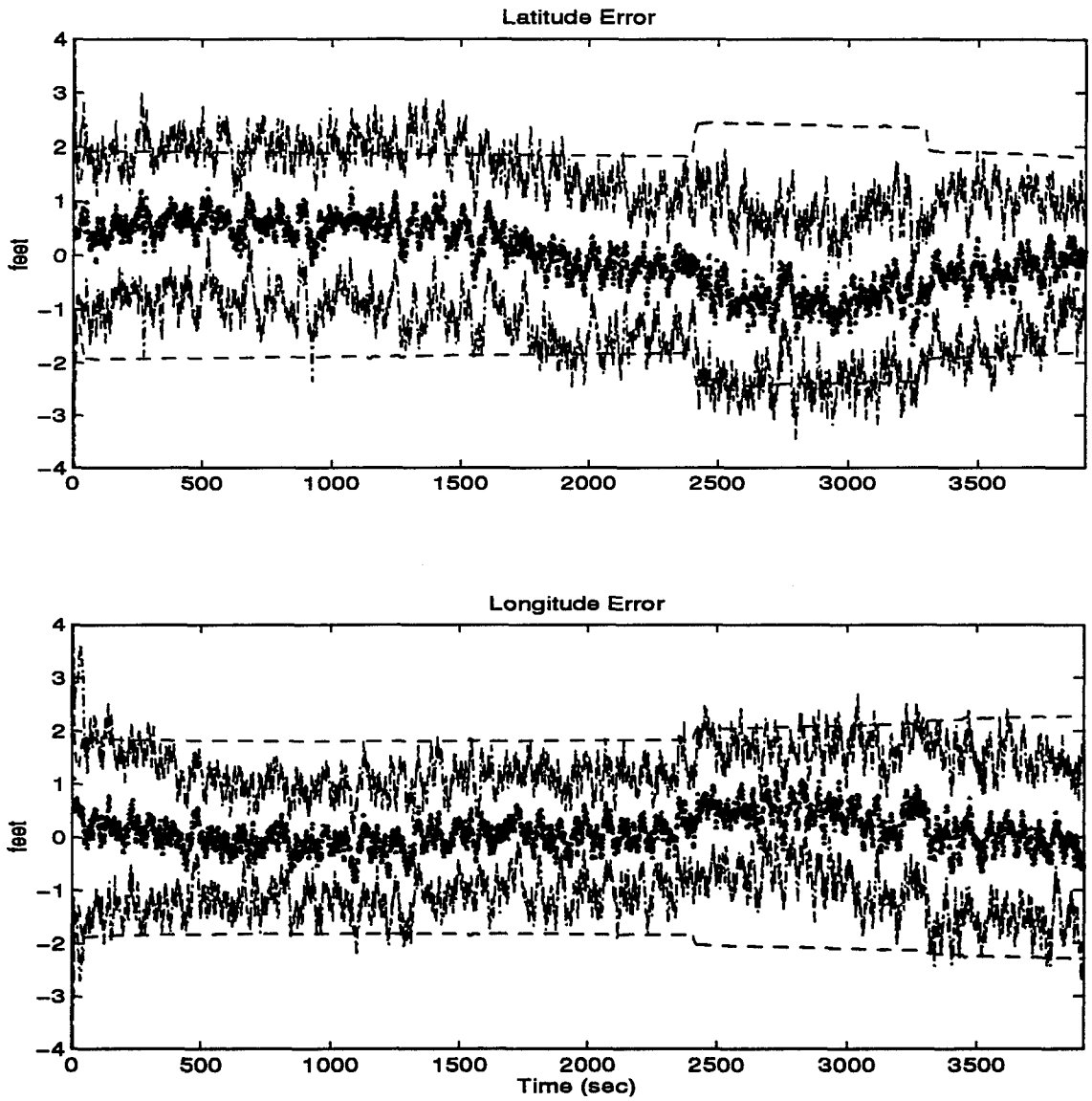

Figure E.31 Latitude and Longitude Error

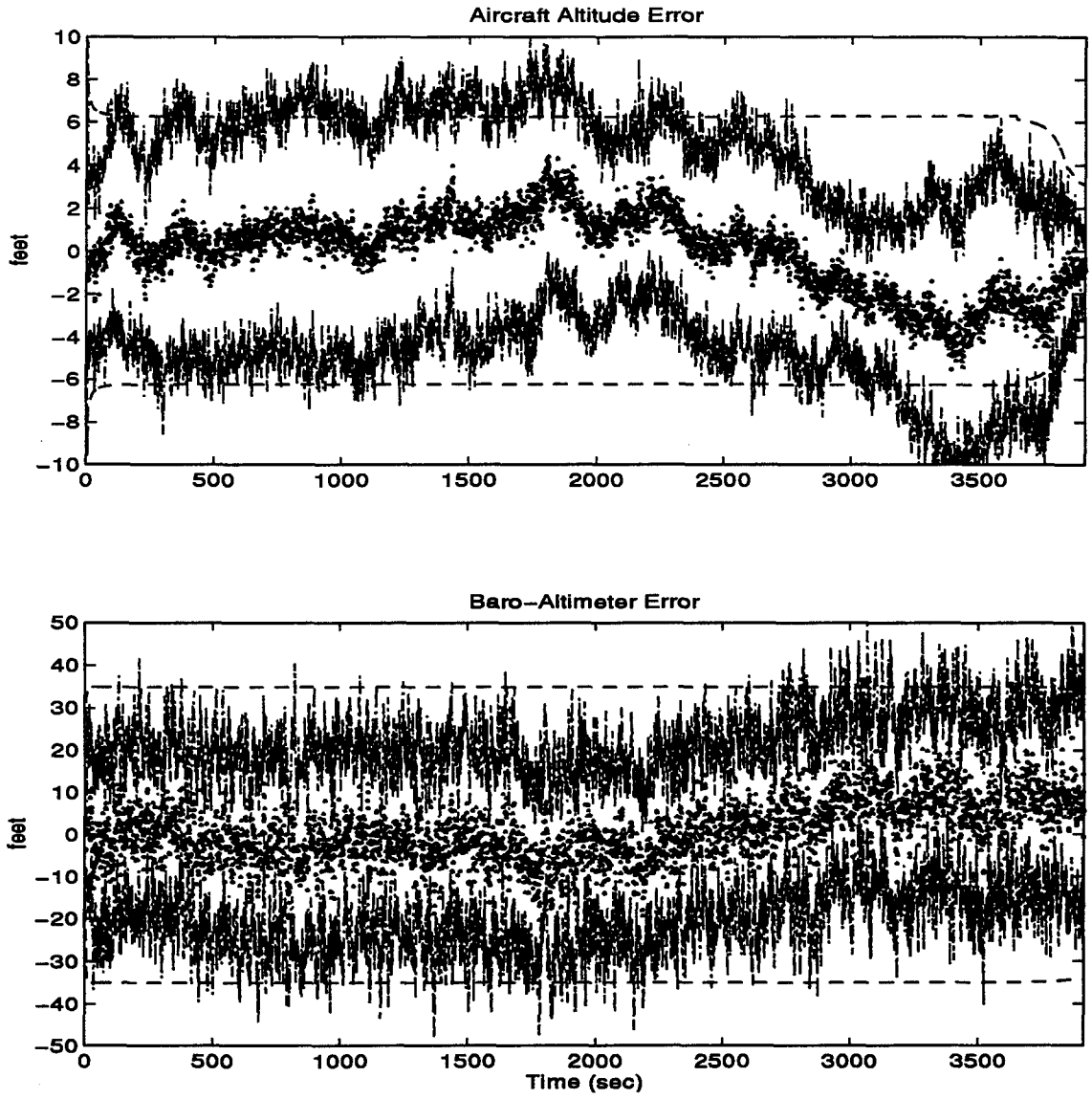

Figure E.32 Aircraft Altitude and Baro-Altimeter Error

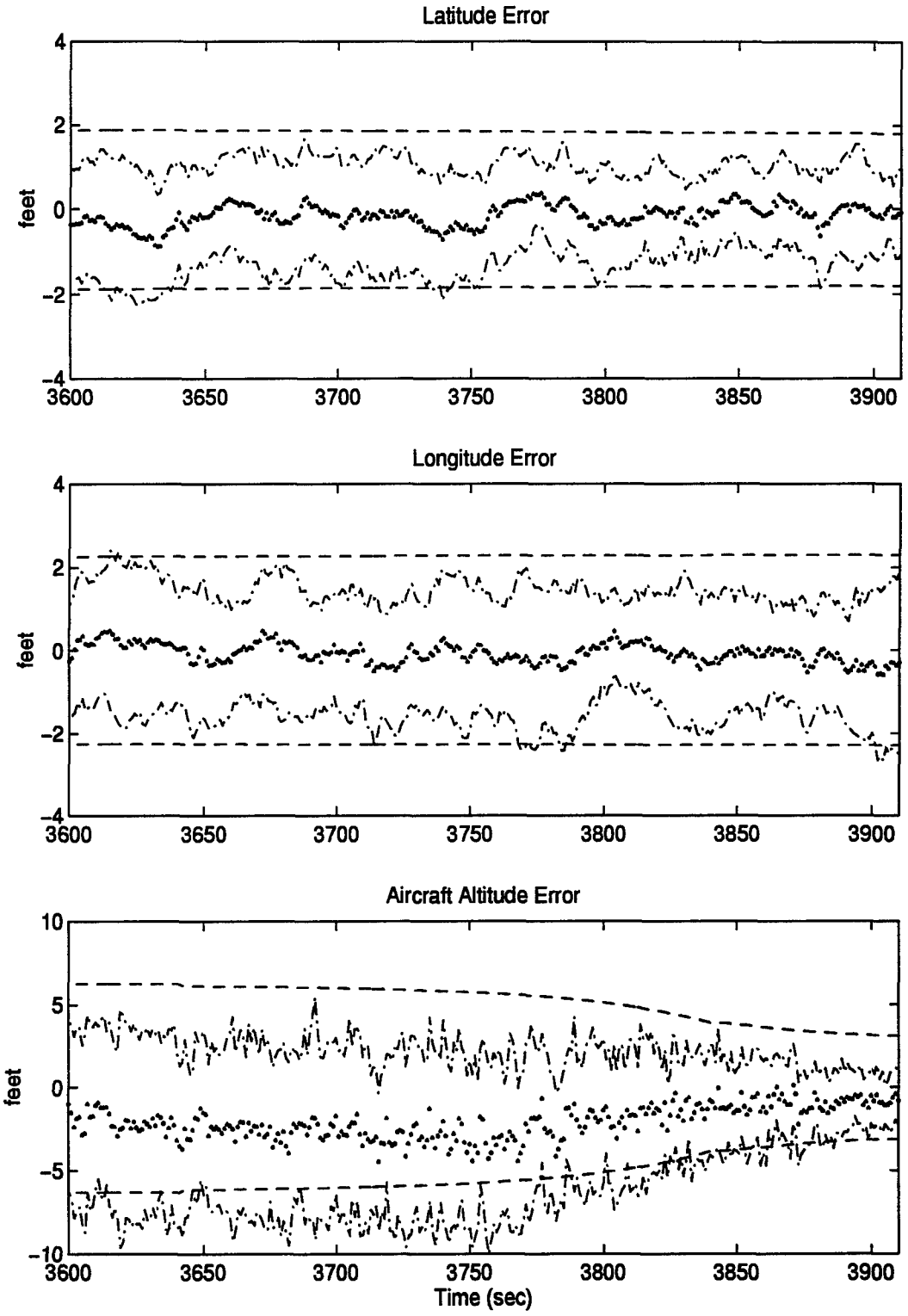

Figure E.33 Latitude, Longitude, and Aircraft Altitude Error

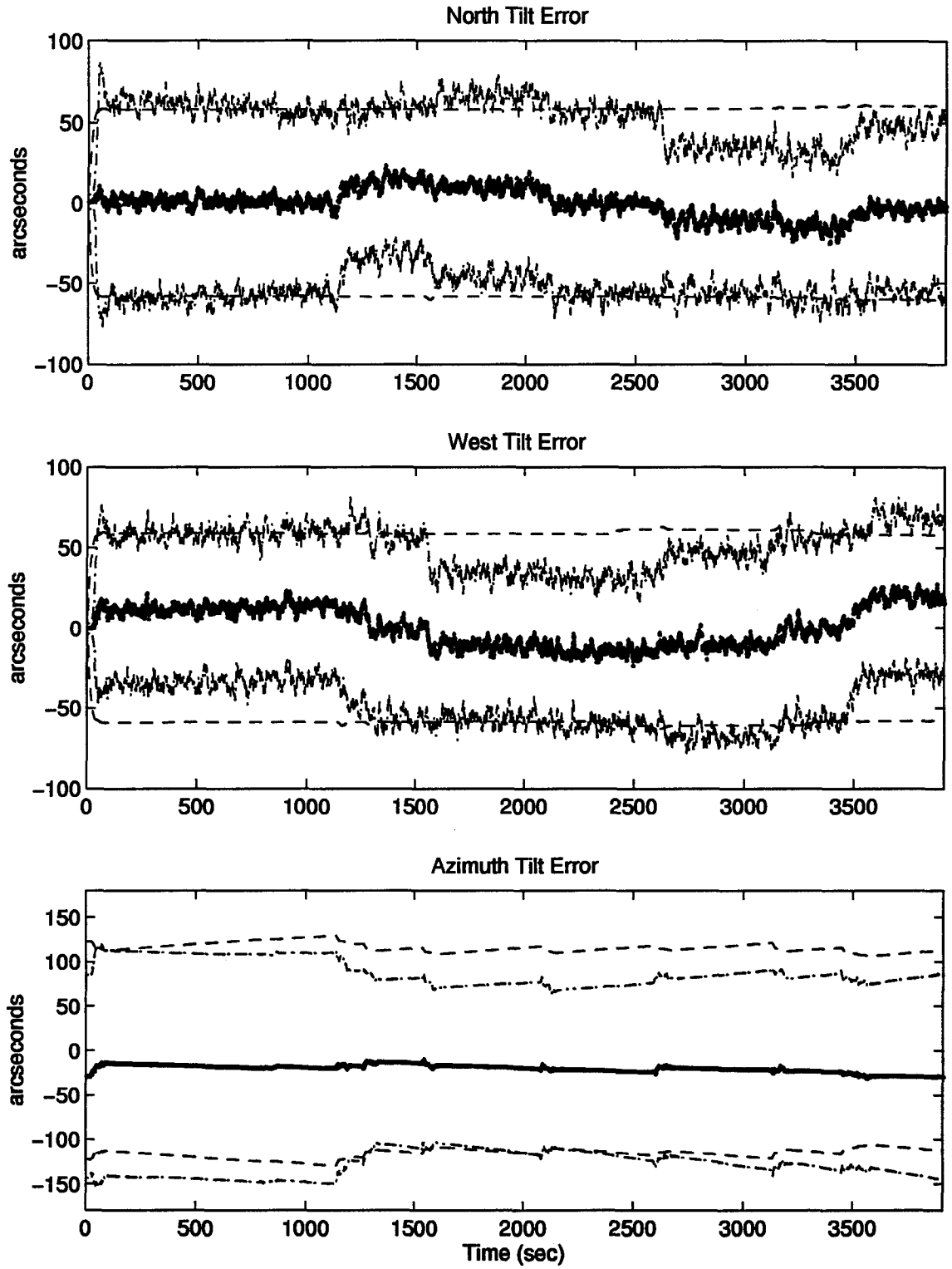

Figure E.34 North, West, and Azimuth Tilt Errors

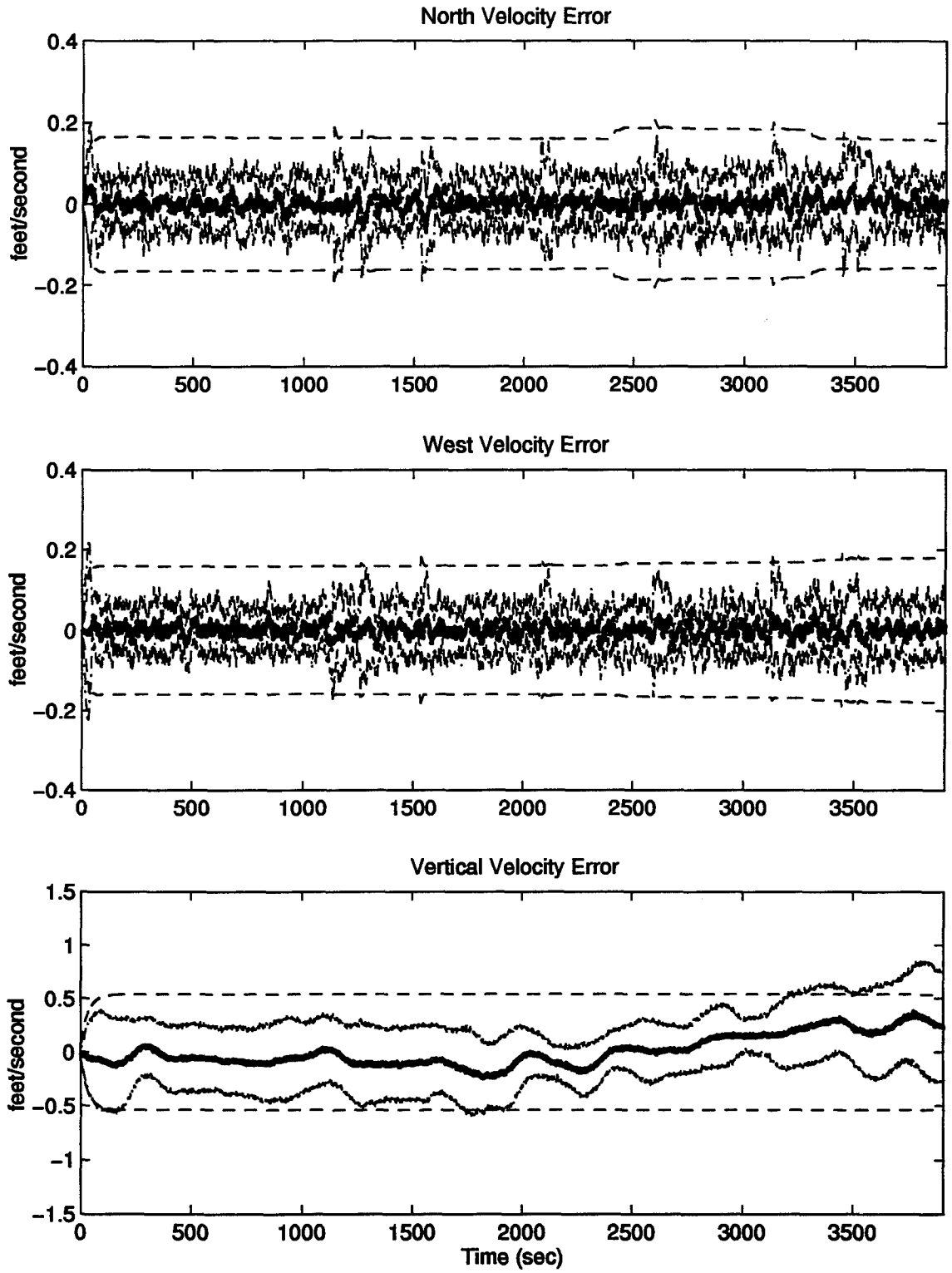

Figure E.35 North, West, and Vertical Velocity Errors

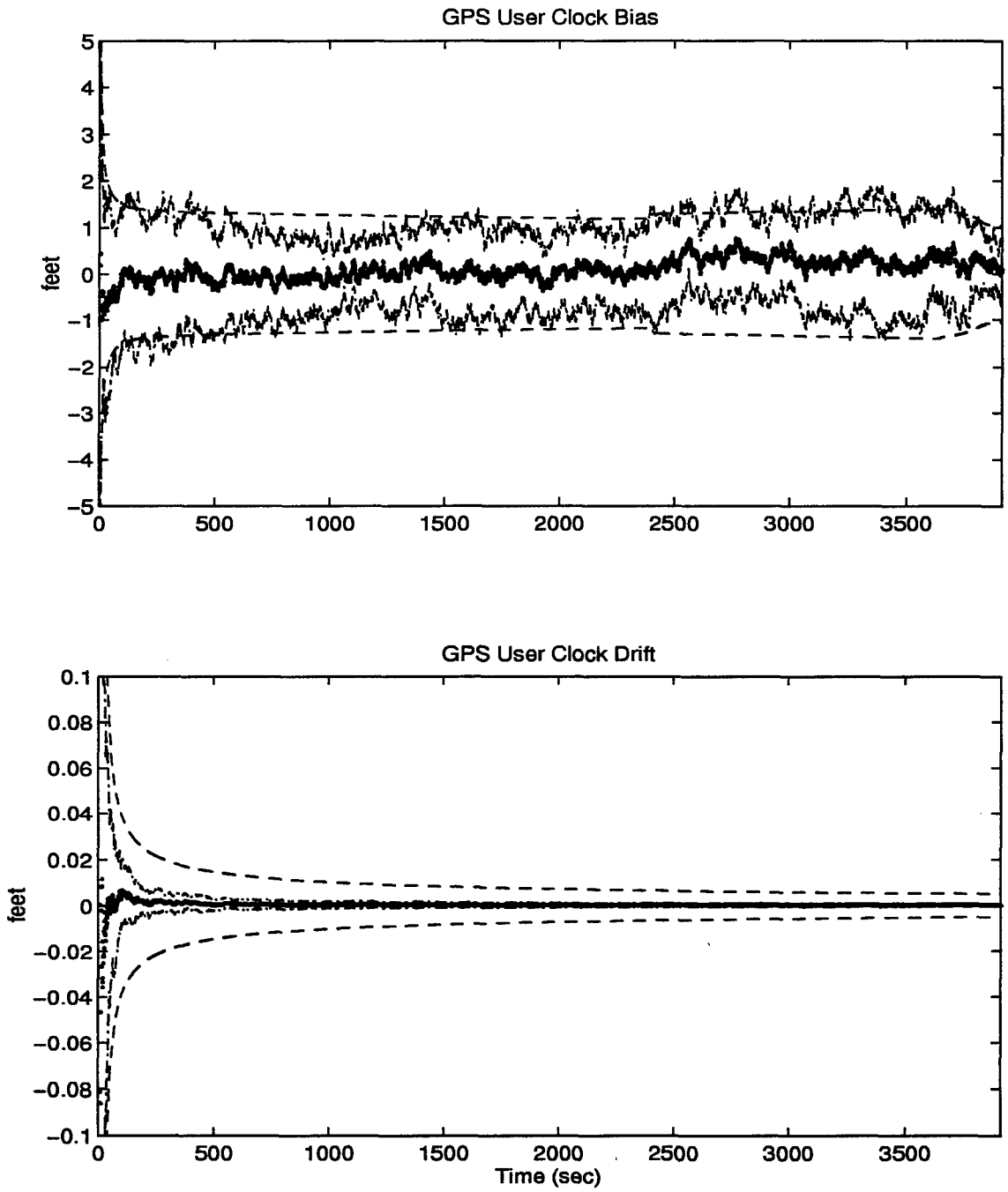

Figure E.36 GPS User Clock Bias and GPS User Clock Drift

Appendix F.

Plots of Case VII through Case XII for Single Engine Aircraft Flight Profile.

Plot Legend

$\cdots$ true error (mean error $\pm$ σ_{true})

- - - filter predicted error ($0 \pm \sigma_{filter}$)

— mean error

F.1 Plots of Case VII: Barometric Altimeter, 0.4 nm/hr INS, Single Pseudolite, and DGPS Using the Single Engine Aircraft Flight Profile.

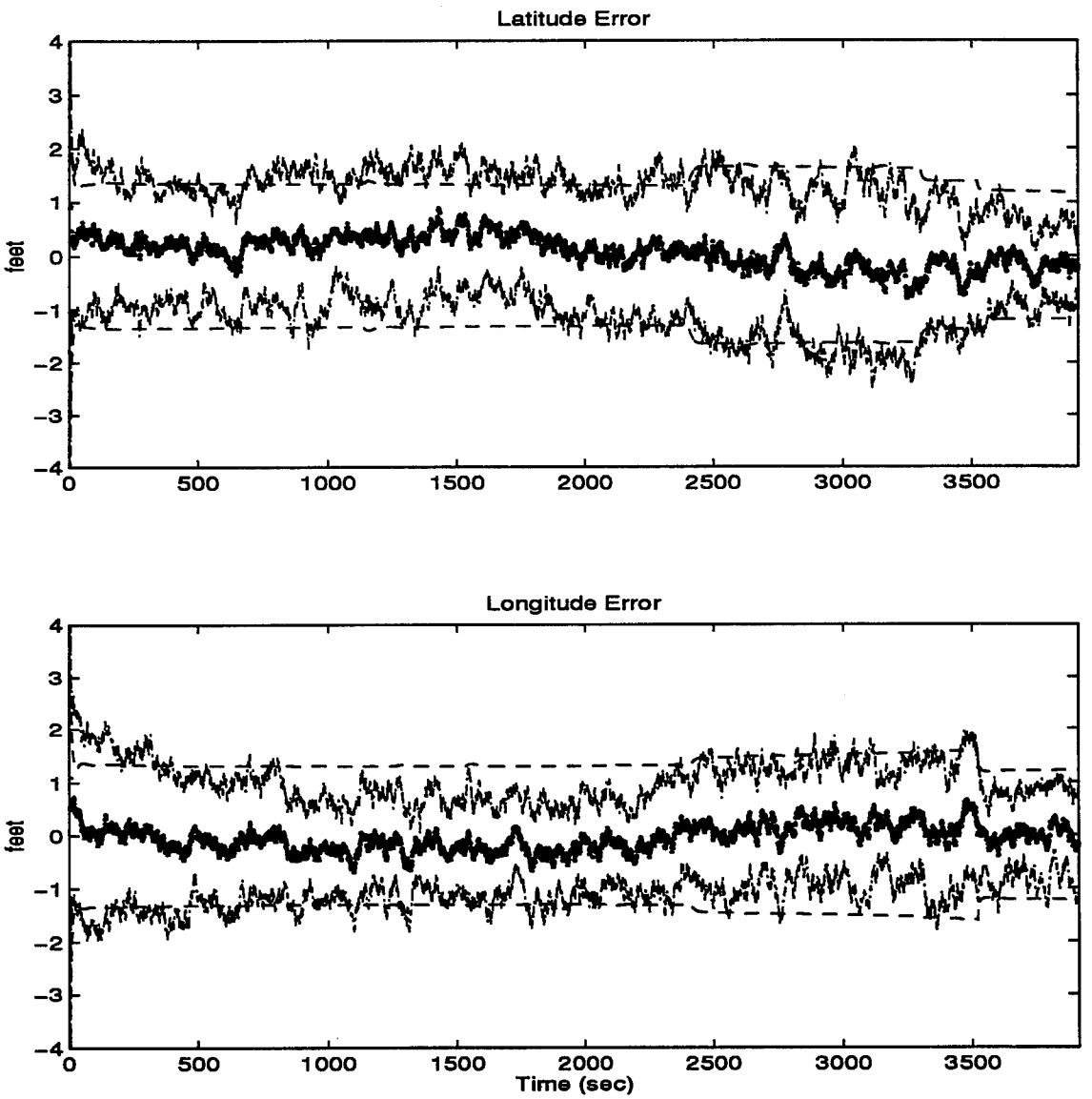

Figure F.1 Latitude and Longitude Error

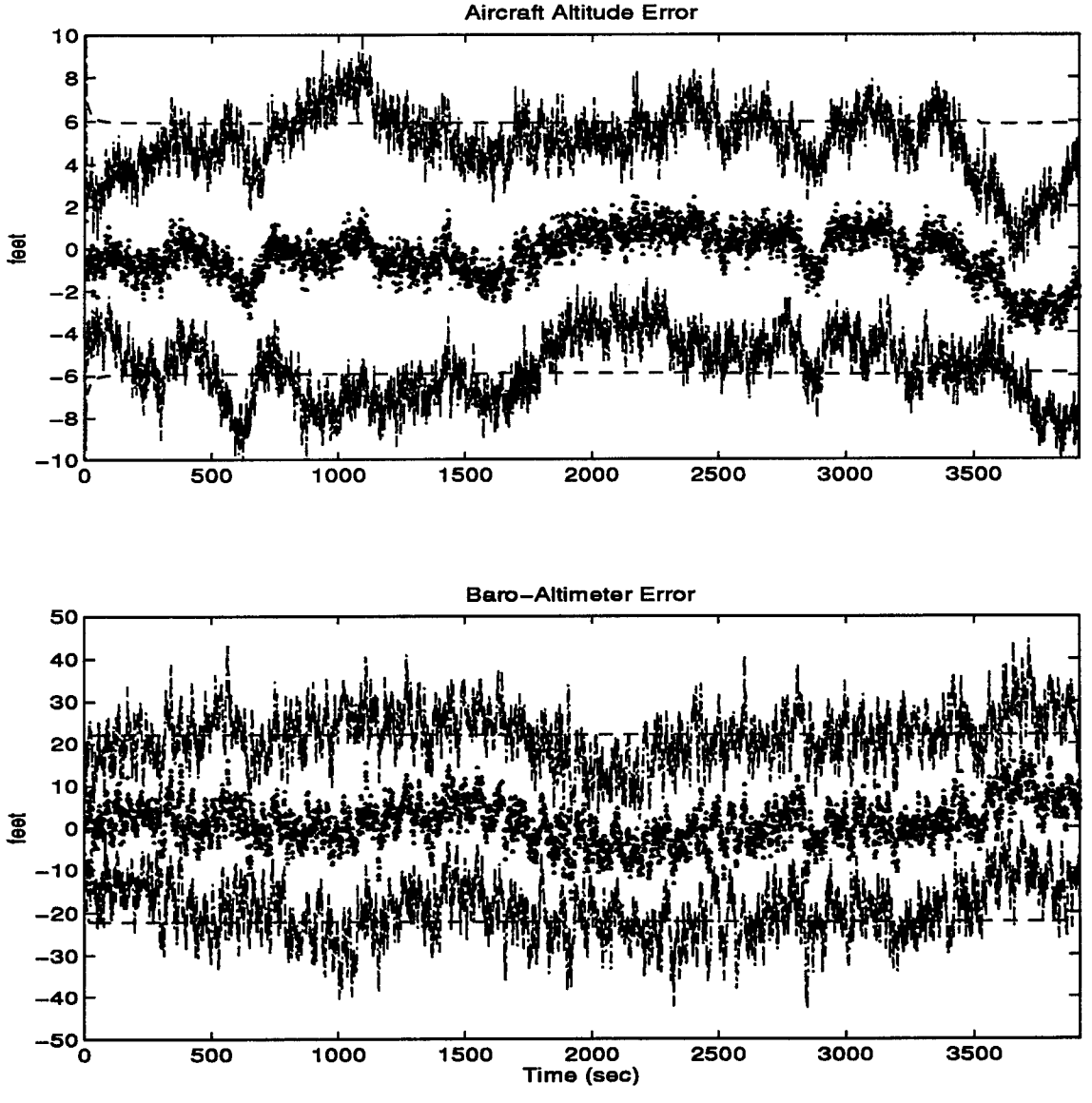

Figure F.2 Aircraft Altitude and Baro-Altimeter Error

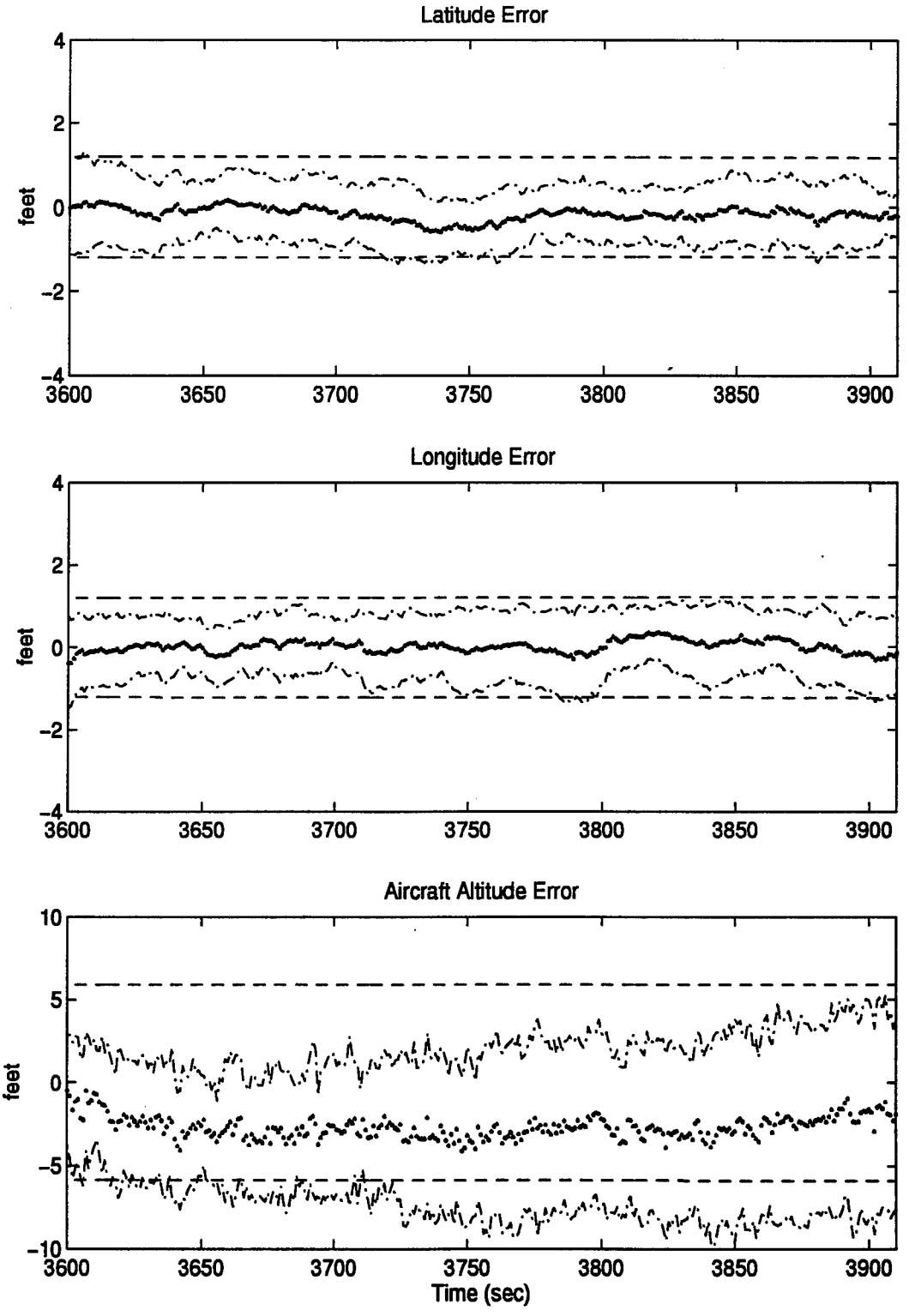

Figure F.3 Latitude, Longitude, and Aircraft Altitude Error

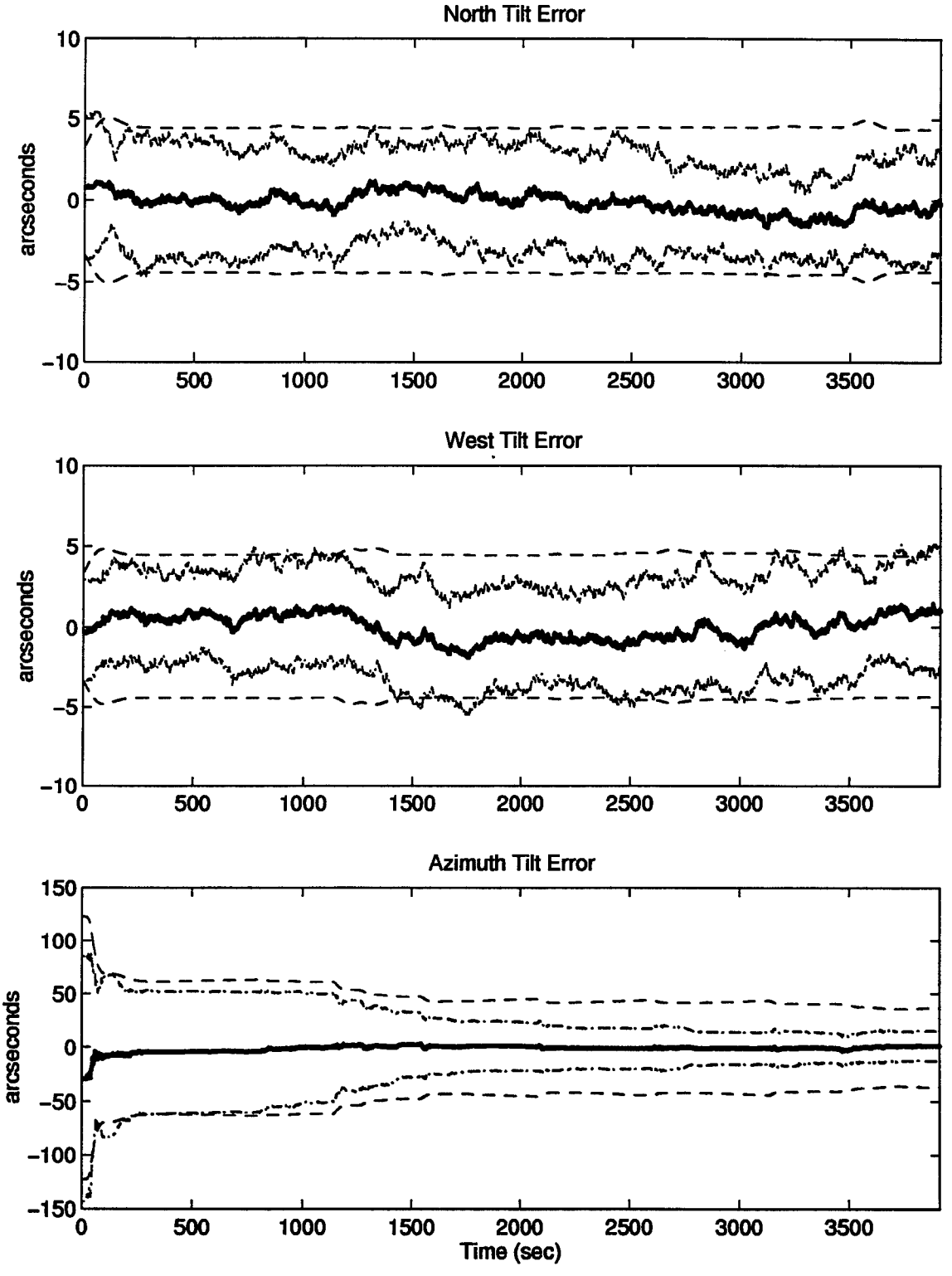

Figure F.4 North, West, and Azimuth Tilt Errors

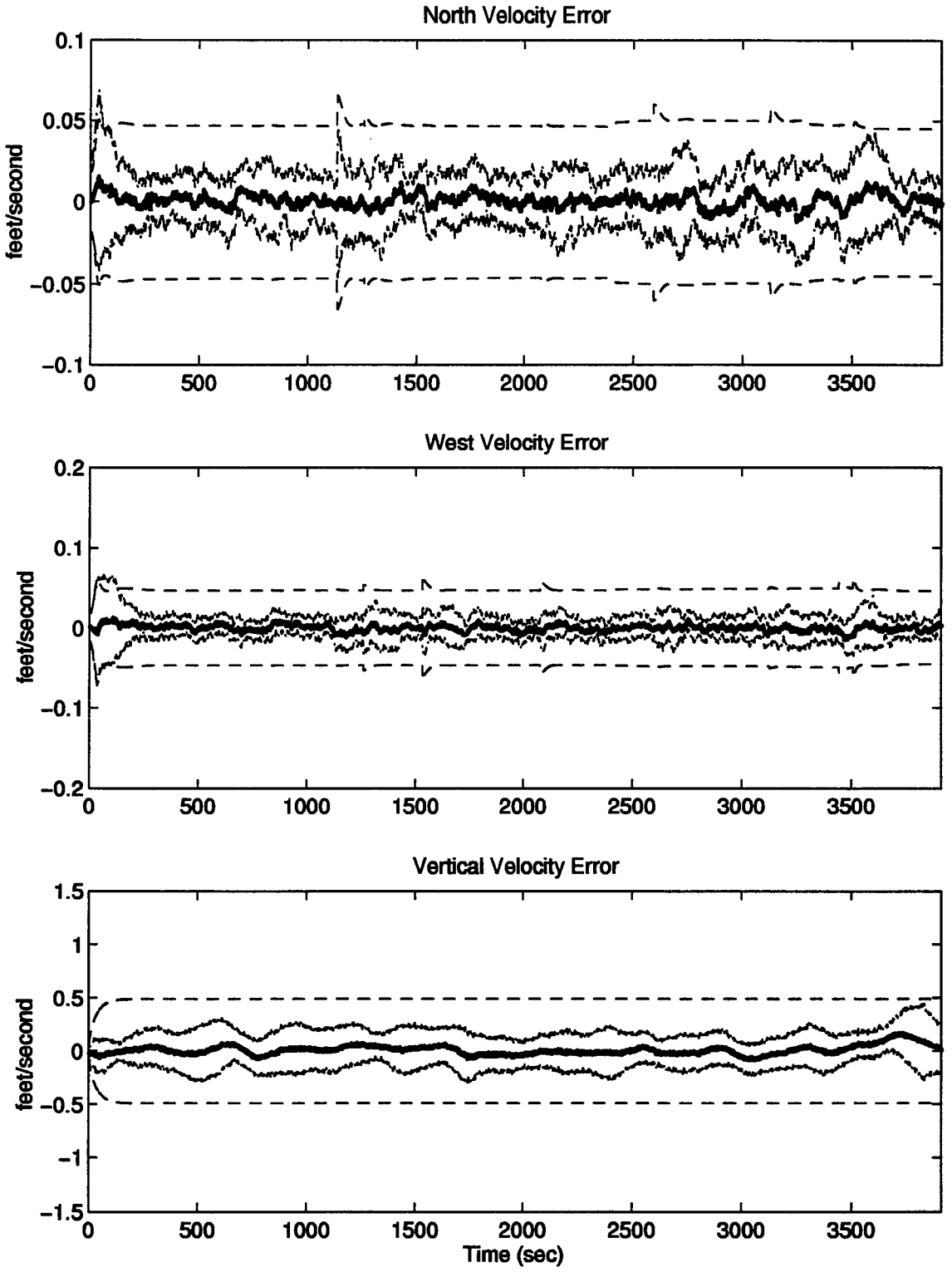

Figure F.5 North, West, and Vertical Velocity Errors

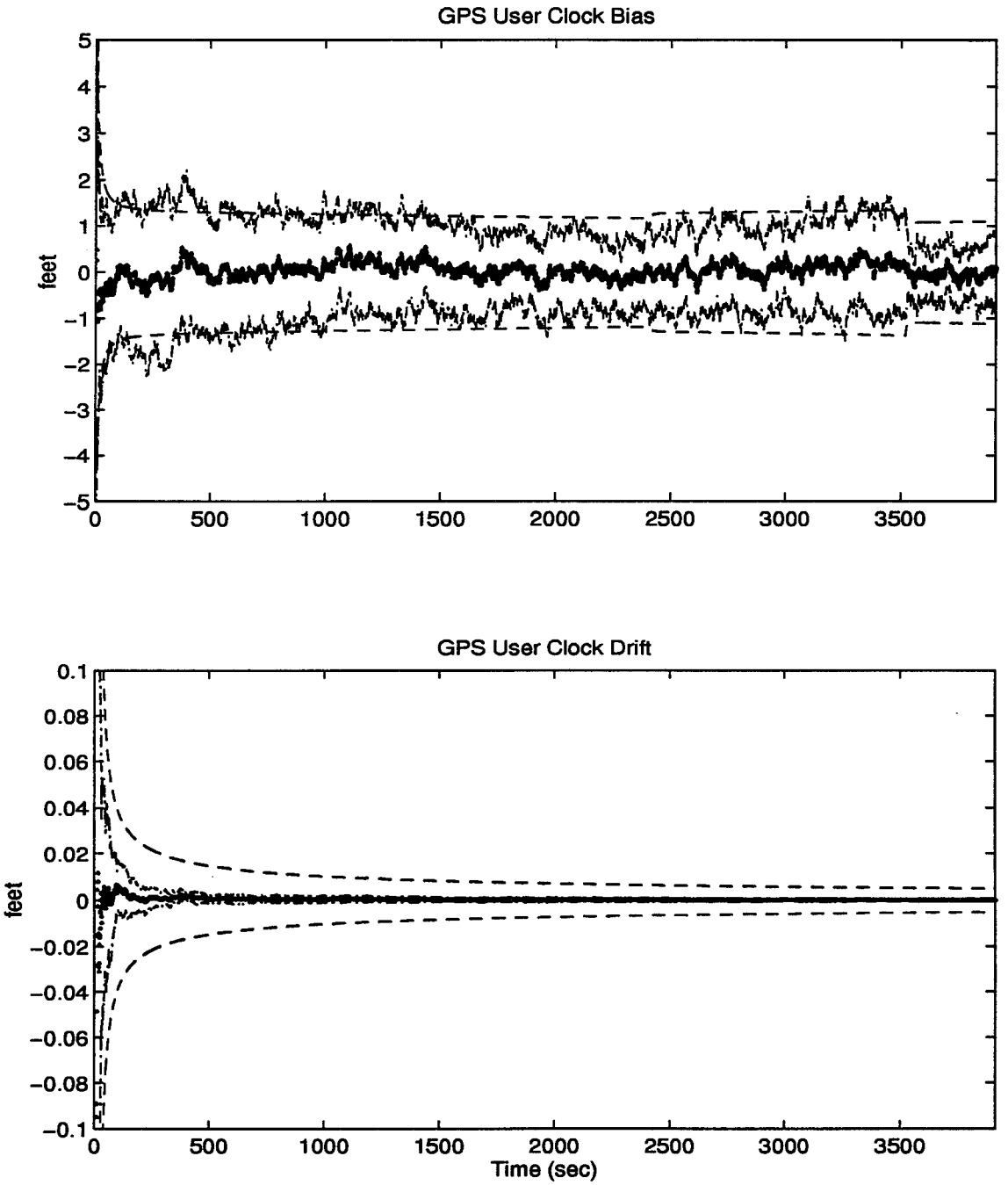

Figure F.6 GPS User Clock Bias and GPS User Clock Drift

F.2 Plots of Case VIII: Barometric Altimeter, 0.4 nm/hr INS, Radar Altimeter, Single Pseudolite, and DGPS Using the Single Engine Aircraft Flight Profile.

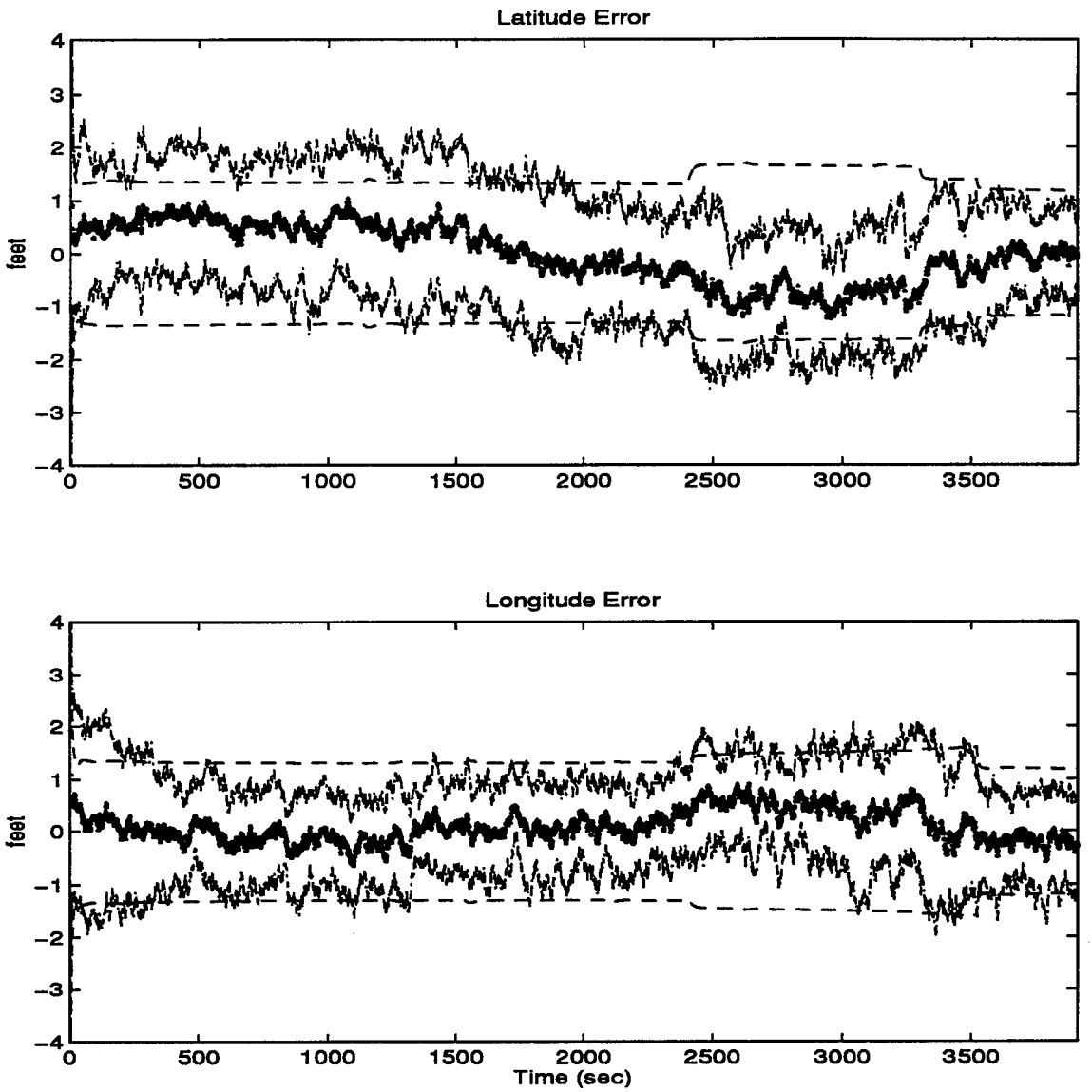

Figure F.7 Latitude and Longitude Error

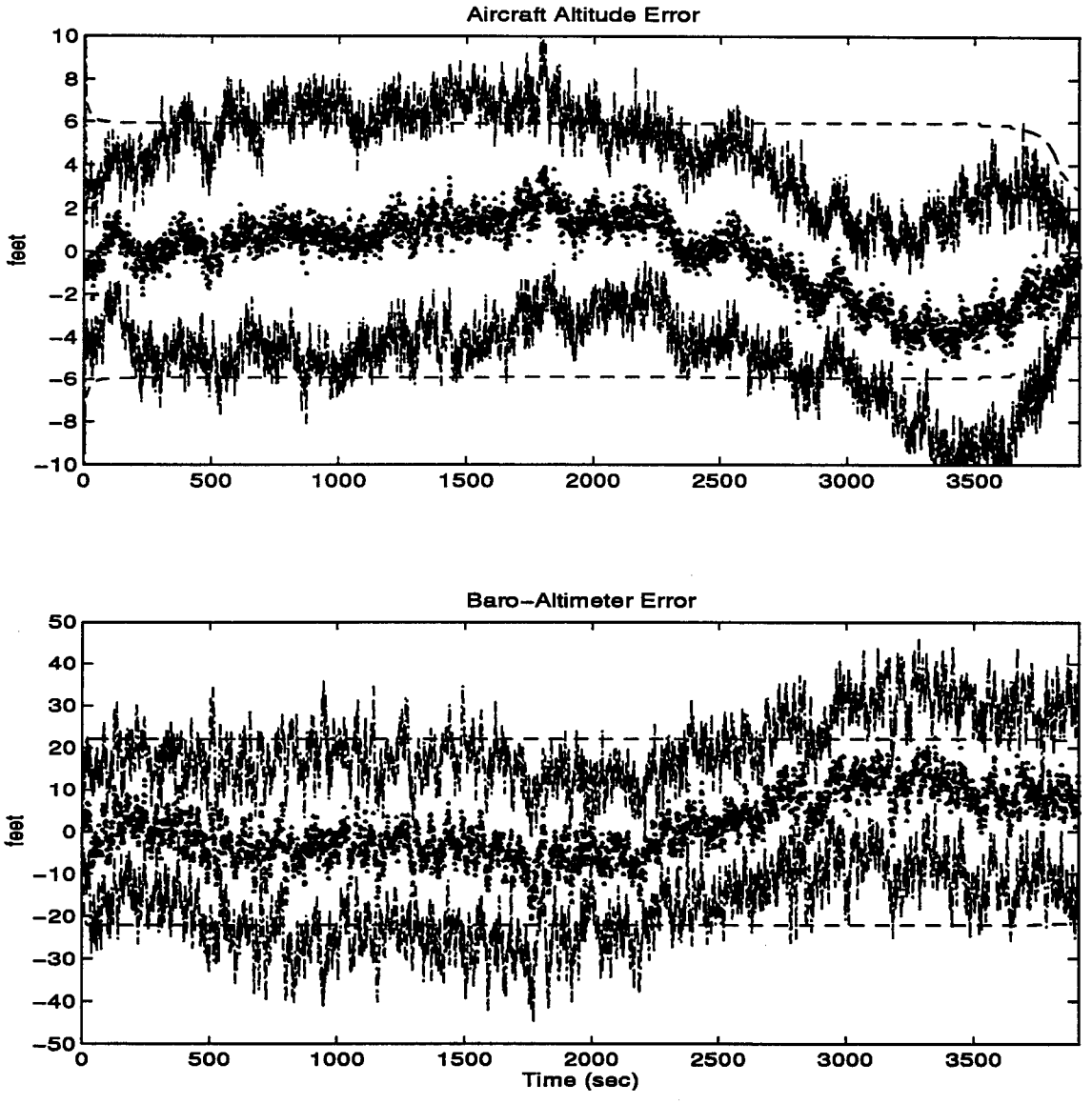

Figure F.8 Aircraft Altitude and Baro-Altimeter Error

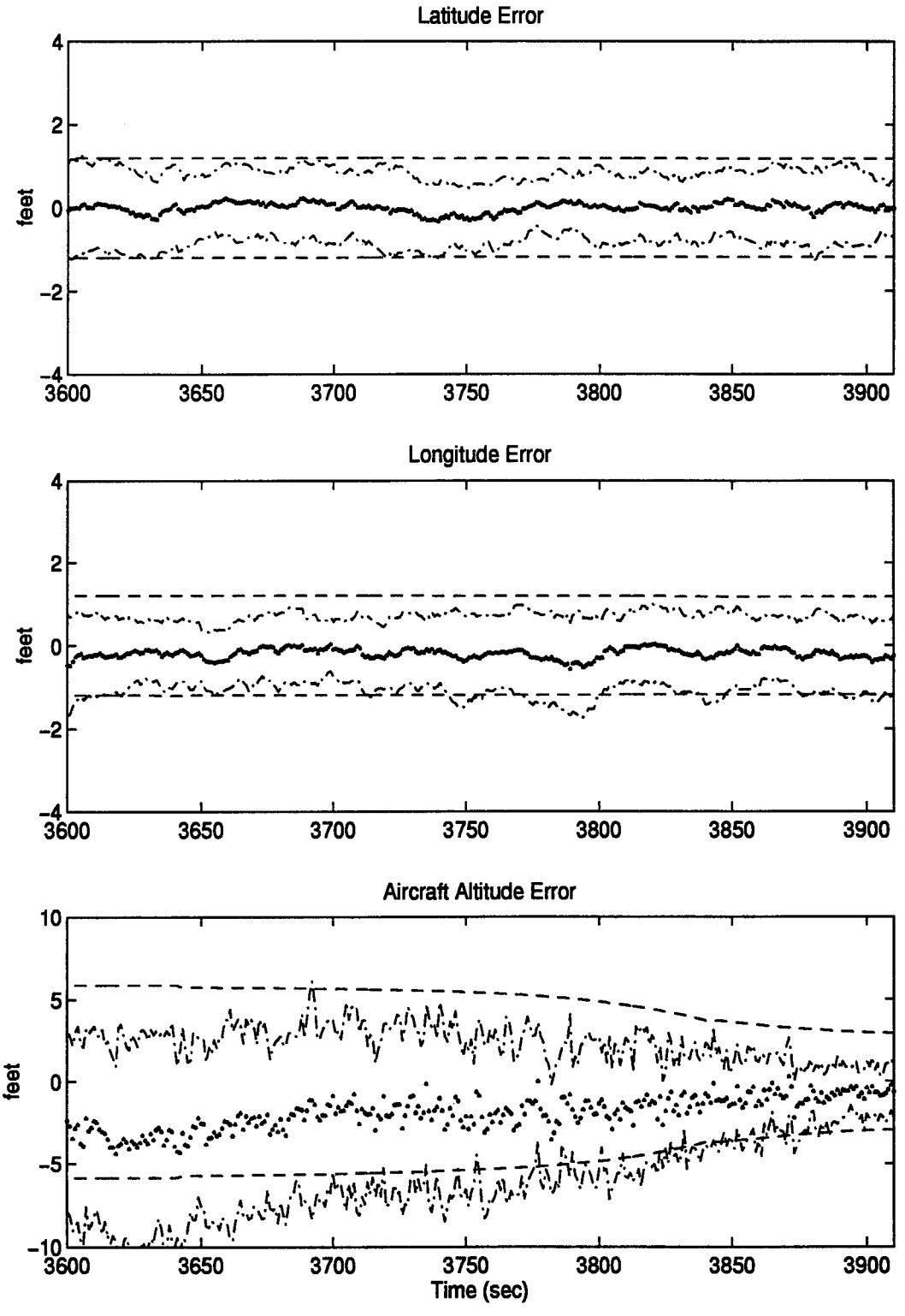

Figure F.9 Latitude, Longitude, and Aircraft Altitude Error

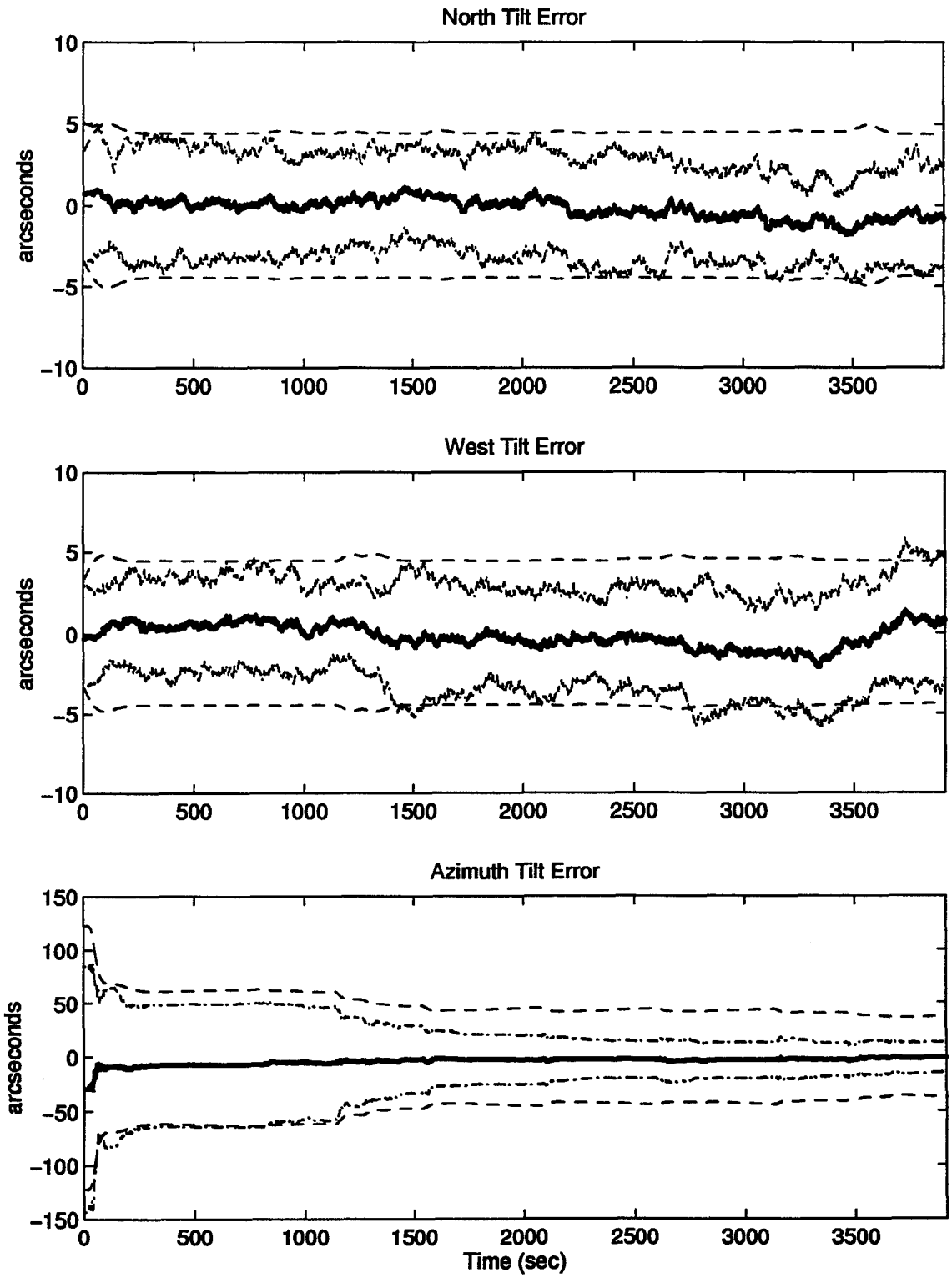

Figure F.10 North, West, and Azimuth Tilt Errors

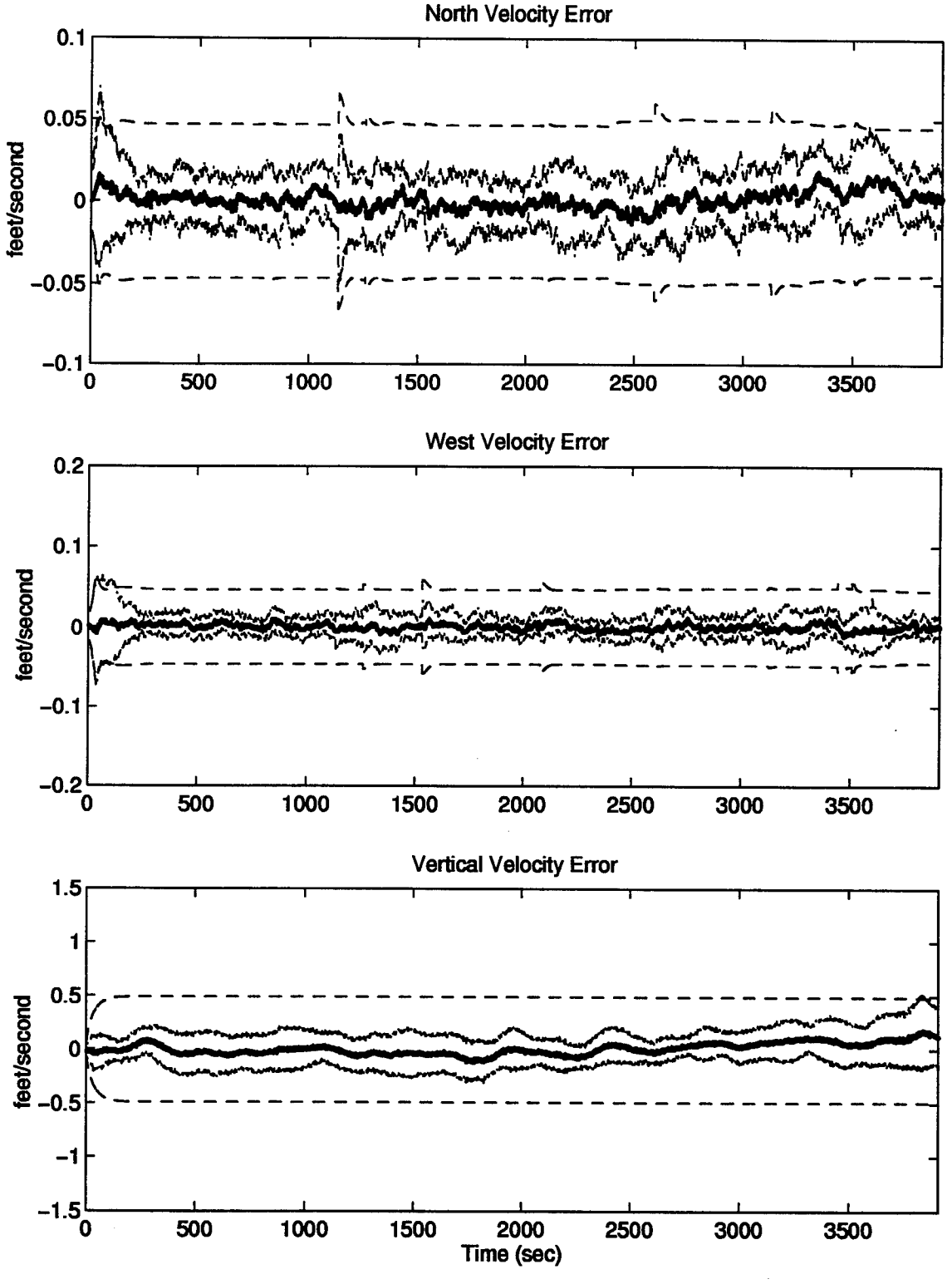

Figure F.11 North, West, and Vertical Velocity Errors

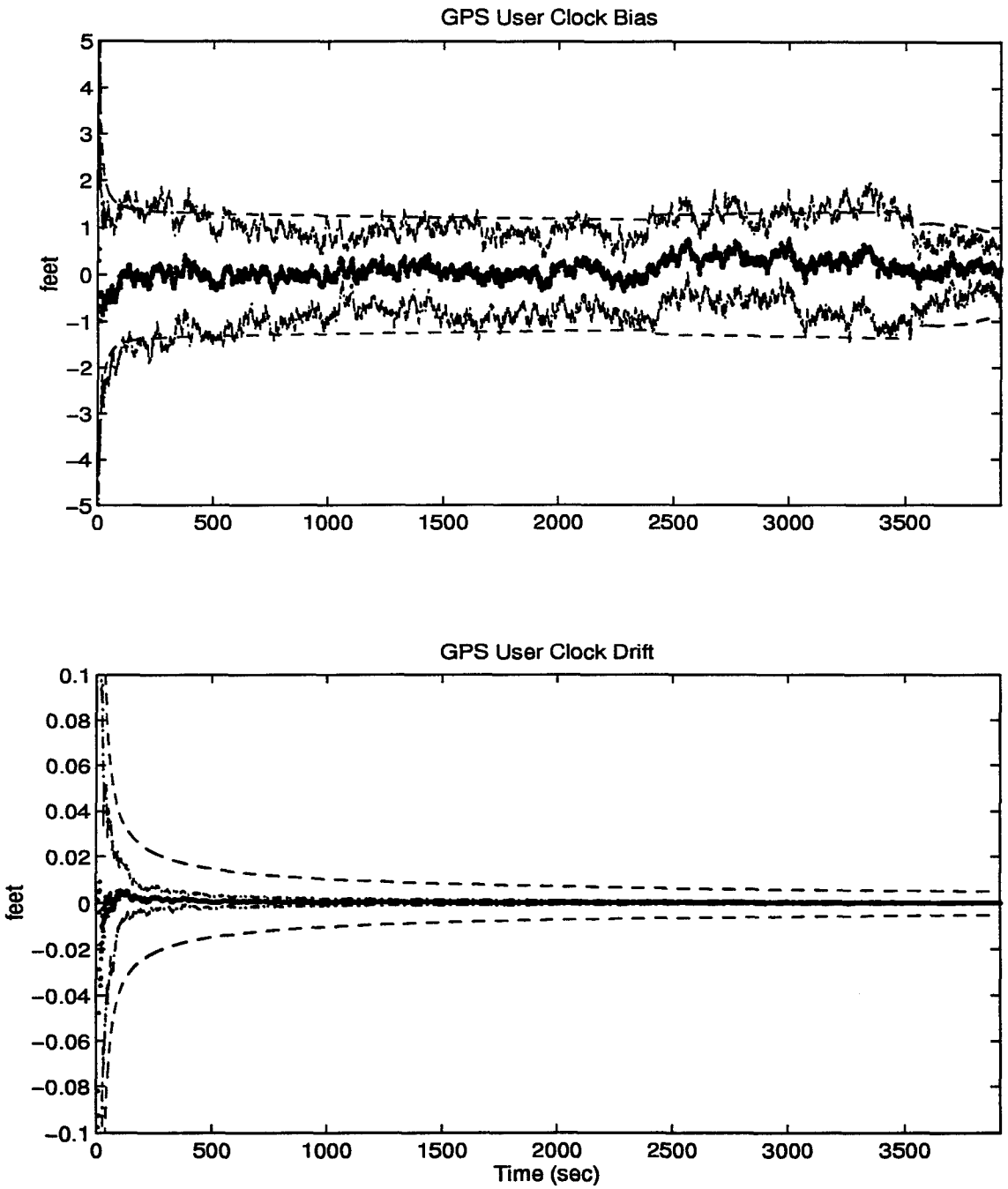

Figure F.12 GPS User Clock Bias and GPS User Clock Drift

F.3 Plots of Case IX: Barometric Altimeter, 2.0 nm/hr INS, Radar Altimeter, Single Pseudolite, and DGPS Using the Single Engine Aircraft Flight Profile.

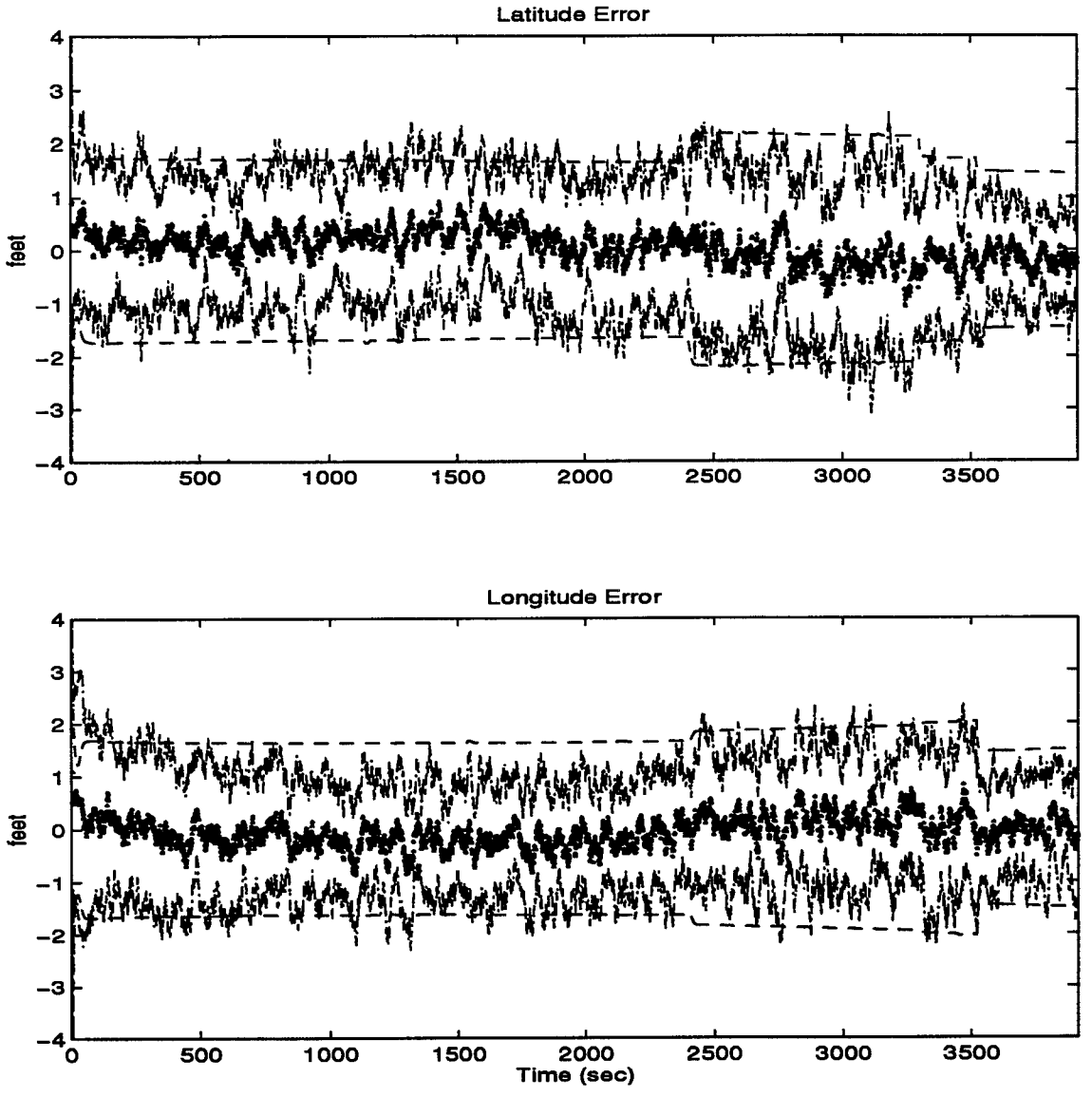

Figure F.13 Latitude and Longitude Error

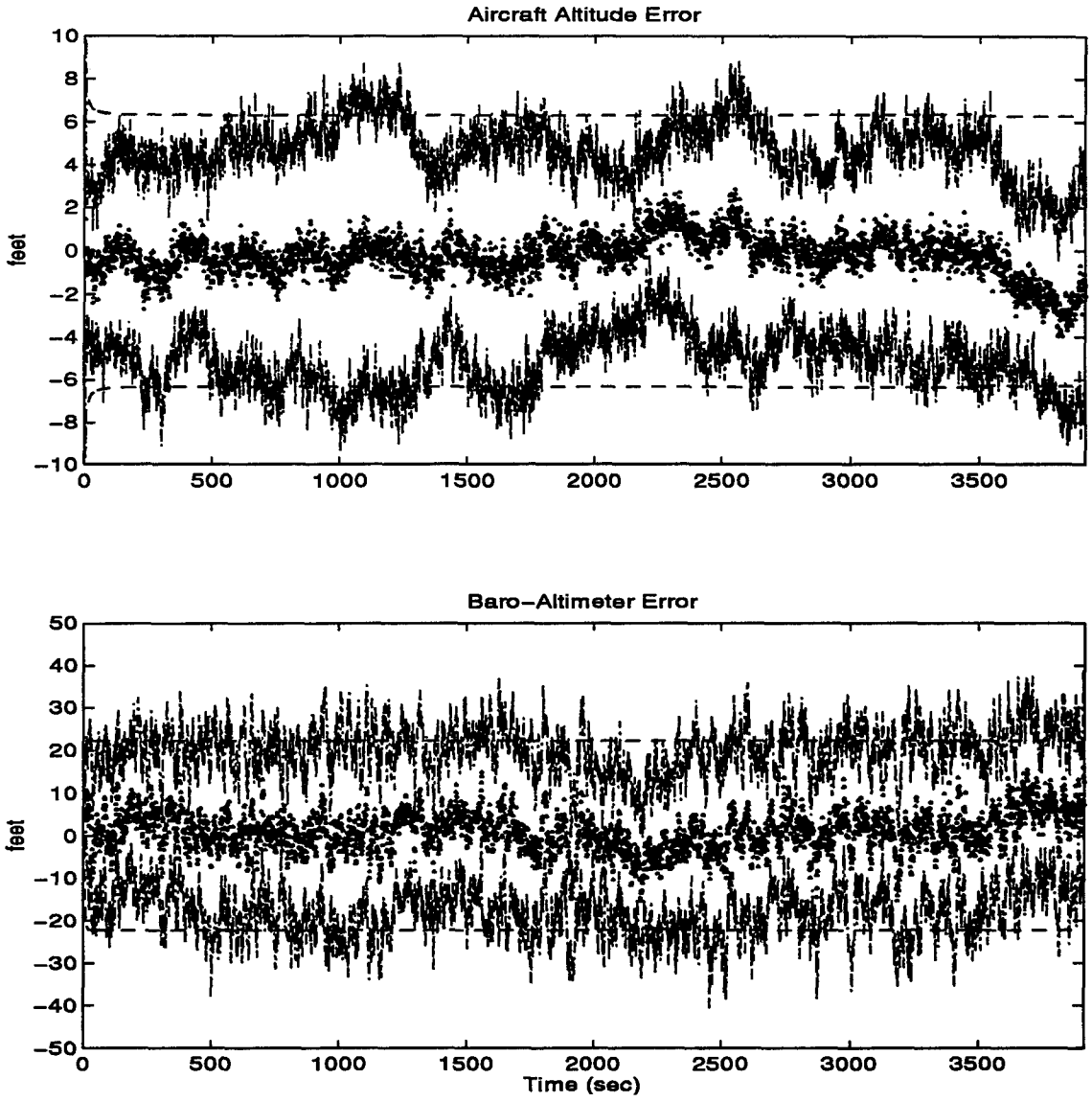

Figure F.14 Aircraft Altitude and Baro-Altimeter Error

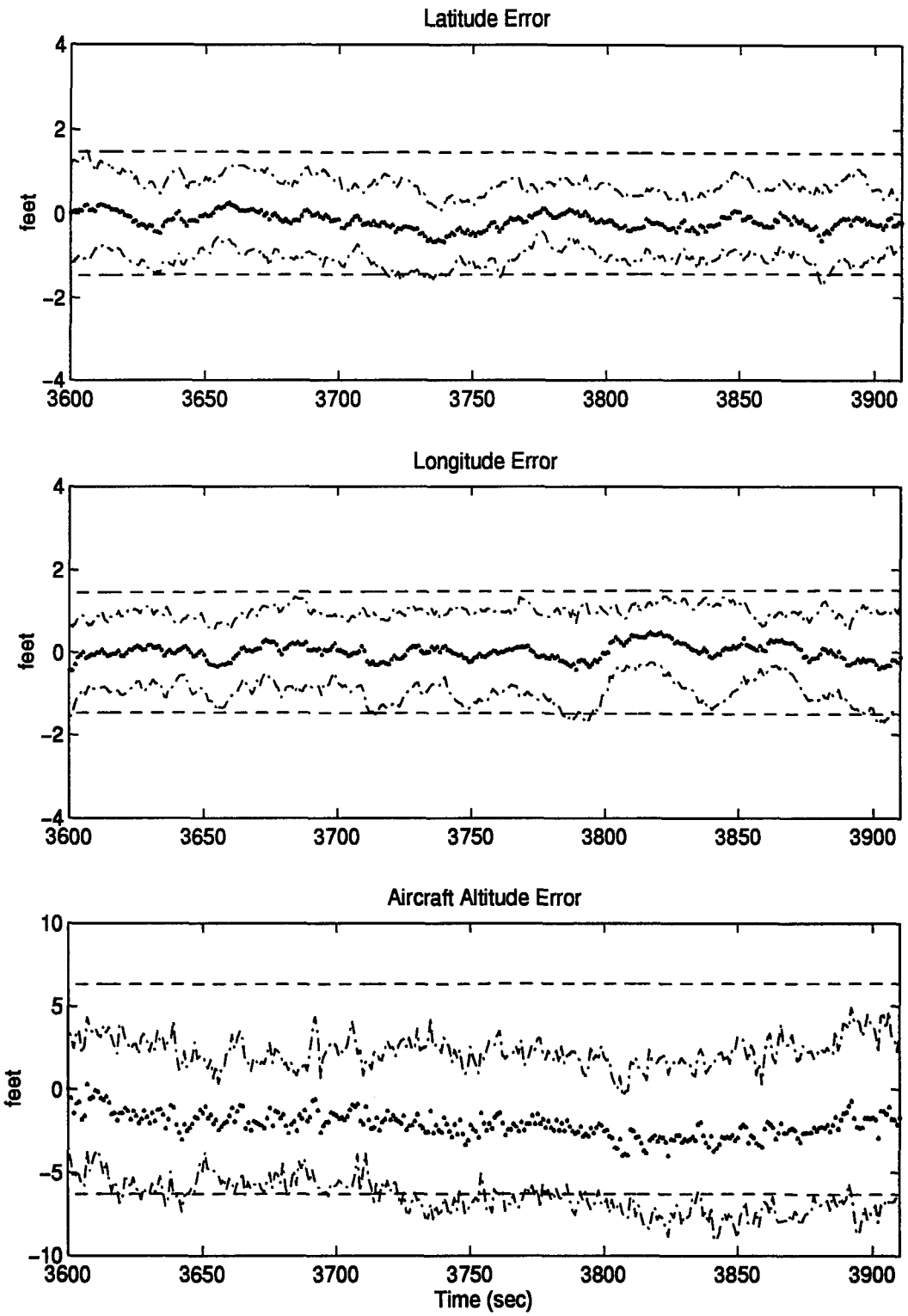

Figure F.15 Latitude, Longitude, and Aircraft Altitude Error

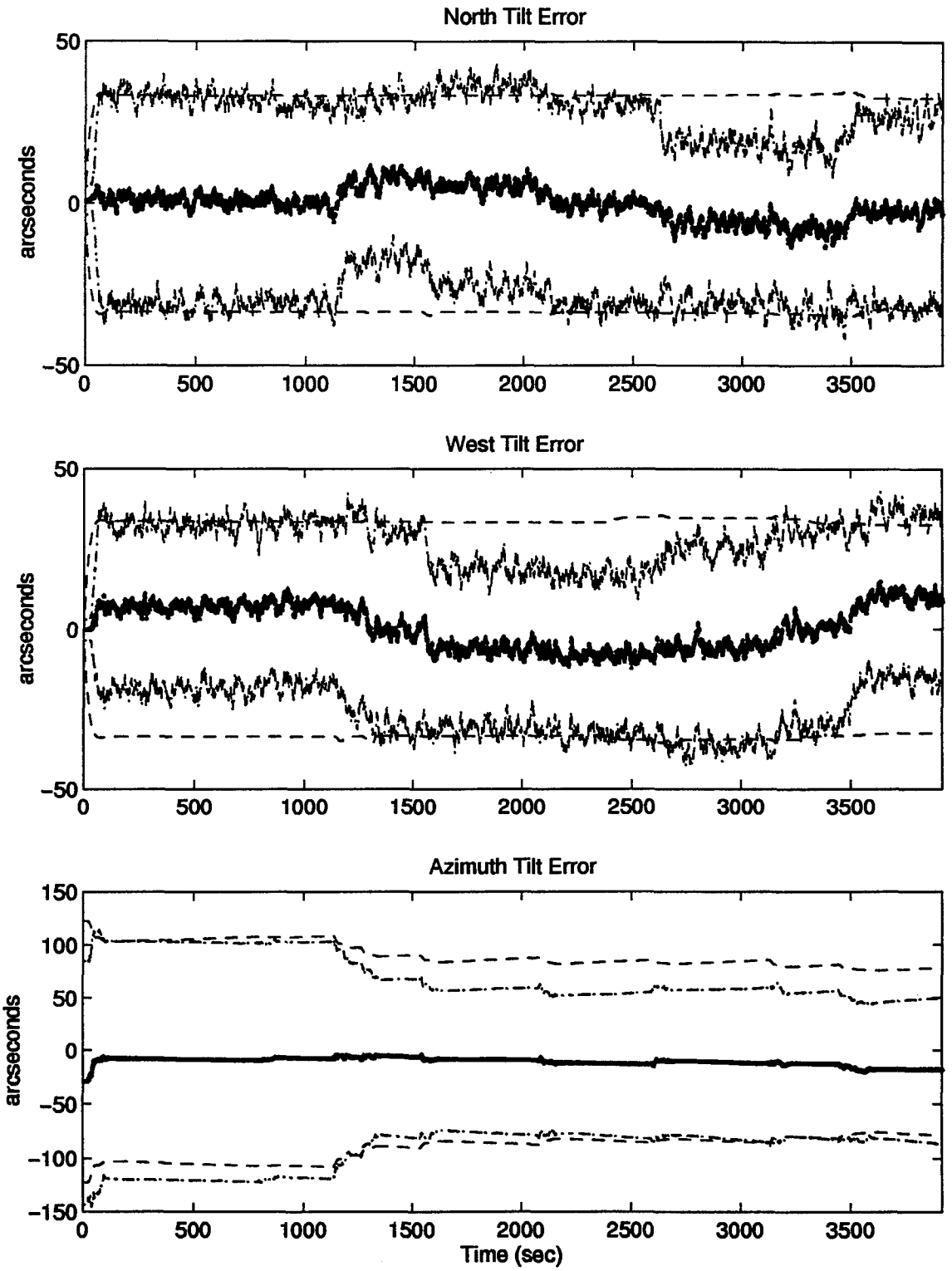

Figure F.16 North, West, and Azimuth Tilt Errors

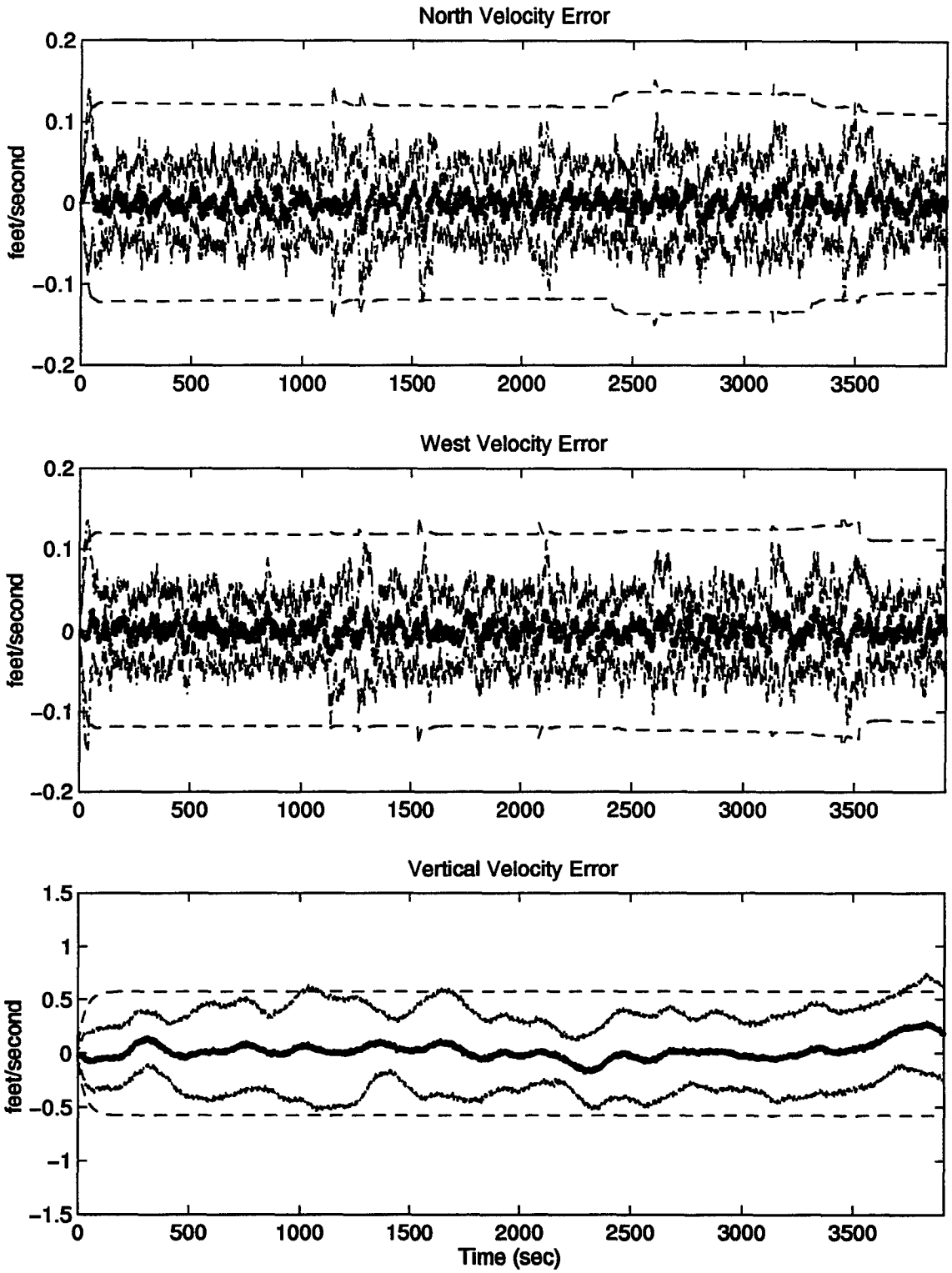

Figure F.17 North, West, and Vertical Velocity Errors

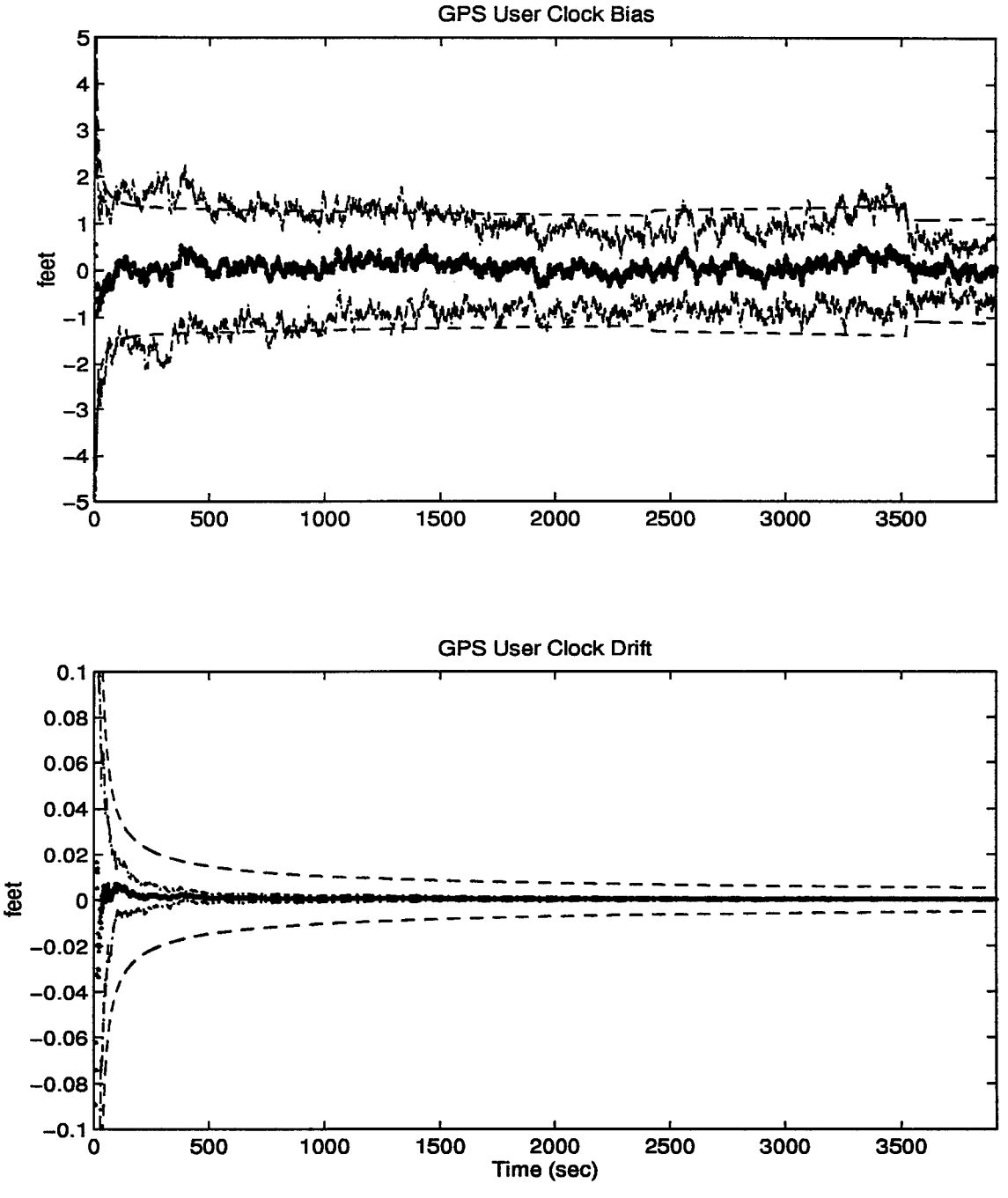

Figure F.18 GPS User Clock Bias and GPS User Clock Drift

F.4 Plots of Case X: Barometric Altimeter, 2.0 nm/hr INS, Radar Altimeter, Single Pseudolite, and DGPS Using the Single Engine Aircraft Flight Profile.

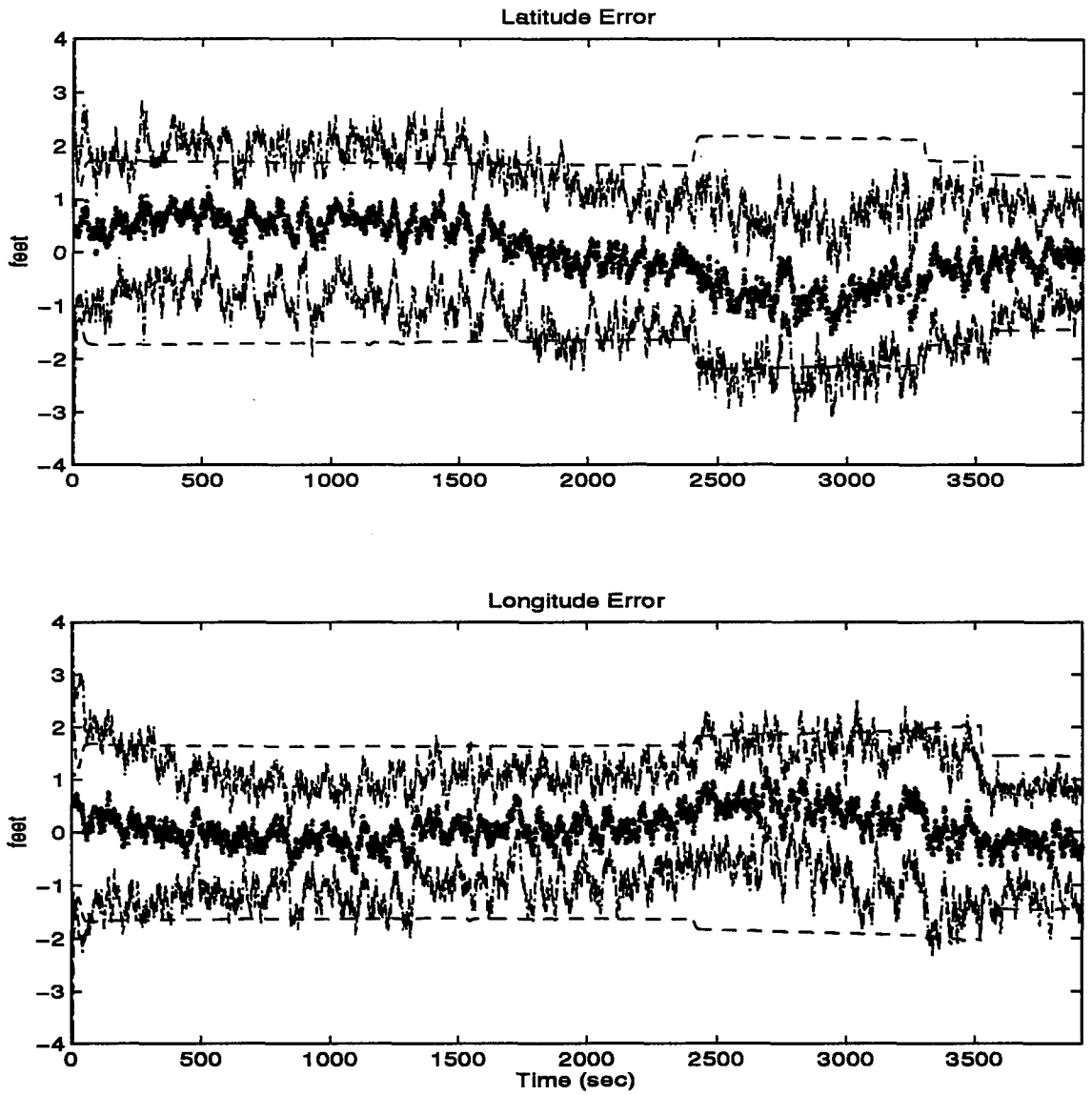

Figure F.19 Latitude and Longitude Error

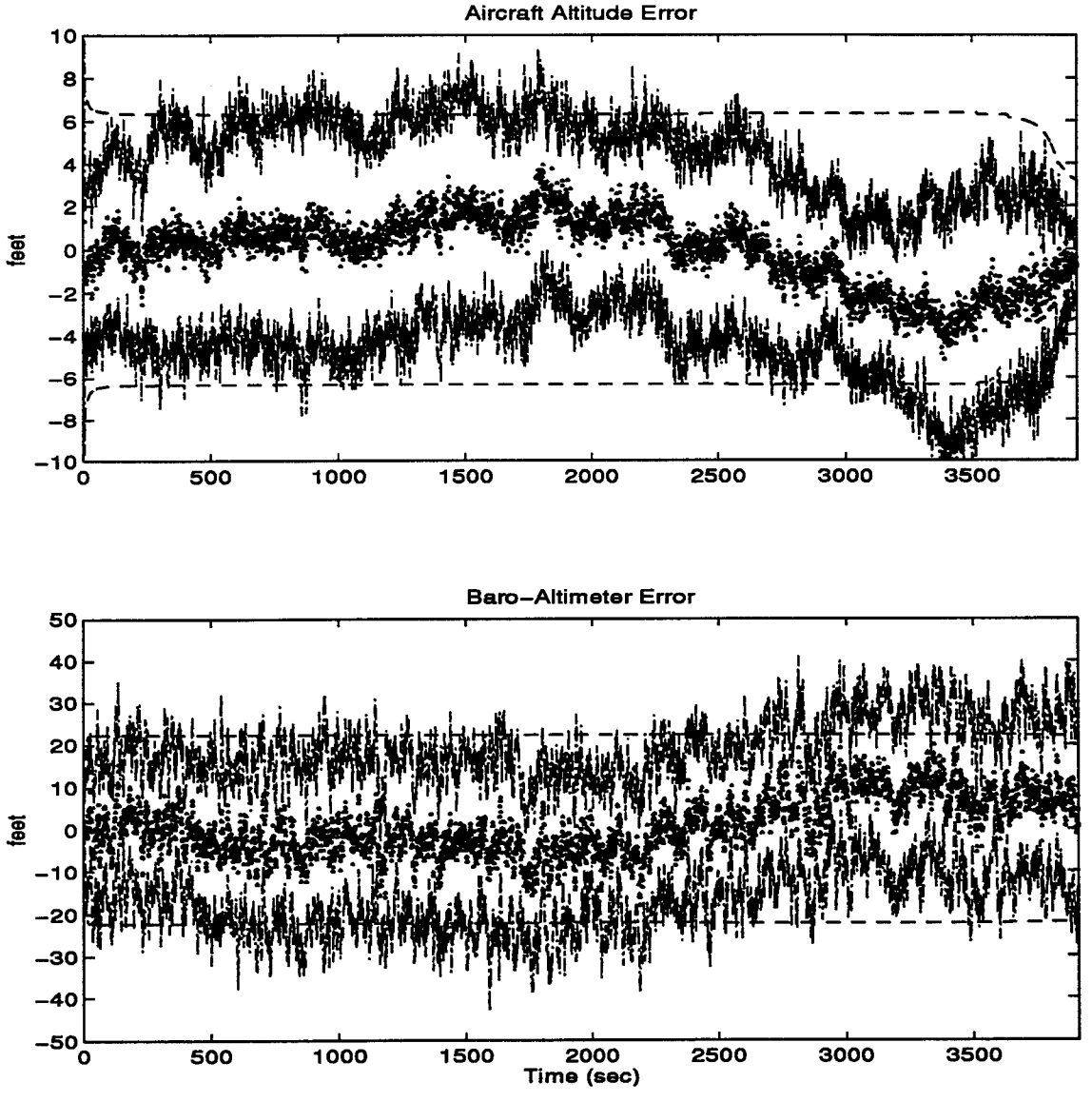

Figure F.20 Aircraft Altitude and Baro-Altimeter Error

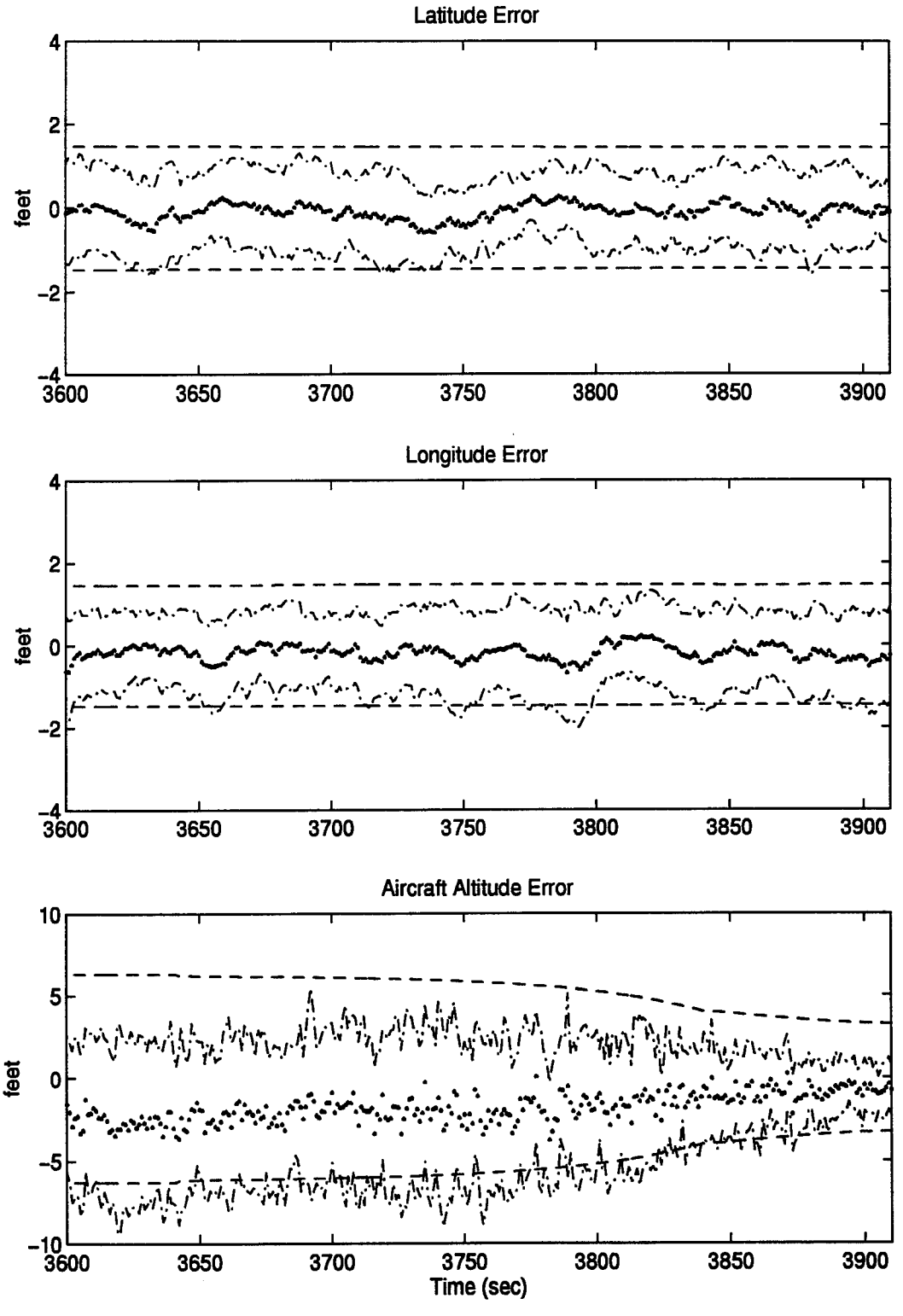

Figure F.21 Latitude, Longitude, and Aircraft Altitude Error

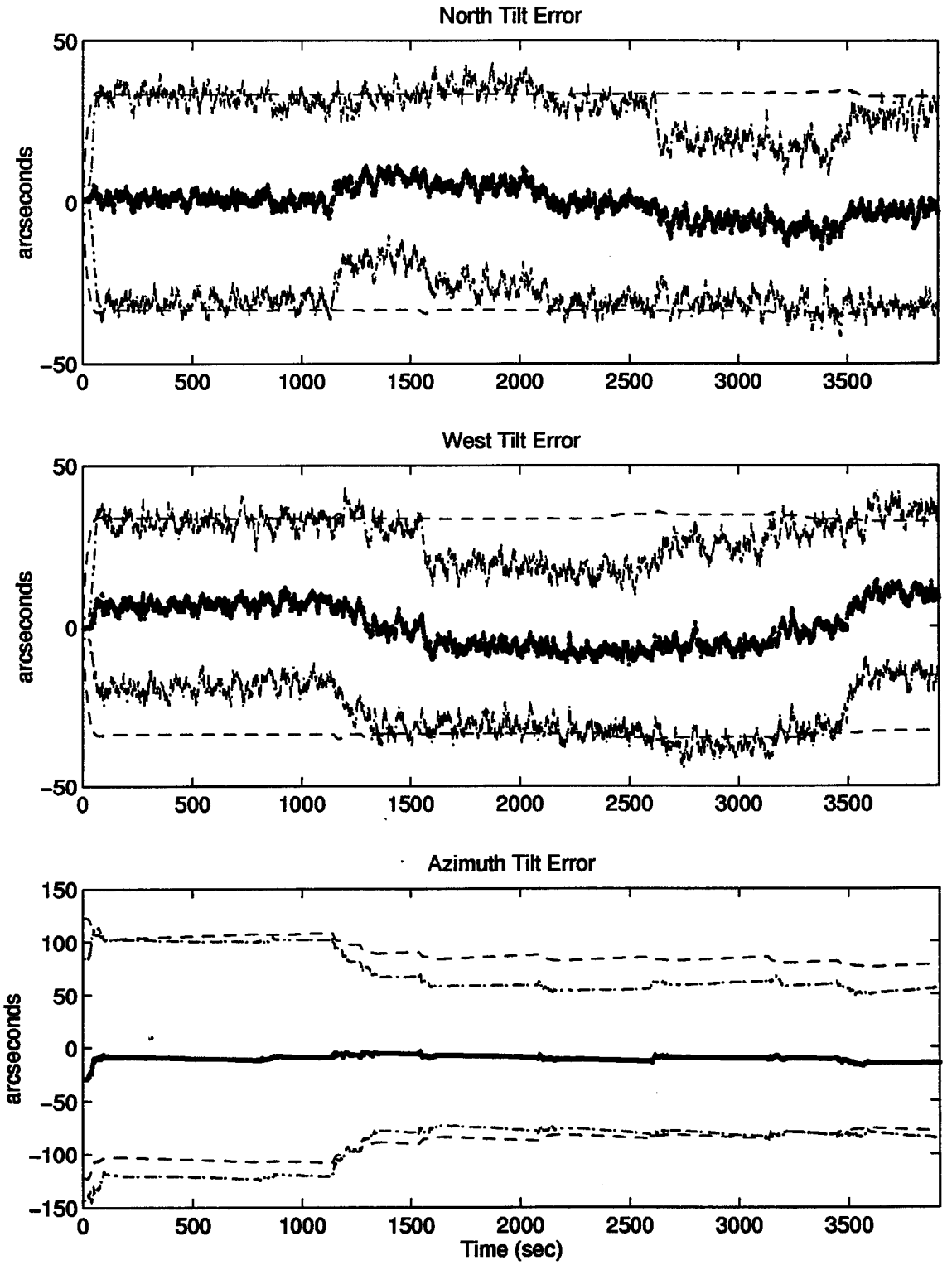

Figure F.22 North, West, and Azimuth Tilt Errors

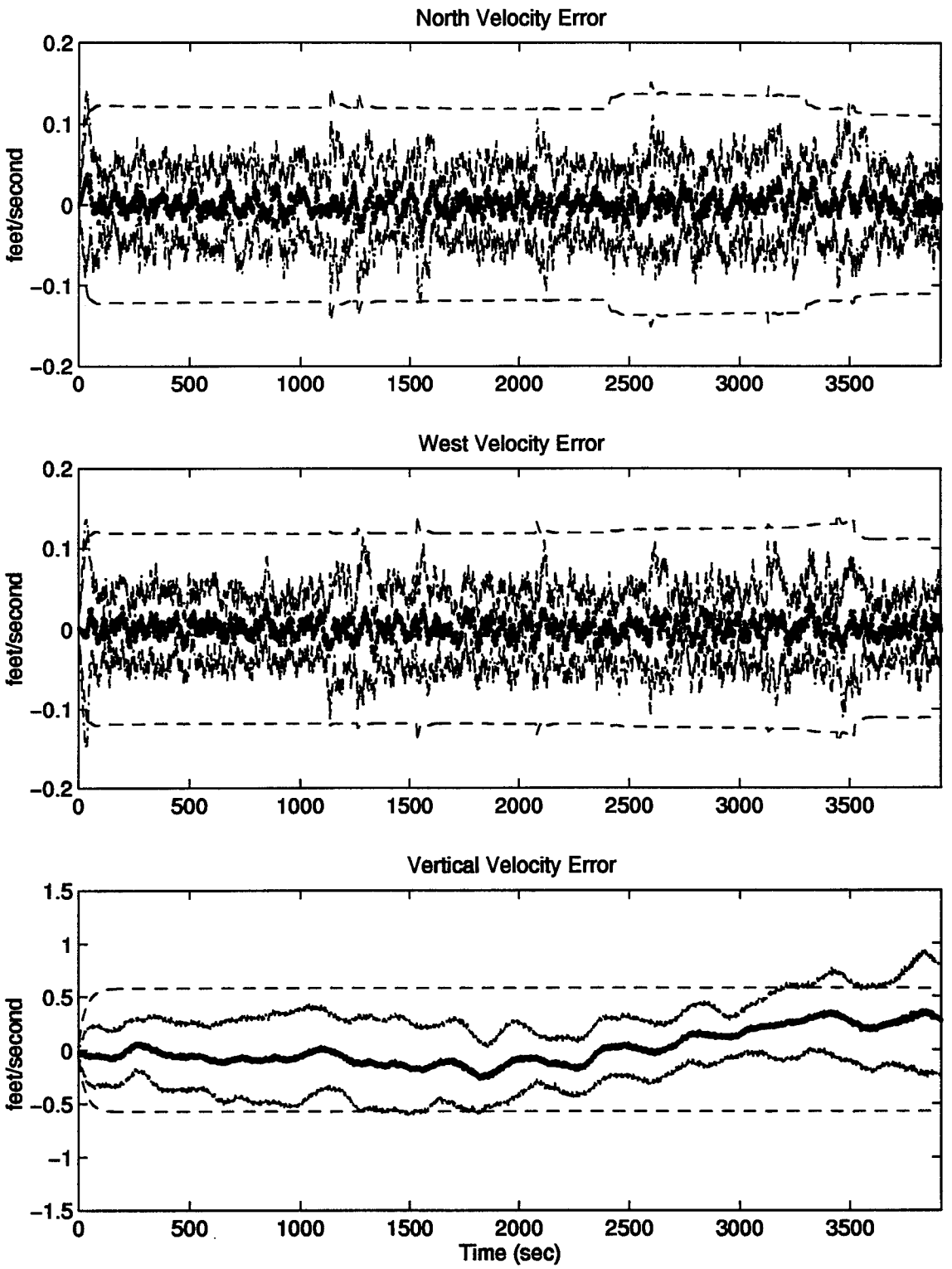

Figure F.23 North, West, and Vertical Velocity Errors

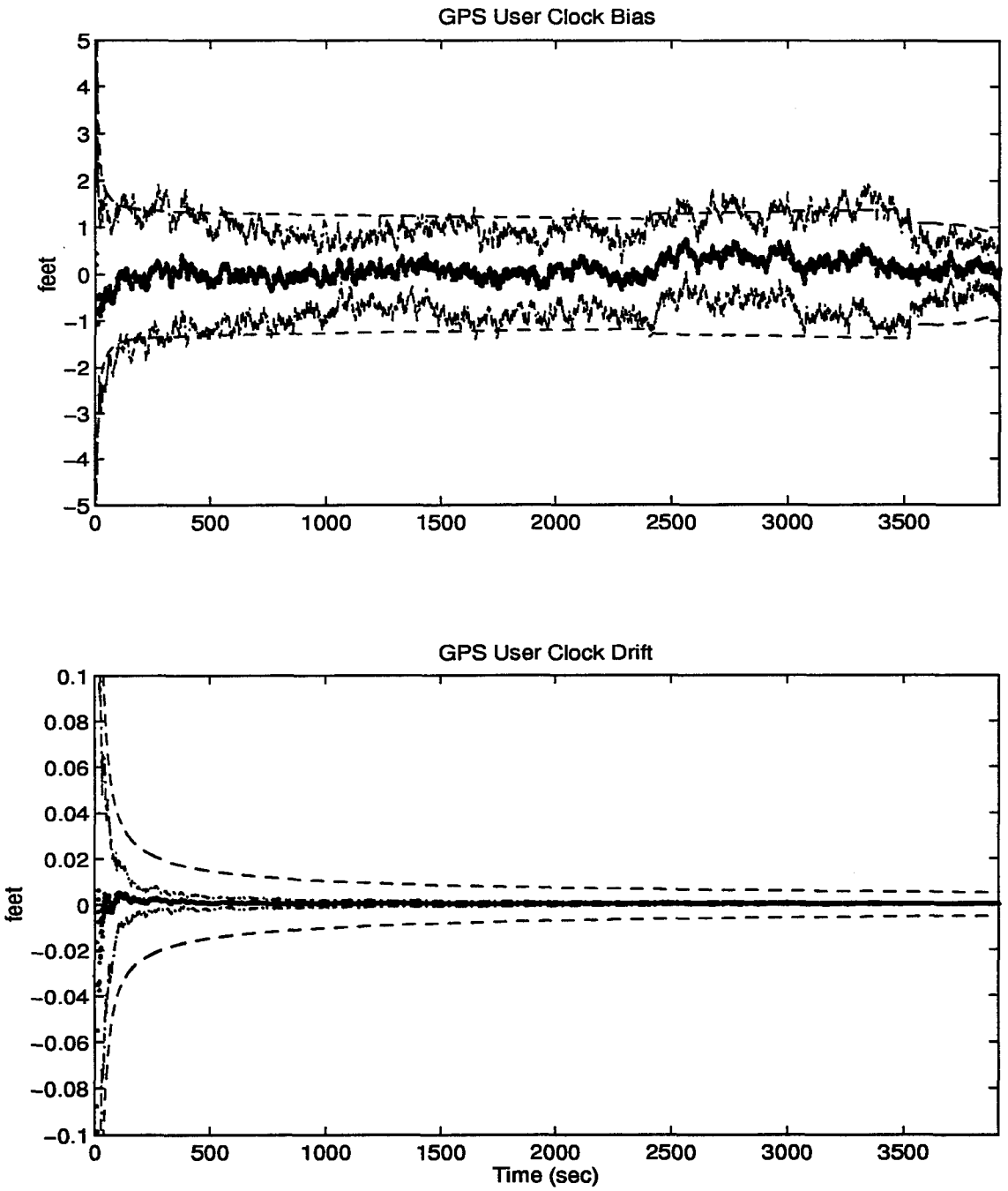

Figure F.24 GPS User Clock Bias and GPS User Clock Drift

F.5 Plots of Case XI: Barometric Altimeter, 4.0 nm/hr INS, Single Pseudolite, and DGPS Using the Single Engine Aircraft Flight Profile.

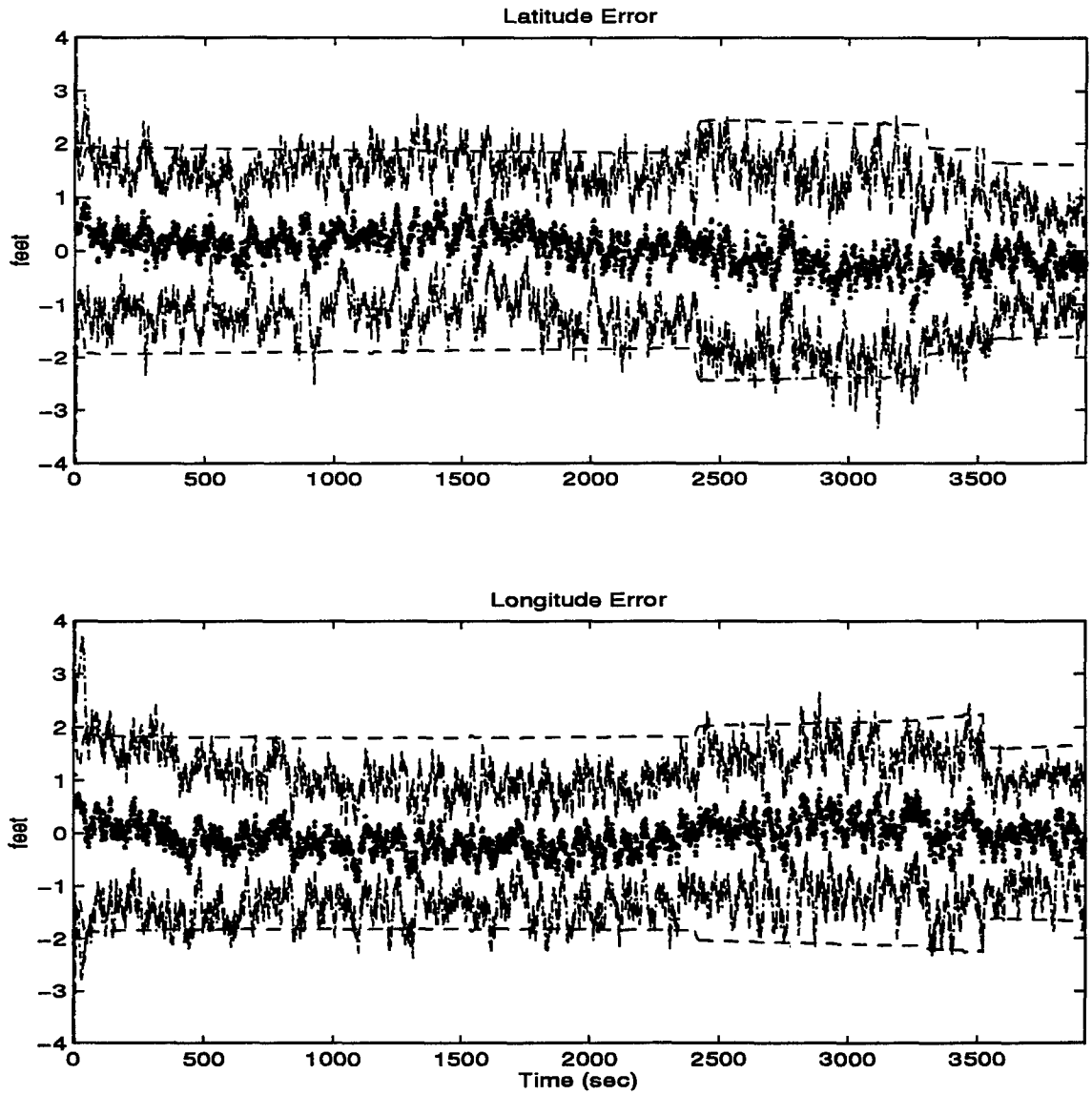

Figure F.25 Latitude and Longitude Error

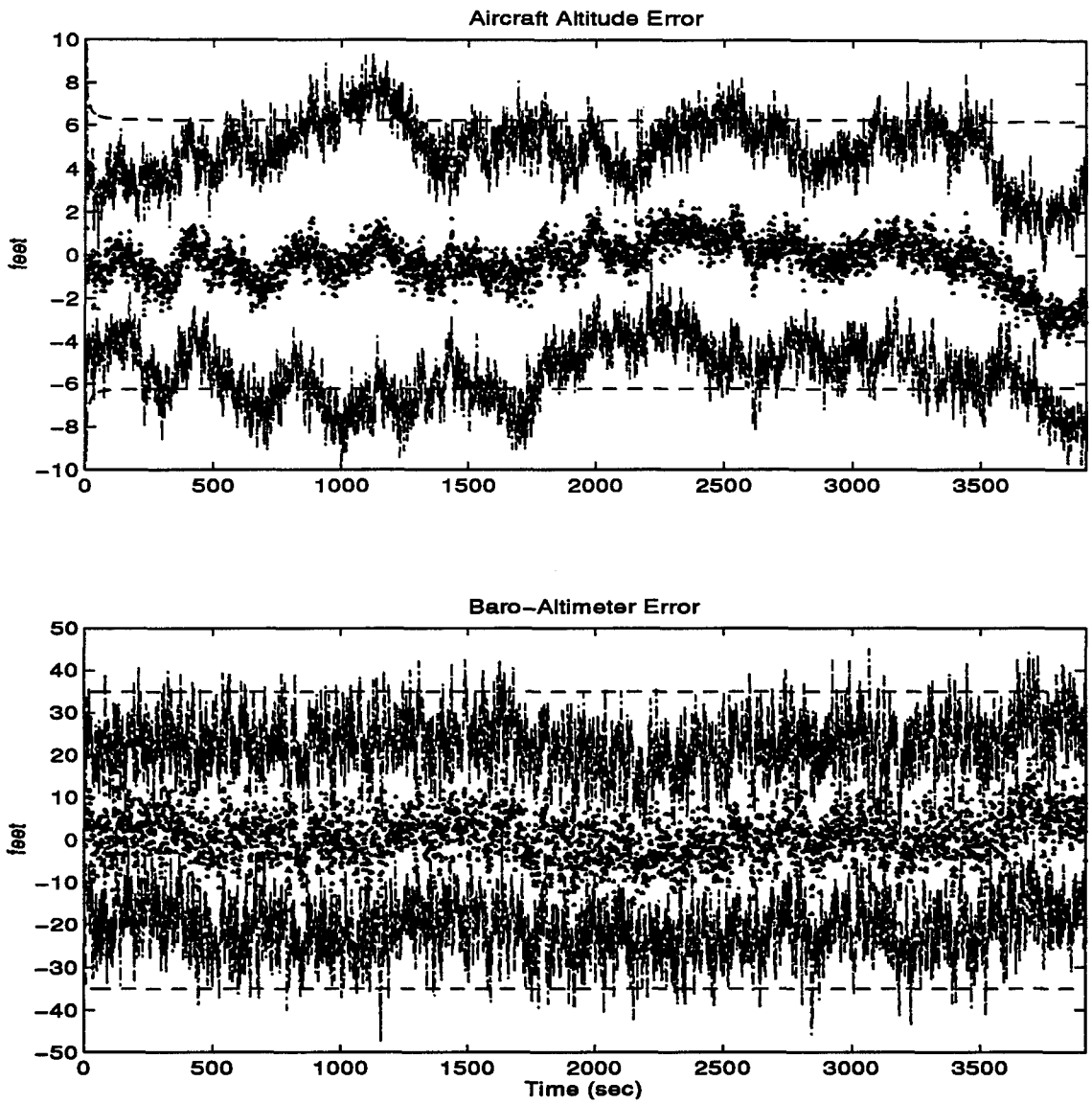

Figure F.26 Aircraft Altitude and Baro-Altimeter Error

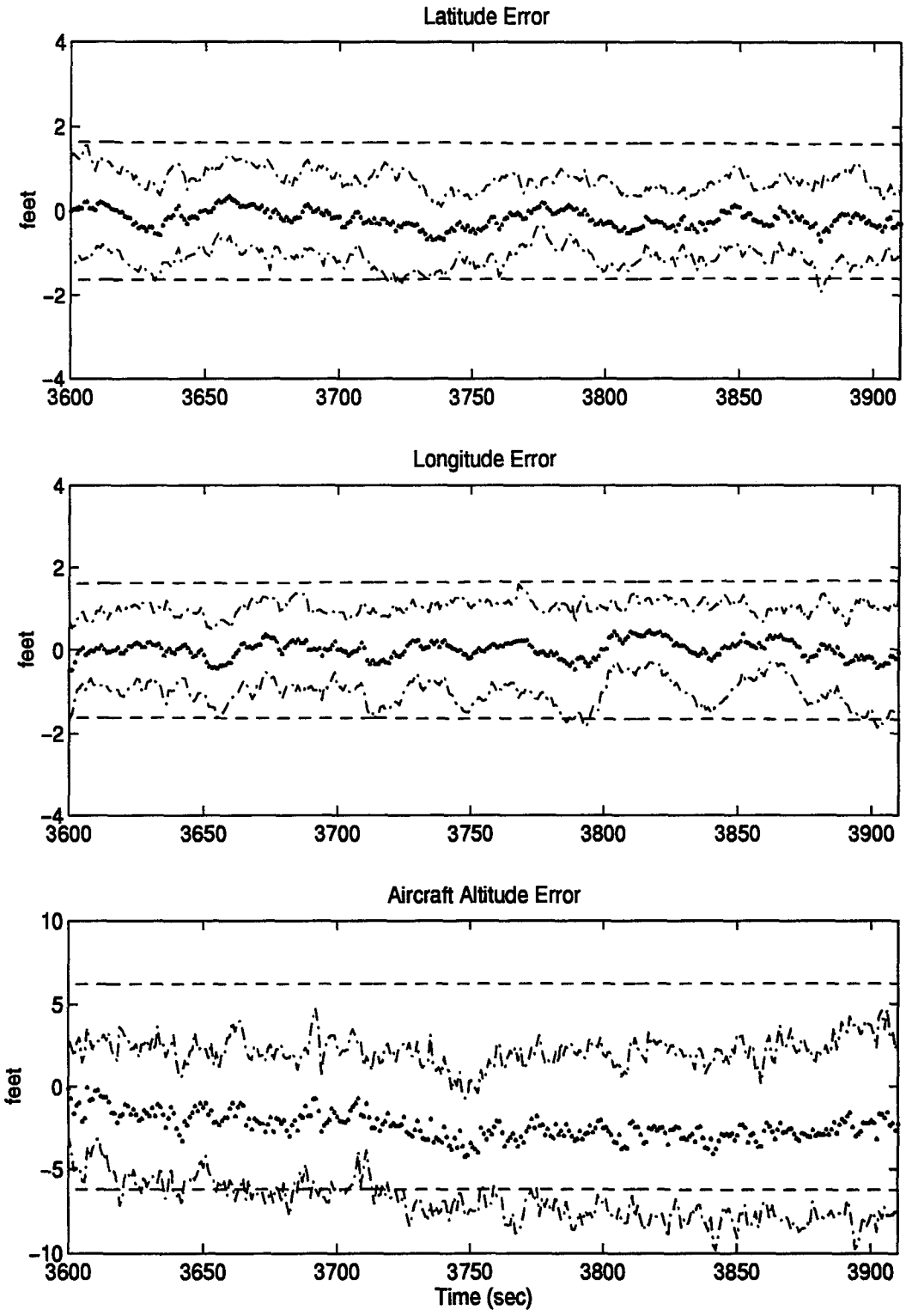

Figure F.27 Latitude, Longitude, and Aircraft Altitude Error

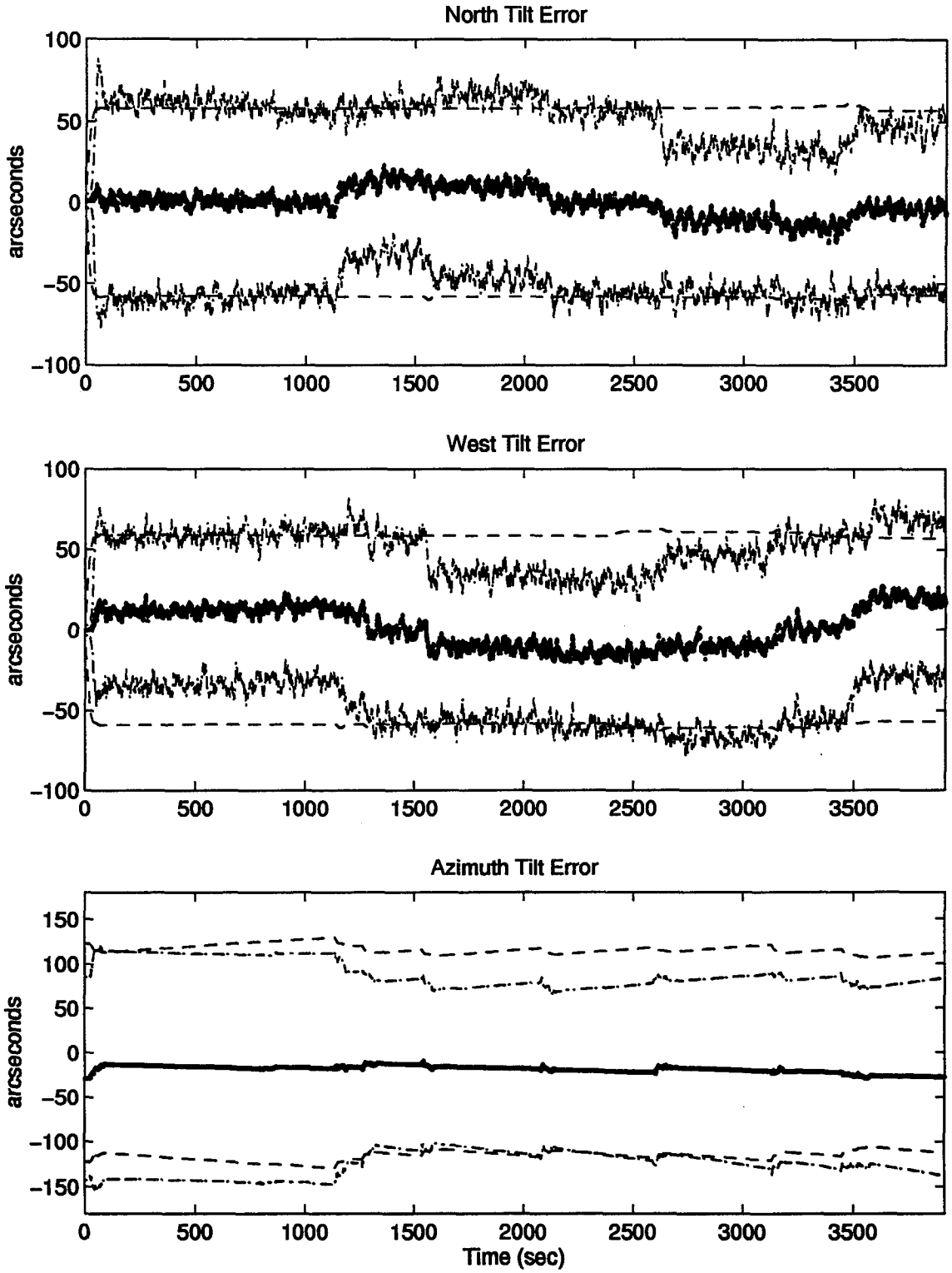

Figure F.28 North, West, and Azimuth Tilt Errors

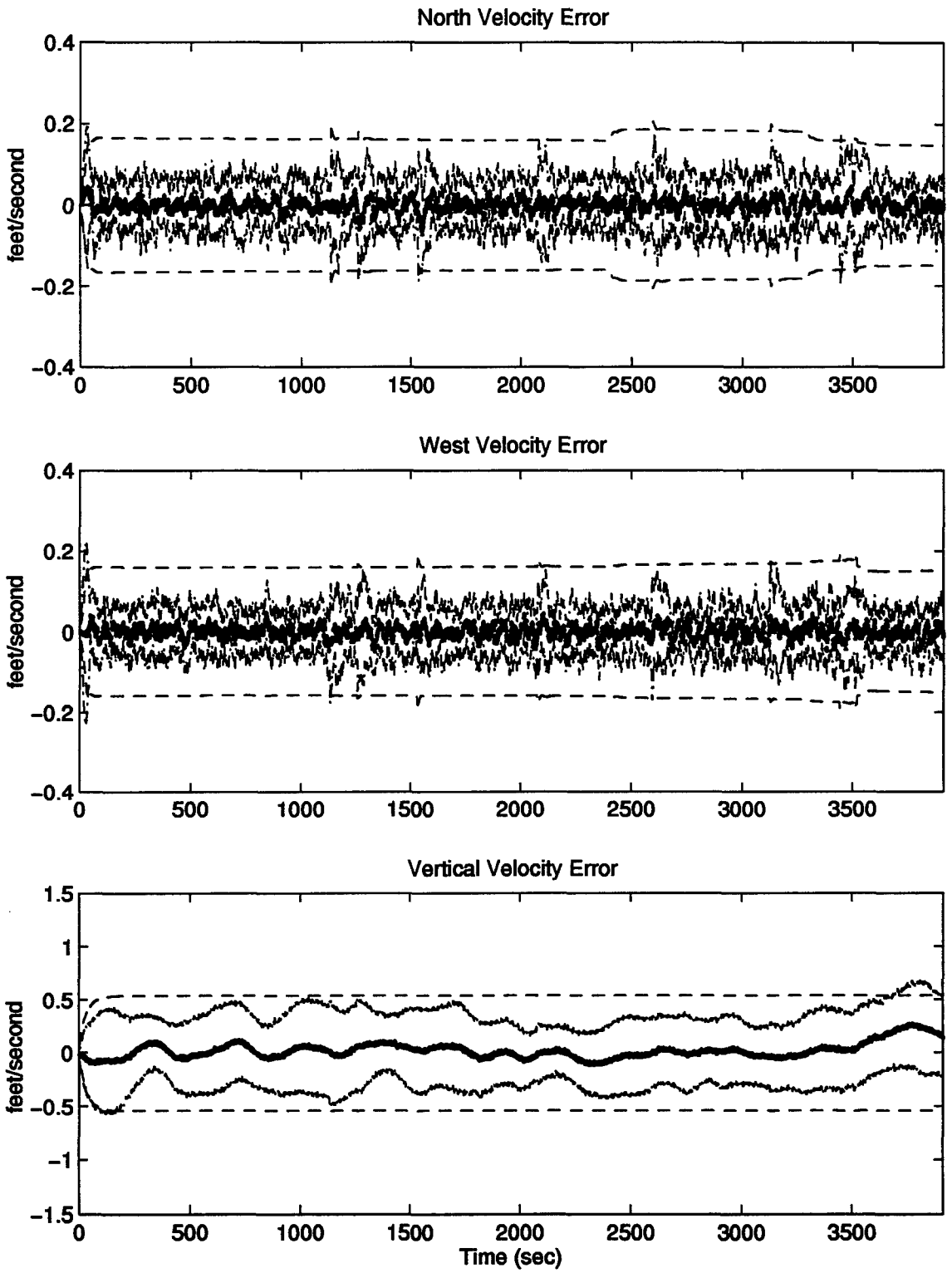

Figure F.29 North, West, and Vertical Velocity Errors

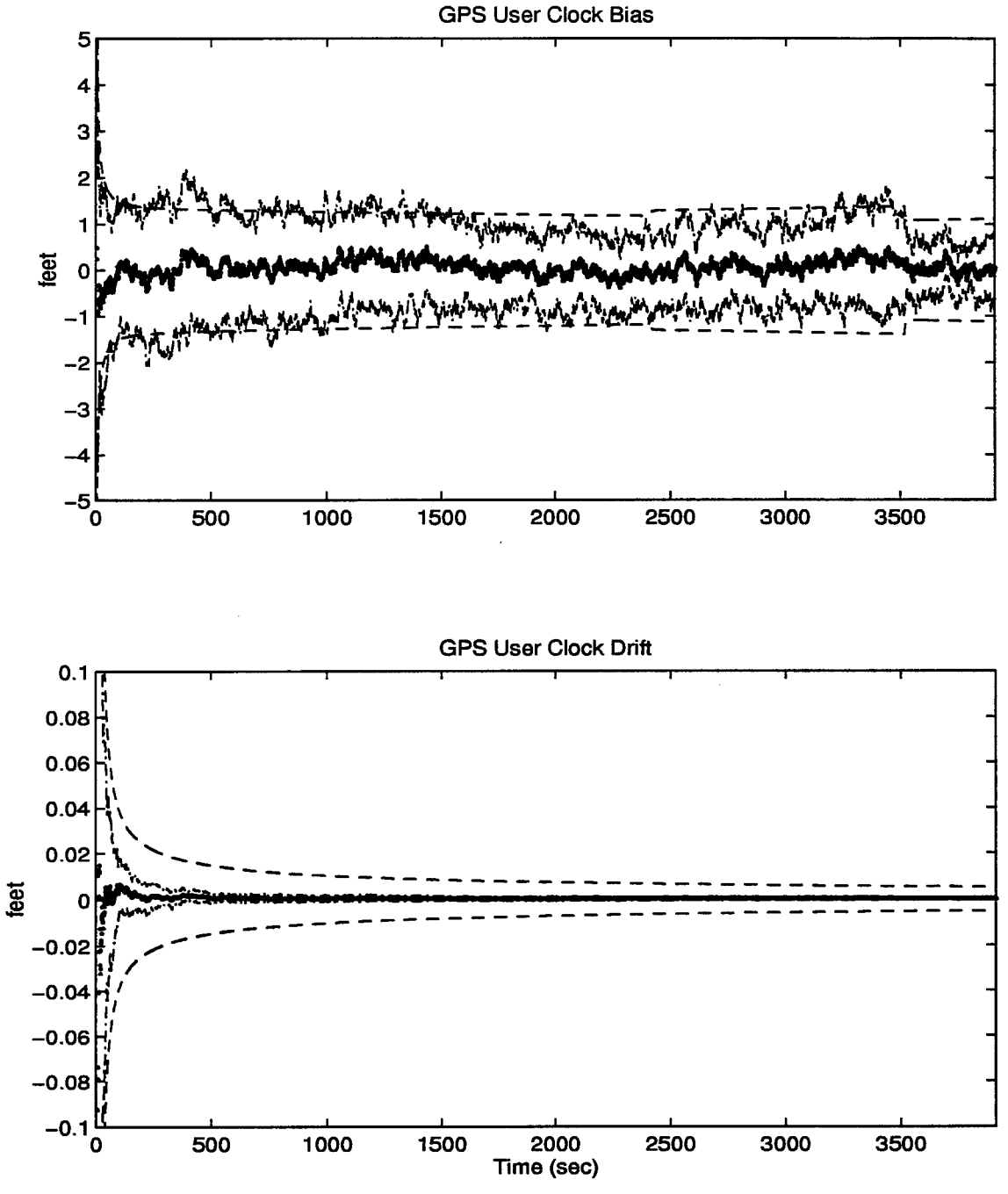

Figure F.30 GPS User Clock Bias and GPS User Clock Drift

F.6 Plots of Case XII: Barometric Altimeter, 4.0 nm/hr INS, Radar Altimeter, Single Pseudolite, and DGPS Using the Single Engine Aircraft Flight Profile.

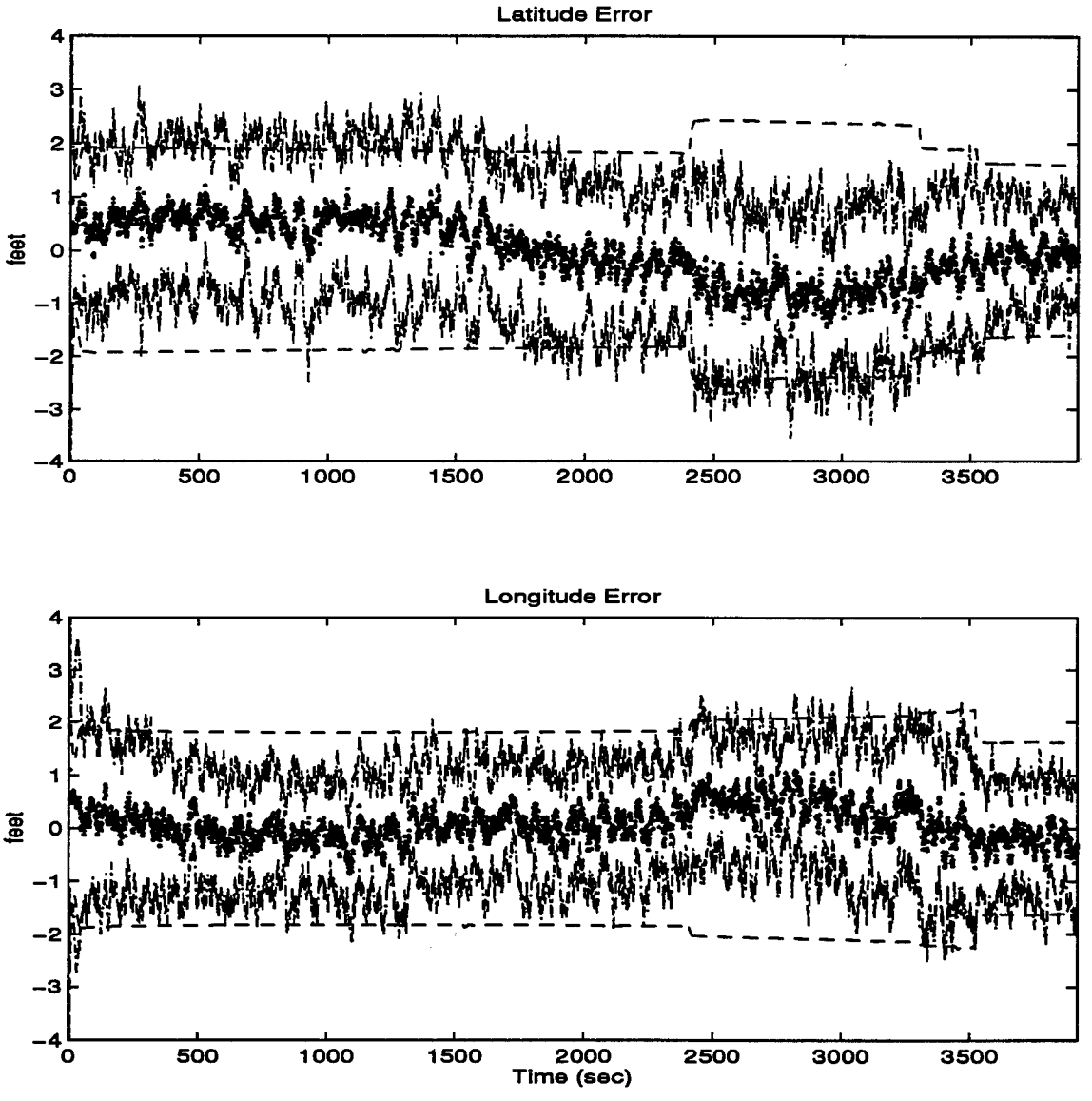

Figure F.31 Latitude and Longitude Error

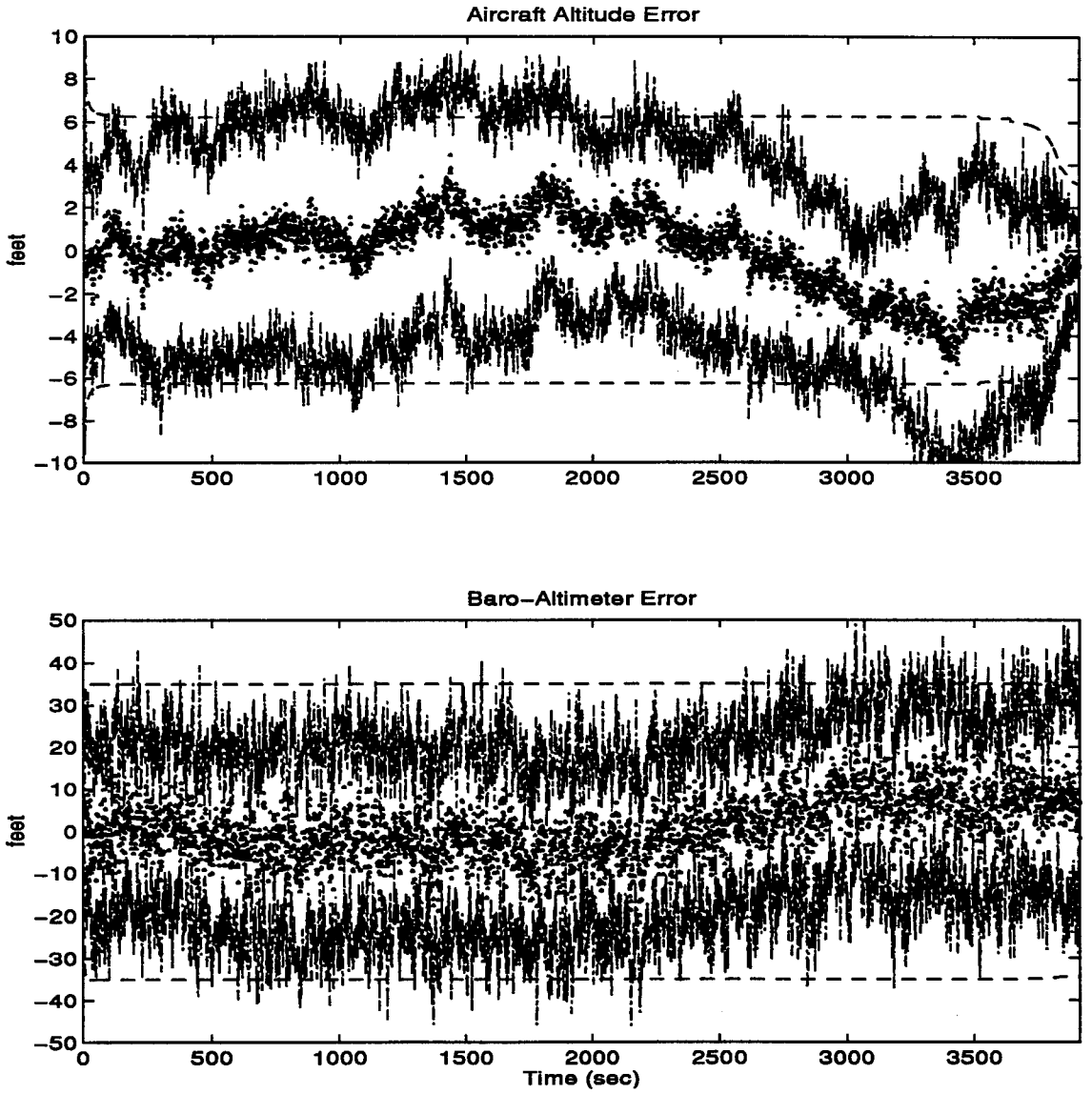

Figure F.32 Aircraft Altitude and Baro-Altimeter Error

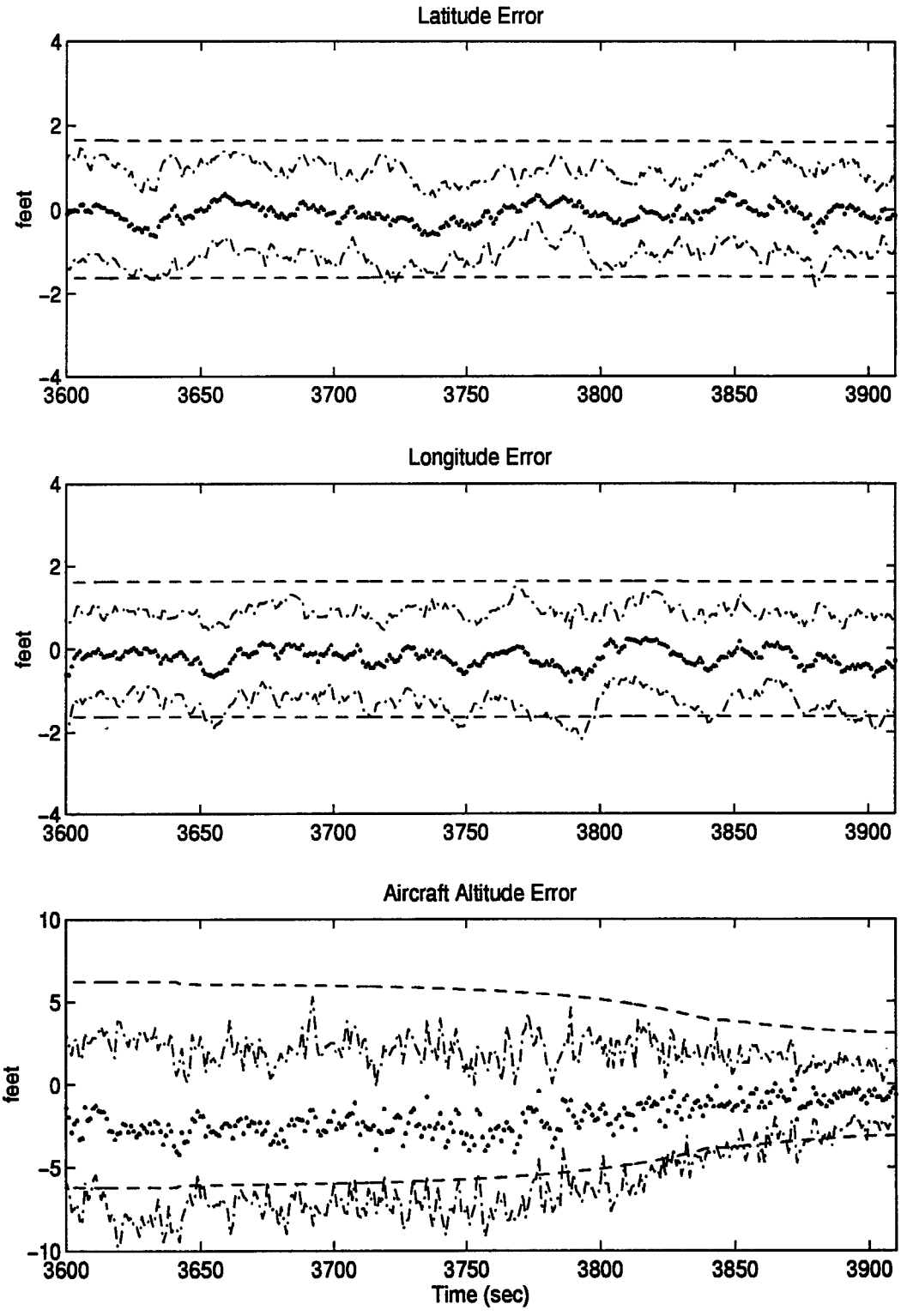

Figure F.33 Latitude, Longitude, and Aircraft Altitude Error

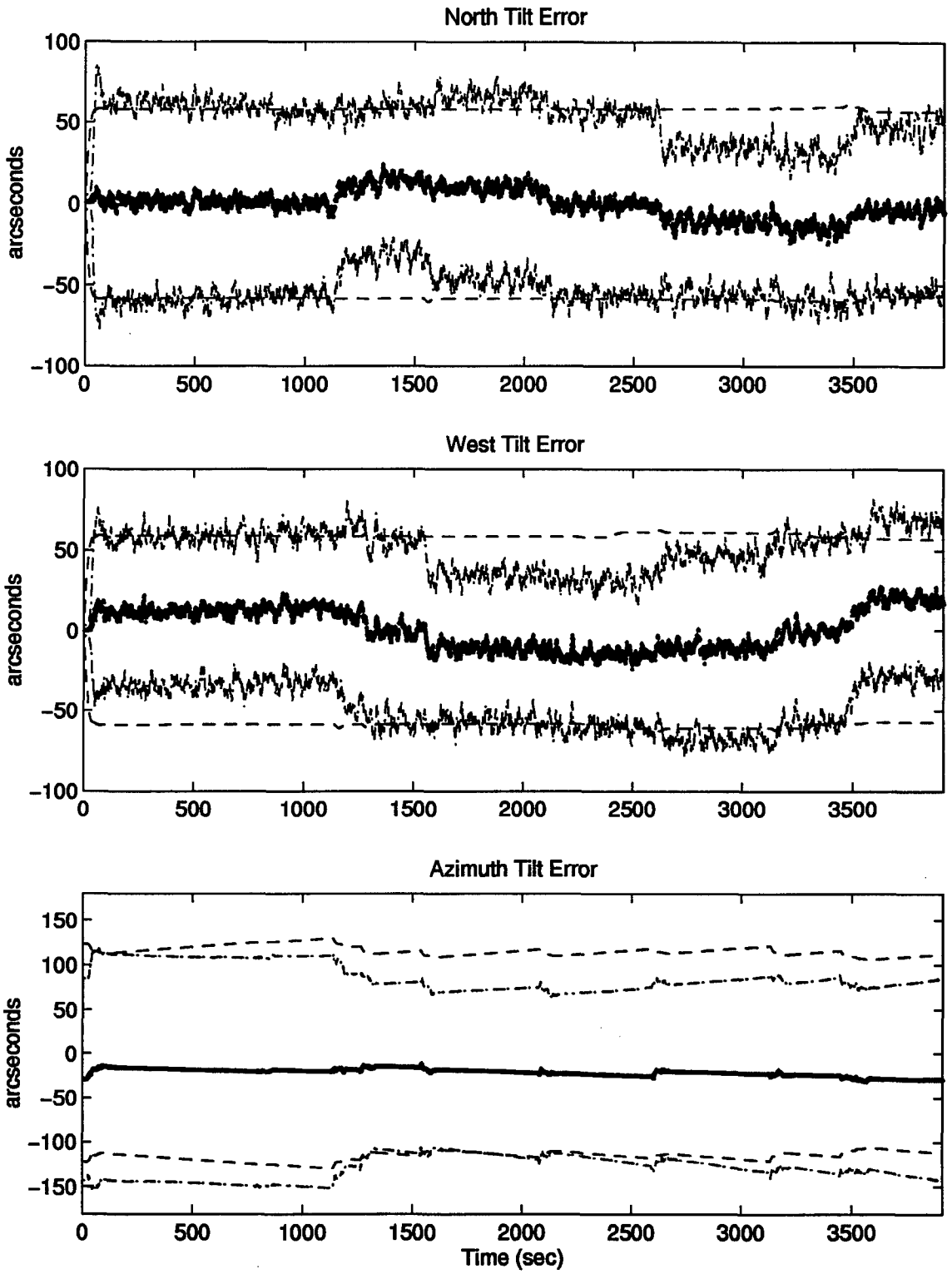

Figure F.34 North, West, and Azimuth Tilt Errors

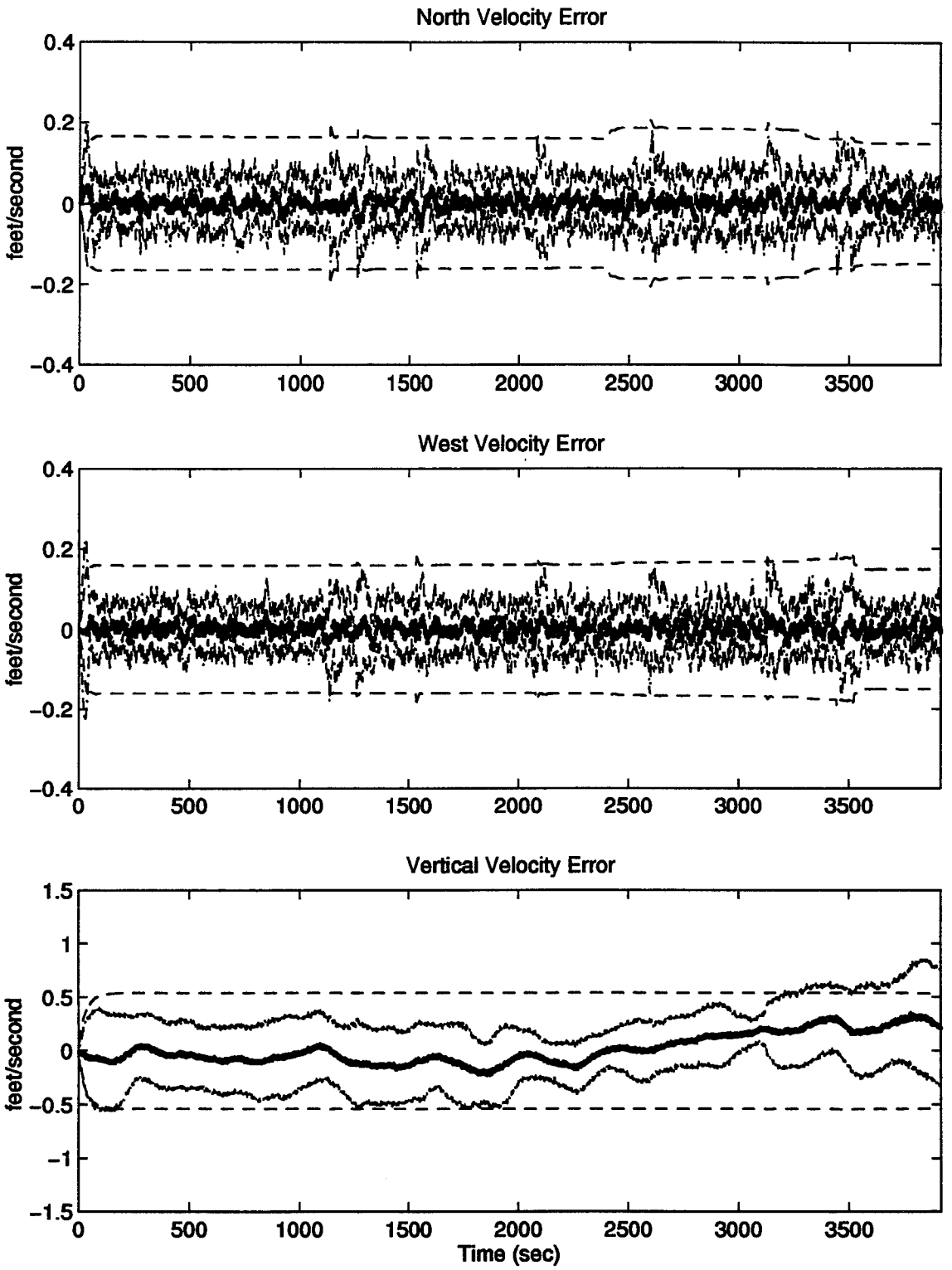

Figure F.35 North, West, and Vertical Velocity Errors

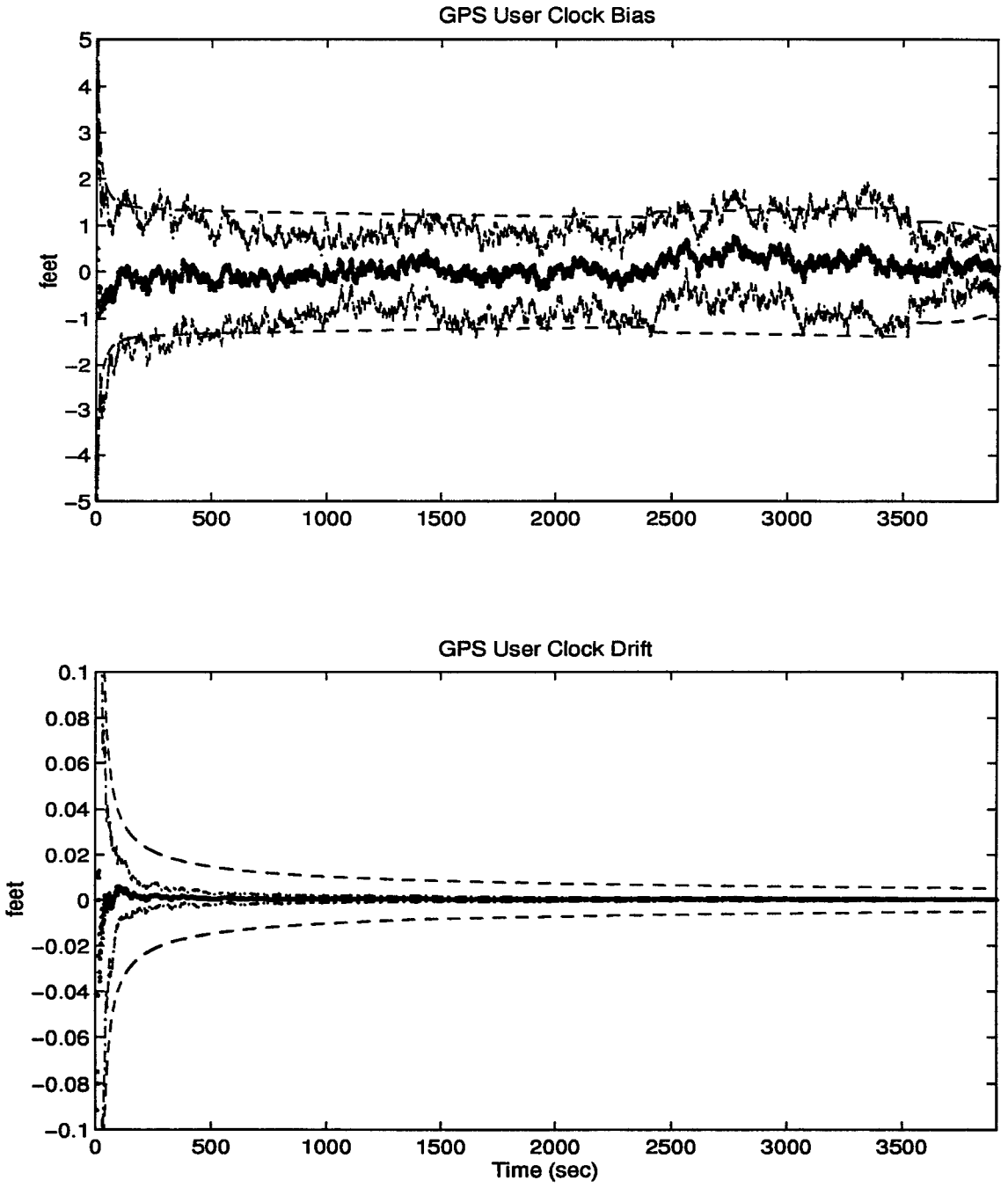

Figure F.36 GPS User Clock Bias and GPS User Clock Drift

Appendix G.

Plots of Case XIII, Case XIV, and Case XV for Single Engine Aircraft Flight Profile. These Cases Present DGPS Measurement Failure in Case I, Case III, and Case V.

Plot Legend

$\cdots$ true error (mean error $\pm$ σ_{true})

- - - filter predicted error ($0 \pm \sigma_{filter}$)

— mean error

G.1 Plots of Case XIII: Barometric Altimeter, 0.4 nm/hr INS, and DGPS Using the Single Engine Aircraft Flight Profile.

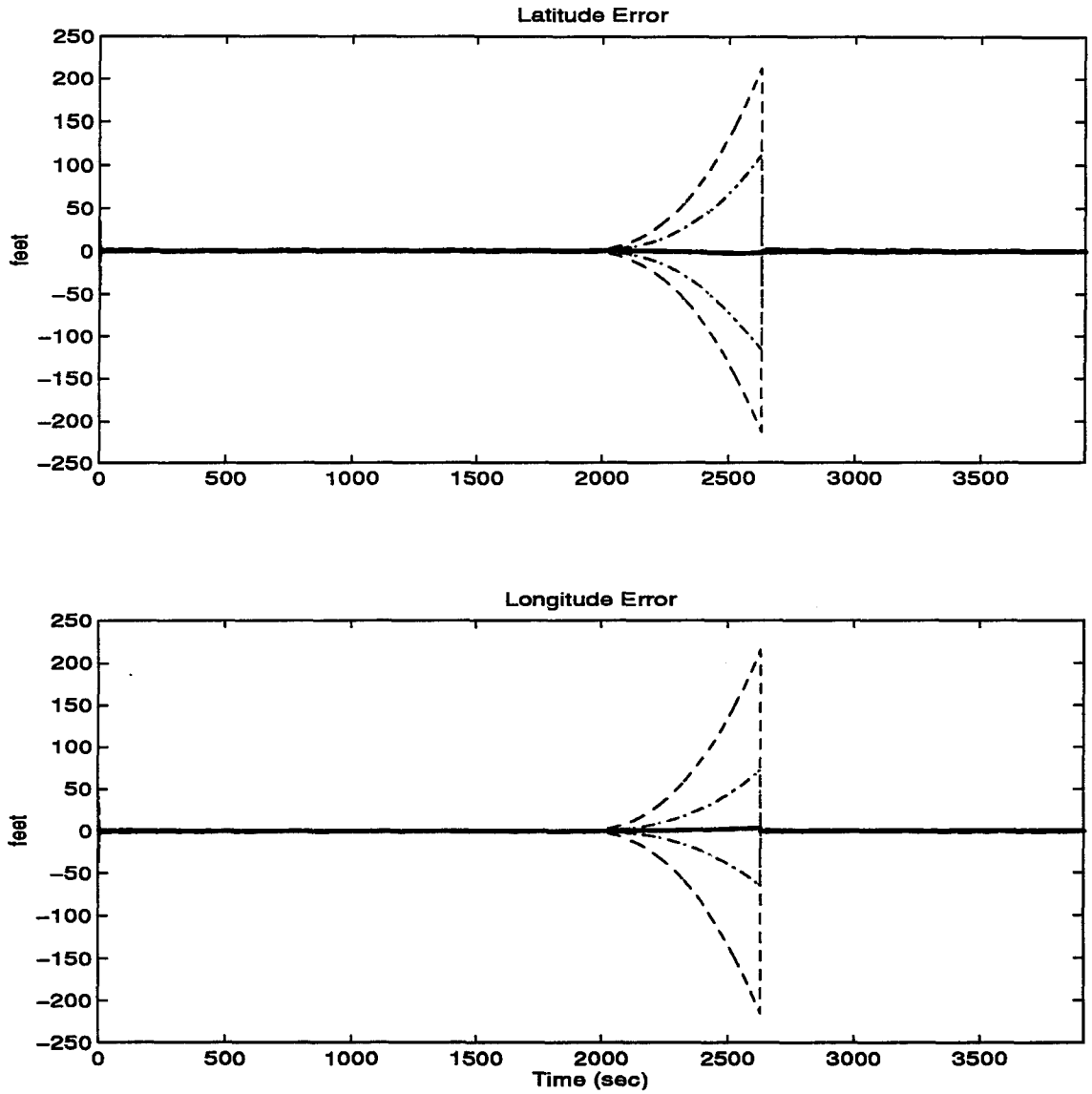

Figure G.1 Latitude and Longitude Error

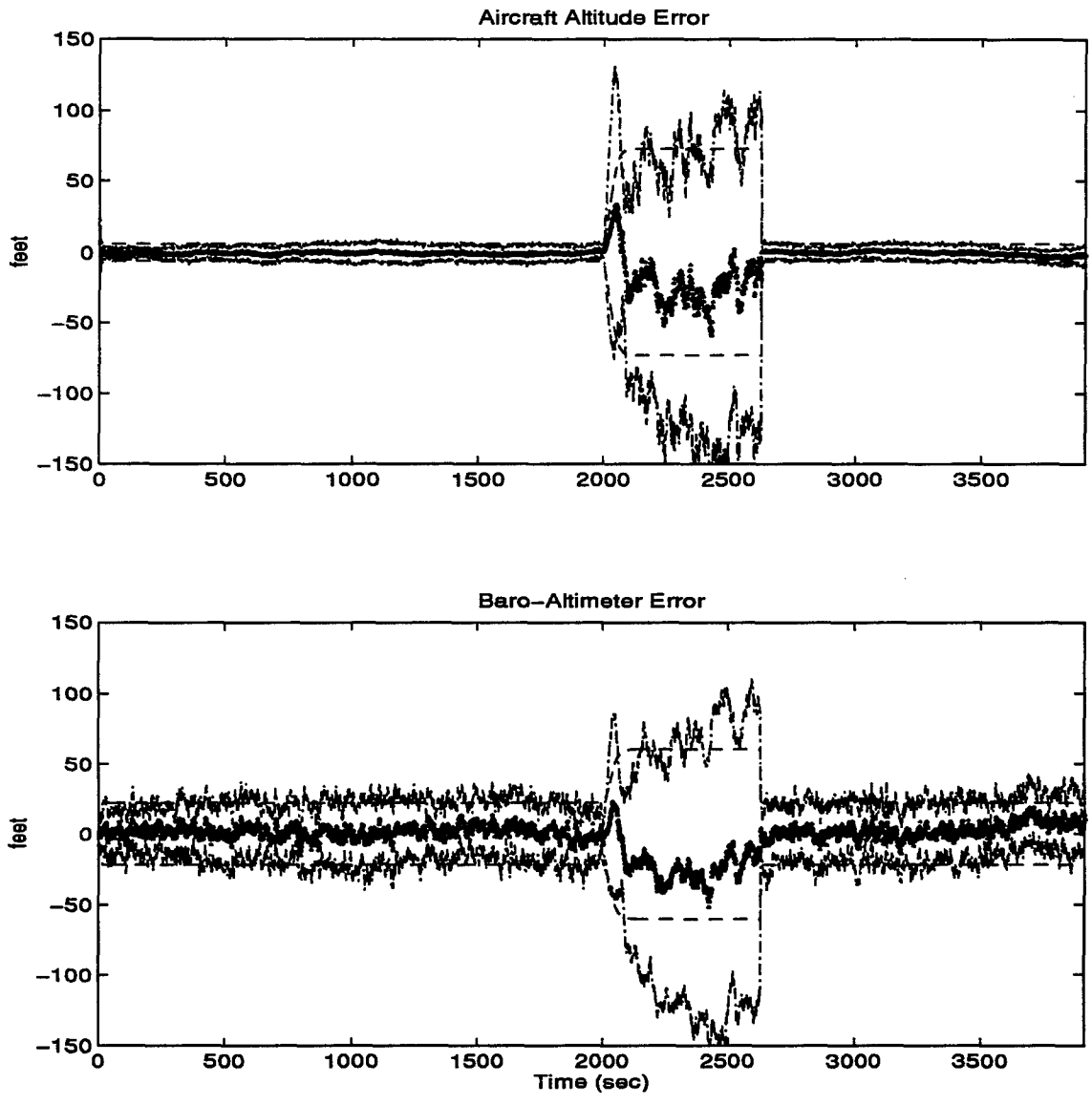

Figure G.2 Aircraft Altitude and Baro-Altimeter Error

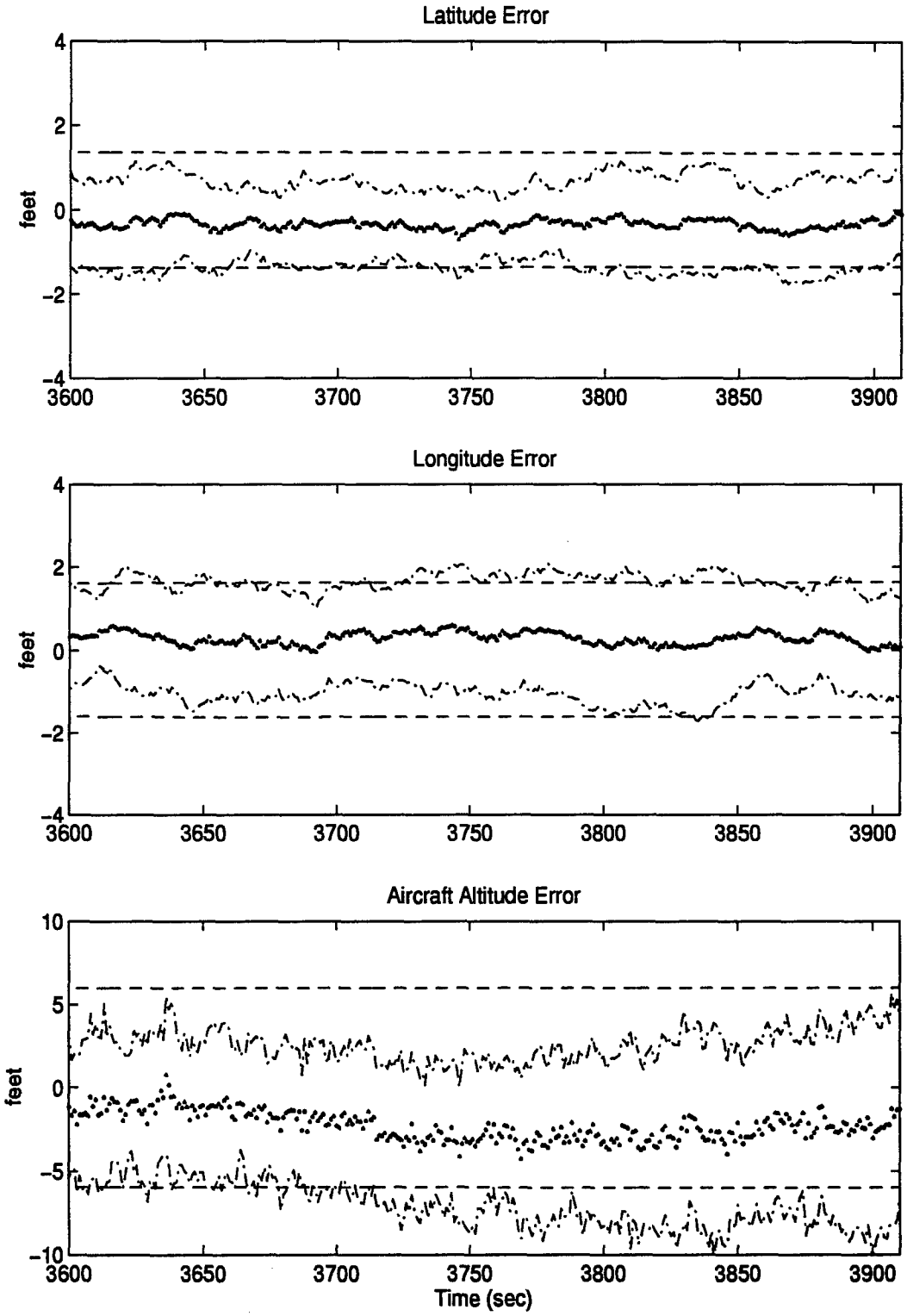

Figure G.3 Latitude, Longitude, and Aircraft Altitude Error

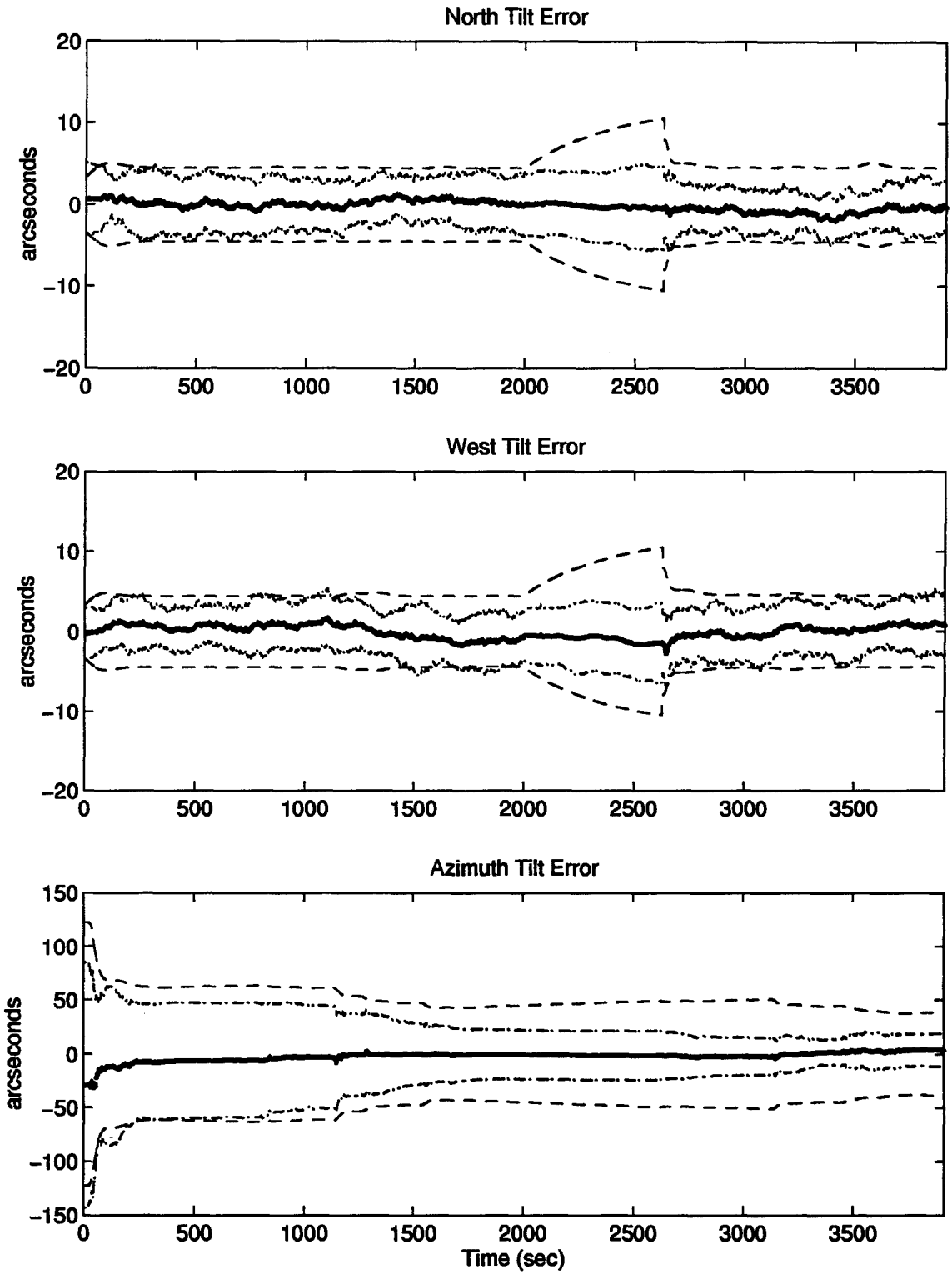

Figure G.4 North, West, and Azimuth Tilt Errors

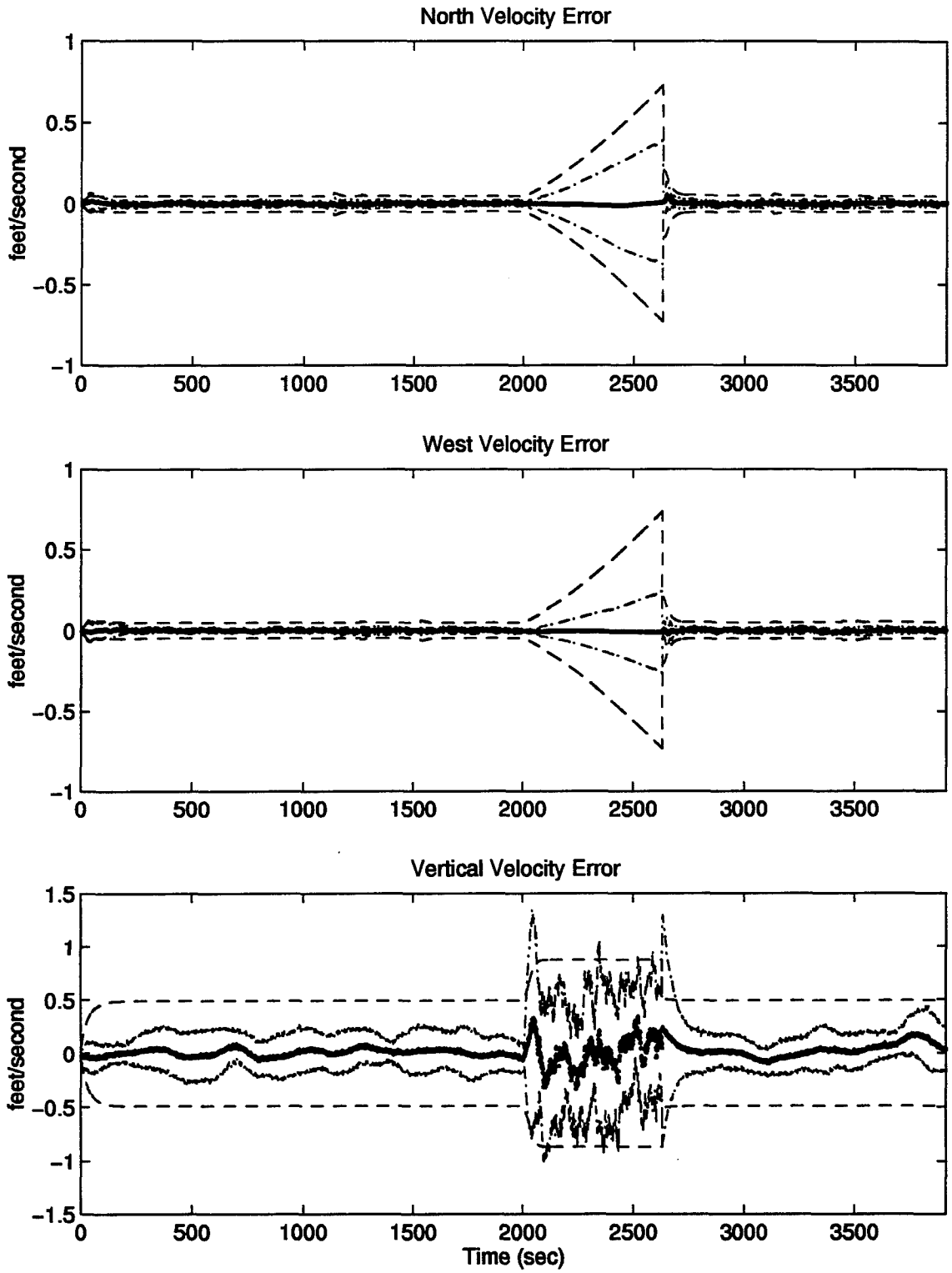

Figure G.5 North, West, and Vertical Velocity Errors

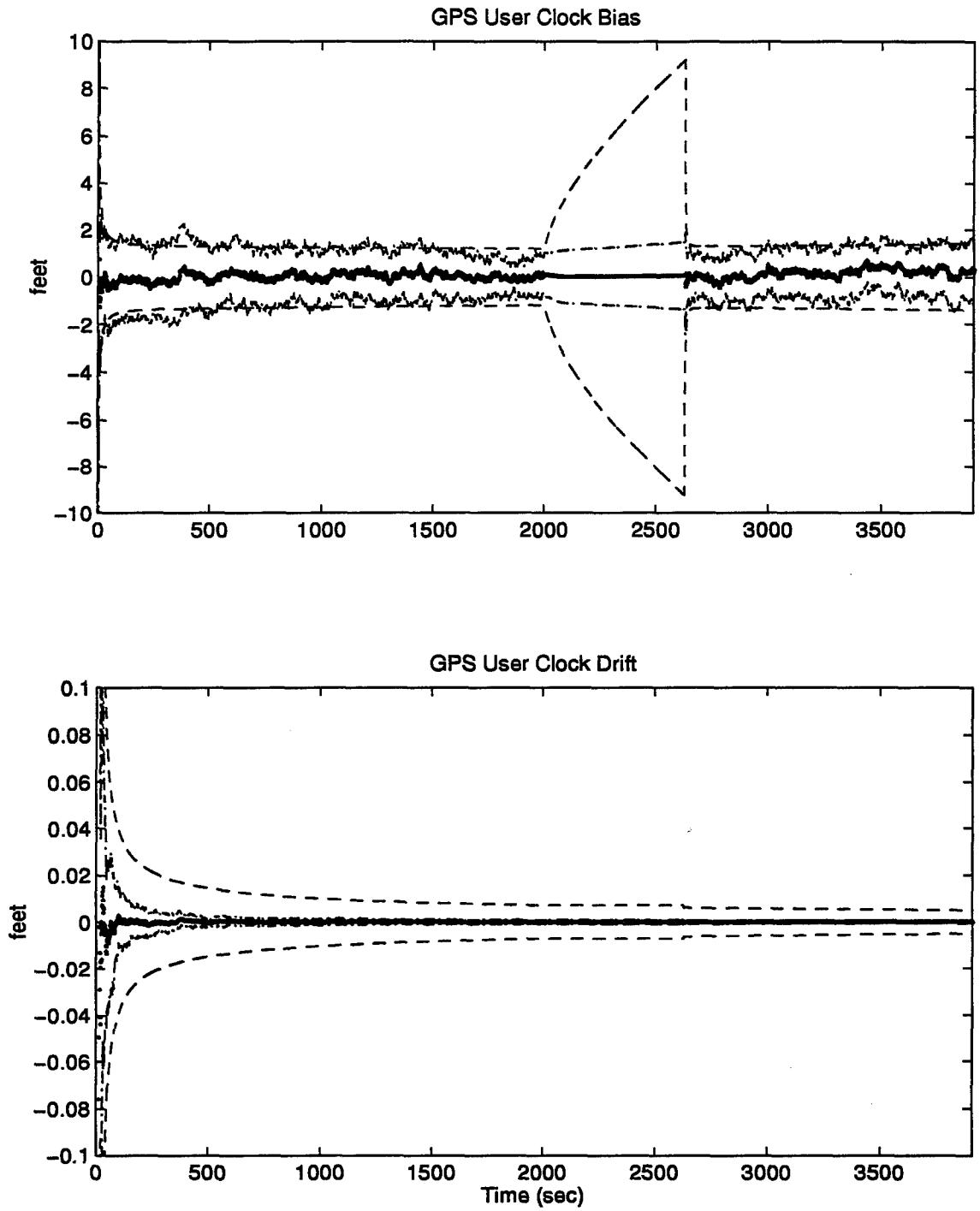

Figure G.6 GPS User Clock Bias and GPS User Clock Drift

G.2 Plots of Case XIV: Barometric Altimeter, 2.0 nm/hr INS, and DGPS Using the Single Engine Aircraft Flight Profile.

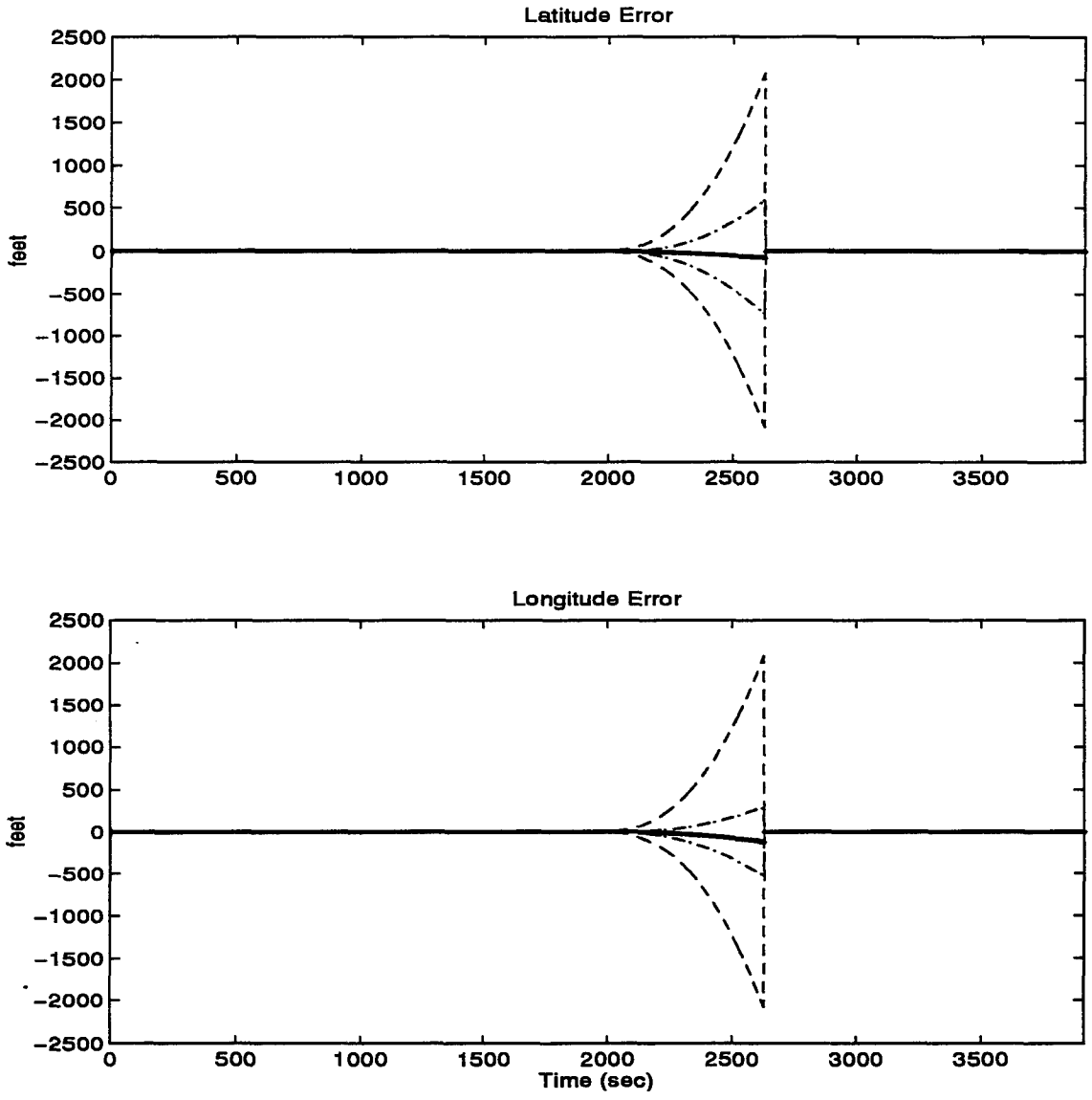

Figure G.7 Latitude and Longitude Error

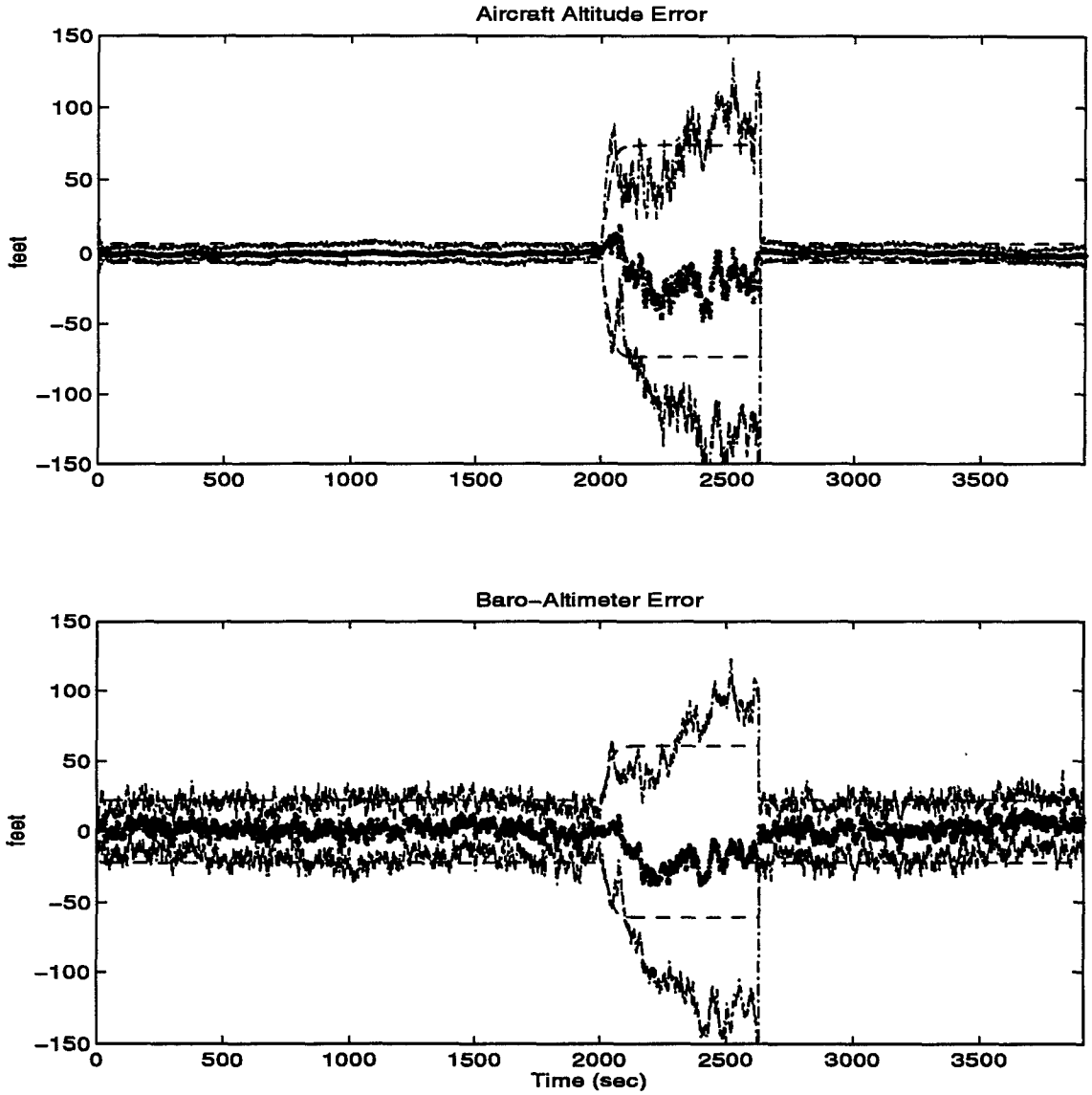

Figure G.8 Aircraft Altitude and Baro-Altimeter Error

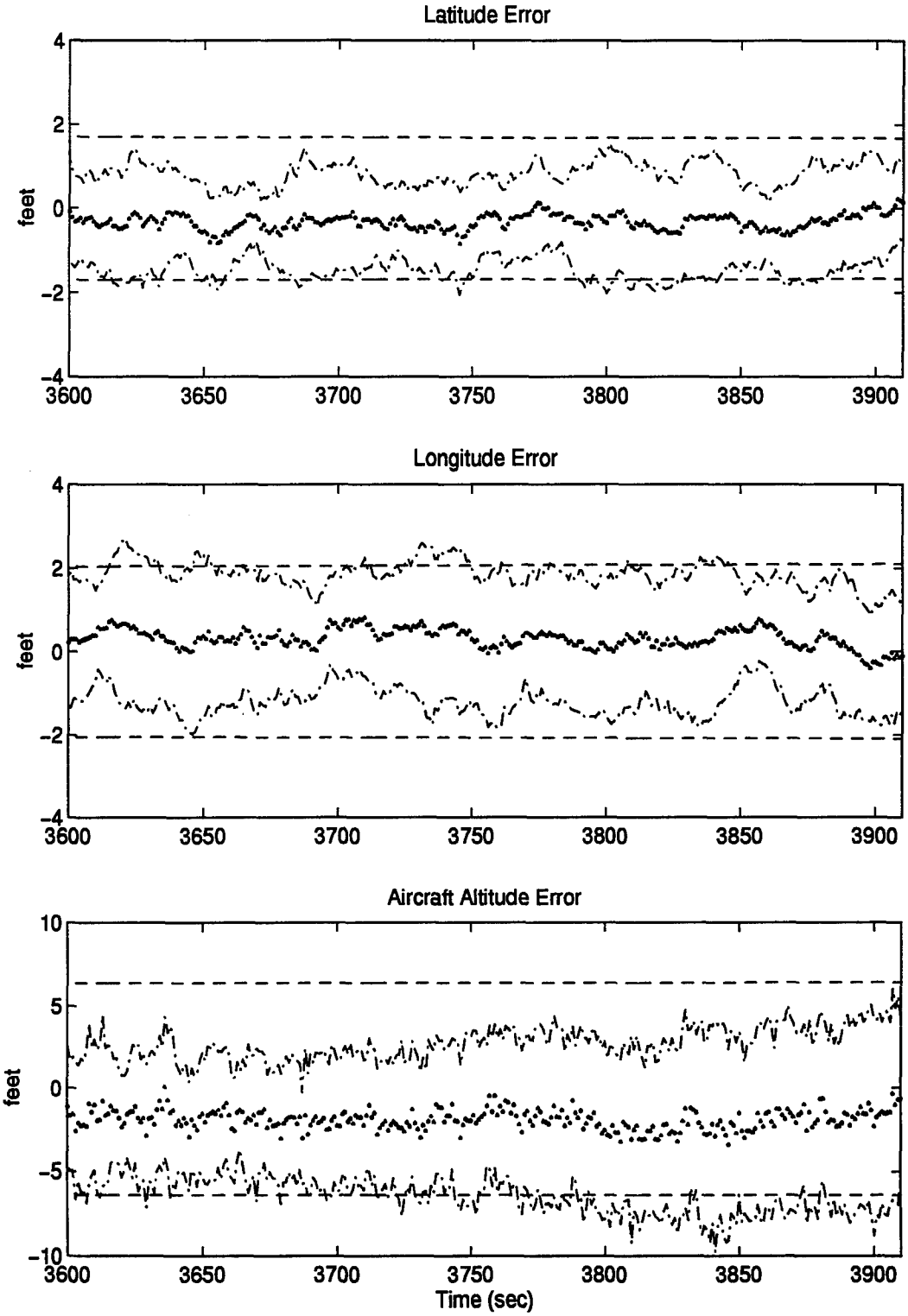

Figure G.9 Latitude, Longitude, and Aircraft Altitude Error

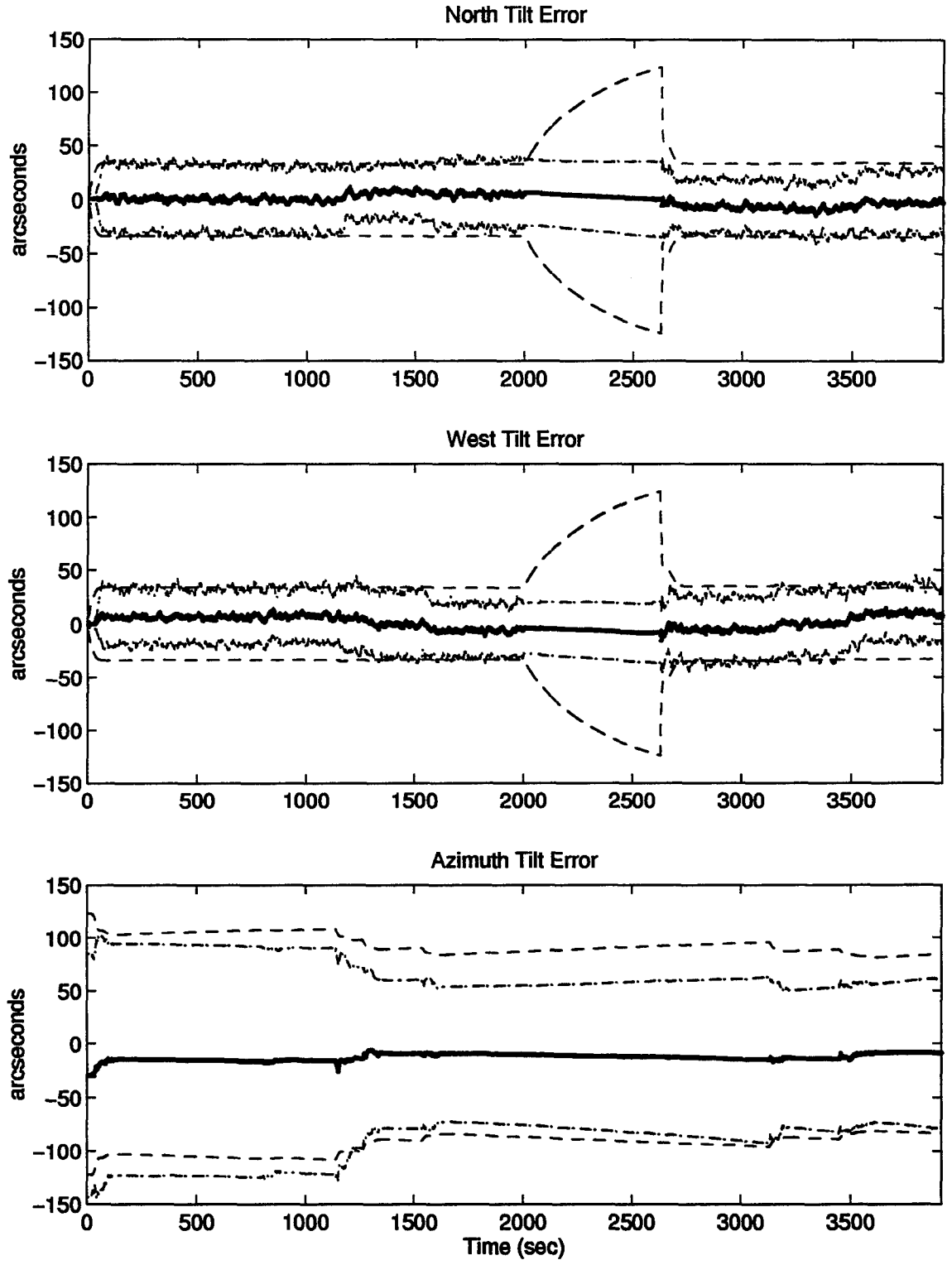

Figure G.10 North, West, and Azimuth Tilt Errors

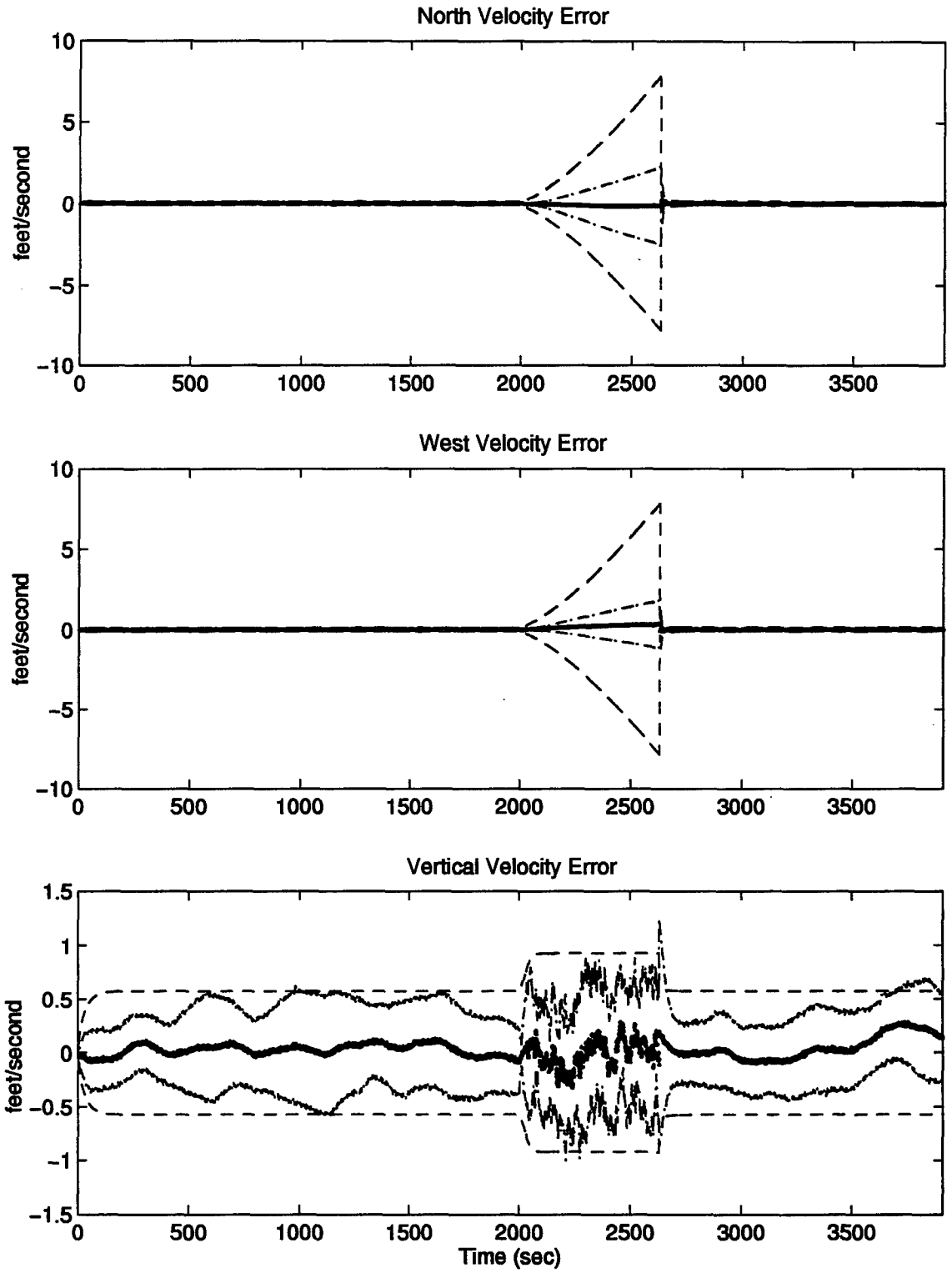

Figure G.11 North, West, and Vertical Velocity Errors

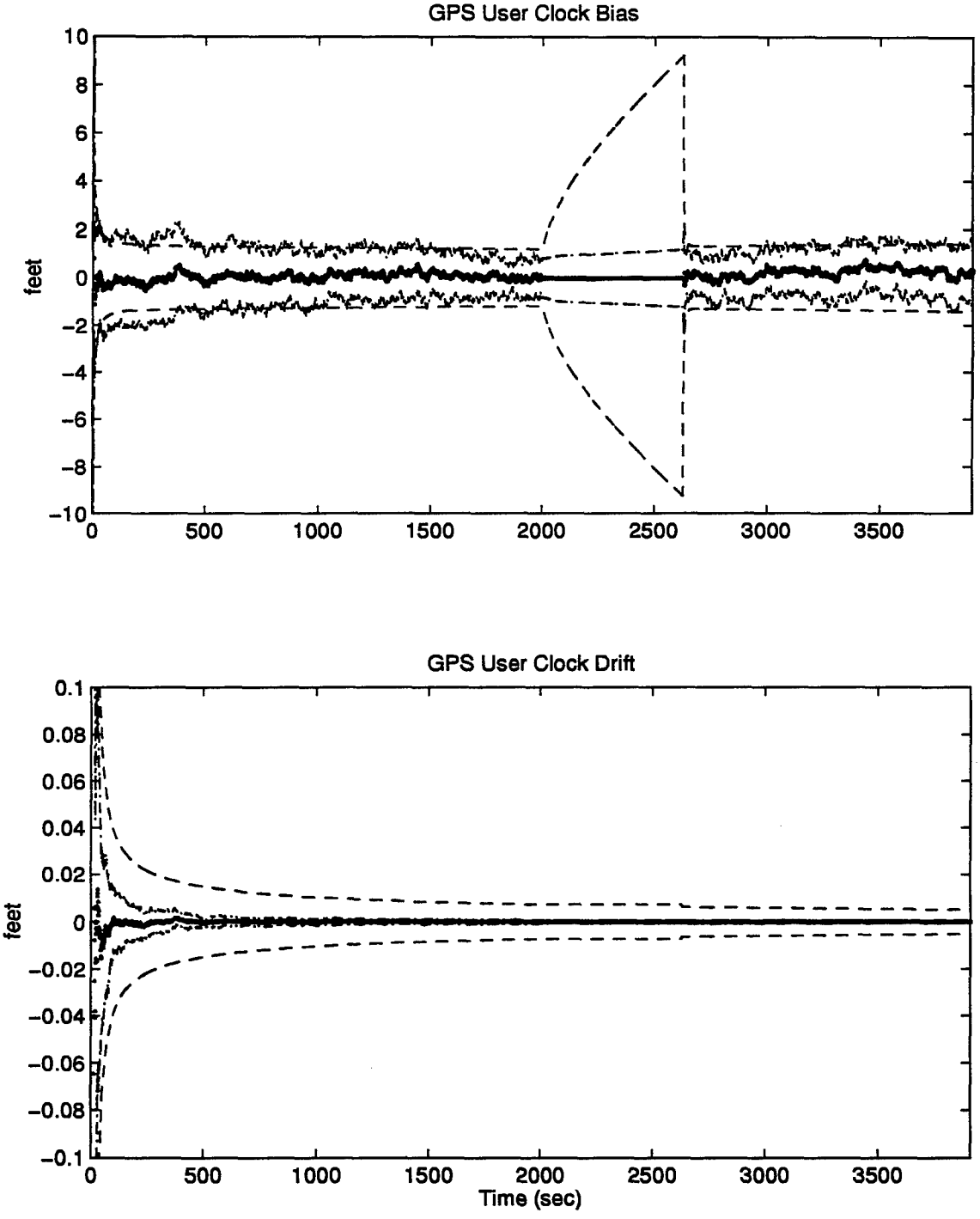

Figure G.12 GPS User Clock Bias and GPS User Clock Drift

G.3 Plots of Case XV: Barometric Altimeter, 4.0 nm/hr INS, and DGPS Using the Single Engine Aircraft Flight Profile.

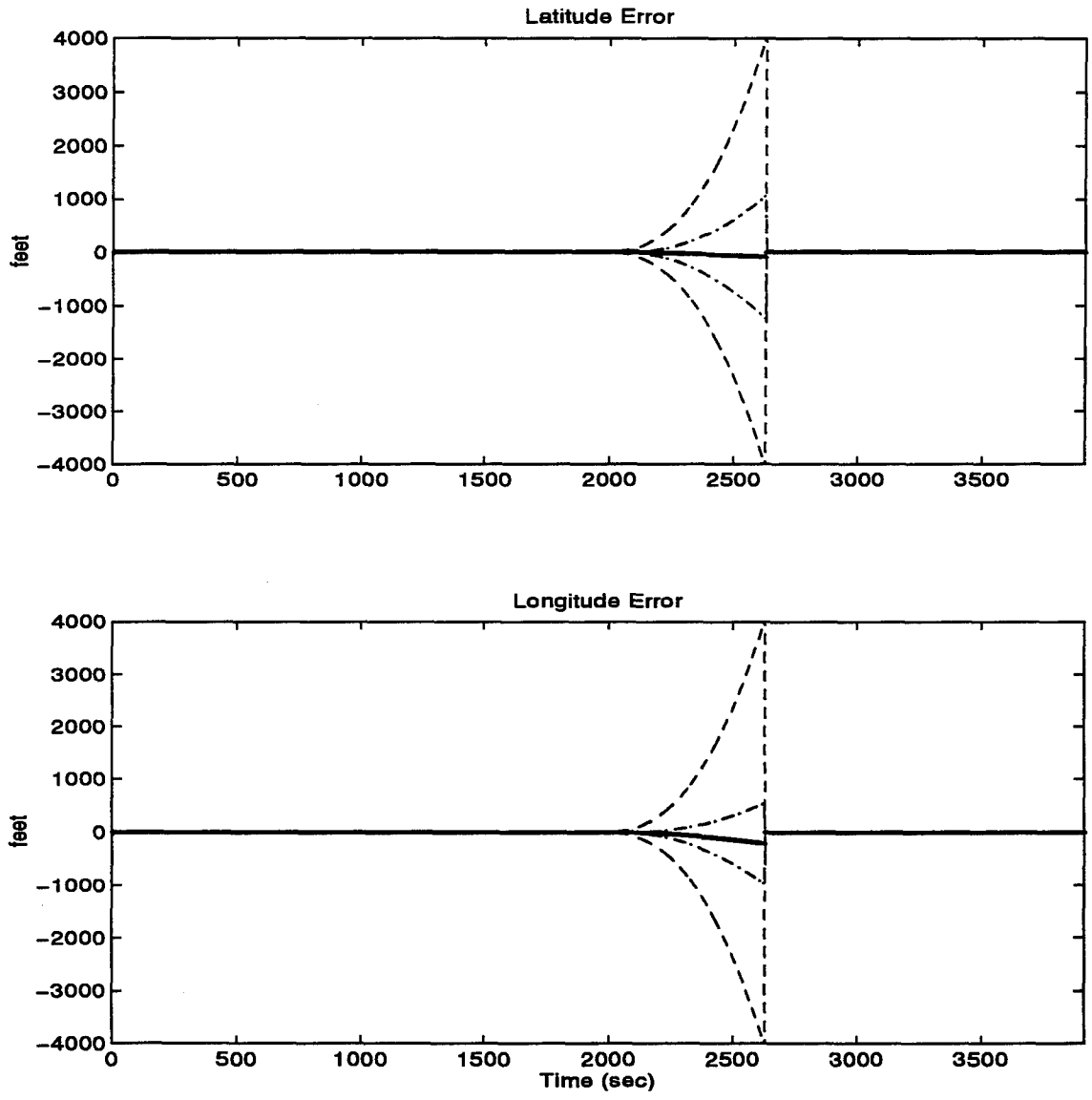

Figure G.13 Latitude and Longitude Error

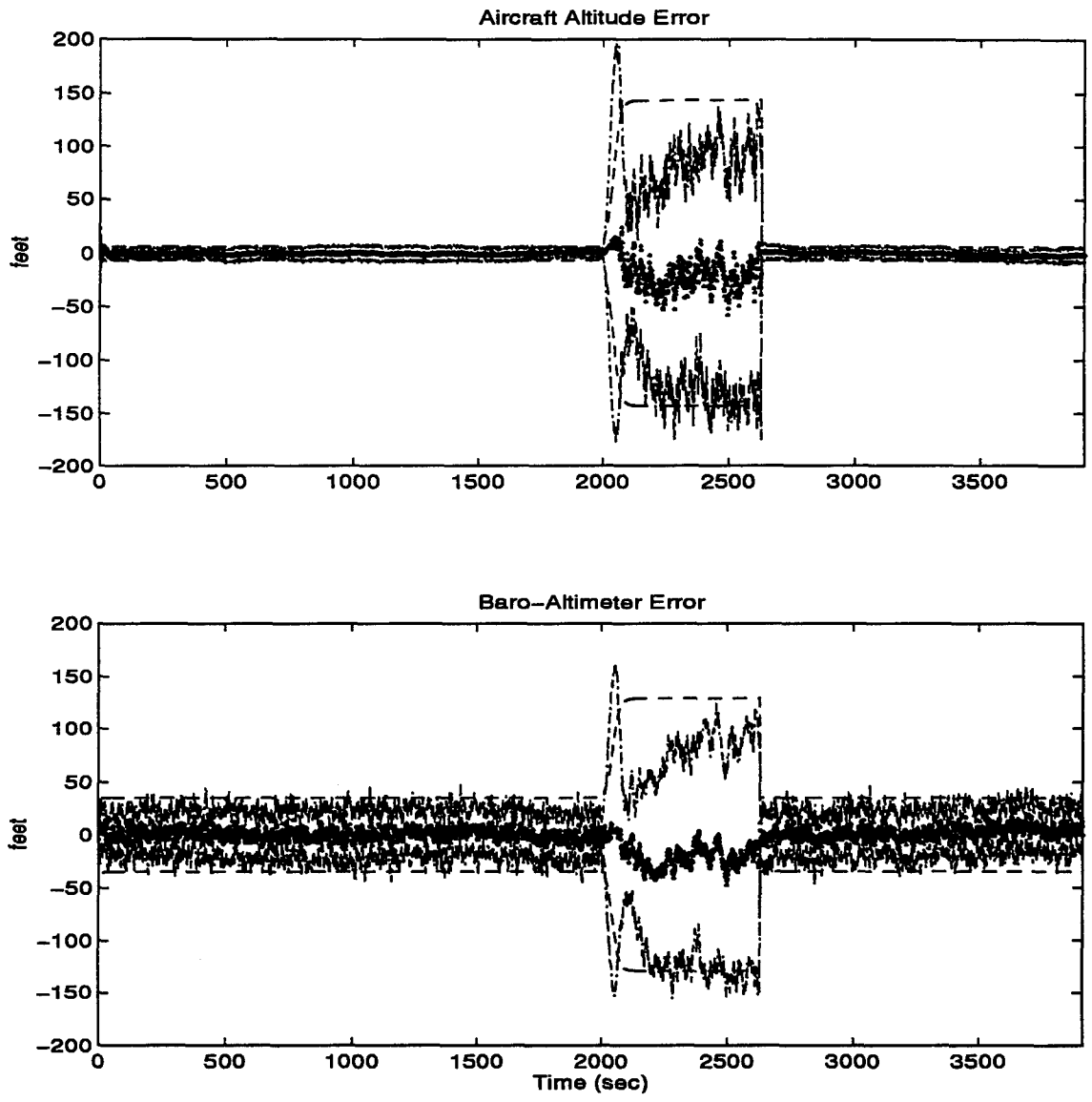

Figure G.14 Aircraft Altitude and Baro-Altimeter Error

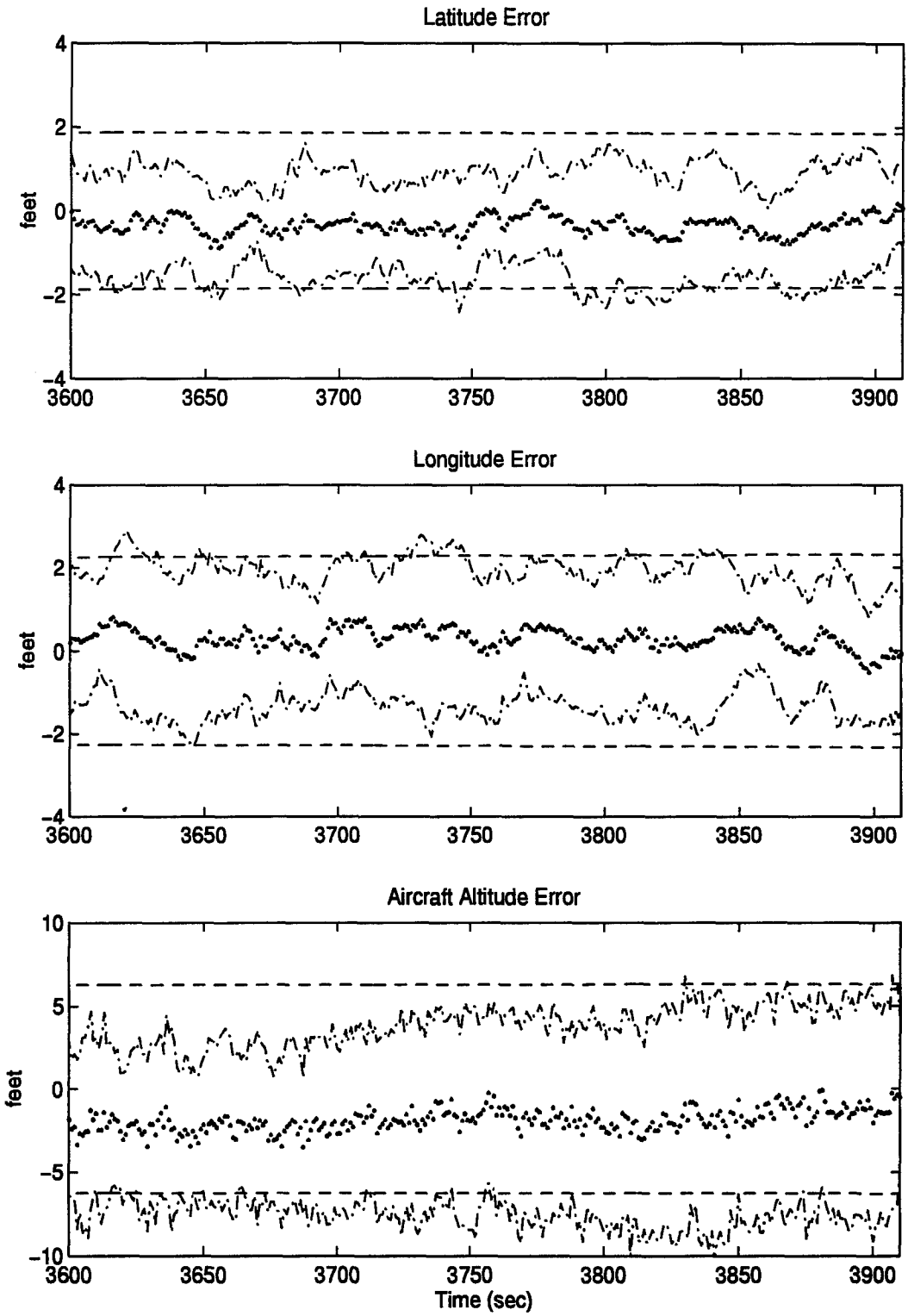

Figure G.15 Latitude, Longitude, and Aircraft Altitude Error

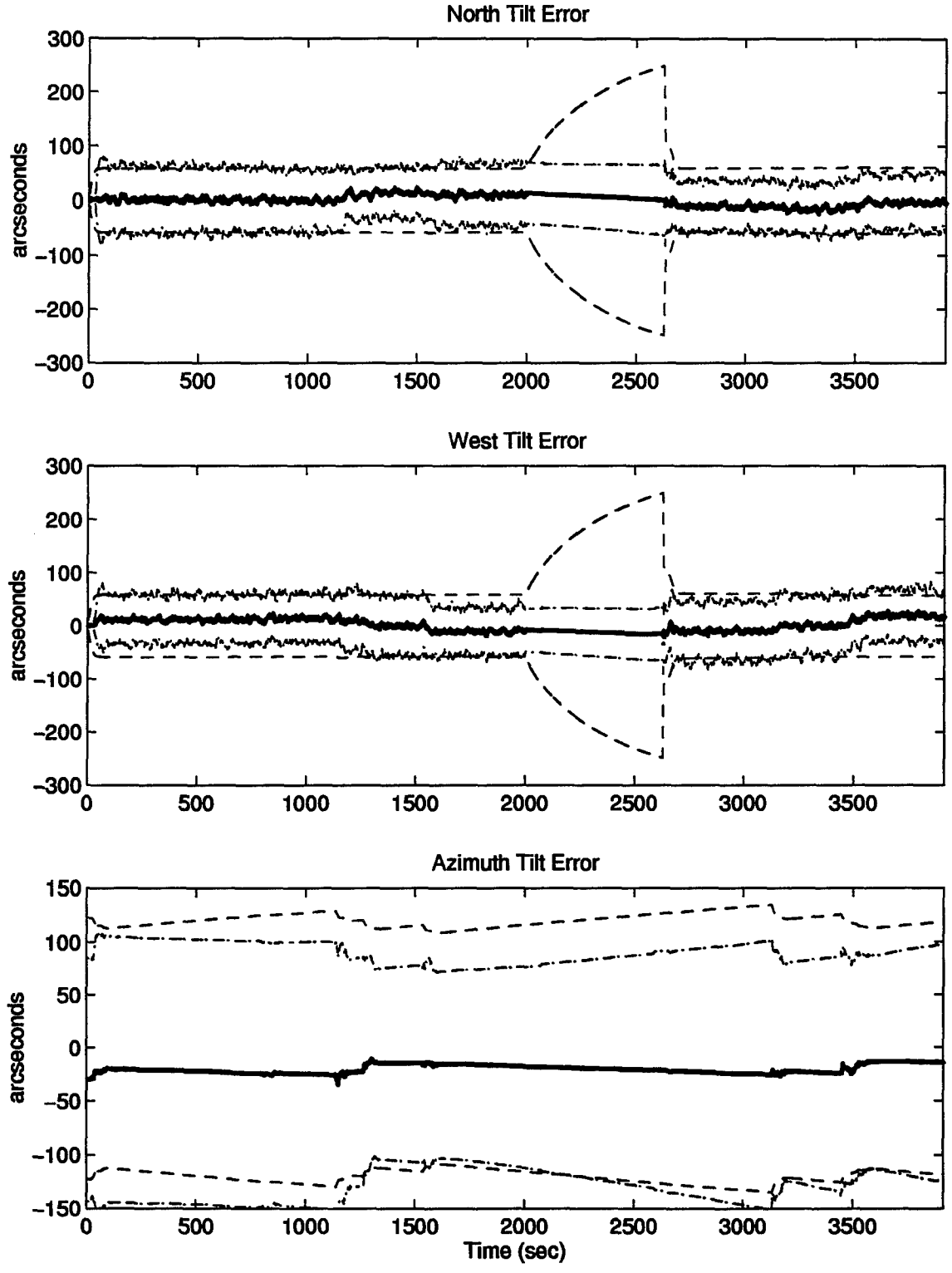

Figure G.16 North, West, and Azimuth Tilt Errors

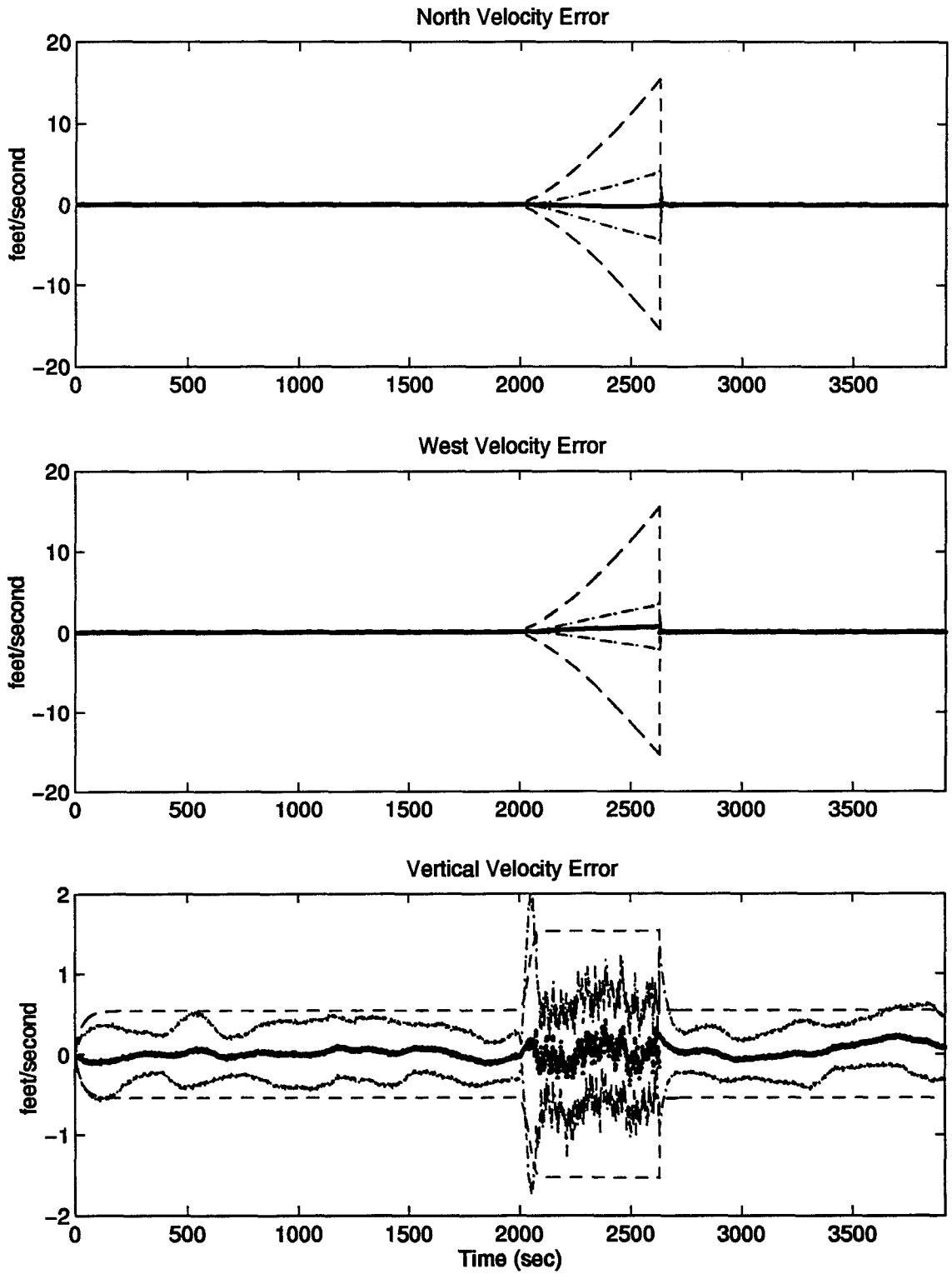

Figure G.17 North, West, and Vertical Velocity Errors

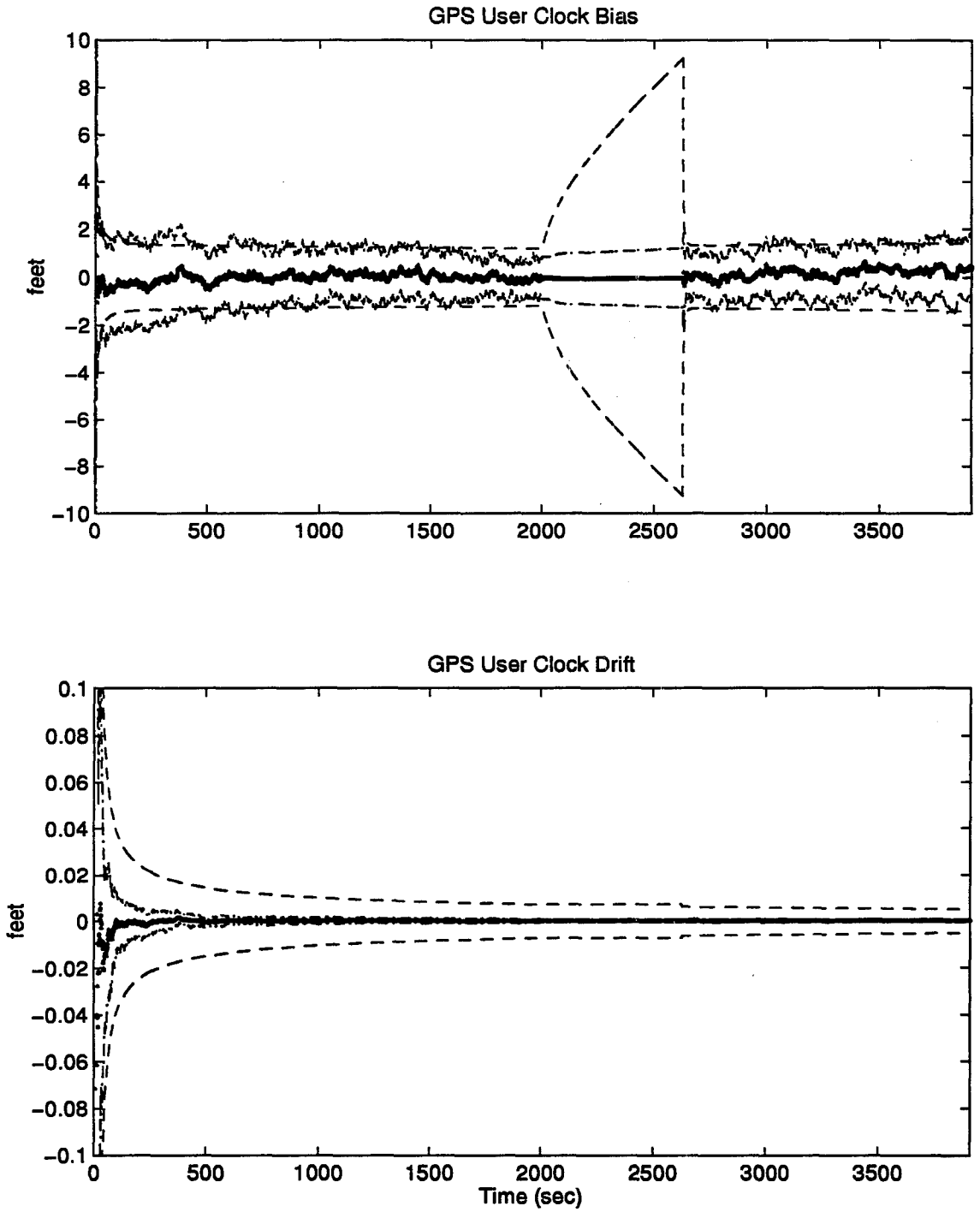

Figure G.18 GPS User Clock Bias and GPS User Clock Drift

Appendix H

FORTRAN source code ADDSV.for, Sample True ephemeris data and Almanac file "051994A.AL3" are contained in this section. In order to interpret Figure H.2, use the following template shown in Table H.1. See SEM 3.6 User Manual for the template of Figure H.3.

*	1994	5	21	4	15	0.00000000
P		6	-3808.264821	-26030.699349	-2199.205556	179.659571
*	YEAR	MONTH	DAY	SV_HOURS	SV_MINUTES	SV_SECONDS
POSITION_INFO		SV#	ECEF_X(in km)	ECEF_Y (in km)	ECEF_Z (in km)	SV Clock Offset (in microsec)

1994	=	YEAR
5	=	MONTH
21	=	DAY
4	=	SV_HOURS
15	=	SV_MINUTES
0.00000000	=	SV_SECONDS
P	=	POSITION_INFO
6	=	SV#
-3808.264821	=	ECEF_X(in km)
-26030.699349	=	ECEF_Y (in km)
-2199.205556	=	ECEF_Z (in km)
179.659571	=	SV Clock Offset (in microsec)

Table H.1 Template for Understanding Figure H - 2.

```
*DECK ADDSV
      PROGRAM  ADDSV
C
C  This program will read in TANKER3 FLIGHT profile, and merge
C  the information with real SV ephemeris data ovtained from the
C  Coast Guard BBS (National Geodetic Survey Ephemeris)
C
C  The output file created will be called "FLIGHT_TANKER3_21my94p4"
C  This file will need to be re-named "FLIGHT" so MSOFE will
C  read it in properly.  Put the "FLIGHT" file in the "runs"
C  directory with your MSOFE_IN file.
C
C  Adopted from J Solomon add.for code:  9 Sep 94  R.A. Gray
C
C
      INTEGER  I,J,K
      REAL  EPHPOS(10000,12)
      CHARACTER   PDATE *10  ,        PTIME *10
      CHARACTER   PTITLE *80, TEMP *80
      INTEGER*4   NRT, NYT
      INTEGER*4   IDFLT(17),  IDCHEK(29)
C
      DOUBLE PRECISION    TKNOT(10000),  UKNOT(10000,29)
C
      DATA  IDCHEK / 1,  2,  3, 40, 40, 40, 43, 43, 43, 5, 7, 8, 9, 14,
     &          16, 17, 18, 60, 61, 62, 60, 61, 62, 60,
     &          61, 62, 60, 61, 62 /
      DATA  NYT   / 29 /
C
C-------
C   #OPEN FILES
C-------
C
C
      OPEN  ( UNIT  = 20,
     &      FILE  = 'FLIGHT',
     &      FORM  = 'UNFORMATTED',
     &      STATUS = 'OLD')
      OPEN  ( UNIT  = 21,
     &      FILE  = '21my94p4',
     &      FORM  = 'FORMATTED',
     &      STATUS = 'OLD')
      OPEN  ( UNIT  = 22,
     &      FILE  = 'FLIGHT_TANKER3_21my94p4',
     &      FORM  = 'UNFORMATTED',    &      STATUS = 'UNKNOWN')
C
C
C-------
C   #READ FLIGHT HEADER
C-------
C
C
      READ  (20) PDATE, PTIME, PTITLE
      READ  (20) NRT, (IDFLT(I),I=1,NRT)
C
C

C   #READ FLIGHT DATA
C-------
C
      DO  100 K = 1, 3920
        READ  (20) TKNOT(K), (UKNOT(K, J), J = 1,NRT)
```

Figure H.1 FORTRAN source code "ADDSV.for"

```
 100    CONTINUE
C
C-------
C   #READ GPS DATA
C-------
C
     DO 200 I = 1,3920
              READ(21,*) TEMP
        READ(21,201) EPHPOS(I,1),EPHPOS(I,2),EPHPOS(I,3)
              READ(21,201) EPHPOS(I,4),EPHPOS(I,5),EPHPOS(I,6)
        READ(21,201) EPHPOS(I,7),EPHPOS(I,8),EPHPOS(I,9)
        READ(21,201) EPHPOS(I,10),EPHPOS(I,11),
    &             EPHPOS(I,12)
C
C    CONVERT FROM KM TO FEET...
C
        EPHPOS(I,1)= EPHPOS(I,1) * 3.2801 * 1000
        EPHPOS(I,2)= EPHPOS(I,2) * 3.2801 * 1000
        EPHPOS(I,3)= EPHPOS(I,3) * 3.2801 * 1000
        EPHPOS(I,4)= EPHPOS(I,4) * 3.2801 * 1000
        EPHPOS(I,5)= EPHPOS(I,5) * 3.2801 * 1000
        EPHPOS(I,6)= EPHPOS(I,6) * 3.2801 * 1000
        EPHPOS(I,7)= EPHPOS(I,7) * 3.2801 * 1000
        EPHPOS(I,8)= EPHPOS(I,8) * 3.2801 * 1000
        EPHPOS(I,9)= EPHPOS(I,9) * 3.2801 * 1000
        EPHPOS(I,10)= EPHPOS(I,10) * 3.2801 * 1000
        EPHPOS(I,11)= EPHPOS(I,11) * 3.2801 * 1000
        EPHPOS(I,12)= EPHPOS(I,12) * 3.2801 * 1000

200   CONTINUE

C
201   FORMAT(5X,F13.6,1X,F13.6,1X,F13.6)
C
C-------
C   #ADD GPS DATA TO FLIGHT DATA
C-------
C
     DO 300 I = 1,3920
       DO 300 J = 1,12
        UKNOT(I,J+17) = DBLE( EPHPOS(I,J) )
300   CONTINUE
C
C
C-------
C   #OUTPUT GPS / FLIGHT DATA
C-------
C
       WRITE  (22) PDATE, PTIME, PTITLE
       WRITE  (22) NYT, (IDCHEK(I),I=1,NYT)
C
       DO  400 K = 1, 3920
         WRITE(22) TKNOT(K), (UKNOT(K, J), J = 1,NYT)
 400    CONTINUE
C
    CLOSE(20), CLOSE(21), CLOSE(22)
    STOP   ' ADD DONE.'
C
    END
```

Figure H.1 (Continued). FORTRAN source code "ADDSV.for"

```
* 1994  5 21  4 15  0.00000000
P  6 -3808.264821 -26030.699349  -2199.205556   179.659571
P 16  22228.030253  -2914.054829  14269.400710   -72.472353
P 17  -1978.539062 -16483.210409  20480.389383   -51.084448
P 28 -14135.480147   5206.630899  21842.559082    14.685241
* 1994  5 21  4 15  1.0000000
P  6 -3807.902060 -26030.482798  -2202.379803   179.659588
P 16  22229.666889  -2913.256477  14267.009251   -72.472371
P 17  -1976.416118 -16484.803199  20479.313405   -51.084449
P 28 -14136.128577   5203.928088  21842.759458    14.685243
* 1994  5 21  4 15  2.00000000
P  6 -3807.539205 -26030.265875  -2205.554003   179.659604
P 16  22231.303287  -2912.458317  14264.617490   -72.472389
P 17  -1974.293373 -16486.396028  20478.236982   -51.084450
P 28 -14136.777174   5201.225288  21842.959367    14.685245
* 1994  5 21  4 15  3.00000000
P  6 -3807.176256 -26030.048580  -2208.728154   179.659621
P 16  22232.939448  -2911.660349  14262.225425   -72.472406
P 17  -1972.170829 -16487.988896  20477.160114   -51.084451
P 28 -14137.425939   5198.522499  21843.158810    14.685247
* 1994  5 21  4 15  4.00000000
P  6 -3806.813214 -26029.830911  -2211.902258   179.659638
P 16  22234.575372  -2910.862573  14259.833058   -72.472424
P 17  -1970.048484 -16489.581803  20476.082800   -51.084452
P 28 -14138.074872   5195.819722  21843.357787    14.685249
* 1994  5 21  4 15  5.00000000
P  6 -3806.450077 -26029.612871  -2215.076314   179.659654
P 16  22236.211057  -2910.064990  14257.440387   -72.472442
P 17  -1967.926339 -16491.174748  20475.005041   -51.084453
P 28 -14138.723973   5193.116956  21843.556298    14.685251
* 1994  5 21  4 15  6.00000000
P  6 -3806.086847 -26029.394457  -2218.250322   179.659671
P 16  22237.846505  -2909.267599  14255.047414   -72.472460
P 17  -1965.804394 -16492.767731  20473.926836   -51.084454
P 28 -14139.373241   5190.414202  21843.754343    14.685253
```

Figure H.2 Sample from National Geodetic OfficeTrue Ephemeris Data

```
25  051994A.AL3
750 32768

1
32
7
 3.61871719360000E-0003  4.03787490677082E-0003 -2.47382546733128E-0009
 5.15368505900000E+0003 -2.18499073561888E-0001 -3.81680029160470E-0001
 9.34495603829844E-0001 -2.47955322270000E-0005  0.00000000000000E+0000
0
1

2
13
7
 1.28645896910000E-0002  3.63542500182467E-0003 -2.64844865770802E-0009
 5.15360546900000E+0003  4.34110874460587E-0001 -8.51847509087840E-0001
-2.11397536351559E-0001 -9.05990600590000E-0005 -3.63797880710000E-0012
0
1

4
34
7
 3.16715240480000E-0003  6.62805331970454E-0003 -2.54658524778148E-0009
 5.15349951200000E+0003 -8.88224868033215E-0001 -3.98996607241964E-0001
 5.56436181933807E-0001  2.76565551760000E-0005  0.00000000000000E+0000
0
1

5
35
7
 2.04277038570000E-0003  4.40408688739476E-0003 -2.64844865770802E-0009
 5.15354834000000E+0003  4.38525794771209E-0001 -7.47885202727681E-0001
-8.79619968280586E-0001  4.19616699220000E-0005  3.63797880710000E-0012
0
1

6
36
7
 6.08873367310000E-0003  5.28146260959343E-0003 -2.48837742344679E-0009
 5.15367529300000E+0003  7.84484770392502E-0001 -9.51250588590547E-0001
 8.06142540736748E-0001  1.81198120120000E-0004  1.81898940350000E-0011
0
1

7
37
7
 6.20937347410000E-0003  6.33813079470329E-0003 -2.47746345635220E-0009
 5.15368798800000E+0003  7.72793384134664E-0001 -8.64231552535642E-0001
-5.47001490125076E-0001  6.96182250980000E-0004  0.00000000000000E+0000
0
1

9
39
7
 2.60972976680000E-0003  3.08419082134277E-0003 -2.61934474550884E-0009
 5.15371142600000E+0003  1.10435722418997E-0001 -2.02198618779358E-0001
 9.39667574686501E-0001 -1.81198120120000E-0005  0.00000000000000E+0000
0
1

12
10
3
 1.45077705380000E-0002  4.65393139879435E-0002 -2.19006317174084E-0009
```

Figure H.3 SEM 3.6 Almanac Data File (051994.al3) Used For: 21 May 94.

```
 5.15351025400000E+0003  2.20944414025568E-0001 -5.63353322948398E-0002
 6.88273665924971E-0001  3.24249267580000E-0005  0.00000000000000E+0000
0
0

14
14
7
 3.12614440920000E-0003  5.97191881407934E-0003 -2.55022323680240E-0009
 5.15373291000000E+0003 -5.47894613209864E-0001  9.78019389301773E-0001
-6.49707535115492E-0001  4.76837158200000E-0006  0.00000000000000E+0000
0
1

15
15
7
 6.81734085080000E-0003  8.10052823333991E-0003 -2.52111932463505E-0009
 5.15363085900000E+0003 -8.77898912451352E-0001  5.72649608752327E-0001
 1.15476012945291E-0001  8.48770141600000E-0005  3.63797880710000E-0012
0
1

16
16
7
 8.64505767820000E-0004  4.97436971769650E-0003 -2.56841289921599E-0009
 5.15353662100000E+0003 -5.44454702377718E-0001 -5.09196621865252E-0001
 1.04387400349130E-0001 -7.24792480470000E-0005  0.00000000000000E+0000
0
1

17
17
7
 7.39622116090000E-0003  8.47055372544914E-0003 -2.51748133561413E-0009
 5.15364502000000E+0003 -8.66931905668387E-0001  6.00263000159655E-0001
 8.30542480168520E-0001 -5.14984130860000E-0005  0.00000000000000E+0000
0
1

18
18
7
 5.53703308110000E-0003  3.05195604672514E-0004 -2.51384334659322E-0009
 5.15374414100000E+0003 -2.32049219860062E-0001  4.18790684681791E-0001
-5.89919703533139E-0001 -7.62939453120000E-0006  0.00000000000000E+0000
0
1

19
19
7
 1.25408172610000E-0004 -2.17437168560882E-0003 -2.66300061379169E-0009
 5.15359960900000E+0003  1.02508064366804E-0001 -8.89521010320165E-0001
 3.50051511019709E-0001  2.86102294920000E-0005  3.63797880710000E-0012
0
1

20
20
7
 4.76932525630000E-0003  5.53512823900381E-0003 -2.63389670162434E-0009
 5.15353125000000E+0003  4.36904307926814E-0001  4.58547696903478E-0001
-2.63615848922248E-0001  5.34057617190000E-0005  0.00000000000000E+0000
0
1
```

Figure H.3 (Continued). SEM3.6 Almanac Data File (051994.al3) Used For: 21 May 94.

```
21
21
7
 1.10397338870000E-0002  3.97873687860613E-0003 -2.57568887725782E-0009
 5.15362597700000E+0003 -5.57345393927682E-0001  8.95620672682456E-0001
 9.14788257969335E-0003 -2.57492065430000E-0005  0.00000000000000E+0000
0
1

22
22
7
 7.18355178830000E-0003  3.68310352426479E-0003 -2.65936262477077E-0009
 5.15354003900000E+0003  4.38924791650606E-0001 -7.99311402531010E-0002
-2.24944476253860E-0001  1.23977661130000E-0004  3.63797880710000E-0012
0
1

23
23
7
 8.32128524780000E-0003  5.13651081681166E-0003 -2.55749921484423E-0009
 5.15359179700000E+0003 -5.46834947341484E-0001 -7.51196023020909E-0001
-1.65312885266793E-0001  5.72204589840000E-0006  0.00000000000000E+0000
0
1

24
24
7
 5.48076629640000E-0003  9.78280379726186E-0003 -2.51020535757230E-0009
 5.15362744100000E+0003 -8.91399160413578E-0001 -6.87911362216682E-0001
 6.78474166136823E-0001  6.27517700200000E-0004  3.27418092640000E-0011
0
1

25
25
7
 5.81312179570000E-0003  8.94565027331417E-0004 -2.63753469064526E-0009
 5.15355957000000E+0003  1.02575664265170E-0001  9.12953036069076E-0001
-7.64856704540744E-0001 -7.62939453120000E-0006  0.00000000000000E+0000
0
1

26
26
7
 8.31842422490000E-0003  4.95530209660800E-0003 -2.45563580494953E-0009
 5.15363476600000E+0003 -2.25428584871805E-0001 -3.30814701228596E-0001
-4.97203227333835E-0001 -6.48498535160000E-0005 -3.63797880710000E-0012
0
1

27
27
7
 1.09333992000000E-0002  2.11908510906553E-0003 -2.61934474550884E-0009
 5.15369824200000E+0003  1.06457355526676E-0001  7.64407505673693E-0001
 5.49562924837777E-0001  2.95639038090000E-0005  0.00000000000000E+0000
0
1

28
28
7
```

Figure H.3 (Continued). SEM3.6 Almanac Data File (051994.al3) Used For: 21 May 94.

```
 5.21230697630000E-0003  8.88444419668218E-0003 -2.45199781592861E-0009
 5.15362744100000E+0003  7.75170821127847E-0001  9.17673683276588E-0001
 3.86364096897161E-0001  1.52587890620000E-0005  3.63797880710000E-0012
0
1

29
29
7
 5.16462326050000E-0003  3.66022239169097E-0003 -2.47382546733128E-0009
 5.15363330100000E+0003 -2.32212423429801E-0001 -5.82052691976437E-0001
 5.61828388466135E-0001  1.33514404300000E-0005  0.00000000000000E+0000
0
1

31
31
7
 5.00249862670000E-0003  6.14358422218893E-0003 -2.48110144537312E-0009
 5.15360058600000E+0003  7.73816318762073E-0001  2.03706971195042E-0001
 9.34471242810989E-0001  1.52587890620000E-0005  3.63797880710000E-0012
0
1
```

Figure H.3 (Continued). SEM3.6 Almanac Data File (051994.al3) Used For: 21 May 94.

Appendix I. Dynamics Matrices and Noise Values

I.1 Definition of Dynamics Matrices

In Chapter 3, the truth and filter model dynamics are defined by the submatrices, F_{Filter}, $F_{INS_{t1}}$, $F_{INS_{t2}}$ and F_{DGPS_t} of Equation (3.3). The F_{Filter} represents the filter dynamics matrix, which is also a submatrix of the larger truth model dynamics matrix [50]. The other three matrices represent the additional truth model non-zero portions of the **F** matrix that simulate the real world [50,55]. Tables I.2, I.3, I.4 and I.5 contain the non-zero elements of the dynamics submatrices F_{Filter}, $F_{INS_{t1}}$, $F_{INS_{t2}}$ and F_{DGPS_t}, respectively. All undeclared variables shown in the following tables are defined in the LN-93 technical report, along with their units [41,50]. The structure of the dynamics matrices in this chapter correspond to the truth model state definitions in Appendix A and to the AFIT thesis (NRS model) by [50,55]. The notation used in Tables I.2 - I.4 in this Appendix is defined in Table I.1.

ρ_x, ρ_y, ρ_z	Components of angular rate of navigation frame with respect to the earth (craft rate), coordinatized in Litton True frame
$\Omega_x, \Omega_y, \Omega_z$	Components of earth sideral rate vector (earth rate), coordinatized in Litton ECEF, with respect to inertial space
a	Equatorial radius of the earth (6378388 meters)
g_0	Equatorial gravity magnitude (32.08744 ft/sec^2)
$\omega_{itx}, \omega_{ity}, \omega_{itz}$	Components of angular rate of navigation frame with respect to inertial space (spatial rate), coordinatized in Litton True frame
V_x, V_y, V_z	Components of vehicle velocity vector with respect to earth-fixed coordinates
A_x, A_y, A_z	Components of specific force, coordinatized in Litton True frame
C_{RX}, C_{RY}	Components of earth spheroid inverse radii of curvature
$\omega_{ibx}, \omega_{iby}, \omega_{ibz}$	Components of angular rate of navigation frame with respect to inertial space (spatial rate), coordinatized in Litton Body frame
$C_{i,j}$	Elements of the transformation matrix C_{body}^{nav}
$\beta\delta_{hc}$	Barometer inverse correlation time (600 seconds)
$\beta\nabla_{xc}, \beta\nabla_{yc}, \beta\nabla_{zc}$	Gyro inverse correlation time constants (5 minutes)
$\beta\delta_{gx}, \beta\delta_{gy}, \beta\delta_{gz}$	Gravity vector error inverse correlation time constants (Velocity/correlation distance)
$\sigma^2_{\delta hc}$	Variance of barometer correlated noise
$\sigma^2_{\nabla xc}, \sigma^2_{\nabla yc}, \sigma^2_{\nabla zc}$	Variances of accelerometer correlated noise
$\sigma^2_{\delta gx}, \sigma^2_{\delta gy}, \sigma^2_{\delta gz}$	Variances of gravity vector correlated noise
$\sigma^2_{\eta bx}, \sigma^2_{\eta by}, \sigma^2_{\eta bz}$	Power spectral density value of gyro drift rate white noise
$\sigma^2_{\eta Ax}, \sigma^2_{\eta Ay}, \sigma^2_{\eta Az}$	Power spectral density value of accelerometer white noise
k_1, k_2, k_3, k_4	Vertical channel gains of vertical channel error model (see figure 2 of [41])

Table I.1 Notation of Variables used in Tables I.2 to I.4

Element	Variable		Element	Variable
(1,3)	$-\rho_y$		(1,8)	$-C_{RY}$
(2,3)	ρ_x		(2,7)	C_{RX}
(3,1)	ρ_y		(3,2)	$-\rho_z$
(4,2)	$-\Omega_z$		(4,3)	Ω_y
(4,5)	ω_{itz}		(4,6)	$-\omega_{ity}$
(4,8)	$-C_{RY}$		(5,1)	Ω_z
(5,3)	$-\Omega_x$		(5,4)	$-\omega_{itz}$
(5,6)	ω_{itx}		(5,7)	C_{RX}
(6,1)	$-\Omega_y$		(6,2)	Ω_x
(6,4)	ω_{ity}		(6,5)	$-\omega_{itx}$
(7,1)	$-2V_y\Omega_y-2V_z\Omega_z$		(7,2)	$2V_y\Omega_x$
(7,3)	$2V_z\Omega_y$		(7,5)	$-A_z$
(7,6)	A_y		(7,7)	$-V_zC_{RX}$
(7,8)	$2\Omega_z$		(7,9)	$-\rho_y-2\Omega_y$
(8,1)	$2V_x\Omega_y$		(8,2)	$2V_x\Omega_x-2V_z\Omega_z$
(8,3)	$2V_z\Omega_y$		(8,4)	A_z
(8,6)	$-A_x$		(8,7)	$-2\Omega_z$
(8,8)	$-V_zC_{RY}$		(8,9)	$\rho_x+2\Omega_x$
(9,1)	$2V_x\Omega_z$		(9,2)	$2V_y\Omega_z$
(9,3)	$-2V_y\Omega_y-2V_x\Omega_x$		(9,4)	$-A_y$
(9,5)	A_x		(9,7)	$\rho_y-2\Omega_y+V_xC_{RX}$
(9,8)	$-\rho_x-2\Omega_x+V_yC_{RY}$		(9,10)	$2g_o/a$
(11,11)	$-\beta\delta_{hc}$		(14,15)	1 ft^2/sec

Table I.2 Elements of the Dynamics Submatrix F_{Filter}

Element	Variable		Element	Variable		Element	Variable
(9,16)	$-k_2$		(9,17)	-1		(9,18)	k_2
(10,9)	1		(10,16)	$-k_1$		(10,18)	k_1-1
(16,10)	1		(16,16)	-1		(17,16)	k_3
(17,18)	$-k_3$		(18,10)	k_4		(18,16)	$-k_4$
(7,19)	C_{11}		(7,20)	C_{12}		(7,21)	C_{13}
(7,22)	1		(8,19)	C_{21}		(8,20)	C_{22}
(8,21)	C_{23}		(8,23)	1		(9,19)	C_{31}
(9,20)	C_{32}		(9,21)	C_{33}		(9,24)	1
(9,11)	k_2		(10,11)	k_1		(17,11)	$-k_3$
(18,11)	$k_4/600$		(18,18)	k_4-1		(9,43)	$C_{33}A_x^B$
(4,25)	C_{11}		(4,26)	C_{12}		(4,27)	C_{13}
(4,28)	$C_{11}\omega_{ibx}$		(4,29)	$C_{12}\omega_{iby}$		(4,30)	$C_{13}\omega_{ibz}$
(5,25)	C_{21}		(5,26)	C_{22}		(5,27)	C_{23}
(5,28)	$C_{21}\omega_{ibx}$		(5,29)	$C_{22}\omega_{iby}$		(5,30)	$C_{23}\omega_{iby}$
(6,25)	C_{31}		(6,26)	C_{32}		(6,27)	C_{33}
(6,28)	$C_{31}\omega_{ibx}$		(6,29)	$C_{32}\omega_{iby}$		(6,30)	$C_{33}\omega_{iby}$
(7,31)	C_{11}		(7,32)	C_{12}		(7,33)	C_{13}
(7,34)	$C_{11}A_x^B$		(7,35)	$C_{12}A_y^B$		(7,36)	$C_{13}A_z^{B'}$
(7,37)	$C_{11}\lvert A_x^B\rvert$		(7,38)	$C_{12}\lvert A_y^B\rvert$		(7,39)	$C_{13}\lvert A_z^{B'}\rvert$
(7,40)	$C_{11}A_y^B$		(7,41)	$-C_{12}A_x^B$		(7,42)	$C_{13}A_y^B$
(7,43)	$C_{13}A_x^B$		(8,31)	C_{21}		(8,32)	C_{22}
(8,33)	C_{23}		(8,34)	$C_{21}A_x^B$		(8,35)	$C_{22}A_y^B$
(8,36)	$C_{23}A_z^{B'}$		(8,37)	$C_{21}\lvert A_x^B\rvert$		(8,38)	$C_{22}\lvert A_y^B\rvert$
(8,39)	$C_{23}\lvert A_z^{B'}\rvert$		(8,40)	$C_{21}A_y^B$		(8,41)	$-C_{22}A_x^B$
(8,42)	$C_{23}A_y^B$		(8,43)	$C_{23}A_x^B$		(9,31)	C_{31}
(9,32)	C_{32}		(9,33)	C_{33}		(9,34)	$C_{31}A_x^B$
(9,35)	$C_{32}A_y^B$		(9,36)	$C_{33}A_z^{B'}$		(9,37)	$C_{31}\lvert A_x^B\rvert$
(9,38)	$C_{32}\lvert A_y^B\rvert$		(9,39)	$C_{33}\lvert A_z^{B'}\rvert$		(9,40)	$C_{31}A_x^B$
(9,41)	$-C_{32}A_x^B$		(9,42)	$C_{33}A_y^B$		---	---

Table I.3 Elements of the Dynamics Submatrix $F_{INS_{11}}$

Element	Variable	
(19,19)	$-\beta\nabla_{xc} = -3.33E\text{-}3\ \text{sec}^{-1}$	
(20,20)	$-\beta\nabla_{yc} = -3.33E\text{-}3\ \text{sec}^{-1}$	
(21,21)	$-\beta\nabla_{zc} = -3.33E\text{-}3\ \text{sec}^{-1}$	
(22,22)	$-\beta\delta_{gx} = -8.22E\text{-}6*\sqrt{V_x^2 + V_y^2 + V_z^2}\ \ ft^{-1}$	
(23,23)	$-\beta\delta_{gy} = -8.22E\text{-}6*\sqrt{V_x^2 + V_y^2 + V_z^2}\ \ ft^{-1}$	
(24,24)	$-\beta\delta_{gz} = -8.22E\text{-}6*\sqrt{V_x^2 + V_y^2 + V_z^2}\ \ ft^{-1}$	

Table I.4 Elements of the Dynamics Submatrix $F_{INS_{t2}}$

Element	Variable		Element	Variable
(43,43)	-1/500 ft^2 / sec		(44,44)	-1/1500 ft^2 / sec
(50,50)	-1/500 ft^2 / sec		(51,51)	-1/1500 ft^2 / sec
(57,57)	-1/500 ft^2 / sec		(58,58)	-1/1500 ft^2 / sec
(64,64)	-1/500 ft^2 / sec		(65,65)	-1/1500 ft^2 / sec

Table I.5 Elements of the Dynamics Submatrix F_{DGPS_t}

I.2 Elements of the Process Noise and Measurement Noise Matrices

This section defines the dynamic noise strengths and measurement noise variances for the truth and filter models. The truth model non-zero dynamics noise strengths are defined in Tables I.6 and I.7. These noise strengths correspond to the driving noises w_{Filter}, w_{INS_t} and w_{DGPS_t} in Equation (3.3). Note that the (4,4) through (9,9) σ^2 terms in Table I.6 are variable names as defined in the Litton technical report [41] and do not represent variance terms typically associated with the notation σ^2 [50,55]. However, the σ^2 terms in "$2\beta_i \sigma_i^2$" in (11,11) through (24,24) are real variances (of the outputs of first order lag shaping filters). The filter dynamics driving noise terms implemented after filter tuning for each respective INS integration (0.4 nm/hr, 2.0 nm/hr and 4.0 nm/hr) are listed in Tables I.8, I.9 and I.10. Finally, the measurement noise variances used in the truth and filter models are presented in Table I.11.

Element	Variable		Element	Variable		Element	Variable
(4,4)	$\sigma^2_{\eta_{bx}}$ = 190.4E-15 $[ft^3/\sec^5]$		(5,5)	$\sigma^2_{\eta_{by}}$ = 190.4E-15 $[ft^2/\sec^4]$		(6,6)	$\sigma^2_{\eta_{bz}}$ = 190.4E-15 $[ft^2/\sec^4]$
(7,7)	$\sigma^2_{\eta_{Ax}}$ = 102.9E-9 $[ft^2/\sec^4]$		(8,8)	$\sigma^2_{\eta_{Ay}}$ = 102.9E-9 $[ft^2/\sec^4]$		(9,9)	$\sigma^2_{\eta_{Az}}$ = 102.9E-9 $[ft^2/\sec^4]$
(11,11)	$2\beta_{\delta hc}\sigma^2_{\delta hc}$= 33.34 $[ft^2/\sec]$		(19,19)	$2\beta_{\nabla xc}\sigma^2_{\nabla xc}$ = 2.75E-11 $[ft^2/\sec^5]$		(20,20)	$2\beta_{\nabla yc}\sigma^2_{\nabla yc}$ = 2.75E-11 $[ft^2/\sec^5]$
(21,21)	$2\beta_{\nabla zc}\sigma^2_{\nabla zc}$ = 2.75E-11 $[ft^2/\sec^5]$		(22,22)	$2\beta_{\delta gx}\sigma^2_{\delta gx}$ = 3.10E-13 $[ft^3/\sec^5]$		(23,23)	$2\beta_{\delta gy}\sigma^2_{\delta gy}$ = 3.10E-13 $[ft^3/\sec^5]$
(24,24)	$2\beta_{\delta gz}\sigma^2_{\delta gz}$ = 3.10E-13 $[ft^3/\sec^5]$						

Table I.6 Elements of Truth Model Process Noise Submatrix for the INS Truth Model

Element	Variable		Element	Variable
(43,43)	0.001 $ft^2/\sec$		(44,44)	0.0004 $ft^2/\sec$
(50,50)	0.001 $ft^2/\sec$		(51,51)	0.0004 $ft^2/\sec$
(57,57)	0.001 $ft^2/\sec$		(58,58)	0.0004 $ft^2/\sec$
(64,64)	0.001 $ft^2/\sec$		(65,65)	0.0004 $ft^2/\sec$

Table I.7 Elements of Truth Model Process Noise for DGPS States

Element	Variable		Element	Variable
(1,1)	1.2E-16 rad^2/sec		(2,2)	1.5E-16 rad^2/sec
(3,3)	0.0 rad^2/sec		(4,4)	20.0 rad^2/sec
(5,5)	28.0 rad^2/sec		(6,6)	85.0 rad^2/sec
(7,7)	0.1 ft^2/sec^3		(8,8)	0.1 E-6 ft^2/sec^3
(9,9)	33,000.0 ft^2/sec^3		(10,10)	16.0 ft^2/sec
(11,11)	2.0 ft^2/sec		(12,12)	0.5 $^2/sec$
(13,13)	5.0E-15 ft^2/sec^3			

Table I.8 Filter Process Noise Q Values for Case Using the 0.4 nm/hr INS

Element	Variable		Element	Variable
(1,1)	1.2E-22 rad^2/sec		(2,2)	1.5E-22 rad^2/sec
(3,3)	0.0 rad^2/sec		(4,4)	3575.0 rad^2/sec
(5,5)	3575.0 rad^2/sec		(6,6)	180.0 rad^2/sec
(7,7)	1000.0 ft^2/sec^3		(8,8)	1000.0 ft^2/sec^3
(9,9)	50,000.0 ft^2/sec^3		(10,10)	2.0 ft^2/sec
(11,11)	2.0 ft^2/sec		(12,12)	0.1 ft^2/sec
(13,13)	5E-15 ft^2/sec^3			

Table I.9 Filter Process Noise Q Values for Cases Using the 2.0 nm/hr INS

Element	Variable		Element	Variable
(1,1)	1.2E-23 rad^2/sec		(2,2)	1.5E-23 rad^2/sec
(3,3)	0.0 rad^2/sec		(4,4)	14,500.0 rad^2/sec
(5,5)	14,500.0 rad^2/sec		(6,6)	520.0 rad^2/sec
(7,7)	500.0 ft^2/sec^3		(8,8)	500.0 ft^2/sec^3
(9,9)	43,000.0 ft^2/sec^3		(10,10)	18.0 ft^2/sec
(11,11)	10.0 ft^2/sec		(12,12)	0.1 ft^2/sec
(13,13)	5E-16 ft^2/sec^3			

Table I.10 Filter Process Noise Q Values for Cases Using the 4.0 nm/hr INS

Measurement	Truth Noise	Filter Noise
Baro Altimeter	2500 ft^2	3500 ft^2
Satellite Vehicles	9 ft^2	30 ft^2
Radar Altimeter	(See function, Chapter 3)	(See function, Chapter 3)

Table I.11 Truth and Filter Measurement Noise R Values for Cases

Bibliography

1. Aeronautical Systems Division, AFSC. *Specification for USAF Standard Form, Fit and Function (F3) Medium Accuracy Inertial Navigation Unit, F-16 Aircraft Application*. SNU84-1/F-16, Revision A, Change Notice 1, Wright-Patterson AFB, OH, 20 Aug 1991.

2. Alexander, Frank. Assistant Director of Flight Operations, Northwest Airlines, St. Paul, MN. Personal Correspondence. 12 September 1993.

3. Bagley, Daniel T. *GPS/INS Integration for Improved Aircraft Attitude Estimates*. MS Thesis, AFIT/GE/ENG/91D-04. School of Engineering, Air Force Institute of Technology, Wright-Patterson AFB OH, December 1992 (AD-A243947).

4. Blackwell, Earl G. "Overview of Differential GPS Methods," *The Institute of Navigation, Volume III*: 89-100 (1985).

5. Blair, Lt Col Jesse (USAF retired). KC-135 Pilot, 121st Air Refueling Squadron, Rickenbaker ANG, OH, Personal Interview. August 1994.

6. Blomenhofer, Helmut, and others. "On-The-Fly Carrier-Phase Ambiguity Resolution for Precise Aircraft Landing," *Proceeding of the ION GPS-93 Sixth International Technical Meeting of the Satellite Division*, Salt Lake City, UT: 821-830 (22-24 Sep 93).

7. Bohenek, Brian J. *The Enhanced Performance of an Integrated Navigation System in a Highly Dynamic Environment*. MS Thesis, AFIT/GE/ENG/94D-01. School of Engineering, Air Force Institute of Technology, Wright-Patterson AFB, OH, December 1994 (ADA-289269).

8. Bose, Sam C. *Five Day Short Course on Inertial Navigation Systems (INS/GPS): Sensors, Systems, Mechanizations, Algorithms, Error Models, Kalman Filtering, System Analysis, Multisensor Integration, Sensor and System Testing with a Unified Treatment of the Similarities and Differences Between Gimbaled and Strapdown and Case Studies of Vertical Channel Stabilization and GPS/INS Kalman Integration*. Course Notes. Technalytics., Canoga Park, CA, 91303, 1994.

9. Bowditch, Nathaniel, LL.D., *American Practical Navigator*, Defense Mapping Agency/Topographic Center, Volume I, 1984.

10. Britting, Kenneth R. *Inertial Navigation Systems Analysis*. New York: Wiley-Interscience, 1971.

11. Burington, Richard Stevens, and Donald Curtis May. *Handbook of Probability and Statistics with Tables*, Handbook Publishers, Inc., Sandusky, OH, 1958.

12. Cohen, Clark. Avionics Research Engineer, Department of Aeronautics and Astronautics, Stanford University. Telephone Interview. November 1994.

13. Cohen, Clark, and others. "Real-Time Flight Test Evaluation of the GPS Marker Beacon Concept for Category III Kinematic GPS Precision Landing", *Proceeding of the ION GPS-93 Sixth International Technical Meeting of the Satellite Division*, Salt Lake City, UT: 841-849 (22-24 Sep 93).

14. Collins Government Avionics Division. Computer Program Product Specification for the GPS Radio Receiver R-2332D (RCVR 3-A) of the User Equipment Segment, NAVSTAR Global Positioning System. Part I of II, Code Ident: 13499, CP-RCVR-3010, Rockwell International Corporation, Cedar Rapids, IO, 9 January 1990.

15. Defense Mapping Agency. Department of Defense World Geodetic System 1984. DMA Technical Report, DMA TR 8350.2, 30 Sep 1987.

16. Department of Defense. *Flight Information Publication, (Terminal) Low Altitude United States Airport Diagrams, Instrument Approach Procedures*. Volume 8, Pages 339-340. 28 April 94.

17. Department of the Air Force. *Flying Training: Instrument Flying*. AFM 51-37. Washington: HQ USAF, 15 July 1986.

18. Department of the Air Force. *NAVSTAR GPS USER EQUIPMENT*. MZI0298.001, US Air Force Space Systems Division, NAVSTAR-GPS Joint Program Office, Los Angeles, CA. February 1991.

19. Department of the Air Force. *Single-Location User, System Effectiveness Model Demonstration Software (Version 3.6) Reference Manual*, Joint Program Office, Directorate of Systems Engineering, Los Angeles CA. March 1990.

20. Department of Transportation. *Automatic Landing Systems,* Federal Aviation Administration, AC 20-57A, Washington, D.C., 12 Jan. 1971.

21. Department of Transportation. *Engineering and Operational Issues Associated with the Application of Satellite-Based Navigation to Precision Approach and Landing*, Revision A, NAS System Engineering Service, Washington, D.C.: Federal Aviation Administration, February, 1992.

22. Department of Transportation. *FAA Satellite Navigation Program Master Plan, FY 93-98*. Washington, D.C.: Federal Aviation Administration, February 15, 1993.

23. Department of Transportation. *FAR-AIM (Federal Aviation Regulations and Airman's Information Manual) Part 1*, Aviation Supplies & Academics, Inc., Renton, WA., 1993.

24. Department of Transportation. *Federal Aviation Administration (FAA) Satellite Navigation Program Master Plan, ARD-70, FY 93-98*, Projected Civil Aviation GPS Operational Implementation Schedule, Washington, D.C.: Federal Aviation Administration, 15 Feb 93.

25. Department of Transportation. *Global Positioning System Information Center (GPSIC) Users Manual.* Bulletin Board Phone Number: (703) 313-5910. United States Coast Guard, Alexandria, VA, September 1992.

26. Farrel, James L. *Integrated Aircraft Navigation.* New York: Academic Press, 1976.

27. Gray, Robert A. *An Integrated GPS/INS/BARO and Radar Altimeter System for Aircraft Precision Approach Landings.* MS Thesis, AFIT/GE/ENG/94D-13. School of Engineering, Air Force Institute of Technology, Wright-Patterson AFB OH, December 1994 (AD-A289280).

28. Gu, Xiaogang. "DGPS Positioning Using Carrier-Phase for Precision Navigation", *Proceedings of the Institute of Navigation 1994 National Technical Meeting*, San Diego, CA: 410-417 (24-26 Jan 94).

29. Hansen, Neil P. *Incorporation of Carrier-Phase Global Positioning System Measurements into the Navigation Reference System for Improved Performance.* MS Thesis, AFIT/GE/ENG/93D-40. School of Engineering, Air Force Institute of Technology, Wright-Patterson AFB OH, December 1993 (AD-A274136).

30. Hilberg, Jochen M. and Thomas Jacob. "High Accuracy Navigation and Landing System Using GPS/IMU System Integration," *IEEE 1994 Position Location and Navigation Symposium*, Las Vegas, Nevada: 298-305 (11-15 Apr 94).

31. Honeywell Military Avionics Division. *Honeywell AN/APN-194 Pulse Radar Altimeter System.* Honeywell Technical Description, Minneapolis: June 1989.

32. Honeywell Military Avionics Division. *Ring Laser Gyro.* Honeywell LaserReady News, Vol 90, Number 2. 1990.

33. Huangqi, Sun, and others. "An Investigation of Airborne GPS/INS for High Accuracy Position and Velocity Determination," *Proceedings of the Institute of Navigation 1994 National Technical Meeting*, San Diego, CA: 801-809 (24-26 Jan 94).

34. Ignagni, Mario. Avionics Engineer, Honeywell Commercial Avionics, Minneapolis, MN. Personal Correspondence. May 1994.

35. Inertial Navigation System, STM 16-829 Vol I & II, *F-16 Block 40 Configuration, Training Manual*, General Dynamics, FortWorth, TX: 10 Jun 90.

36. Institute of Electrical and Electronics Engineers. *IEEE Standard Dictionary of Electrical and Electronics Terms*. IEEE Std 100-1972. New York.

37. Jacob, Thomas. "Landing System Using GPS/IMU System Integration," *Proceedings of the Institute of Navigation 1994 National Technical Meeting*, San Diego, CA: 298-305 (24-26 Jan 94).

38. Kalafus, Rudolph M., and Janis Viscans. "Differential Operation of NAVSTAR GPS," *The Institute of Navigation, Volume II*: 197-214 (1983).

39. Kalman, R.E. "A New Approach to Linear Filtering and Prediction Problems," *Transactions ASME, Series D: Journal of Basic Engineering*, 1960.

40. Kelly, Robert, and Jerry Davis. *RNP Tunnel Concept for Precision Approach and Landing*, RTCA, Inc., SC159 Working Group 4, MT/140, January 1993.

41. Knudsen, L. *Performance Accuracy (Truth Model/Error Budget) Analysis for the LN-93 Inertial Navigation Unit*. Technical Report, Litton Guidance and Control Systems, Woodland Hills, CA: January 1985. DID No. DI-S-21433 B/T:CDRL No. 1002.

42. Kyger, Captain David. Master's Degree Candidate, Air Force Institute of Technology, Wright-Patterson Air Force Base, OH. Personal Interview. 10 June, 1995.

43. Lawrence, David G. Avionics Research Engineer, Department of Aeronautics and Astronautics, Stanford University. Telephone Interview. June 1995.

44. Martin, E.H. "GPS User Equipment Error Models," *The Institute of Navigation, Volume I*:109-118 (1980).

45. Maybeck, Peter S. *Stochastic Models, Estimation, and Control*. Volume 1. New York: Academic Press, Inc., 1979.

46. Maybeck, Peter S. *Stochastic Models, Estimation, and Control*. Volume 2. New York: Academic Press, Inc., 1982.

47. Maybeck, Peter S. *Stochastic Models, Estimation, and Control*. Volume 3. New York: Academic Press, Inc., 1982.

48. Meyer-Hilberg, Jochen, and Thomas Jacob. "High Accuracy Navigation and Landing System Using GPS/IMU System Integration," *IEEE Trans. Position Location and Navigation Symposium, Las Vegas*: 0-7803-1435-2/94, 298-305 (April 11-15, 1994).

49. Milliken, R.J., and C.J. Zoller. "Principle of Operation of NAVSTAR and System Characteristics," *Global Positioning System*, The Institute of Navigation, Volume I. Alexandria, VA 22314, 1980.

50. Mosle, William B. *Detection, Isolation, and Recovery of Failures in an Integrated Navigation System*. MS Thesis, AFIT/GE/ENG/93D-28. School of Engineering, Air Force Institute of Technology, Wright-Patterson AFB OH, December 1993 (AD-A274056).

51. Musick, Stanton H. Electronics Engineer, WL/AAAS-3, Air Force Avionics Laboratory, WPAFB, OH. Personal Conversations. August 1994.

52. Musick, Stanton H. *PROFGEN - A Computer Program for Generating Flight Profiles*. Technical Report, Air Force Avionics Laboratory, WPAFB, OH, November 1976. AFAL-TR-76-247, DTIC ADA034993.

53. Musick, Stanton H., and Neil Carlson. *User's Manual for a Multimode Simulation for Optimal Filter Evaluation (MSOFE)*. AFWAL-TR-88-1138, Wright-Patterson AFB OH: A.F. Avionics Laboratory, AFWAL/AARN-2, April 1990.

54. National Oceanic and Atmospheric Administration. *National Geodetic Survey GPS Orbital Formats*. National Geodetic Information Branch, Rockville, MD. August 1991.

55. Negast, William Joseph. *Incorporation of Differential Global Positioning System Measurements Using an Extended Kalman Filter for Improved Reference System Performance*. MS Thesis, AFIT/GE/ENG/91D-41. School of Engineering, Air Force Institute of Technology, Wright-Patterson AFB OH, December 1991 (AD-A243742).

56. Nielsen, Robert L. *Development of a Performance Evaluation Tool (MMSOFE) for Detection of Failures with Multiple Model Adaptive Estimation (MMAE)*. MS Thesis, AFIT/GE/ENG/93S-37. School of Engineering, Air Force Institute of Technology, Wright-Patterson AFB OH, September 1993 (AD-A274218).

57. Paielli, Russell, and others. "Carrier-Phase Differential GPS for Approach and Landing: Algorithms and Preliminary Results", *Proceeding of the ION GPS-93 Sixth International Technical Meeting of the Satellite Division*, Salt Lake City, UT: 831-840 (22-24 Sep 93).

58. Riggins, Lt Col Robert N., and Capt Ron Delap. Assistant Professors of Electrical Engineering, Air Force Institute of Technology, Wright-Patterson AFB, OH. Course Notes EENG 534/635. 1993-94.

59. Rowson, Stephen V., and others. "Performance of Category IIIB Automatic Landings Using C/A Code Tracking Differential GPS," *Proceedings of the Institute of Navigation 1994 National Technical Meeting*, San Diego, CA: 759-767 (24-26 Jan 94).

60. Savage, Paul G. "Strapdown Sensors," *AGARD Lecture Series No. 95* (June 1978).

61. Schwarz, K. P., and M. Wei. "Aided Versus Embedded: A Comparison of Two Approaches to GPS/INS Integration," *IEEE 1994 Position Location and Navigation Symposium*, Las Vegas, Nevada: 314-322 (11-15 Apr 94).

62. Scull, David. Director of Operations, The Institute of Navigation, 1800 Diagonal Road, Suite 480, Alexandria, VA 22314, Correspondence. 1 Aug 93.

63. Snodgrass, Faron Britt. *Continued Development and Analysis of a New Extended Kalman Filter for the Completely Integrated Reference Instrumentation System (CIRIS)*. MS Thesis, AFIT/GE/ENG/90M-5. School of Engineering, Air Force Institute of Technology (AU), Wright-Patterson AFB OH, March 1990 (AD-A220106).

64. Solomon, Capt Joseph. Research Scientist, Wright Laboratories, Wright-Patterson AFB, OH. Personal Interviews. April 1994 - November 1994.

65. Stacey, Richard D. *A Navigation Reference System (NRS) Using Global Positioning System (GPS) and Transponder Aiding*. MS Thesis, AFIT/GE/ENG/91M-04. School of Engineering, Air Force Institute of Technology, Wright-Patterson AFB OH, March 1991 (AD-A238890).

66. Sutcliffe, Don. Aeronautical Engineer, Boeing Military Aircraft Company. Wichita, KS. Telephone Conversation. August, 1994.

67. The MathWorks, Inc., 21 Elliot Street, Natick, MA 01760. *Matlab*. December 1992. Version 4.0a.

68. Thompson, Paul. Product Marketing, Litton Commercial Avionics. Washington DC. Telephone Conversation. March, 1994.

69. Unternaeher, Bill. Product Marketing, Honeywell Commercial Avionics. Pheonix, AZ. Telephone Conversation. April, 1994.

70. Urbanic, Robert J., and S.H. Musick. "Users' Manual for a Multimode Plotting Program (MPLOT)", Avionics Laboratory, WPAFB, OH, WRDC-TR-90-1077, to be published.

71. van Graas, Frank. Associate Professor of Electrical Engineering, Ohio University. Telephone Conversations. September 1994.

72. Vasquez, Juan R. *Detection of Spoofing, Jamming, or Failure of a Global Positioning System (GPS)*. MS Thesis, AFIT/GE/ENG/92D-37. School of Engineering, Air Force Institute of Technology, Wright-Patterson AFB OH, December 1992 (AD-A259023).

73. Wullschleger, Victor, and others. "FAA/Wilcox Flight Test Results of DGPS System for Precision Approach," *Proceedings of the Institute of Navigation 49th Annual Meeting*, Cambridge, MA: 111-118 (21-23 Jun 93).

74. Wullschleger, Victor. GPS Flight Test Manager, FAA Technical Center, Atlantic City, NJ. Personal Interview. January, 1993.

Vita

Ryan Layne Britton [redacted]. He entered the University of Memphis in Memphis, Tennessee in 1987 on an Air Force ROTC scholarship and graduated Cum Laude in May, 1991 with a Bachelor of Science in Electrical Engineering. Commissioned a Second Lieutenant through ROTC upon graduation, he was assigned to Hanscom AFB, Massachusetts in September, 1991 where he worked as a system engineer and program manager until May of 1994. From June, 1994 till December, 1995 he attended the Air Force Institute of Technology (AFIT), receiving a Master of Science Degree in Electrical Engineering with emphasis in stochastic estimation, navigation and control. Following AFIT, he was assigned to Wright Laboratories at Eglin AFB, Florida.

[redacted]

REPORT DOCUMENTATION PAGE

Form Approved
OMB No. 0704-0188

1. AGENCY USE ONLY (Leave blank)	2. REPORT DATE	3. REPORT TYPE AND DATES COVERED
	December 1995	Master's Thesis

4. TITLE AND SUBTITLE
A DIFFERENTIAL GPS AIDED INS FOR AIRCRAFT LANDINGS

5. FUNDING NUMBERS

6. AUTHOR(S)
Ryan L. Britton
Captain, USAF

7. PERFORMING ORGANIZATION NAME(S) AND ADDRESS(ES)
Air Force Institute of Technology
WPAFB OH 45433-6583

8. PERFORMING ORGANIZATION REPORT NUMBER
AFIT/GE/ENG/95D-03

9. SPONSORING / MONITORING AGENCY NAME(S) AND ADDRESS(ES)
WL/AAAI
Avionics Directorate
Wright-Patterson AFB, OH 45433

10. SPONSORING / MONITORING AGENCY REPORT NUMBER

11. SUPPLEMENTARY NOTES

12a. DISTRIBUTION / AVAILABILITY STATEMENT
Approved for public release, Distribution Unlimited

12b. DISTRIBUTION CODE

13. ABSTRACT *(Maximum 200 words)*

The Department of Defense (DOD) and the commercial airline industry are in the process of replacing the instrument landing system (ILS) for aircraft precision approach landings. The use of differential Global Positioning System (DGPS) is thought to be a viable replacement for ILS precision approaches. This thesis explores the integration of an INS, DGPS, Barometric Altimeter, Pseudolite, and Radar Altimeter for a tanker type and a single engine aircraft precision approach. These devices are integrated using an extended Kalman filter (EKF). For the tanker type aircraft, Federal Aviation Administration (FAA) requirements for a Category I and a Category II precision approach were met when an INS, DGPS, Barometric Altimeter, and Radar Altimeter were integrated. Category III precision approach requirements were met for the single engine type aircraft when the same sensors were integrated.

14. SUBJECT TERMS	15. NUMBER OF PAGES
Global Positioning System, Inertial Navigation System GPS/INS Integration, Kalman Filter, Precision Landings, Differential GPS	376
	16. PRICE CODE

17. SECURITY CLASSIFICATION OF REPORT	18. SECURITY CLASSIFICATION OF THIS PAGE	19. SECURITY CLASSIFICATION OF ABSTRACT	20. LIMITATION OF ABSTRACT
UNCLASSIFIED	UNCLASSIFIED	UNCLASSIFIED	UNLIMITED

GENERAL INSTRUCTIONS FOR COMPLETING SF 298

The Report Documentation Page (RDP) is used in announcing and cataloging reports. It is important that this information be consistent with the rest of the report, particularly the cover and title page. Instructions for filling in each block of the form follow. It is important to ***stay within the lines*** to meet ***optical scanning requirements***.

Block 1. Agency Use Only *(Leave blank)*.

Block 2. Report Date. Full publication date including day, month, and year, if available (e.g. 1 Jan 88). Must cite at least the year.

Block 3. Type of Report and Dates Covered. State whether report is interim, final, etc. If applicable, enter inclusive report dates (e.g. 10 Jun 87 - 30 Jun 88).

Block 4. Title and Subtitle. A title is taken from the part of the report that provides the most meaningful and complete information. When a report is prepared in more than one volume, repeat the primary title, add volume number, and include subtitle for the specific volume. On classified documents enter the title classification in parentheses.

Block 5. Funding Numbers. To include contract and grant numbers; may include program element number(s), project number(s), task number(s), and work unit number(s). Use the following labels:

C	- Contract	**PR**	- Project
G	- Grant	**TA**	- Task
PE	- Program Element	**WU**	- Work Unit Accession No.

Block 6. Author(s). Name(s) of person(s) responsible for writing the report, performing the research, or credited with the content of the report. If editor or compiler, this should follow the name(s).

Block 7. Performing Organization Name(s) and Address(es). Self-explanatory.

Block 8. Performing Organization Report Number. Enter the unique alphanumeric report number(s) assigned by the organization performing the report.

Block 9. Sponsoring/Monitoring Agency Name(s) and Address(es). Self-explanatory.

Block 10. Sponsoring/Monitoring Agency Report Number. *(If known)*

Block 11. Supplementary Notes. Enter information not included elsewhere such as: Prepared in cooperation with...; Trans. of...; To be published in.... When a report is revised, include a statement whether the new report supersedes or supplements the older report.

Block 12a. Distribution/Availability Statement. Denotes public availability or limitations. Cite any availability to the public. Enter additional limitations or special markings in all capitals (e.g. NOFORN, REL, ITAR).

- **DOD** - See DoDD 5230.24, "Distribution Statements on Technical Documents."
- **DOE** - See authorities.
- **NASA** - See Handbook NHB 2200.2.
- **NTIS** - Leave blank.

Block 12b. Distribution Code.

- **DOD** - Leave blank.
- **DOE** - Enter DOE distribution categories from the Standard Distribution for Unclassified Scientific and Technical Reports.
- **NASA** - Leave blank.
- **NTIS** - Leave blank.

Block 13. Abstract. Include a brief *(Maximum 200 words)* factual summary of the most significant information contained in the report.

Block 14. Subject Terms. Keywords or phrases identifying major subjects in the report.

Block 15. Number of Pages. Enter the total number of pages.

Block 16. Price Code. Enter appropriate price code *(NTIS only)*.

Blocks 17. - 19. Security Classifications. Self-explanatory. Enter U.S. Security Classification in accordance with U.S. Security Regulations (i.e., UNCLASSIFIED). If form contains classified information, stamp classification on the top and bottom of the page.

Block 20. Limitation of Abstract. This block must be completed to assign a limitation to the abstract. Enter either UL (unlimited) or SAR (same as report). An entry in this block is necessary if the abstract is to be limited. If blank, the abstract is assumed to be unlimited.